NRL-BuLL-35(Pt.6)   E-2

Bulletin 35
Part 6
(of 7 Parts)

THE
SHOCK AND VIBRATION
BULLETIN

APRIL 1966

A Publication of
THE SHOCK AND VIBRATION
INFORMATION CENTER
U.S. Naval Research Laboratory, Washington, D.C.

Air Gun
pg 119

20011011 085

Office of
The Director of Defense
Research and Engineering

OCT 19 1966

THE
SHOCK AND VIBRATION
BULLETIN

APRIL 1966

The 35th Symposium on Shock, Vibration and Associated Environments was held in New Orleans, Louisiana on 25-28 October 1965. NASA Marshall Space Flight Center was host.

CONTENTS

PART 6

Shock Testing

Specification of Shock

PAPERS APPEARING IN PART 1
Part 1 - Confidential
(Titles Unclassified)

BLAST LOADING OF MODEL ANTENNA STRUCTURES
    R. Kirk Gregory, Southwest Research Institute, San Antonio, Texas

ANALYSIS OF RESPONSE OF EQUIPMENT ON A DROP TEST SHOCK MACHINE
    Robert L. Bort, David Taylor Model Basin, Washington, D. C.

BACKGROUND AND CURRENT STATUS OF UNDERWATER EXPLOSION SHOCK
    SPECIFICATIONS AND TESTING
    Gerald M. Mayer, U.S. Navy Underwater Sound Laboratory, New London, Connecticut

A SIMULATED 25-30 CPS DECK FOR SHOCK TESTING
    Culver J. Floyd, Raytheon Submarine Signal Division, Portsmouth, Rhode Island

MAGNETIC TAPE RECORDING IN A SEVERE MISSILE ENVIRONMENT - A CASE HISTORY
    J. P. White and J. Montsma, Bell Telephone Laboratories, Whippany, New Jersey

LONGITUDINAL VIBRATIONS PRODUCED BY INTERACTION OF THE STRUCTURE, PROPEL-
    LANT FLOW, A COMBUSTION PROCESS IN THE LANCE PROPULSION SYSTEM
    Ernest King Bramblett, II, Rocketdyne, Canoga Park, California

SIMULATION OF IMPULSIVE ENVIRONMENTS BY USE OF PYROTECHNIC DEVICES
    F. A. Ottati, Avco Corporation, Research and Advanced Development Division, Wilmington,
    Massachusetts

PAPERS APPEARING IN PART 2

Vibration Testing

THEORY OF DYNAMIC TESTS OF STRUCTURES
N. Norby Nielsen, Department of Civil Engineering, University of Illinois, Urbana

FATIGUE LIFE UNDER VARIOUS RANDOM LOADING SPECTRA
Sherman A. Clevenson and Roy Steiner, NASA Langley Research Center, Langley Station, Hampton, Virginia

COMBINED BROADBAND AND STEPPED NARROWBAND RANDOM VIBRATION
A. J. Curtis, J. G. Herrera, and R. F. Witters, Hughes Aircraft Company

ON THE USE OF MULTIPLE (MULTI-POINT) RANDOM EXCITATION WITH APPLICATION TO SURVEYOR SPACECRAFT TESTS
A. J. Curtis, H. T. Abstein, and R. J. Varga, Hughes Aircraft Company, Culver City, California

GROUND TEST SIMULATION OF LIFT-OFF AND TRANSONIC VIBRATION EXCITATION MECHANISMS ON THE RANGER SPACECRAFT
Marc C. Trummel, Jet Propulsion Laboratory, California Institute of Technology Pasadena, California

METHODS OF CONTROL OF MULTIPLE SHAKER TESTING SYSTEM
Jack D. Newton, MB Electronics, New Haven, Connecticut

ON SYNERGETIC EFFECTS OF COMBINATIONS OF VIBRATION AND OTHER ENVIRONMENTS
W. P. Rader, J. D. Donahue, H. N. McGregor, and E. R. Wilson, Martin Company, Denver Colorado

A MULTIPLE-FREQUENCY, SHAKE-TESTING TECHNIQUE FOR STRUCTURES WITH RAPIDLY-CHANGING DYNAMIC CHARACTERISTICS
F. J. Hawkins, C. W. Skingle, and G. A. Taylor, Royal Aircraft Establishment, Farnborough, England

A PROGRESS REPORT ON FORCE CONTROLLED VIBRATION TESTING
C. E. Nuckolls and J. V. Otts, Sandia Corporation, Albuquerque, New Mexico

VIBRATION NO SANDWICH PANELS IN A VACUUM
Clemans A. Powell, Jr., and David G. Stephens, NASA Langley Research Center, Langley Station, Hampton, Virginia

THE VIBRATION DESIGN APPROVAL AND ACCEPTANCE TEST PROGRAM FOR THE GEMINI SPACECRAFT - COMPONENT, MODULE AND WHOLE VEHICLE TESTING
James R. Daiber and Vincent S. Noonan, McDonnell Aircraft Corporation, St. Louis, Missouri

TECHNIQUES FOR EXTENDING THE CAPABILITY OF RANDOM EQUALIZATION EQUIPMENT
C. D. Robbins and D. G. Clack, LTV Electrosystems, Inc., Garland Division, Dallas, Texas

A BROADBAND HYDRAULIC VIBRATION EXCITER
H. T. Strandrud, The Boeing Company, Seattle, Washington

ADVANTAGES OF MULTIPOINT CONTROL FRO VIBRATION TESTING OF COMPLETE RANGER FLIGHT SPACECRAFT
Jack L. Cooper, Jet Propulsion Laboratory, Pasadena, California

VIBRATION INPUT CONTROL INVESTIGATION
Roger L. Carlson and Fred A. Chinquist, Honeywell, Inc., Minneapolis, Minnesota

A UNIQUE SUSPENSION SYSTEM FOR LONGITUDINAL VIBRATION TESTING OF LARGE LAUNCH VEHICLES
James A. Schoenster, Jerome Pearson, and Grayson V. Dixon, NASA Langley Research Center, Langley Station, Hampton, Virginia

COMBINED RANDOM VIBRATION AND EXTREME TEMPERATURE TESTING OF INTEGRATED CIRCUITS
James C. Burrus, Texas Instruments, Inc., Dallas, Texas

PAPERS APPEARING IN PART 4

Instrumentation

PAPERS APPEARING IN PART 5

Transportation

A GENERAL SOILS MODEL FOR SHOCK PROPAGATION STUDIES
C.X.C.F. Miranda, University of Detroit, Detroit, Michigan and David C. Kraft, University of Dayton, Dayton, Ohio

PAPERS APPEARING IN PART 7

Prediction of Vibration Environment

TITAN III-C AERODYNAMIC VIBRATION ANALYSIS
F. M. Condos, Martin Company, Denver, Colorado

PREDICTION OF RE-ENTRY VIBRATION
F. A. Smith and F. J. Benedetti, Aerospace Corporation, San Bernardino, California

PREDICTION OF THE BOUNDARY LAYER ACOUSTIC PRESSURE LEVELS OF A BLUNT NOSE RE-ENTRY VEHICLE AT HIGH MACH NUMBERS
H. Saunders and D. E. Nestler, General Electric Company, Philadelphia, Pennsylvania

HIBEX MISSILE VIBRATION ENVIRONMENT CONSIDERATIONS
J. C. Furlong and H. M. Voss, The Boeing Company, Seattle, Washington

MARINER MARS 1964 ACOUSTICALLY INDUCED VIBRATION ENVIRONMENT
R. A. Schiffer and J. R. Hyde, Jet Propulsion Laboratory, Pasadena, California

VIBRATION STUDIES CONDUCTED ON THE GEMINI INERTIAL PLATFORM
Dean Seefeld, Honeywell Inc., Aeronautical Division, St. Petersburg, Florida

GEMINI SPACECRAFT FLIGHT VIBRATION DATA AND COMPARISON WITH PREDICTIONS
James A. Callahan, McDonnell Aircraft Corporation, St. Louis, Missouri

DETERMINATION OF THE WATER IMPACT SHOCK ENVIRONMENT
F. H. Collopy, ITEK Corporation, Lexington, Massachusetts

ORBITAL VIBRATION EFFECTS ON SCIENTIFIC INSTRUMENTS
R. J. Savage, Douglas Aircraft Company, Santa Monica, California

MOBILITY OF A RANDOMLY EXCITED STRUCTURE BY CROSS-CORRELATION AND CROSS-SPECTRAL COMPUTATION TECHNIQUES
Will Gersch and David Sharpe, Purdue University, Lafayette, Indiana

COMPUTATION TECHNIQUE FOR MECHINICAL IMPEDANCE METHODS
James E. Smith, U.S. Navy Marine Engineering Laboratory, Annapolis, Maryland

ANALYTICAL AND EXPERIMENTAL EVALUATION OF DD692 CLASS HULL VIBRATION
J. J. Francis, Boston Naval Shipyard, Boston, Massachusetts and A. R. Paladino, Bureau of Ships, Washington, D.C.

A PRACTICAL APPROACH TO THE PREDICTION OF THE NATURAL FREQUENCY OF PRINTED CIRCUIT BOARDS
James T. Arnold and Fred P. Strother, Jr., Honeywell Inc., Aeronautical Division, St. Petersburg, Florida

MODAL CHARACTERISTICS OF ARBITRARILY-STIFFENED RINGS
John D. Sowers and Nolan P. Hymel, Chrysler Corporation Space Division, New Orleans, Louisiana

MEASUREMENT OF CAPTIVE-FLIGHT VIBRATION RESPONSE FOR AGM-45A (SHRIKE) AND FIREYE BOMB AIRBORNE WEAPONS
A. Weathersbee and W. Parmenter, U.S. Naval Ordnance Test Station, China Lake, California

Damping and Nonlinear Analysis

RESPONSE OF A NONLINEAR DAMPED OSCILLATOR TO RANDOM EXCITATION
A. W. Bell and A. E. Galef, National Engineering Science Company, Pasadena, California

MATHEMATICAL MODELS OF NONLINEAR MULTIDEGREE-OF-FREEDOM STRUCTURES
Walter B. Murfin, Sandia Corporation, Albuquerque, New Mexico

ERRATUM

In Shock and Vibration Bulletin No. 35, Part 5, February 1966, the paper on "Investigation of the Vibration Damping Properties of Viscoelastic Materials Using a Delay-Angle Technique," by Saul A. Eller and Levi Cohen, beginning on page 159, should include the following statement:

"The opinions or assertions contained in this paper are the private ones of the authors and are not to be construed as official or reflecting the views of the Naval Service at large."

SHOCK TESTING

SHOCK TESTING TO SIMULATE RANDOM VIBRATION PEAKS

J. A. Bailie
Lockheed Missiles & Space Company
Sunnyvale, California

Many items of equipment in a variety of vehicles are subjected to both shock and short (nonstationary) bursts of random excitation. It is common practice to analyze these latter events as though they were stationary and measure their severity in terms of spectral density of acceleration. The errors involved and difficulties of doing this are reviewed. Actually, short bursts of random vibration are similar to random shocks, particularly when the failure, if any, is due to the single highest peak (SHP) of the response, rather than to fatigue.

The importance of the SHP as a measure of damage is also discussed. When it is the correct damage criterion, we should attempt to control it and not spectral density. Since the SHP is a random variable, we cannot control it using random excitation, but we can with shock tests. For systems with a single degree of freedom, or those whose sensitivity to damage is known to be confined to a narrow frequency band, the solution is simple, once the statistical distribution of the SHP is known. Available experimental and theoretical data are reviewed. Using the prescribed percentile of the SHP distribution, the shock test as severe as the random excitation is derived. In certain cases, when both stationary random and shock tests are prescribed, the former can be eliminated by deriving a shock test whose highest response peaks at each frequency envelop those of both original tests.

The situation with multi-degree of freedom systems is shown to be significantly more difficult and not amenable to one method of solution. A technique is introduced for extending the results to these situations. Preliminary results obtained on a analog computer for the two degree of freedom system are presented to illustrate certain trends.

There is good reason to believe that the ideas outlined can be used to perform tests that reproduce the damaging potential of certain events more accurately, thereby saving money in acceptance testing by eliminating some of the tests presently being conducted.

INTRODUCTION

The measurement of power spectra of stationary random phenomena and their use in test specifications is part of the scientific literature; see, for example, Refs. (1) and (2). Similar progress in the field of nonstationary phenomena has been much slower due to the inherent difficulties of dealing with processes whose statistics are time dependent. Nevertheless, some advances have been made by Caughey (3), Bendat and Thrall (4), and many others.

However, these papers deal primarily with sources of excitation that are long, compared to the natural periods of the systems, and with systems whose characteristics change relatively slowly. There exists a third type of excitation, which can be heuristically described as "short bursts" of random vibration. Their duration is less than a few seconds and typical examples are the firing of small rocket motors, staging of launch vehicles while the upper stage rocket motor is firing into the interstage, and rapid passage through turbulent regions,

1

earthquakes, etc. This type of phenomenon cannot be adequately handled by the methods outlined in Ref. (1), because of its highly transient nature. We shall now discuss a few ideas that enable us to deal approximately with these events, and show how test specifications can be written to ease the problems of simulating in the laboratory the damaging potential of the events.

SINGLE HIGHEST PEAKS AND THEIR IMPORTANCE

In many structures and items of equipment, the parameter that decides whether or not failure occurs is the single highest stress (acceleration) peak that the structure sees during its service life. This is particularly true of brittle components and those sensitive to a single large load, rather than the cumulative effects of many loading cycles. In dealing with stationary processes, the single highest peak (SHP) seen in a finite time is obviously a random variable and for a simple oscillator its distribution has been solved approximately by Aspinwall (5), whose theory agrees reasonably well with the experimental data obtained on an analog computer by MacNeal and Barnoski (6).

For the short burst random process, with which we are primarily concerned here, there does not appear to be much hope at present of finding a theoretical solution to the distribution of the SHP. For this reason, a preliminary study was conducted to find this distribution using an analog computer. The results (6) will be discussed later. In simulating stationary random phenomena, or any other test for that matter, we exercise control over the important parameter, in this case spectral density. Therefore, in situations where the SHP is the important parameter, we should control it, but this is not possible when using short bursts of random vibration in the laboratory. Therefore, some test that enables us to control the SHP should replace the random test.

SHORT BURSTS OF RANDOM EXCITATION

Highly nonstationary inputs are the most likely situations where the response peaks are important. If one considers short duration random processes as limiting cases of stationary processes and uses spectral density as the measure of severity, troubles immediately arise from two different sources. First, the computation of spectral densities and even rms levels becomes progressively less meaningful as the duration decreases. Second, simulating the events in laboratory vibration tests presents serious difficulties and there is a high probability that the transients which result from switching the shaker on and off far exceed the levels applied during the actual test. Hence, any failures that occur are due to these transients and not the true environment. Another significant point is that for long durations of stationary processes, the SHP that has a prescribed probability of occurrence does not change much as a function of the test duration (Figs. 1 and 2). In other words, the curve of SHP vs T^* has a steep slope for small T^* and becomes less so as T^* increases; controlling the spectral density is the correct thing to do, since the SHP problem is automatically fairly well simulated.

One of the foundations of conventional stationary random process theory is the ergodic hypothesis that entitles us to replace ensemble averages by time averages, etc. For this type of event we should reject this hypothesis and treat the events as true nonstationary processes. One might well ask, "Why not conduct nonstationary random tests on flight hardware?" The reason, of course, is that one cannot control the SHP produced by such processes; it is a random variable. If we assume that, in the laboratory, the nonstationary excitation is produced by multiplying the stationary random process by an envelope function (Fig. 3), the variation in SHP from one test to another increases as the sampling interval (test duration) decreases. Regardless of the method of generation of the excitation, this conclusion must hold for truly random processes. When we are conducting qualification or acceptance tests, this large variation in the important response parameter is clearly undesirable, as it can result in a wide variation of the quality of the hardware that passes the test. We have enough trouble setting the peak we want without using a test whose peak cannot be controlled.

These are the main reasons why the shorter the bursts of random excitation, the less desirable it is to use them in laboratory qualification and acceptance type testing. Our discussion also indicates why these environments are similar to the conventional shock test in which we are concerned with the peak response to a deterministic input. In fact, if we blindly accept the SHP as the only damage criterion, it is an academic question whether a prescribed level is produced by a short random burst or a conventional shock test. However, many components' failure level depends, to some extent, on the frequency content of the excitation. (See Ref. (7) for further discussion of the cause of
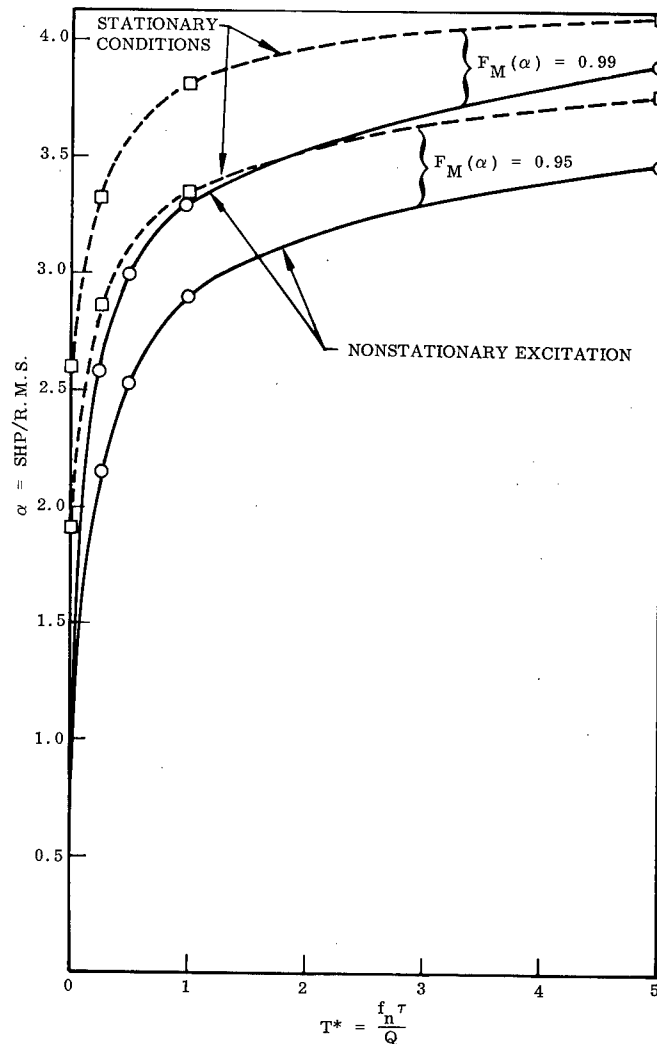
Fig. 1. Response of simple oscillator to
rectangular pulses of random noise (Q = 20)

failures due to shocks.) Hence, for short bursts of random vibration and components that are sensitive to SHP there are a number of reasons why we should proceed as follows in determining the test level:

1. Obtain the probability distribution of the SHP from test data, analog simulation, etc.

2. Decide on the probability of failure that is acceptable or whatever risk one wants to take about the component (2).

3. Find the SHP level that corresponds to the probability level selected in step 2 and conduct a shock test that produces this level.

So far we have implicitly assumed a single degree of freedom system or at least one in which only a single mode is really important. For multi-degree of freedom components the situation is clearly much more difficult as the SHP is a function of the responses in all the modes unless the excitation is narrow band. However, rather than attempt to subject the excitation data to spectral analyses, it is far better to obtain shock spectrum analyses in the conventional manner. Because of the inherent stochastic nature of the data, we expect the shock spectrum level at each frequency to be a random variable. When sufficient data are available to obtain estimates of the distribution at each frequency of interest, we can select a
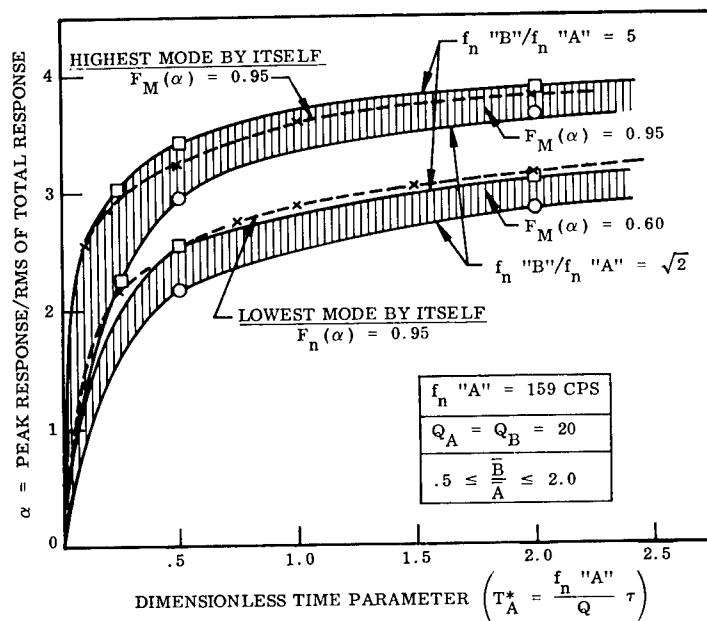
Fig. 2. Summary of results of
two degree of freedom system
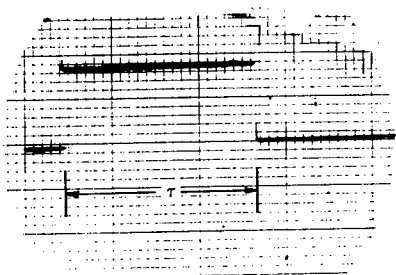
STEP ENVELOPE FUNCTION
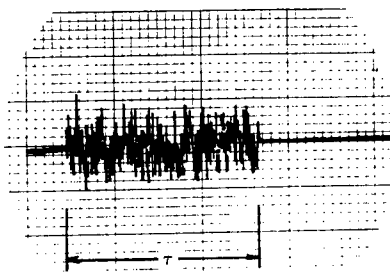
PULSED RANDOM DISTURBANCE

2° FREEDOM SYSTEM		
STEP ENVELOPE – TRANSIENT PROBLEM		
$Q_A = Q_B = 20$	f_n "A" $= 159.1$ CPS	$\dfrac{f_n \text{ "B"}}{f_n \text{ "A"}} = \sqrt{2}$
K = 1	$\tau = 0.0628$ SEC	$T^*_A = 0.50$

NOTE: 200 μ SEC FILTER USED

Fig. 3. Typical excitation

level which has a prescribed probability of being exceeded. A curve through these points can be used as the test level, but it is clearly conservative when failure is due to the response in more than one mode because in doing this we have assumed complete correlation between the levels at all frequencies. This test gives an excessive SHP and is certainly not the only way of selecting the test level.

The question that now arises is "How do we select a shock spectrum that yields the required SHP and the correct frequency distribution of excitation energy?" There does not appear to be a simple way to answer this because of the lack of complete correlation of the times of various modes reaching their independent peaks, and judgment is needed.

The three important characteristics that the test spectrum should exhibit are: (a) the desired SHP, (b) approximate simulation of the frequency content of the excitation, and (c) capability of the shaker to produce the shock spectrum. It is not practical or worthwhile to attempt a closed-form solution because of the wide constraints imposed by conditions (b) and (c); no one solution is optimum for all situations.

There is no doubt that in many practical examples the shock spectrum levels at different frequencies will be only slightly correlated. In these situations, the simulation of the environment presents serious difficulties. If we proceed as just suggested for the case when the spectrum levels are well correlated and shape our test spectrum as proposed, the following difficulties can occur. The high peaks of some of the spectra can be above the test spectrum, and in these regions of the frequency domain the test is not severe enough. If the failure is due to the SHP and is the sum of the responses in many modes, this is not too serious. However, if the failure is due to the response in one mode, the test can be significantly unconservative.

This type of problem is not new in vibration testing, being virtually analogous to the old argument in stationary random testing as to whether the test spectrum should simulate the rms level or envelop the peaks that have a given probability of being exceeded. It appears that we are usually somewhat conservative and tend towards the use of the latter criterion. Also, we do not pay any attention to the correlation of the peaks of the response modes. Clearly there is no hard and fast set of rules that can be applied in every situation and the penalties in

cost, schedule, reliability, etc., should be considered (2).

EXPERIMENTAL DATA ON SHP RESPONSE OF SIMPLE SYSTEMS

The program to obtain preliminary data on this problem was carried out by MacNeal and Barnoski on an analog computer (6). Broadband stationary random noise and the output of an envelope generator were passed through a multiplier to obtain the nonstationary excitation. Figure 3 shows a typical example of the excitation. This input was used to excite the electric analog of both single and two degree of freedom systems which were at rest when the excitation started. The SHP was measured and the test was repeated 100 times for each set of parameters to obtain data on the distribution of the SHP. Barnoski (8) has since repeated the work, obtaining more data points to define the distribution better, but his data are not yet generally available. The data for the single degree of freedom case have been presented in Ref. (9). We shall now discuss typical results from Ref. (6); this work is only the initial step and much remains to be done.

The first point to note is that the SHP is presented as a factor of the rms level, which is desirable only when one is using a stationary process, to obtain the nonstationary excitation in the manner outlined above. In physical nonstationary processes of this short burst variety, the rms level fluctuates from one test to another and, hence, variations in α, the ratio of SHP to rms levels, reflect changes in both SHP and rms. For very short duration inputs, rms is not too meaningful. So one should then work with values of the peaks themselves.

A sample of the results for the single degree of freedom is given in Fig. 1, which illustrates how to obtain a shock test that gives the required SHP. As an example, if we have a system with $Q = 20$, excited by a rectangular pulse of random noise, and $T^* = 1.0$, the level with a 0.01 probability of being exceeded is approximately 3.30. Any shock spectrum which has this level at the system natural frequency is acceptable. However, the practically attainable one most closely following the shock spectrum of the random process is obviously the most desirable.

The data for two degrees of freedom are only the beginning of what is needed to define the problem completely but are described in the following. The SHP to rms ratio, α, was

obtained for each of the two modes individually, and for the complete response of the following system subjected to the rectangular burst of excitation: $f_n(A) = 159$ cps, $f_n(B) = 225$ or 795 cps gives $f_n(B)/f_n(A) = \sqrt{2}$ and 5, respectively; $Q = 20$ for both systems and $T^* = f_n(A)\,\tau/Q = 0.25$, 0.50, and 2.00 denoting excitation durations of 0.0314, 0.0628, and 0.2514 sec. The ratio of rms response levels, σ_B/σ_A in the two modes was 0.5, 1.0, and 2.0.

Figures 4 and 5 show a small sample of the data obtained. The former gives the raw data for $F_M(\alpha)$ vs the ratio of total peak response to the rms of the total response. The latter needs a little explanation. The cross-hatched areas cover a scatter in the results that is due to two entirely different sources. First, the ratio of the rms levels of the two

modes affects the value of α slightly. Second, the increase in the spread for relatively large $F_M(\alpha)$ is due to the small number of trials (100) and can be removed by taking more data. The following comments are derived from these figures:

1. The SHP behavior appears to be slaved to the higher mode, particularly when the natural frequencies are well separated. This is due to the larger number of cycles per unit time in the higher mode and is illustrated in Figs. 2 and 5.

2. The ratio σ_B/σ_A has a small influence on α.

3. Figure 2 presents an interesting summary of the parameters α vs T_A^* with the results

STEP ENVELOPE

f_n "A" = 159 CPS	f_n "B" = 795.5 CPS
$Q_A = Q_B = 20$	$T_A = 0.0628$ CPS

$\alpha_{"C"}$ = TOTAL PEAK RESPONSE/RMS OF TOTAL RESPONSE
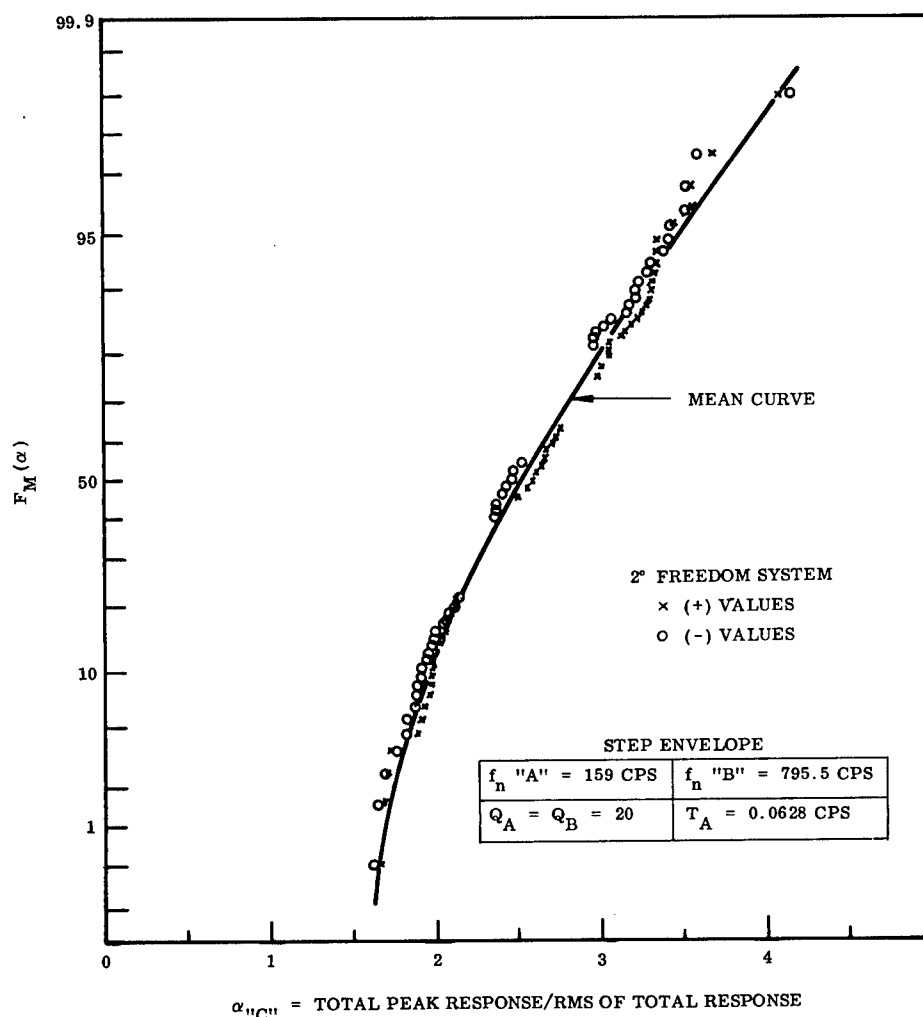
Fig. 4. Typical experimental data

6
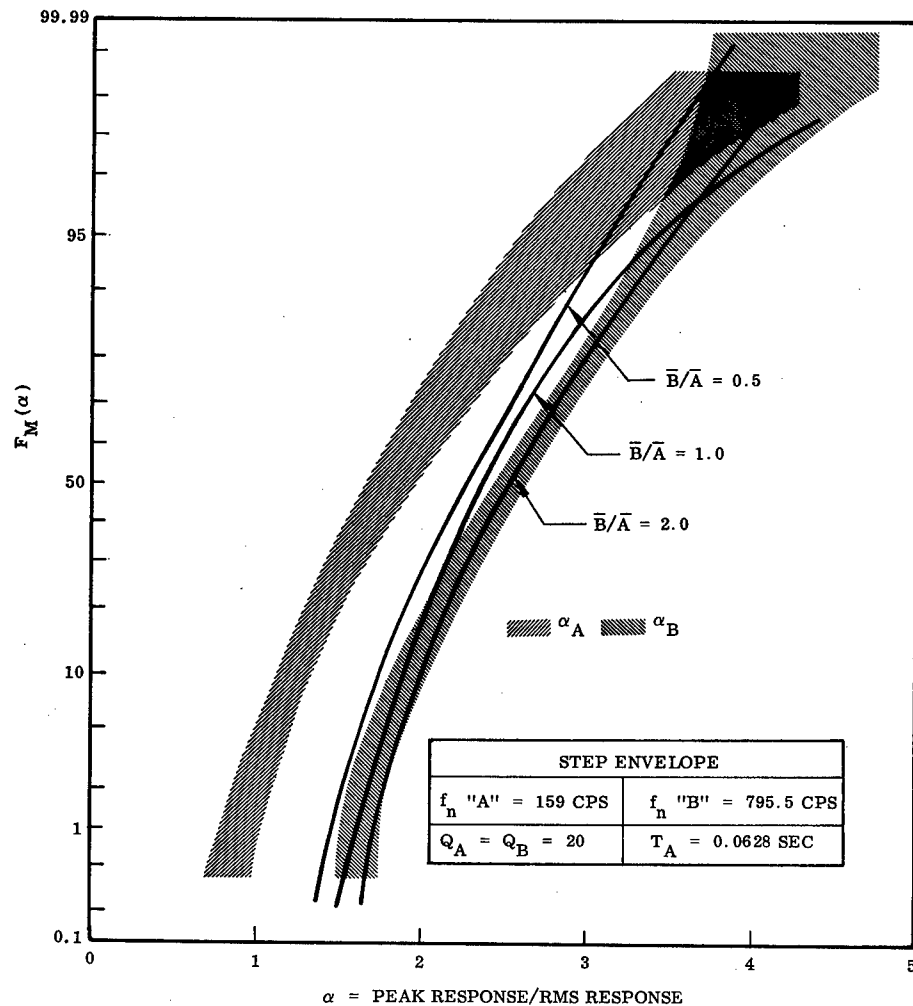
Fig. 5. Typical results for two degree of freedom system

for a single degree of freedom superimposed for the case $F_M(\alpha) = 0.95$.

SHOCKS AND STATIONARY RANDOM TESTING

The SHP could be used as a criterion of test severity when both shock and random acceptance tests are called for. Conducting satisfactory random tests is time consuming and expensive and the question arises: "Which is the most severe?" If the SHP causes failure of an item that is fragile only in a narrow frequency range, it is possible to eliminate the random test on the following basis.

A shock spectrum immediately gives the response (SHP) at each frequency of interest. Using Aspinwall's work and the description of the random test, one simply computes

$T^* = f_n T/Q$, where T is now the duration of the test, and decides the risk one wishes to take (Fig. 6). Once this is done, one uses Fig. 7 to obtain the SHP at each frequency over the range of interest. This information, plotted on the shock spectrum curve, gives effectively a second shock spectrum and the single test shock should be that which envelops all the data. This can be illustrated by an example: a piece of equipment is to be subjected to a half sine shock of 200 g peak and 1.0 ms duration and a random test of 5 sec duration, whose spectral density between 20 and 2000 cps appears as straight lines connecting the following points:

Frequency	PSD (g^2/cps)
20	0.1
400	0.3
1000	0.2
2000	0.1

7
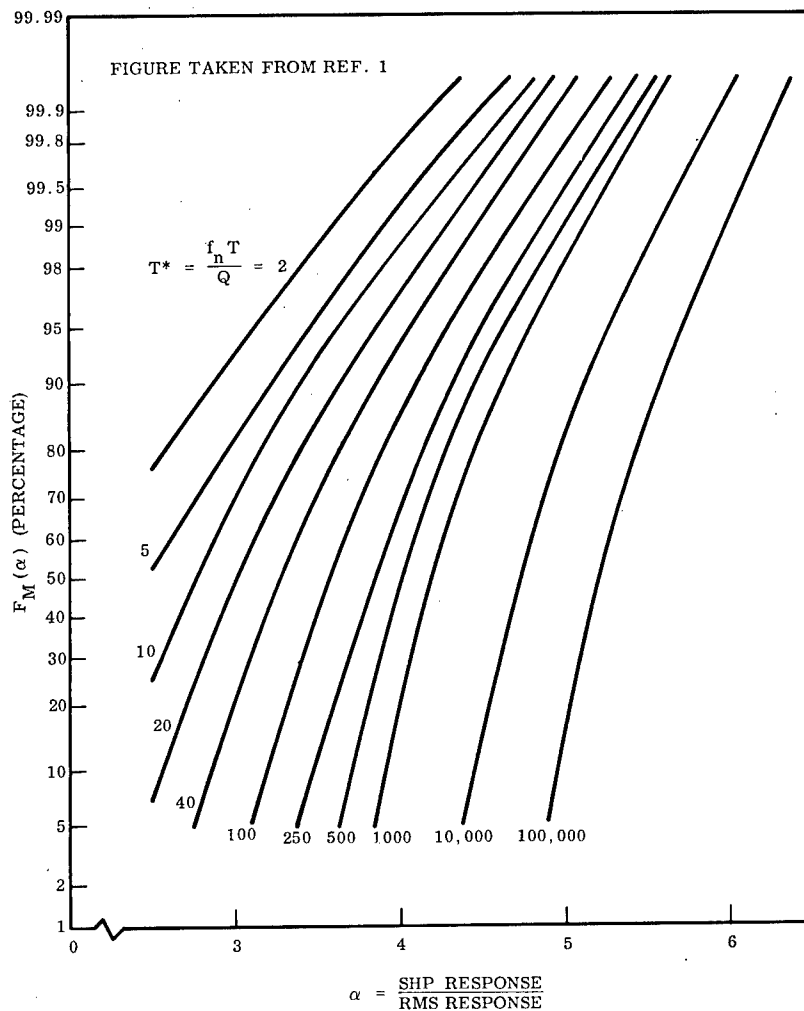
Fig. 6. Probability distribution for single highest
response peak (stationary conditions)

The shock spectrum and the 99th percentile of the SHP response to the above random test are illustrated in Fig. 7. The random test certainly produces the larger peaks at the higher frequencies. If we are restricted to half-sine pulses and want a test that envelops both tests (we might pick the 210 g, 0.8-ms pulse), we produce a slight overtest over a large frequency band. Using devices such as the shock spectrum synthesizer (10), this situation can be greatly improved.

CONCLUSIONS

1. In certain situations, particularly short burst of random excitation, the single highest peak of the response is the parameter which decides the severity (damage) and should be simulated in tests.

2. If nonstationary inputs are used in the laboratory, the SHP varies from test to test. This is undesirable for qualification and acceptance testing.

3. Therefore, it is suggested that shock tests can be used in place of random tests to enable one to control the SHP and insure its repetition from one test to another.

4. Both the experimental determination of the SHP and the shock test to simulate the required level are relatively simple. For multidegree of freedom systems, both problems are far more complex and considerable work remains to be done before they are satisfactorily solved. One of the most important causes of difficulty is the lack of correlation of the peaks in the response modes. However, it must be pointed out that this defect is also inherent in random testing.
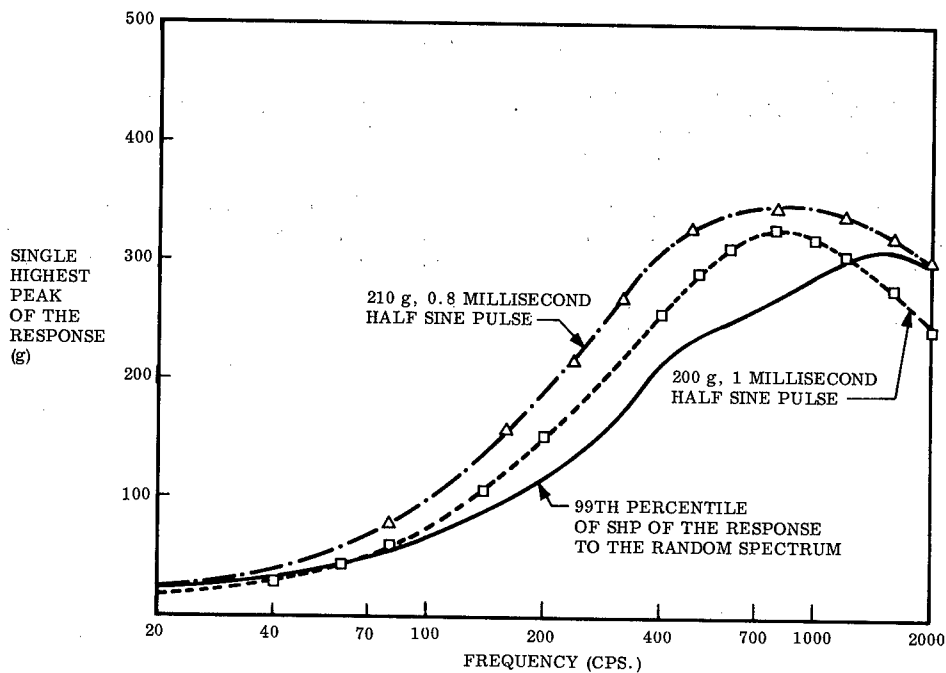
Fig. 7. Single highest peak response (to prescribed random vibration spectrum and half sine shock pulse)

REFERENCES

1. S. H. Crandall, Random Vibration (M.I.T. Press, Cambridge), 1963, Vols. 1 and 2

2. R. E. Blake, "A Method for Selecting Optimum Shock and Vibration Tests," Shock and Vibration Bull. No. 31, Pt. II, p. 88, March 1963

3. T. K. Caughey, Nonstationary Random Inputs and Responses in Random Vibration, Vol. 2 (S. H. Crandall, Ed.) (M.I.T. Press, Cambridge), 1963

4. J. S. Bendat and G. P. Thrall, "Spectra of Nonstationary Random Processes," AFFDL TR-64-198, Nov. 1964

5. D. M. Aspinwall, "An Approximate Distribution for Maximum Response During Random Vibration," AIAA Simulation for Aerospace Flight Conf., Columbus, Ohio, 26-28 Aug. 1963

6. R. H. MacNeal and R. L. Barnoski, "Peak Response of Simple Mechanical Systems to Random Excitation," Computer Engineering Assoc. Rept. ES 182-6, Mar. 1962

7. R. E. Blake, "Near-Optimum Shock Mount for Protecting Equipment from Shock Impulses," Shock and Vibration Bull. No. 35, Part V, 1966

8. R. L. Barnoski, "Response of Mechanical Systems to Nonstationary Random Excitation," submitted to Goddard Space Flight Center under Contract No. NAS 5-4590

9. R. H. MacNeal, R. L. Barnoski, and J. A. Bailie, "On the Response of a Simple Oscillator to Nonstationary Random Noise," submitted to the AIAA Journal

10. G. W. Painter and H. J. Parry, "Simulating Flight Environment Shock on an Electrodynamic Shaker," Shock and Vibration Bull. No. 33, Part III, pp. 85-96, March 1964

DISCUSSION

Mr. Fowler (TRW Systems): Do not the tests that you ultimately select depend on the damping of the system you are testing?

Mr. Bailie: Yes, certainly. I should have said that Q equals 10 was assumed for that particular example.

Mr. Fowler: Normally you do not have that information before you select the test level.

Mr. Bailie: That is perfectly true, but in defining a shock spectrum you are faced with exactly the same problem. So it is certainly no worse than the conventional shock test.

*   *   *

10,000 G SLINGSHOT SHOCK TESTS ON A
MODIFIED SAND-DROP MACHINE

Sam Marshall and LaVerne Root
Collins Radio Company
Cedar Rapids, Iowa
and
Leonard Sackett
University of Michigan
Dearborn, Michigan

A MIL-S-4456 sand-drop shock testing machine was simply and inexpensively modified to obtain impact velocities exceeding 100 fps for small test items. The large drop platform was replaced by one of several smaller test fixtures required for the particular equipment to be shock tested. The fixture and test item are accelerated by 3/4-in. diameter shock cords resembling a slingshot. The fixture is guided in its travel by 3/8-in. diameter steel rods. The guide rods and pulley system were designed so that the spacing between the guide rods may be varied for different size fixture requirements. The velocity attained is dependent on the slingshot drop height and specimen plus fixture weight. From a 10-ft drop height, with the shock cords elongated 100 percent, the machine will accelerate a 7-lb load to a terminal velocity of 150 fps. Pulse shape and duration are determined by the impact material type and configuration. A brief study of some component and equipment shock fragility levels has been performed, and a summary of the data is presented.

INTRODUCTION

To keep pace with the new applications for components and equipment, shock test levels have steadily increased until many present-day requirements are beyond the capability of the more common gravity fall shock testing machines.

A need has been experienced for a shock machine with the capability of providing high g levels of impact. As an example, additional shock fragility data were required for a new component application. The data could not be obtained using the present shock machine which had a maximum impact velocity of 15 fps. To acquire the necessary information, a slingshot type testing device was improvised. The device used an existing overhead hoist, an aluminum table, wire guide rods, and four lengths of 1/2-in. diameter shock cord. A maximum velocity of 80 fps was attained.

Another example was an aircraft cockpit voice recorder which required shock testing to a half sine pulse of 1000 g amplitude and 5-ms duration. The improvised slingshot machine was not capable of accelerating the 43-lb load to the required velocity of 50 fps. To perform this test and similar tests for future requirements, an existing MIL-S-4456 shock machine (sand-drop) was modified to attain higher impact velocities.

Several limitations and design goals were considered:

1. Modification cost, excluding Environmental Department labor, of not more than $1000;

2. Purchased parts to cost $100 per item;

3. Total height of 14 ft;

4. A 150-fps velocity capability for lightweight drop fixtures;

5. A velocity measuring device;

6. A versatile guide and sling system to allow a change in fixture size without a major machine teardown;

7. Use of original sand-drop machine parts wherever possible; and

8. A machine base capable of withstanding the energy levels generated.

DESIGN AND MODIFICATION

Shock cord was chosen as the accelerating material (1). Various sizes were priced, and the 3/4-in. diameter cord was found to offer the best capability within the budget limit. This cord was evaluated for its ability to accelerate a lightweight drop fixture to the design goal of 150 fps. Given the requirement for a terminal velocity of 150 fps, it was calculated, from the manufacturer's data, that the mass load could be increased 35 percent by extending the original drop height of the sand-drop machine from 7 to 10 ft. Figure 1 illustrates the energies available from these two heights. Steel angle beams, similar to the original beams, were used to extend the machine frame to an overall height of 14 ft. Figure 2 illustrates the sling-shot machine.

By using a pulley network, the single length of shock cord appears statically and dynamically as two cords. Two major advantages are realized from this configuration. The unstretched shock cord length can be made nearly equal to the machine height. Forces are equalized on both sides of the drop table when being raised or dropped (or in the event of cord breakage), thus removing all bending moments from the guide rods.

A pulley diameter of 4 in. was chosen to provide a smooth bending radius for the shock cord. Since the bottom set of pulleys are accelerated to a high speed by the shock cord, their weight was reduced as much as practical. Aluminum plate stock 1-1/4 in. thick was used, and the hub was bored to remove the unnecessary weight. (During evaluation of the machine, further reduction in size and weight of lower pulleys was required.) Roller bearings were installed in the pulleys to decrease friction.

By using small diameter guide rods, the surface area and the friction losses are minimized. If a small diameter guide rod is not
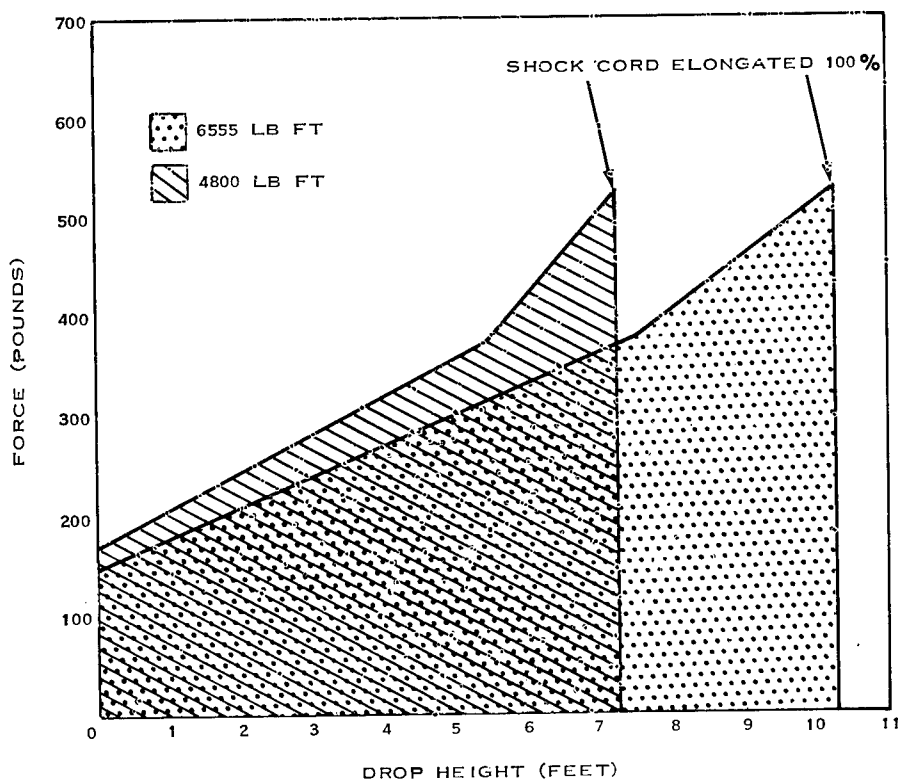
Fig. 1. Force deflection curves of shock machine
using 3/4-in. shock cords

12

TOP LEFT
PULLEY—GUIDE ROD
MOUNTING PLATE

GUIDE ROD
TURN BUCKLE

TOP LEFT
PULLEY

TOP SUPPORT
BEAMS

RETRACTABLE
CORD REEL

EXTENSION BEAMS

GUIDE RODS

LIFT CABLE

MAINTENANCE
PLATFORM

GUIDE ASSEMBLY

SOLENOID RELEAS
MECHANISM

DROP FIXTURE

LIFT
MOTOR

LIGHT
SENSORS

LOWER PULLEY
AND GUIDEROD
MOUNTING PLATES

LIGHT SOURCE

IMPACT
BASE

RUBBER PAD STAC

SHOCK CORD
GUIDES

LOWER LEFT
PULLEY

ANVIL

Fig. 2. Slingshot shock machine

precisely aligned, it can be bowed slightly by the drop fixture without binding on the fixture. The guide rods selected were 3/8 in. in diameter, 12 ft long, and were made from cold rolled steel.

The guide rod ends and pulley systems were fastened to four steel plates, so that each rod end and a pulley are on a common plate. These four plates were clamped in a manner that would permit continuous spacing adjustment

between the guide rods. This allows the drop fixture size and weight to be minimized for each individual test item. Spacing limits are currently 4-in. minimum to 14-in. maximum fixture width.

Because of the limited budget, it was not possible to cut the concrete floor and pour a seismic mass; therefore, another means of distributing the impact forces across the 8-in. thick cement floor was necessary. Although

13

not an ideal seismic mass, a 420 lb steel plate was salvaged from a discarded vibration fixture and welded in place on the original sand box floor. The anvil and the lower pulley plates then were attached to this steel plate.

So that drop fixtures could be quickly changed, the two end portions (guide assemblies) attached to the guide rods were made separate from the drop fixture. Each guide assembly (Fig. 3) is attached to the drop fixture by six 3/8-in. socket-head cap screws. By removing both assemblies, the drop fixture can be easily replaced. If the new fixture is larger or smaller in width, the pulley and guide rod plates then are adjusted to the proper spacing. The guide assembly bearing surface was bushed with oilite bushings on both the top and bottom. (During evaluation a new material for the lower bushings had to be found.)
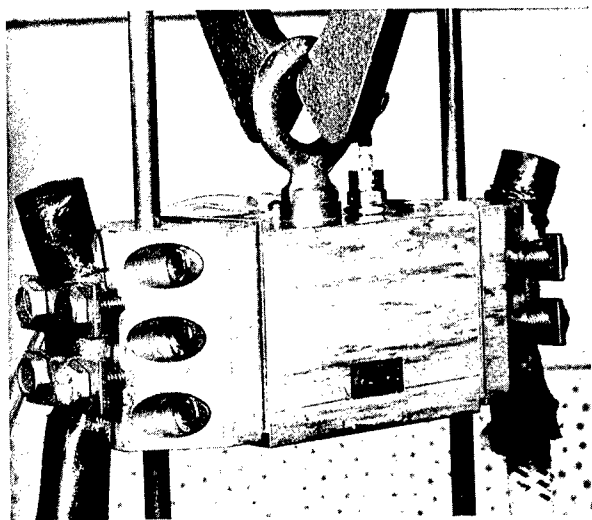
Fig. 3. Drop table assembly

The original lift motor, gear box, cable drum, and release mechanism of the sand-drop machine are used. The increased drop height necessitated a longer lift cable.

Two methods of attaching the release mechanism to the drop table have been used. In the one case, an eye bolt (Fig. 3), similar to that used in the sand-drop carriage, is installed in the center of the drop fixture. When the test item is mounted on top center surface of the drop fixture, a 1/2-in. nylon rope bridle is fastened to opposite ends of the fixture as shown in Fig. 4. Major advantages of using rope are its

Fig. 4. Drop fixture with nylon rope lift assembly

low mass and the nonresonant properties of the resultant lifting assembly.

The shock cord end is coated with a 1/8-in. thick layer of polyurethane rubber and is then clamped to the guide assembly by two straps (Fig. 3). Each strap is attached to the guide assembly by two 3/8-in. bolts. The rubber prevents the clamps from cutting the cord and the end fibers from fraying.

Several safety features have been incorporated. The machine is completely enclosed by industrial fencing, and the bottom 5 ft is covered by plywood. The release mechanism is interlocked with the access door so the drop fixture cannot be released until the door is closed completely.

INSTRUMENTATION

A light-beam system (2) is used to measure the terminal velocity. This system, illustrated in Fig. 5, has two physicians' head lamps as the light sources and two photovoltaic diodes (3) as the sensor elements. Sensor elements

14
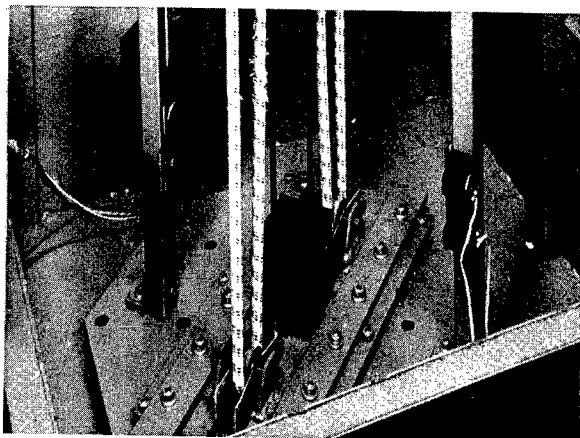
Fig. 5. Velocity measuring system

Fig. 7. Theoretical light sensor circuit output pulse

are located near the impact surface and are vertically spaced 3-1/2 in. apart. The lamps are positioned opposite the anvil from the sensors and have the same vertical spacing as the sensors. The illumination can be varied from 50 to 80 ft-c by adjusting the lamp voltage and/or lamp focus. The output of the sensors drive an electronic circuit (Fig. 6) which has a nominal output of +11 v. As shown in Fig. 7, the voltage drops to approximately +7 v when the upper light beam is cut off by the passing fixture. Whenever the lower light beam is cut

off, the voltage rises to +15 v independently of the state of the upper beam. Therefore, if the electronic timer (Hewlett-Packard Model 524D Counter with a Model 526B Time Unit) start and stop threshold is +10 and +12 v, respectively, the correct time interval will be recorded independent of the object size passing through the light beams. The velocity measurement error is estimated to be less than ±5 percent. Figure 8 is an oscilloscope presentation of the timing pulse.
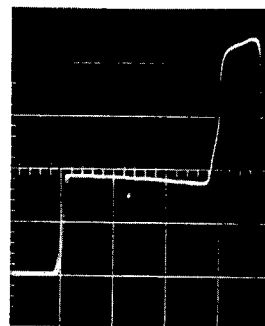
Fig. 8. Oscilloscope display of light sensor output pulse (0.5 ms/div., 2 v/div.), time indicated, 1.93 ms

Fig. 6. Light sensor circuit, schematic diagram

The acceleration pulse is measured by the system in Fig. 9. The accelerometer has been shock calibrated by Endevco Corporation at 500, 3000, and 13,000 g. The sensitivity was 0.62, 0.63, and 0.61 mv/pk g respectively. These sensitivities agree with the 50-cps sinusoidal calibration of 0.62 pk mv/pk g. The capacitance decade box is used as a variable shunt capacitance to reduce the accelerometer sensitivity to that desired for the particular shock level input. The amplifier is used only as a unity gain impedance match. The filter bandwidth is nominally set at 0.2-cps low cutoff and five times the expected pulse duration high

15
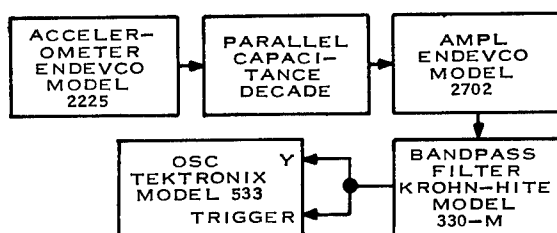
Fig. 9. Shock pulse instrumentation, block diagram

Fig. 10. Shock pulse on 40 durometer neoprene rubber pad (8400 g and 1.2 ms at 150 fps)

cutoff. The oscilloscope is operated at a maximum gain of 50 mv/cm.

EVALUATION OF MACHINE

The slingshot machine was evaluated for impact pulse shape and duration limitations, maximum velocity, and repeatability. The present maximum velocity is 150 fps when using a drop fixture weighing 6 lb. This is an efficiency (measured velocity/theoretical velocity) of 0.82 and is linear over the velocity range of the machine.

Evaluation of impact materials has been limited to 40 and less than 10 durometer rubber and lead. The rubber pads consist of a stack of 1/4-in. or 3/8-in. sheets and yield an impact pulse similar to a half sine wave as shown in Figs. 10 and 11. A cylindrical shaped lead pellet is used and yields a sawtooth or square shape pulse (Fig. 12), depending on the pellet dimensions. Distortion on the leading edge of the shock pulse is decreased by reducing the initial impact area or by covering the pad stack with a soft sponge material. Tests performed to date have yielded shock pulse amplitudes to 12,000 g and pulse durations from 0.3 to 40 ms.

As problems arose during machine evaluation, various changes were made. High speed movies of the pulley action showed that the lower aluminum pulleys continued to rotate in the downward table direction when the table was actually rebounding. This action caused severe cord stretch and failure at the point of clamp attachment. Cord breakage occurred when drops were made on 6 in. of rubber pad at heights exceeding 4 ft. The effective mass of the lower pulleys was decreased by substituting 2-in. diameter hardwood pulleys, which are being used with satisfactory results.

After several high g shocks, the lower set of oilite bushings sheared their retaining pins. They were replaced with nylon bushings and have proven to be very satisfactory. The upper set of bushings also will be replaced with nylon.

To achieve a 150-fps terminal velocity, the shock cord must be elongated 100 percent at the maximum drop height of the fixture. This requires that the cord be prestretched 18.5 percent at the rest position. In an attempt to increase the velocity, one test was made using a cord with approximately 34 percent prestretch. After one shock, the cord was broken in three places. Cord life is in excess of 100 drops if the stretch is kept less than 80 percent.

The fixture center of gravity for one test sample, shown in Fig. 4, was not located at the center between the two guide rods. After a few drops, the guide rods were permanently bent near the point of impact. When the fixture and test item center of gravity are correctly located at the center between the guide rods, this bending is reduced to a negligible factor.
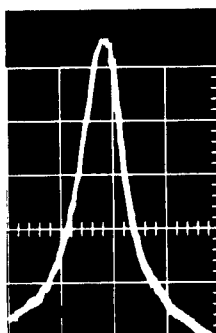
Fig. 11. Shock pulse on less than 10 durometer silicone rubber pad (550 g and 5.4 ms at 30 fps)

16

Severe whipping of the shock cord after impact has caused the cords to jump from the pulley and severely damage the cord covering. Guides have been installed at the lower pulleys to eliminate this problem.

Failure of the accelerometer cable caused by the jerk and acceleration of the drop fixture has been greatly reduced by the use of sleeving (Fig. 3) over the cable. Each end of the sleeving is clamped, thus relieving most of the force from the accelerometer cable.

As a result of these changes, maintenance has been reduced to a visual inspection of the machine and a check of all bolts for tightness after 50 to 100 drops.

Some difficulty has been experienced with the release mechanism cable when drops are made from heights over 5 ft. The cable will not properly unwind from the drum unless a 75- to 100-lb load is applied to the release mechanism as it is being returned to the 5-ft level. A satisfactory solution has not yet been devised to eliminate this problem.

Additional machine characteristics that may be of special interest to test engineers are as follows:

1. Velocity and acceleration, for equal drop heights and cord stretch, are repeatable to ±10 percent for any one setup;

2. The acceleration of the first rebound impact is approximately 10 percent of the initial impact; and

3. The shock level on the floor, 3 ft from the anvil, is less than 0.5 percent of the impact g level.

FRAGILITY TEST RESULTS

Crystals

Two series of tests (4) were run on non-ruggedized 33.7-Mc type CR-23/U crystals. The first tests were performed using three crystals, one in each axis, as illustrated in Fig. 13. Although the crystals are normally clip mounted, for these tests they were potted with wax in the solid aluminum drop fixture shown in Fig. 3. This method was verified by potting an accelerometer in the wax and observing its pulse on a dual-beam oscilloscope together with the pulse of a normally mounted accelerometer. The crystals were checked for frequency and resistance after each drop. The
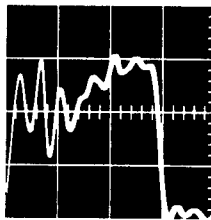
Fig. 12. Shock pulse on lead pellet, 3 in. in diameter and 2-1/4 in. high (2800 g and 1.4 ms at 96 fps)
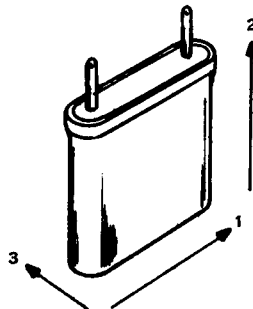
Fig. 13. CR-23/U crystal, axes of applied shock

second test series used the same testing procedure with the exception that the crystals were shocked individually and in plane 3 only. The results of both tests are summarized in Table 1. Inspection of the inoperative crystals showed that they had fractured into two or more pieces. Severe shattering of the crystal resulted when the pulse duration was less than 3 ms.

Crystal Oscillator

The CR-23/U crystal was operated in the third overtone mode on a metal circuit board solid state Pierce oscillator circuit. This circuit board was potted with Sil Guard in a metal can. Wax was used to pot the can in the drop fixture. The transient and permanent frequency deviations were checked for each drop. The maximum permanent deviation was 5 cps. The transient deviation, at the time of impact, is given in Table 2. Inspection after drop No. 30 showed that the crystal had fractured in two pieces.

Voltage-Controlled Oscillator

A substrate voltage-controlled oscillator circuit was tested for permanent frequency shift due to the shock input. The substrate was bonded to the shock table with double-sided pressure sensitive tape. The oscillator was tested in each of three axes, as illustrated in Fig. 14. These data are presented in Table 3.

17

TABLE 1
CR-23/U Crystal

Drop Se- quence	Accel- eration (g)	Dura- tion (ms)	Crys- tal No.	Axis No.	Fre- quency (mc)	Resist- ance (ohms)
Reference data			1	1	33.700174	22
			2	2	33.699884	23.4
			3	3	33.699397	22
			10	3	33.700024	26.8
			11	3	33.700071	23.4
			12	3	33.700182	27.9
			13	3	33.699472	31.5
1	No record ~25	~40	1	1	33.700172	22
			2	2	33.699978	28.2
			3	3	33.699530	22
2	85	20	1	1	33.700126	22
			2	2	33.699924	28.2
			3	3	33.699428	22
3	250	12	1	1	33.700118	22
			2	2	33.699919	28.2
			3	3	33.699428	22
4	>1100 Signal clipped	~3	1	1	33.700122	22
			2	2	33.699916	27
			3	3	33.699438	22
5	>1200 Signal clipped	~5	1	1	33.700155	22
			2	2	33.699939	28.2
			3	3	33.699419	22
6	1500	2.8	1	1	33.700145	22
			2	2	33.699895	27
			3	3	33.699370	22
7	1250	4.5	1	1	33.700154	22
			2	2	33.699916	28.2
			3	3	33.699368	22
8	2250	2.5	1	1	33.700165	22
			2	2	33.699904	28.2
			3	3	Inoperative	—
9	1375	4.4	10	3	33.700026	26.4
10	1150	2.5	11	3	33.700045	22.8
11	680	8.4	12	3	33.700172	27.7
12	2000	1.6	13	3	Inoperative	—
13	1400	5.2	10	3	33.700046	26.8
14	1500	2.5	11	3	Inoperative	—
15	700	8.5	12	3	33.70018	28.6
16	1500	5.0	10	3	33.700061	26.4
17	1600	8.0	12	3	Inoperative	—
18	2700	4.5	10	3	Inoperative	—

18

TABLE 2
Solid State Crystal Oscillator

Drop Sequence	Acceleration (g)	Duration (ms)	Axis No.	Transient Frequency Deviation (cps)
1	No record ~25	~40	3	0
2	25	40	3	0
3	90	20	3	0
4	260	12	3	230
5	240	10	3	230
6	No record ~250	~10	3	—
7	220	13	3	170
8	230	13	3	—
9	100	12	3	0
10	No record		3	—
11	230	4	3	230
12	450	6	3	430
13	380	3	3	530
14	680	1.5	3	2600
15	750	2	3	2200
16	250	12	2	0
17	No record ~500	~6	2	—
18	430	7	2	0
19	600	5	1	0
20	180	11	1	0
21	400	6.7	1	0
22	No record		1	0
23	260	10	1	0
24	800	2.9	1	0
25	600	4.2	1	0
26	680	4.4	1	0
27	1300	3.1	1	0
28	1460	3.3	1	0
29	850	5.4	3	930
30	>1700 Signal clipped	~3	3	Oscillator inoperative

TABLE 3
Substrate Voltage-Controlled Oscillator

Drop Sequence	Accel-eration (g)	Dura-tion (ms)	Impact Velocity (fps)	Axis No.	Fre-quency at 2 V (Mc)	Fre-quency at 8 V (Mc)
Reference data					124.67	142.16
1	25	35	9	1	125.23	142.54
2	70	20	14.5	1	124.95	142.32
3	220	13	29.5	1	125.16	142.41
4	230	11	26	2	125.21	142.63
5	260	10	26.5	3	125.61	143.05
6	600	4.2	26	3	125.60	143.06
7	680	4.4	30.5	3	125.61	143.06
8	1500	2.8	43	3	125.65	143.09
9	>1700 Signal clipped	~3	—	2	125.56	143.01
10	1750	4.5	80	3	125.60	143.04

Microsolder on Aluminum Substrate

A shock test was conducted on 16 substrates with aluminum bonding pads varying in thickness from 6000 to 50,000 Å. Twenty pads on each substrate were tinned with aluminum tin-eutectic solder and a gold-plated Kovar tab was sweated to each tinned area, providing a total of 320 sample bonds. The substrates were subjected to one shock, in axis 2 (Fig. 14) of 6000 g and 0.6 ms. Two of the 320 samples, on 6000 Å pads, failed the bond. This agreed with earlier tests, of another type, showing that pads less than 8000 Å thick are unsatisfactory for micro-soldering.
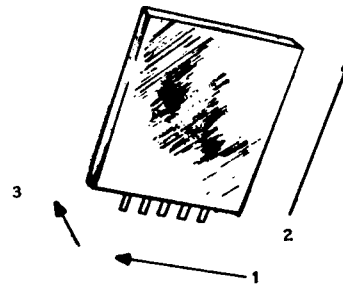
Fig. 14. Voltage-controlled oscilla-tor, axes of applied shock

CONCLUSIONS

1. A terminal velocity of 150 fps has been attained and tests are being performed at this velocity.

2. The cost of modification was approximately $1,000.00 (fabrication of parts) plus 2 weeks of technician time (assembly of machine).

3. The machine has proven to be very versatile. Three separate fixtures have been tested and several more are in the planning stage.

The entire machine is one assembly and could be easily moved to another location.

4. There are several contractual and engineering evaluation requirements that have specified a need for the machine, indicating a high future utilization.

It should be noted that although this machine is versatile and economical to build, it has many limitations. It is not a substitute for the more refined commercially available systems, but should be considered as a stepping stone to bigger and better shock testing machines.

ACKNOWLEDGMENT

REFERENCES

1. J. O. Lonborg, IES Proc., pp. 457-460 (1963)

2. R. Gary Bucke, IES Proc., pp. 247-250 (1963)

3. R. D. Kaus, Electronic Ind., p. 83 (Aug. 1965)

4. J. O. Lonborg, "High Impact Survival," JPL Tech. Rept. 32-647, Sept. 30, 1964

DISCUSSION

Mr. Levin (Bureau of Ships): What were some of the results of testing various components, such as the 23U crystals or any of the very small components?

Mr. Marshall: I did not present any of these results here because we have not done enough testing to set up a failure point. We have too few samples. We are testing some batteries, capacitors, and crystals, but the only testing that has been carried out to any extent at this time was the one that I showed on the crystals. There will be a company report which will contain more component data. If you would care to write to any of the authors at Collins, we will send it. I do have some preprints of the paper too, if anyone is interested.

* * *

SHOCK SPRINGS AND PULSE SHAPING
ON IMPACT SHOCK MACHINES*

Richard O. Brooks
Sandia Corporation
Albuquerque, N. M.

Results are discussed of an investigation conducted to find materials
and practical shock spring designs that can be used to produce differ-
ent shock pulses on impact shock machines. Various materials and
design configurations were experimentally evaluated to determine
through what ranges of stress, energy absorption, and initial strain
rates materials could be used to produce classical pulse shapes such
as the half-sine, triangle, haversine (sine-square), and parabolic cusp.
Springs were designed for particular shock test conditions from this
information. Typical test setups and the recorded pulse shapes (both
noisy and clean) are presented.

Dynamic mechanical properties, such as stress-specific energy rela-
tionships, modulus of elasticity in dynamic compression, coefficient of
restitution, and stress wave propagation velocities were determined for
several types of polymers and plastics. In addition, for rubber spring
designs, the effect of unrestrained and semi-restrained boundary con-
ditions on pulse shape are shown. Three different designs of liquid
shock springs and their pulse shapes are discussed.

INTRODUCTION

Shock pulse generation is a major problem
in the field of mechanical shock testing. The
test engineer often does not have either the time
or the material to develop a requested pulse
shape accurately on a particular shock machine,
so he generates an acceleration pulse which has
only the required amplitude and duration. More-
over, marked differences between recorded and
reported pulse shapes are frequently found if
the pulse shapes generated by several labora-
tories throughout the country are examined and
normalized. For example, the recorded pulse
shape may appear to be a parabolic cusp but is
classified as an approximate half-sine. Conse-
quently, if a shock test is requested, and a cer-
tain shape is specified but a different shape is
generated, the test item will probably not be
subjected to the same "damage potential" as it
would under the requested shock test. There-
fore, an investigation was conducted (1) to find
suitable materials and practical shock spring
designs for good test setups in the generation
of several clean symmetrical pulse shapes for
a variety of shock tests on different impact

shock machines. This paper presents the re-
sults of that investigation.

CLASSICAL PULSE SHAPES

The investigation was concerned with the
generation of four classical symmetrical
shapes, half-sine, triangle, haversine, and
parabolic cusp (Fig. 1). Mathematic expres-
sions for these shapes are given in the Appen-
dix. In Fig. 1, the widths are normalized at the
10 percent level of the maximum amplitude of
the pulse (2, pp. C-9, C-15) because points of
intersection are easier to locate than points of
tangency. If a recorded pulse shape is suffi-
ciently distorted (e.g., the amplitude equal to
five times the width in dimension), one classi-
cal shape can be made to look like another.
The classical pulse shapes differ from each
other in their area (velocity change) and in the
rise and fall times between the 10 and 90 per-
cent levels of the maximum amplitude of the
pulse (2, pp. C-9, C-15). It can be shown that
as a pulse shape changes from half-sine to
haversine to triangle to parabolic cusp, the
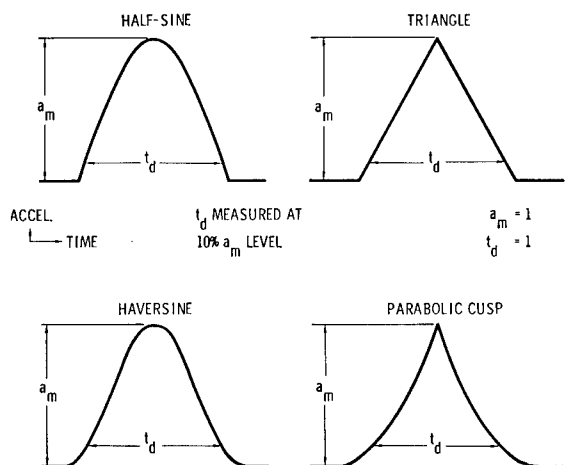
Fig. 1. Four normalized symmetrical pulse shapes

respective areas steadily decrease and the rise and fall times increase.

The shock effect of a particular pulse shape on a linear single degree of freedom system can be examined from the shock spectra; the effect from a second shape can be made the same as the effect from the first by adjusting the amplitude and/or duration of the second pulse shape (3; 4, Ch. 8).

The half-sine and triangle shapes are frequently seen in specifications. The haversine is sometimes called a sine-squared shape or a versine shape if the normalized amplitude is multiplied by two. This shape generally results when a noisy half-sine pulse is cleaned by using certain techniques in the shock spring design. The parabolic cusp is rarely specified; it occurs when well-known shock mitigating or packaging springs are highly compressed during a shock test. The amplitude of the cusp is hard to control accurately since there is so little area near the peak. The haversine is the only one of these four pulse shapes that can be both described mathematically and actually generated. The other shapes can only be approximated because of discontinuities in their profiles that are always smoothed or rounded in actual shock tests. The haversine, therefore, is an excellent shape for a test specification.

The investigation was limited to generating these shapes on impact machines using resilient materials because these machines are frequently encountered in laboratories and are quite versatile for pulse shaping purposes. A typical impact machine is shown in Fig. 2. Two basic problems in classical pulse shape distortion can exist with this type of machine. First, hitting a stationary shock spring surface with a moving carriage surface may have a violent effect on the cleanness of a recorded pulse, especially when the impact velocity is large. The impacted edge of the spring experiences a high-acceleration short-duration impulse to make its velocity equal to the carriage velocity, causing stress waves to be propagated and reflected back and forth in the spring and the carriage. These waves produce ringing (high-amplitude high-frequency vibration) on the basic pulse shape generated as the shock spring is compressed. A similar ringing phenomenon occurs if the shock spring is mounted underneath the carriage; then the velocity of the spring's lower edge at impact suddenly becomes zero. If clean pulse shapes are to be obtained, this ringing must be suppressed. Second, a spring design suitable for a certain pulse shape and shock condition generated on one machine may not be suitable for the same condition generated on another machine unless the relationships between the test item weight, fixture design, and carriage weight are kept similar. Significant feedback forces and undesirable interactions are apt to occur when a relatively large test item is mounted on a small carriage.
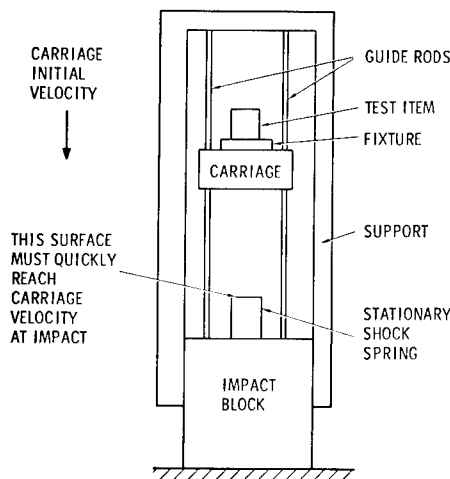
Fig. 2. Impact shock machine

NOMENCLATURE

A   Spring area (sq in.)

A_p Effective piston area (sq in.)

a   Acceleration (g, in./sec/sec)

24

a_m Maximum (faired) acceleration amplitude of the shock pulse (g, in./sec/sec)

B   Apparent dynamic bulk modulus of contained material (psi)

E_c Dynamic modulus of elasticity during compression (psi)

f_c Low bandpass electrical filter upper cutoff frequency (kcps)

k   Spring rate (lb/in.)

L   Spring length (in.)

M   Total impacting mass (lb-sec^2/in.)

Q   Volume of contained material (cu in.)

R   Coefficient of restitution

S   Stress corresponding to the maximum (faired) amplitude, a_m, of the shock pulse (psi)

t   Time (ms)

t_b Duration measured at the base line of the shock pulse (ms)

t_d Duration measured at the 10 percent level of the maximum (faired) amplitude of the shock pulse (ms)

t_r Rise time measured between the 10 and 90 percent levels of the maximum (faired) amplitude of the shock pulse (ms)

U   Spring specific energy (in.-lb/cu in.)

ΔV Velocity change (area) of the shock pulse (g-ms, in./sec)

V_i Carriage impact velocity (in./sec)

V_r Carriage rebound velocity (in./sec)

Subscripts

1, 2   First condition, second condition, respectively

EXPERIMENTAL SETUP AND MATERIAL INVESTIGATION

The dynamic mechanical properties of resilient materials which might be used as impact springs for shock tests were investigated because materials used to generate good desired shapes under certain conditions did not generate good shapes under different conditions, and the literature provided little information on how a material might behave during dynamic compression.

Materials were selected on the basis of their static properties and their availability. The work, in general, consisted of determining ranges of stress, energy absorption, and initial strain rates through which various materials could be used to produce the different classical shapes. This information could then be applied to particular shock test conditions.

In setting up the experiments, one end of a shock spring of known dimensions was placed against a rigid support, and a carriage of known weight was impacted onto the spring. The carriage acceleration-time history was monitored and carriage displacement-time history was either monitored or determined by integration of the shock pulse. (It was assumed that the acceleration of the carriage was caused entirely by the spring force for all tests.) The impact and rebound velocities of the carriage were determined independently. The net velocity change of the carriage was compared to the area under the recorded shock pulse to check instrumentation accuracy. Each test condition was performed three times, and averages were determined when measurable differences were encountered.

Each acceleration-time history was monitored by a piezoelectric accelerometer. Its output signal was fed into a cathode follower whose output signal was photographed on a cathode-ray oscilloscope. In general, all oscilloscope records were unfiltered electrically. When an electrical filter was used, it was placed in the circuit after the cathode follower. The filter was a Gaussian low bandpass type (4, ch. 19, pp. 86, 87) whose upper cutoff frequency selection (gain, -3 db) was governed arbitrarily by the shock pulse rise time shown in Eq. (1).

$$f_c \geq \frac{5}{t_r} , \tag{1}$$

where f_c is the upper filter cutoff frequency (kcps), and t_r is the shock pulse rise time (ms). To classify the shape of a recorded pulse in a shock test, a close comparison of the normalized recorded pulse and the classical pulse was made.

Rubber

Rubber is probably the most common type of material used for pulse generation on impact shock machines. It is also a material whose dynamic mechanical properties differ considerably from its static properties. Fastax movies taken of rubber pads during a shock test show that rubber experiences a significant radial velocity perpendicular to the longitudinal or compression direction. The lateral dimensions can increase over 100 percent, depending on the boundary conditions. This effect does not occur as severely during static compression.

Figure 3 indicates the different pulse shapes, amplitudes, and durations recorded when two neoprene rubber pads (50 Durometer A) were used on one shock machine. One pad (7.6 in. diam. by 1.4 in. thick) was bonded to an impact block. The other pad (7.6 in. diam. by 0.7 in. thick) was bonded to a carriage weighing 227 or 265 lb. The free mating surfaces of each pad were slightly convex. As the kinetic energy absorbed by the material was increased, the shape of Pulses 1, 2, and 3 changed from haversine to half-sine to triangle, respectively, and the shock duration continually decreased. Equipment limitation prevented the application of higher energy levels. As the impact velocity was increased for Pulses 1, 2, and 3, respectively, the amount of high frequency ringing also

increased. Pulse No. 3 was cleaned mechanically with a 4-in. square by 0.5-in. thick medium sponge rubber pad placed in series with the neoprene. Pulse No. 4 was then obtained with about a 5-percent change in both amplitude and duration. Pertinent spring mechanical properties, stress, specific energy, and initial strain rate for each test are shown. (Specific energy is defined as the ratio of kinetic energy absorbed by the spring to the spring volume; initial strain rate is defined as the ratio of carriage impact velocity to impact block pad thickness.) The coefficient of restitution of the spring assembly was 0.84 for Pulse No. 1 and 0.71 for Pulse No. 4. (This coefficient is defined as the ratio of carriage rebound velocity to impact velocity.)

Energy levels above those shown in Fig. 3 were applied to the neoprene by two other shock machines, but the pulses were too noisy, so butyl rubber (30 Durometer A) was then used as the basic shock spring material to produce the clean parabolic cusps shown in Fig. 4. (The 96-lb carriage impacted into a composite spring made up of materials in the following order from top to bottom: one medium sponge pad, 4 in. square by 0.5 in. thick; one butyl pad, 4 in. square by 0.25 in. thick; and one butyl pad, 4 in. square by 1 in. thick. The sponge attenuated any superimposed ringing. The 450-lb carriage impacted into a spring made up of the

① HAVERSINE 38g 10.3 ms	227 lb CARRIAGE	② HALF-SINE 100g 9.0 ms
50 in/sec	IMPACT VEL.	118 in/sec
36 in/in/sec	INIT. STRAIN RATE	84 in/in/sec
190 psi	STRESS	510 psi
8 in-lb/cu-in	SP. ENERGY	44 in-lb/cu-in
③ TRIANGLE 270g 8.4 ms	265 lb CARRIAGE	④ TRIANGLE 255g 8.7 ms
263 in/sec	IMPACT VEL.	263 in/sec
188 in/in/sec	INIT. STRAIN RATE	188 in/in/sec
1570 psi	STRESS	1480 psi
222 in-lb/cu-in	SP. ENERGY	222 in-lb/cu-in

Fig. 3. Pulse conditions generated by typical neoprene rubber spring assembly

	396 in/sec	IMPACT VEL.	612 in/sec
226 in/in/sec	INIT. STRAIN RATE	307 in/in/sec
3960 psi	STRESS	5140 psi
970 in-lb/cu-in	SP. ENERGY	700 in-lb/cu-in
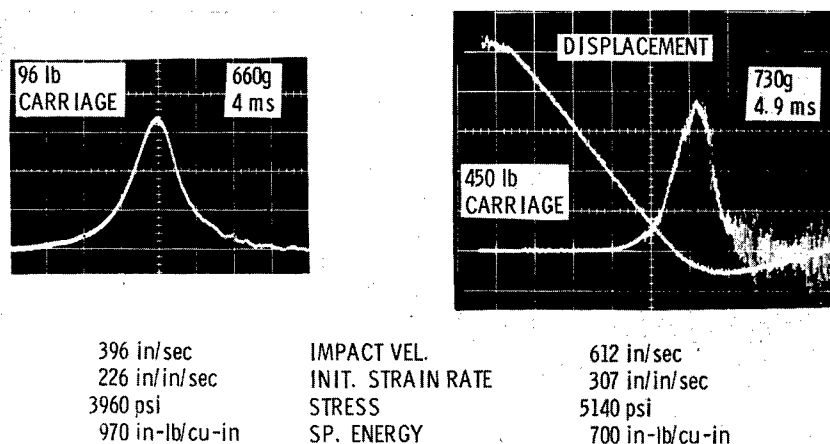
Fig. 4. Parabolic cusps from 30 Durometer A butyl rubber

following materials in the following order from top to bottom: three Ensolite pads, each 8 in. square by 1.25 in. thick; and two butyl pads, each 8 in. square by 1 in. thick. The thickness of the Ensolite, a urethane foam, was ignored in determining an initial strain rate value, but the sponge thickness was included. Ensolite compressed about 80 percent before any appreciable restraint was encountered.) The displacement-time history of the 450-lb carriage, shown on the right, was monitored by an optical tracking device. The slopes of the displacement-time curve just before and just after the acceleration pulse indicated carriage impact and rebound velocities. The ratio of carriage rebound velocity to impact velocity was found to be 0.20. Instrumentation accuracy was checked by adding the impact and rebound velocities together and comparing them to the area under the acceleration pulse. Less than 2 percent difference was found. During the shock, the spring assembly compressed from 5.75 in. to 0.5 in. Pulses such as those shown in Fig. 4 will cause less "damage potential" to a test item than will a half-sine pulse of the same amplitude and duration.

An attempt was made to improve some pulses produced from rubber by imposing a semi-restrained boundary condition on the spring (Fig. 5). Eight dry neoprene rubber discs (each 4 in. O.D., 1.87 in. I.D., and 0.25 in. thick) shown in the upper part of the figure were stacked freely in series and then topped by an aluminum disc and a 0.06-in. thick felt pad. The felt smoothed the pulse start, and the aluminum disc prevented interaction between the felt and rubber during the shock. The spring assembly in the lower part of the figure was made from eight similar rubber discs bonded with Epon VI to eight aluminum discs in series

and topped with felt. Figure 6 shows the pulse shapes generated on the same machine by these two spring configurations, with both test setups having the same initial strain rates and specific energy levels. The stress level of the bonded spring almost doubled the stress level of the free spring but the pulse shape became more nonsymmetrical. The coefficient of restitution for either design was 0.50. The spikes on the upper trace in each record are carriage displacement marks caused by a different carriage pin interrupting a stationary light beam photocell circuit. The distance between pins and the sweep rate of the oscilloscope were used to calculate the impact and rebound velocities (accurate within ±4 percent) and displacement-time histories of the carriage during the pulse (accurate within ±6 percent).

Polymers, Plastics

Besides neoprene, two polymers evaluated were Adiprene, a polyurethane elastomer (hard formulation), and Diene, a stereospecific polybutadiene synthetic rubber mixed with mineral oil (30 percent by weight). Plastics evaluated were Teflon, polyethylene (soft and hard), polypropylene, Delrin (an acetate resin), vinylidene chloride, and a laminated phenolic identified as NEMA Grade LE MIL-P-79B, Form R, type FBE.

All spring materials were cylindrical and, depending on their size, carriage weights of either 12, 90, or 220 lb were used. The weights were capable of impacting at velocities up to 120, 780, and 300 in./sec, respectively. Data were obtained for the mechanical properties of each material by selecting a carriage mass, a particular spring, and then increasing impact

FREE LAMINATIONS

FELT

NEOPRENE RUBBER
50 DUROMETER A

BONDED LAMINATIONS

FELT
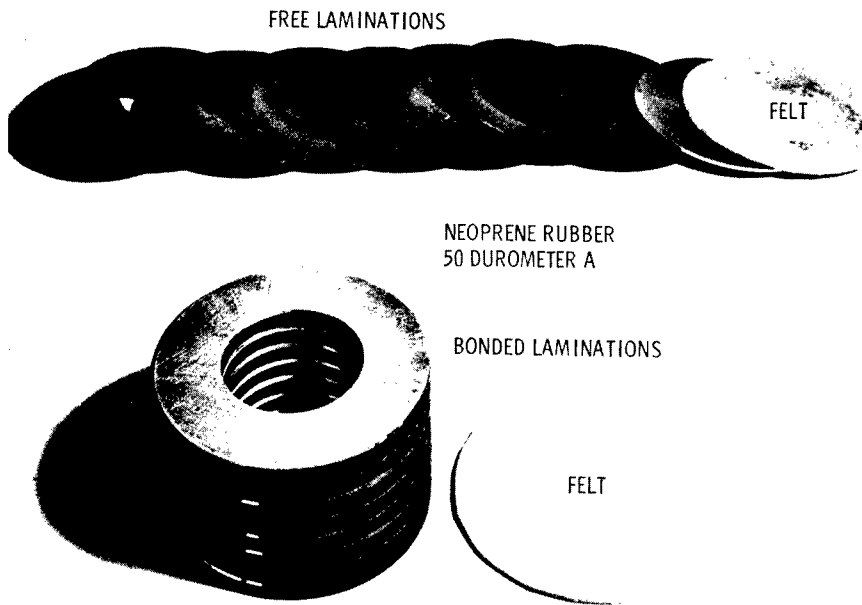
Fig. 5. Rubber spring having different boundary conditions

velocities until either the pulse was distorted from a normalized half-sine shape or the material failed. When a particular shock pulse was too noisy, it was cleaned sufficiently so that a definite faired amplitude could be determined. Faired amplitude is the smooth amplitude throughout the recorded pulse when the unwanted frequencies superimposed on the pulse have been eliminated graphically (2, pp. C-6, C-15). The noisy pulses were generally filtered mechanically by adding nonlinear and highly inelastic material, such as felt or free Diene, in series with the more linear spring material. Sometimes a recorded noisy pulse was electrically filtered to attenuate the amplitudes of the

superimposed high frequencies. At other times, both mechanical and electrical filtering were employed. In any case, the allowable attenuation of the maximum faired amplitude of any pulse after cleanup was 5 percent or less. In Fig. 7, for example, the left-hand record shows a very noisy pulse (electrically filtered at 10 kcps) of approximately 1.5 ms duration having an unknown maximum faired amplitude and rise time. A significant 4-kcps superimposed frequency having some harmonic content can be seen, but the basic pulse shape is not discernible. By employing a low-pass filter having 5-kcps cutoff (center record, Fig. 7), the 4-kcps frequency was not significantly attenuated so a

FREE LAMINATIONS

BONDED LAMINATIONS

AMPLITUDE 85g
RISE TIME 7.8 ms
DURATION 16.0 ms

CARRIAGE
211 LBS

AMPLITUDE 160g
RISE TIME 1.6 ms
DURATION 6.6 ms

1900 psi	STRESS	3600 psi
337 in-lb/cu-in	SPECIFIC ENERGY	337 in-lb/cu-in
76 in/in/sec	INITIAL STRAIN RATE	76 in/in/sec
152 in/sec	IMPACT VELOCITY	152 in/sec
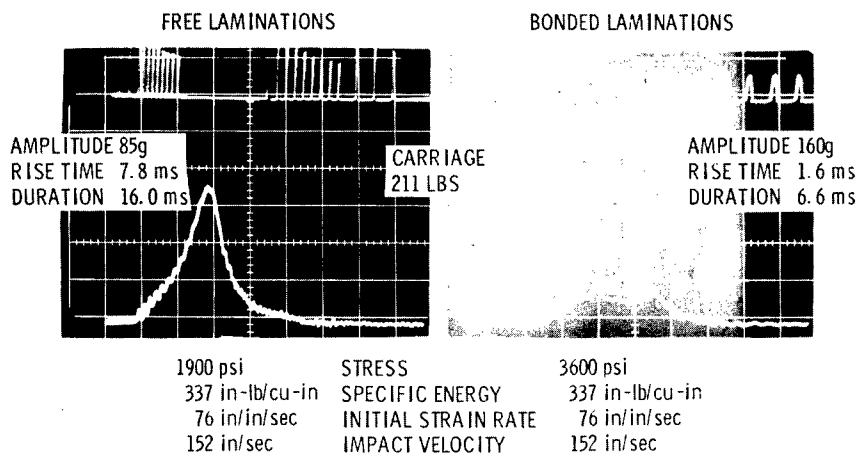
Fig. 6. Comparison of recorded pulses generated
by free and bonded laminated rubber spring

28

ELECTRICALLY FILTERED:
UPPER CUTOFF = 10 KCPS

ELECTRICALLY FILTERED:
UPPER CUTOFF = 5 KCPS

ELECTRICALLY FILTERED:
UPPER CUTOFF = 10 KCPS

MECHANICALLY FILTERED:
$\dfrac{\text{FELT LENGTH}}{\text{PLASTIC CYL. LENGTH}} = 0.03$
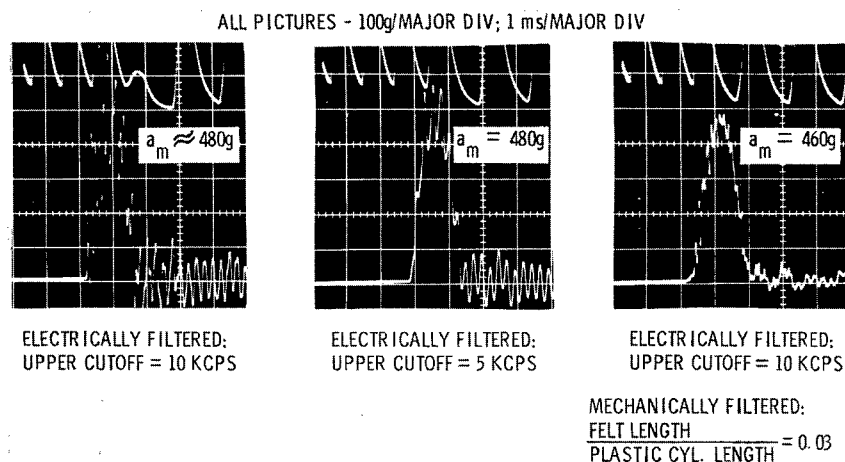
Fig. 7. Noisy pulse records

maximum faired amplitude of 480 g was measured. However, since the filter cutoff frequency did not meet the requirements of Eq. (1), a combination of both mechanical and electrical filtering was tried (right-hand record, Fig. 7). About 4 percent attenuation of the maximum faired amplitude and about 7 percent loss in coefficient of restitution occurred. The amplitude of the 4-kcps superimposed frequency was quite attenuated, indicating that the electrical filter was not necessary. The right-hand record (Fig. 7) was found to be a slightly noisy but satisfactory half-sine pulse. Further pulse smoothing for this test condition would have produced a haversine shape.

Figure 8 shows specific energy-stress relationships of five of the materials investigated. Plotting stress-specific energy data on log-log scales revealed that materials behaving as quasi-linear springs (i.e., having constant moduli of elasticity with increasing stress levels) produced a constant slope equal to that indicated by the dashed line and that they generated half-sine pulses. The solid portion of the curve for each material represents the range of quasi-linear spring behavior, though the materials were also tested in regions shown by the dotted lines. The modulus of elasticity for a quasi-linear spring material can be found from Eq. (2):

$$E_c = \frac{S^2}{2U} , \qquad (2)$$

where

E_c = modulus of elasticity in dynamic compression (psi),

S = stress corresponding to a shock pulse maximum faired amplitude (psi), and

U = specific energy (in.-lb/cu in.).

The modulus of elasticity of the vinylidene chloride used to generate the right-hand pulse in Fig. 7 was 354,000 psi from the calculated dynamic stress-strain curve of the shock pulse and 350,000 psi from Eq. (2).

In Fig. 8, the regions where the slopes of the stress-specific energy curve for any material were greater than that indicated by the dashed line corresponded to shocks that produced either a haversine or triangle shape. Slopes less than that indicated by the dashed line corresponded to shocks where the material yielded. Yielding is not a major problem if only a few shocks are involved, but many shocks in a particular stress range may cause a spring dimension change and, eventually, a shock pulse change. Only Delrin and vinylidene chloride produced half-sines while the spring yielded.

Table 1 summarizes some mechanical properties of the polymers and plastics when they generated half-sine pulses without failure. Coefficients of restitution of some materials were affected by the types of nonlinear series material used and the degree of nonparallelism of the contacting surfaces during impact. Any effects of this nature were incorporated into the mechanical properties of the basic spring material. The effect of different coefficients of restitution on the elastic modulus of a material can be estimated from Eq. (3):
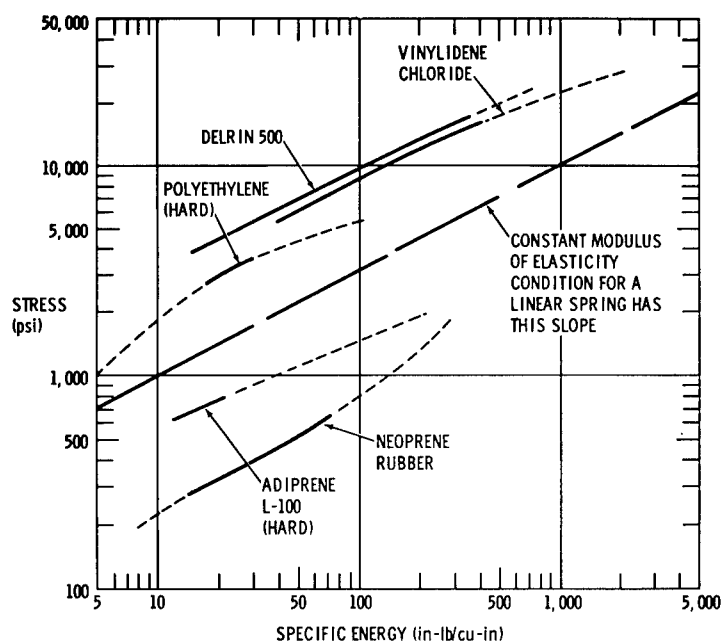
Fig. 8. Stress-specific energy relationships
of several shock spring materials

TABLE 1

Mechanical Properties of Some Materials Capable of Producing a Half-Sine Pulse Shape

Material	Initial Strain Rate[a] (in./in./ sec)	Specific Energy[b] (in.-lb/ cu in.)	Coefficient of Restitution[c]	Maximum Stress[d] (kpsi)	Modulus of Elasticity (kpsi)	Stress Wave Propagation Velocity[e] (in./ms)
Neoprene	100	75	0.77	0.6	2.8	3
Adiprene L-100 (hard)	26	20	0.72	0.8	14	12
Free Diene	270	440	0.16	1.2	2.0	15
Teflon	25	55	0.66	3.4	100	71
Polyethylene (soft)	70	35	0.70	1.5	30	20
Polyethylene (hard)	90	30	0.70	3.7	230	51
Polypropylene	25	30	0.54	4.7	370	65
Delrin-500	50	330	0.67	17	440	57
Vinylidene chloride	100	360	0.56	15	350	52
Laminated phenolic	140	1100	0.77	35	550	65

[a]Ratio of carriage impact velocity to spring length.
[b]Ratio of kinetic energy of carriage absorbed by spring to spring volume.
[c]Ratio of carriage rebound velocity to impact velocity.
[d]No visible failure of material (Diene excepted) or significant pulse distortion.
[e]Material assumed to be homogeneous and isotropic.

30

$$\frac{E_{c2}}{E_{c1}} = \left(\frac{1 + R_2}{1 + R_1}\right)^2 , \qquad (3)$$

where

R_1, R_2 = different coefficients of restitution of a material determined experimentally, and

E_{c1}, E_{c2} = moduli of elasticity of the material corresponding to R_1 and R_2, respectively.

The properties of Diene indicate that, in a free state and for the volume used, the material is highly inelastic, can absorb a large amount of energy when impacted at a high strain rate, and is therefore suitable to suppress the high-frequency ringing of noisy pulses. Stress wave propagation velocities for the materials were calculated from determined values of moduli of elasticity and densities. The effect of different initial strain rates on the mechanical properties of the materials was of some concern. However, varying the initial strain rate between 23 and 128 in./in./sec did not change the mechanical properties of hard polyethylene, so it is likely that the harder materials are also not affected except for pulse cleanness.

A shock spring for any shock pulse condition and machine can be designed from data given in Fig. 8 and Table 1 as long as the following are assumed: maximum amplitude and velocity change of the desired pulse, carriage weight, material type, and coefficient of restitution. Figure 9 shows an example in which a 2000-g, 1.3-ms half-sine shock pulse is to be generated on a shock machine whose total carriage weight is 96 lb and whose impact surface area is 50 sq in. Vinylidene chloride is selected and its coefficient of restitution, 0.56, can be found from Table 1. The necessary carriage impact velocity can be determined once the velocity change of the desired shock pulse is calculated. Spring area is determined from available stock. The maximum expected stress level is calculated from the relationship between spring area, carriage mass, and pulse maximum acceleration. Figure 8 can then be used to find the specific energy of the spring. The volume (and thus the length) of the spring now can be determined, since the kinetic energy of the carriage at impact is known. Several different spring volumes are possible, depending on the area selected. The ratio of spring area to length essentially must be constant if the same spring rate is to be kept, however. The pulse for this example will undoubtedly be noisy, but can be cleaned by using mechanical filters.

Figure 8 for any particular setup is only approximate. Higher coefficient of restitution values than those shown in Table 1 shift the curves upward, while nonlinear series springs added for pulse smoothing shift the curves downward. Precise location of any curve will depend on a particular machine and test setup. If the measured coefficient of restitution during the test is higher than that assumed, the pulse maximum faired amplitude will be higher, and the duration possibly less than expected. This effect can be compensated by reducing the impact velocity necessary and/or adding a nonlinear spring (such as felt or Diene) in series with the primary spring. Enough felt, for instance, could be added to make the noisy pulse

DESIRED PULSE	EQUATIONS		VINYLIDENE CHLORIDE
HALF-SINE 2000g 1.3 ms (ΔV = 683 in/sec) (a_m = 772,000 in/sec^2)	① $V_i = \frac{\Delta V}{1+R}$		
94 lb CARRIAGE AND TEST ITEM (M = 0.244 lb-sec^2/in)	② $S = \frac{Ma_m}{A}$	STRESS (psi)	
	③ $L = \frac{MV_i^2}{2AU}$		

TWO POSSIBLE SPRING DESIGNS

FROM ① :	IMP. VEL.,	V_i = 437 in/sec	V_i = 437 in/sec
SELECT:	AREA,	A_1 = 26.5 sq. in.	A_2 = 13.3 sq. in.
FROM ② :	STRESS,	S_1 = 7,100 psi	S_2 = 14,200 psi
FROM FIGURE:	SP. ENERGY,	U_1 = 67 in-lb/cu-in	U_2 = 290 in-lb/cu-in
FROM ③ :	LENGTH,	L_1 = 13 in.	L_2 = 6.0 in.

Fig. 9. Vinylidene chloride spring designs from stress-specific energy data

31

smoother. (The felt increases the time for the velocity of the upper surface of the spring to reach carriage velocity at the pulse start, thus reducing the traveling stress wave amplitudes, see Figs. 2 and 7.) As felt is added, the primary spring length must be shortened, or the pulse duration will increase. Generally, a clean pulse will be generated if a felt thickness equal to or greater than 0.06 times the primary spring thickness is used in a test setup having an initial strain rate of 70 to 100 in./in./sec.

Figure 10 shows the shock pulse generated with the spring design of Fig. 9 (plastic spring area, 13.3 sq in., length, 6 in.; felt, same area, 0.37 in. thick). The felt, in smoothing the generated pulse, made the shape resemble neither a half-sine nor haversine when normalized, but produced a shape somewhere between the two. Also shown in Fig. 10 is the calculated dynamic stress-strain curve for the pulse. Strain is represented as the ratio of the total deformation of both felt and plastic springs to the original length of the plastic spring. Point A, where the modulus of elasticity becomes constant, corresponds to the maximum positive jerk location of the recorded shock pulse, occurring at the 565-g (4000-psi stress) level. (The maximum jerk for a half-sine pulse occurs at zero amplitude, for a haversine, at the 50 percent level of the maximum amplitude.) The shape of the stress-strain curve of Fig. 10 compares more favorably with the general appearance of the theoretical stress-strain curves of a haversine (Fig. 11) than the curve does with the general appearance of the theoretical half-sine stress-strain curves (Fig. 12). Further discussion of theoretical pulse generation is found in Ref. (1). The present example indicates, to some degree, the problem of generating specified shapes.

The effect of different machine sizes or spring designs on a shock pulse was examined using the same specific energy level and initial strain rate. Two spring designs of the same materials (laminated phenolic and felt) and two carriage weights were selected (Fig. 13). Test results are shown in Fig. 14. The pulse shapes were nearly the same, both resembling a poor haversine. Stress was about 11 percent lower than expected and velocity change 19 percent lower with the parallel spring arrangement. Pulse rise and fall times should have been the same for each arrangement. A lower carriage rebound velocity for the larger machine indicated possible misalignment between carriage and spring impact surfaces. Slight differences in the nominal felt thickness or density also could have contributed to the loss in coefficient of restitution, because the ratio of felt thickness to the phenolic thickness was 0.12. Since one carriage weighed about 18 times the other and multiple contact areas existed in one setup, it is generally agreed that the comparison was satisfactory.

Liquid

Another shock spring material deserving special consideration is liquid. All liquids are somewhat compressible and are highly elastic. A variable rate liquid spring can be a versatile spring, especially when a wide range of shock durations, amplitudes, and carriage weights are involved in testing. Three designs of variable rate liquid springs are currently used at Sandia Corporation. Two of the designs require volume changes, while the third has a constant volume.

One variable rate liquid spring, commercially available, depends primarily on varying the effective fluid volume in generating various duration pulses (Fig. 15). Personnel can control the effective volume of fluid (spring rate)
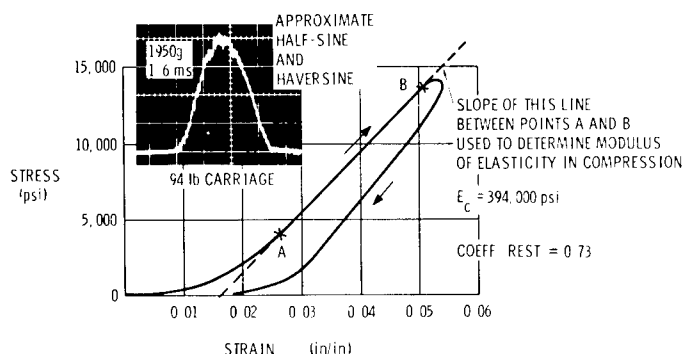
Fig. 10. Dynamic stress-strain curve of shock spring for particular shock test
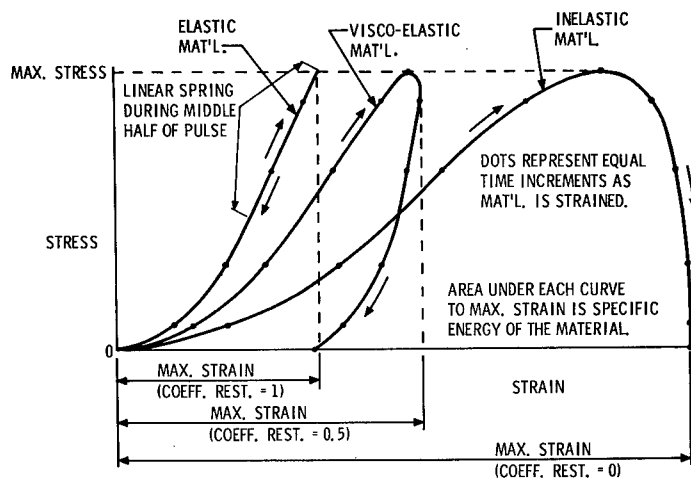
Fig. 11. Theoretical dynamic stress-strain curves
of various materials for haversine pulse generation

by rotating the piston to position an internal
separator. During the positioning, fluid can
flow from one side of the separator to the other
through an open check valve. During the shock,
the external piston assembly is driven into the
cylinder, and the check valve closes to prevent
rapid passage of fluid. The maximum load
rating of the spring can be maintained for any
spring rate setting.

This type of liquid spring is necessarily
heavy for a given size because of the great
pressures contained in the cylinder during the
shocks. Sometimes this weight can be used to
extend the amplitude and duration capabilities

of a machine by mounting the spring on the base
instead of on the carriage.

Because the piston in a liquid spring can-
not be made completely massless, its initial
contact with a surface will cause severe ring-
ing to be superimposed on the pulse. There-
fore, a nonlinear spring must be introduced in
series with the liquid spring. The company that
manufactured the changing volume liquid spring
furnished several nonlinear springs and also
advocated using other mechanical filters to
eliminate a large amount of the noise on the
basic pulse by isolating both the liquid spring
and the test fixture from the carriage.
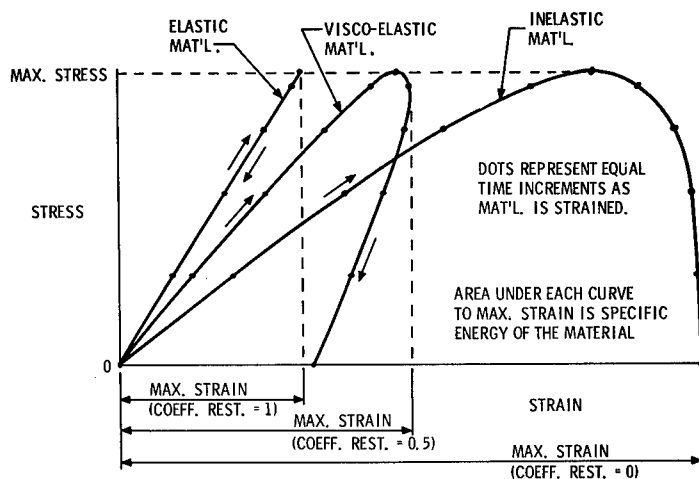
Fig. 12. Theoretical dynamic stress-strain curves
of various materials for half-sine pulse generation

33

LAMINATED
PHENOLIC
1.0 in DIA.,
0.5 in LONG.
FELT, 1 in DIA.,
0.06 in THICK.
SPRING QUAN. 1 EA.
12.3 lb CARRIAGE

LAMINATED PHENOLIC, 3.0 in DIA., 1.0 in LONG.
FELT, 3 in DIA., 0.12 in THICK.
SPRING QUAN. 4 EA. 219 lb CARRIAGE.
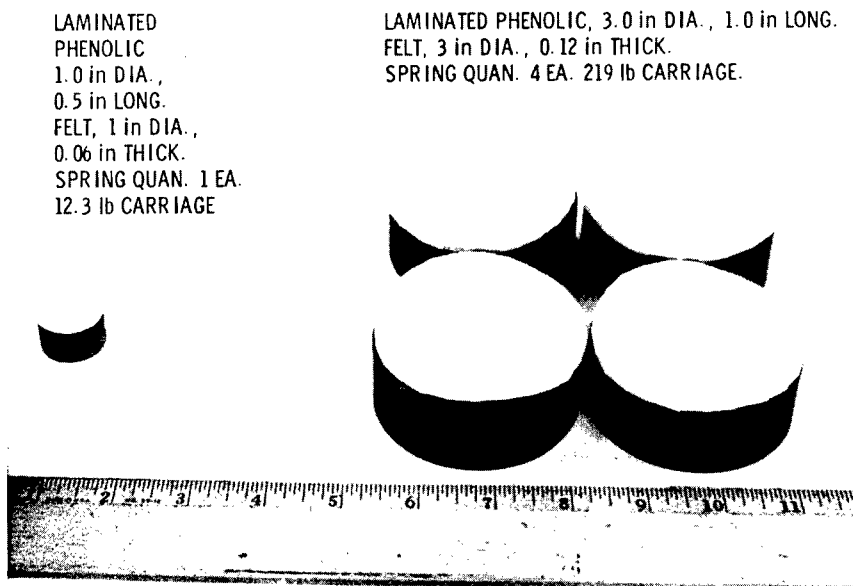
Fig. 13. Two laminated phenolic spring setups

101 in/in/sec	INIT. STRAIN RATE	100 in/in/sec
6120 psi	STRESS	5420 psi
103 in-lb/cu-in	SP. ENERGY	100 in-lb/cu-in

12.3 LB CARRIAGE

219 LB CARRIAGE

50 in/sec	VEL. IMP.	100 in/sec
390g	MAX. ACCEL.	700g
0.90 ms	DURATION	0.90 ms
0.40 ms	RISE TIME	0.35 ms
210g - ms	VEL. CHANGE	340g - ms
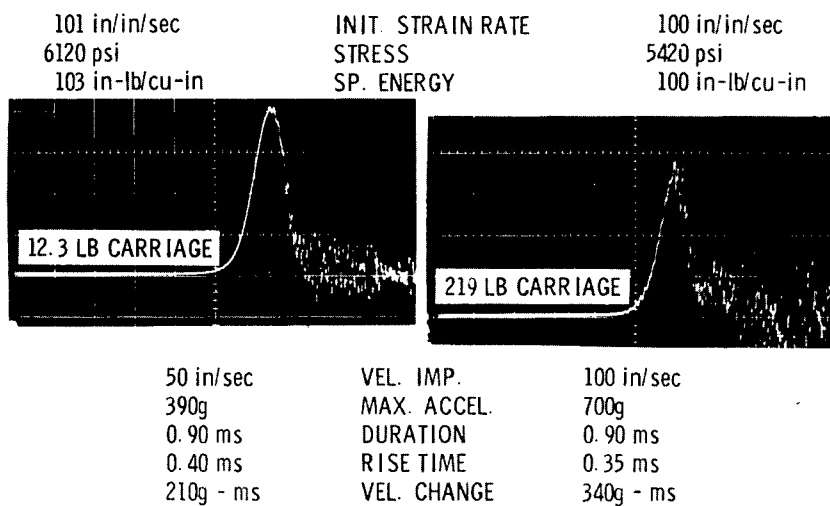
Fig. 14. Comparisons of two different shock tests
on laminated phenolic springs
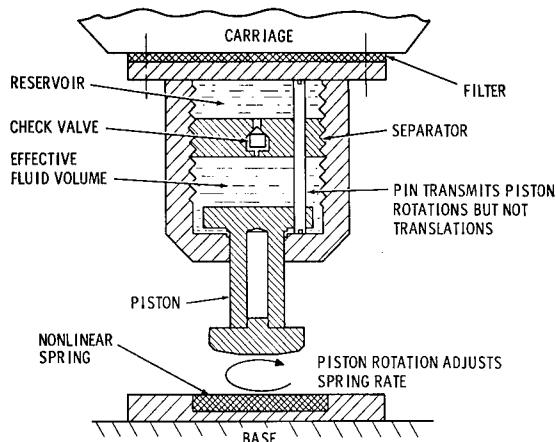
Fig. 15. Commercial variable rate, changing volume, liquid shock spring

One commercial spring, weighing 95 lb, and the filtering technique have been evaluated on two impact machines, an elastic cord accelerated type and a free-fall type, with the carriages (including test item but excluding spring weight) weighing 100 and 250 lb, respectively. Tests were conducted with the spring fastened to the carriage or to the machine base. While the spring rate range varied from 16,000 to 100,000 lb/in. at a maximum load of 42,000 lb, the coefficient of restitution of the spring varied from 0.9 to 0.6, respectively.

Figure 16 shows half-sine pulses at two duration selections with the spring fastened to the 100-lb carriage of the elastic cord accelerated machine. Durations were continuously variable between the values shown. The spring load was about 38,000 lb. In each record, the top trace is the acceleration measured directly on the carriage, and the bottom trace is the acceleration measured on a 23-lb fixture isolated from the carriage by a butyl rubber pad

7 in. square by 0.12 in. thick. The fixture was fastened to the carriage by four each 3/8-in. diam bolts torqued to 15 ft-lb. All pulses were unfiltered electrically, so fixture isolation showed some improvement in clean pulse generation.

Figure 17 shows how pulse amplitudes were increased by placing the spring on the base instead of on the carriage. Unfortunately, the pulses became haversines before they were made sufficiently clean, so the pulse durations were longer than they would have been for half-sines. For each case, different nonlinear spring materials had to be used in series to achieve the desired pulse smoothing.

Figure 18 shows the effects of two different types of mechanical filters used to smooth a given shock generated on the 250-lb carriage machine. Again, all pulses were unfiltered electrically. The left-hand picture was obtained when the mechanical filtering suggested by the company was used on a lower natural frequency carriage than recommended. A satisfactory right-hand record, however, was obtained when a small cylinder of Diene (0.5 in. diam by 1 in. long) was placed between the liquid spring piston and the carriage. The Diene was flattened, but immediately afterwards was manually remolded. These records illustrate the need for custom pulse smoothing for each particular shock machine.

A second type of variable volume spring is the contained Diene spring. This is considered a liquid spring because Diene in a free state is either quasi-solid or quasi-liquid, depending on the time element involved, and a similarity exists in the manner of spring material containment. In a free state at room temperature, a ball of Diene (1 in. diam) flattened due to its own weight to a puddle (2 in. diam) in 19 hr.
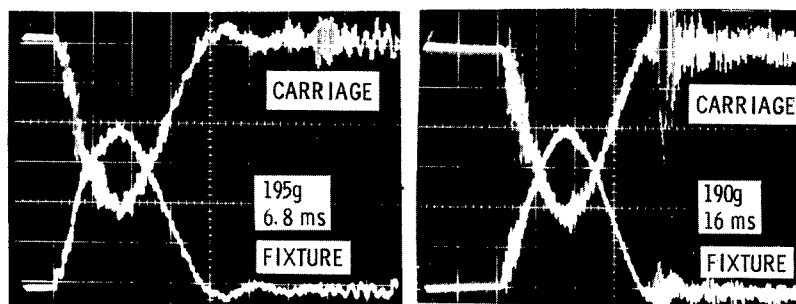
Fig. 16. Typical shock pulses from commercial variable rate liquid spring mounted on carriage of elastic cord accelerated machine

35
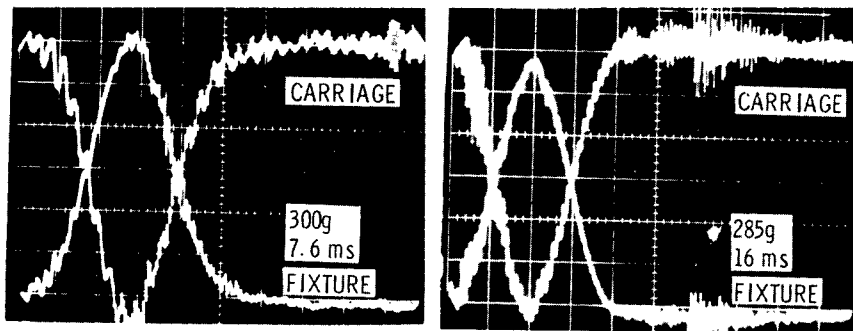
Fig. 17. Typical shock pulses from commercial
variable rate liquid spring mounted on base of
elastic cord accelerated machine

When compressed dynamically, its coefficient
of restitution was approximately 0.16 (Table 1),
indicating material flow. When the Diene was
contained in a cylinder, its coefficient of resti-
tution increased to 0.84, as high as any other
solid or liquid spring used.

Figure 19 is an exploded view of the com-
ponent parts of a Diene spring. No seals were
required around the piston. The Diene was so
viscous that no appreciable leakage occurred,
nor did the piston separate from the cylinder
with rebound velocities experienced. The
spring is made by drilling a hole into a volume
of steel, fitting a piston with a clearance from
0.001 to 0.002 in., and selecting a quantity of
Diene and a thin piece of felt. Spring rate is
controlled by the piston area and by the volume
and apparent bulk modulus of Diene, as shown
in Eq. (4):

$$k = \frac{A_p^2 B}{Q} , \qquad (4)$$

where

k = spring rate (lb/in.),

A_p = effective piston area (sq in.),

B = apparent bulk modulus of contained
material (psi), and

Q = volume of contained material (cu in.).

Figure 20 shows shock pulses (haversines
when normalized) produced by the Diene spring
for two different carriage weights and impact
velocities. Stresses (equal to the internal
pressures) and specific energy levels of con-
tained Diene can be compared to the same
properties of the other materials in Fig. 8.
Contained Diene ranks along with Delrin-500,
except that higher stress levels are possible.
In Fig. 20, the apparent bulk modulus during
compression was essentially constant for the
upper half of each pulse, but differed in the two
setups. This change occurred partly because
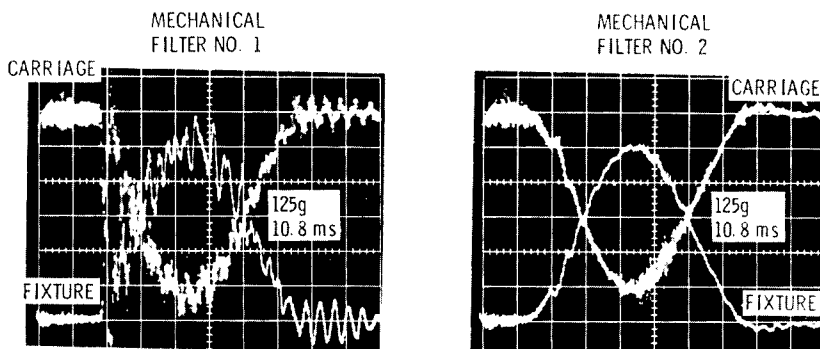
Fig. 18. Mechanical filter effect on pulse smoothing

36

STEEL CYLINDER

"DIENE"

STEEL PISTON

1 in
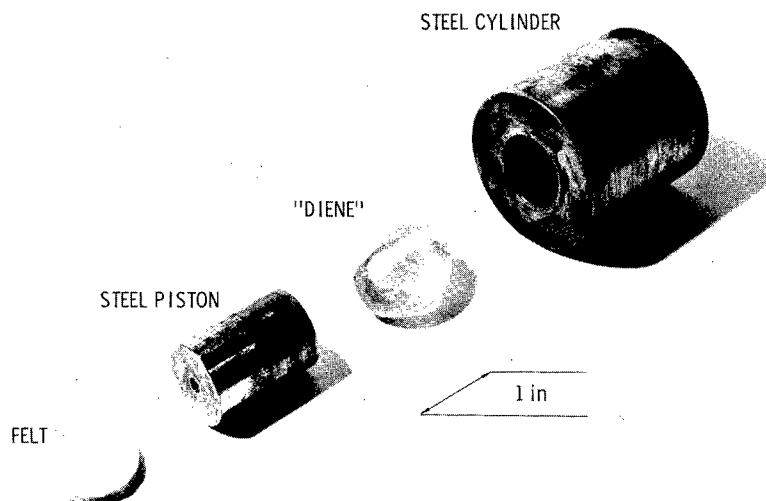
FELT

Fig. 19. Exploded view of contained Diene shock spring

the felt compression during shock was considered part of the Diene compression and because many contained materials do not have a constant bulk modulus. The maximum apparent bulk modulus for each setup was 452,000 and 468,000 psi which corresponded to spring rates of 327,000 and 354,000 lb/in., respectively. The maximum load for either spring rate was 26,000 lb.

The spring of Fig. 19 was subjected to dynamic compression when it was stabilized at the extreme temperatures of -65°F and +160°F. All mechanical properties appeared to be the same as properties at room temperature with one exception: at -65°F, the coefficient of restitution dropped to 0.74.

A variable rate constant volume liquid spring and accessory equipment are shown in Fig. 21. Inside the cylinder are two nonmiscible fluids, such as turpentine and glycerin, with different compressibility factors. Adjusting the ratio of the two volumes by a pump changes the spring rate of the liquid spring. Graduated reservoirs indicate the partial volume of each fluid in the cylinder.

Static load-deflection tests of one spring containing turpentine (80 percent by volume) and glycerin/water mixture (20 percent by volume) indicated the maximum spring rate was 441,000 lb/in. in a 60,000- to 120,000-lb load range. Changing the partial volume of each fluid to turpentine (20 percent) and glycerin/water

| 1300g 1.2 ms | 14 lb CARRIAGE | 100g 4.5 ms | 260 lb CARRIAGE |

185 in./sec	CARRIAGE IMPACT VEL.	56 in./sec
22,300 psi	INTERNAL CYL. PRESS.	31,900 psi
730 in-lb/cu-in	SPECIFIC ENERGY	895 in-lb/cu-in
452,000 psi	MAX. BULK MODULUS	468,000 psi
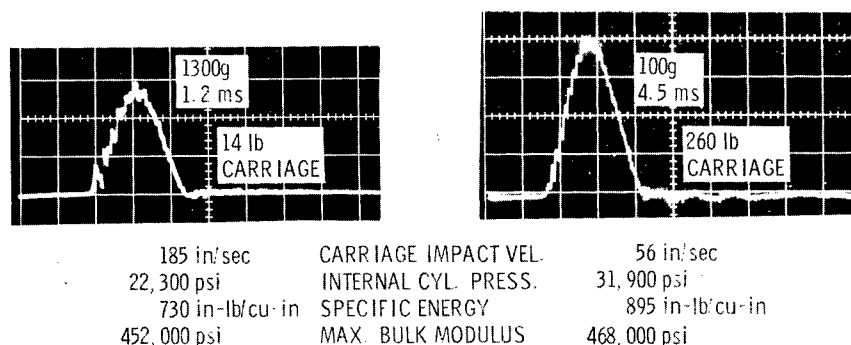
Fig. 20. Shock pulses generated by contained Diene shock spring

37
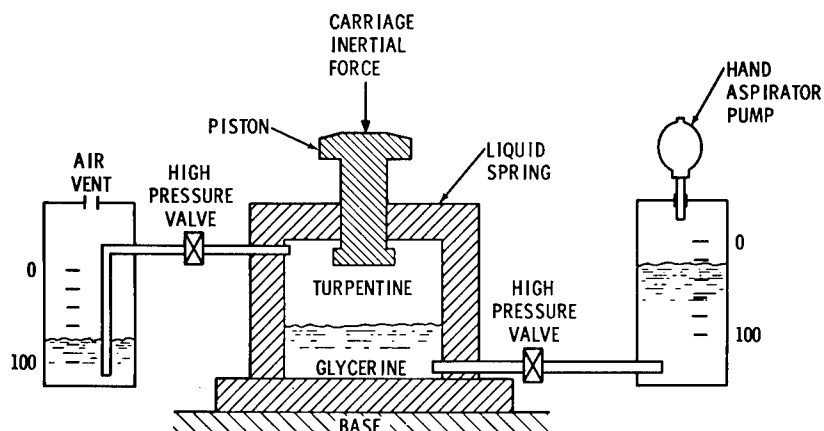
Fig. 21. Constant volume, two liquid,
variable rate liquid shock spring

mixture (80 percent) indicated the maximum
spring rate was 616,000 lb/in. in the 60,000-
to 120,000-lb load range. (The glycerin/water
mixture had a volume ratio of 4/1.) Other fluid
combinations could increase the spring rate
range, but the total available range would prob-
ably be less than that of a changing volume
spring. Actual static bulk moduli correspond-
ing to the two spring rates above were 374,000
and 523,000 psi, respectively. Dynamic tests
were performed and the results were compared
to the static test results. Figure 22 shows
electrically unfiltered records of the triangle
pulse monitored directly on the carriage. Felt
(3 in. diam and 0.25 in. thick) was used between
the spring piston and the carriage. The dynamic

spring rate was found to be 77 percent of the
corresponding static spring rate. The coeffi-
cient of restitution was approximately 0.81.

CONCLUSIONS

Half-sine pulses can be generated on im-
pact shock machines, though this shape only
occurs in a limited range of stress and specific
energy levels for different materials. In gen-
eral, a low modulus material like rubber can
be used for long-duration low-amplitude half-
sine pulses, while higher moduli materials
such as found in plastics can be used to gener-
ate high amplitude short-duration pulses. Both

| 80% | TURPENTINE | 20% |
| 20% | GLYCERIN/WATER | 80% |

260 in/sec	CARRIAGE IMPACT VEL	220 in/sec
25,000 psi	CYLINDER PRESSURE	23,600 psi
640 in-lb/cu-in	SPECIFIC ENERGY	460 in-lb/cu-in
291,000 psi	BULK MODULUS	399,000 psi
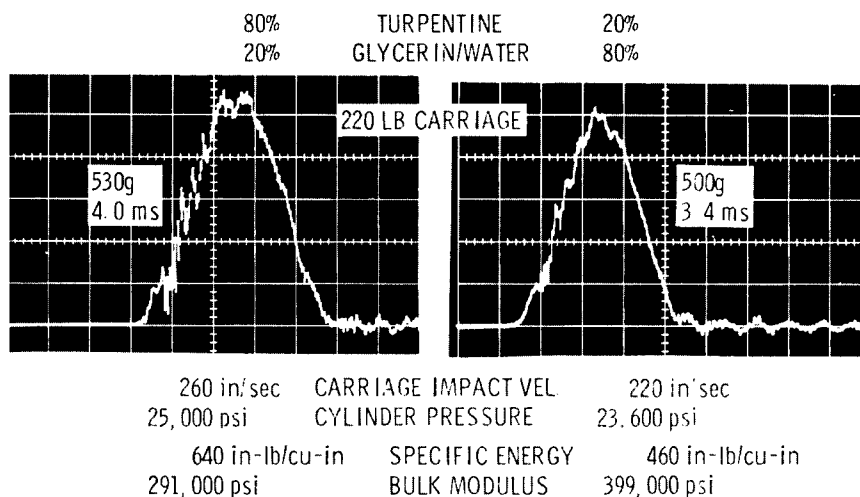
Fig. 22. Pulses obtainable with constant volume
variable rate liquid spring

of these materials are relatively cheap. Liquid springs, while more expensive, can be used over a wide range of shock durations for a given load. Quasi-liquid springs can be made cheaply and appear to be similar to plastic springs in performance. If not overstressed, liquid and plastic springs can last indefinitely. Unfortunately, the half-sine pulses generated by any medium are usually noisy when the carriage impact velocity is greater than 100 in./sec. The pulses can be made cleaner by placing nonlinear springs in series with quasi-linear springs, but when this is done, the generated pulses tend to become haversines.

A triangle pulse, while often specified, is difficult to generate because of three discontinuities in its shape. When these pulses are generated, the sharp corners are rounded, giving most triangles a haversine or parabolic cusp appearance. Triangle shapes can be obtained using rubber, polyethylene, or liquids in a narrow range of the stress-specific energy curves. Again, noise is a problem, and its suppression means using an additional nonlinear spring in series with a nonlinear spring. Of all symmetrical shapes, the triangle seemed to be the most difficult to generate.

Parabolic cusp shapes can be generated with nonlinear springs such as rubber and Ensolite. Unfortunately, the maximum amplitude is hard to control accurately for many shocks even though the pulse velocity change may be constant. These pulse shapes are usually quite clean.

The haversine shape is the easiest to generate and is relatively free from noise over the largest range of shock conditions. It is the only classical shape of the four considered that has no discontinuities in its profile. The haversine is the best shape that could be standardized to eliminate confusion in the identification of a recorded shape.

Test setup techniques and dynamic properties of several materials are now available to design springs to produce new shock conditions on selected machines. The use of multiple springs in series and/or parallel arrangements will widen the possibilities of pulse shapes and conditions.

REFERENCES

1. R. O. Brooks, "Shock Springs and Pulse Shaping on Impact Shock Machines," Sandia Corp. Tech. Memo. SCTM 65-443, Sept. 1965

2. "Sandia Corporation Standard Environmental Test Methods," SC 4452C(M), July 1964

3. R. O. Brooks, "Shock Testing Methods," Sandia Corp. Tech. Memo. SCTM 172-62A(73), Sept. 1963, pp. 57, 59-62

4. C. M. Harris and C. E. Crede, Shock and Vibration Handbook (McGraw-Hill, New York), 1961, Vol. I

Appendix

MATHEMATICAL EXPRESSIONS OF FOUR CLASSICAL PULSE SHAPES

Half-sine:

$$a = a_m \sin\left(\frac{\pi t}{t_b}\right) \qquad 0 \leq t \leq t_b$$

Haversine:

$$a = \frac{1}{2} a_m \left[1 - \cos\left(\frac{2\pi t}{t_b}\right)\right] \qquad 0 \leq t \leq t_b$$

Triangle:

$$a = \frac{2a_m}{t_b} t \qquad 0 \leq t \leq \frac{t_b}{2}$$

$$a = 2a_m \left(1 - \frac{t}{t_b}\right) \qquad \frac{t_b}{2} < t \leq t_b$$

Parabolic cusp:

$$a = \frac{4a_m}{t_b^2} t^2 \qquad 0 \leq t \leq \frac{t_b}{2}$$

$$a = 4a_m \left(1 - \frac{t}{t_b}\right)^2 \qquad \frac{t_b}{2} < t \leq t_b$$

where

a = amplitude at any time t ($a = 0$ for $t > t_b$);

a_m = maximum amplitude; and

t_b = pulse duration at base line.

DISCUSSION

Mr. Root (Collins Radio Co.): Have you used this mechanical filtering beyond 50 fps or so? This is where we start to get into trouble at Collins.

Mr. Brooks: We do use it as far as 90 fps. Eventually, we will be going up to 150 fps because the techniques will still work. All that is necessary is to have a certain ratio of mechanical filter length to the normal spring length. The ratio which I have found to work in most cases is about 12 percent. In other words, the filter dimension will be one-eighth of the spring mentioned.

Dr. Vigness (U.S. Naval Research Lab.): I am not too sure that he should call this a filter to begin with. It is just something to change the spring constants when the impact is first beginning. However, it might be called a filter. It is merely a matter of semantics. Anyhow, it seems to work quite nicely. I might make two comments: We have often used polyurethane for the spring material, and we find it is much tougher than rubber or any of the other rubber-like materials. Also, if lead or a plastic material is used and if there is a little grease or uncleanliness on the impacting surface, the type of impact will be changed enormously.

* * *

SHOCK TESTING A SPACECRAFT TO SHOCK RESPONSE
SPECTRUM BY MEANS OF AN ELECTRODYNAMIC EXCITER

G. A. Gallagher
M.I.T. Lincoln Laboratory
Lexington, Massachusetts
and
A. W. Adkins
Littleton Research and Engineering Corporation
Littleton, Massachusetts

A spacecraft is shock tested by means of an electrodynamic shaker, using shock response spectra instead of pulse wave forms as test criteria. The specified spectrum was that of a 0.4-ms, 375-g peak half-cycle sine pulse.

Obtaining a clean pulse for 100- to 200-lb test specimens to such a specification is virtually impossible for a shaker of 24,000-lb peak random capacity, because damping of ringing encroaches severely on shaker capacity. Ringing, however, contributes appreciably to the shock response spectrum and is useful, rather than troublesome, when the spectrum is the test criterion. Rigid body calculations would indicate that the shaker was used successfully at more than eight times its rated capacity. Such calculations do not properly represent the phenomenon, although they are sometimes used.

The technique has been successfully used for shock testing a family of satellites. There appears to be no alternative technique now under development for producing high-frequency shock spectra in large test items, except in ordnance testing. Here again, the shock response spectrum is used as the test criterion. Obvious advantages in using the electrodynamic shaker for shock testing are economies of equipment and test setup time.

INTRODUCTION

The short duration (0.4 ms) of the half-cycle sine pulse specified for the Titan IIIA shock environment necessitated development of a new shock test technique for the Lincoln Experimental Satellite (LES) family.

Although a conventional drop test machine would give a reasonably clean pulse for component testing, it would not do so for the complete spacecraft. The same difficulty was experienced when attempts were made to shock test the spacecraft with an electrodynamic shaker.

As is probably true in most cases, the important property of the shock was its shock response spectrum, defined as the maximum acceleration experienced by a simple resonator subjected to a given shock, plotted as a function of the natural frequency of the resonator. It is a mathematical property of the shock input and is not related to the test specimen response (1). The actual shock data on which the specification was based did not remotely resemble a half-cycle sine pulse, or any other simple pulse form. The half-cycle sine pulse merely provided a convenient means of describing the shock; it was chosen only because it had the correct shock response spectrum.

The same shaker which appeared to be inadequate for a 0.4-ms 150-g peak half-cycle sine pulse has proved to be fully capable of producing a shock whose response spectrum is approximately that of a 375-g peak half-cycle sine pulse of the same duration. This shaker is an MB Electronics Model C-126, which is rated at 24,000 lb peak random capacity. In some of the tests the total moving weight, that is,

spacecraft, adapter, slip table and armature, has been as much as 540 lb (Fig. 1). The force required to drive a rigid body weighing 540 lb at 375 g is 202,000 lb. The shaker could be used at more than eight times its nominal capacity because the moving mass was not rigid. Much of this advantage would be lost if ringing were suppressed for the sake of a clean pulse.

TEST PROCEDURE

Figure 2 illustrates the block diagrams for the test equipment and data reduction setups. The test specimen was fastened to the shaker table in the same fashion as it would be for conventional vibration testing. An Exact Waveform Synthesizer, Type 200, was used to generate the input signal to the shaker power amplifier. The output of a monitor accelerometer was recorded on analog tape, and the shock response spectrum was later calculated from the tape record using an analog computer. The monitor accelerometer was mounted at the base of the test specimen to record the appropriate input shock motion.

A dual-trace oscilloscope provided for a photo-oscillograph of the shaker amplifier input signal, in addition to the signal from the monitor accelerometer. The latter gave an approximate indication of the adequacy of the test, but final judgment had to wait for calculation of the shock response spectrum.

Figure 3 shows the photo-oscillograph and shock response spectrum for a typical pilot test. The operator picked a half-cycle sine pulse and adjusted its level so that the monitor accelerometer signal looked as though the shock might be nearly adequate. The shock response spectrum proved to be inadequate in the 1000- to 2000-cps region.

The revised input signal and shock response spectrum is shown in Fig. 4. The new signal consists to two pulses at 1000 cps, followed by two at 2000 cps, and two at 3000 cps. The new spectrum is higher than necessary in the 2000- to 3000-cps region, as perhaps might have been foreseen, and slightly deficient at 650 cps. The shock was judged to be adequate, and further refinement was not attempted.

The trapezoidal pulse form was used mainly because it was easy to dial on the waveform synthesizer. Reversing the direction of the shock is accomplished by reversing the polarity of the waveform synthesizer output signal. The technique has been successfully used in performing shock tests on three generations of LES.

CALCULATION OF SHOCK RESPONSE SPECTRUM

To date, a general purpose analog computer has been used for calculation of the shock
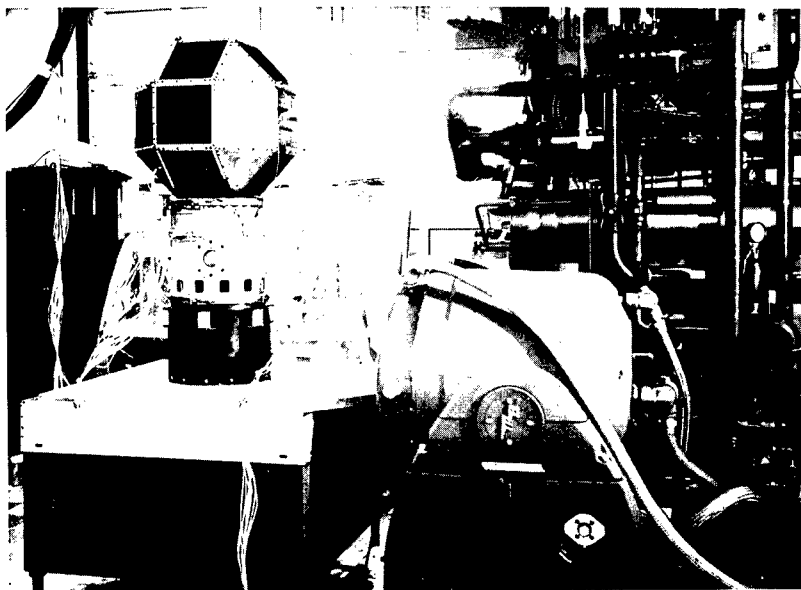
Fig. 1. Prototype LES mounted on slip table for shock and vibration testing

SHOCK TEST SET-UP
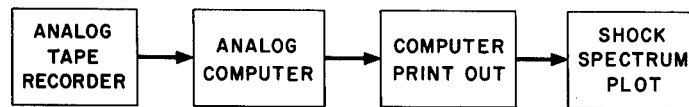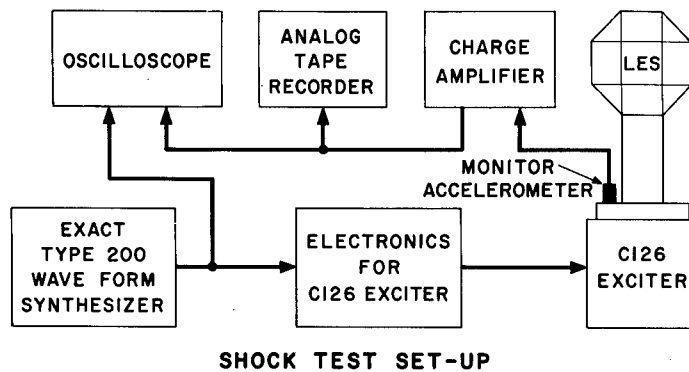
Fig. 2. Block diagrams for equipment setups
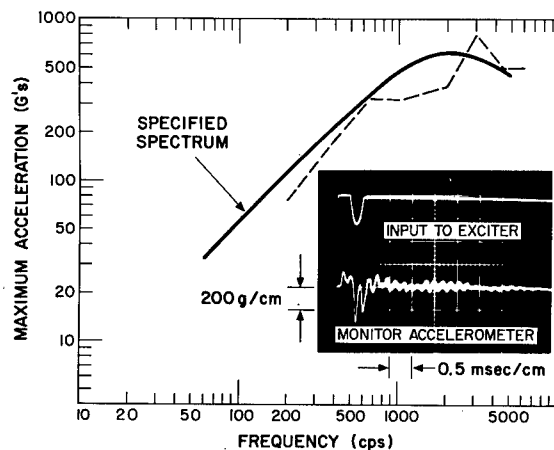
Fig. 3. Shock response spectrum for half-cycle sine input
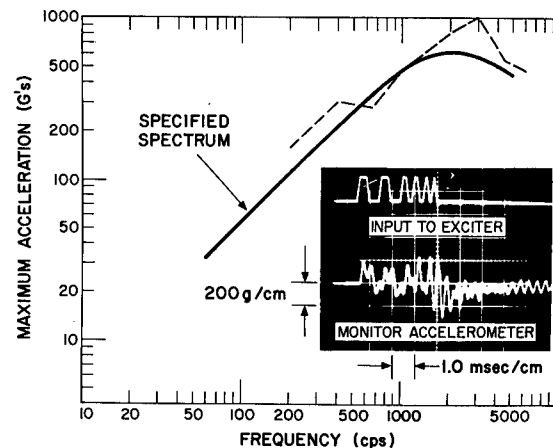
Fig. 4. Shock response spectrum for compound pulse input

response spectrum. It solves the equation for a simple mechanical resonator:

$$\ddot{r} + 2\zeta\omega\dot{r} + \omega^2 r = -\ddot{s},$$

where r is the displacement of the resonator's mass relative to the support, $\ddot{s}$ is the acceleration of the support given by the tape record of the monitor accelerometer signal, ω is the natural frequency of the resonator in radians per second, and ζ is the damping ratio. Dots denote differentiation with respect to time. The acceleration relative to inertial space is

$$\ddot{x} = \ddot{r} + \ddot{s},$$

and this result is drawn by the computer on a strip chart. The equation is solved for some ten values of ω, and the maximum value of $|\ddot{x}|$, the absolute value of the response acceleration, is found for each ω by visual inspection of the ten output charts. This provides for ten points on the shock response spectrum, since $|\ddot{x}|$ is the ordinate of the spectrum and $\omega/2\pi$ is the abscissa.

It should be remembered that ω and ζ are properties of a set of ideal resonators which exist only in the imagination and are in no way related to the test specimen. Although properties of the test specimen do influence the

43

relation between the shaker amplifier input signal and the resulting monitor accelerometer signal, they do not otherwise influence the shock response spectrum. The spectrum is a mathematical property of the monitor accelerometer signal.

The decision to use an analog computer for calculation of shock response spectra was influenced by the immediate availability of a computer and personnel familiar with it. For those who have foreknowledge of the adequacy of the test technique and leisure for planning and preparation, a general purpose analog computer probably is not the best choice.

Whereas the shock response spectrum has usually lagged a day or more behind the test, it would be desirable to present the test operator with the shock response spectrum 10 minutes after performance of the test. If access to a remote digital computer is available by means of a console in the laboratory, as well as an analog-to-digital tape converter and a digital X-Y plotter, reduction of the time lag to 10 minutes should be relatively easy.

Another possible means is suggested by the fact that the simple LCR filter is the electrical analog of the simple mechanical resonator. If the input and output terminals are properly arranged, the output voltage is the analog of the corresponding mechanical resonator acceleration when the input voltage is the monitor accelerometer signal. The monitor tape record could be played back through a band of such filters and the output recorded on a multi-channel oscillograph.

A special purpose analog computer for calculation of shock response spectra has recently appeared on the market (2,3).

CONCLUSIONS

1. A 24,000-lb peak random capacity shaker has been found adequate for testing spacecraft, weighing as much as 195 lb, to shocks whose response spectra are as severe as that of a 0.4-ms 375-g peak half-cycle sine pulse, even though, without a special test setup (4-7), it appears to be incapable of producing a clean pulse of this form for the same test specimens.

2. The capacity of the shaker is not believed to have been reached.

3. Shock testing, when done by a shaker, requires little laboratory equipment beyond that needed for vibration testing.

4. Shock testing by a shaker provides a great saving in time, since the same test setup can be used for both shock and vibration testing.

5. The prospects are good for automated calculation of shock response spectra at reasonable cost.

REFERENCES

1. C. T. Morrow, Shock and Vibration Engineering (John Wiley and Sons, New York), 1963, p. 105

2. J. S. Forte, "Shock Analysis and Synthesis," Rept. Proc. IES, 1965, p. 263

3. "New Shock Testing System by Ling Utilizes Existing Electrodynamic Shaker Fixtures," Environmental Quarterly, 11 (3):38 (Sept. 1965)

4. W. A. Hay and R. M. Oliva, "An Improved Method of Shock Testing on Shakers," Rept. Proc. IES, 1963, p. 241

5. D. J. Dinicola, "A Method of Producing High Intensity Shock with an Electrodynamic Exciter," Rept. Proc. IES, 1964, p. 253

6. W. R. Miller, "Shaping Shock Acceleration Waveforms for Optimum Electrodynamic Shaker Performance," Shock and Vibration Bull. No. 34, Pt. 3, pp. 345-354, Dec. 1964

7. J. M. McClanahan and J. R. Fagan, "Shock Capabilities of Electrodynamic Shakers," Rept. Proc. IES, 1965, p. 251

DISCUSSION

Mr. Schell (AF Flight Dynamics Lab.): Why did you use a shaker rather than a shock machine?

Mr. Gallagher: On the shock machine that we have available in our laboratory, the overall weight of the test specimen and the counterbalance that would be necessary for transverse axes approaches 1000 lb. The drop height required to provide initially the 150-g peak half-cycle 0.4-ms pulse was 0.040 in. This was virtually impossible to do without some exotic means of lifting the drop table this minute amount. It was also discussed with the Monterey Research Laboratory, and a bungee cord system was considered. I was advised at that time that it would require a great deal of development cost and time which we could not afford. It was primarily because of the low energy level and short time duration of the pulse that we used the shaker.

Mr. Lyon (Bolt Beranek & Newman): Did you monitor the vibration levels on the sensitive portions of the spacecraft during the shock test?

Mr. Adkins: We did record accelerations at various points on the satellite.

Mr. Lyon: In that event, could you comment on the relative magnitudes of the acceleration levels at points remote from the point of excitation as opposed to those right at the point of excitation?

Mr. Adkins: They were low. I cannot give you exact numbers, but they were low.

Mr. Bresk (Monterey Research Lab.): In setting up the analog into which the shock pulse was fed, was damping included in the analog at all, or were these undamped systems?

Mr. Adkins: We worked it with 5 percent damping, if I remember correctly.

*   *   *

DESIGN AND PERFORMANCE CHARACTERISTICS

OF A WATER JET ACTUATOR

Robert L. Henderson
Sandia Laboratory
Albuquerque, New Mexico

In response to a need for a velocity generator to provide a 400-fps im-
pact velocity with a 3000-lb test sled, a Water Jet Catapult was designed
and fabricated. The design of the facility is discussed, along with a
description of the major components and the predicted and measured
performance of the facility. Reference is also made to a small low-
velocity generator, designed using the same basic principles.

INTRODUCTION

During the last decade, the science of
weaponry has had to adjust itself to an entirely
new realm of environments. The delivery con-
ditions experienced by World War II bombs
were very different from the environments en-
countered by modern weapons, in either mis-
sile delivery or high-speed low-level aircraft
delivery techniques. As the delivery techniques
have changed, the problems facing environmen-
tal testing organizations have also changed.
One of the major changes, and one which has
caused much concern, is the increase in impact
velocity associated with the new techniques and
the greatly increased shock levels generated by
the impact.

WATER JET ACTUATOR

In the late 1950's, as the changes were be-
ginning to make themselves known, the Environ-
mental Test Facilities Design Division of Sandia
Corporation projected the impending need for a
large-capacity medium-speed shock test facil-
ity. Several types of propulsion systems were
considered before the water jet actuator princi-
ple was chosen. The system was to be patterned
after the Catapult that was then in operation at
Langley Aeronautical Laboratory, Langley Field,
Virginia. There were to be two basic changes
in the system to adapt it to the specific needs
of Sandia.

To aid in illustrating the importance of
these changes, it might be appropriate to de-
scribe briefly the principle of the Water Jet
Catapult that is in use at Langley Field, and
then consider the changes made. The Catapult
is basically a single-bucket linear turbine: a
stream or jet of water is forced through a noz-
zle at a high velocity. This stream impinges on
a turn-around bucket attached to the back of a
sled supported on a set of tracks. The momen-
tum change resulting from the change in direc-
tion of the water results in a force being applied
to the bucket. This force then accelerates the
sled down the track. The Langley facility uti-
lizes an L-shaped plenum chamber to hold the
water and a motor-operated valve to allow the
air to flow from the reservoir into the plenum.
The system is fired by opening a 1/4-turn valve
at the front of the nozzle. The power stroke is
stopped by closing this same valve. Since this
valve is motor operated, the control of power
stroke is not as precise as was desired by
Sandia.

To provide better control of stroke dura-
tion and thereby achieve tighter control of the
final carriage velocity, the motor-operated air
valves were replaced in the Sandia design with
a quick-acting actuator-type valve to admit the
air into the plenum chamber. A frangible dia-
phragm was used at the front of the nozzle
rather than the 1/4-turn valve. This greatly
shortened the lag time between activation of the
firing circuit and the emission of a stable
stream of water from the nozzle. The dia-
phragm was scored to permit rupture at some
nominal pressure (approximately 250 psi). The
lag between the opening of the quick-opening
valve and the rupture of the diaphragm per-
mitted the pressure in the plenum chamber to
reach a maximum value immediately after the
water began to flow, thereby producing an al-
most instantaneous high velocity in the stream

of water and allowing almost the entire quantity of water to be used for the power stroke.

The second major design change was from an L-shaped plenum to a horizontal cylinder with a movable piston to keep the air separated from the water during firing. The position of the piston relative to the nozzle determines the quantity of water expended on each shot, making it possible to vary the duration of the power stroke. By manipulating both the air pressure used to propel the piston and the quantity of water ejected, a continuous set of sled velocities can be obtained between 75 and 400 fps.

Figure 1 is a schematic of the operation of the water jet system.

Air Storage System

The air storage system is composed of four steel vessels obtained through a government surplus depot. They have a volume of 70 cu ft each at a rated pressure of 4000 psi. The manifold system is mild steel tubing pressure tested for operation at 3600 psi. Between each tank and the manifold is a motor-operated valve. The total volume of the manifold is approximately 80 cu ft. This means that with the storage vessels standing at 4000 psi and then opened to allow flow into the manifold, the pressure will drop to 3600 psi. When the quick-opening valve is actuated, the combined pressure losses through the valve into the plenum chamber reduce the maximum pressure attained in the plenum to 3400 psi, or 100 psi below the design pressure of the plenum.

Firing Valve

Figure 2 is a schematic of the quick-opening or firing valve. The operation of the

valve is quite simple. The portion of the valve above the piston is partially filled with oil. Low-pressure nitrogen (125 psi) is introduced above the oil to insure positive seating of the valve. To actuate the valve, high-pressure air is bled from the main air line into the firing chamber. Once the piston has traveled enough to lift the seal ring from the valve body, the fire air pressure is able to act over the entire bottom surface of the piston, forcing the valve to open. As the piston moves upward, the oil is forced through the orifice in the oil chamber. This acts as a viscous damper to help control the speed of the piston. The oil-orifice combination also reduces the piston oscillation which would occur if the piston were stopped by an air cushion only. The valve seal material in the original design was Zytel nylon. Following each of the first two shots, the valve failed to reseal. Disassembly disclosed that the nylon material had been deteriorated by some heating mechanism, as shown in Fig. 3. Explanation of the seal damage was referred to the aerodynamics and materials experts while the second replacement was fabricated from a linen-filled phenolic plastic. At the most recent disassembly, this seal was unmarked and completely serviceable.

Plenum

Figure 4 illustrates the arrangement of the plenum. The plenum piston is a three-piece fabrication, with a 12-ring composition chevron seal. The front and rear sections are manganese bronze castings, and the center section is aluminum. The chrome-plated rod at the rear of the piston acts as a guide and is also used to indicate the velocity of the piston during a shot. The protrusion attached to the front of the piston is part of the piston braking system. The protrusion or snubber enters the nozzle orifice and reduces the area available for water
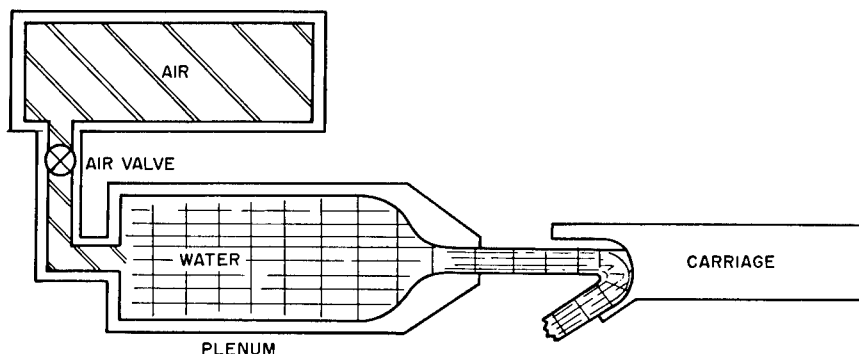
Fig. 1. Schematic of water jet catapult system
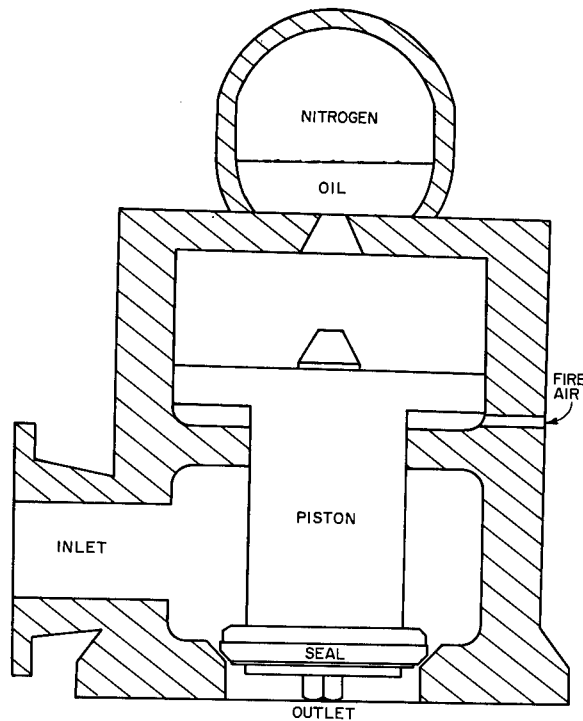
Fig. 2. Firing valve for water jet catapult

flow. This flow restriction results in reduced water flow rate, thereby slowing the piston. The diameter of the cylindrical portion of the snubber is 0.020 in. smaller than the minimum nozzle diameter, resulting in the piston being essentially stopped as the snubber enters the orifice. The open annulus allows the trapped water to escape, and the piston comes to rest against the converging portion of the nozzle. The magnitude of the main deceleration is approximately one fourth that of the piston acceleration for a given shot. Portions of the nozzle and piston coming in contact have matching contours to prevent deformation due to the high air pressure that is still acting on the piston. This residual pressure is approximately 70 percent of the original storage pressure and is contained in the system by the piston. Following a shot, the motor-operated valves between the air storage tanks and the manifold are closed before the pressure in the manifold and plenum is exhausted. This conservation of

Fig. 3. Firing valve seal after first shot,
fire pressure of 1500 psi

49
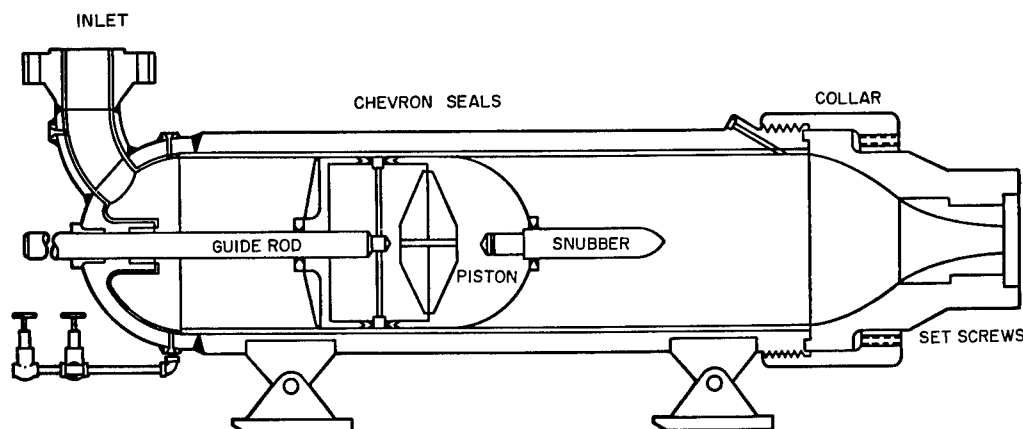
Fig. 4. Plenum assembly for water jet catapult

air pressure in the storage tanks greatly reduces the time required to return the system pressure to a given level.

The plenum itself is a low carbon steel weldment with a stainless steel liner formed on the inside. The contoured section at the rear of the plenum was flame sprayed with aluminum and sealed to prevent corrosion. The nozzle was machined from a stainless steel forging and has a replaceable insert in the throat, in case this area should ever be damaged. The nozzle is held in place by a large threaded collar or nut. The collar is screwed into place and then pressure is applied to the nozzle by a ring of set screws placed in the collar and bearing on the nozzle.

The inside diameter of the plenum is 36 in., and the maximum stroke is about 8 ft. This allows approximately 57 cu ft of water to be expended per shot. The minimum nozzle diameter is 5.6 in. This means the ratio of the velocity of the piston to the velocity of the water ejected is $5.6^2/(36)^2$ or 0.0244, and results in a minimum amount of energy being stored in the moving piston.

For most of the recent shots fired, the portion of the plenum behind the piston has also been filled with water. This reduces the time delay between valve opening and diaphragm rupture and reduces the pressure loss due to expansion into the plenum. This addition also results in the standardization of these two values, regardless of the position of the piston in the cylinder.

Momentum Exchange Bucket

The design of the proper contour for a momentum exchange bucket was the subject of much investigation. It was determined that a parabolic curve allowed extraction of the maximum amount of energy from a jet. A parabolic bucket with a parabolic cross section was optimum. However, as is often the case, theory and fabrication are two different worlds. Forming a parabolic bucket strong enough to withstand the applied loads would have been prohibitively expensive. A compromise was made and the bucket was fabricated from two standard 10-in. stainless steel pipe fittings, a 90 degree elbow and a 45 degree elbow. A 15-in. to 10-in. reducer was welded to the input opening of the bucket to reassure the pessimists associated with the project. The entire bucket assembly was polished to reduce the energy loss due to friction in the bucket.

Braking System

Since it is now known that the carriage can be propelled down the tracks, the next consideration must be stopping it in some controlled manner. In the original facility concept, two test methods were envisioned. The first concept was impact of the carriage into a shock-mitigating or pulse-shaping material attached to a massive impact block, as was done on other impact shock test machines. The second testing method was to stop the sled and allow the test item to continue in free flight into a prepared target. So that the original performance

50

capabilities could be realized, the muzzle end of the track would have to be free of obstructions for the free flight test and also have a large impact block for the standard test. The impact block must be massive and must be supported so that it would appear to have an infinite mass as seen from the impacting sled. The obvious solution to these contradicting conditions was to provide a large impact block supported on a carriage whose wheels rested on large curvature rockers. The block is fabricated in ten 22,000-lb sections to facilitate handling and can be completely removed from the track trough. The rockers provide a system with a very low natural frequency which makes the mass appear infinite, even though it is only about 250,000 lb, including the weight of the carriage.

The different types of tests would require quite different treatment of the test carriage during braking. In the direct impact test, the carriage could, in some cases, follow the test item into the impact material. However, in many cases this would be quite undesirable. Some tests require that the carriage be stopped to allow free flight of the test item into the target. To provide this type of braking action, the contour of the rail cross section was changed for the last 86 ft of track. The standard rail section and the thickened section are both shown in Fig. 5. Also shown is the carriage slipper with brake material locations and clearances. Between the two types of rails is a section that tapers from one to the other.

For the standard tests, where the carriage is impacted into some pulse-shaping material on the front of the impact block, it is imperative that the brakes not engage until after the impact has taken place. The impact block was placed as near the muzzle of the track as practical, which required that the sled travel over a portion of the thickened rail section before impact. To allow this, still providing the braking force necessary to prevent rebound of the carriage back into the nozzle and plenum, a second set of slippers were designed that can travel over both rail profiles; then on impact, an inertia-operated valve opens, dumping air from a small high-pressure reservoir on the sled onto the top of the movable sections of the brakes. This forces the braking surface against the rail, thereby stopping the carriage. The time required for the valve to open, for air to flow through the valve and the connecting tubes and to build up pressure on the braking surfaces prevents distortion of the test pulse due to superposition of the braking force. Since the rebound velocity will always be considerably less than the impact velocity, and since
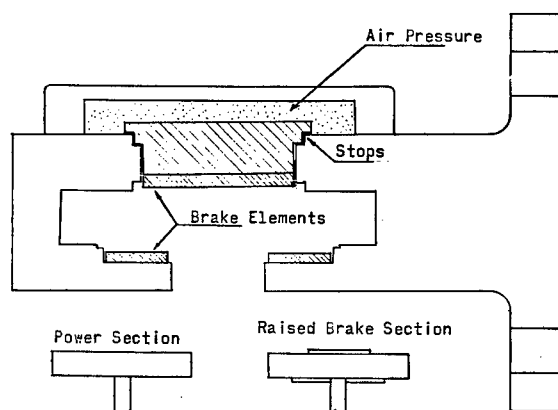
Fig. 5. Cross section of track and large brake slippers

over 150 ft of track are available between the impact block and the plenum nozzle for stopping the sled, the braking area on this set of shoes is much less than on the shoes designed for use with the tapered rail. This makes the shoes themselves much smaller and reduces the forces and moments associated with the impact of the carriage.

A sintered iron brake material was used on both sets of shoes to provide braking force. The sintered material also allows higher brake pressures to be applied without degrading the material and gives a slightly higher coefficient of friction than can be provided by other materials.

Track

The track for this facility has two parallel rails with a length of 186 ft, including 118 ft of standard T-section, 12 ft of transition, and the remainder, the special braking rail. The rails were fabricated in 12-ft sections from stainless steel.

PERFORMANCE

Prior to, during and after the design of this facility, computations were made to determine the performance that could be expected from the device. Since the principle of operation was patterned after the Langley Catapult, the theoretical evaluations were made following the mathematical developments reported by Joyner and Horne (1).

Starting with the familiar expressions,

pv^n = constant for polytropic expansion of air

51

(since the weight of air involved remains constant, volume may be substituted for specific volume), and

$$V_j = 2g \, \frac{144 \, p^{1/2}}{W}$$

for efflux of a noncompressible liquid from an orifice, they develop an expression for the velocity of the water emerging from the nozzle as

$$V_j = V_j^0 \, (1 + C_2 \, t_j) \, \frac{-n}{n+2} \, ,$$

where

$$C_2 = \frac{\left(\frac{n}{2} + 1\right) V_j^0 \, A}{U^{-0}} \, ,$$

V_j = water velocity at any time t_j,

V_j^0 = initial water velocity,

U^{-0} = initial air volume in cubic feet,

n = polytropic gas constant, and

A = area of jet in square feet.

In the case we are considering $A = 0.165$ sq ft, $U^{-0} = 360$ cu ft, $t = 0.75$ sec, and $n = 1.4$. The term in parentheses varies from 1 to 0.9, which would indicate that the jet velocity remains essentially constant.

Using this information and impulse and momentum principles, the approximate equations of motion were obtained as follows:

$$a_c = \frac{1}{R} \, (V_j - V_c)^2 \, ,$$

$$V_c = \frac{V_j^2}{\dfrac{R}{t_c} + V_j} \, ,$$

and

$$S_c = V_j t_c - \frac{R \, \log V_j t_c + R}{R} \, ,$$

where

a_c = acceleration of carriage,

V_c = velocity of carriage,

S_c = displacement of carriage,

t_c = time measured from initial impact of water on carriage, and

$R = w_c / [wA(1 - \cos J)]$, where

w_c = weight of carriage,

w = specific weight of water in pounds per cubic foot,

A = area of stream in square feet, and

J = angle through which water is turned.

Again, since the volume of the storage vessel is so much greater than the volume of water ejected, these approximate equations yield solutions that are almost identical to the exact mathematical solutions.

From the equation for acceleration, the expression for force output of the deflected stream can be obtained as:

$$F = (V_j - V_c)^2 \, wA(1 - \cos J) \, .$$

If we consider a maximum performance shot, the maximum accelerating force can be calculated as 260,000 lb at that instant when the carriage velocity is zero. With this amount of thrust available, it would be expected that a given velocity can be obtained in a shorter distance than is possible with most other velocity generators.

Since completion of the facility, the data obtained in tests have been checked against the predicted performance. Figure 6 shows the comparison between the performance predicted by the equations, as plotted by a digital computer, and the performance measured on one test. Figure 7 is a composite of data collected in actual tests, compared to performance that could have been predicted prior to testing. As it turned out, the only parameter that could not have been predicted accurately prior to testing was the pressure drop between the storage vessels and the back of the piston. Once this value has been established, the performance of the device can be predicted.

Figure 8 is the oscillograph record of a typical shot. There are several significant events shown, e.g., the absence of measurable piston acceleration between the initial impulse and the braking pulse, as well as the apparent linearity of the piston displacement curve. These measurements justify our previous assumption that the piston velocity and the
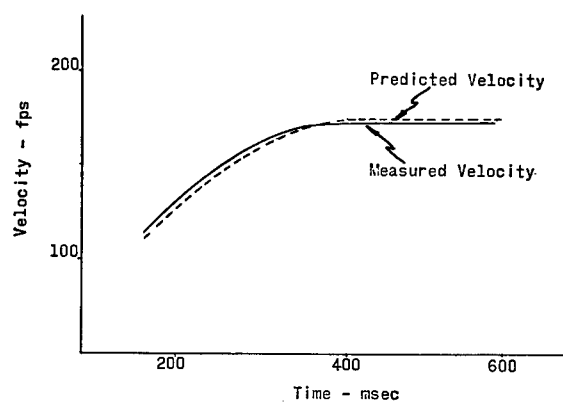
Fig. 6. Comparison of computed
and measured carriage velocity
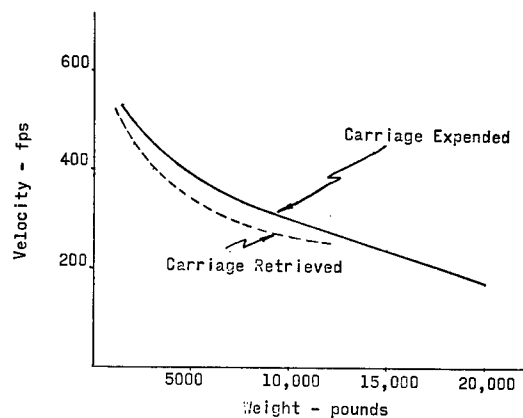
Fig. 7. Predicted maximum velocity
capability of water jet catapult vs
carriage weight
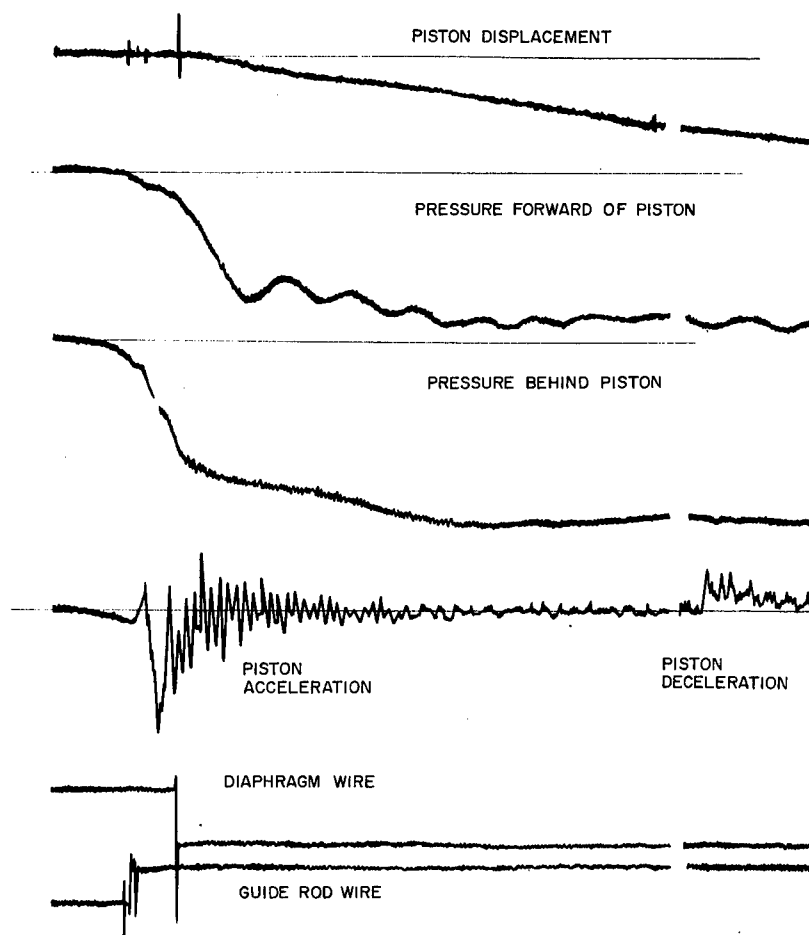
Fig. 8. Typical oscillograph record of water
jet catapult test, all values plotted vs time

resulting water velocity remain essentially constant during a shot. The similarity between the pressure measured in the front and the rear of the plenum (100 psi typical differential) reinforces this contention and indicates that a refined high-pressure seal across the piston is not a necessity. The amplitude of the deceleration pulse indicates that the snubber is indeed performing as designed and that the piston is not impacting against the nozzle. The step functions in the two bottom traces were generated by the breaking of wires attached to the rear of the piston guide column, and to the diaphragm in the nozzle. These traces show that there is a time lag between the start of piston motion and the rupture of the diaphragm. They also show that the pressure in the front of the piston is rising at the time of water emission.

"LITTLE SQUIRT" DEVICE

While the construction and checkout of the Water Jet Catapult was in progress, a similar but much smaller device was being designed and fabricated. This "Little Squirt" is incorporated as a velocity generator to test pullout devices. It has a maximum fire pressure of 50 psi, a nozzle diameter of 0.575 in. and a maximum water velocity of 265 fps. Its bucket was machined into the rear of the test carriage, which weighs 15 lb and has reached velocities of 65 fps.

The design and performance problem areas for this device were much the same as for the Water Jet, with one notable addition. The fire chamber (plenum) and nozzle are not integral parts of the same assembly in the Little Squirt.

In fact, they double back upon one another. The resulting problems of stream stabilization were solved by the addition in the nozzle of straightener vanes which reduced the turbulence of the water and allowed the stream to remain intact.

CONCLUSIONS

Since the performance evaluation of these two facilities has been essentially completed, the results can be summarized in a very simple manner. Whether it be in a large-scale Water Jet or a Little Squirt, a stream of water is a simple, safe, predictable and relatively inexpensive way to accelerate a test carriage along a track. The mathematical expressions that describe the performance of the system are straightforward and accurate. The necessary hardware, with the exception of the nozzle contour, does not require tight machining tolerances. Proper valve arrangement can make it possible to retain much of the air pressure in the system, thereby increasing the time between tests. Some 50 shots conducted on the Water Jet have proved the system to be as repeatable and reliable as any other system now being used to accelerate large masses. The absence of any explosive propellant and the large forces attainable help make this system more attractive to anyone wishing relatively high accelerations, short test tracks, and maximum safety.

REFERENCE

1. U. T. Joyner and W. B. Horne, "Considerations on a Large Hydraulic Jet Catapult," NACA Tech. Note 3203, July 1954

DISCUSSION

Mr. Forkois (U.S. Naval Research Lab.): What is the intactness of the stream itself?

Mr. Henderson: It depends, of course, on the pressures and water velocities. We operate with a power stroke on the sled of about 3/4 sec. The facility was designed for a 100-ft power stroke. In other words, we are able to hit that bucket out 100 ft from the nozzle. With lower air pressures, which means lower water velocities, almost 1 sec of acceleration can be achieved from the system. We shoot about 60 cu ft of water in a full stroke. It is possible to position the piston in the plenum in such a manner that varying volumes of water can be used. This means the power stroke then can vary, but the maximum that we have been able to get is about 3/4 sec.

Dr. Vigness (U.S. Naval Research Lab.): You might mention also the velocity and the velocity time or acceleration time relations for your sled.

Mr. Henderson: This, again, is variable. Velocities have been generated up to 400 fps on the smaller sled. With the maximum stream velocity, we can get a 250,000-lb force on that sled. From this it varies as a difference in the water velocity to the carriage velocities. It goes from the 250,000 lb down, and the accelerations and final velocities would vary.

Dr. Vigness: Your accelerations have been in the order of about 100 g or so?

Mr. Henderson: Yes, on our sled they run about 80 g. We are running with about a 3500-lb sled.

*   *   *

REENTRY OVERPRESSURE SHOCK SIMULATION TEST*

William R. Kampfe
Sandia Corporation
Albuquerque, N. M.

A test series simulating reentry conditions during a possible overpres-
sure blast was conducted on a large reentry vehicle (RV). The dynamic
blast simulation was achieved by impacting a propelled sled into a non-
propelled sled containing the instrumented RV. The impact amplitude
and duration were controlled by having cutter bars on the propelled
sled and shear-shaped metal attached to the nonpropelled sled. The
impact forces were distributed around the RV and applied to its shell
by phenolic microballoons which completely surrounded the reentry
shield surface. Before full-scale testing could begin, scale-model
tests were necessary to develop the material shearing method and to
select the proper material to surround the reentry shield surface.
This testing technique was developed on an 18-in. high g actuator in
approximately 12 months.

INTRODUCTION

The Environmental Testing Department of
Sandia Corporation was originally approached
in June 1962 on possible methods of simulating
reentry conditions during an overpressure
blast. There were two basic problems: to
produce the desired shock pulse and to simu-
late the distributed aerodynamic load on the
surface of the reentry vehicle (RV).

The original desired shock pulse was to
have a 20-ms rise time up to 51 g and then
spike up to 119 g with a rise time of about 0.5
ms, dwell at 119 g for 5 ms, and then decay
back to zero in approximately 25 ms (Fig. 1).
The 5-ms dwell time represents the length of
time necessary for the slowest component in
the system to respond.

The first two phases of the curve are rela-
tively simple to accomplish using shaped honey-
comb or a similar material. The real problem
exists during the decay portion of the pulse.
One remote possibility would be to use a com-
bination of honeycomb, springs, and large hy-
draulic dampers.

It was felt that the desired shock pulse
could be obtained through a metal shearing de-
vice much easier than by the previously men-
tioned method. The metal shearing device will
be discussed in more detail later.

The second problem could be solved by
using a material of varying thickness, which
would be sandwiched between the RV and a
specially designed jig or nest fixture.

It was proposed to mount the RV in a non-
propelled sled cavity on the rocket sled track
so that the longitudinal axis of the RV is hori-
zontal. The RV was to be isolated from the
nonpropelled sled or nest by a sheath of foam
tailored to apply the desired pressure distri-
bution across the surface of the RV. This total
assembly was to weigh approximately 15,000 lb
and would be tested in the following manner.
The assembly would be placed on the track with
slippers so that it would be free to move along
the track. A large mass weighing three times
that of the nonpropelled or stationary sled, or
45,000 lb, would be accelerated by approximately
30 HVAR rocket motors and impacted into the
stationary assembly at a velocity of 150 fps
(Fig. 2). By means of a metal shearing device
placed between the propelled sled and the non-
propelled sled assembly, the desired pulse
shape would be transmitted to the RV (Fig. 3).
The nonpropelled sled or nest fixture was to be
instrumented with 25 flush-mounted pressure
transducers to measure the pressure distribu-
tion over the surface of the RV.

Development of Technique

All of the unknown parameters were deter-
mined in three stages:

Fig. 1. Shock pulse

Note:
  Although the cutter bars are
depicted for clarity as mounted directly on
the rams, the cutter bars were actually taped to the
metal shearing device. Taping the cutter bars to the metal
shearing devices eliminated possible misalignment between the two
sleds and ensured that the cutter bars were struck precisely by the rams.
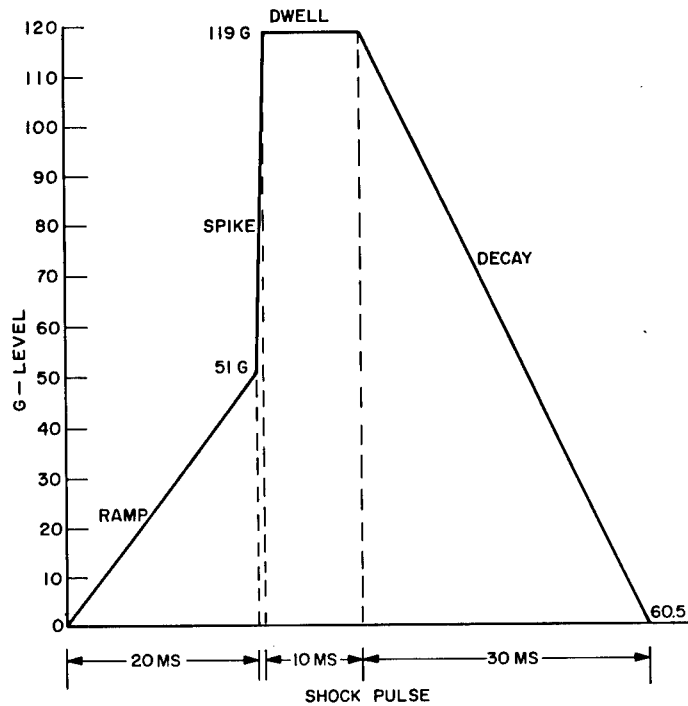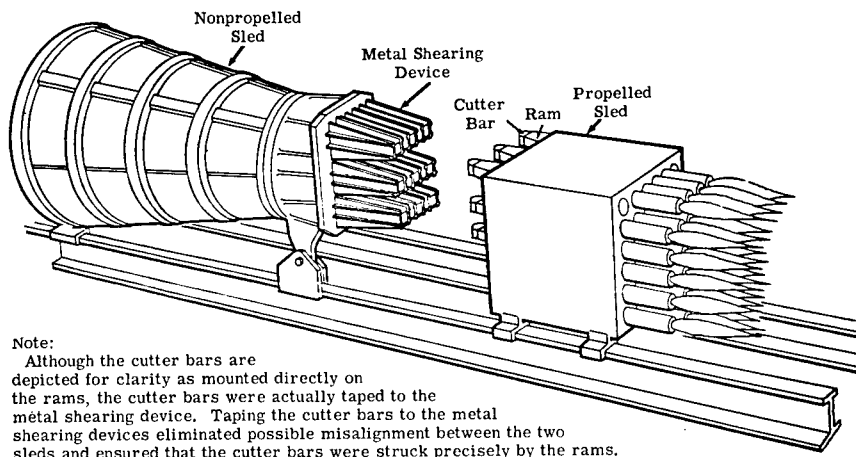
Fig. 2. Propelled and nonpropelled sleds
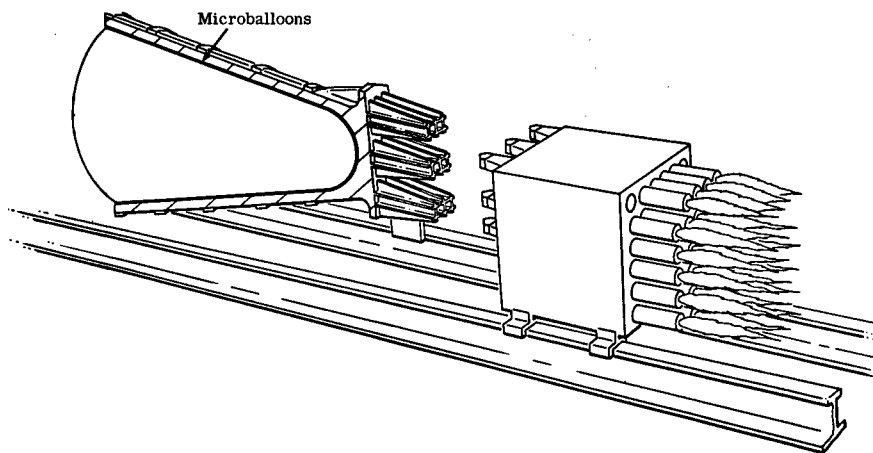
Fig. 3. Cutaway showing microballoons

First — 1/10-scale static and dynamic tests;

Second — 1/6-scale dynamic tests; and

Third — full scale tests.

Scale model tests were a necessity, since the full scale RV was approximately 120 in. long and 90 in. in diameter.

Stage 1

Objectives — The objectives of the 1/10-scale tests were as follows:

1. To determine if rigid foam would give a controlled pressure distribution under static loading;

2. To prove the analysis for determining the correct thickness and densities of rigid foam to be used;

3. To determine the response of the rigid foam under dynamic loading, and

4. To select a material which could be poured and could replace rigid foam.

Test Facilities — Test facilities included a Baldwin Universal test machine, a 15-ft accelerated shock machine, and an 18-in. horizontal actuator.

Test Articles — The test articles consisted of a 1/10-scale aluminum model with ten flush-mounted miniature load cells, an aluminum cavity, and two sheaths of rigid foam.

The miniature load cells were a Sandia design and consisted of a 1/2-in. diameter aluminum column approximately 15/16 in. long with a necked down rectangular cross section 1/8 x 3/8 x 1/2. Two biaxial strain gages were mounted on opposite flats of the necked down area and then wired to complete a four-arm bridge with the longitudinal gages and the lateral gages in opposite arms of the bridge to cancel out bending as much as possible (Fig. 4).

Instrumentation — Ten load cells measured the forces present during the static test with the Baldwin Universal test machine. These load cells were located in a longitudinal plane with five cells located at 0, 22-1/2, 45, 67-1/2, and 90 degrees on the nose, with the five remaining cells equally spaced along the frustum.

Two accelerometers were mounted on the aluminum model and the cavity, and one displacement gage was placed between the 1/10-scale model and the aluminum cavity. These instruments, plus the ten load cells, were used to monitor tests on both the 15-ft accelerated shock machine and the 18-in. horizontal actuator.

Procedure — The following technique was used to determine the proper material thickness for a particular desired pressure. Since phenolic microballoons were finally selected as the material to simulate the aerodynamic loading, their thickness determination will be discussed.

First, the required normal pressures were obtained from the given normal pressure distribution curve for this particular RV when subjected to 119 g overpressure shock (Fig. 5).

57
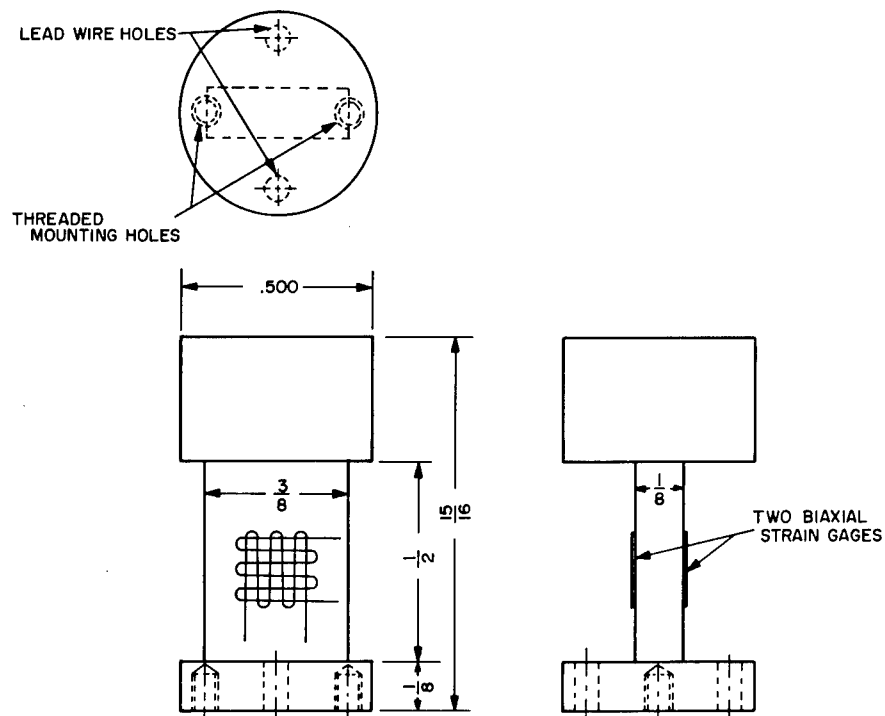
Fig. 4. Miniature load cell
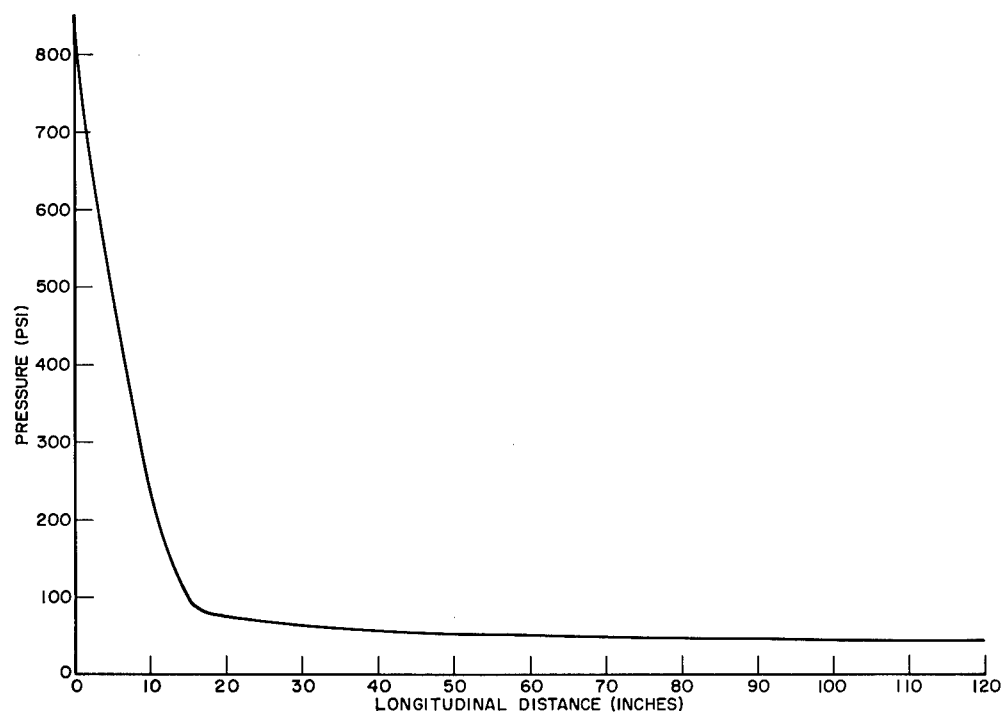
Fig. 5. Normal pressure distribution curve for 119.5 g

The surface of the RV was divided into 18 stations. The spherical portion of the RV was divided into seven stations because it witnessed both high pressures and a large gradient.

By assuming a practical original material thickness at the nose or Station 1, a longitudinal deflection ΔX can be determined by using a stress-strain curve for the material to be used, in this case phenolic microballoons (Fig. 6). The required pressure for Station 1 is 840 psi, and from Fig. 6, a 56.8 percent deflection is necessary to develop that pressure. If the original thickness is 0.272 in., then $\Delta X = 56.8$ percent of 0.272 = 0.154 in. Now knowing ΔX, ΔN for all points can be determined, since the angle α is already known for each point from the geometric shape (Fig. 7). For point 1, $\Delta N = \Delta X$, since cos 0 = 1.

After computing ΔN for all points, and also knowing the percent deflection required to develop the necessary pressure at a particular point, the required thickness can be determined as follows:

$$\text{Required thickness} = \frac{\Delta N}{\% \text{ deflection}} .$$

These values are given in Table 1.

The main drawback of the technique was the fact that the stress-strain curve for the phenolic microballoons was determined statically and not dynamically. However, the curve was corrected somewhat by working backwards using pressures recorded during the 1/10-scale model dynamic drop tests.

Results — A total of seven static tests, 19 drop tests, and four 18-in. actuator tests were conducted using the 1/10-scale model. The first static test and the first four drop tests established the first three objectives; however,
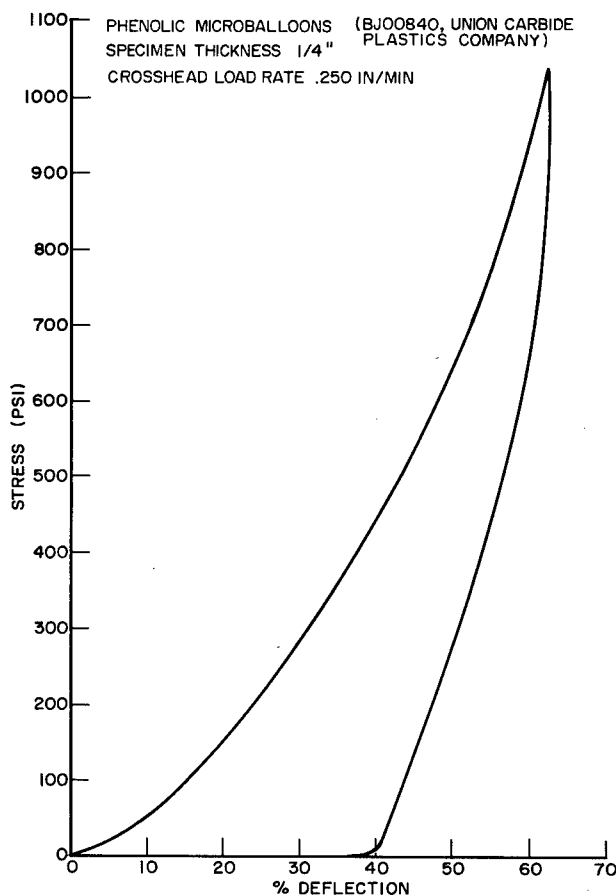
Fig. 6. Phenolic microballoon stress-strain curve

TABLE 1
1/10-Scale Contour Using Stress-Strain Curve

Station Number	Longitudinal Distance (in.)	Pressure (psi)	ΔN Deflection (in.)	Deflection (percent)	Thickness (in.)
1	0	840	0.1545	56.8	0.272
2	0.17	690	0.1423	51.7	0.275
3	0.67	385	0.1087	36.6	0.297
4	1.02	230	0.0858	26.2	0.327
5	1.21	175	0.0732	21.8	0.335
6	1.42	120	0.0595	17.1	0.348
7	1.58	73	0.0333	12.5	0.267
8	2.26	63	0.0333	11.3	0.295
9	3.19	57	0.0333	10.5	0.317
10	4.09	53	0.0333	10.0	0.333
11	4.99	51	0.0333	9.7	0.344
12	5.89	48	0.0333	9.5	0.351
13	6.79	47	0.0333	9.3	0.358
14	7.69	45	0.0333	8.9	0.374
15	8.59	44	0.0333	8.8	0.379
16	9.49	43	0.0333	8.7	0.383
17	10.39	43	0.0333	8.7	0.383
18	12.00	43	0.0333	8.7	0.383

they also established the fact that very close tolerances were necessary in the machining of both the contour and the rigid foam. Also, after close inspection of the prime RV, discontinuities were observed at each of the two joints connecting the three sections of the RV. Therefore, the remainder of the 1/10-scale model tests were used to investigate such materials as glass and phenolic microballoons, partially expanded styrofoam beads, and three different sizes of ground cork, all of which could be poured into the contour cavity between the RV and the nest. Phenolic microballoons were found to be a very satisfactory material for developing the necessary distributed pressure.

Conclusions — It was concluded that Stage 1 fulfilled all four of the original objectives.

Stage 2

Objectives — The objectives of the 1/6-scale model tests were as follows:

1. To develop a metal shearing device for generating the desired shock pulse, and

2. To determine if the pressure transducers could be located in the nest fixture rather than the RV surface.

Test Facility — The 1/6-scale dynamic tests were conducted using an 18-in. horizontal actuator.

Test Articles — The test articles consisted of a 1/6-scale aluminum model with ten flush-mounted pressure transducers and an aluminum nest or cavity sled with nine flush-mounted pressure transducers on the inside contour of the nest. The pressure transducers were identical to those used in the 1/10-scale model. Also, a metal shear fixture and a Stentor tool steel cutter were used.

Procedure — The procedure for determining the material thickness was identical to that of the 1/10-scale model tests. The 1/6-scale model was ballasted to weigh 1/36 that of the full-scale RV. This was done so that the same pressures and accelerations required by the full-scale RV could be applied to the 1/6-scale model, since the area of the 1/6-scale model is (1/6) squared.

$\Delta N = \Delta_X \cos^\alpha$
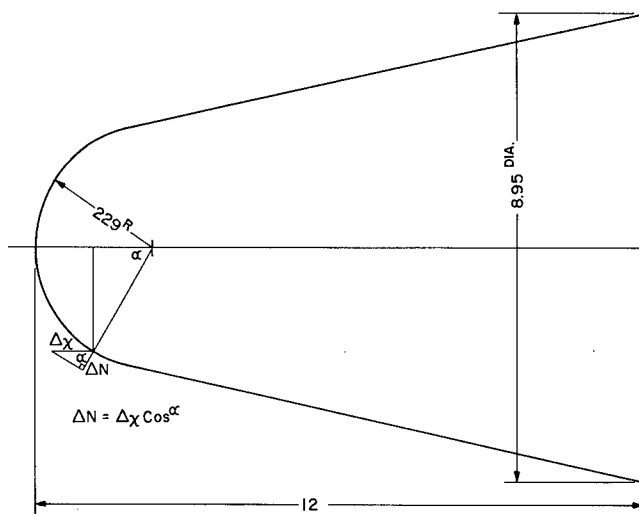
Fig. 7. Drawing of 1/10-scale model

To keep the length of the metal shear device to a minimum and the velocity of the moving or ram sled to a minimum, the moving or ram sled was designed to weigh three times that of the stationary sled or nest sled.

The contour of the metal to be sheared was determined by plotting the acceleration curves of both the stationary and moving sleds and then integrating each twice to determine displacements.

The acceleration curve of the stationary sled was one of the original desired shock inputs (Fig. 8). Since the forces between the two sleds must always be equal and opposite, and the moving sled weighs three times more than the stationary sled, the moving sled acceleration curve has just 1/3 the amplitude of the stationary sled acceleration curve (Fig. 9). Using the conservation of momentum equation, mass of moving sled × velocity of moving sled = mass of both sleds × their final velocity, or

$$M_1 V_1 = (M_1 + M_2) V_2 ,$$

or

$$V_1 = \frac{4}{3} V_2 ,$$

V_2 is determined by integrating the acceleration curve of the stationary sled.

The length of shear metal required to generate the ramp phase up to 51 g is determined in the following manner. From Fig. 8, the moving sled travels 3 ft during the first 20 ms, and from Fig. 9, the stationary sled travels 0.2 ft,

the difference being the length of metal necessary to produce the ramp phase, or 2.8 ft. The remainder of the shear metal is determined in the same manner.

After the first metal shear test, it was established that the force generated was relatively independent of the shearing velocity and only dependent on the metal thickness.

Results — Seven separate metal shear tests were conducted in developing the final metal shear fixture. Figure 10 represents forces generated by various metal thicknesses. The 1008 to 1010 mild steel was found to shear the smoothest.

For the first four metal shear tests, the Stentor tool steel cutter heat-treated to Rockwell C-48-52 was mounted on the ram or moving sled and required precise alignment. Keeping to proper alignment was difficult on the 18-in. actuator and would be even more difficult on the rocket sled track; therefore, a new technique of inserting the cutter in the metal shear fixture or the stationary sled was used on the remaining metal shear tests and was found to be very successful.

Two 1/6-scale dynamic tests were conducted on the 18-in. actuator using rigid foam. These tests indicated that the pressure transducers in the model and the nest mounted opposite one another gave the same reading.

Conclusions — It was concluded that Stage 2 fulfilled both of the original objectives. Also, it was concluded from these tests that the desired 0.5-ms rise time between the ramp and

61
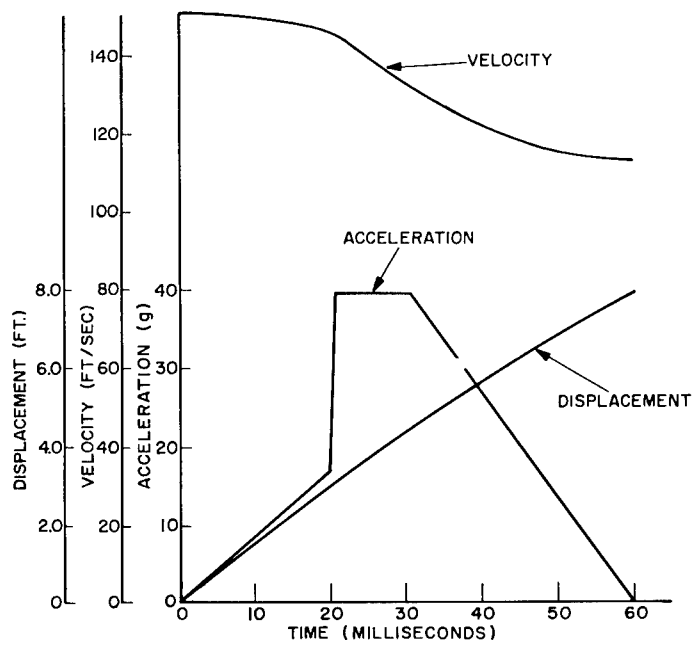
Fig. 8. Moving sled acceleration, velocity, and displacement curves
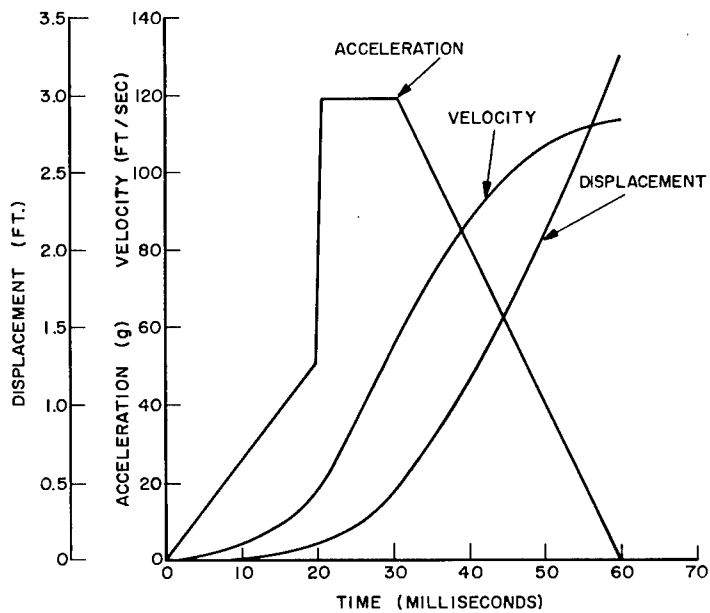
Fig. 9. Stationary sled acceleration velocity, and displacement curves

62
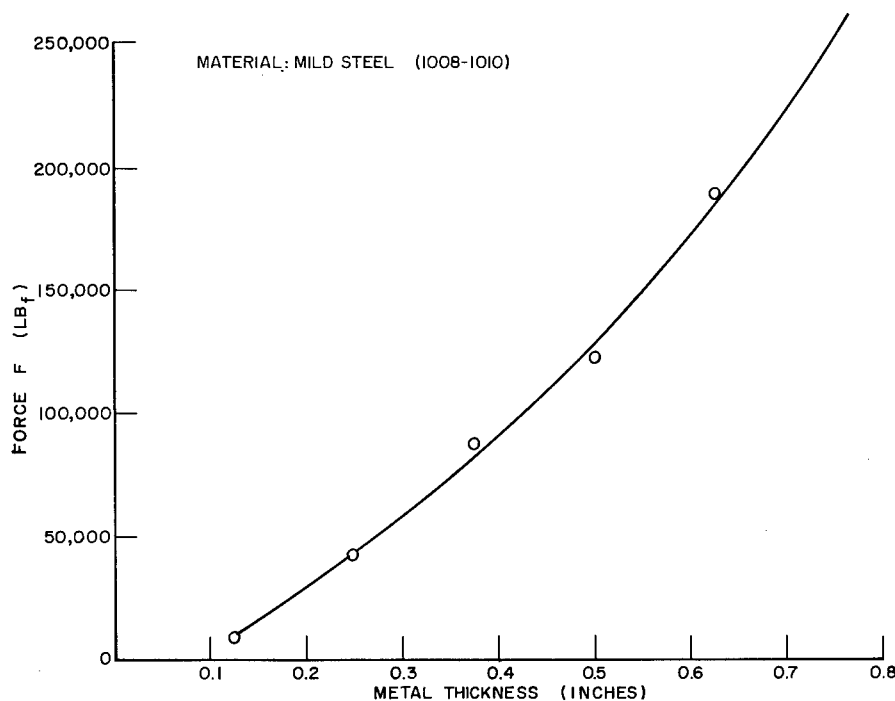
Fig. 10. Results of metal shear tests (four thicknesses of metal shown on the abscissa cut to obtain forces shown on ordinate)

spike phase could not be transmitted through the original 60-in. long metal shear fixture. At this time a new shock input was adopted, which had a 15-ms ramp up to 51 g and then spike up to 119 g with a rise time of about 0.5 ms, dwell at 119 g for five ms, and then decay back to zero in approximately 20 ms (Fig. 11). This modification reduced the length of the metal holding fixture to 36 in.

Stage 3

Test Facility — The sled track for these tests is located in Area III, Sandia Corporation, Albuquerque, New Mexico. The track is used for both impact and recoverable shots. The rails weighed 115 lb/yd with a 4-ft 8-1/2-in. separation. Sleds on which the test specimens are mounted were custom-fabricated and are powered by solid propellant rocket motors. Facility characteristics are as follows:

Length, 3000 ft;
Maximum velocity, 3000 fps to date;
Impact acceleration, dependent on target, specimen and velocity; and
Specimen weight, dependent on sled design.

Test Articles — The test articles for the full-scale tests were as follows:

1. Nonpropelled or nest fixture of aluminum (Fig. 12);

2. Propelled sled of steel (Fig. 13);

3. Nine metal shear fixtures patterned directly from the fixture developed during 1/6-scale model tests (Fig. 14);

4. Three separate reentry vehicles.

Instrumentation — The pressure between the nest fixture and the RV were monitored with 25 flush-mounted Sandia designed pressure transducers located in the nest (Fig. 15).

As many as 58 crystal accelerometers mounted on various RV components were monitored on some tests. Three Statham accelerometers and three displacement gages were also monitored. All instrumentation was monitored by hard-wire through three cannon explosive connectors and approximately 200 ft of cable back to two instrumentation trailers. The nonpropelled sled displaced less than 4 ft during the shock signature; therefore, the instrumentation cable was detached from the nonpropelled sled by activating the explosive connectors after 10 ft of travel.

63
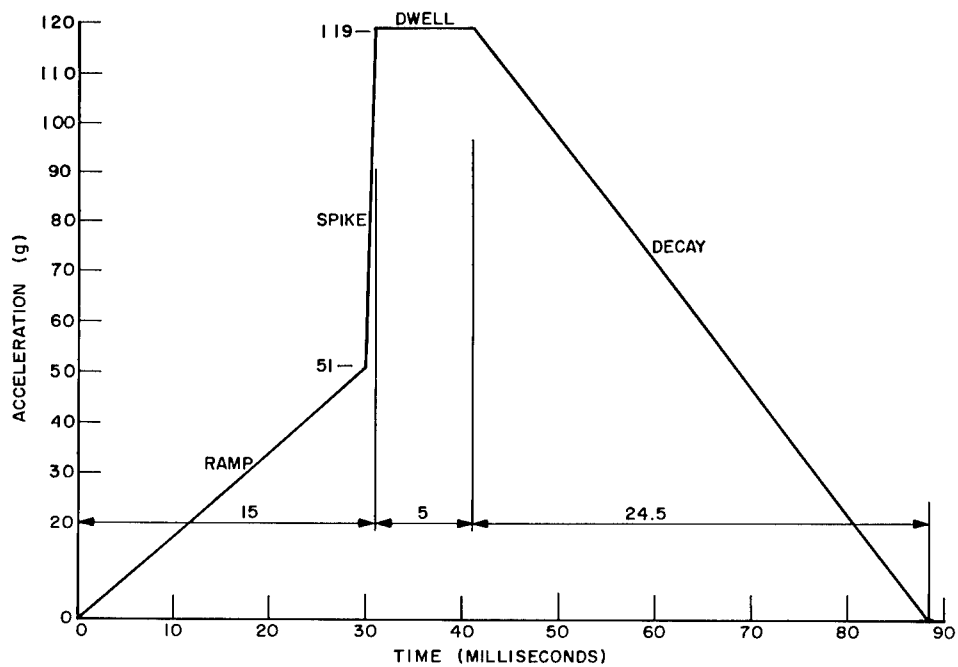
Fig. 11. Final input pulse

Fig. 12. Nest sled

64
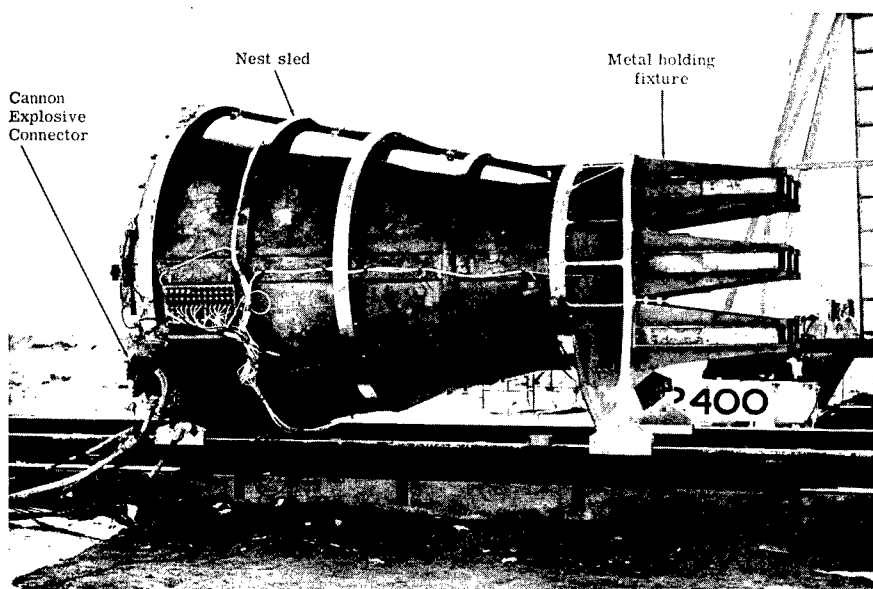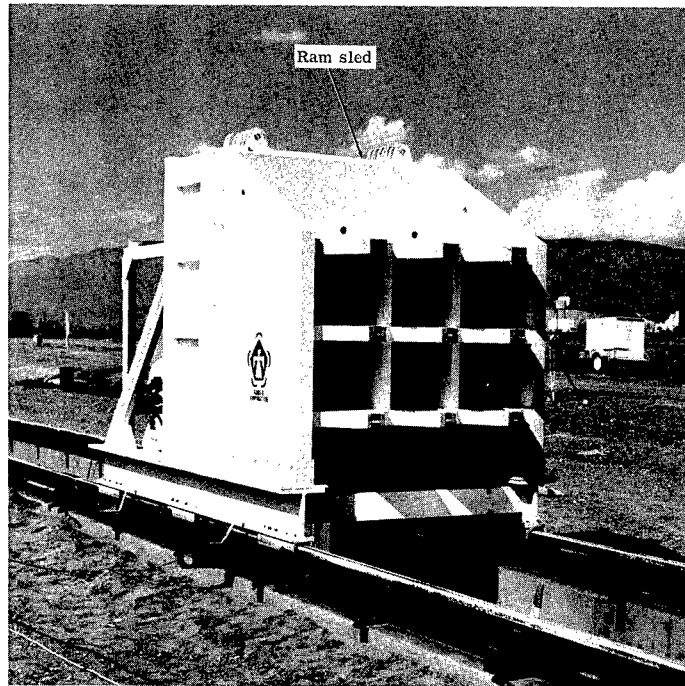
Fig. 13. Ram sled
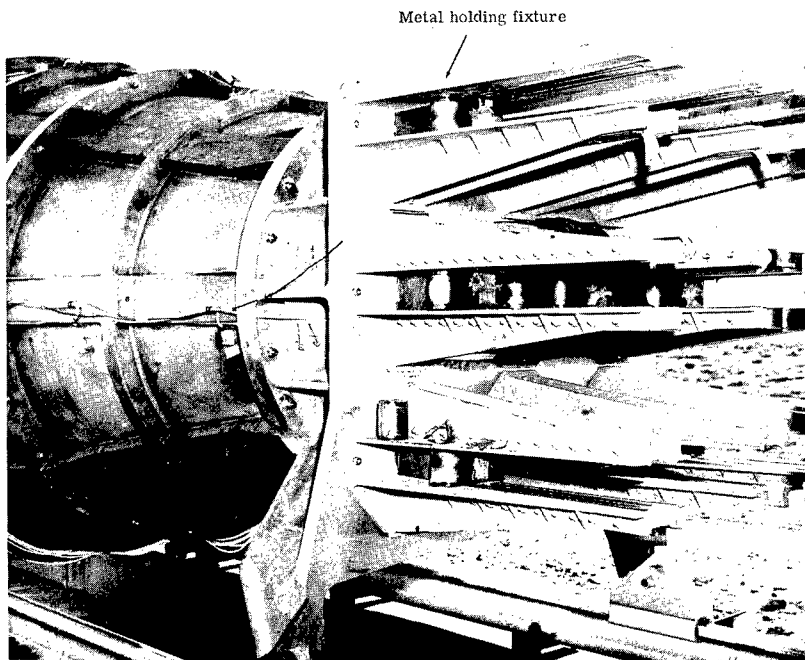
Fig. 14. Metal holding fixtures
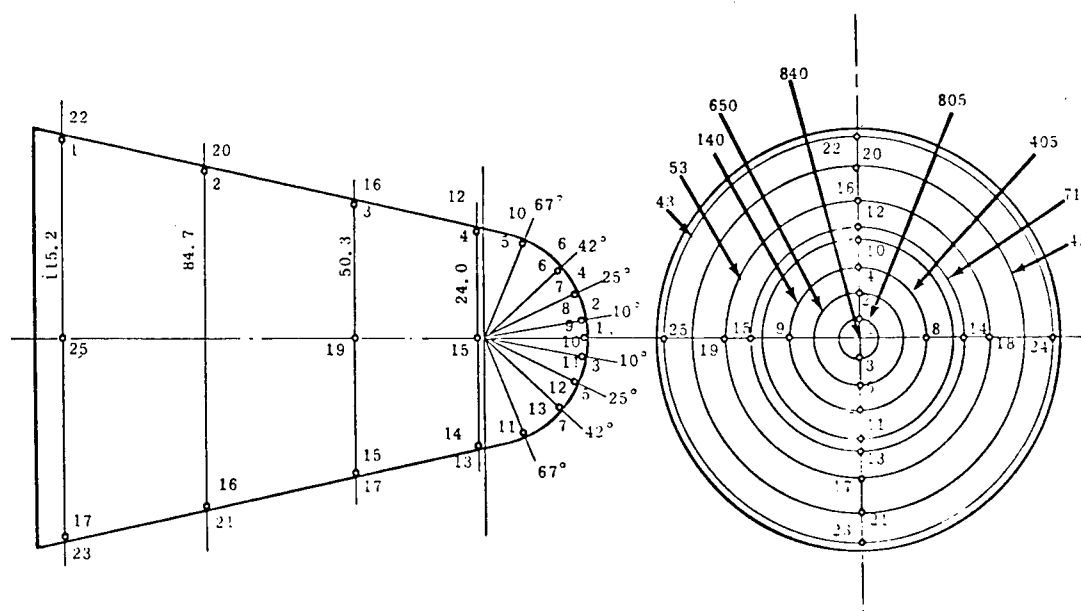
Fig. 15.   Pressure transducer locations

Procedure — The shape of the cavity between the nest and the RV was patterned directly from the scale-model tests. For the test setup, the nest sled (Fig. 12) was pivoted about the front shoes into the vertical position. While in the vertical position, the RV was lowered into the nest, nose down. After the RV was properly aligned in the nest, the phenolic microballoons were poured and vibrated into the gap or cavity between the RV and the nest, and then sealed off with a 1-in. × 1-in. aluminum angle. Next, the nest with the RV was lowered to the horizontal position and the metal holding fixtures were bolted to it (Fig. 12). This entire assembly weighed approximately 15,000 lb. The ram sled (Fig. 13) weighed 45,000 lb. It was accelerated using rocket motors and impacted into the nonpropelled nest sled at a velocity of 100 fps. The maximum force generated during the shearing of the metal was 1,790,000 lb (Fig. 14).

Once the necessary metal thicknesses and lengths were determined for the 100 percent tests, the 1/3- and 2/3-level test loads were developed. Since nine metal shearing fixtures were used, the 1/3-load level was obtained by using metal for developing the 119 g load in only three of the nine fixtures. The 2/3 load level was obtained by using metal for developing the 119 g load in six of the nine fixtures.

All nine of the metal shearing fixtures contained metal for developing the ramp up to the 51 g load for the 1/3- and 2/3-load and 100 percent level tests.

The necessary impact velocities for shearing the required metal for the 1/3- and 2/3-level tests were determined. First, the total strain energy was computed by summing the strain energies for the ramp, dwell, decay portions of the shock pulse, and a safety zone. Calculations were carried out for the 2/3-level test in the following manner. The nonpropelled sled with the RV weighed 15,300 lb. By multiplying this weight by the 51, 96, and 37 g, the following forces were obtained:

$$F = Ma$$

$$= \frac{15,300}{g} \times 51 \; g = 780,000 \; lb \; ,$$

$$F = \frac{15,300}{g} \times 96 \; g = 1,470,000 \; lb \; ,$$

and

$$F = \frac{15,300}{g} \times 37 \; g = 567,000 \; lb \; .$$

By referring to the cross section of the shear metal configuration (Fig. 16),

$$\text{Strain energy in ramp} = \frac{780,000 \; lb \times 1.51 \; ft}{2}$$

$$= 588,000 \; ft\text{-}lb \; ;$$

$$\text{Strain energy in spike and dwell} = 1,470,000 \; lb$$

$$\times 0.395 \; ft = 581,000 \; ft\text{-}lb;$$

66
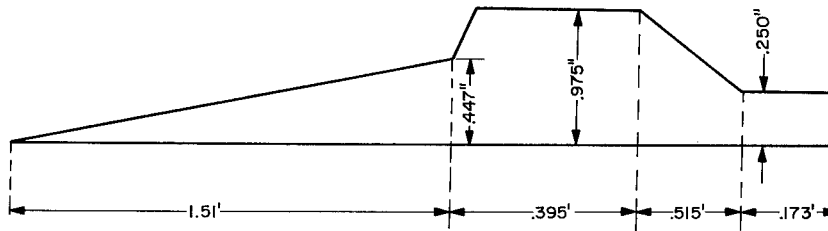
Fig. 16. Cross section of shear metal configuration

Strain energy in decay $= \dfrac{(1,470,000 + 567,000)}{2} \, 0.515$

$= 490,000 \text{ ft-lb}$,

and

Safety strain energy $= 567,000 \times 0.173$

$= 98,200 \text{ ft-lb}$.

Summing all strain energies minus safety zone:

$$
\begin{array}{r}
588,000 \\
581,000 \\
\underline{490,000} \\
1,659,000 \text{ ft-lb}
\end{array}
$$

This strain energy is equal to the difference in kinetic energy of the system before and after impact; that is,

Strain energy = KE before – KE afterwards ,

KE before impact $= 1/2 \, \dfrac{(45,900)}{32.2} \, (V_1^2)$,

KE afterwards $= 1/2 \, \dfrac{(61,200)}{32.2} \, (V_2^2)$.

Since $V_2 = 3/4 \, V_1$,

Strain energy $= 1/2 \, \dfrac{(45,900)}{32.2} \, V_1^2$

$- \, 1/2 \, \dfrac{(61,200)}{32.2} \, (3/4 \, V_1)^2$

$= V_1^2 \, (711.1 - 534.0)$

$= V_1^2 \, (177.1)$.

Transposing,

$V_1^2 = \dfrac{\text{strain energy}}{177.1}$,

$V_1 = \sqrt{\dfrac{\text{strain energy}}{177.1}}$

$= \sqrt{\dfrac{1,659,000}{177.1}}$

$= 96.75 \text{ fps}$.

Results — Nine full-scale tests were conducted. Two tests were conducted on a prototype RV at the 1/3-load level. Seven tests were conducted with a prime RV: one at 1/3, one at 2/3, three at 100 percent, and two at 125 percent load levels. When interpreting the results, it was a major problem to determine accurately the total load that the RV witnessed in any particular test. Both an accelerometer technique and a technique of mechanically integrating the pressure readings were used to determine the total loads.

CONCLUSIONS

This technique for simulating reentry conditions during an overpressure blast had one big drawback; i.e., it did not permit the RV to react as a completely free body as it would in outer space. This limitation was known from the beginning, but it was still felt to be a good simulation for the interior components. The big advantage of this technique was that it was a nondestructive type test, and that a complete postmortem could be performed after each test. Additional information on this program may be obtained from two Sandia reports, SC-WD-64-682, and RS 7331/302.

*   *   *

67

SHOCK TESTING WITH HIGH EXPLOSIVE

INITIATED GAS DETONATIONS*

W. M. Sigmon, Jr.
Sandia Corporation
Albuquerque, N.M.

The development is described of a simple, convenient method of con-
trolling pulse rise times in explosive gas tests. The pulse rise time
on a test item subjected to an explosive pressure loading is a function
of the rate or velocity at which the shock wave sweeps over the affected
surfaces. The sweep velocity is, in turn, a function of the angle at
which the shock wave meets the test item surface.

The method devised for control of rise times, or sweep velocities, con-
sists of using small strands of solid high explosives to propagate the
gas detonation. By properly positioning the explosive strands relative
to the test item surface, a wide range of shock pulse sweep velocities
is possible. This method lends itself well to large or complex shapes.

Tests to investigate the performance of this method were conducted in
four types of setups: (a) frangible wooden chambers, (b) a rectangular
steel chamber, (c) a 16-in. diameter 14-ft long detonation tube, and (d)
a 26-in. diameter 130-ft long tube. The gas mixture ordinarily used
was hydrogen and oxygen, with Primacord as the solid explosive.

Experimental results generally confirmed predictions. Shock front
sweep velocities of as high as 30,000 fps were obtained. The results
indicate that high explosive initiated gas detonations will provide pres-
sure pulses controllable in amplitude, duration, and rise time for blast
load simulation and other shock tests requiring similar pulses.

INTRODUCTION

Pressure pulses from detonating gas mix-
tures have been successfully used to produce
mechanical shock loadings of test items (1).
This technique is particularly useful for labo-
ratory duplication of blast loading conditions.
Basically, the procedure consists of placing the
test item in a tube, gun or other chamber filled
with an explosive gas mixture. Detonation of
the mixture creates a high-velocity shock wave
which impinges upon the test item surface. The
force exerted by the shock wave generates a
shock acceleration pulse, provided the test item
is mounted so that it is free to accelerate. Fig-
ure 1 shows an idealized acceleration-time his-
tory typical of those produced by detonation
wave loading:

Three parameters are ordinarily of prime
importance in designing a shock test using
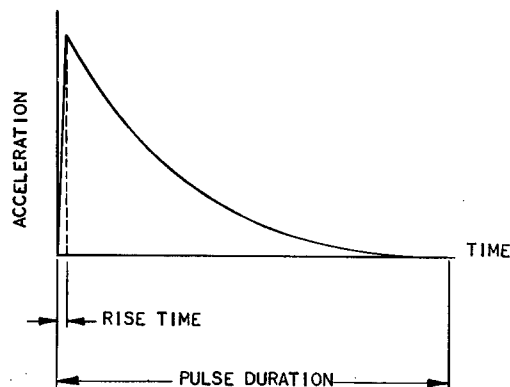
Fig. 1. Idealized blast wave rigid
body acceleration-time history

explosive gases: (a) the peak pressure or ac-
celeration amplitude, (b) the pulse duration,

---

and (c) the pulse rise time. Control of the peak pressure is a relatively simple matter. Both theory and experiment have shown that the peak pressure in a gas detonation wave is essentially a constant multiple of the initial unburned mixture pressure, the value of the constant depending on the composition of the mixture (2-7). Almost any desired peak pressure, and corresponding peak acceleration of a test item, may be obtained by varying the initial pressure and composition of the explosive gas mixture. Previous experiments have also shown that pulse durations may be controlled by proper design of the geometry of the setup, particularly the detonation tube length and volume (8). However, the third parameter of importance, pulse rise time, has received little attention in previous explosive gas work. Therefore, an investigation was launched to develop a simple repeatable method of controlling the shock pulse rise time on a test item subjected to a gas detonation loading.

THEORETICAL DEVELOPMENT

The pulse rise time on a test item subjected to an explosive loading is defined as the time required for the pressure force to rise from an initial value to its peak value. In general, pressure cannot be applied instantaneously to the entire test item surface. Some finite period of time is required for the detonation wave to sweep over the affected areas. This sweep time corresponds to the rise time of the pressure force. The pressure rise time within the wave front itself is only a fraction of a microsecond and ordinarily will be negligible compared to the time required for the wave to travel over the test item.

Pressure force rise time is therefore seen to be a function only of the rate or velocity at which the detonation wave sweeps over the test item surface, for a test item of a given size and shape. Consequently, in the following discussion, sweep velocity, instead of actual rise time, will be the parameter of interest. Sweep velocity, defined as the rate at which a pressure change engulfs a test surface, may differ considerably from the detonation wave velocity. This will be illustrated by the examples of Fig. 2 in which the test item is a simple flat plate.

In Fig. 2a, the plate surface is parallel to the direction of detonation wave propagation. The sweep velocity (V_S) is then identical to the detonation velocity (V_D). In Fig. 2b, the plate has been rotated 90 degrees to face directly into the oncoming detonation wave. Pressure will be applied instantaneously over the entire

surface; therefore, the sweep velocity is infinite and the rise time is zero. Figure 2c illustrates the general case. The surface is oriented at some arbitrary angle (α) to the wave front. Wave velocity (V_D) is the component of sweep velocity (V_S) in the direction of wave travel. The sweep velocity is then

$$V_S = \frac{V_D}{\sin \alpha} . \qquad (1)$$

Another approach which yields the same result is to compute the time required for the wave to travel the length of the test surface projected in the direction of propagation. Referring to Fig. 2c:

$$X_1 = X_2 \sin \alpha . \qquad (2)$$

Also,

$$X_1 = V_D t , \qquad (3)$$

where t is the sweep time interval. Therefore,

$$X_2 = \frac{V_D t}{\sin \alpha} , \qquad (4)$$

and

$$V_S = \frac{X_2}{t} = \frac{V_D}{\sin \alpha} . \qquad (5)$$

Since the two factors which determine sweep velocity are detonation velocity and detonation wave incidence angle, one might reasonably expect to control sweep velocities by varying either or both of these factors. In actual practice, however, relatively little can be accomplished by attempting to change gas detonation velocities. Detonation velocity is a physical constant of an explosive gas mixture, and practically all known mixtures have velocities which fall within the range of 6000 to 12,000 fps (2). Consequently, sweep velocities may be varied by a factor of only two at most by using mixtures having different detonation rates. Therefore, the primary means of sweep velocity control must be by control of the detonation wave incidence angle. While this method of control appeared from the beginning to be more versatile and promising, its development was actually dictated by the need for pressure force rise times with sweep velocities well beyond the maximum velocity of 12,000 fps obtainable from a gas detonation alone with incidence angle, α, equal to 90 degrees.

If the test item were a simple flat plate, such as in the example of Fig. 2, changing the detonation wave incidence angle would only require rotating the plate. This is not possible

WAVE FRONT

V_D, DETONATION WAVE VELOCITY

$V_S = V_D$

V_S, SWEEP VELOCITY

TEST SURFACE

LENGTH, X
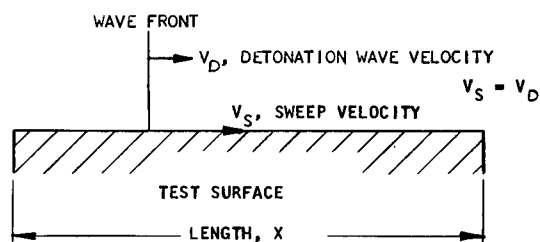
(a) WAVE PROPAGATING PARALLEL TO TEST SURFACE

WAVE FRONT

V_D

$V_S = \infty$
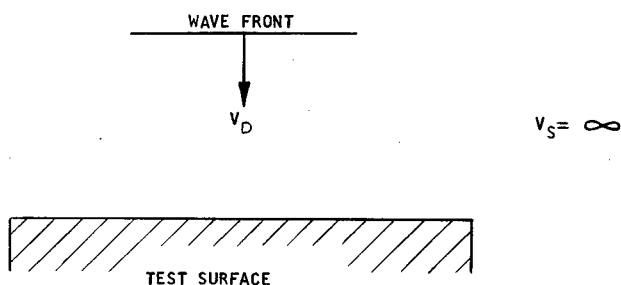
TEST SURFACE

(b) WAVE PROPAGATING DIRECTLY INTO TEST SURFACE

WAVE FRONT

V_D

X_1

α

V_S

X_2

$V_S = \dfrac{V_D}{\sin \alpha}$
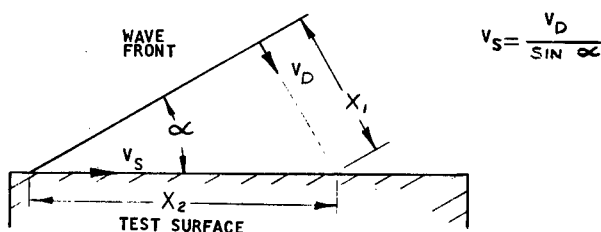
TEST SURFACE

(c) GENERAL CASE, WAVE AT OBLIQUE INCIDENCE WITH TEST SURFACE.

Fig. 2. Examples of detonation wave intercepting test surface

with a more complex shape because all parts of the test item would not be at the same angle with the wave front. A method had to be devised to obtain the proper angular orientation of wave front to test item over all affected areas of the test item simultaneously.

The proposed test method consisted of using small amounts of solid high explosives in strands or strips to propagate the gas detonation. As shown in Fig. 3, the gas detonation front would propagate outward from the solid explosive strand at the gas detonation velocity while the point of initiation would necessarily propagate at the solid explosive detonation rate. Detonation velocities are normally much higher in solid explosives than in gases; values of 20,000 fps or more are common (9). The resulting gas detonation wave would form at some

angle to the solid explosive strand, the magnitude of the angle being a function of the two detonation velocities.

If the gas detonation is assumed to propagate spherically outward from a point of initiation (point 0 in Fig. 3), in some time, t, the wave will have traveled a radial distance, r, given by

$$r = V_D t . \tag{6}$$

During the same time period the solid explosive detonation has traveled a distance, y, given as

$$y = V_E t , \tag{7}$$

where V_E is the detonation velocity in the solid explosive. The angle, β, between the wave front and explosive strand may then be determined:

71

VOLUME FILLED WITH EXPLOSIVE GAS

α = ANGLE OF INCIDENCE OF GAS DETONATION FRONT
β = ANGLE BETWEEN DETONATION WAVE FRONT AND EXPLOSIVE STRAND
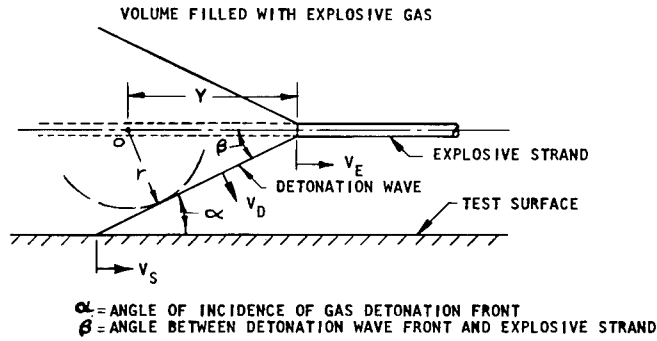
Fig. 3. Detonation wave initiated by solid
explosive strand, strand parallel to test
surface

$$\beta = \arcsin\left(\frac{r}{y}\right) = \arcsin\left(\frac{V_D}{V_E}\right). \qquad (8)$$

Since the angle is a function only of the respective detonation velocities, which are constants, it too will be a constant.

Explosive strand initiation thus provides a convenient means of orienting the gas detonation shock wave relative to a test surface. The simplest case is shown in Fig. 3, where the explosive strand is laid parallel to the test item surface. In this case, the angle between the wave front and the test item is the same as the angle between the wave front and explosive strand, and the sweep velocity may be found by combining Eqs. (1) and (8), noting that $\alpha = \beta$ in this particular case:

$$V_S = \frac{V_D}{\sin \alpha} = \frac{V_D}{\sin \beta} = \frac{V_D}{\sin\left(\arcsin\frac{V_D}{V_E}\right)} = V_E . \qquad (9)$$

That is, for the special case where the initiating explosive strand is parallel to the test surface, the sweep velocity is identical to the solid explosive detonation velocity. Actually, this could have been determined by inspection. If the wave angle remains constant as stated previously, then both ends (the point of initiation and the point of contact) must necessarily travel at the same velocity.

Next, let us consider the general case in which the explosive strand is at some angle ϕ, with the test surface, as shown in Fig. 4. The wave front meets the test surface at the angle α. From inspection of the geometry, it is seen that

$$\alpha = \beta - \phi . \qquad (10)$$

Proceeding as before, combining Eqs. (1), (8), and (10), the general equation for sweep velocity is found as

VOLUME FILLED WITH EXPLOSIVE GAS

ϕ - ANGLE OF INCLINATION OF STRAND TO TEST SURFACE
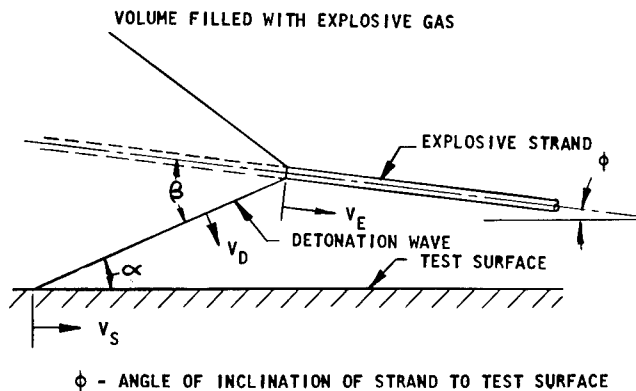
Fig. 4. Detonation wave initiated by solid
explosive strand, general case

72

$$V_S = \frac{V_D}{\sin \alpha} = \frac{V_D}{\sin (\beta - \phi)} = \frac{V_D}{\sin \left(\arcsin \dfrac{V_D}{V_E} - \phi\right)} .$$

$$\text{(11)}$$

Since the denominator in Eq. (11) is a sine function, it will always have an absolute value between zero and one. Therefore, the sweep velocity will always be equal to or greater than the gas detonation velocity; i.e., the gas detonation velocity is the lower limit of pressure wave sweep velocity for a test item being loaded by a solid explosive propagated gas detonation. There is no theoretical upper limit, for as the denominator in Eq. (11) approaches zero, sweep velocity approaches infinity, the case shown in Fig. 2b.

It is to be expected that variations in the angle at which the wave strikes the test surface will have an effect on the pressure exerted on the surface. Two distinct values of peak pressure are associated with a detonation wave in a gas. These are the static pressure and the reflected pressure (5). Static pressure, sometimes called overpressure or sidewall pressure, is the pressure exerted on a surface at right angles to the wave front, as in Fig. 2a. Reflected pressure, also known as total or head-on pressure, is the pressure exerted on a surface facing directly into the oncoming wave, as in Fig. 2b. As one might expect, the reflected pressure is much higher than static pressure because of the kinetic energy delivered by the flowing detonation products. For most explosive gases, reflected pressures are about 2.5 times greater than static pressures (6).

While considerable information is available from the literature concerning static and reflected pressures in detonations, very little has been said concerning the pressure produced by a wave at oblique incidence to a solid surface. For a first approximation, an equation was derived based on the assumption that pressure would be a simple function of the cosine of the angle (α) between the wave front and test surface:

$$P = P_S + (P_R - P_S) \cos \alpha \qquad \text{(12)}$$

where

P = pressure on test surface,

P_S = static detonation pressure,

P_R = reflected detonation pressure, and

α = same as in Fig. 4.

Equation (12) is not an exact relationship, but merely an interpolation of pressures between two known extreme values, those for α equal to zero and to 90 degrees. Another assumption inherent in the foregoing analysis is that the detonating solid explosive strand contributes nothing to the pressure exerted on the test item surface. This condition may not be realized in the actual test setup, and actual pressures are likely to be higher than those predicted by Eq. (12).

One conclusion which may be drawn from Eqs. (10) and (11) is that the angle α must be relatively small if sweep velocities are to be much above the gas detonation velocity. For small values of α, Eq. (12) states that the pressure will be nearly the reflected pressure, P_R. Furthermore, for small angles, the pressures will be relatively unaffected by angle changes which produce considerable variations in sweep velocity. For example, decreasing α from 30 to 15 degrees would nearly double the sweep velocity, but would produce only about 11 percent change in pressure. A test designer would therefore be able to choose different sweep velocities or rise times in a given setup without materially affecting peak pressures and accelerations.

EXPERIMENTAL EQUIPMENT AND PROCEDURES

A number of tests have been performed to study experimentally the behavior of high explosive initiated gas detonations and to develop practical shock test methods using the forces generated by these detonations. The procedures and equipment common to all tests will be described first, followed by descriptions of each type of setup.

For most tests, the explosive gas was the stoichiometric mixture of hydrogen and oxygen, the detonation characteristics of which are listed in Table 1. The hydrogen-oxygen mixture was chosen because the constituent gases are stable, nontoxic, readily available commercially, and relatively low in cost. No special handling procedures are required, other than those required for any flammable gas, and pure water vapor is the only detonation product.

Acetylene-oxygen mixtures were used in several tests. Acetylene mixtures are not generally suitable for the types of tests we are considering because it is unstable at high pressures and produces undesirable detonation products. However, acetylene-oxygen detonations yield approximately twice the pressures

TABLE 1
Detonation Characteristics of Stoichiometric Hydrogen-Oxygen Mixture (5)[a]

Characteristic	Theoretical	Observed
Static pressure (atm)	18.59	18.6
Reflected pressure (atm)	44.18	62.5 pk 33.8 avg[b]
Detonation wave velocity (fps)	9360	9500

[a]Composition: $2H_2 + O_2$ by volume; initial pressure: atmospheric; combustion equation: $2H_2 + O_2 \rightarrow 2H_2O$.
[b]For first 100 μsec of pulse.

of hydrogen-oxygen mixtures under the same initial conditions. In certain instances, the pressure advantage might possibly outweigh the disadvantages in other areas. For this reason, data on acetylene detonations were desired to supplement hydrogen-oxygen data.

The gases used in our tests were drawn from commercial cylinders. A simplified schematic of the metering arrangement is shown in Fig. 5. The required mixture proportions were obtained by adjusting the gas volume flow rates by means of a needle valve and flowmeter in each line. Check valves were also inserted in each line as a safety measure to prevent detonation pressure or flame from reaching the metering equipment and gas bottles. The flowing gases were mixed at a tee connection near the test fixture. Upstream or metering pressures were always at least twice the maximum test fixture pressure so that flow rates would not change appreciably as the test fixture filled.
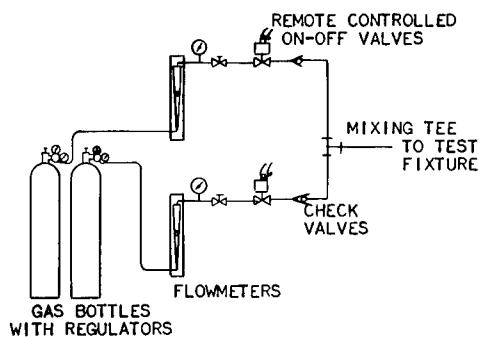
Fig. 5. Schematic diagram of gas metering equipment

Any air initially present in the test fixture had to be removed prior to firing; otherwise, its presence would have degraded detonation pressure and velocity. If the fixture was well sealed, the air was evacuated with a vacuum pump. For unsealed fixtures, the normal procedure was to flush out the air by passing several volume changes of the explosive mixture through the fixture.

The solid high explosive used was a commercial detonating fuse, Primacord, manufactured by the Ensign-Bickford Company. Primacord is a strong flexible cord, of plastic tape and textile braid, containing a core of high explosive. The particular core load used in our tests was 25 grains of PETN per foot of cord. Primacord is relatively insensitive to accidental firing from heat, impact, or electrical discharge. It may be handled with ease and safety, and it is available as an off-the-shelf item, at low cost, from most construction or mining supply houses. When properly initiated, it detonates at the rate of 21,000 fps (10).

The Primacord was initiated by a detonator of the exploding-bridge-wire type, Model SE-1, manufactured by Mound Laboratories. This detonator contains 0.25 gm of PETN plus 0.05 gm tetryl booster. The choice of detonator was based on safety considerations. The SE-1 contains no sensitive primary explosives, and the probability of an accidental firing from heat or static discharge is quite low, much less than that for ordinary blasting caps. The detonators were fired by a special circuit which discharged a 3.5-mfd capacitor at 5000 volts into the detonator bridge wire.

The first tests were performed in frangible wooden chambers such as the one shown in Fig. 6. These chambers were 26.5 in. square, 12 to 18 in. deep inside, and were made of 3/4-in. thick fir plywood walls set on a 1-1/2-in. thick plywood base. The tops were of 0.010-in. thick Mylar plastic film supported on an open wooden grid. Five to nine strands of Primacord were strung through the box parallel with the base surface. These strands were gathered together at one end to a single detonator, and all strands were of equal length between the detonator and the box. The explosive gas mixture was introduced through a hose near the base. Three pressure transducers, enclosed in steel slugs for protection, were mounted in the base, flush with the surface.

The wooden chambers were, of course, one-shot setups, with a new chamber required for every test. However, the chambers were convenient for several reasons: (a) they were
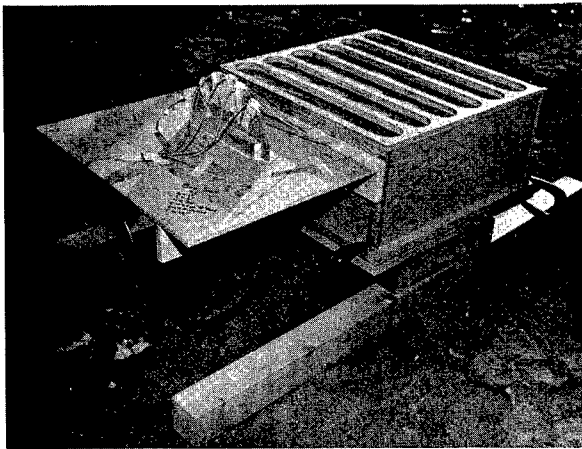
Fig. 6. Typical wooden chamber
explosive test setup

Fig. 7. Rectangular steel
explosive test chamber

quickly and easily fabricated; (b) any modifica-
tions desired on a particular test could be made
on the site by test personnel using only basic
hand tools; and (c) after the explosion the cham-
ber would remain intact long enough to permit
the required measurements to be made, but yet
would disintegrate before shock wave reflections
could be set up which might obscure the data.

The primary purpose of the wooden cham-
ber tests was to investigate the sweep velocities
and pressures created by a Primacord initiated
gas detonation, and, if possible, confirm the pre-
dictions given by Eqs. (11) and (12). Several
other parameters were also studied, including
the effects of varying the amount of Primacord,
varying the distance between the Primacord and
the test surface (base), and changing the com-
position of the gas mixture.

Information gained from the wooden chamber
tests was then used to design and construct a
permanent steel chamber and firing table for
additional tests. The steel chamber, shown in
Figs. 7 and 8, is made of standard structural
steel channels welded together to form a rec-
tangular chamber. The chamber is bolted to a
firing table, consisting of a 5-in. thick slab of
steel on a set of legs. Five pressure trans-
ducers are mounted in the firing table flush
with the surface. Explosive gases are intro-
duced through a pipe fitting in the table. Inside
dimensions of the chamber are 36 by 60 in., and
the depth is 12 in. The chamber was designed
so that additional sections could be stacked on
the present assembly to give greater volumes,
although this has not been done on any tests
to date.
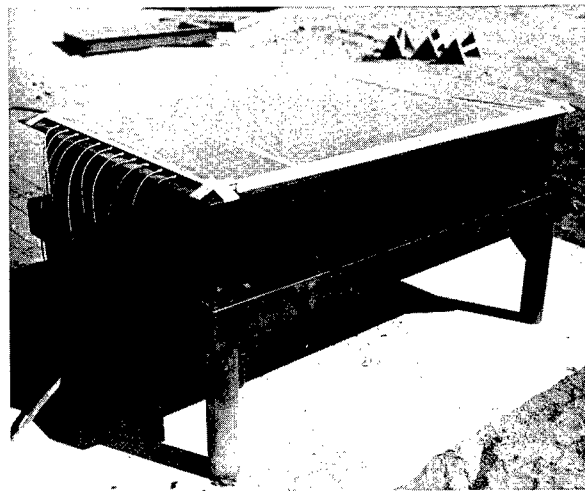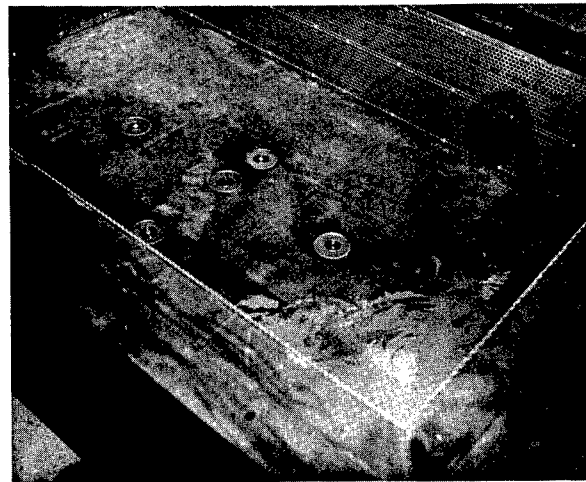
Fig. 8. Interior of rectangular
steel explosive test chamber

For a test, the chamber is covered by a
sheet of plastic film on a wooden frame. This
blow-off cover eliminates a potential reflection
surface, as well as permitting escape of the
detonation products so that excessive pressure
forces are not exerted on the chamber walls.

The high explosive strand array was at-
tached to the wood and plastic cover. For dif-
ferent tests the arrays were oriented at differ-
ent angles with respect to the table surface to
investigate the validity of Eq. (11) relating
sweep velocity to explosive strand angle.

An interesting design feature of the steel chamber is a perforated liner shown in Fig. 8; the purpose of the liner is to damp out shock wave reflections from the walls. This concept has been previously used in hypervelocity shock tunnels and in an explosive gas powered projectile launcher (1,11). The liner, consisting of perforated sheet metal, is mounted on standoffs 3 in. from the inside wall surfaces.

Both the wooden and steel chambers were designed for research into the aspects of high explosive initiated gas detonations, although either could be easily adapted to actual shock testing of small components. However, the relatively small dimensions and volumes of these chambers limited pulse durations to less than 1 ms. To produce longer duration pulses, tests were performed in two detonation shock tubes. The first shots were fired in a 16-in. diameter, 14-ft long tube. While even a tube of this length will not produce much longer pulses than those obtained in the small chambers, the first tests were performed in it mainly to study the effects of a cylindrical explosive strand array.

The Primacord for a test in the 16-in. tube was strung on a cylindrical wooden frame about 6 ft long, shown in Fig. 9, which closely fit the inside diameter of the tube. The test item was a simple aluminum cone about 18 in. long containing pressure transducers mounted flush with the cone surface. The cone was suspended by wires at one end of the tube and in the center of the Primacord array, as shown in Fig. 10. Transducer cables were protected by being enclosed in several feet of hydraulic hose. Plastic covers on the ends of the tube contained the explosive gas mixture until firing. One strand of Primacord was connected from the array to a detonator at the opposite end of the tube from the test item.
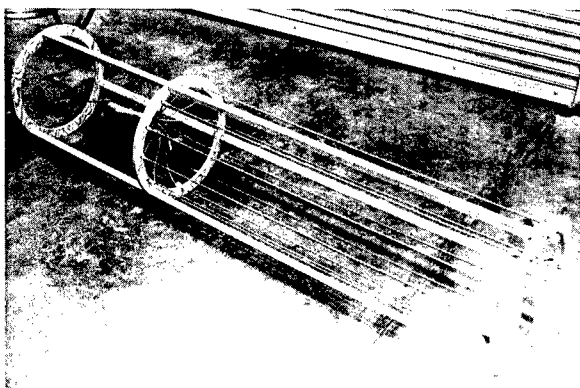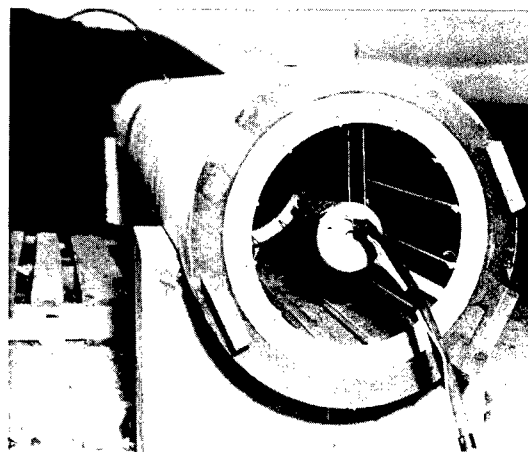
Fig. 10. Setup for test in 16-in. tube

Tests in the 16-in. tube were followed by a number of tests in a larger diameter, much longer tube, obtained by converting the Sandia Corporation 26-in. air gun facility to explosive gas operation. The air gun has been in use for several years for shock testing large items with compressed air supplying the driving force. It consists of two 16-in. naval rifles bored to 26 in. inside diameter and joined end-to-end to form a barrel 90 ft long. The explosive gas conversion consisted of the addition of 40 ft of steel pipe, with an inside diameter of 29 in., to one end of the gun barrel. The extension formed the test section containing the test item and all instrumentation. The result is a detonation tube 130 ft long, with a total volume of nearly 600 cu ft.

An instrumented cone, very similar to the one used in the 16-in. tube tests, but containing additional transducers, was used as a test item. The cone was rigidly mounted to a transverse strut located inside the test section, 20 ft from the end. Rigid mounting of a test item would not be the normal procedure in an actual mechanical shock test because test specifications usually include an acceleration or velocity change. However, the primary objective of these initial investigations was to evaluate the applied pressure pulse, the characteristics of which are virtually independent of test item motion. Since no motion was required, rigid mounting could be used, thereby reducing the possibility of damage to the test item and instrumentation, and generally improving the amount and quality of data obtained.

Primacord, loaded with 25 grains of explosive per foot of length, was used as the solid explosive in the 130-ft gun tests. For the first few tests the strands were arrayed on cylindrical

Fig. 9. Explosive strand array for 16-in. tube test

wooden frames, very similar to those used in the 16-in. tube, shown in Fig. 9. Twelve strands of Primacord were equally spaced around the frame, and were tied together to a single strand at one end. When the frame was loaded into the gun, the single strand of Primacord was strung the full length of the barrel to a detonator at the opposite end of the gun from the test item. This arrangement assured that the entire volume of explosive gas in the gun ahead of the test item was detonated before the Primacord and gas layer surrounding the test item was initiated. The object was to have the solid and gaseous explosives in the vicinity of the test item provide the desired sweep velocity and initial peak pressure. Then the flow of the large volume of detonation products from the gases in the tube ahead of the test item would produce the long duration decay portion of the pulse.

Pressure records from the first few Primacord initiated shots in the 130-ft gun contained undesirable multiple peaks during the first 2 or 3 ms following the initial peak. These additional peaks were suspected to be the result of transverse shock wave reflections between the test item surface and the gun wall. In an attempt to reduce these reflections, a perforated sheet metal liner was inserted into the 29-in. diameter test section, surrounding the test item. The liner was approximately 26 in. in diameter, leaving a gap of about 1.5 in. between the liner and tube wall. In several tests the Primacord strands were located in this gap, attached to the outside of the liner, and in one test the strands were arrayed on the inside of the liner. The number and spacing of Primacord strands was the same for all tests, with or without the perforated liner. Figure 11 shows one of the liners loaded with Primacord and ready for insertion in the gun.

Since the test item was a cone, and since the explosive strands were always laid parallel to the gun wall, the angle between explosive strands and test surface was simply the cone half-angle. For the particular combination of cone angle, gas mixture, and solid explosive initiation used in the 130-ft gun tests, the anticipated sweep velocity was 30,000 fps. The expected pressure normal to the cone surface was 43 atm, assuming no pressure contribution from the Primacord. A pulse duration of 12 ms was predicted, based on results of previous experiments in smaller tubes.

In all tests, the pressures were measured with commercially available piezoelectric transducers. Several makes and models were used. Signals were recorded on magnetic tape and played back at reduced speed into a paper recording oscillograph. The overall frequency response of the system, from transducer to oscillograph recording, was flat within 10 percent from 0 to 40,000 cps and 3 db down at 80,000 cps. Velocities were determined from the times required for the shock front to pass across two or more pressure transducers known distances apart. The output of each transducer triggered a pulse circuit. The pulse circuit outputs were mixed and displayed on a cathode ray oscilloscope screen, from which times were read for velocity computations. Velocity measurements were considered accurate to within 3 percent.

EXPERIMENTAL RESULTS

The results of ten tests performed in the frangible wooden chambers are presented in Table 2. A typical pressure-time record is shown in Fig. 12.
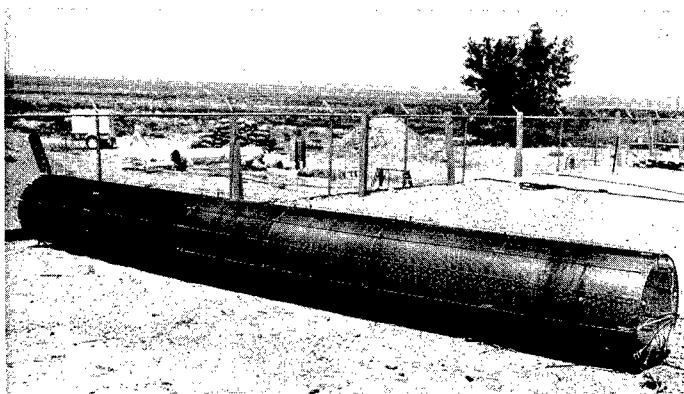
Fig. 11. Perforated metal liner and explosive strand array for 130-ft gun test

77

TABLE 2

Results of Explosive Tests in Frangible Wooden Chambers[a]

| Test No. | Chamber Depth (in.) | Primacord | | | Gas Mixture | Sweep Velocity (fps) | Peak Pressure[d] (atm) | Pulse Duration[d] (ms) |
		Standoff[b] (in.)	No. of Strands	Spacing[c] (in.)				
A-2	12	11	7	4	$C_2H_2+O_2$	20,000	68.3	0.30
A-3	12	11	7	4	Air	—	33.3	0.30
A-4	12	11	7	4	$C_2H_2+O_2$	21,400	67.5	0.40
A-5	12	6	9	3	$C_2H_2+O_2$	21,500	75.0	0.19
A-6	12	3	9	3	Air	19,000	75.0	0.08
A-7	12	3	9	3	$C_2H_2+O_2$	20,000	74.2	0.11
A-8	18	17	5	5.5	$C_2H_2+O_2$	20,700	60.8	0.36
A-9	18	17	5	5.5	$2H_2+O_2$	21,500	40.8	0.28
A-11	12	11	7	4	$2H_2+O_2$	20,000	50.8	0.25
A-13	15	9	7	4	$2H_2+O_2$	20,000	46.7	—

[a]Computed sweep velocity = 21,500 fps for all tests, computed peak pressure = 93.0 atm for $C_2H_2+O_2$ mixture and 41.7 atm for $2H_2+O_2$ mixture.
[b]Distance between Primacord and test surface.
[c]Distance between Primacord strands.
[d]Average from three transducers.
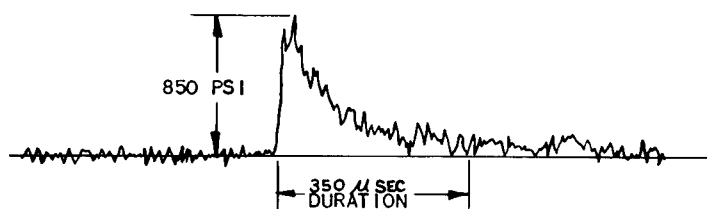
WOOD CHAMBER TEST NO. A-4
GAS: $C_2H_2 + O_2$ AT ATMOSPHERIC PRESSURE
SOLID EXPLOSIVE: 7 STRANDS OF 25 ^{GR}/FT PRIMACORD

Fig. 12. Typical pressure-time record
of test in wooden chambers

The results may be briefly summarized as follows:

1. Both stoichiometric hydrogen-oxygen and equimolar acetylene-oxygen mixtures at atmospheric pressure were detonated without difficulty by Primacord.

2. Sweep velocities were of the order of 20,000 fps, agreeing well with the computed value.

3. Peak pressures agreed reasonably well with predicted values for hydrogen-oxygen mixtures, but were 20 to 28 percent lower than

predicted values for acetylene-oxygen mixtures.

4. Pressures from the Primacord alone were appreciable, even at standoff distances of as much as 11 in. (Test No. A-3); however, pressures from the Primacord and gas did not appear to be directly additive. In fact, the data suggested that the maximum pressure is determined by either the Primacord or the gas, whichever is higher, and is not the sum of both.

5. Pulse duration varied according to the thickness of the gas layer between the Primacord and measuring surface, and appeared to be independent of the total volume of the chamber. This was an expected result because the only portion of the gas set in motion in the direction of the test surface would be that portion between the initiating explosive and the test surface.

The tests in the steel chambers were primarily to confirm predicted values of sweep velocity for different explosive strand inclination angles. Results of six shots are given in Table 3. Excellent agreement of computed and measured velocities was obtained. The relatively small disagreement at the larger angles was probably caused by a slight sag in the Primacord strands, since only a limited amount of tension could be applied to the strands without changing their explosive characteristics.

Agreement of computed and measured pressures in Table 3 is only fair. The pressure-time records for the steel chamber tests were practically identical in appearance with those for the wooden chamber tests, shown in Fig. 12.

Six Primacord initiated shots were made in the 16-in. diameter tube, with the conical test item. The explosive gas mixture in all tests was stoichiometric hydrogen-oxygen. The measured shock front sweep velocities on the test item surface were 27,000 to 33,000 fps, with an average value of 29,000 fps. These values are in good agreement with the computed value of 30,000 fps. More important, however, the agreement indicated that the test method was applicable to three-dimensional test items and explosive strand arrays as well as to flat surfaces as in the chamber tests.

Ten tests were performed in the 130-ft gun facility to evaluate the performance of Primacord initiated hydrogen-oxygen in a tube designed to produce long pulse durations. Results and pertinent setup data are presented in Table 4. Several tests in the series (Nos. 1, 3, 6, and 8) were control shots made with no solid explosive present to study the pressure pulse from the gas detonation alone. The last four shots in the series were made with the cylindrical perforated metal liner in place surrounding the test item (Fig. 11). In tests Nos. 7 and 9, the Primacord strands were attached to the outside of the liner, so that the liner was between the explosive strands and the test item, while in test No. 10 the Primacord was on the inside surface of the liner.

The results of the 130-ft gun tests may be summarized as follows:

1. Excellent agreement between computed and measured values of sweep velocity was obtained.

2. Agreement of computed and measured pressures was only fair. Possible reasons for the discrepancies will be discussed later.

TABLE 3
Results of Explosive Tests in the Rectangular Steel Chamber[a]

Test No.	Primacord Angle[b] (degrees)	Sweep Velocity (fps)		Peak Pressure[c] (atm)	
		Computed	Measured	Computed	Measured
1	0	21,500	21,300	41.7	38.3
2	0	21,500	21,000	41.7	38.3
3	0	21,500	21,500	41.7	30.0
4	5	26,300	26,500	42.5	31.3
5	7.5	29,600	28,800	42.9	45.0
6	10	33,400	31,300	43.2	50.0

[a]Gas mixture: $2H_2 + O_2$; initiator: 11 strands of 25 gm/ft Primacord, spaced 3 in. apart, entering chamber 12.5 in. above test surface.
[b]Angle between Primacord and test surface.
[c]Normal to test surface, 12 in. from nearest Primacord strand.

TABLE 4
Results of Explosive Tests in the 130-Ft Gun Facility[a]

Test No.	Sweep Velocity (fps)		Peak Pressure (atm)		Pulse Duration[b] (ms)
	Computed	Measured	Computed	Measured[b]	
1[c]	9,500	8,800	22.4	27.9	—
2	30,000	33,700	43.0	65.8	—
3[c]	9,500	10,300	22.4	22.5	10.0
4	30,000	30,300	43.0	52.5	12.0
5	30,000	33,300	43.0	66.6	11.1
6[c]	9,500	9,500	22.4	24.4	9.7
7[d]	30,000	30,500	43.0	39.2	13.6
8[cd]	9,500	9,200	22.4	14.6	13.1
9[d]	30,000	—	43.0	34.2	—
10[d]	30,000	—	43.0	67.8	10.5

[a]Gas mixture: $2H_2 + O_2$ at atmospheric pressure; initiator: 12 strands, 25 gm/ft Primacord, equally spaced on 26-in. diameter cylindrical frames, 7 to 20 ft long.
[b]Average from three transducers.
[c]Explosive gas only (no Primacord used) in these tests.
[d]Perforated liner in place.

3. Pulse durations agreed reasonably well with the predicted value of 12 ms. Pulse durations were difficult to measure accurately because the long gradual decay did not permit an exact determination of the end of the pulse.

4. Tests with the perforated liner were accompanied by considerably lower pressures on the test item when the Primacord was between the liner and tube wall, compared to pressures in tests without the liner or with the explosive on the inside liner surface.

A typical test item pressure-time record is shown in Fig. 13 for a test in the 130-ft gun with no solid explosive present, thereby illustrating the effect of the gas detonation alone. The pulse shape is the classical blast pressure history, consisting of a very fast rise followed by a long exponential decay. Figure 14 is a typical pressure record from a Primacord initiated explosive gas test, with all other setup conditions the same as for the test producing the record of Fig. 13. The peak pressure is considerably higher in the record of Fig. 14, which is to be expected because of the different shock front incidence angle. However, several severe peaks and dips are noted in the first few milliseconds of the pulse. These multiple peaks are suspected as being the shock front reflecting back and forth between the test item and tube wall. The intended purpose of the perforated liner was to break up or damp out any reflections, but the liner design used thus far, a simple cylinder concentric with the gun bore, has proven ineffective. Pressure records from tests with the liner, such as the one in Fig. 14, showed only moderate reductions in the multiple peaks when compared to records of tests without the liner. In any case, the multiple

220 PSI

10 MILLISECONDS DURATION

26 INCH GUN TEST NO. 8
GAS: $2H_2 + O_2$ AT ATMOSPHERIC PRESSURE
SOLID EXPLOSIVE NOT USED.
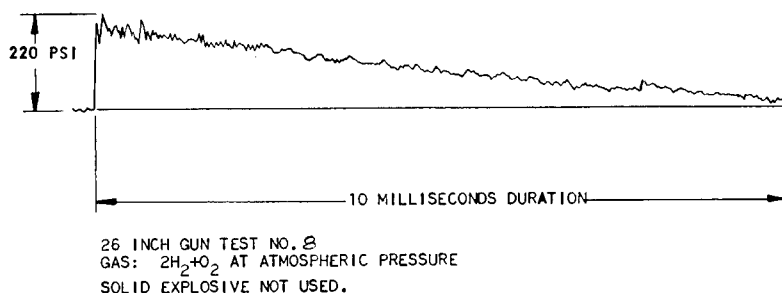
Fig. 13. Typical pressure-time record of explosive gas test in 130-ft gun, solid explosive not used

80

575 PSI

|←————————10.8 MILLISECONDS DURATION————————→|

26-INCH GUN TEST NO. 10
GAS: $2H_2 + O_2$ AT ATMOSPHERIC PRESSURE
SOLID EXPLOSIVE: 25 $^{GR}/_{FT}$ PRIMACORD,
                  12 STRANDS ON 26-INCH DIA.
                  CIRCLE
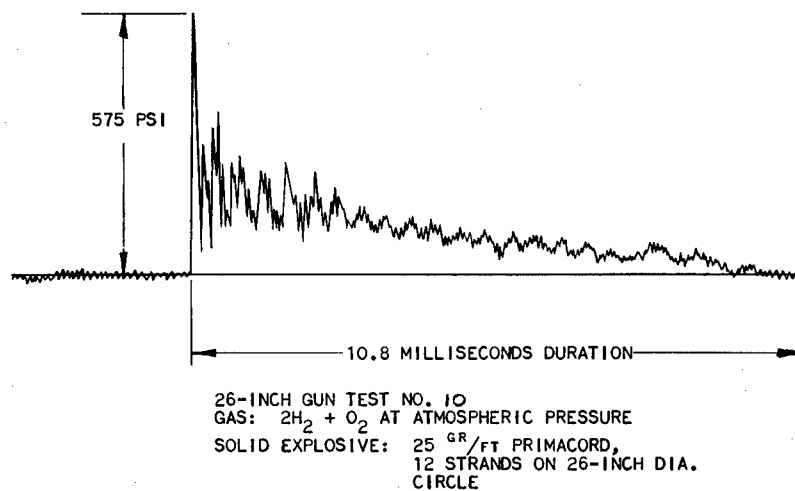
Fig. 14. Typical pressure-time record of solid explosive
initiated explosive gas test in 130-ft gun

peaks fade away after about 2 or 3 ms, and the remainder of the pulse very closely resembles that for the simple gas detonation, shown in Fig. 13.

CONCLUSIONS

The results of the tests have shown that the usefulness of explosive gas loading as a means of mechanical shock testing may be considerably extended by employing solid explosive strands to propagate the gas detonation. Shock front sweep velocities, and hence pressure force or acceleration pulse rise times, may be controlled over a wide range of values by proper orientation of the explosive strands. The method works equally as well on three-dimensional shapes or simple flat surfaces.

Excellent agreement has been obtained between measured sweep velocities and those computed by the equations developed in earlier paragraphs. Agreement of measured and computed pressures has been only approximate, however. Several reasons for the discrepancies have been advanced. First, the equation for pressure was only an interpolation and was not derived from gas dynamics theory. Second, the transducers may not have had suitable transient response characteristics to follow the initial portion of the pulse. Either overshoot or attenuation could have resulted, depending on the ratio of the particular pulse rise time to the

transducer natural period. Investigations are now underway to develop instrumentation capable of more accurate measurement of blast pressures. Finally, pressures from the solid explosive strands were not negligible and could have caused reading to be higher than predicted. Tests are planned in which smaller strands of explosive, such as extruded PETN, will be used to reduce this effect.

Tests are also planned for additional investigation of methods for eliminating the multiple peaks seen in the pressure records of 130-ft gun tests. The problem appears to be one of designing a baffle arrangement which would eliminate shock reflections without altering the desired pulse characteristics. Design and fabrication of various baffle arrangements are now in progress. Use of smaller amounts of solid explosive might possibly help by reducing the intensity of the initial peak, and this too will be studied.

The use of solid explosive initiated gas detonations promises to be a means of obtaining shock pulses difficult to produce by more conventional test procedures. Pulse rise time, duration, and amplitude may be varied over wide ranges. Test setups may be simple and inexpensive. The explosive strands may be mounted on wooden or wire frames conforming to practically any test item size and shape, and the assembly may be enclosed in a plastic bag of explosive gas for short-duration low-pressure tests or in a rigid tube or chamber for longer duration or high-pressure loadings.

81

REFERENCES

1. W. M. Sigmon, "Shock Testing with Explosive Gases," Shock and Vibration Bull. No. 34, Pt. 5, pp. 311-327, Dec. 1964

2. B. Lewis and G. von Elbe, Combustion, Flames and Explosions of Gases (Academic Press, New York), 1961, pp. 511-554

3. W. Jost, Explosion and Combustion Processes in Gases (McGraw-Hill, New York), 1946, pp. 160-192

4. A. G. Gaydon and I. R. Hurle, The Shock Tube in High Temperature Chemical Physics (Reinhold, New York), 1963, pp. 257-282

5. D. H. Edwards, G. T. Williams, and J. C. Breeze, J. Fluid Mech., 6:497 (1959)

6. R. L. Gealer and S. W. Churchhill, "Detonation of Hydrogen-Oxygen Mixtures at High Initial Pressure," ASTIA Doc. AD 202 043 (MICH-5-P-Squid), Sept. 1958

7. W. Doering and G. Burkhardt, "Contributions to the Theory of Detonation," Air Material Command Tech. Rept. No. F-TS-1227-1A, May 1949

8. M. R. Johnson and M. J. Balcerzak, "A Detonation Tube Drive for Producing Hypersonic Flows in a Shock Tube," Proc. 3rd Hypervelocity Techniques Symposium, Mar. 1964, pp. 116-134

9. Fundamentals of Explosives, U.S. and Foreign, Spec. Text No. 9-2900-1, Ordnance School, Aberdeen Proving Ground, Md., Jan. 1953

10. Primacord Detonating Fuse Handbook (Ensign-Bickford Company, Simsbury, Conn.), 1960

11. R. R. Flagg, "Advances in Shock Tunnel Driving Techniques," Proc. 3rd Hypervelocity Techniques Symposium, Mar. 1964, pp. 89-115

*   *   *

A METHOD OF PRODUCING LONG-DURATION
AIR-INDUCED GROUND SHOCK USING HIGH EXPLOSIVES

Eugene Zwoyer, George Triandafilidis
and James Stras
University of New Mexico
Albuquerque, New Mexico

Simulation of the effects of a nuclear weapon using the Long-Duration
High-Explosives Simulation Technique (LDHEST) is described. The
principal objectives of LDHEST are: (a) to produce a predictable peak
pressure on the bottom surface of an underground cavity; (b) to produce
a predictable exponential decay in pressure with time; and (c) to cause
the generated shock front to move across the bottom of the cavity with
predictable velocity.

This LDHEST program consists of detonating high explosives in under-
ground cavities of varying dimensions. Each cavity is constructed by
opening an excavation which later is covered with a select backfill re-
ferred to as a surcharge. The walls and bottom of the open excavation
form the walls and bottom of the cavity. Primacord is placed in a hor-
izontal plane at a specified height within the cavity, and the surcharge
is placed over the cavity. The bottom surface of the surcharge forms
the top of the cavity, and the Primacord and surcharge are supported
on a structural system within the cavity. When the Primacord is deto-
nated, a blast pressure is applied to all surfaces of the cavity. The
bottom surface, the loaded area of interest, is instrumented with pres-
sure gages. At detonation, the surcharge accelerates upward, allowing
the volume of the cavity to increase, as a result of which the blast
pressure decreases.

Preliminary results include: (a) peak overpressure as related to the
weight of explosives per cubic foot of cavity; (b) shock-front velocity as
a function of weave angle of the Primacord; and (c) an indication that
the duration of the pressure pulse is a function of the area-perimeter
ratio of the cavity. In addition, it is shown that the pressure environ-
ment of a 17-kt nuclear weapon can be simulated.

INTRODUCTION

Objective

Since the moratorium imposed by the Nu-
clear Test Ban Treaty on atmospheric testing
of nuclear weapons, increased emphasis has
been placed on finding ways and means of simu-
lating the mechanical effects of nuclear weap-
ons. This search is mainly due to the continu-
ing need to test hardened systems and keep
them updated to provide protection against
nuclear weapons.

This paper describes a method which is
believed to provide the most promising way of
simulating an air-blast-induced ground shock
caused by nuclear weapons in a superseismic
region. The method utilizes the detonation of
high explosives in a confined configuration to
attain long durations and is designated as the
Long-Duration High-Explosives Simulation
Technique (LDHEST).

Nuclear Weapons Simulation

To simulate the proper nuclear environ-
ment for a given weapon yield at a given range
from ground zero (point of explosion), it is
necessary to reproduce an input-loading func-
tion which at the ground surface has the same
characteristics as a nuclear explosion. These
characteristics are peak overpressure, shape
of the decay of overpressure with time to im-
part the necessary impulse to the ground

surface, and shock-front velocity associated with the particular peak overpressure of interest.

Figure 1 illustrates the relationship between weapon yield in megatons (Mt) versus the range in feet from ground zero parametricized with respect to peak overpressure (1). By assuming arbitrarily that it is of interest to reproduce the effects of a 1-Mt weapon and utilizing the data from Fig. 1, Fig. 2 illustrates the decay of peak overpressure with range. Figure 2 also indicates that the peak overpressure decays very rapidly at close range from ground zero. For instance, for a 1-Mt weapon the peak overpressure at 1,500 ft is 1,000 psi while at only 2,250 ft from ground zero the peak overpressure rapidly decays to 300 psi.

The velocity of the shock front is a function of peak overpressure, and consequently depends also on the range from ground zero. Figure 3 illustrates the relationship between shock-front velocity and peak overpressure (2). Again for a 1-Mt weapon the shock-front velocity for the 300-psi peak overpressure is 4,800 fps, while for the 1,000-psi level it is 8,700 fps.

The shape of the pressure versus decay time curve is important in a simulation technique because it represents the impulse imparted to the ground. Figure 4 illustrates the rate of pressure decay with time for both the 1,000- and 300-psi peak overpressures, respectively, for a 1-Mt weapon (3). It is apparent from Fig. 4 that the 1,000-psi overpressure decays at a much faster rate than the 300-psi peak overpressure. It is also of interest to note that the 1,000- and 300-psi peak overpressures have comparable total positive-phase durations which amount to about 1.2 and 1.0 sec, respectively (3). It should be emphasized that both durations are quite long and they impose a major problem in any nuclear weapon simulation technique.
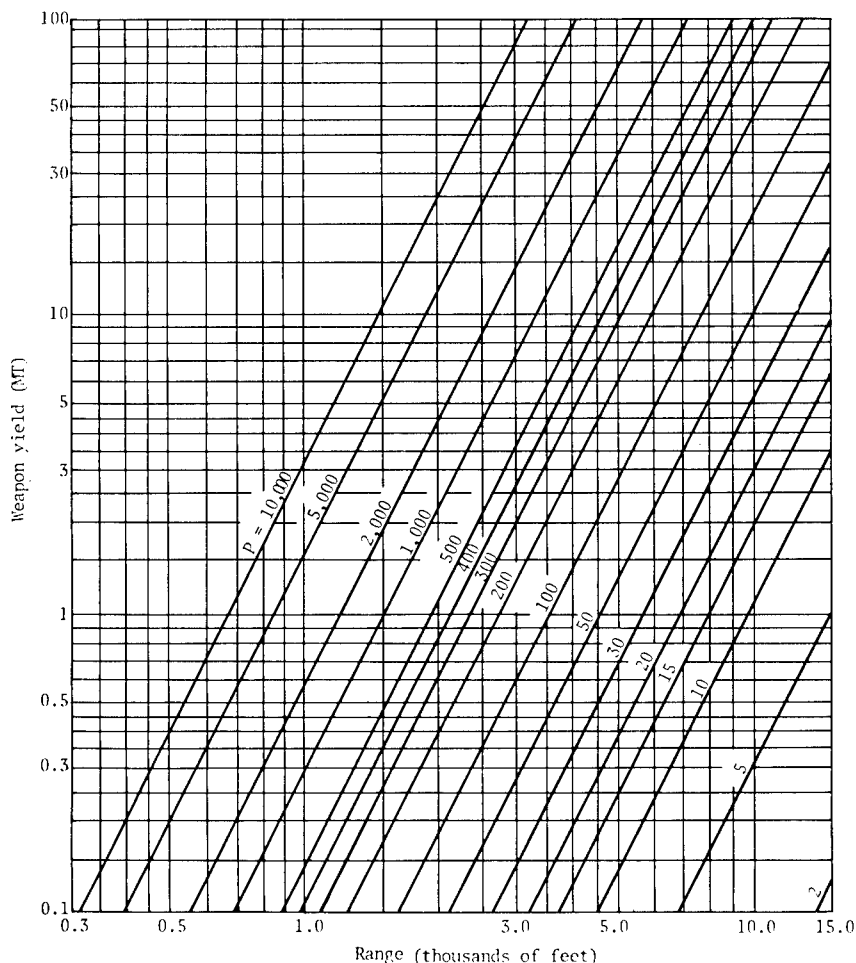
Fig. 1. Peak overpressure at ground surface vs range for various surface-burst weapon yields at sea level

84
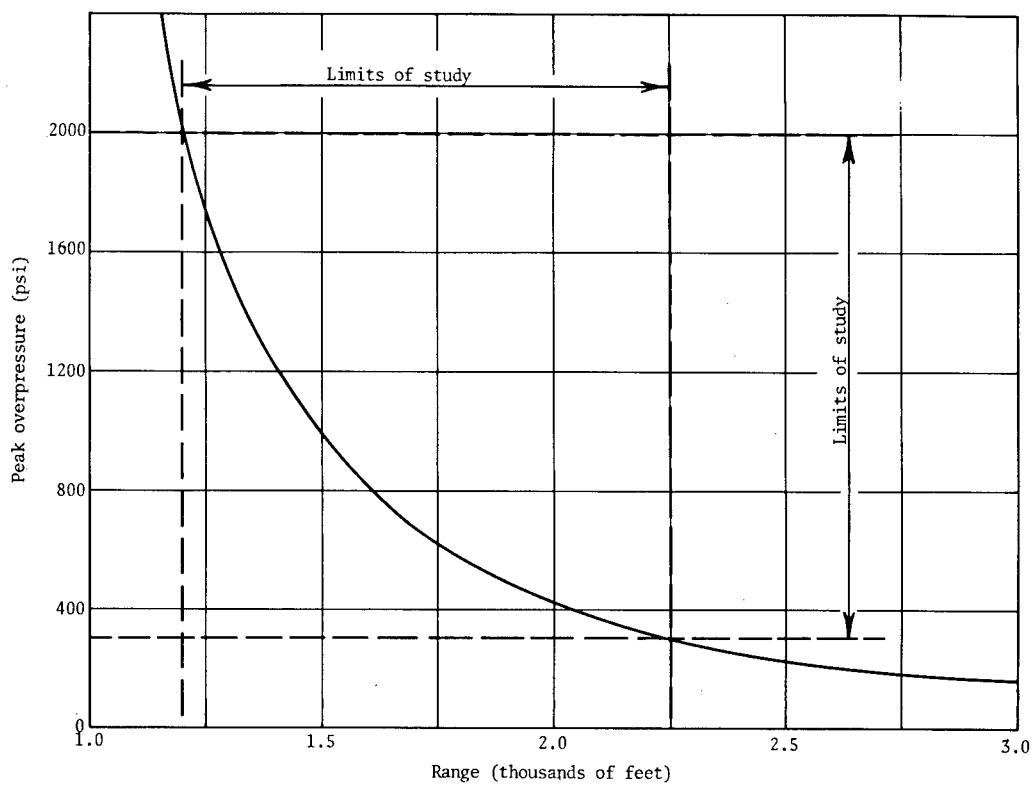
Fig. 2. Peak overpressure vs range for 1-Mt weapon,
surface burst at sea level
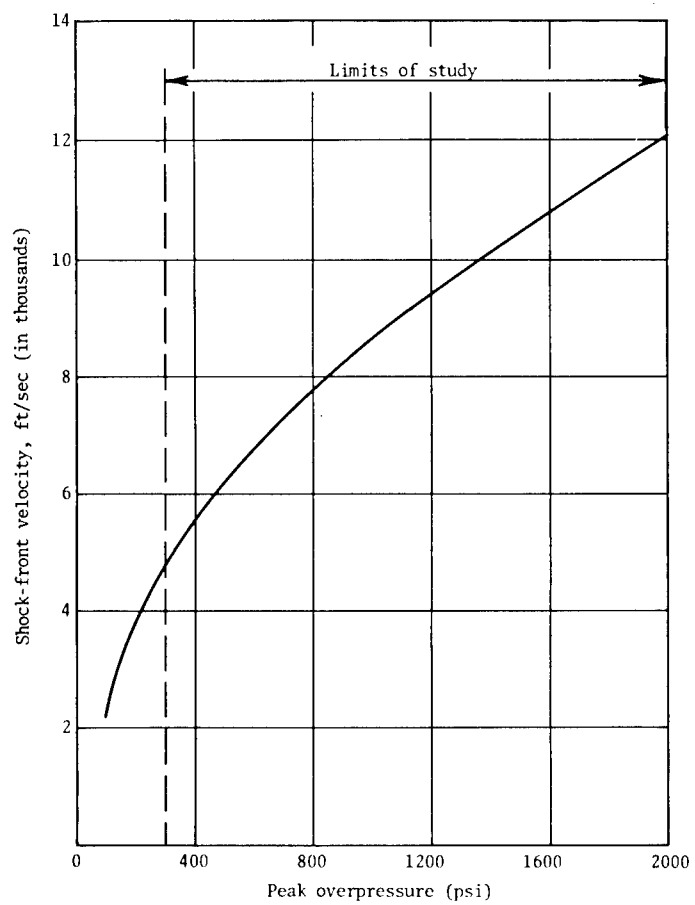
Fig. 3. Shock-front velocity vs peak overpressure
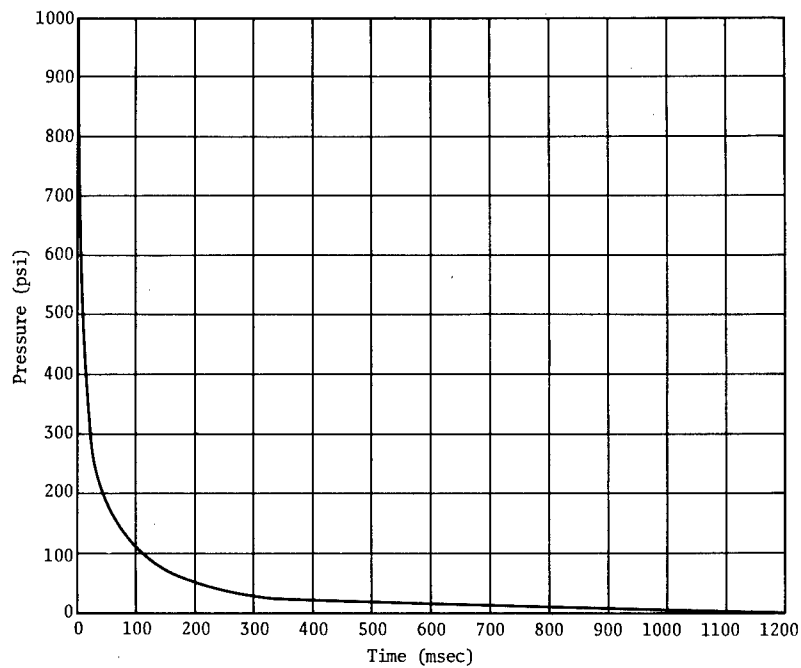
(a) Range, 1,500 ft; 1,000-psi overpressure simulation
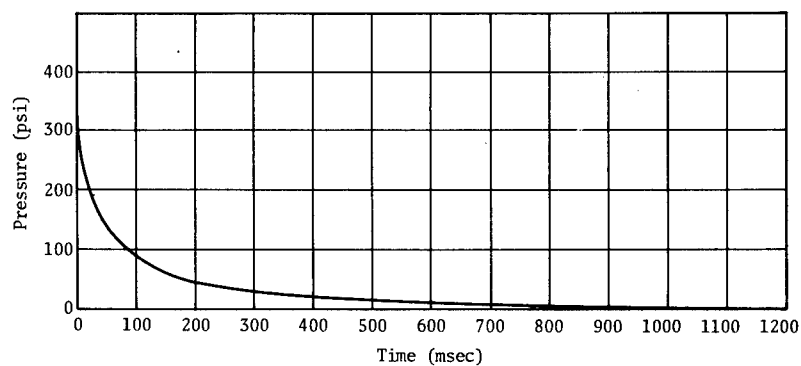
(b) Range, 2,250 ft; 300-psi overpressure simulation

Fig. 4. Pressure-time relationships for 1-Mt surface burst

Figure 5 represents the impulse, i.e., the area under the curves of Fig. 4 for the 1,000- and 300-psi overpressures as a function of time. For a 1-Mt weapon, the total impulse for the 1,000-psi peak overpressure is about 51 psi-sec and for the 300-psi peak overpressure is about 34 psi-sec.

Due to the large positive-phase durations associated with nuclear weapons, it is practically impossible to simulate an input trace that would impart to the ground the true total impulse. Although the response of structures buried in soil subjected to air-induced ground shock is dependent on the total loading function, satisfactory results can be obtained by reproducing peak pressures and only a portion of the total impulse. As a matter of fact, if testing scaled-down models of prototype structures was desired, it would be preferable also to scale down the positive-phase duration of the pressure pulse. It has therefore been assumed that a satisfactory simulation could be achieved for buried structures and free-field experiments if the initial portion of the pressure-time trace could be reproduced to one-half of the peak overpressure.

Figure 6 shows the relationship between percent of impulse and of peak overpressure for both the 300- and 1,000-psi peak overpressures. For instance, at times corresponding to 50 percent of the peak overpressure, the impulse for the 300-psi peak overpressure curve (Fig. 4b) is 30 percent of the total impulse while for the 1,000-psi peak overpressure (Fig. 4a) it is only 18 percent. The time durations corresponding to one-half the peak overpressures are 37 ms for the 300-psi peak overpressure and 14 ms for the 1,000-psi peak overpressure (Fig. 4). If the difficulties associated with reproducing long durations in a simulation technique are kept in mind and the 50-percent peak overpressure criterion is accepted, it becomes obviously easier to simulate high overpressure levels, but only by sacrificing relatively large amounts of impulse imparted to the ground.

Background

Both in-house and under contracts, the Civil Engineering Branch of the Air Force Weapons Laboratory (AFWL) has worked on the development of a technique to simulate the
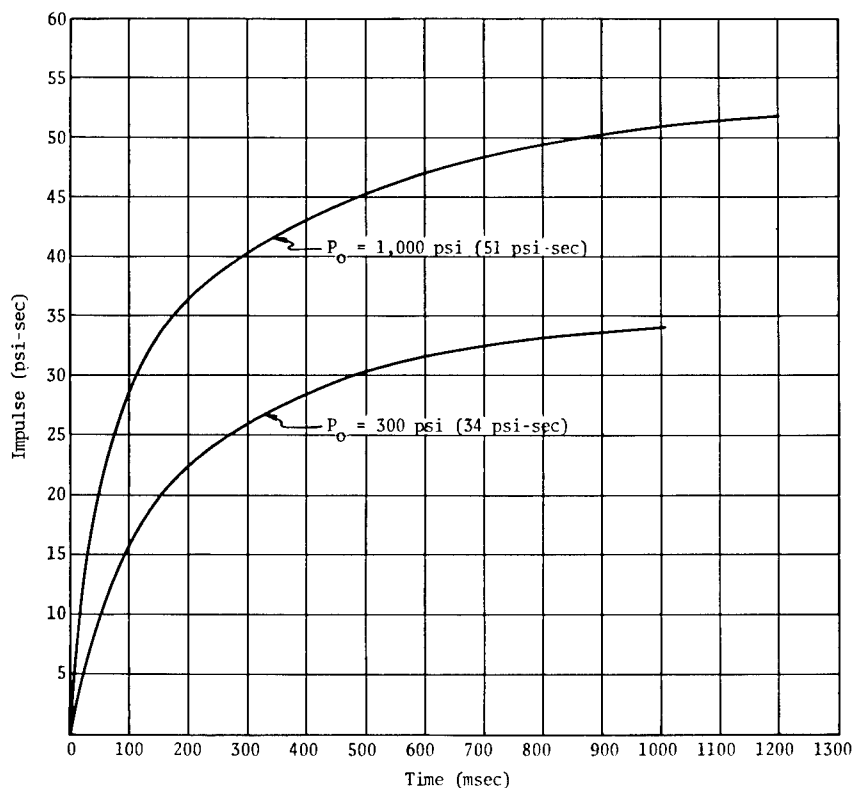
Fig. 5.   Total impulse vs time for 300- and 1,000-psi
peak overpressures, 1-Mt weapon
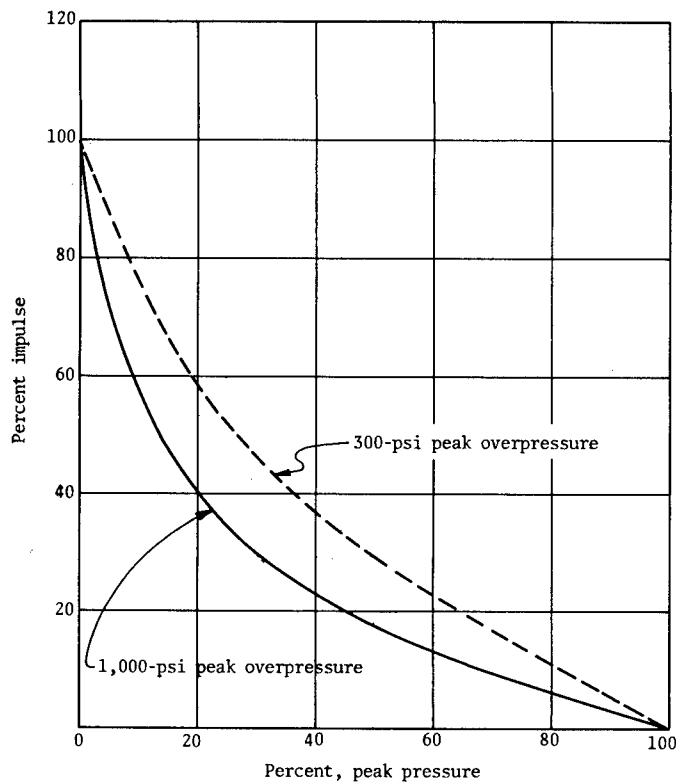
Fig. 6. Percent impulse vs percent peak
pressure for 300- and 1,000-psi peak
overpressures, 1-Mt weapon

mechanical effects of nuclear weapons. So far
two approaches have been investigated. One
utilizes detonable gaseous mixtures; the other,
detonation of a Primacord matrix. In both
methods, a surcharge, which may consist of a
column of water or soil overburden, is placed
above the explosion cavity to confine and con-
tain the gaseous products of the explosion long
enough before complete venting to achieve the
long durations necessary for simulating the
effects of nuclear weapons.

The earliest attempt to simulate a nuclear
explosion, as well as the application of the con-
cept of overburden to achieve long durations, is
attributed to work done at Stanford Research
Institute (SRI) (4) under contract with the De-
fense Atomic Support Agency. The SRI fired a
number of shots utilizing a pit 5-1/2 by 11-1/2
ft in which mixtures of detonable gases only
were exploded. In general, the results of the
SRI study pointed out the feasibility of the con-
cept of overburden to attain long durations, with
the size of the pit an important parameter in
simulating long durations. Although the SRI
study failed to indicate that nuclear shock-front

velocities could be simulated with mixtures of
detonable gases, subsequent tests by the Air
Force were successful.

Under Air Force contract the MRD Division
of the General American Transportation Corpo-
ration (5) experimented with the concept of a
Primacord matrix in conjunction with an over-
burden to simulate nuclear weapons effects.
Two tests were performed utilizing a pit 15 by
30 ft in which simulation of a 300-psi peak
overpressure environment was attempted. Both
efforts failed in creating the proper environ-
ment, but indicated a technique which with fur-
ther development has proven to be successful.

The Civil Engineering Branch of the Air
Force Weapons Laboratory, in an in-house ef-
fort designated as Phase I (6), conducted exper-
iments to develop and refine both the gaseous
mixture and Primacord matrix techniques, as
well as to examine more closely the overburden
concept of simulating long durations. Under
the Phase I study, seven shots were fired uti-
lizing a pit 20 by 40 ft. The results of the study
indicate that both the gaseous mixture and

89

Primacord matrix techniques were adequate in simulating the desired nuclear environment. Nevertheless, more emphasis and weight were placed on the Primacord matrix concept because it proved easier and safer for field use as well as being more economical.

Following Phase I, Phase II (7) of the study was initiated in an attempt to prove the feasibility of the method in loading large areas which would be of greater interest in performing tests on hardened facilities. Two tests were performed under Phase II. The first experiment consisted of loading an area 96 by 150 ft in which a 300-psi peak overpressure was simulated. The second experiment* was constructed utilizing an area of 88 by 96 ft and creating an environment of 600-psi peak overpressure. Following the Phase II study, another test was also conducted on specific mechanical components of a hardened system. This test, the BSD test,* was conducted in a pit 40 by 96 ft under a 300-psi peak overpressure environment.

Under Air Force contract, the Eric H. Wang Civil Engineering Research Facility (CERF), operated by the University of New Mexico, has also conducted three LDHEST experiments.* The main purpose of these experiments was to investigate the feasibility of creating larger peak overpressures, as well as to test certain hardware under high-pressure environment. The first two tests were performed in a pit 32 by 36 ft in an attempt to create 1,000-psi peak overpressure while the third test was performed in a pit 40 by 48 ft with a 600-psi peak overpressure environment.

SIMULATION TECHNIQUE
  PARAMETERS

In simulating a nuclear weapon it is necessary to reproduce the following primary parameters:

1. The peak overpressure resulting at certain range from ground zero due to a given weapon yield;

2. The shock-front velocity associated with the specific peak overpressure of interest; and

3. A pressure-time trace that would impart the necessary impulse to the ground.

—————————
*Results of these tests have not yet been reported.

Due to the long durations associated with nuclear explosions it is proposed to simulate the pressure-time history only up to the time corresponding to one-half the peak pressure for a given weapon yield.

The parameter that affects peak overpressure in a simulation technique is the charge density (amount of explosives per unit volume of cavity). The velocity with which the shock front propagates in the cavity is a function of the detonation velocity of the explosives. We will confine our discussion to Primacord since only this type of explosive has been used in the tests to be described. Primacord is a high-velocity explosive known as PETN (pentaerythritetetranitrate). It is a nonhygroscopic crystalline solid which melts at about 284°F. The solid crystalline core is wrapped in a plastic casing. The explosive in the core is detonated by a blasting cap. Primacord is commercially available in a variety of core loads ranging from 10 to 400 grains per foot. When initiated, it detonates along its length at a velocity of about 21,000 fps. It is therefore obvious that to simulate shock-front velocities that are realistic with respect to actual nuclear environments, the detonation front must be slowed. The desired nuclear shock-front velocity is achieved in the simulation technique by weaving the Primacord at a predetermined angle. Therefore, the weave angle of the Primacord is also an important parameter in attaining the necessary shock-front velocity associated with the specific peak overpressure of interest.

To be able to simulate the pressure-time trace even up to times corresponding to one-half of the peak overpressure, it is necessary to contain the explosion within the detonation chamber by retarding the venting of the detonation gases to the atmosphere. To achieve retardation, an overburden (soil surcharge) is placed on top of the detonation chamber; thus, the amount of soil surcharge is another major parameter that affects the pressure-time history in the simulation technique. Since venting at early times is prevented by a soil surcharge, the density and method of placement of the surcharge are also likely to affect the degree of confinement of the explosion. All other conditions remaining the same, venting is most likely to be affected by the boundary conditions of the test pit. For a given size of loaded area, the greater the perimeter length of the cavity the greater the amount of venting to be expected. It is therefore likely that the size of the loaded area will also be an important parameter in the simulation technique. Besides these major parameters, the position of the charge within

the cavity and the depth of the detonation cavity are likely to influence the results of the simulation technique.

To investigate all the parameters in a systematic fashion, the research program consisted of five series of tests as shown in Table 1. In the first four series of tests, each of the parameters was varied independently. Only in Series I was more than one parameter varied at the same time because charge density and weave angle were assumed to be variables independent of each other. To maintain an economically feasible research program, the size of the cavity was 8 by 20 ft for all test series, with the exception of some tests in Series V. In Series V, the principal variables were charge density, weave angle of Primacord, surcharge,

and cavity size, all chosen from results obtained in Series I through IV. The objective of Series V was to determine if the results of Series I through IV produced enough valid information to design an LDHEST experiment reliably.

The influence of boundary conditions on venting and duration will be investigated by comparing the results of the parameter study with available data from large size experiments (see Background); and, if necessary, additional experiments will be designed to close any gaps existing at the conclusion of this investigation.

Since all the tests outlined in Table 1 have not yet been completed, only those for which data are available are presented.

TABLE 1
LDHEST Parameter Study

Series	Test	Cavity Dimensions (ft)			Charge Position Measured from Top of Cavity (ft)	Charge Density of Cavity (lb/sq ft)	Weave Angle (degrees)	Surcharge (lb/sq ft)	Number of Primacord Racks	Principal Variables
		Width	Length	Depth						
I	1	8	20	4	2.0	0.074	8.6	1,000	1	Charge density and weave angle
	2	8	20	4	2.0	0.140	13.5	1,000	2	
	3	8	20	4	2.0	0.180	16.0	1,000	2	
	4	8	20	4	2.0	0.220	18.3	1,000	2	
	5	8	20	4	2.0	0.408	25.3	1,000	4	
II	1	8	20	4	1.0	0.074	18.3	450	1	Position of charge in cavity
	2	8	20	4	2.0	0.074	18.3	450	1	
	3	8	20	4	3.0	0.074	18.3	450	1	
III	1[a]	8	20	4	2.0	0.14	13.5	1,000	2	Surcharge
	2	8	20	4	2.0	0.14	13.5	600	2	
	3	8	20	4	2.0	0.14	13.5	450	2	
	4	8	20	4	2.0	0.14	13.5	300	2	
IV	1	8	20	3	1.5	0.22	18.3	1,000	2	Depth of cavity
	2[a]	8	20	4	2.0	0.22	18.3	1,000	3	
	3	8	20	5	2.5	0.22	18.3	1,000	4	
	4	8	20	6	3.0	0.22	18.3	1,000	4	
V	Use best values as determined from Series I-IV									Charge density, weave angle, surcharge and cavity size

[a]Indicates duplicate tests.

TEST FACILITY

The size of the cavity for the tests in this study, with the exception of some tests in Series V, is 8 ft wide and 20 ft long. The depth varies from 3 ft to 6 ft with most of the tests conducted in a 4-ft deep cavity. The surcharge (soil overburden) varies from 300 to 1,000 lb/sq ft corresponding to approximately 3 and 10 ft of overburden, respectively. The cavity is constructed underground, and the top of the surcharge is flush with the ground surface. An excavation of from 9 to 18 ft is required, depending on the amount of surcharge and the depth of the detonation chamber for a particular test. The plan view of the bottom of the excavation is about 14 ft wide and 26 ft long. The

longitudinal walls of the excavation are cut almost vertical, and the transverse slopes are cut on a 1 vertical to 3 horizontal to provide access for the excavating equipment. The excavation configuration allows for a backfilling at least 3 ft wide all around the periphery of the cavity.

Construction

Figure 7 shows a plan view and a typical cross section of the test facility. Wooden posts 8 by 8 in. are precut to the required length, which depends on the height of the detonation chamber and the depth of embedment of the posts in the floor of the cavity. The posts are
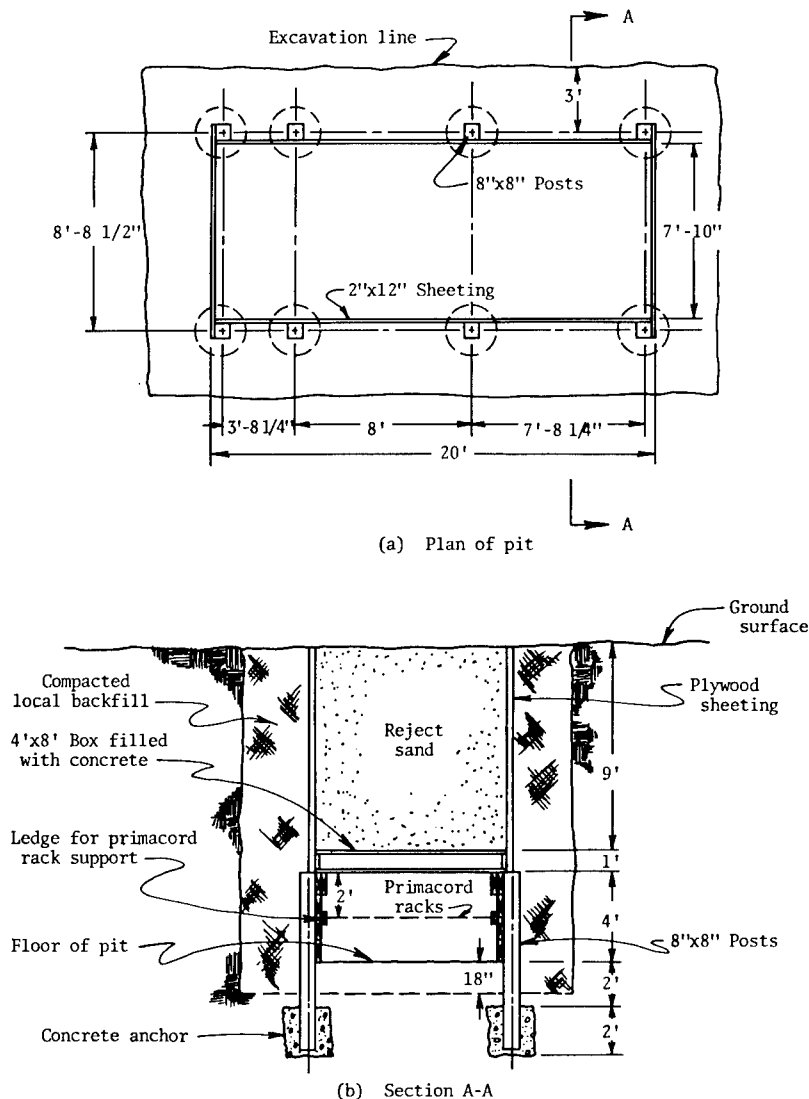

(a) Plan of pit

(b) Section A-A

Fig. 7. Details of pit construction

92

normally spaced at intervals in multiples of 4 ft on center. At the location of each post, holes about 2 ft in diameter and 2 ft deep are excavated. The posts are set in the holes and the holes are filled with concrete. The upper level of the concrete in the holes is 2 ft below the floor of the cavity. The floor of the cavity is overexcavated by about 18 in. to allow for the placement of all instrumentation within a select backfill material.

As shown in Fig. 7, the wooden posts are lined along the periphery of the test cavity with 2- by 12-in. plywood sheeting up to their top to form the sides of the detonation chamber (cavity). The top of the detonation chamber is covered with wooden boxes 4 by 8 ft in plan. The boxes are constructed from plywood sheets, 4 by 8 ft by 3/4 in., to form a bottom and by nailing 2- by 12-in. joists along the periphery of the plywood. The wooden boxes are reinforced by nailing additional 2- by 12-in. joists between 8- and 12-in. centers running along the 8-ft length of each box. The 8-in. joist spacing is used for the 1,000-lb/sq ft surcharge pressures. The ribs between the 2- by 12-in. joists are filled with concrete prior to placement of the surcharge. Five adjacent wooden boxes, spanning the 8-ft width of the pit, are required to cover the entire detonation chamber. To inhibit excessive venting, the 8- by 8-in. posts, as shown in Fig. 7b, are not carried to the ground surface. To provide for a well-defined block movement of the surcharge above the detonation chamber, 1/2-in. thick plywood sheets are tacked around the periphery of the wooden boxes. The plywood sheets extend to the top of the surcharge, although such a precaution is not warranted in large test facilities. The 3-ft wide trough along the periphery of the detonation chamber is subsequently filled with local compacted backfill up to the top of the detonation chamber. While the outside of a box is being filled with compacted backfill, the inside of the box is simultaneously filled with reject concrete sand in small lifts (6 to 8 in.). The purpose of this procedure is to avoid excessive lateral pressures on the plywood sheeting which is not adequately braced to withstand large pressures.

The compacted backfill is placed close to optimum water content, and its density is controlled by making moisture-density measurements with a rubber-balloon apparatus. The surcharge, reject concrete sand, is rained into the boxes through a clamshell, and density measurements of the surcharge are made with a nuclear density device.

The construction procedure described here was adapted as a result of four small-scale tests (4 by 8 ft in plan) which were performed strictly to study surcharge behavior through high-speed photographs. Tests 1 and 2 of Series I utilized a somewhat different procedure, but it was not satisfactory and was abandoned when the results of the four small-scale experiments became available.

Primacord

The Primacord is woven on racks made of 2- by 4-in. lumber as shown in Fig. 8. The racks are 88 in. wide and 118 in. long and fit inside the detonation chamber. They are supported on ledges which are attached to the 2- by 12-in. sheeting at the appropriate depth in the chamber. The racks are positioned in the detonation chamber before placement of the wooden boxes that support the surcharge. Plywood gusset plates on all four corners and a 2- by 4-in. cross brace in the middle of the rack are used to stiffen the racks. The 2- by 4-in. lumber along the periphery of the rack is notched at top and bottom at adequate intervals to accommodate the Primacord at the required angle of weave (Fig. 8). As previously explained, the purpose of weaving the Primacord at an angle is to slow down the propagation velocity of the shock front. The sine of the required weave angle (Fig. 8) is determined by dividing the required shock-front velocity by the detonation velocity of the Primacord (21,000 fps). To cover the entire test cavity, two racks of the size shown in Fig. 8 are required for each row of Primacord. Adjacent racks in the same plane are laced together with Primacord of the same core load to provide continuity in the lacing pattern and to insure spontaneous detonation. At the firing end of the detonation chamber a transverse strand of 400 grains per foot of Primacord ties all incoming individual strands together.

Three strands of 54-grain Primacord are connected to the 400-grain transverse strand to form the plane-wave generator. All three strands are taped together and enter the detonation chamber encased in a plastic tubing. Two of the three strands are short; only one is connected to a blasting cap. A spare line with a duplicate blasting cap is also provided to initiate the explosion, in case the first cap does not go off. If more than one row of racks is used, the racks are interconnected before they leave the detonation chamber to enter the plastic tubing (Fig. 9).

The required charge density is achieved by one or more of the following methods:
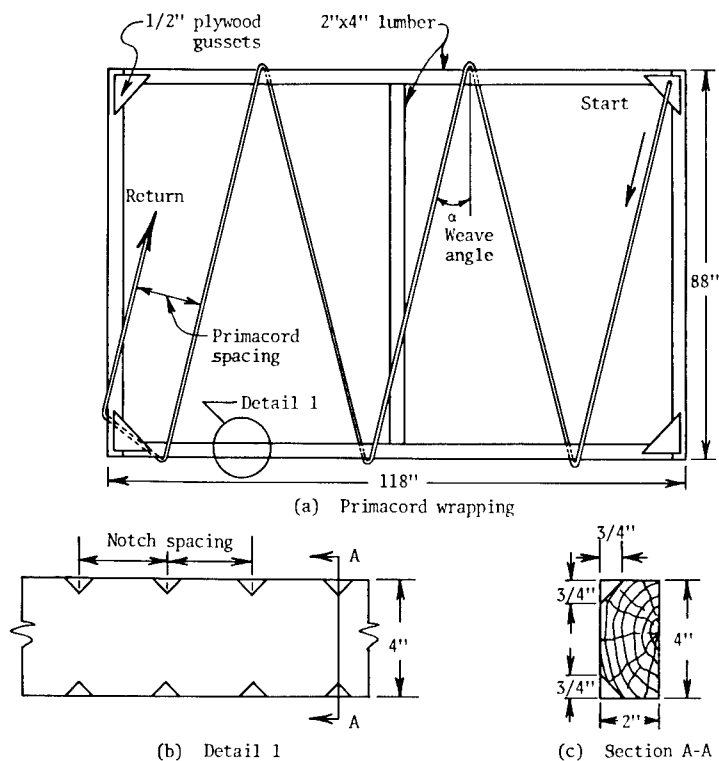
Fig. 8. Primacord racks and wrapping

1. Adjusting the spacing of the Primacord matrix;

2. Selecting the proper core load of Primacord; and

3. Using an adequate number of racks.

In this testing program low-charge densities can be attained by using a single rack, but the high-charge densities may require as many as four racks (Table 1). A minimum of 3-1/2 in. of clearance between strands is necessary to avoid sympathetic detonation.

Instrumentation and Data Recording

The floor of the cavity is overexcavated by about 18 in. and subsequently backfilled. Over-excavation allows placement of all transducers within a select backfill in which uniform soil conditions can be achieved. The only measurements of interest throughout this study are pressure-time traces and arrival times of the shock front as the detonation progresses from the firing end to the reflection end of the cavity. These measurements can be taken with pressure gages that are capable of surviving the test environment. Two types of pressure gages have been used: the Norwood, Model 111,

bonded strain gage pressure transducer and the UNM Soil Stress Gage.

The Norwood was used for both air pressure-time traces and for arrival times of the shock front. It is rugged enough to withstand the LDHEST environment up to pressures of 2,000 psi, and it has a low-frequency response, 20 kc, which causes a considerable amount of ringing when subjected to air shock. In the tests the gage is mounted on a canister, as shown in Fig. 10, with its sensing element flush with ground surface. Considerable difficulty was experienced during the early stages of the program in obtaining interpretable traces. It should be emphasized, however, that to attribute the uninterpretable traces to an inherent weakness of the transducer would be unjust since the environment produced by the air shock contains very high-frequency components on which are superimposed innumerable reflections from the boundaries of the detonation chamber. It is of interest to note that at least an interpretable trace can be attained by mechanically filtering out a portion of the high-frequency oscillations (hash). To accomplish this, UNM soil stress gages were buried at shallow depths, ranging from 6 to 48 in., in an attempt to determine from the measurements the peak intensity of the input at the surface.

94

Blasting cap

Plywood

Random
backfill

Compacted
backfill

Reject sand
backfill

Wooden boxes
filled with concrete

Plastic
tubing

1 strand

2"x12" Sheeting

400-grain
primacord

Primacord
racks

3 strands, 54-grain,
taped together

3

1

Instrumentation
placement layer

Virgin soil

8"x8" Post

Concrete
anchor

Fig. 9. Details of Primacord initiation,
longitudinal section through pit

95

Gage stations

(a) Instrumentation plan

(b) Section A-A
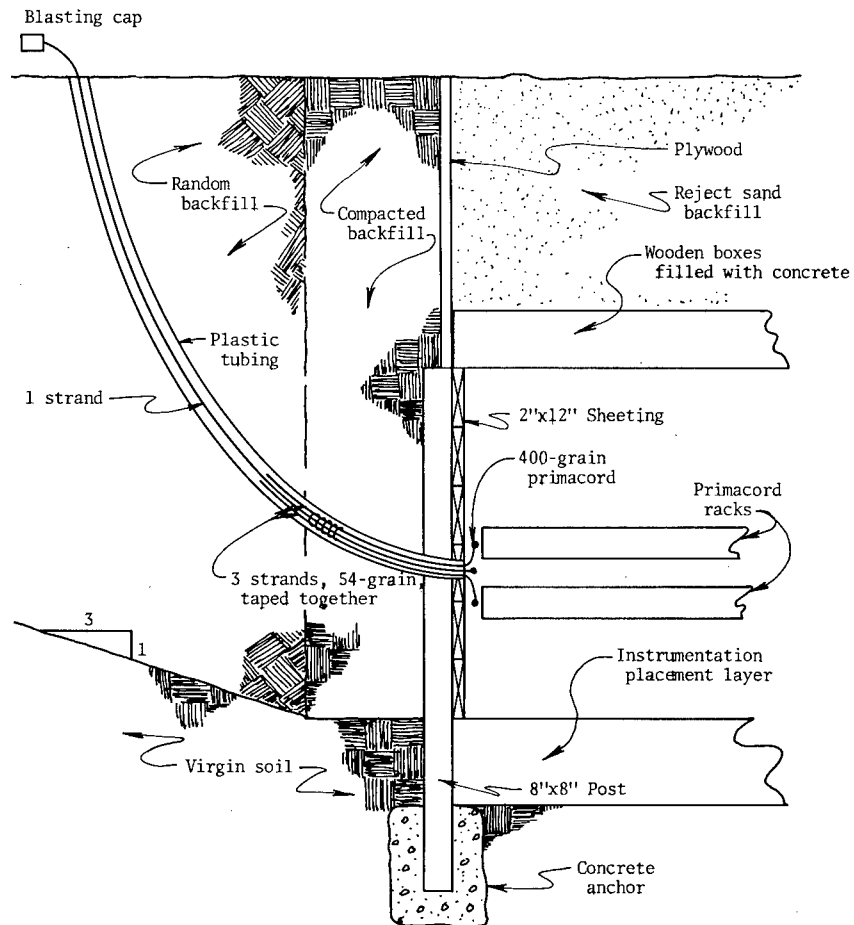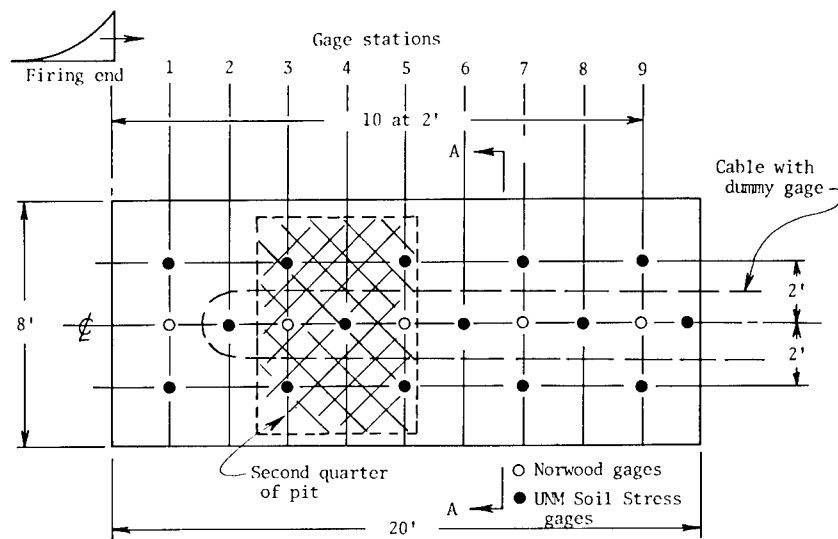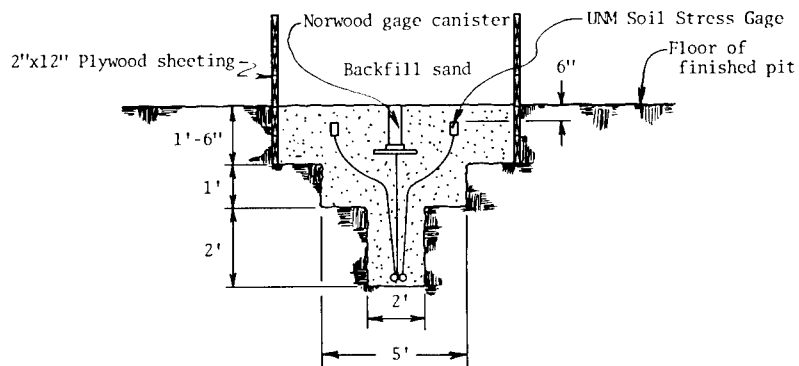
Fig. 10. Instrumentation layout

96

The UNM soil stress gage was developed and built at the Eric H. Wang Civil Engineering Research Facility, operated for the Air Force by the University of New Mexico (8). This gage utilizes semiconductor strain gages in a full bridge. The strain gages are mounted on a short column with an annular ring between the column and the gage casing. The gage has a frequency response over 100 kc and a pressure range of 0 to 2,000 psi. It has performed excellently when tested under both static and dynamic loading conditions. UNM soil stress gages have been used buried at 6, 24, and 48 in. The data from these gages show conclusively that the concept of mechanical filtering can be applied effectively by burying the gages from 6 to 24 in. without any appreciable stress-attenuation effects. Of course, the deeper the burial the more effective is the filtering mechanism but the greater the attenuation becomes, due to the inelastic behavior of the soil and the geometric dispersion of the stress.

On the basis of a few preliminary tests (Series I, 1 through 4), it was decided to use Norwood air pressure gages for times of arrival and UNM soil stress gages buried at a depth of 6 in. for pressure-time records. The instrumentation layout, shown in Fig. 10, consists of five Norwood surface pressure gages, used mainly for determination of times of arrival and shock-front velocity, and 15 UNM soil stress gages for pressure-time histories. All cables are buried, as shown in Fig. 10, in a 4-ft deep instrumentation trench. An additional channel was utilized in which a dummy gage is placed outside the test pit while its shielded but otherwise unprotected cable is laid on the bottom of the instrumentation trench. The purpose of the additional channel was to assess the noise level in the cable when exposed to the same test environment. With cable burial at 4 ft, the noise level even in the high-pressure shots has been negligible.

The electronic signals produced by the pressure transducers are recorded on a United Electro Dynamics (UED) data-recording system which consists of AMPEX CP-100 magnetic tape recorders and associated switching and timing equipment. Each tape has 14 channels, one of which is used to record an IRIG-A time code. A common-time channel which is located at the first transducing station, closest to the firing end, is recorded on all tapes. The common-time channel is used to determine times of shock-front arrival at different stations. The magnetic tapes are run at a speed of 60 ips, and the electronic signal from each transducer is recorded FM which provides a bandwidth of 20 kc. The stored data are played back, displayed on oscilloscopes, and then photographed on Polaroid film at different sweep speeds. Figure 11 is a schematic of the electronic recording system.

RESULTS

General

It must be kept in mind that the study is not complete and that the results presented are those derived from selected experiments. Every effort has been made to present unbiased data, but further testing may disclose new
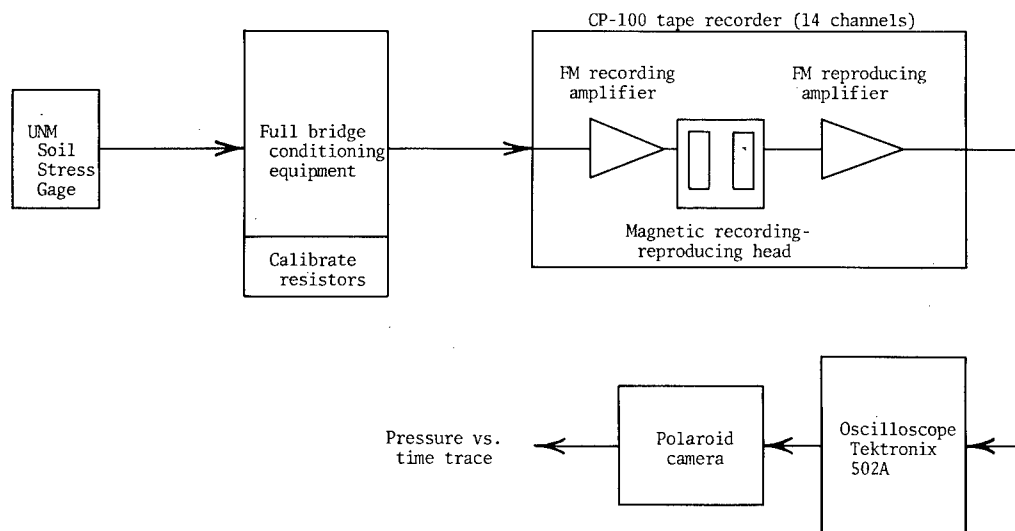

Fig. 11. Schematic of electronic recording system

variables and relationships. The Parameter Study tests from which results are reported here are given with their physical parameters in Table 2. These include tests 3, 4, and 5 of Series I, all three tests of Series II, and test 1 of Series III which was a replica of test 2 of Series I. (The first two tests of Series I are not reported since the data were obscured by cable noise and instrumentation failure.) The results of the Air Force Weapons Laboratory Phase II experiment (7) are also included for comparison with the Parameter Study.

All data presented from the Parameter Study were taken from Polaroid photographs of the pressure-gage response described previously. Data from the Phase II experiment were electronically digitized and plotted. In the Phase II experiment, Norwood gages were used to measure air pressure, and UNM gages monitored the stress in the soil near the surface. To compare the results of the Phase II experiment with those of the Parameter Study, only data from near-surface (6-in. burial) UNM gages were utilized for both cases. Thus, inconsistencies which may have resulted from comparing the records of different types of gages were avoided.

To remove boundary effects from the data, an area of the cavity was chosen where a number of gages appeared to give the most consistent results and which was far enough from either end of the cavity to reduce as much as possible effects caused by the shock-wave reflections off the ends. The length of the cavity

was divided into quarters and analysis of the data indicated that the second quarter from the firing end (Fig. 10) best suited the above conditions. All data presented represent the average values of the pressure-time results from that area. It is a fortunate coincidence that these data represent a fair average of data for the entire cavity.

Peak Overpressure

Figure 12 shows the experimentally determined trend of the peak pressure versus charge density relationship. The numbers beside each point identify the Series and test. The location of the center of gravity (c.g.) of the Primacord rack was at the center of the cavity for all points shown in Fig. 12. Although more testing must be done, a definite trend has been established, and the fact that the point representing test II-2 follows the trend of the remaining points lends substance to the assumption that the initial-shock pressure is independent of the surcharge pressure. The variation of peak pressure with the location of the center of gravity of the Primacord rack is shown in Fig. 13. In a 4-ft deep cavity, the peak pressure appears to rise as the explosive is positioned closer to the ground.

Shock-Front Velocity

The shock-front velocity was assumed to be a function of only the angle of weave of the

TABLE 2
Test Parameters for Reported Results

Series	Test	Charge Density (lb/cu ft)	Angle of Weave (degrees)	Surcharge Pressure (lb/sq ft)	Z^a (ft)	Cavity Height (ft)	Pit Dimensions (ft)
I	1 [b]	0.0740	8.80	1028	2.0	4	8 x 20
	2 [b]	0.1350	12.50	1045	2.0	4	8 x 20
	3	0.1720	15.00	1031	2.0	4	8 x 20
	4	0.2150	18.00	1064	2.0	4	8 x 20
	5	0.4020	24.75	1045	2.0	4	8 x 20
II	1	0.0726	17.83	439.3	1.0	4	8 x 20
	2	0.0710	17.83	438.5	2.0	4	8 x 20
	3	0.0770	17.83	452.5	3.0	4	8 x 20
III	1	0.1415	12.58	1081	2.0	4	8 x 20
AFWL	Phase II	0.0725	8.80	500	0.5	3	96 x 150

[a]Distance of c.g. of explosive from cavity roof.
[b]Data not included in the results because of instrumentation failure due to excessive cable noise.
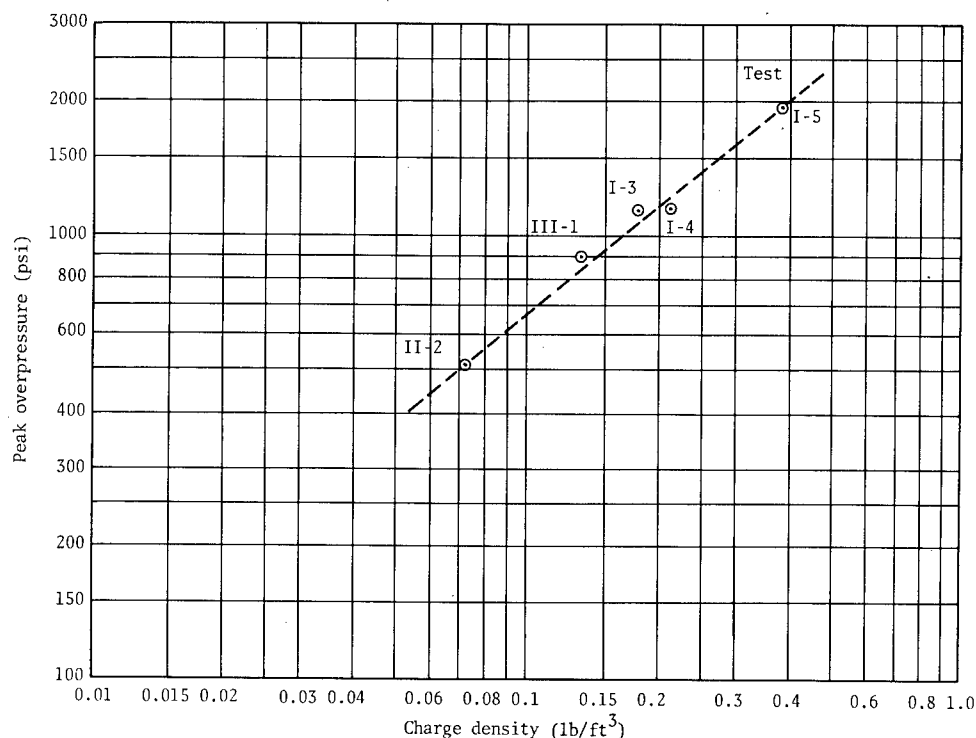
Fig. 12. Peak overpressure vs charge density

Primacord lattice. Figure 14 compares the experimentally determined, shock-front-velocity data plotted as a function of angle of weave to a curve calculated by multiplying the detonation velocity of the Primacord by the sine of the weave angle. The dashed line represents the trend of the data, ignoring the data from tests I-3 and I-4 where sympathetic detonation was suspected. Multiple racks were used in these tests, but it is believed that they were placed too close to each other. In test I-5 the spacing between the racks was increased, and this appeared to rectify the problem of sympathetic detonation.

Duration of Pressure Pulse

The experiments designed to determine the influence of the pit parameters on pulse durations have not yet been completed, and few results are available. Series I and II of the Parameter Study were designed primarily to examine determinations of peak pressure and shock-front velocity. The duration to one-half peak pressure varied from 7.7 ms for test III-1 to 3.0 ms for test I-4, a band which was too narrow for interpretation. The situation was much the same regarding total duration of the pulse, which averaged about 110 ms for Series I with a 20 percent scatter band. Although the

durations were disappointingly short, it must be remembered that the 8- by 20-ft test cavity is relatively small, and there is evidence that durations may be greatly affected by the ratio of the area to the perimeter of the cavity. Table 3 compares test I-3 with the AFWL Phase II experiment (7). Test I-3 was chosen to compare with the Phase II experiment because the ratios of peak pressure to surcharge were very nearly the same. Series V, in which the size of the pit is varied, will shed more light on variation of durations with area-perimeter ratio, but on the basis of this comparison a trend is apparent. It indicates that a higher value of the area-perimeter ratio results in longer durations.

NUCLEAR WEAPON
  EQUIVALENCY

The pressure-time environment of an LDHEST experiment can usually be roughly equated with the effects, at some range, created by a nuclear weapon of some yield. For example, a pressure-time trace was chosen from test I-3 which represents as closely as possible an average of the traces from the second quarter of the cavity. This trace was integrated, and the resulting impulse was used, according to the cube foot scaling law (2), to determine an

99
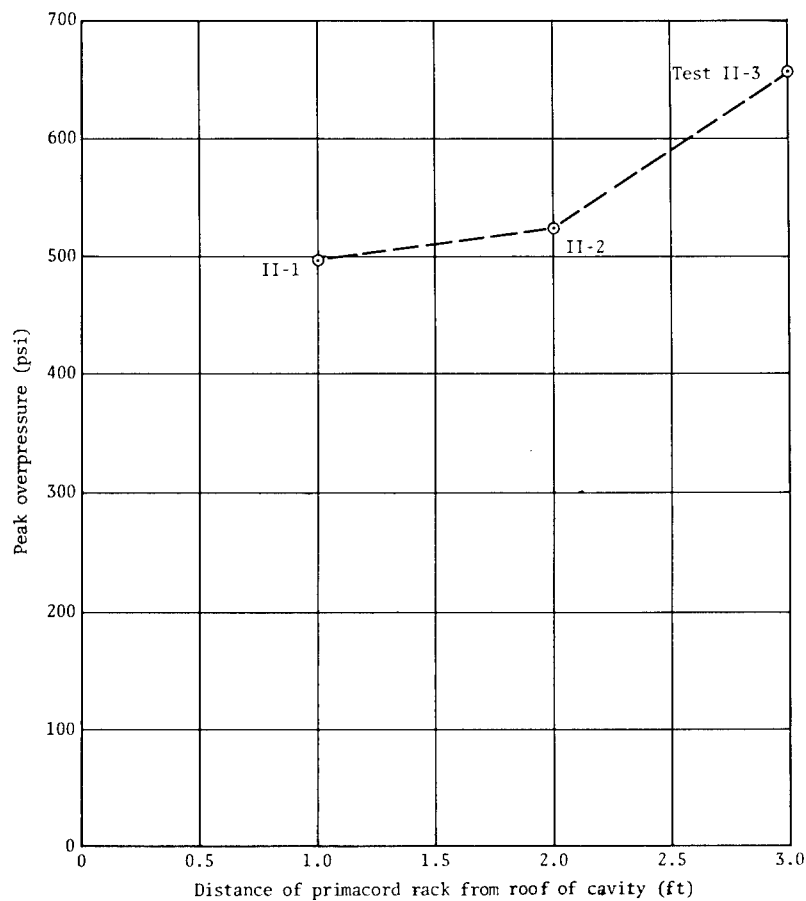
Fig. 13. Peak pressure vs distance
of rack from roof of cavity

TABLE 3
Comparison of Test Parameters for AFWL Phase II Experiment with CERF Test I-3

Test	Peak Pressure/ Surcharge Pressure (psi/lb/sq ft)	Area/ Perimeter (ft)	Duration to One-Half Peak Pressure (ms)	Total Duration (ms)
AFWL Phase II experiment	1.20	29.0	18.6	170
CERF test I-3	1.34	2.9	3.3	90

equivalent yield weapon of 17 kt. The pressure-time curve produced by such a weapon at a range of 360 ft from ground zero was found to approximate closely that of the trace. Figure 15 shows the trace for test I-3 superimposed on the calculated pressure-time curve for a 17-kt weapon (3) at a range of 360 ft from ground zero, and Table 4 summarizes the important parameters.

Table 4 indicates that although the total impulses of test I-3 and the 17-kt weapon compare favorably, the total durations of the two pulses are quite different. This discrepancy can be explained by the fact that the pressure-time trace of test I-3 is not monotonically decaying as in the case of a nuclear weapon burst. The LDHEST pressure-time trace contains random peaks and troughs which on the average

100
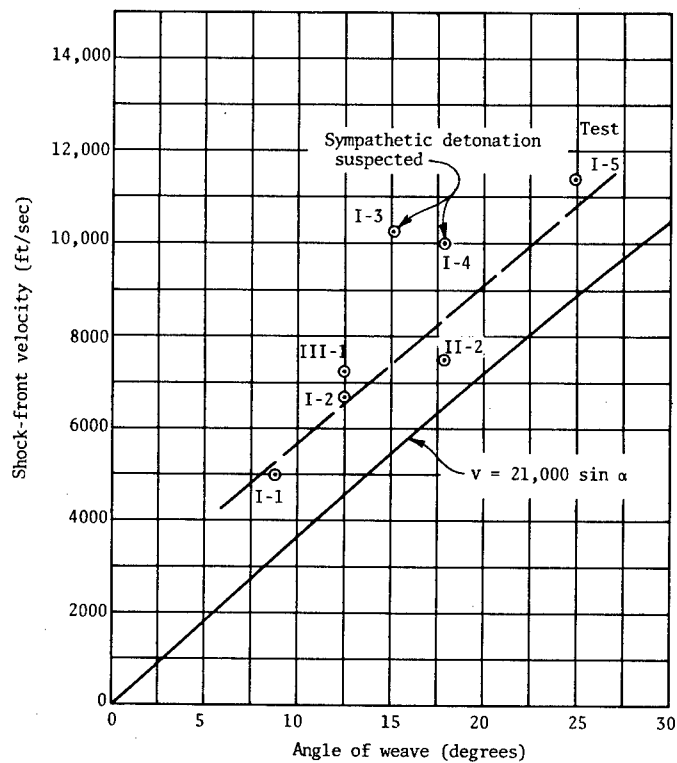
Fig. 14. Shock-front velocity vs angle of weave
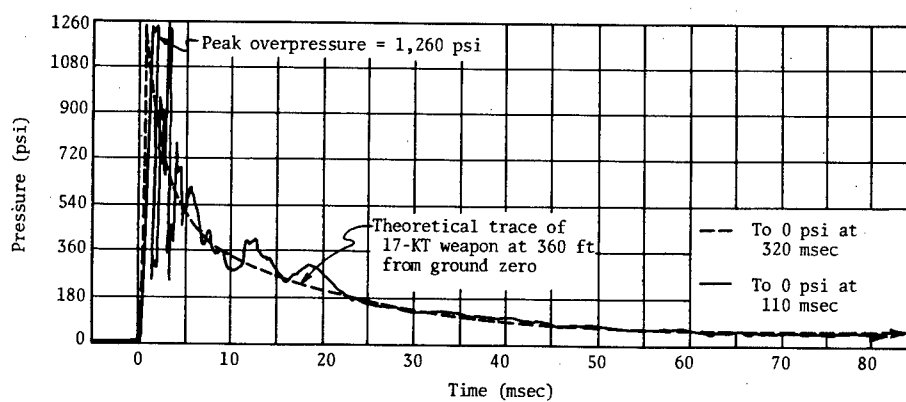
Fig. 15. Typical trace from test I-3

TABLE 4
Comparison of Phenomena from Test I-3 with Those from a 17-KT Weapon

Source of Phenomena	Peak Pressure (psi)	Duration to One-Half Peak Pressure (ms)	Total Duration (ms)	Total Impulse (psi-sec)
Test I-3	1,240	4.0	110	15.7
17-kt weapon	1,240	3.2	320	15.7

produce more impulse at early times, thus compensating for the loss of impulse due to the shorter total duration of the LDHEST pulse.

DISCUSSION

The pressure at the shock front caused by the detonation of a high explosive is known to be a function of the weight of explosive detonated, the density of the explosive, and the distance between the explosive and the point at which the pressure is measured (9).

For the Parameter Study it was assumed that the initial peak pressure was a function of charge density and possibly the vertical position of the center of gravity of the explosive in the cavity. Since the initial pressure pulse had been observed (7) to be far too short in duration to cause appreciable movement of the large surcharges used for the study, it was also assumed that the initial peak pressure was independent of surcharge pressure. The trend indicated by Fig. 12 substantiates these assumptions; it points to a definite relationship between peak pressure and charge density for tests I-3, I-4, I-5, and III-1, all of which had nearly the same surcharge pressure. The point representing test II-2 follows the trend, even though only conducted at roughly one-half of the surcharge pressure of the other tests.

As the Primacord rack is moved closer to the ground, an increase in peak pressure occurs as shown in Fig. 14. The initial pressure imparted to the ground is the reflected pressure caused by the reflection of the shock front off the ground surface. The shock-front pressure in air decreases as the distance from the explosive is increased (9), so that a larger air-shock pressure was reflected as the explosive was moved nearer to the ground surface.

Within the range of ratios tested, the plot of shock-front velocity versus angle of weave of the Primacord shown in Fig. 14 appears to be displaced above the predicted sine curve by a constant amount. The trend of the data in the range studied indicates the possibility of describing the functional relationship between shock-front velocity and weave angle as follows:

$$u = v \sin \alpha + c ,$$

where

u = shock-front velocity,

v = velocity of Primacord detonation (21,000 fps),

α = angle of weave of Primacord, and

c = a constant (units of velocity).

Based on the data gathered so far, a tentative value of 2,000 fps could be assigned for c, but more testing is necessary before this value is assigned.

The assumption of the dependence of the shape of the wave and the total duration of the pressure pulse on the ratio of the area to the perimeter of the cavity appears to be justified to some extent by the comparison in Table 3. If two test pits are constructed with cavity heights which are approximately the same (within 2 to 5 ft), then the percent of gas lost by venting around the perimeter would appear to be a function of the ratio of the area to the perimeter for a given charge density and surcharge pressure. The durations and shape of the wave were assumed to be a function of this ratio and also of the ratio of peak pressure to surcharge pressure, the latter being a measure of the expanding volume of the cavity.

For some configurations (i.e., a large pit with low surcharge pressures and initial high-peak pressures), the ratio of peak pressure to surcharge pressure may be the predominant parameter affecting durations, whereas for other configurations, the ratio of the area to the perimeter may be the most important. For example, the tests in Series I possessed ratios of low-peak pressure to surcharge pressure, so that the comparison of one of these tests

with the larger AFWL Phase II experiment indicated a marked increase of duration to one-half peak overpressure as the ratio of the area to the perimeter increased. It is realized that durations may, for some test configurations, be equally a function of both of these parameters, and the final results of the Parameter Study should provide further evidence.

Initially, it was hoped that the pressure-time environment generated by the Parameter Study Series I tests would be comparable to that of a large-yield weapon, but the fact that the pressure-time environment of a 17-kt weapon was generated is encouraging.

CONCLUSIONS

Based on the data obtained from the Parameter Study and a few selected Air Force experiments, the following tentative conclusions may be drawn:

1. Peak overpressure is related to charge density, and there is evidence to support the assumption that it is not a function of surcharge pressure. The final results of Series III tests, in which the charge density is held constant while the surcharge pressure is varied, will provide further information on this point.

2. Peak overpressure is related to the location of the center of gravity of the explosive above the floor of the test cavity.

3. Shock-front velocity is a function of the angle of weave of the Primacord and, within the range of values tested, a reasonable function has been proposed.

4. The duration of the pressure pulse and the wave shape appear to be a function of the ratio of the area to the perimeter of the cavity. It is believed that the wave parameters may be a function of the ratio of peak pressure to surcharge pressure, and Series III tests are designed to study this relationship (for a small area-perimeter ratio).

5. The pressure-time pulse generated in test I-3 closely represents that of a 17-kt weapon at a range of 360 ft from ground zero.

In summary, the results obtained from the LDHEST experiments are encouraging. A maximum pressure of 1,900 psi was generated in test I-5. If a pressure of this magnitude can be coupled with the relatively long durations which apparently can be achieved in a large pit, the impulse generated may be sufficient to allow the simulation of the free-field soil displacements, velocities, etc., which would be induced by a large-yield weapon. The limits of the size of the weapon which can be simulated remain to be defined, and the results of the Parameter Study will be very useful in designing experiments to determine these limits.

ACKNOWLEDGMENT

REFERENCES

1. N. M. Newmark and J. D. Haltiwanger, Air Force Design Manual, Principles and Practices for Design of Hardened Structures, AFSWC TDR-62-138, Dec. 1962

2. S. Glasstone (ed.), The Effects of Nuclear Weapons, rev. ed., U.S. Department of Defense, U.S. Atomic Energy Commission, April 1962

3. H. L. Brode, A Review of Nuclear Explosion Phenomena Pertinent to Protective Construction, The Rand Corp., R-425-PR, May 1964

4. J. K. Croby et al., "Feasibility of Simulating the Mechanical Effects of a Nuclear Explosion Using Non-Nuclear Explosives," DASA-1264, Dec. 1961

5. F. R. Kurz, "Investigation of Air-Blast-Induced Ground Motion Technique Using High Explosives," MRD Div., General American Transportation Corp., unpublished report to AFWL, Nov. 1964

6. Gerald P. D'Arcy, Harry E. Auld, and Gerald G. Leigh, "Simulation of Air-Blast-Induced Ground Motions (Phase I)," AFWL TR-65-11, April 1965

7. Harry E. Auld, Gerald P. D'Arcy, and Gerald G. Leigh, "Simulation of Air-Blast-Induced Ground Motions (Phase II)," AFWL TR-65-26, April 1965

8. R. E. Lynch, "Development of the University of New Mexico Soil Stress Gage,"

Tech. rept. to AFWL, to be published 1965

9. Stuart R. Brinkley and John G. Kirkwood, "Tables and Graphs of the Theoretical Peak Pressures, Energies, and Positive Impulses of Blast Waves in Air," NDRC Rept. No. A-327, OSRD Rept. No. 5137, May 28, 1945

DISCUSSION

<u>Dr. Sevin (IIT Research Inst.)</u>: I think the Hess technique is extremely ingenious and I am sure it will have great application. There is yet another parameter that in your presentation was not explicitly considered which we think is critical in controlling the initial time decay rates. That is the compressibility properties of the soil being loaded and that of the surcharge. In the Weapons Lab Phase II report, which you have not specifically mentioned, using the compressibility data or elastic property data of the soils with which you dealt, we did a preliminary one-dimensional compressibility analysis including the compressibility effects of the surcharge and the soil being loaded. We came out very very close to the average measured pressures and substantially closer than the theoretical predictions based on a rigid body surface and rigid body overburden motion. If this is the controlling mechanism, which we strongly suspect it to be, it seems to us that during the times perhaps of 10 to 20 ms, the order of times of the double transient wave through the surcharge, the rate of decay is essentially independent of the depth of surcharge, at least for 5 ft or more of material. It will be at least in the kiloton range and not in the desired megaton range. I would be interested if you could comment on any work that

you are doing related to the influence of compressibility.

<u>Dr. Zwoyer</u>: Thank you, Dr. Sevin. On some of the tests which were not a part of our parameter study, we had targets placed on the bottom and on the top of the surcharge, and recorded what happened with Fastax cameras. Although one cannot get very precise measurements this way, there was not any noticeable compressibility in the surcharge. In the same experiment we had targets anchored to the bottom of the cavity, just below the surface, and those targets moved downward appreciably. The cause of the initial growth of the cavity is an immediate large displacement of the ground surface, rather than the upward motion or compressibility of the surcharge. We do not have a systematic program outlined at this time to study that, but it is an interesting feature. If it turns out that we are unable to get the durations that we think we can get, this is perhaps one possible explanation. We will design some tests to study it. Some of our experiments do indicate that we are reproducing rather accurately the initial portion of the pressure-time curve for weapons above 500 kt, not the total positive phase duration, but the initial 150 ms.

* * *

STRUCTURAL AND FUNCTIONAL TESTS OF A FULL-SCALE

GEMINI RENDEZVOUS AND RECOVERY SECTION AND

AN AGENA TARGET DOCKING ADAPTER AS SUBJECTED

TO AN ORBITAL MOORING SHOCK ENVIRONMENT

N. E. Stamm and J. F. Siller
McDonnell Aircraft Corporation
St. Louis, Missouri

The McDonnell Structures and Dynamics Laboratory conducted a series of tests, simulating full-scale Gemini and Agena orbital moorings, to qualify structurally and functionally the Gemini Rendezvous and Recovery (R & R) Section and Agena Target Docking Adapter (TDA) Assembly as subjected to the mooring shock environment. The R & R section and TDA assembly were each mounted on fabricated steel frameworks with the composite vehicle assemblies each simulating the mass, c.g. location, and three-axis mass moments of inertia of their respective production vehicles for an orbital configuration.

The test vehicles were suspended as simple pendulums, 56.67 ft in length, with a gimbal system at each c.g. providing the vehicles with five degrees of freedom for small values of pendulum displacement. The Gemini test vehicle was pulled back and then allowed to swing forward through a predetermined distance to attain various vehicle limit and ultimate closing velocities. Vehicle attitudes and locations of impacts were also controlled. Selected accelerations, loads, displacements, and bending moments of various mooring system components and vehicle rigid body accelerations were recorded.

INTRODUCTION

The NASA-Gemini Space Program will, as a prelude to the Apollo lunar landing, conduct a series of rendezvous missions between a Mc-Donnell-built Gemini Spacecraft and an earth-orbiting Agena-D Target Vehicle, equipped with a McDonnell Target Docking Adapter.

Establishing techniques to effect a rendezvous between orbiting vehicles, prior to the Apollo mission, is an essential step, since it is in this manner that the Apollo astronaut will return from his lunar excursion to the orbiting command module. Rendezvous and mooring capabilities are also tentative prerequisites for the successful staffing and supplying of future manned orbiting laboratories.

This paper discusses methods employed by the McDonnell Structures and Dynamics Laboratory in conducting a series of simulated orbital moorings for the structural and functional qualification of the full-scale production-type Gemini Rendezvous and Recovery (R & R) Section and the Agena Target Docking Adapter (TDA) Assembly. An earlier paper, presented at the 33rd Shock and Vibration Symposium, discussed a 1/4-scale mooring test conducted by McDonnell to evaluate design concepts and establish mooring parameters for a successful mission. Mooring is that phase of the Gemini rendezvous mission when contact is established between vehicles and consists of impact, latching, and rigidization of the moored vehicles at the, now adjacent, interfaces.

Four objectives of the test program were to:

1. Qualify production hardware for limit and ultimate mooring impact loads;

2. Demonstrate satisfactory latching, rigidizing, and release system operation subsequent to the impact environment;

3. Compare latching capabilities with 1/4-scale results; and

4. Demonstrate the emergency release system.

The structural and functional qualification of the TDA assembly and the R & R section, as subjected to the mooring shock environment, is only one phase of a rigorous qualification program which the mooring system and its components must undergo.

DESCRIPTION OF SPECIMENS

General

The Gemini and Agena test vehicles were assembled from fabricated steel structures and the production mooring hardware (R & R section and TDA assembly). The vehicle assemblies were designed to simulate the mass, c.g. location, and three-axis mass moments of inertia of their production prototypes.

Each vehicle was suspended as a simple pendulum with an effective length of 56.67 ft, measured from the c.g. of each vehicle to the overhead pivot point. One-third of the suspending cable mass was considered effective and was added to the total vehicle mass. The free end of each cable terminated in a gimbal system centered at the vehicle c.g. The relatively long pendulum lengths, combined with the gimbal systems, provided the vehicles with two translational degrees of freedom (for small values of pendulum arc) and three angular degrees of freedom. Testing was restricted to conditions which utilized these five degrees of freedom, with the vehicles being reoriented to meet conditions requiring the vertical, or sixth degree of freedom. The vehicles are shown in a pretest condition in Fig. 1.

Agena TDA Assembly

The portion of the TDA assembly which receives the Gemini vehicle during the docking maneuver is conical in shape and is coated internally with a dry film lubricant. The leading edge of the TDA cone is notched at the top to receive an indexing bar on the Gemini R & R section which keys the vehicles together if a roll misalignment exists. The cone is supported by a system of seven fluid-filled dampers, arranged to dissipate energies inherent with the relative lateral, longitudinal, or roll motions which might exist between the vehicles. The dampers which act parallel to the longitudinal axis are spring loaded and also meter fluid during their return strokes. This prevents vehicle rebound following impact and also returns the cone to a ready position if latching has not occurred and the astronaut desires to withdraw and attempt another entry.

The dampers which dissipate energy associated with lateral vehicular motion also serve to keep the cone laterally centered prior to the mooring operation. The dampers were designed to perform this function in an orbital, zero-g environment, but could not center the cone during the 1-g mooring test environment. This required a method of counterbalancing the cone which would induce a minimum amount of restraint in the cone-damper system. Counterbalancing of the cone was achieved through the use of a shock-cord spring rated at 3.4 lb/in. The spring arrangement, including associated hardware, is shown in Fig. 2.

A boom which supports the TDA transponder antenna was extended to its full 85-in.
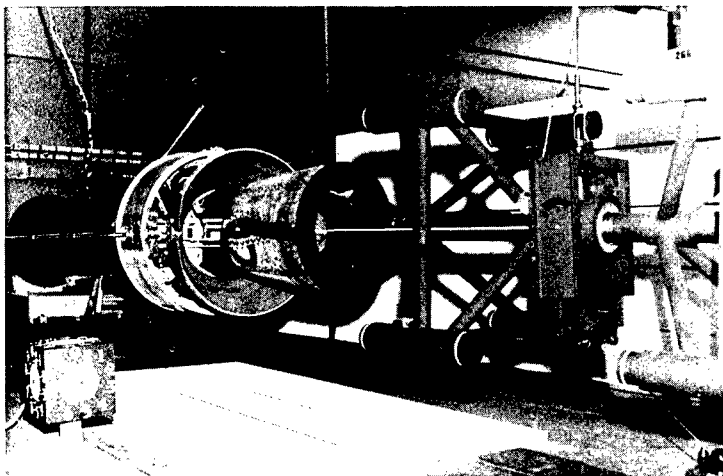

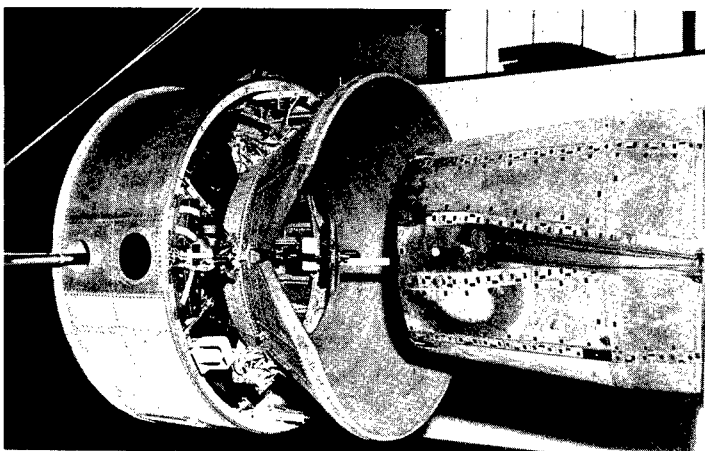Fig. 1. General arrangement of Gemini Agena mooring test setup

Fig. 2. Gemini R&R section and Agena TDA assembly with TDA cone counterbalance system installed and indexing slot horizontal

length and the antenna, located at the extreme end of the boom, was removed. Instrumentation, having the same mass as the removed antenna, was added to the end of the boom.

The apex of the TDA cone has an interrupted ledge or shelf, spaced circumferentially every 120 degrees with a partially recessed spring-loaded latch located at each shelf segment. It is against this shelf that the leading edge of the Gemini R & R section must ultimately rest to effect a successful mooring maneuver. The R & R section contains three receptacles which engage the TDA latches, and all three latches must be engaged before rigidization of the vehicles can be achieved. After complete latch engagement has occurred, the TDA mooring drive motor automatically begins pulling the cone and attached Gemini vehicle down onto three structural hard points.

The vehicles may be unrigidized by astronaut command through the umbilical connection existing between vehicles and established during the rigidization cycle. This is the normal mode and includes energizing the latch release mechanism actuator which retracts all latches. Should the vehicles fail to unrigidize or separate, an emergency release system, contained in the Gemini R & R section, may be used. Following their retraction by the actuator, all latches are automatically extended within 30 seconds; it is during this period that the astronaut must effect the Gemini withdrawal, if he so desires. The latches are returned to the extended position to be prepared for future mooring maneuvers.

Gemini R & R Section

The inability to separate the moored vehicles by normal methods would require activation of the emergency docking release system. Activation of the system separates each latch receptacle from the R & R section through a pyrotechnic device, resulting in the complete severance of mechanical linkage between the two vehicles. The three voids in the R & R section skin, left by ejection of the latch receptacles, are covered by individual, pyrotechnically activated, door assemblies. The skin openings are covered to protect recovery components, housed in the R & R section, from elevated temperatures encountered during the vehicle reentry phase.

The indexing bar on the R & R section, which engages the TDA cone slot, was fully extended. Reflective tape was installed on the leading edge of the R & R section during the latter stages of the test program to determine the ability of the tape to remain intact and in place during impact and subsequent chafing between the R & R section and TDA cone. The purpose of the tape was to improve the Gemini radar image for ground tracking stations during orbit.

The Gemini vehicle was equipped with a modified 1600-lb capacity electromagnet, located beneath the vehicle c.g. and integral with the gimbal housing. The magnet was used to restrain the vehicle while in a pulled-back or ready state prior to testing..

107

SETUP AND PROCEDURE

Various vehicle attitudes, impact locations on the TDA cone, and limit and ultimate relative vehicle closing velocities were attained by pulling back, positioning, and then releasing the Gemini vehicle. The Agena vehicle was maintained in a static condition prior to impact. Restraint and release of the Gemini vehicles was accomplished through the electromagnet located below its c.g. Limit and ultimate values of lateral and longitudinal closing velocities were: lateral, 0.50 and 0.58 fps; longitudinal, 1.50 and 1.75 fps. Drifting or other undesirable movement of the vehicles during the pretest period, which would destroy their alignment, was averted by the use of a light restraint placed at the aft end of each vehicle. Optical tooling was used to align the vehicles prior to testing. The test setup is shown in Fig. 1.

Since the vehicles were not free to translate along the supporting cables' axes, tests which required misalignment of the vehicles in a pitch plane required that the vehicles be rolled with their pitch planes parallel to the ground. Misalignment of the vehicle c.g. was accomplished by laterally adjusting the Gemini overhead pivot point, from ground level, through hydraulic pumps and cylinders. Location of the Agena overhead pivot point was fixed.

For tests which required impact of the R & R section on the TDA cone at locations ahead of the cone shelf, the Gemini overhead pivot point was adjusted so that the vehicle attained a maximum velocity midway between the initial impact point and impact at the cone shelf. The maximum velocity was greater than the desired velocity in this case, but was an effective compromise to attain approximately equal kinetic energies at initial impact and impact at the cone shelf. Dissipation of energy following initial impact, resulting from friction losses and cone deflections, prevented the kinetic energies at the two impact locations from being exactly equal.

One series of tests was conducted to impose the maximum anticipated loading on the R & R section indexing bar and to impart a maximum amount of energy about the roll axis to the TDA damping system. A relative roll velocity between vehicles was induced by placing an eccentric mass on the Gemini vehicle disengaged at approximately one-half the time required for the vehicles to close. The test setup for this condition is shown in Fig. 3. The relative roll velocity at impact was 10 degrees/sec and was in addition to the lateral and longitudinal closing velocities. Prior to testing, the torque resulting from the eccentric mass was reacted by a roll restraining device, with the restraint removed simultaneously with vehicle release. The indexing slot on the TDA cone was vertical for this series of tests.

The TDA mooring drive motor was energized for each test and automatic rigidization of the vehicles occurred during tests in which all three
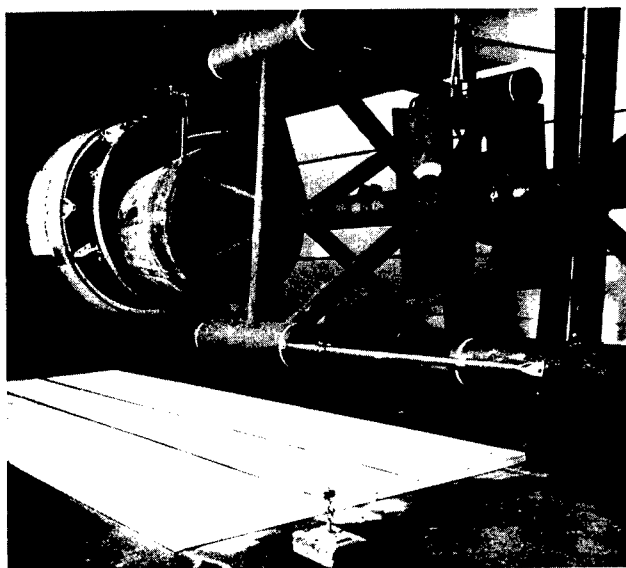

Fig. 3. Gemini test vehicle shown prior to initiation of relative vehicular roll rate

TDA latches engaged. Following tests in which partial or no latching occurred, all non-engaged latches were manually engaged and the vehicles were then rigidized. The mooring drive motor was energized through the TDA/R & R umbilical connection to unrigidize the test vehicles.

A comparison was made between the mooring capabilities of the full-scale vehicles and results obtained during the 1/4-scale model development tests. Vehicle attitude and alignment boundaries within which latching might occur were defined during the 1/4-scale tests. The comparison consisted of a series of ten tests duplicating impact parameters of selected tests conducted with the 1/4-scale models.

The last phase of the test program was the qualification of the emergency docking release system. The system was tested for three Gemini/Agena moored configurations: vehicles latched and rigidized, vehicles in a loose-latch condition with the leading edge of the R & R section resting against the TDA cone shelf, and vehicles in a loose-latch condition with the R & R section moved aft to the limits of the TDA latch restrictions. No data were recorded during this series of tests.

The following data versus time were recorded for all impact testing: TDA damper loads and strokes, transponder antenna transverse accelerations at the extended boom extremity, latch release mechanism actuator transverse accelerations, R & R section indexing bar bending moments, longitudinal and lateral accelerations at the c.g. of each vehicle, and angular acceleration about the Agena suspending cable axis.

All tests were recorded on film at 64 frames/second and included coverage from three views: profile, plan, and end. Films were correlated with all test data through the use of a clock, which appears in each film. The clock recorded elapsed time to the nearest 0.01 sec, with a reference impulse appearing on all data corresponding to a visual indication of zero time on the clock.

RESULTS

Structural failures, component malfunctions, excessive loads, binding, or other deleterious effects did not occur during the test program. Latching capabilities for various impact parameters of the full-scale test vehicles equipped with production mooring hardware compared favorably with vehicle attitude and alignment boundaries established during the 1/4-scale mooring tests.

*   *   *

EXTENSION OF SHAKER SHOCK CAPABILITIES

James M. McClanahan and John Fagan
Astro-Electronics Division
Radio Corporation of America
Princeton, New Jersey

The scope of this evaluation (the extension of shaker shock capabilities by dc biasing the driver coil) is limited to data obtained by double integration of the acceleration waveform. This determination of the positive and negative displacement from a zero-deflection position of the shaker moving element indicates possible extension of shock capability. The restriction of scope was necessitated by technical problems involved when an attempt was made to "jury rig" a biasing setup for this evaluation. One shaker manufacturer indicated that a blocking capacitor was required to block the dc current through the power amplifier output transformer and prevent saturation of the transformer. The mathematical evaluation of acceleration data indicated that the extension of capability is worth the cost of a biasing unit. The greatly improved frequency response of the overall shock console allows for more repeatable control of the undershoot by greatly reducing the interaction between the leading edge and trailing edge of the input pulse. This increased control of undershoot provides an increase of shaker shock acceleration capability in long-time-duration half-sine shock pulses with the specimen coupled to the moving element. It is not anticipated that sawtooth shock capability will be extended with the improved control, due to the low axial resonance and the shaker-and-power amplifier dynamics.

DISCUSSION

An attempt was made to jury rig a dc bias for a shaker system to evaluate the gain in shaker shock capability. A test setup of on-hand equipment was made as closely as possible to that described by Ben Reznek [1]. The object of the dc bias is to deflect the shaker moving element statically to permit utilization of the full distance between shaker limits. The static deflection required would be either plus or minus, depending on the input pulse waveform and the shock pulse direction. The jury rig was completed and provided excellent control of shaker deflection, but the shock pulse was lost. Discussion with equipment manufacturers, who are currently marketing shaker displacement dc bias units, revealed that some of the optional items cited by Reznek [1] are required. The manufacturer informed us that the blocking capacitance in series with the output transformer is required to prevent saturation (Fig. 1). A very large value of capacitance and inductance would be required; both become very expensive in large values.

Since the jury rig was impractical and insufficient time was available for procuring capital equipment, a double integration of the shock acceleration pulse was utilized to evaluate the possible gain in shock capability by dc biasing of the driver coil. This single and double integration was done graphically utilizing the Simpson Rule for approximating integrals. The half-sine resultant curves are shown in Fig. 2. Note that the peak displacements occur in time-phase with minimum velocity, and the peak acceleration occurs midway between velocity peaks.

A single sawtooth shock pulse was evaluated to determine the displacement characteristics of the shaker with the required input. The results were similar to that of the half sine only in that the displacement is in one direction. The displacement follows the pattern predicted by McClanahan and Fagan [2]. This similarity should occur as both pulse shapes are generated by the leading and trailing edge of the input pulse (i.e., half-sine input, half-sine output or integrated-sawtooth input, and sawtooth output). Both the half-sine pulse of Ref. [2] and the sawtooth evaluated in this paper utilize an uncoupled slip table with some form of striker-and-anvil arrangement between the slip table and the shaker head.
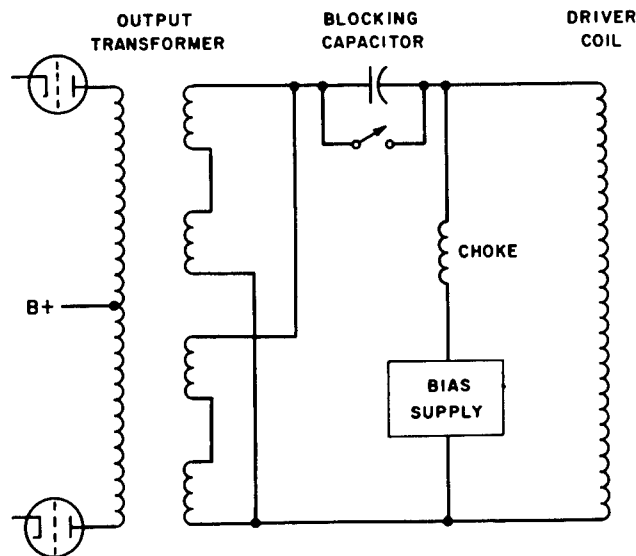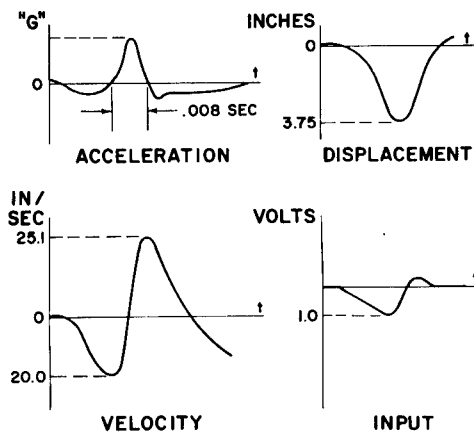
111

Fig. 1. Typical shaker dc bias

Fig. 2. Typical half-sine
pulse on C10VB

There are three possible areas which could limit the extension of shaker shock capability by dc biasing of the driver coil: (a) actual plus-and-minus deflection of near equal value, (b) velocity limit (voltage output limit from the power amplifier), and (c) shaker protective device (amplitude protector) triggering. In all tests using double integration, the deflection was much greater in one direction than the other. The peak velocity attained was well below that of the shaker-power amplifier capability limit. Evaluation from the double integrated data indicates that both areas (a) and (b) above, would not be limiting factors to an extension of capability by dc biasing of the driver coil. Without the actual dc biasing system, we

were unable to determine the interaction of the amplitude protector and the applied shock pulse.

In the previously completed study of shaker shock capability (2), directly coupled half-sine shock testing was restricted to 8 ms or less. Note the extension of low-frequency response (Fig. 3) when the revised shock console is used. This extension of shaker shock capability was attained by electronically inverting the output of the shock console. The method described by Hay and Oliva (3) utilized an isolation transformer for pulse inversion. This imposed a low-frequency-response penalty, producing the uncontrollable undershoot for long-time-duration half-sine shock pulses. The electronic pulse inversion was accomplished by modifying an MB N504 amplifier. The modification was the addition of a plate-load resistor having a value equal to the cathode resistor of the cathode follower output and insertion of a bypass capacitor across the 5-cps filter. Figure 4 is a picture of the modified shock console; the schematic of the modification is shown in Fig. 5. The shock console was modified from the configuration shown in Fig. 6 to that shown in Fig. 7.

DIRECT COUPLED HALF SINE

The shock test method to utilize the increased control capability of the shock console was that described by Hay and Oliva (3). This method utilizes an input wave shape of a ramp function followed by a half cosine. The undershoot of the half cosine can easily be controlled with the isolation transformer removed. The
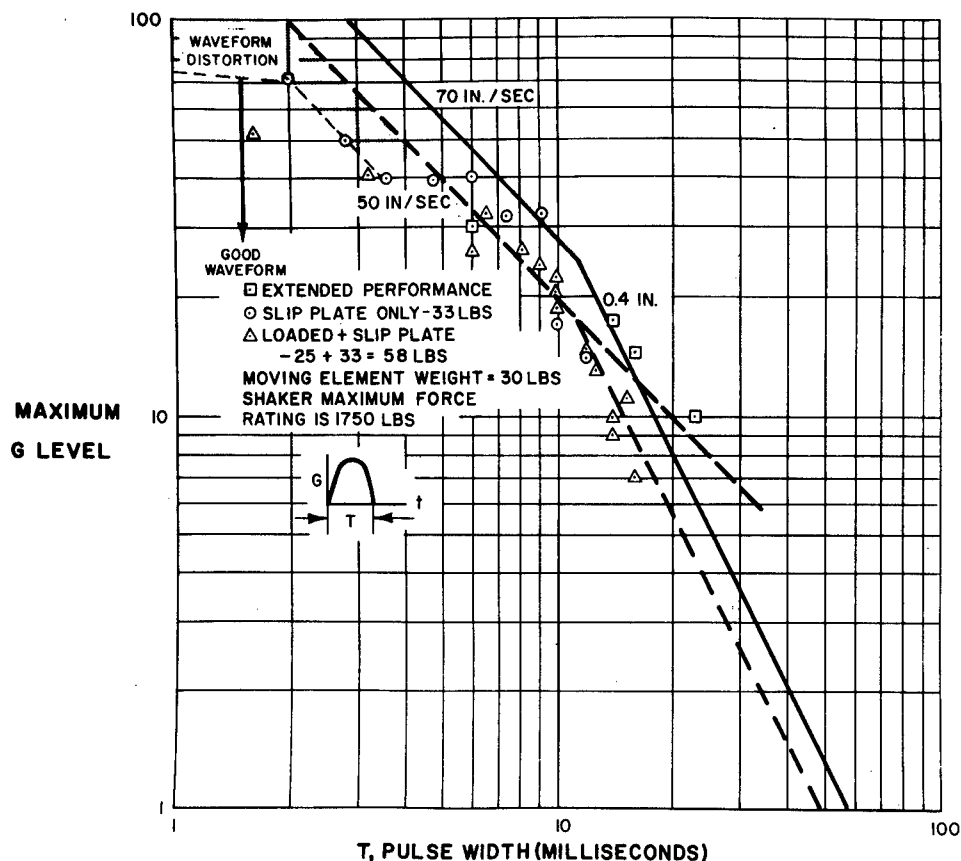
Fig. 3. Half-sine shock on M.B. C10VB

modification also eliminated the interaction be-
tween increments at the leading edge of the
ramp and the trailing edge of the half cosine.
This interaction made the shock test setup very
time-consuming and, on occasion, very frustrat-
ing. With the interaction problem corrected, a
new technique can be employed in optimizing
the pulse shape. The exact waveform synthe-
sizer can be put in the repetitive mode and the
shaker energized at a low level. The pulse is
then optimized by adjusting the amplitude of the
increments of the exact waveform synthesizer.
This optimization is, of course, accomplished
with only the fixture and monitor accelerome-
ter mounted on the shaker. The technique is
described in the RCA half-sine shaker shock
testing procedure given in the appendix.

UNCOUPLED SAWTOOTH
   SHOCK TESTERS

Sawtooth shock testing on a shaker must be
accomplished with the slip table fixture uncou-
pled from the shaker and driver through a
striker and anvil of some design. This method

is described in detail by Dinicola (4). The input
to the shaker is essentially an integrated saw-
tooth with a sharp fall off on the trailing edge.

This input to the shaker produces a saw-
tooth shock pulse with excessive undershoot.
The slip table fixture is butted against the
shaker head. A hardened steel block (striker)
is attached to both the slip table and shaker
head. Grease is applied to the mating surfaces
to eliminate chatter during the rise of the saw-
tooth pulse.

SHAKER CHARACTERISTICS

The input waveform requirements are af-
fected by the characteristics of the shaker and
amplifier. The voltage versus acceleration
(E/G) curve of the shaker reveals the frequency
range in which the shaker reacts as a velocity
generator and the frequency range at which the
shaker reacts as an acceleration generator.
The half-sine input waveform for the velocity
generator portion of the shaker response curve
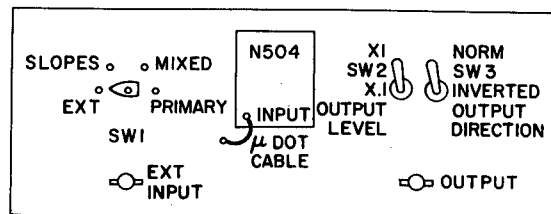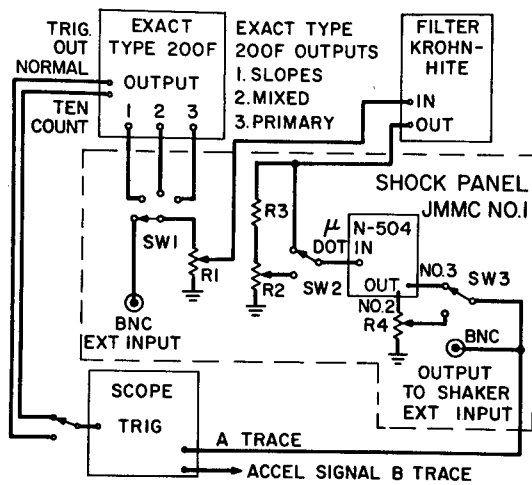is the ramp function followed by a half cosine.

113

Fig. 4. Modified M.B. N504
shock test console

Fig. 5. Schematic diagram of modification
to N504 amplifier
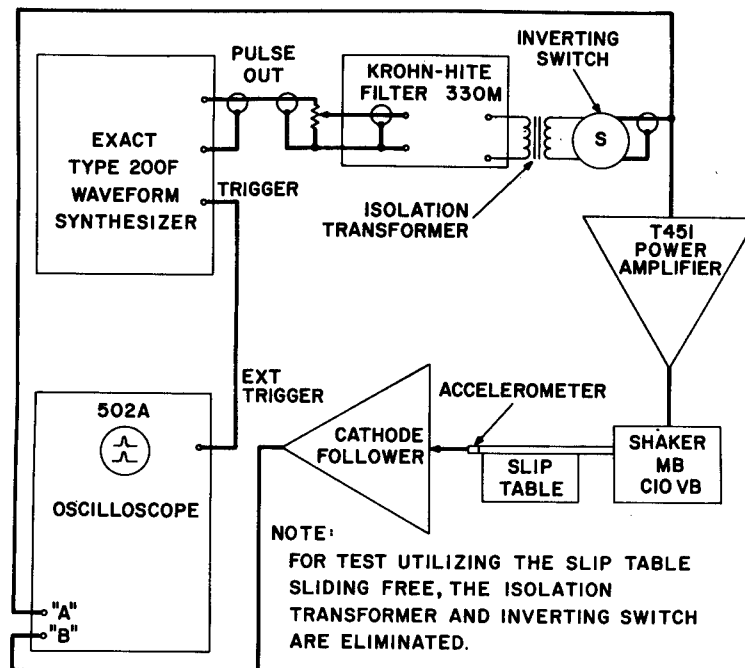
114

Fig. 6. Electronic isolation test setup

Fig. 7. Transformer isolation test setup

115

Figure 2 is an example of this input waveform and response. The half-sine input for the acceleration generator portion of the shaker response curve is a half-sine input. Figure 8 is an example of this input waveform and response. The MB C10VB, which has a very flat response curve, is an example of a shaker which requires a change of input waveform at a 5-ms pulse width. The MB C210 does not have a flat response and, therefore, does not require a change in input.
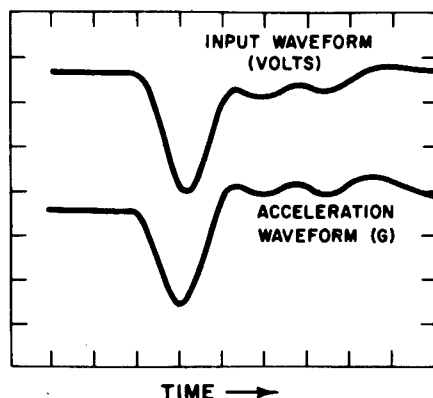

Fig. 10. C210 E/G curve

Fig. 8. Input and output wave-form in acceleration generator frequency range

The response curves for both the C10VB and C210 are shown in Figs. 9 and 10. These response curves verify the reason for the input waveform. This would also affect the sawtooth input waveform. In the velocity generator area of the response, a sawtooth input would be required for a sawtooth output.
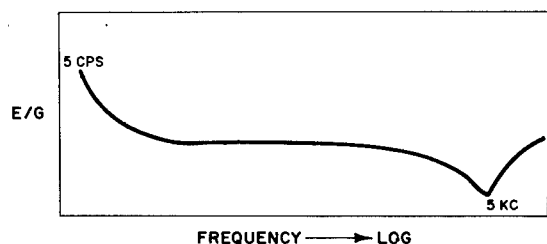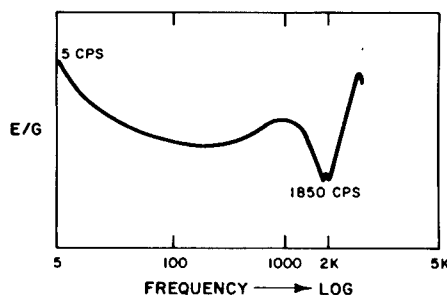

Fig. 9. C10VB E/G curve

An academic treatment of input versus output of the shaker and amplifier system would also consider the effects of starting conditions on the mechanical spring-mass system of the shaker armature and flexures.

The general solution of the differential equation of motion of a vibrating system consists of a particular solution (which goes to zero with time) and a steady state solution. In shock testing with shakers, the particular portion of the general solution would intuitively have an effect on the input and output dynamics of a shaker and amplifier system. This effect cannot be visualized by inspecting an E/G curve.

CONCLUSION

Shock capabilities of shakers can be extended by the use of armature dc biasing. The degree of extension would be limited by the shaker and amplifier and firing characteristics of the AP circuit. This would be predictable (i.e., utilizing the manufacturers vibration velocity limit for the shaker and amplifier combination).

Optimizing low-frequency response of the shaker shock console by providing electronic pulse inversion makes possible the realization of the advantage of reduced fixturing and reduced test time. This is especially true when the test specification will allow shock testing in an axis after completion of vibration in that axis. This would be true for all three axes of half-sine shock testing (directly coupled) and for the two slip table axes for sawtooth shock testing (slip table uncoupled).

REFERENCES

1. Ben Reznek, "Elimination of Static Shaker Deflections by DC Armature Biasing," Proc. IES (1963), pp. 425-431

2. J. McClanahan and J. R. Fagan, "Shock Capabilities of Electrodynamic Shakers," Proc. IES (1965)

3. Warren A. Hay and Ralph M. Oliva, "An Improved Method of Shock Testing on Shakers," Proc. IES (1963)

4. D. J. Dinicola, "A Method of Producing High Intensity Shock With An Electro-Dynamic Exciter," Proc. IES (1964)

Appendix

SHAKER SHOCK TESTING PROCEDURE

1.0 Half-sine shock pulse with test unit and fixture bolted to shaker.

   1.1 Connect output of shock test portable console (JMC-1) to shaker amplifier system. Connect accelerometer output to scope.

   1.2 Exact Waveform Synthesizer settings.

      1.2.1 All 50 matrix knobs (both red and black) full CCW.

      1.2.2 "Output amplitude" full CW.

      1.2.3 "Time/Increment" at 1 ms.

      1.2.4 "Trigger Source" at internal.

      1.2.5 "Trigger Mode" at normal.

NOTE: For most testing, only the top three rows of the Exact matrix need be used. To switch out the bottom two matrix rows, first set the "Time/ Increment" full CCW. Observe the 5 neon lights arranged in a vertical column at the right of the 50 matrix knobs. When the bottom two lights representing the bottom two matrix rows are NOT LIT, switch the two rows to OFF. The row switches are arranged in a vertical column to the left of the matrix knobs. Reset the "Time/Increment" to 1 ms.

   1.3 JMC-1 panel settings.

      1.3.1 Function selector to primary.

      1.3.2 N504

         1.3.2.1 "Function" to amplify.

         1.3.2.2 "Hi-P Filter" to 5 cps.

         1.3.2.3 "Gain" to X1.

      1.3.3 "Output Level" switch to X1.

      1.3.4 "Output function" switch to normal.

1.4 Set Khron-Hite filter for maximum bandpass.

1.5 Set scope panel switch to normal.

1.6 Turn first black matrix knob full CW and observe increment amplitude change on scope. Adjust scope trigger to where this increment is the first displayed increment of the scope sweep. Set both scope beams to monitor DC SIGNALS ONLY. (This is important.) Return first matrix knob full CCW.

1.7 Generating the pulse.

      1.7.1 Program the Exact unit as shown in Fig. A-1.
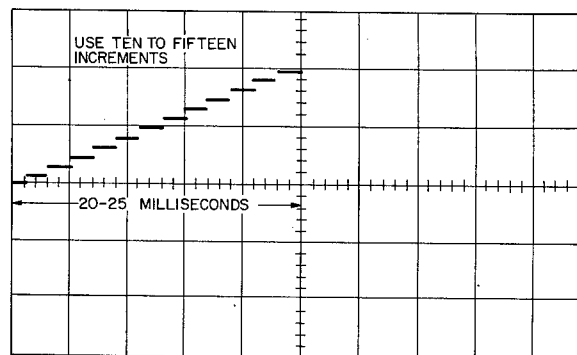

Fig. A-1. Exact program for half-sine pulse

      1.7.2 Reduce high-frequency cutoff on Khron-Hite filter until pulse smooths out. Set trailing edge of ramp pulse to desired half-sine time duration as indicated in Fig. A-2.

      1.7.3 Mount fixture on shaker, do NOT mount the test item. Check accelerometer setting, monitor accelerometer signal on scope (DC mode only). Set amplitude
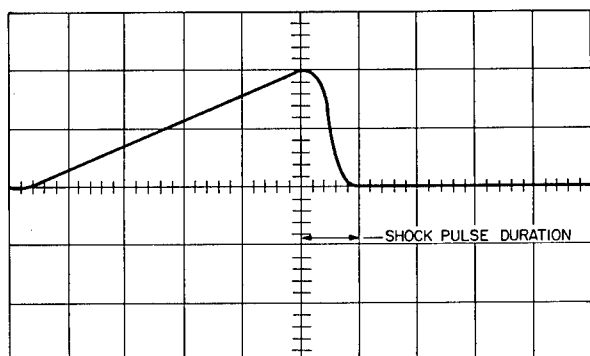
117

Fig. A-2. Filtered exact program
for half-sine pulse

Fig. A-4. Touch-up of
exact program

protector to 0.95 in. D.A. Set
Exact "Trigger Mode" at Pro-
gram Count.

1.7.4 Push "Reset" button on the Ex-
act; this will initiate the pulse
into the shaker system. Slowly
raise the shaker-power ampli-
fier gain while repeatedly push-
ing the reset button. The half-
sine pulse will be indicated by
the accelerometer. If the pulse
is not a clean half-sine, try
"touching up" by gradually
changing programmed incre-
ments of the Exact and observ-
ing the effect on the acceleration
signal. Figures A-3 and A-4
show an example of a common
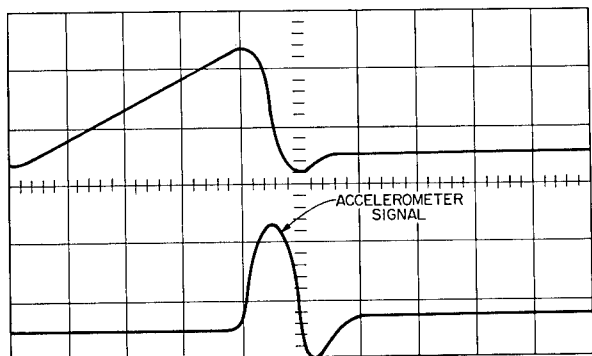type of "touching up" that might

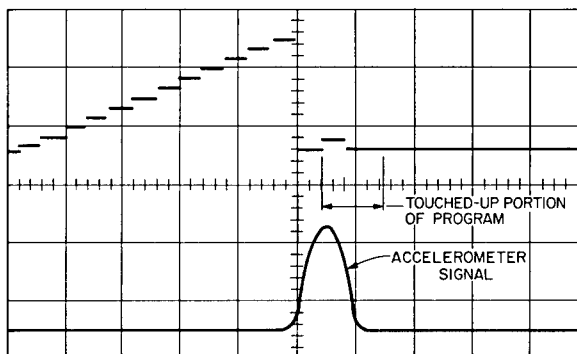Fig. A-3. Filtered exact program
before touch-up

be necessary. OBTAIN THE
TEST SPECIFIED PULSE.

1.7.5 Turn the P.A. gain down and bring
the shaker system to standby.
Mount the test item to the fixture.

1.7.6 Switch the "X1 - X 0.1" of the
JMC-1 panel to 0.1.

1.7.7 Bring the system to operate;
slowly raise the gain pot of the
P.A. while repeatedly operating
the reset button on the Exact
until the g level of the pulse
reaches 1/10 the test level of
the pulse. NOTE THE GAIN
SETTING OF THE P.A. POT.
Turn the pot back to zero.

1.7.8 Switch the "Output level switch"
of the JMC-1 panel to X1. Set
the Polaroid camera on the scope
to monitor the test pulse. Raise
the gain pot on the P.A. to EX-
ACTLY the setting noted in the
previous paragraph. Open the
camera shutter. Push the reset
button on the Exact. Close the
camera shutter. The Polaroid
photo is the record of the test
pulse. Turn the P.A. gain pot to
zero.

1.7.9 To reverse the pulse direction,
switch the "output function" of
the JMC-1 panel to "inverted."

*   *   *

118

A NEW AIR GUN FOR SHOCK TESTING

Evan W. Gray and Tom B. Linton
Quality Evaluation Laboratory
U.S. Naval Weapons Station
Seal Beach, California

Water entry subjects a weapon to unique two-phase shocks, consisting of a high-g, short-duration, spike phase at splash, followed by an in-water drag phase, wherein an initial acceleration decays as the weapon approaches a terminal sinking velocity. The U.S. Naval Weapons Station at Seal Beach, through the facilities of the Quality Evaluation Laboratory, has the task assignment of simulating the water entry tests on pre-production and periodic production samples of SUBROC weapon components. Guidelines for the air gun design to perform the tests came from the U.S. Naval Ordnance Laboratory at White Oak, in the form of test specifications and air gun methods of test as developed at that Laboratory.

A principal departure in the gun is a fast-opening valve, which provides air pressure rise time at the piston in such a short time as to produce piston accelerations comparable to mechanically released pistons. The specific capability to simulate two-phase water entry shocks does not preclude the capability to produce a wide spectrum of shock tests. In the two-phase test, the spike phase is generated by impacting a moving piston against a stationary test item platform. Thus a relatively massive piston is used with consequent reduction of spurious ringing. Velocity change spikes of 30 fps in 1/4 ms are attainable, plus drag phase accelerations of over 1000 g. Lesser values are readily and repeatably available by adjusting force pressure and volume, and by platform-to-piston spacing. Force pressures on the piston range up to 286,000 lb at 2000-psi firing pressure.

The 61-ft long gun, weighing about 25,000 lb, rests on three pairs of rollers set in shallow V-inclines. Gun firing and piston oscillation reactions are absorbed by oscillation of the gun in the V-inclines. Test items are mounted on a platform within a hollow free piston. Gun pressures and piston accelerations are monitored in addition to test item responses as required. Transmission of signals from the piston has been accomplished by several types of cables brought from the piston out the muzzle end of the barrel. Instrumentation includes oscilloscope, oscillograph, tape recorder, and peripheral equipment.

An air gun of advanced design is used to simulate water entry shocks of SUBROC weapon components. Features include a fast-opening valve, spike-generating piston, repeatability, and flexibility of operation and instrumentation. The report gives design requirements, hardware installation, instrumentation, and results to date.

INTRODUCTION

High-speed water entry of missiles such as the SUBROC weapon imposes high and unique shock forces on missiles and components. Characteristically, a high-value short-duration shock spike is created at splash impact, and is immediately followed by a longer duration drag shock which decreases to small value at the terminal sinking velocity. The air gun of this report shock tests components of SUBROC by applying the spike and drag phases of the shock from a state of rest, then decelerating at a negligibly small value against an air column in the closed barrel of the gun. The test item is mounted in its fixture on a platform in a closed hollow piston. After firing the gun to accomplish the shock test, the piston oscillates to rest within the barrel; the energy and consequent number of oscillations are minimized by

a "catch tank" connected to the muzzle by a check valve. As a result of the catch tank arrangement, less than half of the firing energy is dissipated in piston oscillations; the remainder is exhausted to the atmosphere. The piston is loaded and removed from the muzzle end of the gun and is positioned within the closed barrel by manipulating breech and muzzle air pressures. The 25,000-lb gun is mounted on three sets of rollers set in shallow V-inclines to dissipate gun-piston momentum exchanges by longitudinal oscillations of the gun.

Instrumentation presents two principal problems: (a) ringing induced in the piston load assembly by the 2500 Hz fundamental frequency of the 1/4-ms spike, and (b) transmission of piston and test item responses from a piston moving at high speed in a closed barrel. The ringing problem has been somewhat minimized by a relatively massive piston design, and additional help may be found in damping methods yet to be explored. Complete elimination of induced ringing is not anticipated, nor is it likely to be desired if simulation of field shock characteristics is to be maintained. The second problem of signal transmission is largely resolved by the use of cables of shielded signal wires. Neither very heavy cables nor the light low-noise type survive the energetic piston attack, but several commercial types have survived a dozen or more shots. The "survival" cables are not low noise, so transducers in the piston either are of the low-impedance bridge type, or require a low-impedance local amplifier. For single-phase shock tests, the piston platform is clamped, and peak g-levels are on the order of 1000. For two-phase shocks, the main piston still sees about 1000 g for the highest accelerations needed for SUBROC tests, but the platform-piston impact spike reaches toward 10,000 g. Thus, test item and platform transducers are required to survive 10,000 g, while piston transducers need to survive only the 1000 g or a little more. When separate local amplifiers are used with test item accelerometers, they are mounted on the piston proper, where their survival is greatly enhanced.

The air gun air supply is rated at 2000 psi firing pressure and is adjustable at any pressure up to that maximum. At a design firing cycle time of 30 min per average test, storage bulk is minimized by the use of 5000 psi supply, regulated to 2000 psi for the gun. Flexibility and reliability is aided by the use of three 15-cu ft/min compressors paralleled to three 5-cu ft water volume receivers. Valving permits any combination of compressors and receivers to be used at one time. Dryers and filters are used between the compressors and the high-pressure receivers.

The high air pressures used and the high piston energy dictate great care to provide safe operation. ASME pressure vessel and pressure piping codes were required in applicable construction, including hydrostatic and air pressure testing, and the use of pressure relief valves and burst diaphragm assemblies. The building is isolated, with flashing red lights to warn of testing in progress. A mound of earth outside the muzzle end of the building prohibits unauthorized piston travel toward the ocean beaches a mile away. Explicit operational procedures are rigidly followed, including some originated by the technicians who operate the gun. The 143-sq in. piston area and 53 ft of potential piston travel in the barrel means high exit velocity of the piston if the muzzle door is open, even with small air pressures. As little as 0.1 psi will slide the piston in the chrome-plated barrel. A minimum of three persons are required during testing: an engineer, an electronics technician, and a test mechanic. No more than six persons are allowed in the building during a test, and none of these persons is allowed in the main gun room. Mirrors are used to help monitor the gun area during testing. Splinter-proof cubicles are provided for live storage of explosive test items, and are used also for instrument and tool storage. The compressor room is enclosed by 16-in. thick reinforced concrete walls and a 3/8-in. thick steel door, locked against unauthorized entry. The roof is light "fly-away" construction, but the plan is to have it fall down from age rather than blow off from a blast.

TEST REQUIREMENTS

The three following levels of two-phase water-entry testing are typical of those performed on a number of different test items over the first 6 months of acceptance testing with this air gun. The specifications read about as follows:

1. Spike phase: 28- to 32-fps velocity change in 0.2 to 0.3 ms; drag phase: initial acceleration 1000 g minimum, and 650 g minimum average for 15 ms.

2. Spike phase: 24 to 26 fps velocity change in 0.2 to 0.3 ms; drag phase: initial acceleration 700 g minimum, and 450 g minimum average for 15 ms.

3. Spike phase: 16 to 20 fps velocity change in 0.2 to 0.3 ms; drag phase: initial

acceleration 100 g minimum, and 75 g minimum average for 15 ms. (Some of the test procedures do not spell out the duration and average acceleration value of the drag phase.)

TEST METHOD

1. The test item is installed in its fixture and bolted to the piston platform.

2. Accelerometers are installed and piston signal connections are made.

3. Platform spacing is set in accordance with test spike phase requirements.

4. Platform with test item and accelerometers is bolted to the piston.

5. Piston is inserted into muzzle end of gun barrel, and pushed to about 3 ft from muzzle end toward breech. Signal cable is arranged in the 3-ft barrel space, and the muzzle door closed and secured with (12) 1-1/4-in. nuts.

6. Muzzle pressure is applied to send piston to breech where piston proximity indicator signals contact.

7. Muzzle pressure is increased to predetermined deceleration pressure value, typically 50 psi.

8. Firing sequence performed at the control panel. Just prior to firing the tape recorder and oscillograph are started, then stopped a few seconds after the fire button is pushed.

9. Pressure is bled from breech and muzzle, and muzzle door is opened.

10. Breech pressure is carefully applied to bring piston to muzzle end of barrel, with a safety bar across the muzzle opening, and a mirror view into the muzzle.

11. Plug in breech end of barrel is removed to insure atmospheric pressure only in barrel behind piston; piston is then manually moved from barrel to piston handling cart.

12. Test item is removed from piston, and data are entered in log and on test report sheet.

Additional precautionary and make-ready actions are performed before and after the test sequence, such as pressurizing or bleeding the supply air lines, activating or securing the pressure regulators, starting and stopping the flashing red warning lights, checking and setting instruments, determining firing pressure level (from previously charted performance data), and checking the accumulator water supply.

ADDITIONAL CAPABILITIES

Testing to date has utilized a "water volume" firing air pressure of 2.3 cu ft. At 1500 psi firing pressure, this amounts to about 100 atm, or some 2300 cu ft atmospheric air supply per test shot. By blocking off at the various junctions, the firing pressure water volume can be readily set at about 1, 2.3, 3.6, 6, and 11 cu ft, and continuously adjusted by water fill of the fire pressure upper receiver between 11 and 18 cu ft. There is no intention of using the larger volumes at the highest available pressure, because we like the muzzle end just about the way it is. Rather, the large firing volumes at reasonably low pressure provide long duration accelerations to the piston for performing high shocks at the muzzle end with suitable stopping means, such as honeycomb material for constant-g decelerations.

A rotary valve is available for placement between the fast-opening valve and the breech end of the gun barrel, for moderate pulse shaping capability. In use, the fast-opening valve is synchronized with the rotary valve by SCR and relay circuitry with timing.

HARDWARE AND PERFORMANCE
   ILLUSTRATED

A plan view of the total air gun facility is shown in Fig. 1. The 61-ft gun was well suited for the long room of the building already available. Controls and instruments are in an adjacent side room, in line with a series of cubicles ideally meeting the needs of explosive test item storage, with splinter-proof construction, but also providing storage and work spaces for instruments, tools, and equipment. At the upper left is a hydraulic lift hand truck with fixturing used to service the breech end of the gun. At the right end of the gun, near the muzzle, is a specially designed cart for handling the piston load with test item. An earth mound outside the right end of the building serves to shield traffic on nearby streets from the muzzle end. High pressure air at 5000 psi is compressed, filtered, dried, and stored in the compressor room at the lower left. Reinforced concrete walls 16 in. thick and a heavy steel door are arranged to contain flying objects in case of explosion. Pneumatic lines follow the course
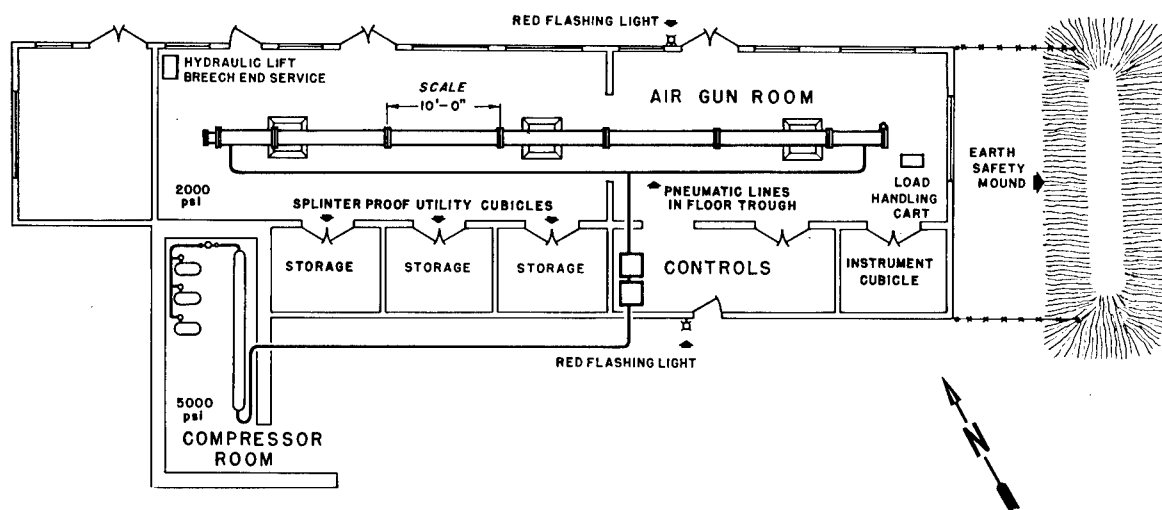
Fig. 1. Seal Beach 13-1/2-in. air gun facility arrangement

of the heavy black line from receivers to controls to gun. The controls receive air regulated from the 5000-psi supply to 2000 psi, and any fraction of the 2000 psi may be used at the gun.

The compressor room exterior, looking north, is shown in Fig. 2. Note the open space above the 7-ft high concrete walls, and the light shed roof. By these means accidental blast pressure is released without damage to the walls, and they in turn give maximum protection against horizontally flying objects. Signs warn of the high pressure, and the steel door of the compressor room is padlocked against unauthorized entry.
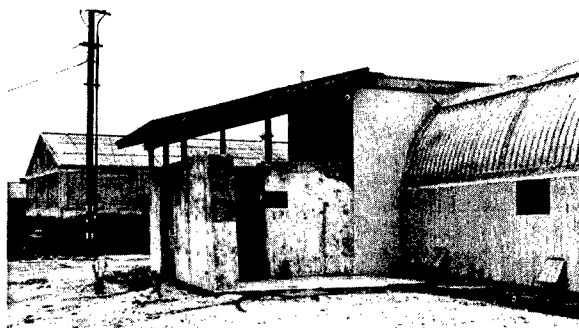
Figure 3 shows the interior of the compressor room with three Ingersoll-Rand 15-cu ft/min 4-stage 5000-psi compressors at the left. Flexible air lines lead from the compressors to a wall-mounted line, from there to the filter and dryers mounted on the far wall, and then to the three receivers shown at the right. Valves at the far end of the receivers allow any of the receivers to be isolated from the supply line. Welded and bolted steel receiver racks are anchored to wall and floor. Electric controls on the far wall allow manual operation of the compressors with the three switches shown, while the upper contactors are actuated from the control room. The compressors are individually controlled.

A closer view of some of the compressor and line details is shown in Fig. 4, along with the manual disconnect electric switches and the filter and dryers. For periodic hydrostatic testing to 7500 psi, the compressors are blocked

Fig. 2. Compressor room exterior

off, and the filter and dryer elements are removed.

The near end of the receivers of Fig. 5 show individual regulators which feed the control room supply line. Between tests, the valves at the regulators may be closed and the control panel valve opened to exhaust. A valved drain is shown at the bottom end of each receiver, and angling up to the right are relief valves set at 5250 psi. Between the blowoff and relief valves are burst diaphragm assemblies selected to blow at 5500 psi. Exhausting from the safety valves is carried out over the top of the wall. The manifolding exhaust arrangement will be replaced by separate exhaust lines.

In the main gun room the muzzle end of the gun is shown in Fig. 6 with the muzzle door open, and the major portion of the piston exposed. The upper tube is termed a catch tank because it traps the piston compressed air
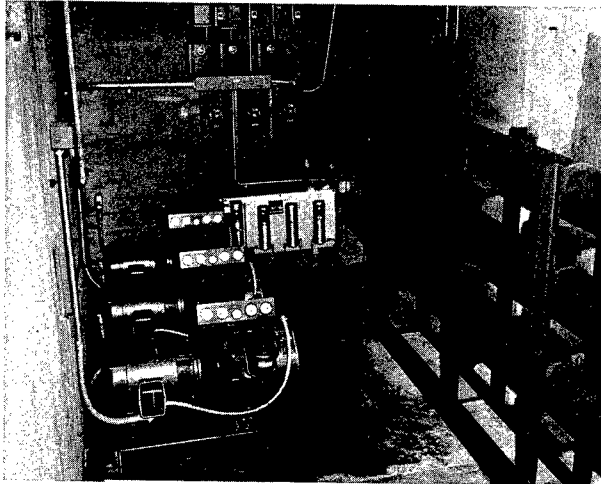
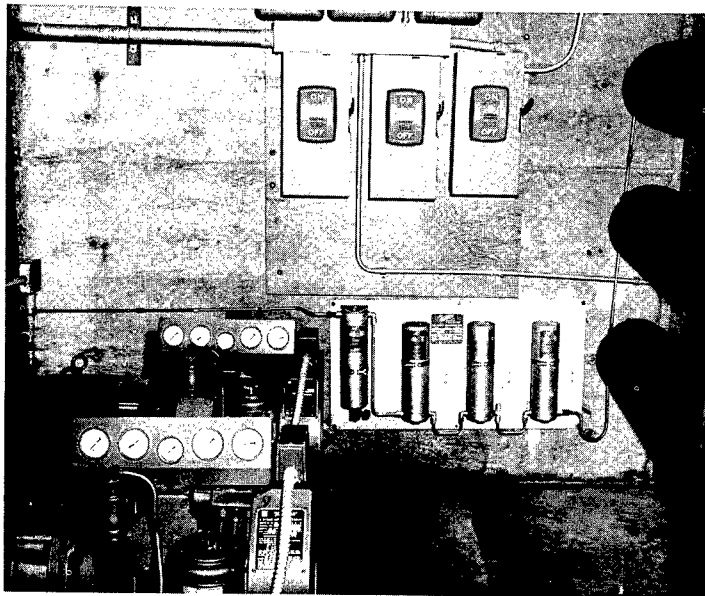Fig. 3. Compressor room interior
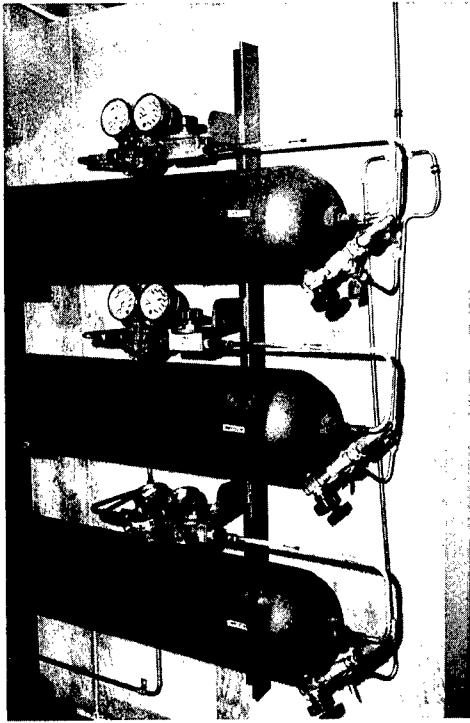

Fig. 4. Compressor room panel end

Fig. 5. Compressor room
regulators and receivers

from the muzzle by the large check valve shown
between the catch tank and the muzzle of the
gun. The round support at the far end of the
catch tank is mechanical only, not an air pas-
sage.

A close-up of the muzzle end of the gun
with the door open is shown in Fig. 7. The
piston, containing the test item, is pushed a
little way into the barrel to allow room for the
signal cable. This style of nylon braid-covered
cable is no longer used, because the soft cov-
ering tended to wedge between the piston and
barrel. Conventional vinyl-covered cables
using shielded wires survive the high-velocity
piston impacting about as well as any so far
tried. On the bottom face of the barrel flange
is shown the muzzle door closed indicator
switch. The same type of switch installed at
the breech end of the barrel to indicate piston
contact failed to survive the air pressure, and
was replaced by an inductive proximity pickup
of special potted design.

An overall view of the air gun from the
muzzle end is shown in Fig. 8. Note the over-
head Spectra-Strip 12-conductor signal cable
terminating on a terminal block from which a
cable drop enters the muzzle door. This spe-
cial Spectra-Strip cable has 6 shielded and 6
unshielded wires. An identical line runs from
the breech end, so 24 signal wires are normally
available in the control room. Note the 12 in-
ternal wrenching high-strength nuts securing
the muzzle door. An electric impact wrench is
used on them. At the lower left of the muzzle
door is an electric line to allow control room
actuation of a solenoid valve to fill and bleed
the muzzle. The manual valve just above the
electric junction box is a manual bleed for
safety and convenience. The pneumatic line
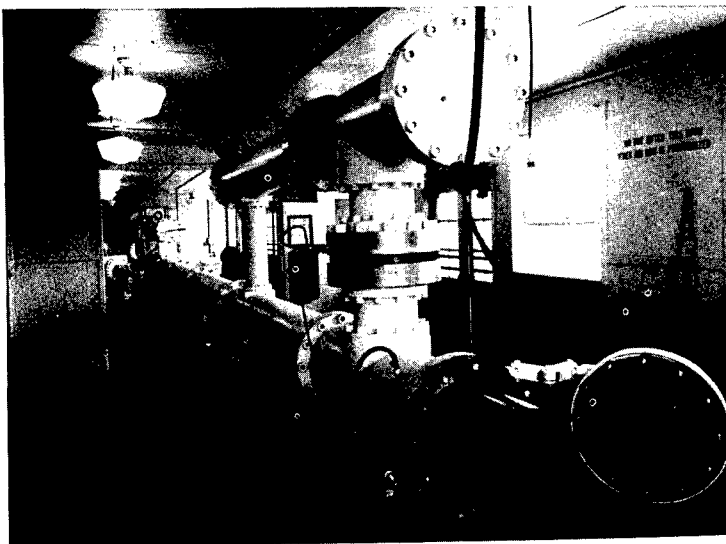from the barrel to the catch tank insures

Fig. 6. Seal Beach 13-1/2-in. air gun,
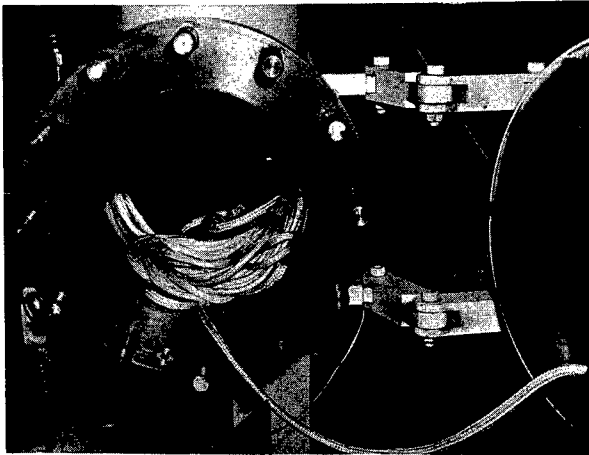muzzle end open, showing piston load
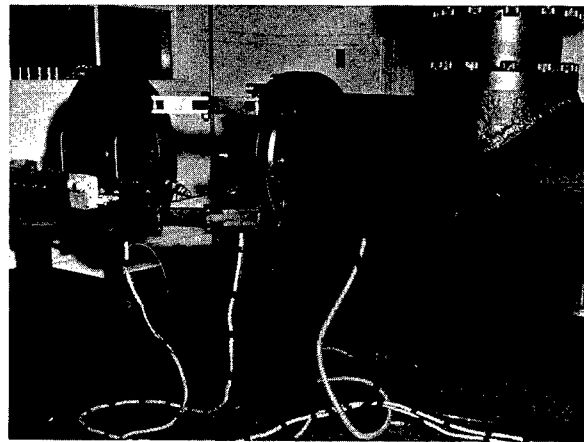
124

Fig. 7. Muzzle end open,
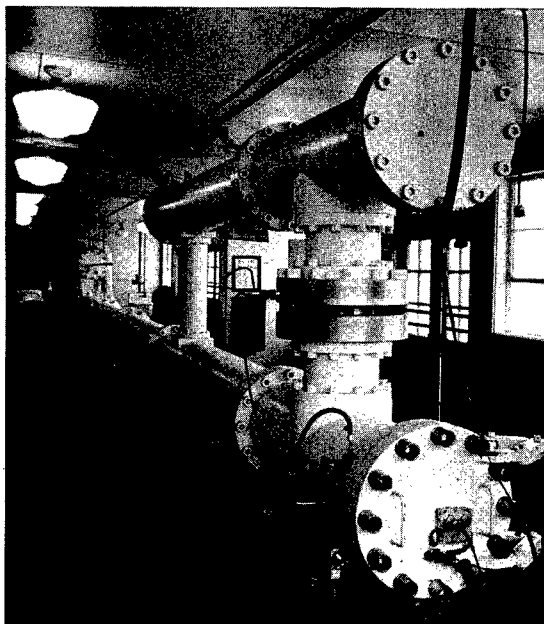showing signal cable

Fig. 9. Muzzle end details

Fig. 8. General view from muzzle end

Figure 9 shows the muzzle from another angle (and at an earlier time) with additional details. The salient nylon line helped some signal cables survive an extra few shots, but did not keep the low noise cable, here shown taped to the line, from breaking in the first fraction of an inch of piston travel after gun firing. Projecting from the muzzle door is a pressure relief valve intended to provide some reduction of muzzle door shock in case the piston ever travels beyond the check valve riser. Considering the ratio of piston area to relief valve flow area, the value of the relief valve is seen to be small. One of the six barrel pressure transducers is seen near the barrel end flange. They are arranged in three pairs, each pair being on opposite sides of the barrel. Other illustrations show their locations. The muzzle door is rather difficult to manipulate on the hinge arrangement shown, and is to be replaced. At the left, partially hidden by the muzzle door, is the piston handling cart with a cushioned piston cradle. A pneumatic line and an electric control line are seen to emerge from a gutter in the floor. The covered gutters extend along the air gun and into the cubicles and the control room.

A quarter end view of the breech end of the air gun is shown in Fig. 10. The fast-opening valve assembly slips into its housing and is attached by the large row of socket cap screws. At the side of the fast-opening valve flange is the firing solenoid from which rises the valve lock accumulator. Three flexible pressure lines are seen to emerge from the gutter. One goes to the near end of the fast-opening valve to provide valve close pressure and valve close bleed. A branch from that line goes to the top

complete bleeding of air pressure from the catch tank. At the far end of the air gun is seen the manifold allowing free flow of air from the upper fire pressure accumulator down into the fast-opening valve assembly, and then into the breech against the piston load. At the left of the manifold is a rotary valve assembly, not so far used, intended to shape the firing pulse when connected between the fast-opening valve and the barrel.

125

Fig. 10. Breech end looking forward

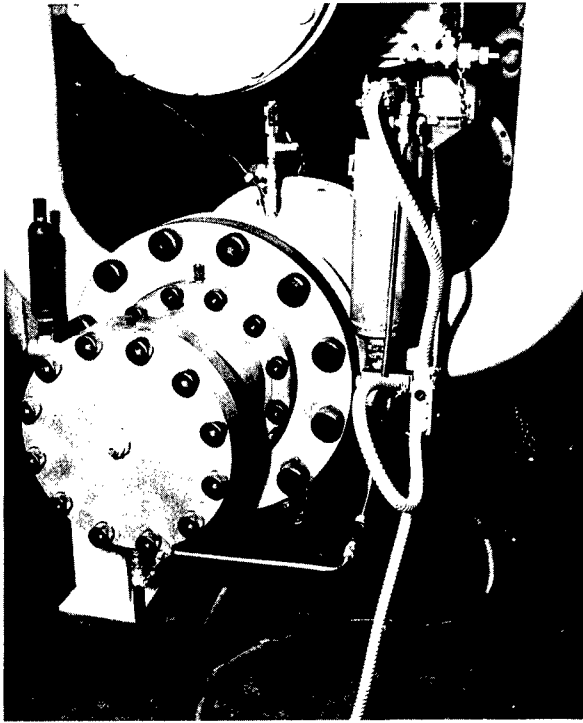Fig. 11. Breech looking aft, right side

Fig. 12. Breech end of barrel, left side

of the accumulator where actuation of a sole-noid valve allows the accumulator to be pres-surized, while the check valve visible prevents back flow. Another pressure line furnishes firing pressure in the fast-opening valve cham-ber, and in the manifolds and upper breech ac-cumulator, when so arranged. The third pres-sure supply line furnishes valve open pressure to a small area of the fast-opening valve. A safety relief valve and burst diaphragm assem-bly may be seen protruding from the top of the fast-opening valve housing.

Figure 11 shows, from the right side of the air gun, the forward quarter view of the fast-opening valve installation with attached mani-folds. The fire pressure line enters at the bot-tom and the breech bleed solenoid is at the side of the flange. One of the two breech pressure transducers may be seen angling into the weld junction of the barrel with its flange. From the breech accumulator we see a drain valve pro-jecting downward, and the bottom portion of a water sight gage which is sometimes used.

The pedestal-mounted charge amplifier of Fig. 12 is connected to a breech pressure transducer by low-noise cable, and to the overhead cable run by conventional shielded wire. The roller gun support shown is one of three pair along the length of the air gun.

They ride in shallow V-inclines of 2-degree slopes, which for the 5 or 6 in. of longitudinal gun oscillation at firing, produces a rise of about 0.10 in. The V-incline support frame is anchored to the floor, and the chains provide safety against overturning, primarily in case of earthquake. The small accumulator at the right side of the illustration connects to the water

126

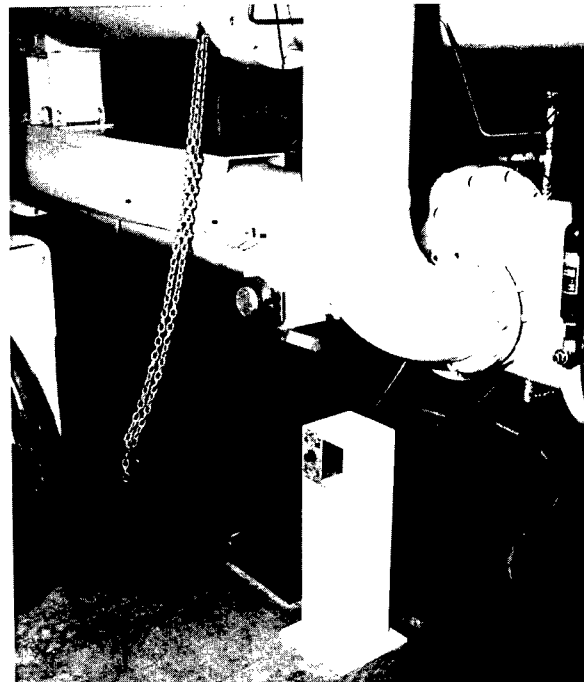portion of the fast-opening valve, and minimizes O-ring stresses by accommodating residual pressure unbalance of the nominally balanced-during-travel fast-opening valve piston. The machined flat top of the channel welded to the top of the barrel provides for insertion of the rotary valve by pulling the fast-opening valve-manifold-breech accumulator assembly back away from the gun barrel. The breech accumulator support column is then bolted to the top of the machined channel rearward of where shown.

Figure 13 shows the instrumentation and electric and pneumatic controls at one end of the control room. Overhead are seen the exhaust, or bleed, lines leading to the building exterior. From the top of the center rack we see the following instruments: three Astrodata amplifiers, six Kistler power amplifiers, Tektronix dual trace storage oscilloscope, Midwestern oscillograph, custom patch panel, four Systems Research signal conditioners at the left, and our own source and indication for piston proximity at the right. At the right is the pneumatic control panel whose operation is described later. The largest air gage on the angled shelf is a standard which sees the supply pressure. Not shown is a gage later added to monitor compressor room receiver pressure. A detailed list of the instruments is given in Table 1.

The pneumatic control diagram is shown in Fig. 14. Note that some valves are manually operated, and some are solenoid valves. The corresponding electric control diagram is shown in Fig. 15. These diagrams are largely self-explanatory.

The instrumentation block diagram of Fig. 16 shows the principal instrumentation used. Piston instrumentation requires local amplifiers because low-noise cables do not survive the shocks, and amplifiers or bridge-type accelerometers have exhibited a high shock failure rate. Satisfactory shock resistant units are still in process, complicated by nontechnical problems. However, sufficient successful instrumented shots have been accomplished to set up factors for our pressure transducers, and the demonstrated consistency of pressure-accelerometer correlation minimizes the need for frequent accelerometer readings. The really damaging spike phase shock is monitored by the empirical values derived from experience by NOL/White Oak with their copper ball accelerometers, and these accelerometers are used on every test shot for record. Attention to detail in mounting transducers in the piston, and in signal wiring, is a prime requisite
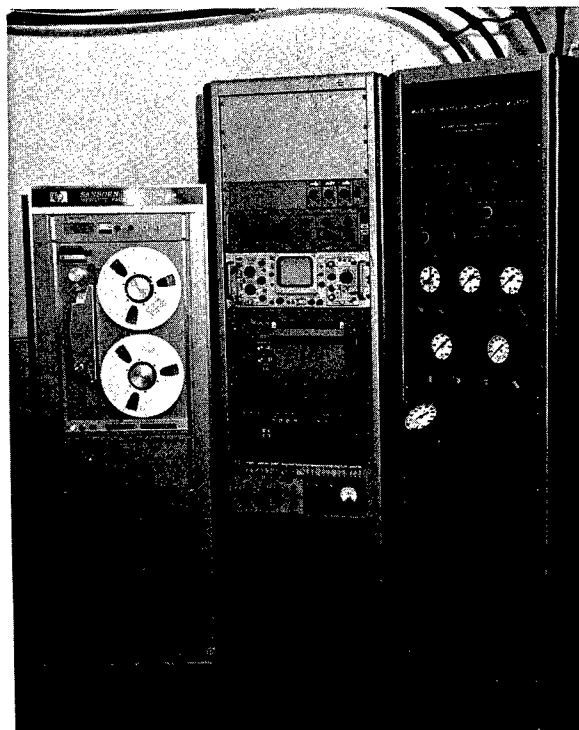

Fig. 13. Controls and instruments

for valid data acquisition. The tape recorder with record speed of 60 ips and playback at 1-7/8 ips gives a time magnification of 32 for driving the oscillograph. This time expansion is essential to catch the faster responses, and helpful in response analysis.

The fast-opening valve is shown in Fig. 17, removed from its housing in the gun. The valve element itself is seen to have the appearance of a piston within a sleeve. Note that the valve element in operational sealing comes forward out of the sleeve and seals within the mating bore of the fast-opening valve housing. Those O-ring seals which slide or are exposed to high-velocity air are bonded in place.

The fast-opening valve is shown in cutaway diagram fashion in Fig. 18, with peripheral information to help explain its operation. The valve performs its function in the test firing by operations in the sequence of the circled numbers:

1. The piston is brought to the breech, after muzzle door is closed, by closing the Decel Bleed valve and cracking open the Decel Press valve (all at the control panel).

2. Piston arrival at the breech end of the barrel is signalled by the proximity indicator.

127

TABLE 1
List of Instrumentation

Location	Visual Gage Range (psi)	Signal Conditioner	Pickup	Amplifier	Power Amplifier	Record and Display
(a) Pressure Instrumentation						
Fire Chamber	3000		10KΩ	A141V	K567	
Breech	—		K601A	K566C	K567	
Center	—		K601A	K566C	K567	
Muzzle ⎫	300 Panel		K601A	K566C	K567	
Muzzle Tank ⎭	1500 Tank		10KΩ	A141V	K567	
						Oscillograph MW 800, 25-channel
Compressor Regulator Control Panel:	300/2000/5000 6000/3000					
"Source"	3000 Working 2000 Transfer Std					
"Force"	3000 (Same as "Fire Chamber" above)					
"Valve Close"	3000					
"Valve Open"	3000					h p - Sanborn 3917B,
"Decel Press"	300					7 channel FM
	1500 (Same as "Muzzle Tank" above)					(plus voice)
(b) Load Acceleration Instrumentation						
Platform		None	K808A			
Platform		None	Copper ball (NOL/WO)	On order None	K567 None	Storage oscilloscope Tektronix 564
Piston		—	K808A			3A72 dual trace plug-in
Piston		SR3560	E2216PR	On order	K567	3B3 time base w/delay
Piston		SR3560	Statham	A141	K567	Plug-in
				A141	K567	
(c) Other Instrumentation						
Electronic Filter Bench Micrometer, 0.0001 in. (for Copper Balls)						

3. Addition of Decel Fill pressure is continued until the predetermined pressure is attained — typically 50 psi of "decelerating" pressure in the muzzle length of the barrel and in the muzzle catch tank. The "water volume" of the decelerating pressure is then about 70 cu ft.

4. Valve Close pressure valve is opened until about 1500 psi is indicated.

5. Trapped water or air is bled to establish unbalanced piston areas as seen by the water (in fast-opening valve).

6. Accumulator Pressure solenoid is operated; deceleration pressure bleed occurs simultaneously. Water in the fast-opening valve is now pressurized, and with the unbalanced valve piston, the valve is locked in place by the water column.

7. Valve Open pressure, typically 900 psi, is introduced. This pressure tending to open the valve is restrained by the water locking force.

8. Firing Pressure to the predetermined value is introduced. This can range up to 2000 psi; test shots have been performed for record in the range of 500 to 2000 psi.
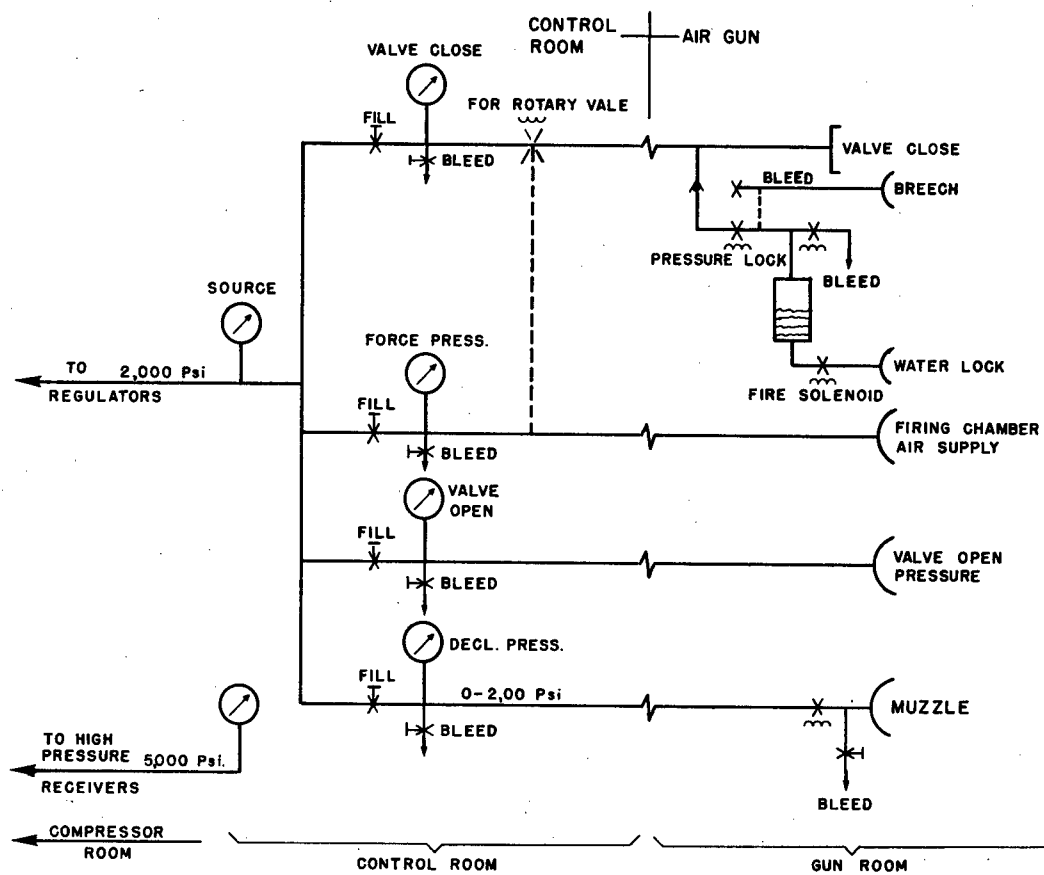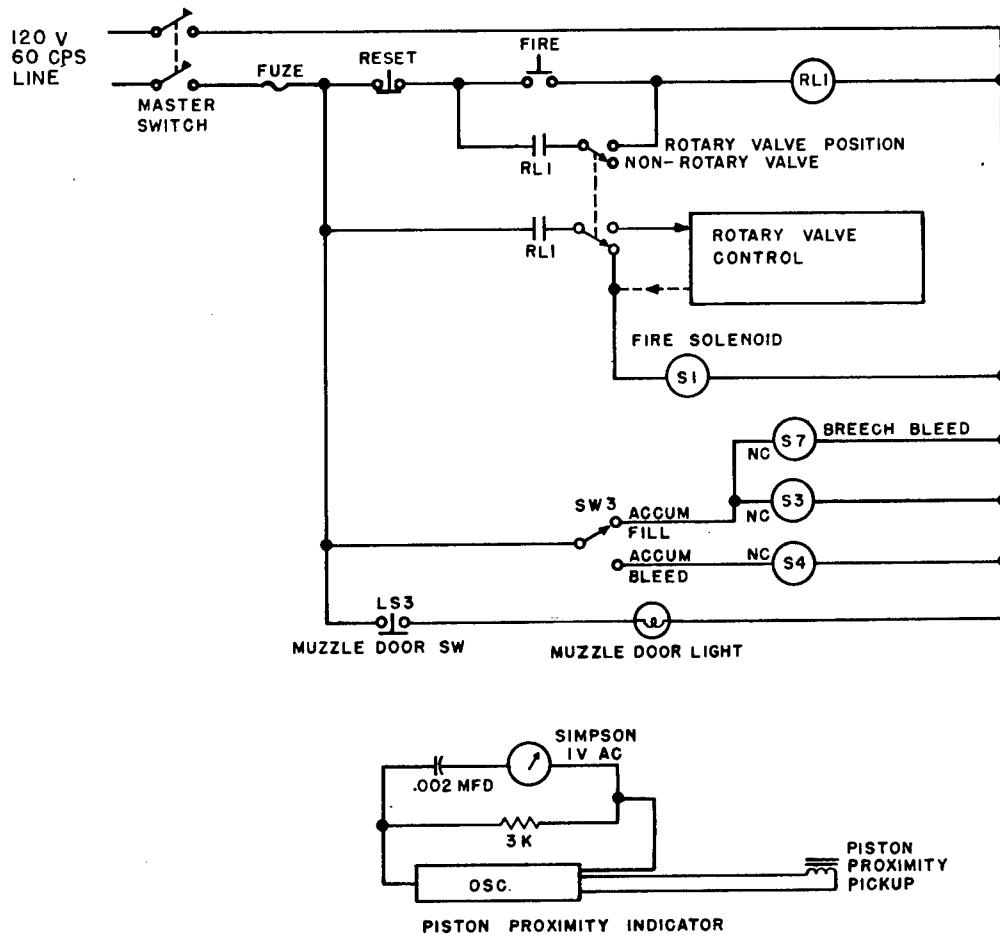
Fig. 14. Pneumatic control diagram

Fig. 15. Electric control diagram

130

PRESSURE
TRANSDUCER
(KISTLER 601A)
CHARGE
AMP.
(K566)
POWER
AMP.
(K 567)

RESISTIVE
PRESSURE
TRANSDUCER
($\frac{1}{4}$ WATT, IOK, CARBON)
BRIDGE
CONDITIONER
(SR. 3560)
AMPLIFIER
(ASTRODATA 141)

ACCELEROMETER
(KISTLER 808A)
CHARGE AMP.
(SPECIAL Hi-g)
POWER AMP.
(K 567)

OSCILLOSCOPE
(TEKTRONIX 564 STORAGE)

OSCILLOGRAPH
(MIDWESTERN 800)

TAPE RECORDER
(HP-SANBORN 3917 B)   PLAYBACK

VOICE TRACK

COPPER BALL
ACCELEROMETER
(NOL/WO)
BENCH
MICROMETER
.0001"

Fig. 16. Typical instrumentation block diagrams

Fig. 17. Fast-opening valve removed,
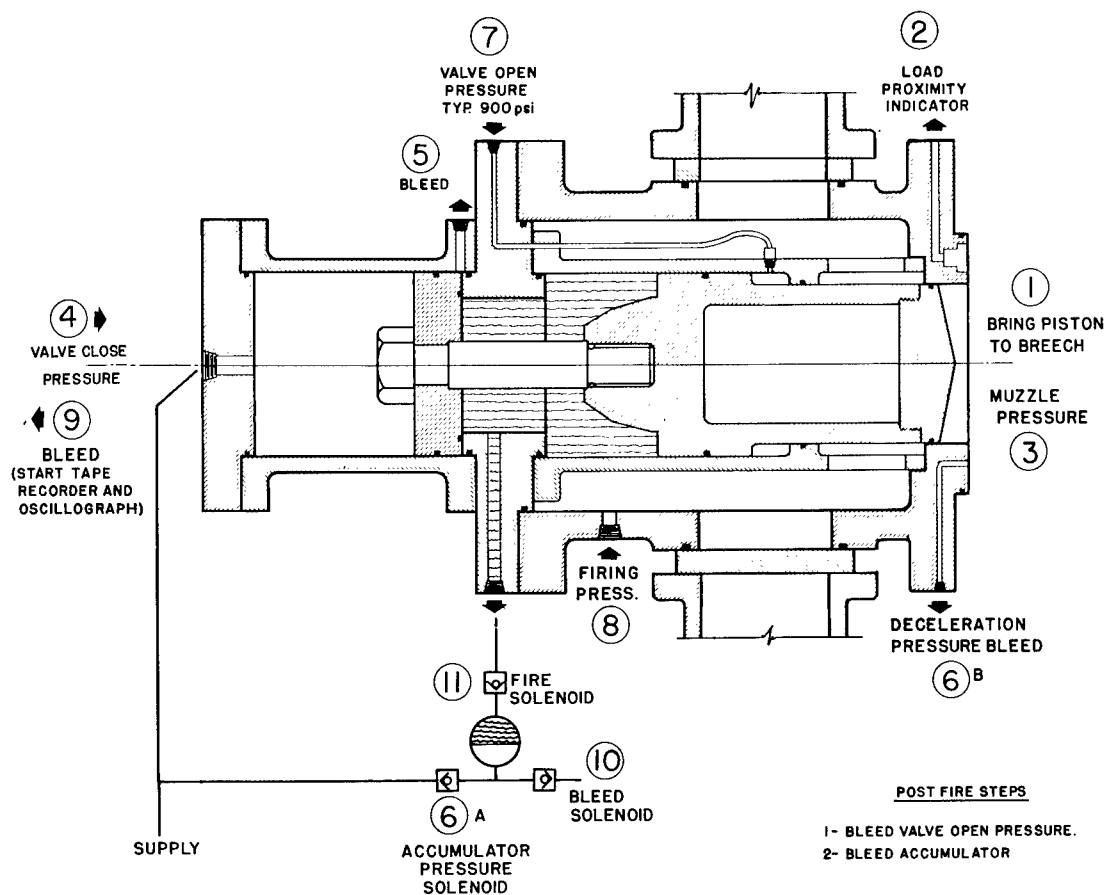forward end

131

Fig. 18. Fast-opening valve diagram

9. Tape recorder and oscillograph are started, and Valve Close pressure is bled. Note that leaking O-ring seals and leaking solenoid valves may allow the gun to fire at this stage, hence the recorder and graph starting to insure record capture.

10. Accumulator solenoid is bled, now ready to fire.

11. Fire solenoid button is pushed.

Post-firing actions include securing the instruments, bleeding off breach and muzzle pressures, removing breech barrel plug, opening muzzle door, carefully applying breech pressure to push piston to muzzle opening, inspecting and stowing signal cable, transferring piston to cart, and removing test item.

Note on Fig. 18 the manifold connections; at the upper one on the diagram a doughnut spacer is used, and at the lower connection a solid disc is shown. This is one of the methods used to vary firing chamber volume.

The muzzle check valve of Fig. 19 allows most of the air, pushed to the muzzle end of the gun by the initial piston rush from the breech, to escape into the catch tank, and then restrains the back surge by checking the air back flow. Elongated flat steel strips are spring loaded over a multitude of elongated holes in the 16-in. diameter valve plate. Through that plate the net flow area is about 60 percent of the vertical tube passage area, and about 40 percent of the piston load area. Upward forces on the poppets by the high-velocity air broke some of the original cantilever spring mounts, so the broken units were replaced by new poppet types, with no subsequent failures. No static air sealing is desired; downward leakage helps bleed off catch tank air after each shot.

Muzzle check valve dynamic effectiveness is plotted from pressure recordings on Fig. 20. Kistler pressure transducers were placed in the muzzle barrel wall and in the muzzle catch tank, rather than adjacent to the check valve in locations of highest air velocity. The ramps and oscillations superimposed on the basic
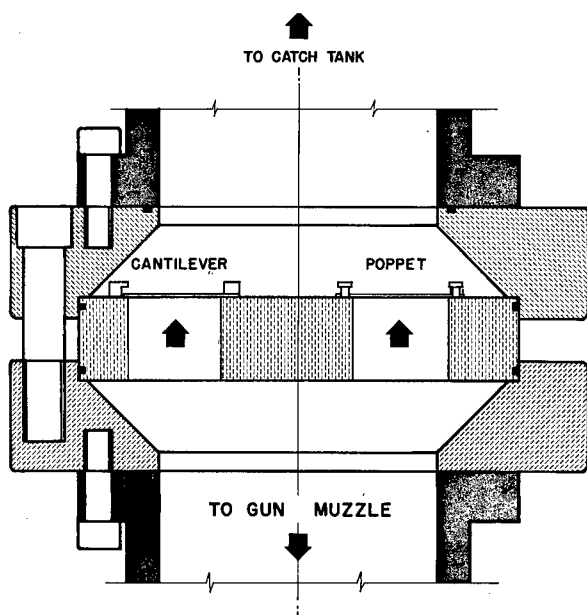
132

Fig. 19. Muzzle check valve diagram

Fig. 20. Muzzle check valve
performance chart

pressure curves indicate air pressure waves
triggered by nonlinear check valve opening and
closing. The basic curves clearly show that
the check valve does pass the air upward with
negligible restriction, and that the check does
hold the catch tank pressure while the piston
travels back toward the breech. We can see
that by the time the piston has traveled back
toward the breech, at 350 ms after fire, the
muzzle pressure is somewhat below initial
pressure (the zero pressure of the curves is
actually the 50-psi initial deceleration pres-
sures; then pressures read off the curves are
50 psi higher than shown, when referred to at-
mospheric zero gage pressure). The 350-ms
time indicated for the piston to make its first
excursion to and from the muzzle end is typical;
based on rough estimates that the piston travels
35 ft forward and 20 ft back, the velocity aver-
age is on the order of 150 fps.

The piston carriage of Fig. 21 is the test
item carriage; in terms of gun performance, it
is the piston load. Weight as shown, less ac-
celerometer, is 142 lb, including 19 lb for the
platform assembly. End area of the piston is
143 sq in. The surfaces are hard anodized. A
mere 5- to 10-lb endwise force will slide the
piston in the hard-chromed bore of the gun bar-
rel. The basic acceleration forces on the piston
load range up to about 1100 g in normal usage.
The test item and platform may see up to
10,000 g during the first phase of two-phase
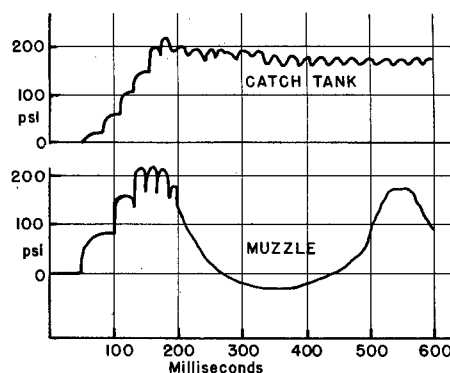shocks. The platform is restrained from

bouncing after initial impact by circumferential
spring-loaded platform locks. The platform
has performed impact shocks with dummy test
loads up to 43 lb in weight and 16 in. in length,
although missile components thus far have been
tested with considerably lighter loads, typically
10 to 20 lb for component and fixture. Speci-
men mounting holes on 1-1/2 in. centers are
3/8-16 threads in Keensert stainless steel in-
serts. Platform impact spacing parallelism is
closely held. Preventing metal to metal con-
tact by one layer of cloth adhesive tape is the
rule for the 1/4-ms duration spike phase; some
hundreds of impacts have resulted in no visible
deterioration. This piston arrangement with
the relatively heavy piston impacting the lighter
test item provides easy attainment of very
short-duration responses. Cushioning on the
exterior muzzle end of the piston, and on the
muzzle door interior, is an aid to signal cable
survival. The cable connector attaching nut is
used when signal acquisition time is from fir-
ing to piston at rest, but in that case, cable
breakage sometimes occurs on the piston back
stroke, as a result of cable knotting. The pre-
ferred and usual method is to leave the nut un-
locked, so that the cable disengages near the
end of the initial forward piston stroke, and
piles up against the muzzle end cushion, thus
acquiring the essential forward acceleration
data and dropping out the usually trivial piston
oscillatory accelerations. Signal cable survival
is then generally excellent and dependable.

The general air gun arrangement is shown
in Fig. 22, with principal data listed. The
breech end is at the left, with fast-opening
valve, manifolds, and firing pressure accumu-
lator. The muzzle is at the right end, with the
muzzle check valve and muzzle catch tank
above. The muzzle door is opened to load and
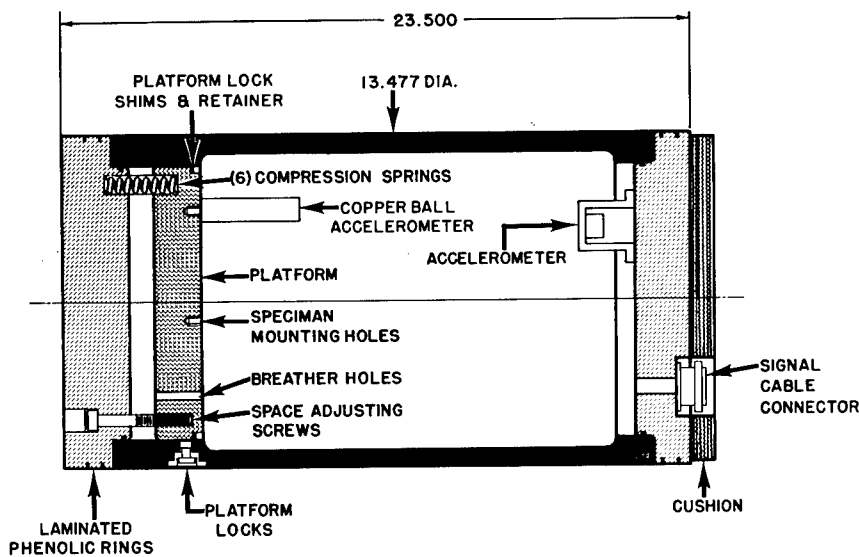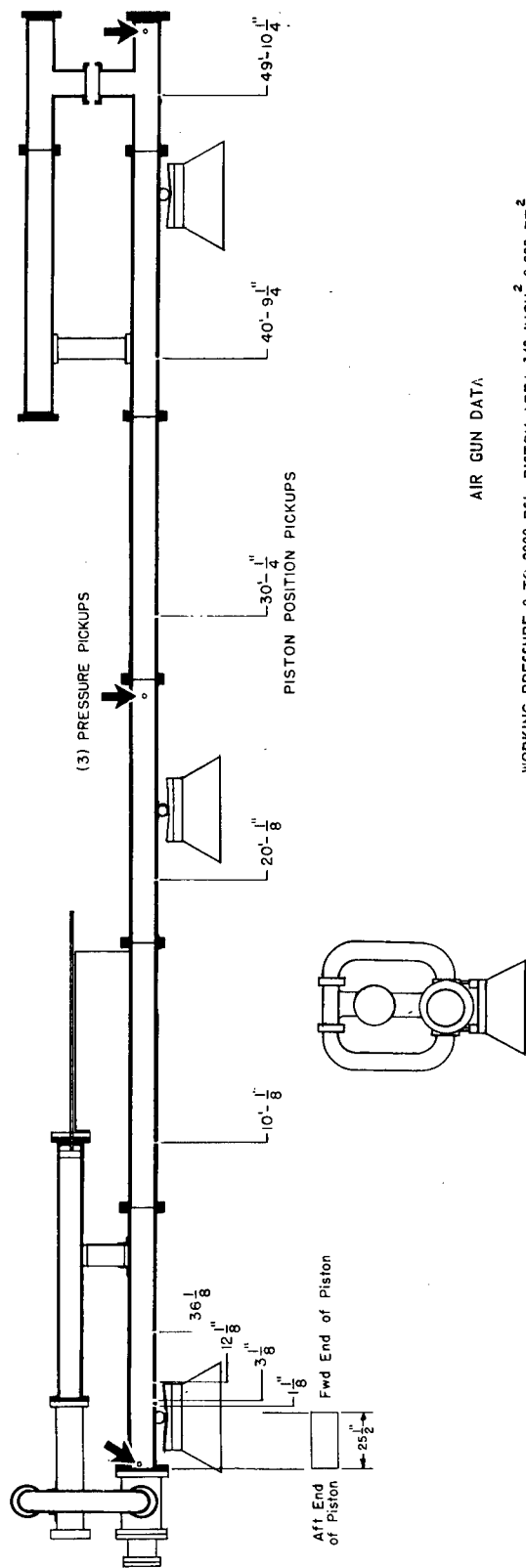unload the piston. Three pressure pickup

133

Fig. 21. Piston load (test item carriage) diagram

locations are pointed out on the figure; at each location two pickups are positioned on opposite sides of the barrel, for a total of six. These signal pressures are at the breech, center, and muzzle. Because of the high velocity attained by the piston over a portion of its travel, the effective air pressure force behind the piston is less than indicated by the pressure transducers, while the pressure force on the front of the piston is greater by virtue of stagnation (velocity head) pressure build-up.

A series of dimensions from the floating piston view show that initial piston travel reaches piston position sensors. Signals from these locations, when recorded on the oscillograph, yield time-distance relations as plotted on Fig. 23. The sensors consist of 1/8-in. diameter potting of hairpin-shaped magnet wire; these are connected in series with shunt resistors to yield a voltage step function on the oscillograph record. They are designed to minimize the size of holes in the gun walls, are expendable by being clipped off as the piston passes, and made in groups of 20 by molding in a Teflon mold. They remain in the barrel until replaced by new ones, and are held in place against barrel air pressures by T-screws, as seen in Fig. 12. Fire pressure volume is adjustable from about 1 to 18 cu ft water volume. A piston and extension rod are shown in the fire pressure accumulator; water fill forward of the accumulator piston can vary the air volume from 18 down to about 9 cu ft. Blocking of the manifolds at the top reduces the fire pressure volume to about 3.5 cu ft. Blocking one manifold at the top and one at the

bottom (Fig. 18) results in 2.3 cu ft, and the smallest available volume is that of the fast-opening valve housing, just under 1 cu ft, when both manifolds are blocked off. The last line of data omitted + and = signs; the muzzle volume should be listed 54.5 + 15.0 = 69.5 cu ft at 50 psi. The overall length of the gun as shown is 59 ft; with the rotary valve (not shown on the figure) installed, the overall length is about 61 ft.

A revealing test for looking at the speed of opening of the fast-opening valve is shown in Fig. 24. The usual firing sequence was performed, except without a piston load, and with no muzzle pressure applied. Pressure transducers at the breech, center, and muzzle reveal pressure rise sequencing characteristic of a shock wave traveling back and forth in the gun barrel past the transducers. Note the gun has less than perfect reflecting surfaces at both breech and muzzle. When the fast-opening valve element retracts to initiate the shot, a hole 8-1/2 in. in diameter connects the gun barrel to the fire chamber volume of 2.3 cu ft; the breech reflecting surface is thus washer shaped rather than a full disc. While the muzzle end has a full disc, a minor shunting effect exists at the catch tank branch. On initiation of firing, the shock front emerging from the valve hole expands to the barrel wall at an angle which substantially misses the breech pressure pickup, as indicated by the very weak first response of the breech transducer. Following the dotted lines from left to right tracks the sequence of pulses and shows that the major pressure occurs as expected at the full flat face

134

(3) PRESSURE PICKUPS

PISTON POSITION PICKUPS

PRESSURE PICKUPS

49'-10 1/4"

40'-9 1/4"

30'- 1/4"

20'- 1/8"

10'- 1/8"

36 1/8"

12 1/8"

3 1/8"

1 1/8"

25 1/2"

Fwd End of Piston

Aft End of Piston

BREECH END VIEW

AIR GUN DATA

WORKING PRESSURE 0 TO 2000 PSI. PISTON AREA 143 INCH; 0.993 FT.^{2}

AIR PRESSURE FORCE ON PISTON 0 TO 286,000 POUNDS.

CALIBER 13 1/2" DIA. X 55' INSIDE BARREL.

VALVE OPENING 8.47" DIA.; AREA 56.3 INCH^2 ; 0.39 FT.^{2}

MAX. PISTON TRAVEL 53 FEET.

WEIGHT OF GUN APPROX. 25,000 POUNDS.

TYPICAL PISTON WEIGHT 142 LB. INCLUDING 19-POUND PLATFORM.

MAX. TEST ITEM AND FIXTURE 10" DIA. X 16"; 50 POUNDS WEIGHT.

CUBIC SIZES

BARREL TO CHECK VALVE	56.5 FT.^{3}	MUZZLE RECEIVER TO CHECK VALVE 15 FT^3
BREECH ACCUMULATOR	15.0 FT.^{3}	WITH TYPICAL LOW-ENERGY SHOT
(2) MANIFOLDS	4.6 FT.^{3}	FIRE VOLUME 2.3 .9, 3.2 FT.^{3} AT 1500 PSI
FAST-OPENING VALVE	0.9 FT^3	MUZZLE VOLUME 54.5 15, 69.5 FT.^{3} AT 50 PSI

Fig. 22. Seal Beach 13-1/2-in. air gun general diagram and data
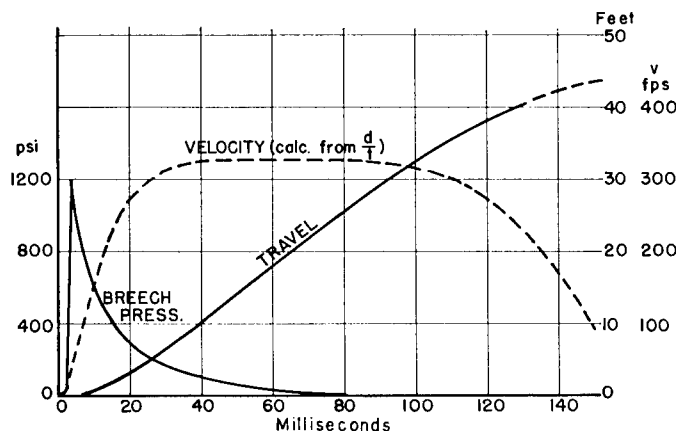
135

Fig. 23. Breech pressure, load travel,
load velocity vs time

of the muzzle door. The first pulse reflected from the muzzle gives the center transducer its biggest bang, but then that strong pressure front is irreparably damaged by dissipating considerable energy in the breech fire chamber labyrinth. Subsequent pulses are somewhat leveled, then rather quickly die out by loss of energy to the breech fire chamber and other imperfect surfaces.

A typical test shot with platform clamped to yield drag phase only is shown on Fig. 23. The travel curve (distance vs time for the piston load) is obtained from the "clip-off" piston position indicators, in relation to the oscillograph timing markers. The breech pressure curve is slightly smoothed for this particular curve

from the oscillograph trace. The piston velocity curve is calculated from the travel vs time curve, and shows about 325 fps velocity over a considerable distance. The piston load of 154 lb, including test item and fixture, was inadvertently left off the illustration. End of piston travel (direction reversal) is not shown, but occurs at about 160 ms, as can be deduced by extrapolating the travel and speed curves. The 930 g peak noted in the illustration title was picked off another curve relating firing pressure to g-levels as measured by Endevco 2261 and Statham strain gage accelerometers.

Basic gun performance is charted on Fig. 25 showing peak accelerations of the piston load, without spike phase, obtained with various
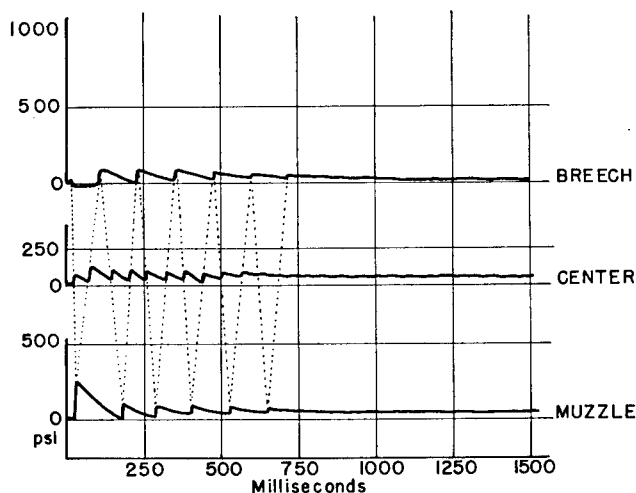

Fig. 24. Barrel air pressure
vs time, without load

136

firing pressures. For these data, a 155-lb load was used (142-lb piston plus 13-lb fixture). From the relations $F = ma = Wg = pA$, we obtain for this gun the relation $g = 143 \ p/W$, and from that relation we calculate g from the air pressure and piston load weight. The calculated g-curve is merely a reference; the piston is going away too fast for the static calculation to be accurate, but the experimentally derived curves, such as this one shown relating firing pressure to peak g with various piston loads and chamber volumes, enable prediction of actual results without pretest shots, except under special circumstances.

charted in Fig. 26, and by piston load weight as charted in Fig. 27. On both charts velocity change is the ordinate plot, and all data imply a 1/4-ms duration for the spike pulse, insured by parallel metal contact of the impact faces. We see considerable flexibility to meet various spike velocity change requirements, and it is not at all limited by the curve limits so far examined. Note especially that the origins of Fig. 27 lie far to the left and down from the axes shown, and a moderate firing pressure of 1000 psi was used. Not shown on that chart is the piston weight of 154 lb, including a dummy fixture.

Figure 28 shows a routine drag phase alone shot, with breech, center, and muzzle pressure pickups recording a number of translational piston oscillations in the barrel, over a time of nearly 1-1/2 sec. The initial pressure rise is here compressed by the time scale used. The superimposed numbers on the curves give pressure values for comparing the three curves. We see in the high muzzle peaks another example of the breech fire chamber pressure damping. The pips along the center transducer curve show that after the first pulse is uncovered by the piston, only stagnation pressure at the forward end of the piston is significant enough to register. The squiggles on the first muzzle pressure rise are the result of the characteristic nonlinear check valve action. Note the gradual increase of the piston "turn-around" time from an initial value of about 350 ms. This piston oscillation frequency of approximately 3 Hz is several times as fast as the natural gun frequency of rocking in its cradle. For perhaps 3 sec after firing, the gun goes through a sort of longitudinal St. Vitus
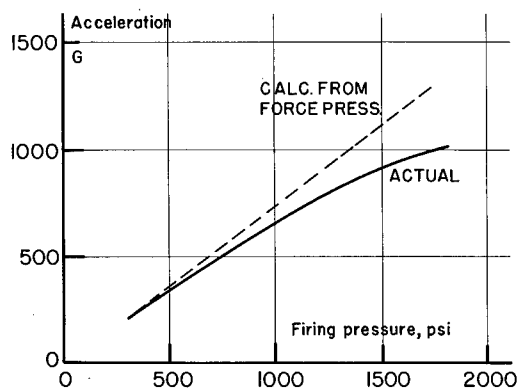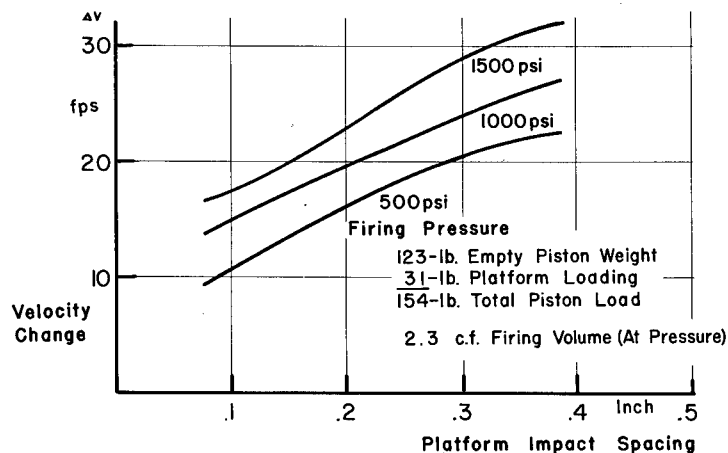

Fig. 25. Acceleration vs firing pressure

The first, spike, phase of the two-phase water entry shock is affected mainly by platform to piston spacing and fire pressure, as

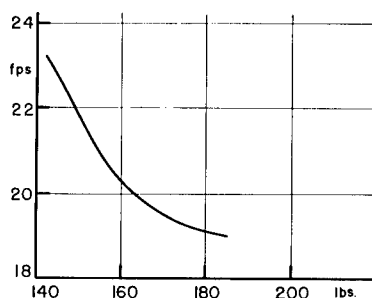

Fig. 26. Impact load velocity vs impact spacing

137

Fig. 27. Impact load velocity vs load
weight, 0.25-in. platform spacing

dance, showing the pronounced effect of the
piston oscillations on the natural gun oscilla-
tions.

A typical test item mounted in its fixture
on the piston platform is shown in Fig. 29. The
test item on the breech end of the piston is
ready to be attached to the piston body. Only
6 of the 24 attaching cap screws are used; as
few as 2 or 3 would suffice, since no significant
tensile forces can act on the piston ends. Stain-
less steel solid inserts are used here as else-
where for tapped holes in the aluminum piston
parts. Note the adjustable height of the piston
handling cart, and the caster wheels with brake.
Three copper ball accelerometers are mounted,
before the test, on the platform to obtain an
average value for the three positions and to
verify that the platform was properly mounted
parallel to the mating piston impact surface.

In addition to the copper ball accelerome-
ters mounted on the platform, Endevco 2261

and Statham accelerometers were mounted on
the interior of the muzzle end of the piston to
monitor the basic piston acceleration. The
copper ball accelerometers are actually stand-
ardized to indicate velocity change, rather than
acceleration, of the short-duration metal to
metal impacts. Deformation of a copper ball by
a hard steel "hammer" of the accelerometer is
multiplied by a factor, depending on the particu-
lar accelerometer type, to arrive at the veloc-
ity change number for these short-duration
high shocks of the first phase of the water entry
shocks.

Figure 30 shows test curve responses on
the test item shown in Fig. 29. Acceleration
and pressures are shown plotted against time
in milliseconds. The fire chamber pressure
was 1200 psi, and as the second curve from the
top shows, continued to supply air to the barrel
for the 160 ms it took the piston to travel some
35 or 40 ft from start position. In contrast, the
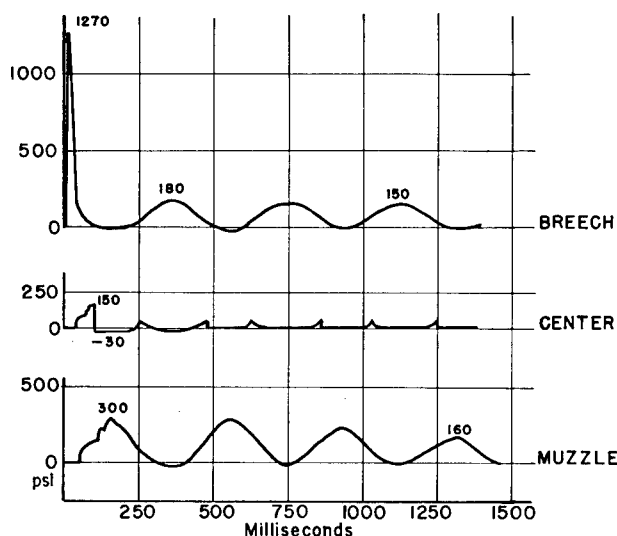breech pressure dropped to its limiting value,
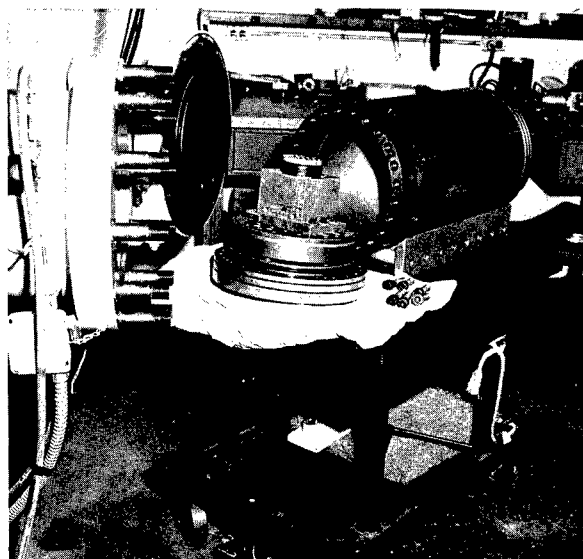

Fig. 28. Barrel air pressure
vs time, 154-lb load

138
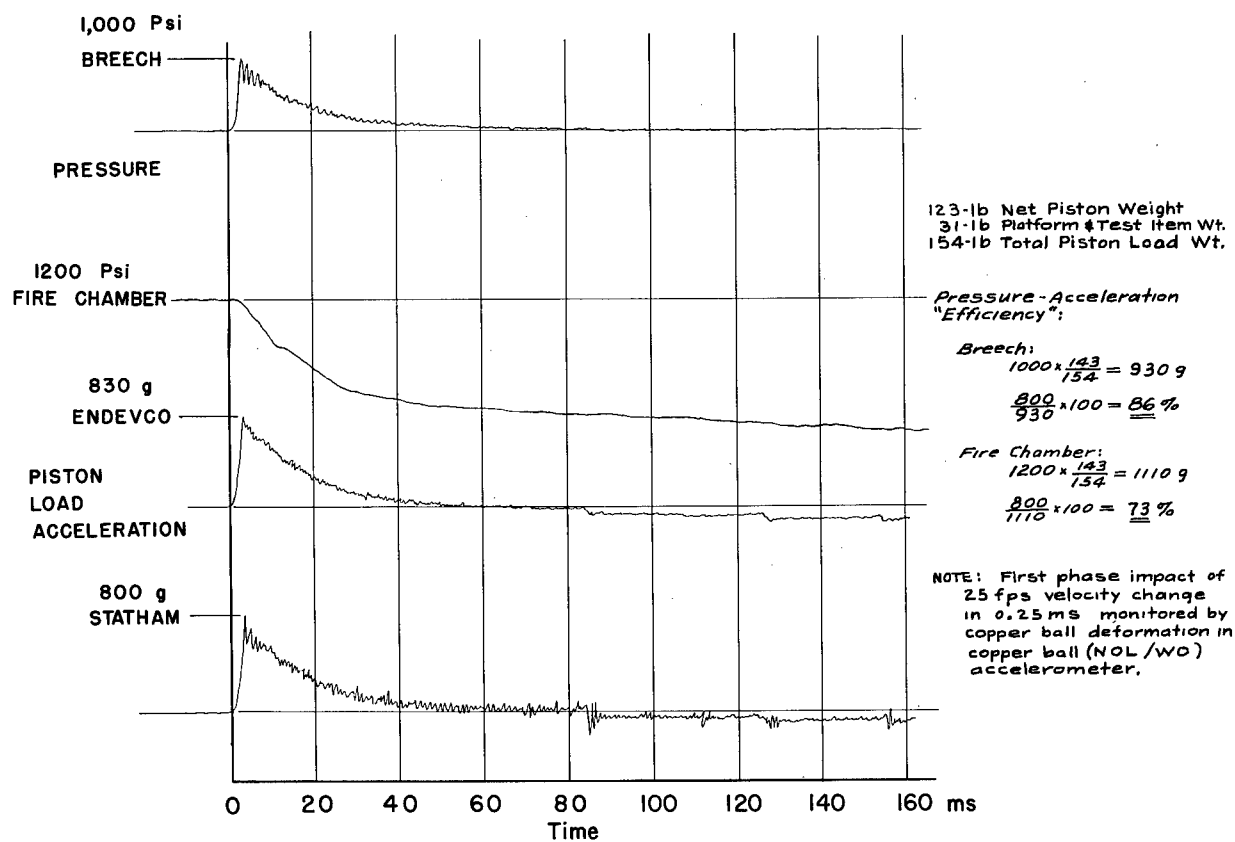
Fig. 29.   Test item in fixture, on platform

123-lb Net Piston Weight
 31-lb Platform & Test Item Wt.
154-lb Total Piston Load Wt.

*Pressure-Acceleration
"Efficiency":*

Breech:
$$1000 \times \frac{143}{154} = 930 \, g$$

$$\frac{800}{930} \times 100 = \underline{\underline{86 \, \%}}$$

Fire Chamber:
$$1200 \times \frac{143}{154} = 1110 \, g$$

$$\frac{800}{1110} \times 100 = \underline{\underline{73 \, \%}}$$

NOTE: First phase impact of
    2.5 fps velocity change
    in 0.25 ms monitored by
    copper ball deformation in
    copper ball (NOL/WO)
    accelerometer.

Fig. 30.   Typical test shot responses

139

approximately zero psig, within 100 ms, after which the decreasing piston velocity was matched by air velocity from the fire chamber. The peak effective breech pressure labeled 1000 psi is really more like 800 psi, as can be seen by averaging the reverberation oscillations. The acceleration ringing of the lowest curve is so much more than that of the next higher Endevco response that transducer resonance, rather than piston ringing, was indicated. Follow-up checks indicated that the Statham needed replacement or repair. This typifies our main problem, that of instrumentation, for verifying the excellent and dependable gun performance. From the extensive instrumentation failures emerges a clear rule of thumb: on the piston load put only high shock resistant pickups, avoiding integral amplifier and bridge types, and use separate local amplifiers shock-mounted in the piston and away from the platform.

CONCLUSIONS

The Seal Beach 13-1/2-in. air gun is a versatile and reliable test facility for the conduct of a wide variety of shock tests, including the two-phase water entry weapon component requirements, and other high-energy tests. The fast-opening valve provides acceleration rise times on the order of 2 to 3 ms with a 150-lb piston load. The present test item piston carriage provides for spike phase shocks of 1/4-ms duration and 30-fps velocity change, with test items up to 10 in. in diameter and 16 in. long, weighing up to 50 lb. The 55-ft long barrel provides cushioned stops of very low reverse accelerations, typically around 50 g for initial accelerations of over 500 g. Twelve-conductor cable pushed ahead of the piston load during the test shot enables a variety of piston load and test item responses to be recorded on

the 7-channel 0- to 20-kc tape recorder, and 25-channel oscillograph, and viewed on a dual trace storage oscilloscope. A 45-cfm compressor system with 5000-psi receivers provides ample air capacity and pressure for full utilization of the air gun's capabilities. With the gun operating at any pressure up to 2000 psi and 18-cu ft fire pressure storage, a wide range of shots may be accomplished, from low-pressure high-volume to high-pressure low-volume. The fire pressure storage energy grosses about 9,000,000 ft-lb; test packages up to the 13-1/2-in. bore size may be accommodated; muzzle door closed impact tests may be performed; muzzle door open shots to the outside may be done; and with the rotary valve, pulse shaping is intended. This gun is already performing well in backing up our defense efforts; it will do much more.

ACKNOWLEDGMENT

*　　*　　*

INVESTIGATION OF PARAMETERS AFFECTING DYNAMIC PRESSURES IN SUPER PRESSURE GENERATOR USED FOR CANNON BREECH FATIGUE STUDIES

R. R. Lasselle, J. E. Zweig,
and M. A. Scavullo
Watervliet Arsenal
Watervliet, New York

INTRODUCTION

With the advent of a mobile type of combat unit, the need has become urgent to develop lighter "heavy" weapons requiring new approaches to cannon design. Not too many years ago, the philosophy commonly used in gun design was "if it fails, beef it up," or even "if it looks like it is going to fail, beef it up." This resulted in very heavy, cumbersome weapons for their firepower. Testing consisted of very slow and expensive field firings with little data applicable to future designs.

The requirements for an increasingly effective firepower-to-weight ratio has produced weapons with smaller wall ratios, higher pressures, more severely loaded threads, etc., and many more small cuts in the pressure vessel for the minor components required for more automatic operation. Material yield strengths have been increased substantially and cold working has been used to meet the above requirements. However, this has added the problem of increased notch sensitivity.

Lead times from concept to standardization have been cut so that a weapon can be in the hands of using troops somewhat before it becomes obsolete. This has generated a need for techniques to get preliminary cannon fatigue information rapidly in a controlled laboratory test. A technique is required whereby full fatigue tests can be run on prototype cannon pressure vessels early in the design stage even before an operating mechanism is detailed.

BACKGROUND

The loading desired for a laboratory testing machine for cannon breech assemblies is a fluid pressure pulse essentially half sine in form with a peak pressure of from 40,000 to 100,000 psi (depending on the weapon) and a time to peak of approximately 3 ms. For this to be an effective fatigue machine, it should deliver several thousand of these pressure pulses in a relatively short period.

The equipment being developed to do this kind of testing uses a compressed air- or steam-operated pile hammer as an energy source. The hammer impinges on a piston fitted into a shortened or stub tube attached to the cannon breech assembly. This is shown in sectional view in Fig. 1. The stub tube is smooth bored and packings are provided on the piston to seal a fixed amount of fluid in the chamber of the test weapon. The falling weight of the hammer drives the piston into the chamber compressing the fluid. The thermal cycle is not simulated, but this is considered an advantage rather than a disadvantage since, if the heat energy generated per round were put into the test for each cycle, the temperature buildup would very severely limit the rate of testing. (Rapid testing is one of the main advantages of the present system.) Also, the areas of interest are usually separated from the propellant gases by 1 to 2 in. of steel and, therefore, remain at low enough temperatures that material yield strength is not affected either during field or laboratory tests.

The size and capacity of test rigs have grown over the years as the need arose, starting with a 37-mm weapon requiring a hammer of only a few hundred pounds up to the latest facility able to test the largest weapons, currently manufactured, to maximum design loads. However, to keep pace with current trends in gun design it is desirable to investigate test parameters to maximize the thrust capability of this facility.

This new facility, in operation approximately 18 mo, is designed around a Vulcan Iron
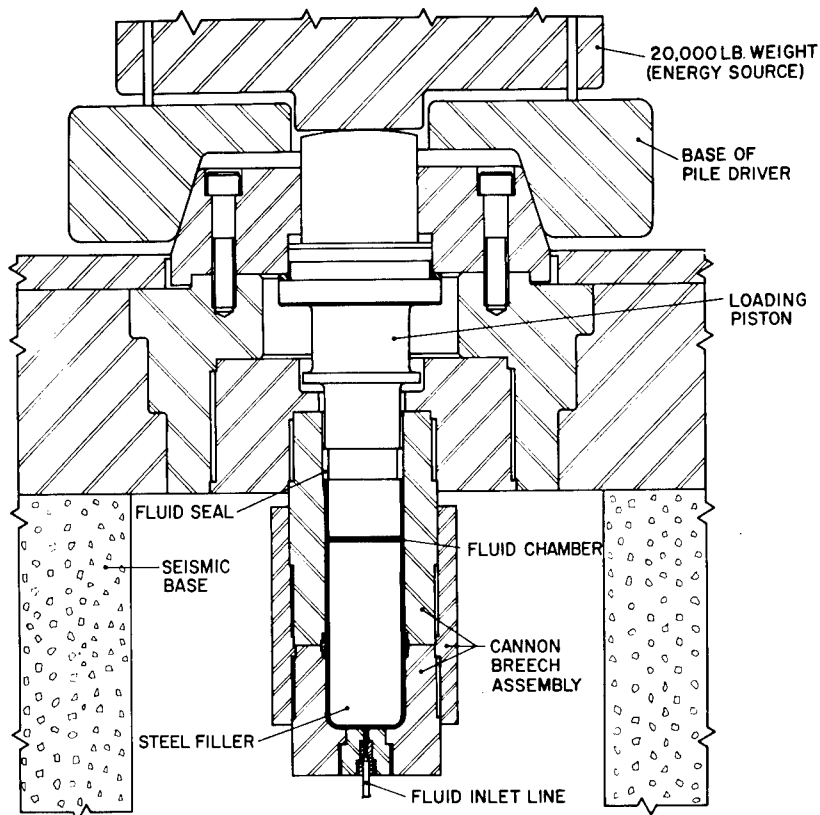
Fig. 1. Sectional view of impact test facility

Works 020 hammer which has a 20,000-lb free-fall weight with maximum drop height of 3 ft and can operate at 60 to 70 cpm. The test assembly is mounted on a 300,000-lb reinforced concrete seismic base that floats on shock pads. The facility can currently produce a peak thrust of 2.5 million pounds with a rise time of 5 to 7 ms.

The load is monitored with strain gages mounted around the body of the piston and readout is on a Tektronix 535 scope with Q units. For this test a pressure gage has been designed so that actual measurements of pressure can be made at points in the weapon chamber rather than depending on only the gross thrust information which the piston strain gage bridge provides. The gage is a thick wall cylinder with fluid on the inside and strain gages mounted on the outside. A sectional view of an installed gage appears in Fig. 2 and a photograph of a completed gage in Fig. 3. The piston bridge is calibrated directly by pressurizing the chamber of the weapon through the fluid inlet line, to full operating loads, using a Harwood Engineering Company 200,000-psi intensifier system. The pressure gage is calibrated with an American
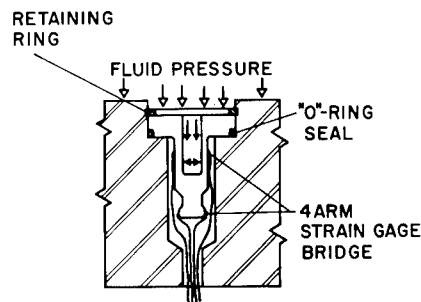

Fig. 2. Pressure gage

Instrument Company 100,000-psi dead weight tester.

STATEMENT OF THE PROBLEM

The problem of interest in this paper has two aspects, namely:

1. To determine factors affecting pressure pulse so that peak thrust can be maximized through proper design; and
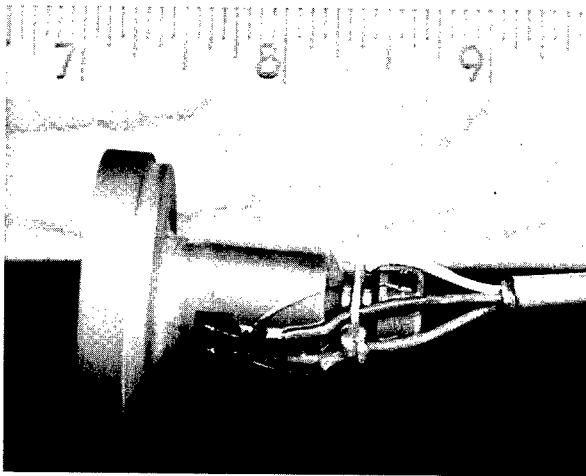
142

Fig. 3. Pressure gage

examination of the effects of top, annular, and bottom clearances on the dynamic pressure in both the top and bottom of a pressure vessel. A cannon tube, chamber and coupling were used as the pressure vessel for this particular test. The cannon components, the dynamic test setup and an adjustable filler piece, as well as the position of the pressure transducers, are shown in Fig. 4. The top and bottom clearances may be adjusted by removing the adjustment shims shown in this figure. The top clearance is adjustable from 0.1 to 1.35 in. and the bottom clearance from 0.035 to 4 in. The filler piece was constructed to have an annulus of 0.002 in. for the initial study and can be machined to any larger annulus desired. A study of the pressure time pulse was chosen as the most expedient method for examining these variables both independently and in combination.

2. To ascertain what pressure gradients may exist in the chamber of the test weapon and determine the factors governing them.

APPARATUS

The test program and subsequent data reduction were directed toward the isolation and

The pressure-time pulse was provided by impacting the 20,000-lb hammer on a piston. A cam-operated quick release mechanism and bridge crane was used in place of steam operation to give single drops of the hammer from various heights. Figure 5 is a photograph of the mechanical setup with the operator at the release mechanism. The impacting hammer provides a pressure pulse which is sensed by
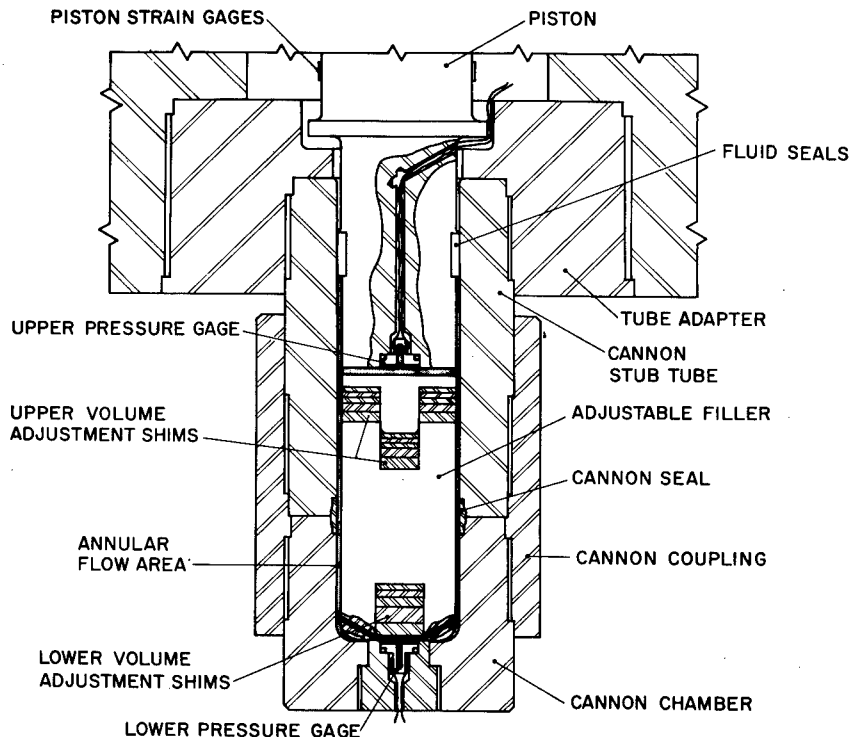

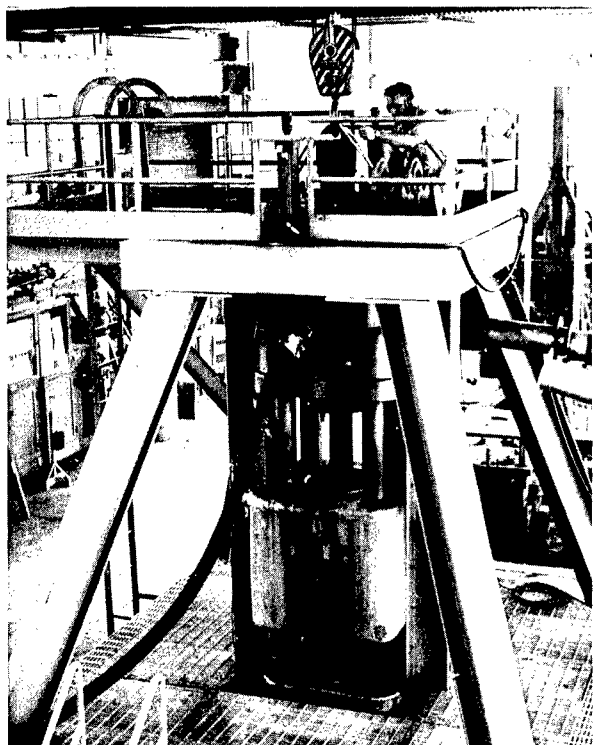Fig. 4. Experimental apparatus for pressure-volume-flow study

Fig. 5. Test apparatus

the pressure gages (shown in Figs. 2 and 3) in the top and bottom of the pressure vessel.

PROCEDURE

In each case a preload pressure of 2000 psi was introduced into the system. The hammer was raised to the desired height and released. The ensuing pressure pulse was monitored by the pressure gages shown in position in Fig. 4. The signal from the pressure transducers was monitored on a dual trace oscilloscope and a photograph made on Polaroid film. The data then are in the form of a pressure-time pulse for the two transducers.

Tests were conducted with various hammer drop heights and top clearances for a given bottom clearance and annulus. The bottom clearance was varied and the tests rerun. When all tests were completed, the filler was machined to a new annular clearance and the previous schedule was rerun.

RESULTS

Representative pressure-time pulses are shown in Figs. 6 through 9. The scope sweep rate for all cases is 4 ms per major abscissa division. The details for each figure are given in Table 1. The top trace is the top pressure gage output. The bottom trace is the bottom pressure gage output, except for Fig. 8 where it is the piston bridge output.

A more complete summary of results is shown in Figs. 10 through 12.

In Fig. 10 maximum pressures are plotted as a function of top clearance for a 3-ft drop height and 0.002-in. annular clearance. The bands are wide enough to encompass the slight change in pressure created by changing bottom volume and the experimental scattering. This same description applies to Fig. 11 except that here bands have been drawn for a 0.012-in. annular clearance with Fig. 10 reproduced for comparison.

In Fig. 12 maximum pressures are plotted as a function of hammer drop height for a 0.002-in. annular clearance and for two top
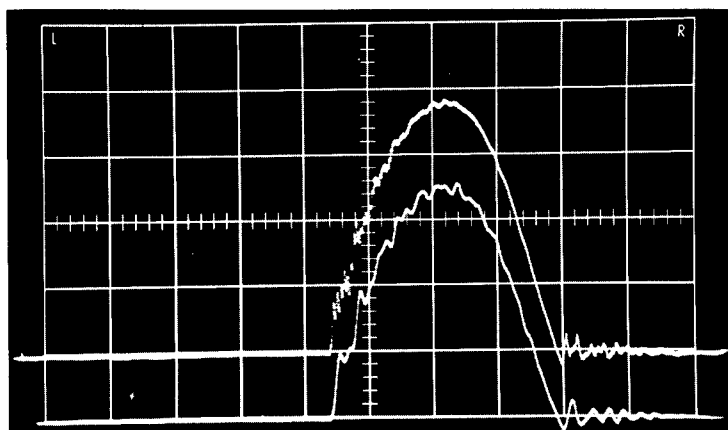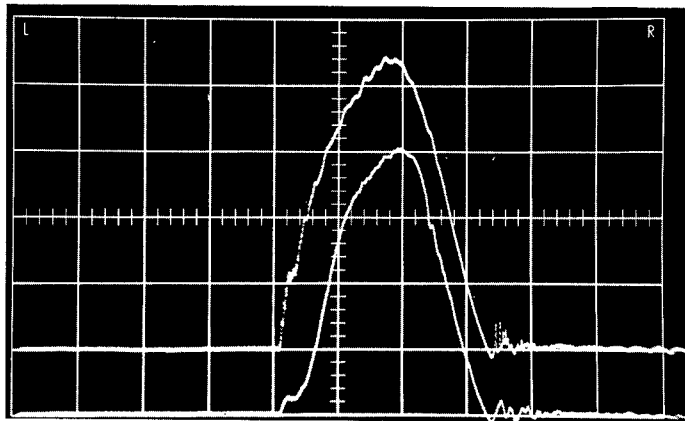

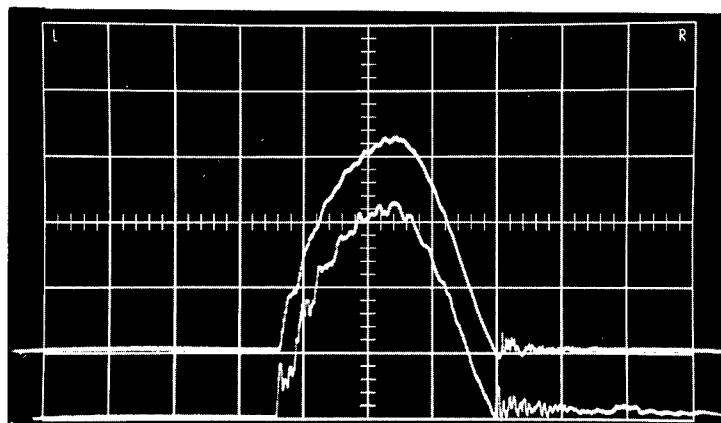Fig. 6. Pressure-time pulse

144

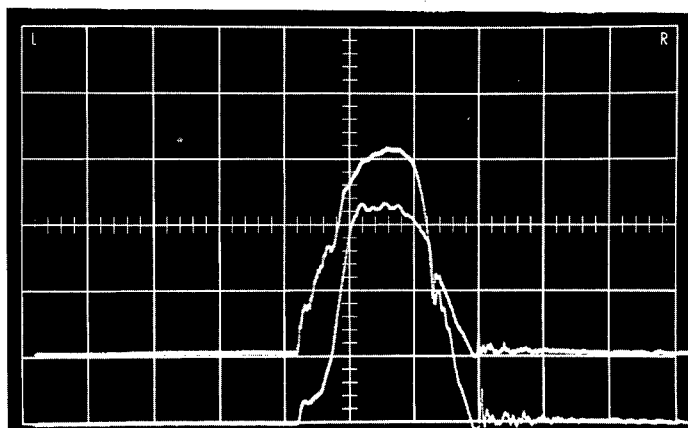Fig. 7. Pressure-time pulse

Fig. 8. Pressure-time pulse

Fig. 9. Pressure-time pulse

145

TABLE 1

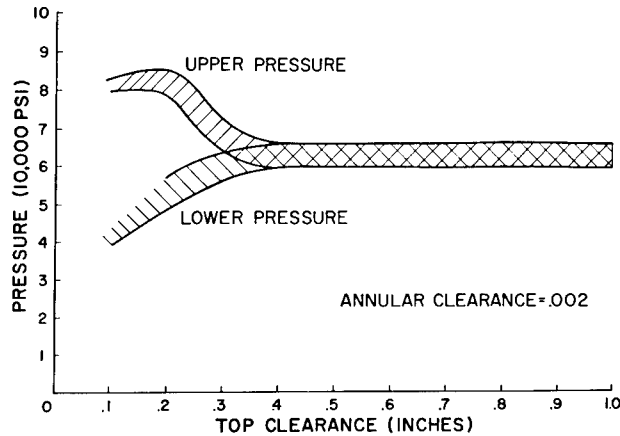| Figure	Top Clearance (in.)	Bottom Clearance (in.)	Annulus Clearance (in.)	Drop Height (in.)	Top Trace Max. Press. (psi)	Bottom Trace Max. Press. (psi)
6	1.35	0.25	0.002	6	21,000	21,000
7	1.35	0.25	0.002	36	60,000	60,000
8	1.35	0.25	0.002	21	44,000	46,000
9	0.2	0.25	0.002	36	86,000	49,000

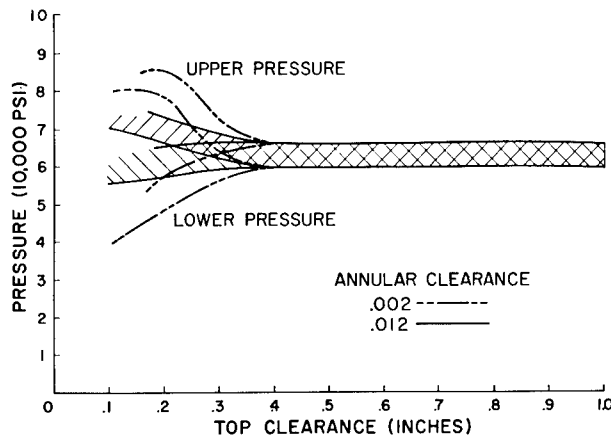Fig. 10. Variation of peak pressures with top clearance

Fig. 11. Variation of peak pressures with top clearance

clearances. The band widths primarily represent the variation of pressure along the filler piece from the top to the bottom of the chamber; i.e., the top of the band is the pressure at the chamber top and the bottom of the band is the pressure at the chamber bottom. The two top clearances illustrated are representative of two characteristic "families" of results. With a top clearance of 0.2 in. or less, the large pressure decay from the top to the bottom of the chamber was noted, while for a top clearance of 0.35 in. or more this decay was much less.
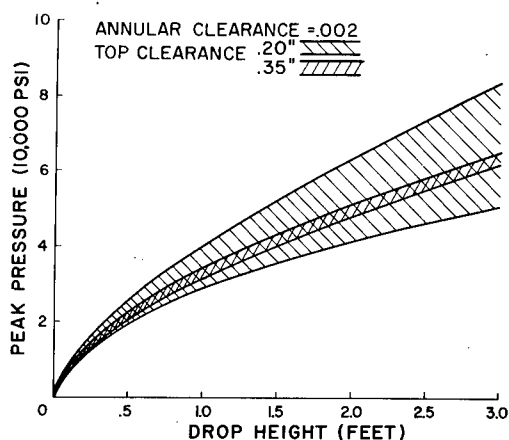
146

Fig. 12. Variation of peak pressure
with hammer drop height

DISCUSSION

The characteristic pressure pulses shown in Figs. 6 through 9 have a general half-sine form with certain deviations apparently created by the fluid properties.

Resistance to fluid flow through the annulus offers a possible explanation for much of this deviation. Total flow from the top to the bottom of the chamber is determined by the pressure difference between these two ends and the duration of this pressure difference. Stated another way — it may be said that the area under the pressure time pulse for the top of the chamber represents the total "driving potential" available to push fluid from the top, through the annulus, and into the bottom. However, if flow rate is not linearly proportional to driving pressure the actual area is not a quantitative measure of total flow. If, for example, flow rate did not rise as fast as pressure, a short-duration high-pressure pulse would not push as much fluid through the annulus as a longer duration lower pressure pulse with the same integrated area. Flow of an incompressible fluid with constant viscosity through a fixed area would exhibit just this type of behavior; that is, pressure drop is proportional to velocity (flow rate) to some power greater than one, for example $\Delta p \, \alpha \, v^{7/4}$ for turbulent flow.

The actual experimental setup does not offer such easy analysis. Flow is undoubtedly quite complex — there are density changes, viscosity changes, and flow area changes. The increase in viscosity with pressure and the above-mentioned velocity dependence on pressure would tend to reduce total flow for the short-duration high-pressure pulse, while the increase in density and flow area would have the opposite effect.

The area under the pressure-time curve for the top of the chamber is a measure of the total impulse imparted by the falling weight. Therefore, for a given drop height, this area should only vary to the extent that the coefficient of restitution varies from case to case.

The following observations may be made about the actual experimental data:

1. For a given drop height, total area under the pressure-time curve does not vary significantly.

2. When there is a relatively large top clearance, as in Figs. 6 through 8, the pressure pulses for the top and bottom are similar with about the same maximum pressure.

3. When there is little top clearance as in Fig. 9, the pressure pulses are quite different. Now the maximum top pressure is much higher than the maximum bottom pressure. (For this case the pressure sensitivity for the bottom trace is double that for the top trace).

4. When there is little top clearance, there is a pressure reversal or "blip" on the decaying side of the top pressure pulse (see Fig. 9). The "blip" coincides with the time when the bottom pressure exceeds the top pressure, thus indicating a flow reversal through the annulus.

These observations support the conclusion that the "effective resistance" of the annulus is less with higher top clearances, in which case there is a longer duration but lower pressure top pulse. Therefore, the nonlinear increase in pressure loss with flow velocity and the increase in viscosity with pressure must be the dominant effects. This conclusion is further supported by the comparison of results obtained for a 0.002-in. annulus with those obtained for a 0.012-in. annulus (Fig. 11).

Figure 12 illustrates the dependence of maximum pressure on hammer drop height. If the system was linear and perfectly elastic, this dependency would show pressure varying as the square root of drop height, that is, linearly with impact velocity. The actual curves show pressure increasing somewhat faster than with the square root of drop height. This may be caused by the fluid which, in a closed vessel, has a characteristic "hard" spring behavior. Also, the previously mentioned increase in annulus "effective resistance" at the higher pressures would give the system the overall characteristics of a "hard" spring.

The experimental results are compared with a simplified analytical model illustrated in

147

Fig. 13. In this model the elasticity of the piston, fluid, gun parts, and base bridge are lumped into a single spring. Varying the experimental parameters is equivalent to varying the stiffness of this spring in the model. Since, in the experiment, this stiffness could not be directly measured, comparison with the model was limited to a plot of maximum pressure vs time to maximum pressure, which is also illustrated in Fig. 13. There is rough agreement between the experimental and analytical results. Note that there are two "families" of experimental points. Those points below the analytical curve are for cases where the pressure pulses were similar to those in Figs. 6 through 8, while those points above the analytical curve are for cases where the pressure pulses were similar to those in Fig. 9; that is, they have the previously referred to "blip." This is further evidence that high annulus "effective resistance" as illustrated by Fig. 9 tends to increase the overall stiffness of the system.

CONCLUSIONS

For the range of variables considered, the following conclusions may be noted:

1. A uniform pressure can be obtained in the weapon chamber if certain combinations of top and annular clearances are maintained.

2. The maximum pressure is relatively insensitive to total fluid volume from some minimal volume to several times that volume.

3. Bottom chamber volume has little effect on maximum pressure up to any requirement for fitting the filler piece to a cannon chamber contour.

4. The results of the investigation indicate that mere variation in fluid volume cannot appreciably increase the maximum thrust level of the fatigue facility. A continuing program is being conducted to determine what other steps may be taken to uprate the facility.
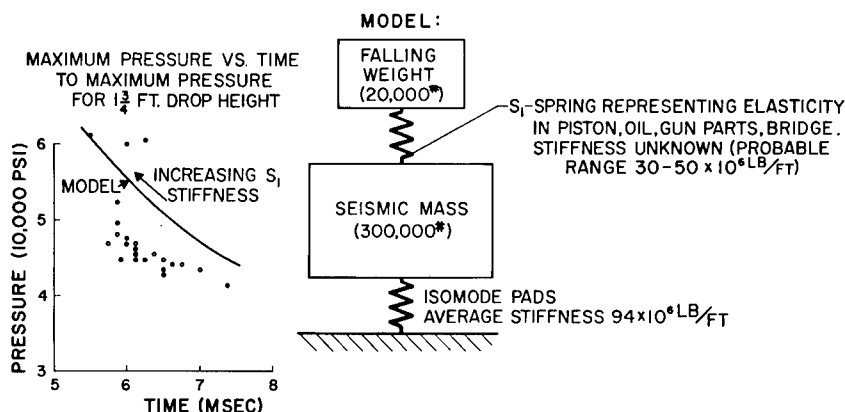

Fig. 13. Comparison of experiment with simplified analytical model

* * *

THE DOUBLE FORCE PROGRAMMER SHOCK TESTING

METHOD—A NEW TECHNIQUE FOR CONTROLLING

SHOCK PULSE WAVEFORMS*

F. H. Mathews
Sandia Corporation
Albuquerque, N.M.

A shock testing technique, the double force programmer method, is described which can be used to generate a wide variety of unusual shock pulse shapes and can be applied to most shock machines. Two honeycomb springs, placed between three carriages, are used to generate the desired acceleration-time pulse on the center (test item) carriage. A test is conducted when one of the outer carriages (ram) impacts into the two stationary carriages. The strength and shape of the honeycomb springs are adjusted to produce the desired test item acceleration history. The method was used with a pneumatic actuator to shock test a 450-lb test item carriage by applying a triangular shock pulse of short rise followed by a long decay. These results are used to illustrate several problems which occurred during the test series. Analytical methods are developed which predict required honeycomb spring geometries. A parameter study is described in which effects of honeycomb rate sensitivity and restitution are investigated.

INTRODUCTION

The problem of qualifying components for use in a field shock environment is normally approached by measuring or computing the individual component response. The damage potential of this shock-induced response is then analyzed, and a suitable, but not identical, laboratory shock test is conducted to qualify the component for further field investigation. This approach encounters difficulty if applied to a major subassembly, because the complex interactions between components severely restrict the shape and duration of shock pulses which adequately simulate the field environment for all of the components. The test engineer is therefore called upon to develop shock testing techniques to generate these special shock pulses. Ideally, any such technique should be easy to apply, adaptable to existing shock facilities, and meet the normal requirements of safety, low cost, and repeatability.

The double force programmer shock testing method described in this paper can be used to generate a wide variety of shock pulses while meeting these requirements.

DOUBLE FORCE PROGRAMMER METHOD — FREE IMPACT SETUP

The double force programmer method produces the desired shock pulse during an impact between three masses, as shown schematically in Fig. 1. The forces required to accelerate a test item are generated by crushing two honeycomb blocks which act as force programmers. A shock test is conducted when a moving ram mass impacts into the stationary test mass. During this impact, forces are developed between carriages by the crushing honeycomb. Hence, the force time history generated by either ram or anchor programmers may be controlled by properly shaping the honeycomb. One important restriction applies: the force between adjacent masses cannot decrease until these masses achieve equal velocity. While the programmers are crushing, the force must either increase or hold constant. Hence, as the ram mass crushes the pointed portion of the ram programmer (Fig. 1), an increasing force · is generated, followed by a constant force as the uniform programmer section is crushed.

a) INITIAL IMPACT BETWEEN RAM AND TEST MASSES

b) FIRST CONTACT BETWEEN TEST AND ANCHOR MASSES-RAM PROGRAMMER PRODUCES DOMINANT FORCE

c) LATE PHASE OF IMPACT-BOTH PROGRAMMERS PRODUCE COMPARABLE FORCES

d) COMPLETION OF TEST-ALL MASSES ARRESTED BY BRAKES
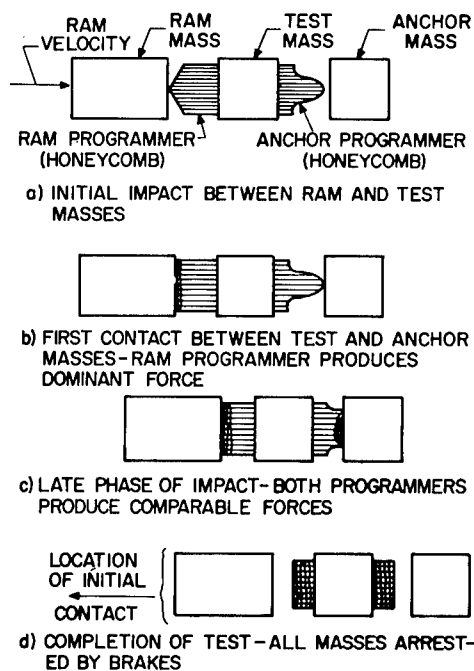
Fig. 1. Schematic of free impact test

Fig. 2. Idealized acceleration and velocity histories required to produce triangular test mass acceleration

The function of the anchor programmer is to produce a resisting force which can be subtracted from the ram force in a manner allowing complete control of the entire test carriage acceleration history. Thus, after obtaining the rising portions of the acceleration pulse (Fig. 1a), the anchor mass and programmer contact (Fig. 1b), and as both programmers crush (Fig. 1c), the net force acting on the test mass decreases, thus forming the decaying portions of the test mass acceleration. Finally, as the three masses achieve equal velocities, they are separated by restitution and braking forces and brought to a stop without further contact.

Idealized acceleration and velocity time histories required to produce a short-rise, long-decay, triangular-shaped acceleration-time pulse are illustrated in Fig. 2. Ram and anchor accelerations are of opposite sign, so the resulting forces subtract to produce a triangular acceleration pulse on the test mass. The velocity traces indicate that during impact, the ram mass always moves toward the test mass, which in turn always moves toward the anchor mass, except at the time c' when all carriage velocities are equal. Therefore, the ram programmer is being progressively crushed during time a through c', while the anchor programmer is being crushed during time b through c'. Because of this continual crushing, the honeycomb programmers may be shaped to the
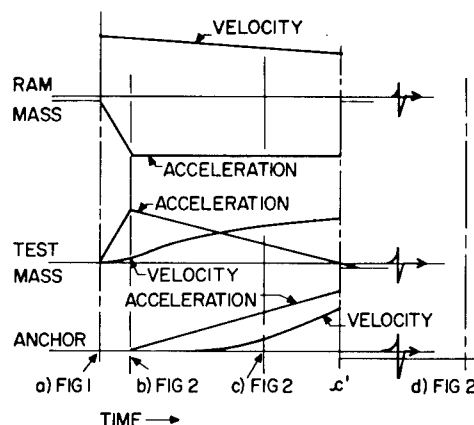
required force profiles by adjusting their areas as a function of crush depth.

The double force programmer technique was used to produce a 300-g triangular shock pulse on a 450-lb test mass with the setup shown in Fig. 3. A pneumatic actuator brought the 1600-lb ram to the required velocity. This ram mass then contacted the ram programmer and produced the free impact sequence shown in Fig. 1. Each carriage was equipped with friction brakes which arrested the carriages independently and without further impact after approximately 40 ft of travel.
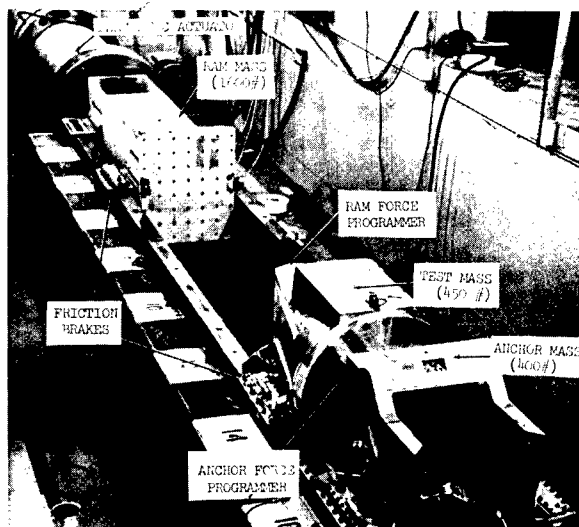

Fig. 3. Setup for shock test -- longitudinal axis

A close-up of the setup used for tests in a lateral axis is shown in Fig. 4. Both programmers were placed on the test mass so that crushing would occur on the contact surfaces of the ram and anchor masses. This permitted the honeycomb length to smooth the force generated by the honeycomb. In addition, felt pads placed between the honeycomb and the test mass acted as mechanical filters to smooth further the honeycomb forces.

Acceleration results obtained with this set-up are shown in Fig. 5. These records indicate that each carriage responded approximately as indicated in the idealized case depicted in Fig. 2. There are three important exceptions. First, the ram and test masses resonated during the shock pulse. This problem was somewhat alleviated by using mechanical filtering between the honeycomb and test mass. However, the problem of designing test fixturing of large physical size and high-frequency response is fundamental and is made more difficult with this setup, since the test carriage must provide opposing faces through which the anchor and ram forces pass. This design restraint further increases test carriage size, thus reducing natural frequency.

A second exception to ideal behavior is that the honeycomb programmers exhibited restitution, hence producing some rebound after crushing was completed. As a result, both ram and anchor accelerations end with a gradual decay rather than with the immediate termination assumed in Fig. 2.
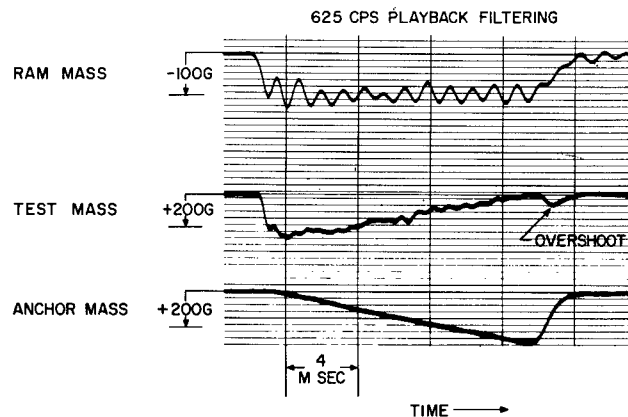

Fig. 4. Close-up of test setup -- lateral axis

Fig. 5. Acceleration results obtained
using setup of Fig. 3

The final deviation from ideal performance is the acceleration overshoot occurring at the end of the test mass acceleration. Controlling overshoot, which may be either positive or negative, and which was frequently of greater amplitude than indicated in Fig. 5, proved a most difficult problem to which no entirely satisfactory solution has been proposed. Overshoot results from a difference in the forces generated by the two programmers during the final stages of impact. It is at this time that both programmers are developing near maximum forces, which must cancel almost exactly to produce the desired low test mass acceleration. If these two forces are not identical due to some small error in either crush strength or impact velocity, or due to a difference in restitution between the two programmers, an acceleration overshoot will result. This is the major problem affecting the repeatability and preciseness of the double force programmer method. It was, therefore, the subject of an analysis discussed in a later section of this paper.

A final problem encountered during the double force programmer tests was that the aluminum honeycomb used in the ram programmer split and buckled along the bonded joint between cells, without producing the desired crush force. Some improvement was achieved by cutting the ram programmer so that the wedge of buckled honeycomb cells formed during crush of the pointed honeycomb section was always oriented across the bond line between cells. Then the splitting force caused by this wedge was not directed normally to the honeycomb bond line, and splitting was reduced. In future tests, honeycomb of improved bond strength is expected to yield better performance.

ANALYSIS

Two analytical investigations were conducted in support of the double force programmer tests. The first, based on the assumption of ideal plastic honeycomb behavior, was used to determine honeycomb profiles, the required ram mass impact velocity, and the necessary relationship between carriage masses. The second investigation determined the effect of restitution, honeycomb strain rate, and various experimental errors. The force diagram used in each of these investigations is shown in Fig. 6, and mathematical symbols are defined as follows:

M_R = ram weight (lb);

M_T = test weight (lb);

$$\Sigma F_R(t) = F_{RB} - F_{RT}(t) \qquad \Sigma F_A(t) = F_{AB} + F_{TA}(t)$$

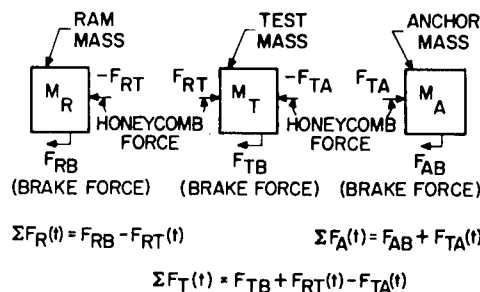$$\Sigma F_T(t) = F_{TB} + F_{RT}(t) - F_{TA}(t)$$

Fig. 6. Force diagrams used during analysis

M_A = anchor weight (lb);

F_{RB} = ram mass braking force (lb);

F_{TB} = test mass braking force (lb);

F_{AB} = anchor mass braking force (lb);

F_{RT} = force between ram and test masses (lb);

F_{TA} = force between anchor and test masses (lb);

X = displacement of ram mass (ft);

Y = displacement of test mass (ft);

Z = displacement of anchor mass (ft);

Δ_1 = honeycomb crush between ram and test masses (ft);

Δ_2 = honeycomb crush between test and anchor masses (ft);

σ_c = crush strength of honeycomb (psi);

A = area of honeycomb (sq in.);

t_m = shock pulse rise time (ms);

t_o = shock pulse duration (ms);

$f(x)$ = actuator force, a function of displacement (lb);

M_R' = weight added to ram by test machine parts during impulsive impact (lb);

ℓ = free space between ram and ram programmer (ft);

Σ = force summation;

152

· = first time derivative;

·· = second time derivative;

a = coefficient of rate sensitivity (lb-sec/ sq in.-ft); and

b = coefficient of elastic restitution (lb/ sq in.-ft).

The force time profiles required for an ideal system are shown in Fig. 7. The test mass force time curve is derived from desired acceleration requirements. Hence,

$$\Sigma F_T(t) = M_T \ddot{Y}(t) = F_{TB} + F_{RT}(t) - F_{TA}(t) ,$$

where $\ddot{Y}(t)$ is the desired test mass acceleration pulse and includes deceleration during braking. The remaining force time curves are determined from the force diagrams in Fig. 7, with the additional requirement that only increasing or constant force histories are permitted. Hence,

$$\Sigma F_R(t) = -F_{RT}(t) + F_{RB} \quad \text{when} \quad 0 \leq t \leq t_m,$$

$$= -F_{RT}(t_m) + F_{RB} \quad \text{when} \quad t_m \leq t \leq t_o$$

describes the force acting on the ram mass during the shock pulse, while

$$\Sigma F_A = 0 \quad \text{when} \quad 0 \leq t \leq t_m,$$

$$= F_{TA}(t) + F_{AB} \quad \text{when} \quad t_m \leq t \leq t_o$$

describes the anchor force history. Therefore, the force time history acting on each mass is implied by the desired shock pulse. It follows that the force contribution due to the honeycomb may be assessed and honeycomb programmers of proper shape may be formed. A discussion of the detailed procedures required to predict the programmer shapes follows.
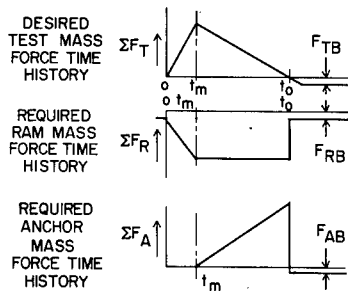

Fig. 7. Ideal force time histories on each mass during impact

FREE IMPACT ENERGY REQUIREMENTS

If the test item force time curve and its mass are known, the impact velocity required of a ram and the required mass of the anchor can be determined in the following manner. The test item velocity change from 0 to t_o is given by:

$$\dot{Y}(t_o) = \int_0^{t_o} \ddot{Y} \, dt = \int_0^{t_o} \frac{\Sigma F_T(t)}{M_T} \, dt .$$

It is required that on completion of the test item acceleration pulse at t_o, both ram carriage and anchor carriage attain the velocity $Y(t_o)$, assuming no elastic recovery of the programmer. The anchor velocity change is given by

$$\dot{Z}(t_o) = \int_{t_m}^{t_o} \frac{\Sigma F_A(t)}{M_A} \, dt = \dot{Y}(t_o) .$$

Solving this equation for the anchor mass gives

$$M_A = \int_{t_m}^{t_o} \frac{\Sigma F_A(t)}{\dot{Y}(t_o)} \, dt .$$

During the time $0 \leq t \leq t_o$, the ram carriage is slowed from its initial impact velocity, $\dot{X}(0)$, to its final velocity $\dot{X}(t_o) = \dot{Y}(t_o)$, as indicated in the following equation:

$$\dot{X}(0) = \int_0^{t_o} \frac{\Sigma F_R(t)}{M_R} \, dt + \dot{Y}(t_o) .$$

Hence, the ram impact velocity $\dot{X}(0)$ and the required anchor mass M_A may be computed for a desired test item acceleration pulse and test item mass. Notice that any ram mass M_R could be used. However, the ram will normally be much heavier than either test or anchor masses, since a large ram reduces the ram programmer crush distance.

FORCE PROGRAMMER SHAPES

The force programmer shapes are determined by assuming an ideal plastic model of the honeycomb material. With this model, the honeycomb follows the stress-strain curve shown in Fig. 8. Then the force generated by the honeycomb programmer as it crushes is related to the crush stress σ_c and the area by
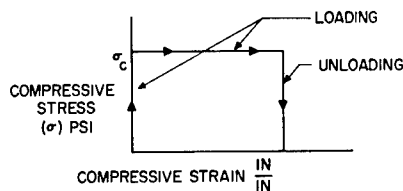
$$F = \sigma_c A ,$$

153

Fig. 8. Ideal plastic be-
havior of honeycomb as-
sumed during analysis

and the required honeycomb area is given as a function of t by

$$A(t) = \frac{F(t)}{\sigma_c} .$$

The position of each mass during the impact can be calculated from the forces acting. Hence,

$$X(t) = \int_0^t \left(\dot{X}(0) + \int_0^t \frac{\Sigma F_R(t)}{M_R} \, dt \right) dt ,$$

$$Y(t) = \int_0^t \int_0^t \frac{\Sigma F_T(t)}{M_T} \, dt \, dt ,$$

$$Z(t) = \int_0^t \int_0^t \frac{\Sigma F_A(t)}{M_A} \, dt \, dt .$$

The amount of honeycomb crush is given by

$$\Delta_1(t) = Y(t) - X(t) ,$$

$$\Delta_2(t) = Z(t) - Y(t) ,$$

where $\Delta_1(t)$ is the crush of the first honeycomb programmer and $\Delta_2(t)$ is the crush of the second programmer. Using the values of $\Delta(t)$ and $A(t)$, each programmer can be cut to the shape required for the desired pulse.
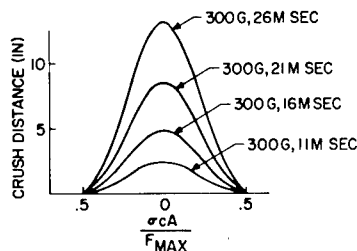
IMPULSIVE IMPACT

These equations were programmed for a digital computer solution in which the force required from each programmer was determined as a function of crush height. The profiles of several ram and anchor programmers are shown in Fig. 9. Additional honeycomb, not shown in Fig. 9, must be included to accept the crushed honeycomb without bottoming. In all cases, the desired shock pulse was triangular in shape with a 1-ms rise and the indicated

duration. The profiles of Fig. 9 indicate large ram programmer crush depths when long-duration pulses are required. In view of previously mentioned difficulties with buckling and splitting of honeycomb, some method of decreasing crush depth would be desirable. This may be accomplished with an actuator setup in which the impact occurs while the ram mass is still being accelerated by the actuator. This setup is depicted in Fig. 10, which includes the additional terms required for analysis of this problem. The three masses are placed in their initial rest position, with a free space (ℓ) between the ram and the first programmer. When the actuator is fired producing a thrust force, described here as a function of displacement [f(x)], both the ram mass and the actuator parts are accelerated, picking up velocity while closing the space ℓ. The ram carriage then contacts the ram spring, producing the ram acceleration history depicted in Fig. 10. Because the ram is taking energy from the actuator during this impact, its average velocity is lower and the required crush deformation of the ram programmer is reduced. The acceleration records shown in Fig. 10 are those compiled assuming ideal honeycomb behavior. During the impulsive impact depicted in Fig. 10, the ram programmer crushed 14 in., compared to 25 in. using the free impact setup.

Several actuator experiments conducted using the impulsive technique confirmed that
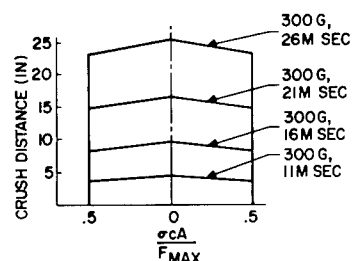
a) RAM PROGRAMMER HONEYCOMB PROFILES

b) ANCHOR PROGRAMMER HONEYCOMB PROFILES

Fig. 9. Honeycomb pro-
files required for triangu-
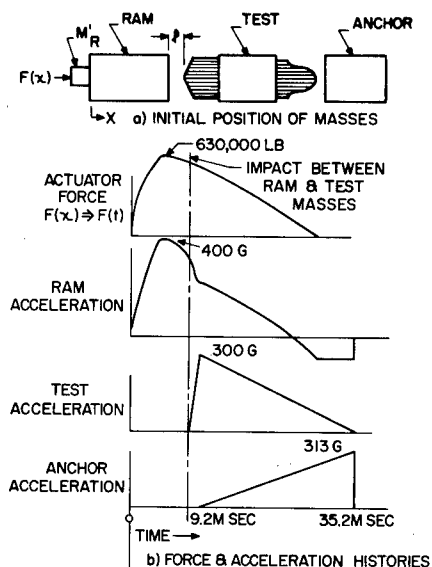lar shock pulses using setup
of Fig. 3

154

Fig. 10. Setup and motion histories calculated for impulsive impact

the analysis was adequate. In addition, these tests indicated that adding the mass and length of moving test machine parts decreased the natural frequency of the ram system, causing increased resonance of the ram carriage.

ANALYSIS OF NONIDEAL BEHAVIOR

It has already been demonstrated that precise control of the test mass acceleration may be obtained in the case of ideal plastic honeycomb. However, the honeycomb force programmers may exhibit properties of restitution and rate-dependent crush strength which constitute a major departure from ideal behavior. The effect of these properties, as well as the effect of variations in other test parameters, were investigated analytically. Honeycomb profiles determined from the preceding ideal plastic assumption were used in this analysis, which solved for the carriage motions resulting during a free impact. By assuming various amounts of rate sensitivity and restitution or by changing some other test parameter, the computed result could be used to indicate how the assumed change from ideal plastic behavior influenced test results.

A rate-sensitive model of honeycomb was formulated as indicated in Fig. 11 and is described by the following set of equations:

$$\sigma(\Delta, \dot{\Delta}) = \sigma_0 + a\dot{\Delta}, \qquad \text{if } \dot{\Delta} > 0, \qquad (1)$$

$$= \sigma - b(\Delta \text{Max} - \Delta), \qquad \text{if } \dot{\Delta} \leq 0, \qquad (2)$$
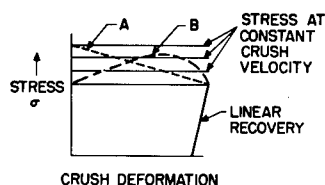

Fig. 11. Assumed model of rate-sensitive honeycomb; A is loading path, followed by ram programmer, while B is loading path, followed by anchor programmer

and

$$\sigma(\Delta, \dot{\Delta}) = 0, \qquad \text{if } \sigma_0 \leq b(\Delta \text{Max} - \Delta). \qquad (3)$$

Hence, the honeycomb was assumed linearly dependent on crush velocity during loading, and followed a linear rate-independent recovery during unloading. With this model, the ram programmer would follow a force deformation curve similar to A in Fig. 11, while the anchor programmer would follow the B curve.

Several of the acceleration-time histories computed using this analysis are given in Figs. 12 through 18. A key to these figures is provided in Table 1. In all cases the programmer profiles were those computed assuming ideal plastic honeycomb. Restitution figures (120,000 lb/in. recovery) were based on rebound velocity obtained during tests using the setup of Fig. 3.

Figures 12 through 14 indicate the effect of variations in ram impact velocity, assuming restitution with no rate sensitivity. The impact conditions of Fig. 12 were determined from perfect plastic energy requirements. Because of restitution, this impact velocity was too high, resulting in a trailing acceleration overshoot on the test mass. Overshoot occurred because the ram programmer continued supplying force to the test mass after the anchor force was reduced by rebound of the anchor mass. The ram impact velocity was reduced approximately 5 percent to obtain the computed acceleration results shown in Fig. 13, which is the closest approach obtained to the desired 300-g 16-ms shock pulse.

Figure 14 indicates the effect of a further reduction in ram velocity (10 percent) as might occur due to poor control of setup conditions. These computed results indicate that acceptable experimental results may be obtained using honeycomb exhibiting restitution, provided
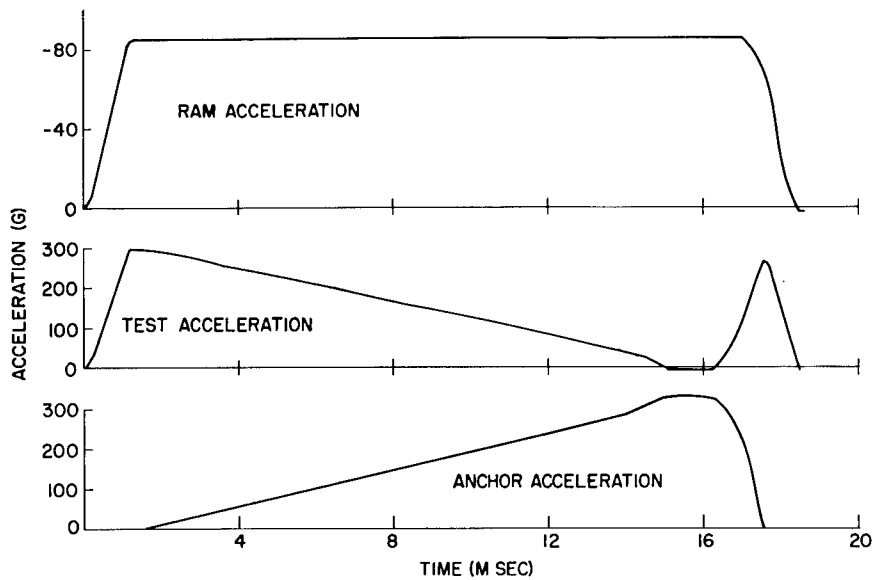
155

Fig. 12. Computed acceleration results allowing for restitution -- excessive ram impact velocity of 121 fps

Fig. 13. Computed acceleration results allowing for restitution -- ram impact velocity reduced to 116 fps
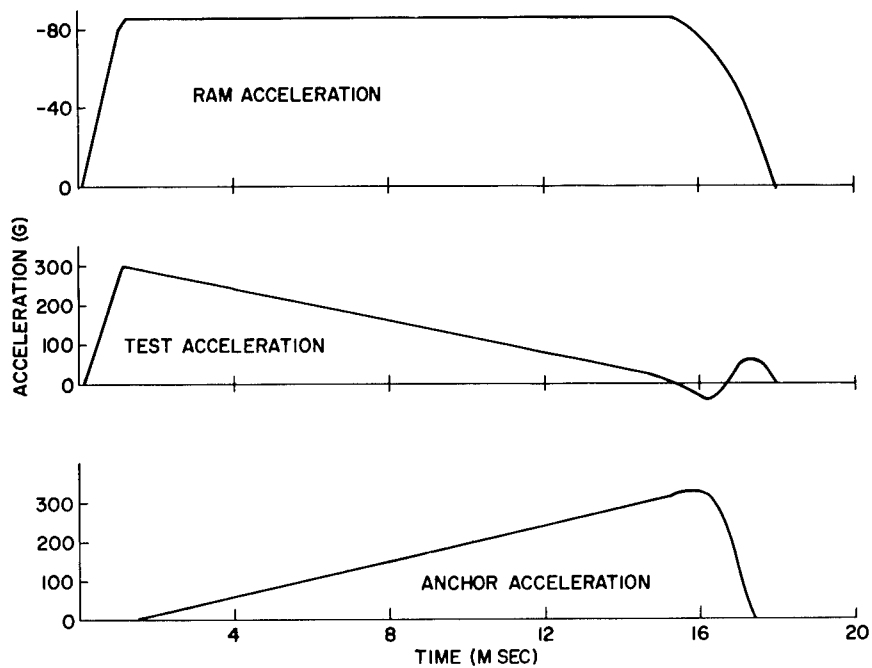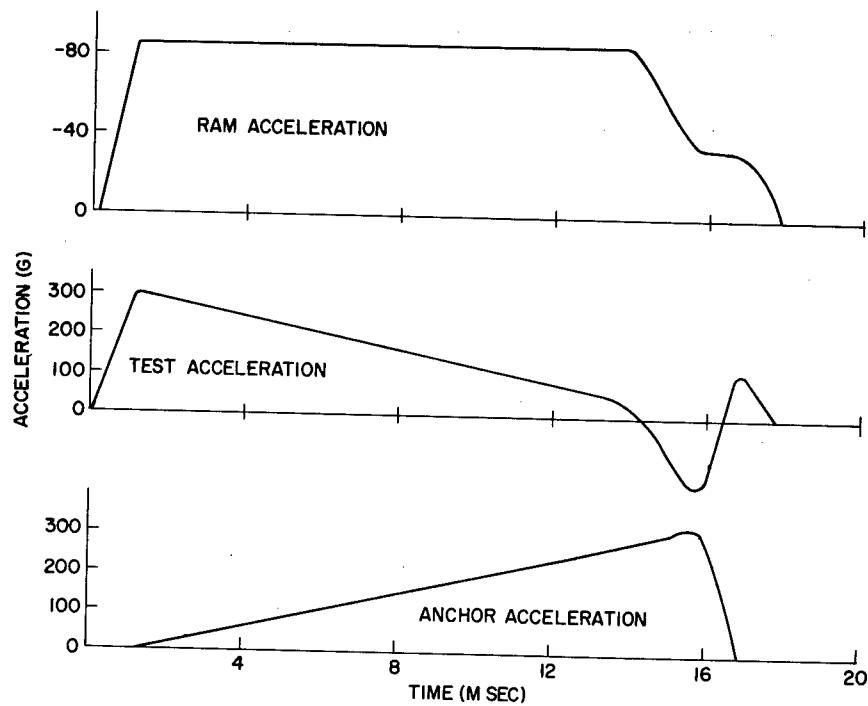
156

Fig. 14. Computed acceleration results allowing for
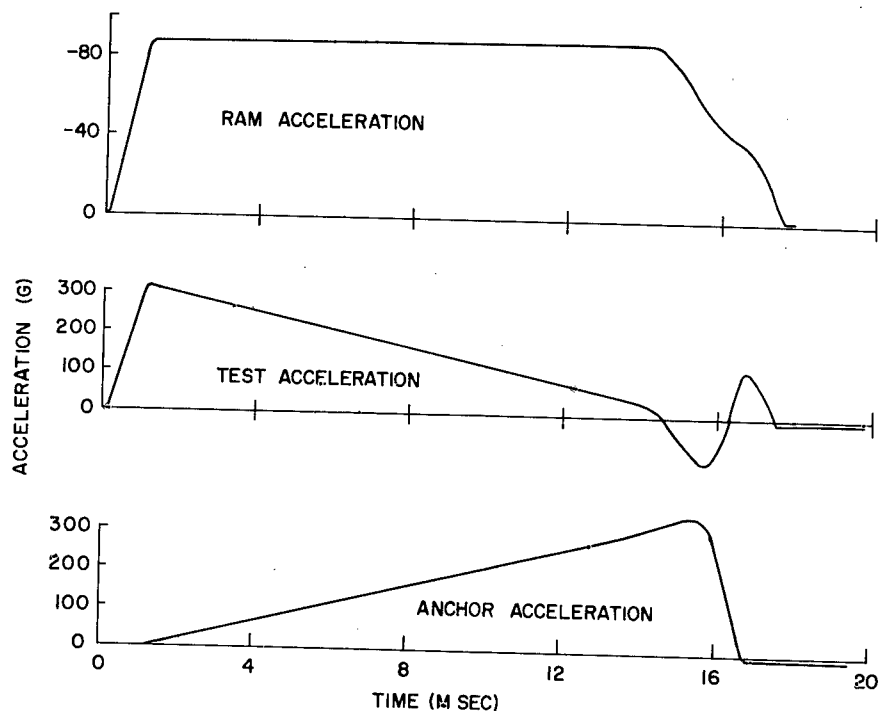restitution -- ram impact velocity reduced to 110 fps

Fig. 15. Computed acceleration results allowing for
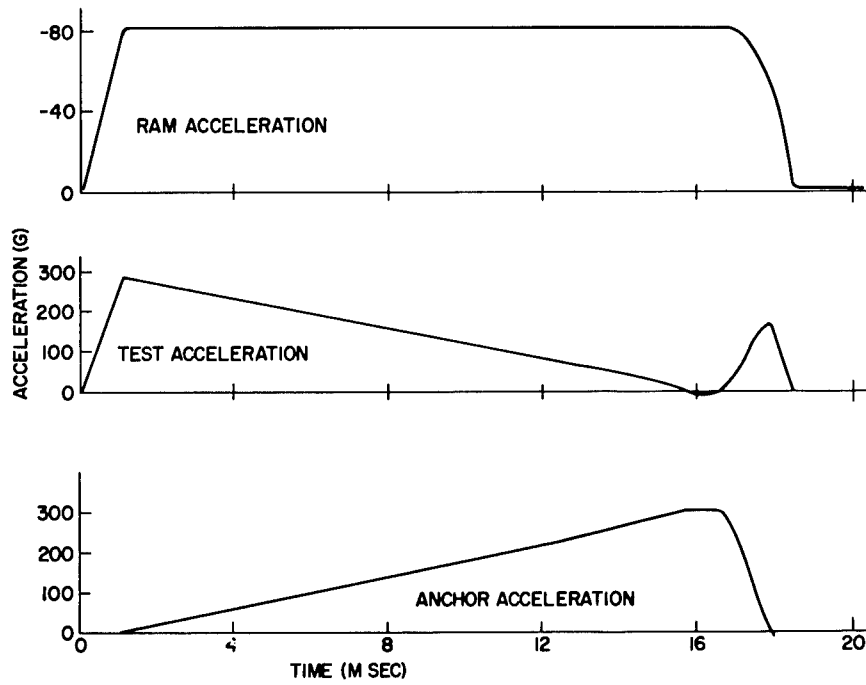restitution -- high honeycomb crush strength

157

Fig. 16. Computed acceleration results allowing for restitution -- low honeycomb crush strength
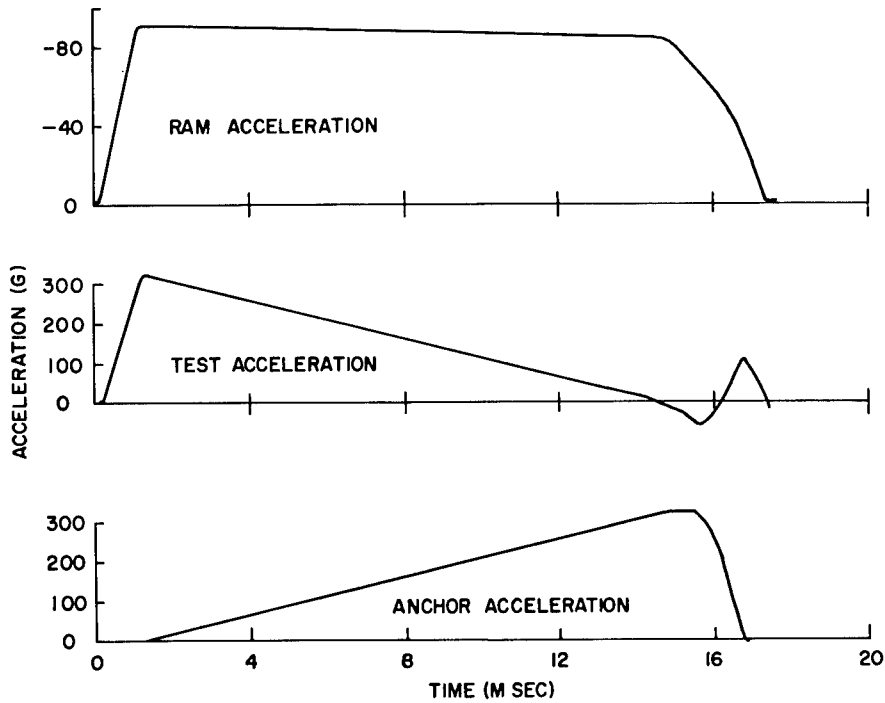

Fig. 17. Computed acceleration results allowing for restitution and rate sensitivity
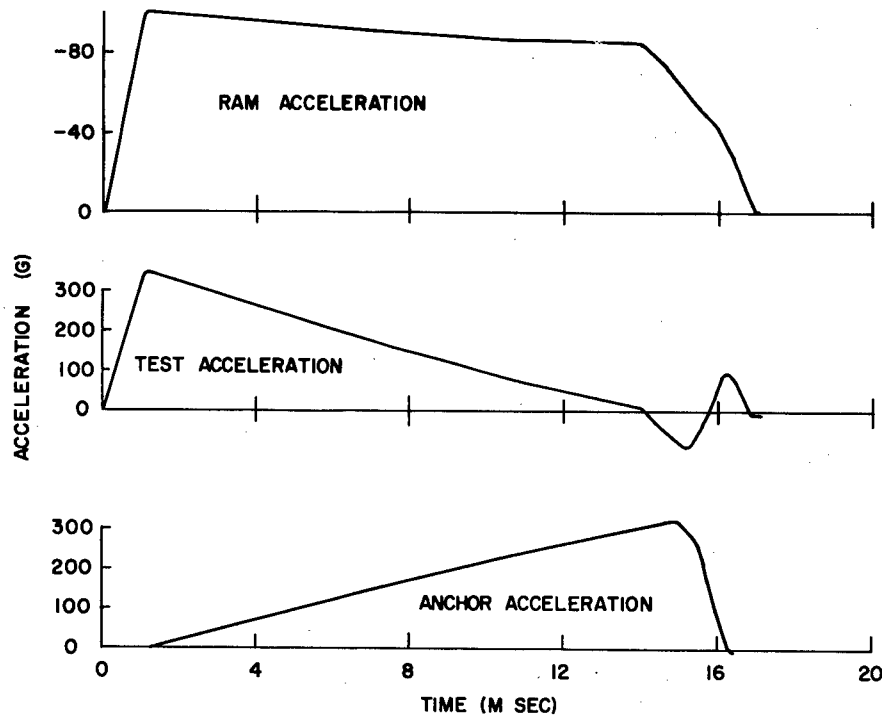
158

Fig. 18. Computed acceleration results allowing for restitution and increased rate sensitivity

TABLE 1
Conditions Investigated in Figs. 12 Through 18

Figure	Honeycomb Descriptions	Test Conditions	Comments
12	Ideal plastic with 120,000 lb/in. restitution.	M_R = 1600 lb F_{RB} = 3000 lb M_T = 450 lb F_{TB} = 900 lb M_A = 416 lb F_{AB} = 450 lb $\dot{X}(0)$ = 121 fps	Honeycomb profiles and impact velocity from ideal plastic analysis.
13	Ideal plastic with 120,000 lb/in. restitution.	Same as 12 except $\dot{X}(0)$ = 116 fps	Ram impact velocity reduced to account for restitution.
14	Ideal plastic with 120,000 lb/in. restitution	Same as 12 except $\dot{X}(0)$ = 110 fps	Ram impact velocity reduced to account for error in test control.
15	Ideal plastic with 120,000 lb/in. restitution. Honeycomb crush strength increased 5 percent without compensating change in programmer area.	Same as 12 except $\dot{X}(0)$ = 116 fps	
16	Ideal plastic with 120,000 lb/in. restitution. Honeycomb crush strength increased 5 percent without compensating change in programmer area.	Same as 12 except $\dot{X}(0)$ = 116 fps	
17	Rate sensitive with 10 percent increased strength at 116 fps crush velocity. 120,000 lb/in. restitution.	Same as 12 except $\dot{X}(0)$ = 116 fps	
18	Rate sensitive with 20 percent increased strength at 116 fps crush velocity. 120,000 lb/in. restitution.	Same as 12 except $\dot{X}(0)$ = 116 fps	

159

proper adjustments are made in the ram impact velocity. They also indicate that precise control of ram impact velocity is essential, and minor deviations will result in considerable under- or overshoot.

The effects of either high or low honeycomb crush strength, as well as restitution effects, are indicated in Figs. 15 and 16, in which ram impact velocity had been reduced to the conditions of Fig. 13. Both programmer profiles were those computed for ideal plastic honeycomb, but their crush strength was assumed either 5 percent higher or lower than would be required ideally. Once again, major under- and overshoot was predicted near the end of the test mass acceleration, indicating the need for precise honeycomb strength control. In practice, honeycomb crush strength can be measured dynamically during a drop table test, and simple allowances can be made for variations in each lot. However, if the honeycomb is subject to random splitting and buckling, these effects can easily lead to much greater overshoot than indicated in Figs. 15 and 16.

Dynamic crushing tests performed on a drop table indicate that honeycomb is subject to velocity sensitive behavior, which increases honeycomb crush strength with increased loading rate. The honeycomb programmers were assumed to exhibit 10 and 20 percent linear hardening at a 116-fps loading velocity in addition to restitution to produce the results of Figs. 17 and 18. Once again, under- and overshoot occurs after termination of the primary pulse. Velocity sensitivity most strongly influences the interaction between ram and test masses, since it is here that the largest loading velocity occurs. Hence, the early phases of the test mass acceleration history show higher than desired acceleration, which in turn brings the test mass up to ram velocity earlier than the anchor mass, with a resulting undershoot terminating the pulse. However, the assumed velocity sensitivity caused less under- and overshoot than errors either in ram velocity or in honeycomb crush strength.

This analysis of nonideal behavior has indicated that if the honeycomb departs from perfect plastic behavior and exhibits restitution or rate-sensitive behavior, suitable results may be obtained with programmers whose profiles were determined from ideal plastic assumptions. It is necessary that ram impact velocity be reduced and then precisely controlled.

Further parameter studies are under way to investigate the effect of adjustments in the ram mass and possible gains resulting from a

deliberately excessive anchor mass. It is hoped these studies will indicate better control methods.

APPLICATION TO OTHER SHOCK TESTING EQUIPMENT

The double force programmer method may be applied to other types of shock testing equipment, including air guns or drop tables. The drop table setup is depicted in Fig. 19. A test is conducted by releasing both anchor and test mass, allowing them to impact against a stationary anvil to produce the desired acceleration. For some applications, it may be possible to replace the honeycomb ram programmer by an elastic spring. The method may also be applied to air guns using either a free impact or impulsive impact setup, as shown in Fig. 20. Test operation would be similar to the actuator setup, except that enough free volume must be provided between pistons to prevent compressed gas from influencing test results. In addition, the muzzle pressure, which acts only on the anchor piston, may cause second impacts. In some cases, it may be feasible to modify the
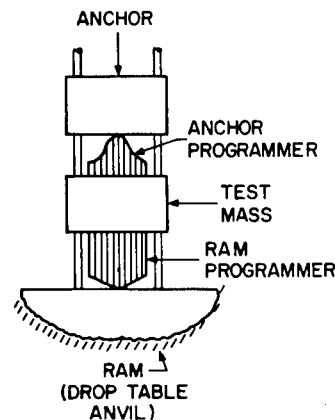

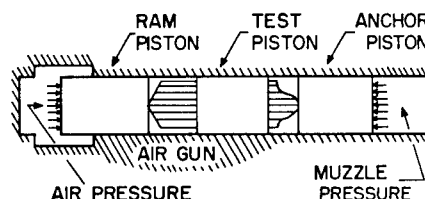Fig. 19. Application of double force programmer to drop table

Fig. 20. Application of double force programmer to air gun

normal air gun pulse simply by an impact between test piston and anchor, thus eliminating entirely the requirement for a ram piston and ram programmer.

CONCLUSIONS

In conclusion, the double force programmer method has proven a useful testing technique which allows control of the entire acceleration-time history occurring on a massive test item. The analysis required to apply the method is straightforward and easily set up for digital computer solution. The method is versatile and can be used to obtain a variety of either symmetrical or nonsymmetrical shock pulses. In addition, it is applicable to most existing shock testing equipment, including actuators, air guns, and drop tables. The method requires considerable care in application, which suggests that it be applied only to those tests where unusual shock pulse shapes are essential. The double force programmer method suffers from spurious accelerations which may occur as the primary shock pulse is completed. Controlling these accelerations requires close test control.

*   *   *

SPECIFICATION OF SHOCK

AEROSPACE SHOCK TEST SPECIFIED AND
MONITORED BY THE RESPONSE SPECTRUM

K. Kuoppamaki, Consultant
Riverside, California
and
R. A. Rouchon
Lockheed Missiles and Space Company
Sunnyvale, California

Laboratory data are presented on two recent developments in testing for shock: (a) a continuous frequency, constant Q, shock spectrum analysis technique; and (b) a shock spectrum synthesis technique employing electrodynamic shakers. Data presented show that shock spectrum simulation is a practical laboratory test method for general shock testing, combined shock and vibration testing, and for shock to remote areas via long signal transmission line. The present shock simulation methods are discussed, as well as the methods of specifying the shock environment. Damage potential of shock spectrum testing is compared to that of standard pulse shape testing. Inaccuracies resulting from pulse shape distortion are illustrated and the accuracy of shock spectrum simulation is compared to that of standard pulse simulation. Present electrodynamic shaker limitations are discussed and a shaker system for pyrotechnic event simulation is described. It is recommended that aerospace shock tests be specified and monitored by the response spectrum.

INTRODUCTION

The Aerospace industry can now move toward subjecting flight hardware to more realistic shock tests. The practice of using the standard pulse shapes (half-sine, sawtooth, etc.) to simulate the damage potential of complex shock motions results in subjecting the hardware to loads far in excess of that necessary. This is an unrealistic overtest. The intent of shock testing, according to Vigness, is that "shock machines simulate the important characteristics of shocks that occur in field environments; or that the shock machines have a damage potential which by analysis is shown to be similar to that of a composite field shock environment against which protection is required" (1, p. 26-1).

Shock testing for field environments has been accomplished for many years by simulation of standard pulse shapes. This technique was useful when the major portion of the shock environments was due to quasi-standard pulse-

generating events such as occur during transportation and handling. However, it has been recognized for some time that most of the shock events experienced by aerospace hardware are not the standard pulse type but are complex shock motion. Unfortunately, because of the lack of suitable laboratory equipment, no change in the method of simulation followed this awareness.

With the development of the electronic analog of the reed gage, along with the use of electrodynamic shakers for shock spectra simulation, shock environments can now be specified by shock response spectrum and simulated by complex shock motions.

DESCRIPTION OF SHOCK
PHENOMENON

The shock phenomenon is generally described by two parameters, time and amplitude, or frequency and peak response (shock spectra). The parameters, time and amplitude, are

163

common laboratory terms and need no explanation here. Shock response spectra parameters, however, are not widely used in the test laboratory and should be defined.

Shock response spectrum is generally defined as the maximum response of a series of single degree of freedom systems, as a function of the frequencies of the systems, to a given shock excitation (2). It should be recognized that the application of shock response spectra assumes that the structure has a specific amount of damping and is responding as a second-order system. This differs from a Fourier spectrum which makes neither assumption (1, p. 23-10). A correlation does exist between the Fourier spectrum and residual spectrum if the system has zero damping. However, further discussion in this subject is beyond the scope of this paper (1, p. 23-10; 3, 4).

Historically the classical reed gage consists of a number of mechanical systems-reeds which are considered to respond as single degree of freedom systems, each having a different natural frequency (1, pp. 23-29). This mechanical reed gage has been used to measure the shock response spectrum in the past, but with limited success due to its bulkiness and difficulties in the readout of high-frequency data.

SELECTION OF STANDARD PULSE SHAPES

The present method of selecting the standard pulse shape to be used for laboratory simulation of the spectra content of a complex shock motion is generally accomplished by the following steps (Figs. 1 and 2):

1. Estimates of the expected test shock spectrum are obtained.

2. The shock spectra of available amplitude-time traces from test recordings of prominent transients are plotted.

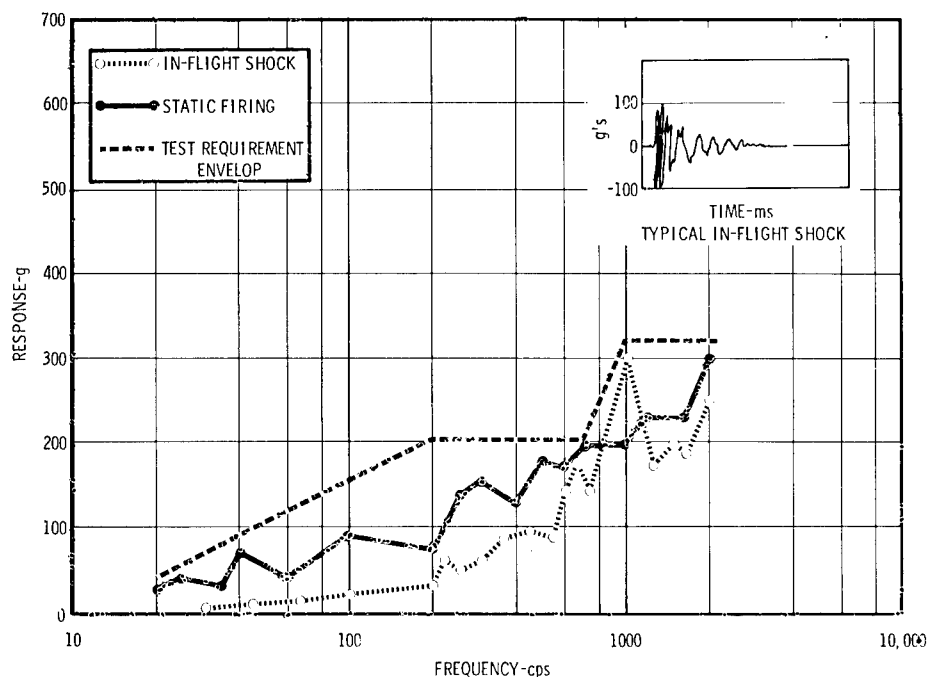3. The estimates and the shock spectrum curves are compared to all available data from

Fig. 1. Test requirement. The test requirement envelope is described by a listing of following format:

"Amplitude (g)	Frequency (cps)
50	80
200	200
200	700
320	1000
320	2000

Connect the coordinate points with straight lines on a semilog plot; log frequency, linear amplitude."
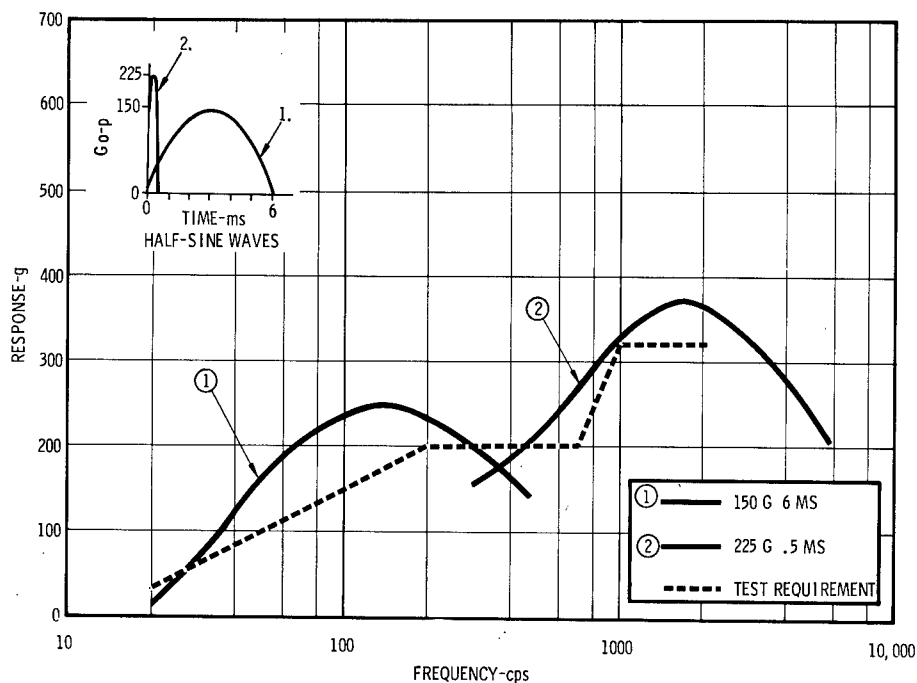
164

Fig. 2. Enveloping test requirement with response spectrum of half-sine pulses. When the test requirement is presented in form of an envelope of response spectrum, the test by velocity shock machine is performed by choosing pulse shapes (1 and 2) with shock response spectra which will envelop the required response amplitudes. (Note: The amount of damping included in process of establishing a response spectrum shall be indicated. The presented spectra are based on 5 percent damping.)

previous tests, and the test requirement curve is specified.

4. Standard pulse shapes (whose spectra content are known) are selected to envelop the test requirement.

It should be noted as shown in Fig. 2 that the half-sine pulses selected only approximate the test requirement. This inaccuracy cannot be overcome using standard pulse simulation. When a standard pulse is actually experienced by the aerospace hardware, a pulse with the same characteristic is selected for laboratory simulation.

SELECTION AND SPECIFICATION OF SHOCK SPECTRUM ENVELOPE

The selection of a shock spectrum to be used for laboratory simulation is accomplished as mentioned above except, of course, that standard pulses are not selected. The shock spectrum itself is specified by giving a table of frequency versus response g values. These

values are plotted with frequency along the abscissa (log) and response g along the ordinate (linear) with straight lines connecting the points as shown in Fig. 1.

COMPARISON OF DAMAGE POTENTIAL

The standard pulse has a significant velocity content. This pulse may be called a velocity shock. Simulation of a standard pulse on an impactor or electrodynamic shaker (5) results in subjecting the test specimen to a severe velocity shock. This is in contrast to the much smaller velocity content of a complex shock motion, as shown in Fig. 3.

The velocity content of a shock is very important since the damage potential of any velocity shock is related to the ability of an item to store the energy change fed into it without failing (6). The effects of local resonances are not considered here. The velocity content of the majority of complex shock motions resulting from pyrotechnic events is negligible (7).

165

$$V_A = \int_{t_0}^{t_1} A\,dt$$

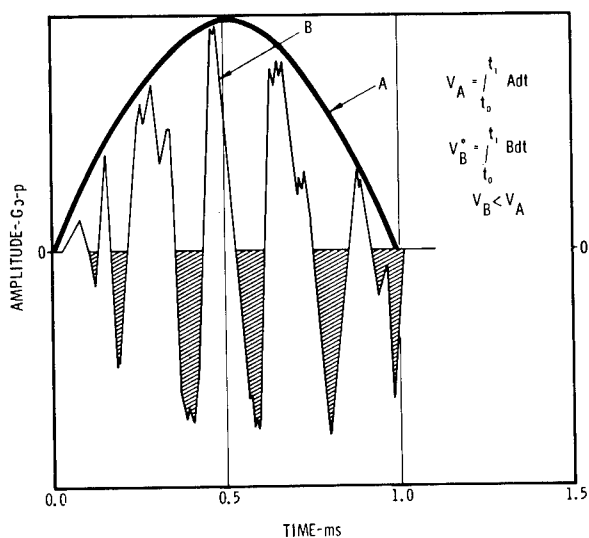$$V_B = \int_{t_0}^{t_1} B\,dt$$

$$V_B < V_A$$

Fig. 3. Standard pulse vs complex shock motion in respect to velocity content. Difference in velocity content of an impact pulse A and complex shock B is shown by difference in area under amplitude/time trace. Positive and negative sides of complex shock motion are close to identical in velocity content.

Since pyrotechnic events and other complex shock motions make up a great majority of the complex shock motions experienced by aerospace hardware, the use of a standard pulse to simulate the spectral content of a complex shock motion frequently results in severe overtesting, as shown by the following example.

While attempting to qualify a particular part, three small screws designed to shear during a pyrotechnic event showed a high incidence of failure when subjected to a half-sine pulse of 200 g, 1 ms. The part was subjected to eight complex shock motions simulated with an electrodynamic shaker and the new shock spectrum simulator. All eight spectrum levels exceeded that of the half-sine by at least 50 percent; however, no failures were observed. The part was then subjected to several static firings and no failures were noted. It was concluded that the failures were due to the velocity content of the half-sine pulse, and the test specifications were changed.

It is believed that this type of problem is not uncommon in the industry. The cost of the exercise described above was approximately $3,000.00. Consider for a moment how many times similar events have caused retesting, redesign, or some other delay in test programs.

ANALYSIS OF STANDARD PULSE SIMULATION

It is generally known that laboratory simulation of the standard pulse shapes does not necessarily agree with the analytical response spectrum for the particular pulse. The major reason for this disagreement is the response characteristic of the total moving mass. This includes the test specimen, holding fixture, and tester table. Pure standard pulse shapes are generally not achieved in the test laboratory.

An analysis of several half-sine pulses was made to obtain some measures of the magnitude of deviation from the true analytical curve. The shock response spectra of twenty-three 150-g 1-ms half-sine pulses, performed on routine hardware (using an Impact Model 2424 Drop Tester) were compared. These pulses were recorded on magnetic tape during routine testing. All 23 pulses were considered to be within the standard amplitude/time limits. Figure 4 shows a plot of the maximum and minimum spectrum deviation from the analytical curve. The upper shock response spectrum curve has a value of 272 g at 1600 cps and the lower curve has a value of 192 g at 820 cps. This represents a total deviation of 78 g or +28 and -22 percent from the analytical curve. The allowable pulse tolerances are ±15 g and ±0.4 ms. Half-sine pulses within these tolerances would produce a shock spectrum deviation and shift the resonant frequency point as shown in Fig. 5. A comparison of the allowable limits to those obtained above shows that the limits in response g were exceeded by 17 percent, while the frequency shift tolerance limits were exceeded by 44 percent.

Similar deviations were noted when simulating 2-, 7-, and 9-ms pulses on this same machine. In general, as the pulse duration increased, the spectral content decreased and the pulses became more triangular. The decrease in spectral content is consistent with the fact that the amplification factor of a triangular pulse is 1.34 instead of the 1.64 for the half-sine. It is expected that deviations as wide or wider would be observed if several different shock testing machines were used to develop the same pulse. These data indicate possible undertesting with respect to response spectrum. A substandard part may pass an undertest but fail when subjected to the proper test levels.

COMPLEX SHOCK MOTION SIMULATION

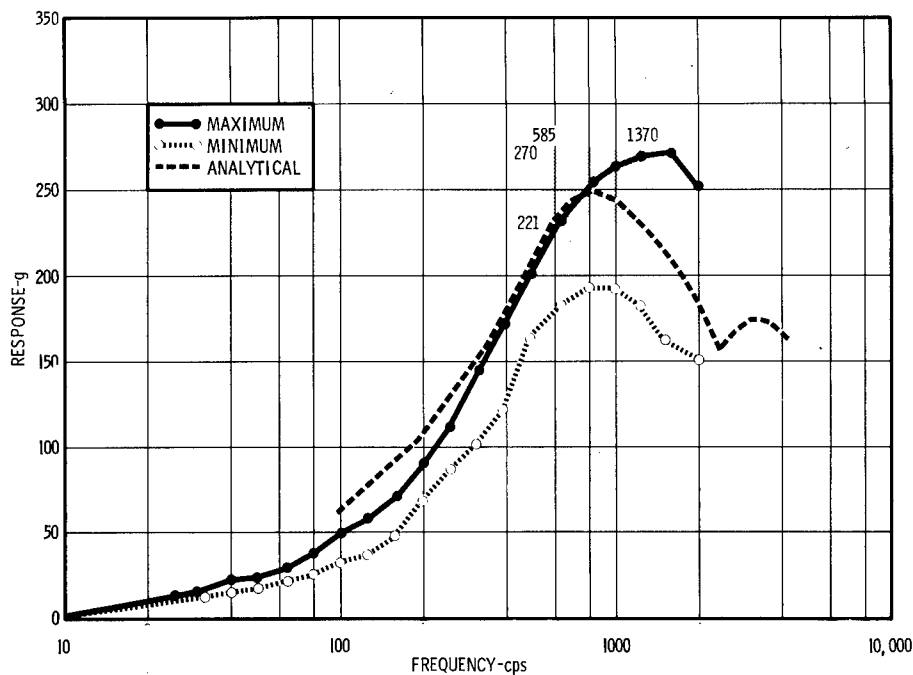Now that a continuous frequency, constant Q, shock spectrum synthesizer/analyzer has

Fig. 4. Maximum and minimum spectra of half-sine pulse tests. Response spectra of 23 corresponding impact pulse shock tests (all within test requirements of Fig. 5) indicate wide variety in response spectra.
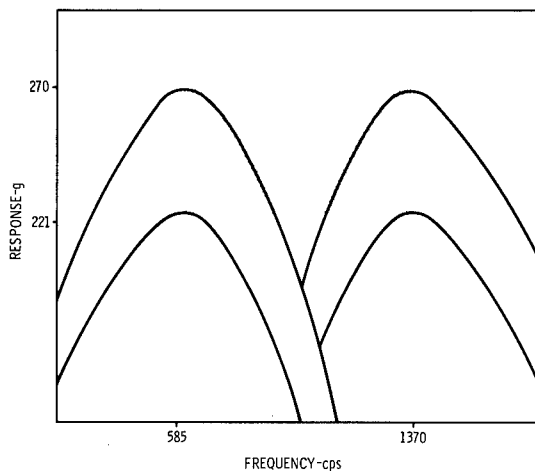

Fig. 5. Resulting spectral deviation based on amplitude time specification of shock pulse. Allowed margins in performing a shock pulse test, 150 ± 15 g, 1 ± 0.4 ms, results with scatter in response shown by shaded area in Figs. 4 and 5.

been developed for laboratory use and shown to be a practical tool (3), the gates are opened for the return to the reed gage principle for monitoring of shock simulation. This type of shock

testing is simulated using an electrodynamic shaker and the shock spectrum synthesizer/ analyzer as described by Painter and Parry (3). Briefly, the procedure is a process whereby the test requirement shock response spectrum is synthesized point-by-point, using the synthesizer/analyzer and an electrodynamic shaker. The transient produced by the shock synthesizer, shown in Fig. 6, closely resembles a typical in-flight transient shown in Fig. 1. The velocity content and damage potential of the synthesized transient can be shown to be much closer to that of the in-flight transient than that of the standard pulse. The length of this transient is controlled by the lowest frequency component (in the spectrum to be simulated) and is derived by ringing a bank of third-octave B and K filters with a unit impulse.

Simulation of shock spectrum on a shaker is not without problems. For adequate simulation it is important that the transducer location and mounting of the transducer is the same in laboratory testing as during the measurement of the environment to be simulated. In the illustrated case this requirement was well met. The flight measurements at the location shown in Fig. 7 resulted in the spectrum shown in Fig. 8, indicating a response of 17 g shock at 68 cps. This response is increased to 21 g at 68 cps in
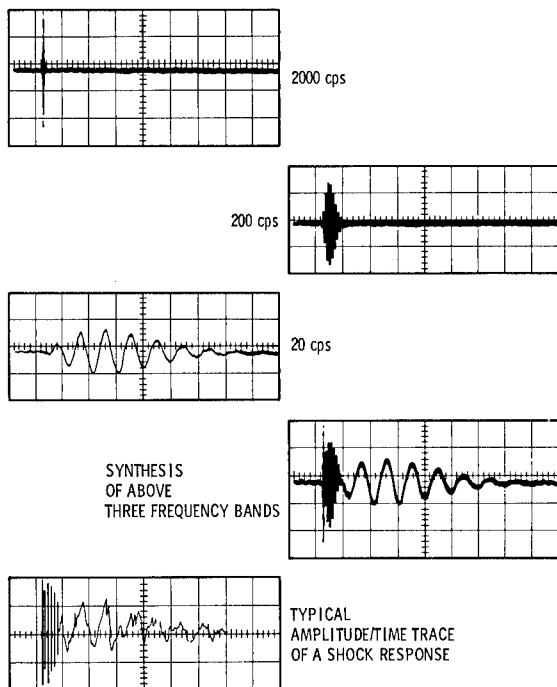
167

Fig. 6. Shock synthesis. Synthesis of frequency bands 2000, 200, and 20 cps is shown in time domain to illustrate similarity of synthesized shock motion with typical trace of flight shock motion. Traces illustrate capability of shock synthesizer to shape shock response to correspond with specific type of shock in respect to overall shape of shock motion and decay characteristics of its amplitude/time trace.

Fig. 7. Test specimen mounted on 20,000-force pound shaker for shock testing

the test specification. The spectrum shown also indicates that the shaker was equalized below the level of flight amplitudes and that the shaker power was increased for the test shock to reach the specified test level. The amount of accuracy which can be reached in shaping the spectrum is only a technicality. The tolerances to be maintained can be reduced to any practical level with relatively small additional expense, time permitting. However, the nonlinearities in the shaker table and test item combination can produce deviations in the shape of the spectrum, as well as marginal differences between the required spectrum and the response at the test. Reduction of such nonlinearities is an interesting engineering problem. In the illustrated case, this difference, however, was relatively small, as shown by the response spectrum of Fig. 8.

By definition, the number of peaks per frequency contained in the complex shock transient is the third dimension of shock response spectra
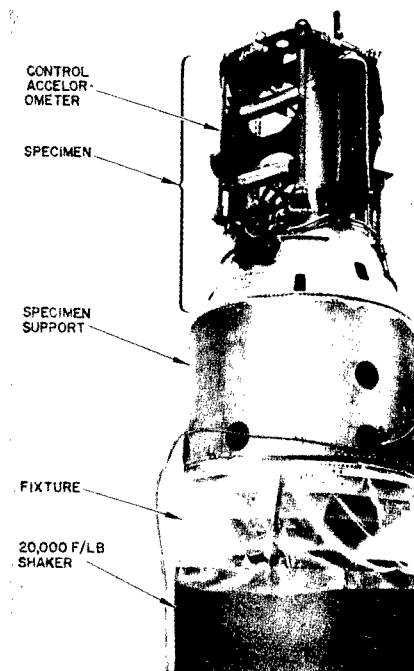
(1, 23-29). It is thought that with slight increases or decreases in damping, control of this dimension may be possible in the very near future.

Painter (8) has described the close correlation between the digital and analog analysis of the spectra simulated in the test laboratory at Lockheed, Sunnyvale. These two analyses agree within 10 percent.

MONITORING OF FORCE

The techniques of force measurement appear to be advancing to a state of practical application (9) in the description of flight environments.

Once force is measured (at the point of the measured acceleration), the combined data of force and acceleration, in form of response spectra, will greatly improve the use of electrodynamic shakers in testing for vibration and shock. Considerable amount of shaker capability goes into pushing up antiresonant notches to a level which would represent forces far above those experienced in flight. With force data, adjustments in acceleration requirements can be made.
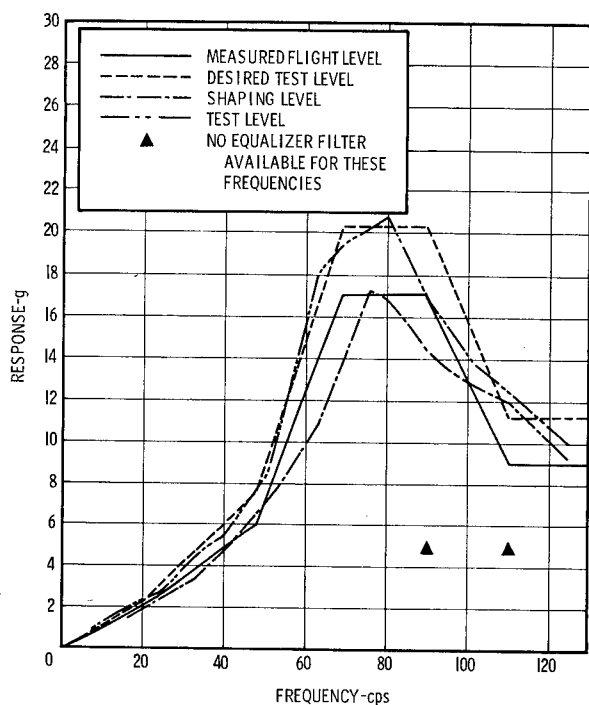
168

Fig. 8. Response spectra of Fig. 7 test. Test level has been increased 24 percent above envelope of flight measurements. Shaping of response spectrum with shock synthesizer was performed below flight amplitudes. Test represents preliminary state with incomplete capability in shaker equalization network. Accordingly, amplitudes above 100 cps remained above flight amplitudes at shaping level because of missing equalizer filters and response at 90 cps could not be increased to required level for same reason. These deficiencies can be easily corrected, but correcting of nonlinearity 76- and 80-cps peaks requires further study of problems involved.

PRESENT SHAKER LIMITATIONS

The majority of shaker equipment in use today is limited to a sinusoidal displacement of 1 in. double amplitude, a velocity of 70 to 100 ips, and a bare table acceleration of 100 g o-p. It has been determined, as shown in Fig. 9, that the standard continuous duty curve for a Ling Model A246 shaker does not hold for transient testing. It is increased by a factor of 3. This factor must be applied to determine the peak g rating of this shaker because it is designed to produce peaks three times its random force rating. The random force rating of the Ling Model A246 is 6000 force-pounds. Shock spectrum values in excess of 1500 response g (produced by pyrotechnic events) are beyond present shaker equipment capabilities. The major shortcoming we have encountered in using shakers

for the shock spectrum testing is that our power amplifiers do not have sufficient peak power capability. A shaker system to simulate shock spectra for the majority of present pyrotechnic events would consist of a shaker which has a lightweight armature (possibly 100 lb maximum) with high transitory velocity and acceleration capability (approximately 200 ips and 1000 peak g) and a power amplifier capable of delivering 600 kva peaks. The performance curve for the shaker is shown in Fig. 10. It is believed that such a shaker system is not beyond the present state of the art.

COMBINED ENVIRONMENTS

During the course of shock spectrum testing, it was determined that the synthesized shock transient signal and the random vibration signal from an automatic equalizer/analyzer could be imposed on the input terminals of the power amplifier at the same time, resulting in combining shock and vibration (Figs. 11 and 12). It is clearly seen by these figures that shock spectrum testing can be performed during random testing without significant alterations of the shock environment. The random environment was also not significantly altered.

LONG LINE TRANSMISSION

It was also determined that shock spectrum simulation is practical over long transmission lines. The spectrum shape imposed is shown in Fig. 8 and the test specimen mounted on a 20,000 force-pound shaker is shown in Fig. 7. The shaker was located in a test laboratory approximately 1 mile from the synthesizer/analyzer system. Present plans are to locate the synthesizer/analyzer in Lockheed's Centralized Vibration Signal Control Center and supply shock spectrum simulation to all of LMSC.

CONCLUSIONS AND RECOMMENDATIONS

For the past 10 years, monitoring of shock simulation has been based on the amplitude time trace of the shock pulse. This was primarily due to the lack of a practical tool for quick readout of the resulting shock response spectrum. This spectrum is an indicator of damage potential in accordance with the reed gage principle (1, pp. 23-29). The present developments in laboratory simulation and analysis techniques make it possible to reject the use of an amplitude/time trace of the transient
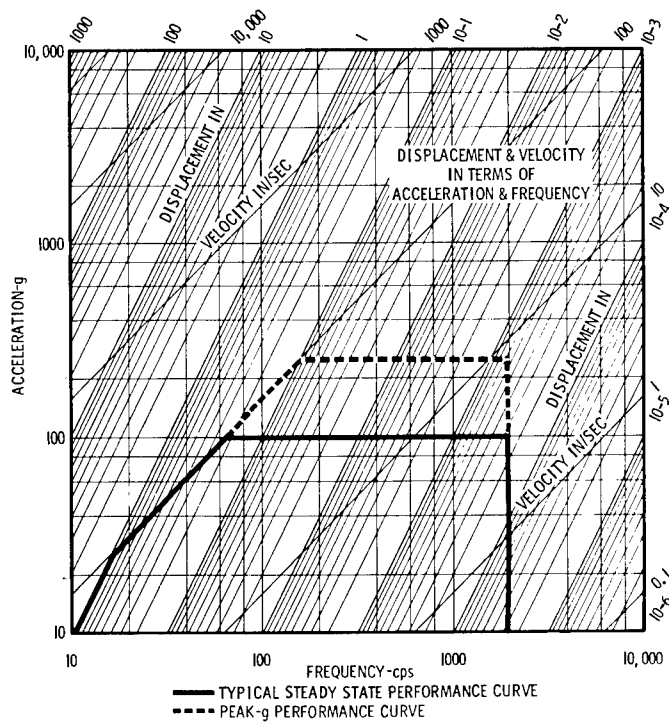
TYPICAL STEADY STATE PERFORMANCE CURVE

PEAK-g PERFORMANCE CURVE

Fig. 9. Typical steady state performance curve is altered when considering peak g capabilities of shaker

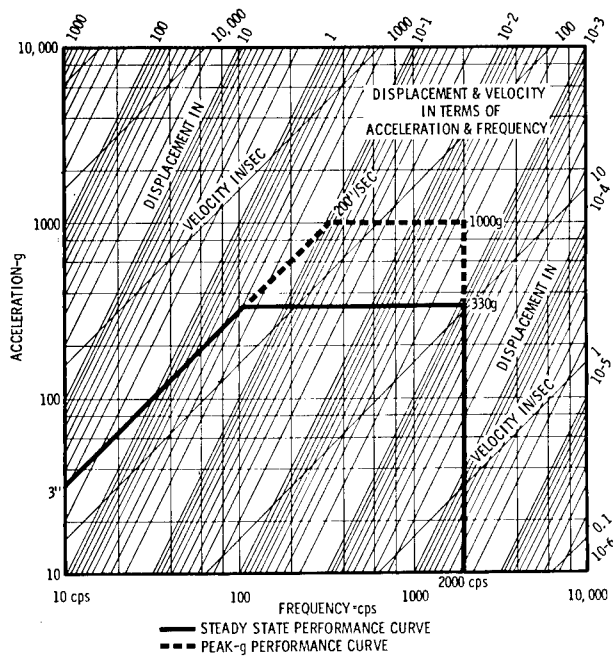**STEADY STATE PERFORMANCE CURVE**
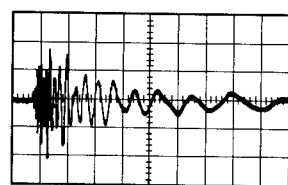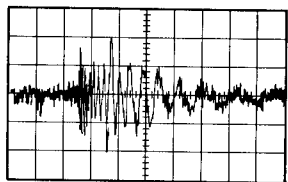
PEAK-g PERFORMANCE CURVE

Fig. 10. Performance curve of shaker capable of simulating pyrotechnic events. Shaker would be capable of generating energy necessary for simulating shock spectrum of 3000 response g.

170

Prior to Random Test
500 mv/div
10 ms/div

Fig. 11. Amplitude/
time trace of shock,
synthesized on electro-
dynamic shaker with
and without 10 g rms
random vibration

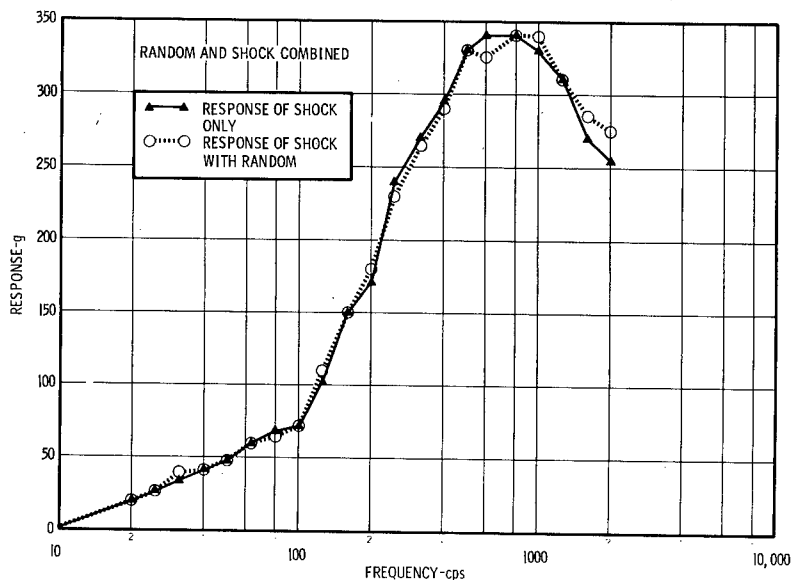During Random Test
500 mv/div
10 ms/div

Fig. 12. Response spectra of synthesized
shock motion samples of Fig. 11

as the basis for quantitative description in establishment of design criteria and test specification. It is now practical to use shock spectra for quantitative descriptions.

A return to the original reed gage philosophy is recommended, not only in describing the actual shock environment, but also in monitoring its simulation during all types of aerospace shock testing.

ACKNOWLEDGMENT

REFERENCES

1. C. M. Harris and C. E. Crede, Shock and Vibration Handbook (McGraw-Hill, New York), 1961

2. Irwin Vigness, "Elementary Considerations of Shock Spectra," Shock and Vibration Bull. No. 34, Part 3, pp. 211-222, Dec. 1964

3. G. W. Painter and J. H. Parry, "Simulating Flight Environment Shock on an Electrodynamic Shaker," Shock and Vibration Bull. No. 33, Part 3, pp. 85-96, March 1964

4. E. H. Schell, "Spectral Characteristics of Some Practical Variations in the Half-Sine and Saw-Tooth Pulses," Shock and Vibration Bull. No. 34, Part 3, pp. 223-251, Dec. 1964

5. W. R. Miller, "Shaping Shock Acceleration Waveforms for Optimum Electrodynamic Shaper Performance," Shock and Vibration Bull. No. 34, Part 3, pp. 345-354, Dec. 1964

6. R. Lowe and R. D. Cavanaugh, "Correlation of Shock Spectra and Pulse Shape with Shock Environment," J. Inst. Environ. Eng. 1(1): 24-28 (Feb. 1959)

7. V. R. Paul, "Mechanical Shock from Frangible Joints," Shock and Vibration Bull. No. 33, Part 4, pp. 63-71, March 1964

8. G. W. Painter and H. J. Parry, "A Continuous Frequency Constant Q Shock Spectrum Analyzer," Shock and Vibration Bull. No. 35, Part 4, 1966

9. G. W. Painter, "Use of Miniature Force Transducers in the Measurement of Shock and Vibration Environments," Shock and Vibration Bull. No. 34, Part 4, pp. 45-53, Feb. 1965

DISCUSSION

Dr. Morrow (Aerospace Corp.): The basic problem concerning you today is the same as was dominant in my mind in 1955 when I took part in writing a specification in terms of a shock spectrum. I did not have very strong feelings as to what sort of a pulse was used in the test laboratory, but I have seen some of the results of the widely prevailing practice of trying to match a complex wave with a half-sine wave by trying to superpose them without any deeper examination of damage potential. It seemed to me that we needed something better than this. The sort of thing that you are doing now, this deviation from the standard shock pulses, does look like something that is well worth exploring a good deal more. Did you have any difficulty maintaining a reasonably smooth spectrum? Are any nulls generated that are bothersome or does it generally work out without too much difficulty?

Mr. Rouchon: We do have difficulty. After we pass 1000 cps, we get into the area where things start moving quite easily. It is a matter of sufficient equalization. With Mr. Painter's analyzer, we analyze every third octave. It is a continuous frequency analyzer so we can analyze any points in between.

Dr. Morrow: This is a matter of equalization of the shaker, not a synthesis of the waveform you are to apply?

Mr. Rouchon: That is right.

*   *   *

SPECIFICATION OF ACCELERATION PULSES

FOR SHOCK TESTS

Irwin Vigness
U.S. Naval Research Laboratory
Washington, D.C.

Descriptions are given of methods by which acceleration pulses used for shock testing can be described and have their tolerances specified. Illustrations are given of measured acceleration pulses obtained from usual shock machines to illustrate differences between generated and specified shock pulse motions. From these differences it is possible to estimate what tolerances are reasonable at this time.

INTRODUCTION

When the principal purpose of a shock test is to require that an equipment be of some standard robustness or when the future environment of the equipment can only be expressed in general terms, the shock test is often specified in terms of an acceleration pulse.

An acceleration pulse, or shock pulse, consists of an excitation involving a unidirectional acceleration of relatively large magnitude applied over a relatively short time. Acceleration values are zero, or relatively small, before and after the pulse interval.

A shock pulse can be precisely described by a graphical representation of the acceleration as a function of time, by its mathematical equation, or by giving its Fourier spectra (two spectra required for a complete description). Shock spectra can be used for additional descriptions. Important characteristics of a pulse can be described by such factors as its duration, area, rise time, drop-off time, magnitude, and superimposed characteristic frequencies.

If a pulse has high frequency oscillations superimposed upon it, the "smoothed" or "faired" pulse should be used to describe the shape of the fundamental pulse. The faired pulse is the pulse obtained by sketching a line through the centerline of the high-frequency components.

The contents of this paper are limited to descriptions of pulse shapes commonly specified for shock tests, and to methods by which pulse characteristics and their tolerances can be described. In addition, a group of illustrations is given which illustrates the shapes of measured pulses. These demonstrate differences between a pulse of ideal (specified), and the shapes of corresponding pulses which are generated by shock machines.

PULSE DESCRIPTION BY CHARACTERISTIC VALUES

Characteristic values useful for providing a description of a pulse in terms of a few numerical values are illustrated in Fig. 1. For pulses of less than a few milliseconds duration it may be adequate to describe the pulse by giving only the maximum magnitude, the maximum faired magnitude, the duration, and the velocity change (area under curve). If more detail is desired, rise time, drop-off time, and superimposed oscillations may be added. While the velocity change can be measured by many methods, it is usually most convenient to determine its value by graphical integration of the area under the acceleration pulse. This is illustrated in a later section.

PULSE DESCRIPTION BY NOMINAL VALUES

When a measured pulse does not differ from an ideal pulse by more than prescribed values (tolerances), the measured pulse is sufficiently like the ideal pulse to be considered equivalent. The values which describe the ideal pulse will then be nominal values for the measured pulse.
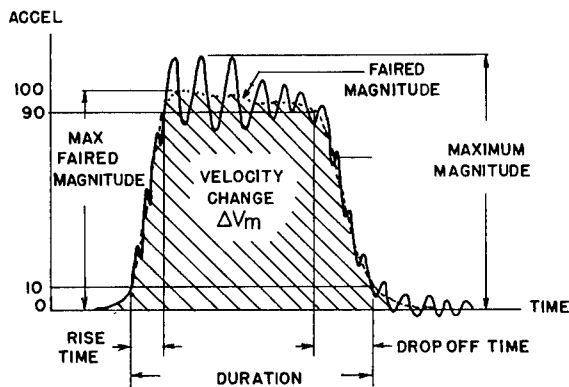
Fig. 1. Acceleration pulse on which terms descriptive of the pulse are illustrated. Rise time, in this case, is taken as time for faired pulse magnitude to go from 10 to 90 percent of maximum value. Similarly, drop-off time is time taken for faired pulse magnitude to drop from 90 to 10 percent of maximum value. The pulse duration, in this case, is time between initial and final 10 percent magnitude points. (See Appendix for more general definitions.) The area under either faired or unfaired curve is equal to velocity change, ΔV_m, where m indicates that velocity change is for a measured pulse. For an ideal or theoretical pulse, the subscript i is used. (Patterned after figure in Sandia Corp. Rept. SC-4452C(M), July 1964.)

The tolerances permissible are a matter of individual judgment and practicality. Hence, they are subject to change according to the situation and state of the art of shock machines.

However, standards for general present-day conditions are desirable and some proposals* as to how these tolerances should be given are illustrated in Figs. 2 through 8. It is probable that the numerical values involved will be subject to considerable change. However, this method of specifying tolerances, and of expressing the nominal characteristic values of a measured shock pulse as those of the equivalent ideal pulse, will probably become more widely used.

The sloping terminal-peak sawtooth pulse (Fig. 6) and the sloping-end trapezoidal pulses (Fig. 8) are included because a study of practically obtainable waveforms indicated that these slopes represented an average of what present-day machines deliver. The author prefers the pulses with the vertical ends (Figs. 5 and 7) as they presumably are what are being strived for.

VELOCITY-CHANGE REQUIREMENT

The velocity change associated with a shock pulse is an important damage parameter. It is also relatively easy to measure and to control with reasonable accuracy. With tolerance limits defined by envelopes as shown in Figs. 2 through 8, it is possible, with the values given, to have

*MIL-STD-202, method 213, the International Electrotechnical Commission, and a NATO committee are considering shock pulse specification in these manners. A similar approach is included in MIL-STD-810.
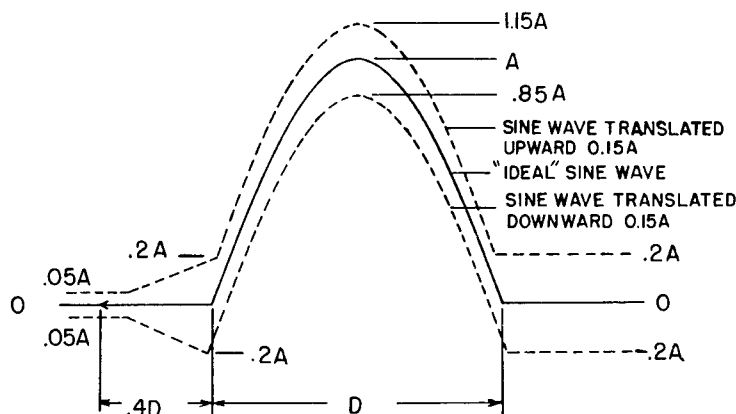

Fig. 2. Half-sine acceleration pulse with tolerance envelopes. Amplitude of pulse is A and duration is D. Velocity change associated with pulse is $\Delta V_i = 0.636DA$ (D expressed in seconds and A as acceleration). ΔV_m (measured) must be equal to $\Delta V_i \pm 10$ percent. Tolerances proposed for a revision of MIL-STD-202, method 213.
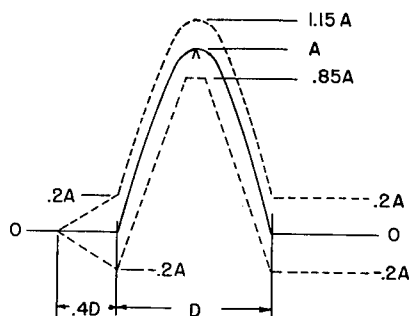
174

Fig. 3. Half-sine acceleration pulse with tolerance envelopes. Velocity change associated with pulse is $\Delta V_i = 0.636DA$ (D expressed in seconds and A as acceleration). ΔV_m (measured) must be equal to $\Delta V_i \pm 10$ percent. Tolerances proposed by IEC/50A/WG1.
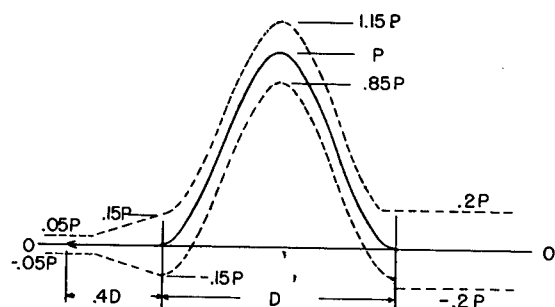

Fig. 4. Versed-sine, or haversine, acceleration pulse with tolerance envelopes. Maximum value is P and duration is D. Tolerance curves are obtained by translating the versed-sine curve upward and downward a distance of 0.15P. Velocity change associated with pulse is $\Delta V_i = 0.5DP$ (D expressed in seconds and P as acceleration).

Fig. 5. Terminal-peak sawtooth acceleration pulse with tolerance envelopes. Maximum value is P and duration is D. Velocity change associated with pulse is $\Delta V_i = 0.5DP$ (D expressed in seconds and P as acceleration). ΔV_m (measured) must be equal to $\Delta V_i \pm 10$ percent.

Fig. 6. Sloping terminal-peak sawtooth acceleration pulse with tolerance envelopes. Maximum value is P and duration is D. Peak values of pulse and tolerance envelopes are 0.1D from end of pulse. Velocity change associated with pulse is $\Delta V_i = 0.5DP$ (D expressed in seconds and P as acceleration). ΔV_m (measured) must be equal to $\Delta V_i \pm 10$ percent.

a velocity change associated with the area between the upper limit and the zero g axis which is over 50 percent greater than that associated area between the lower limit and the zero g axis. This large value is undesirable and could be taken advantage of by those who could control their shock pulse shapes with good accuracy. As the velocity change is relatively easy to control and measure, it is usually thought advisable to require the actual velocity change associated with the measured pulse to be not different from the nominal value by more than a given amount (on the order of 10 percent).
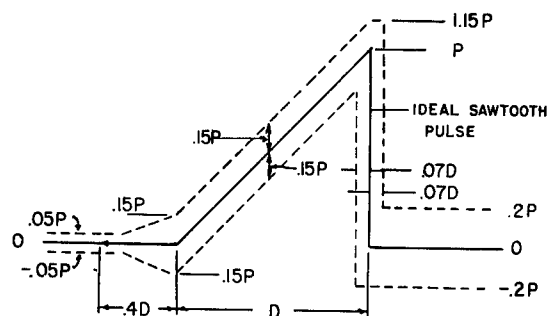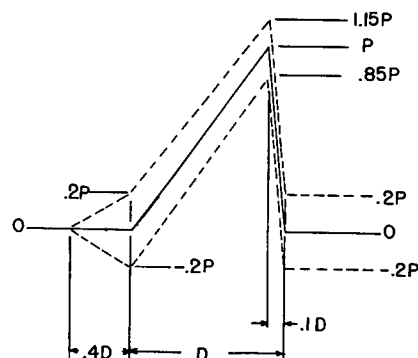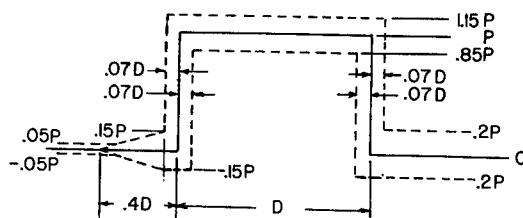

Fig. 7. Rectangular acceleration pulse with tolerance envelopes. Maximum value is P and duration is D. Velocity change associated with pulse is $\Delta V_i = DP$ (D expressed in seconds and P as acceleration).
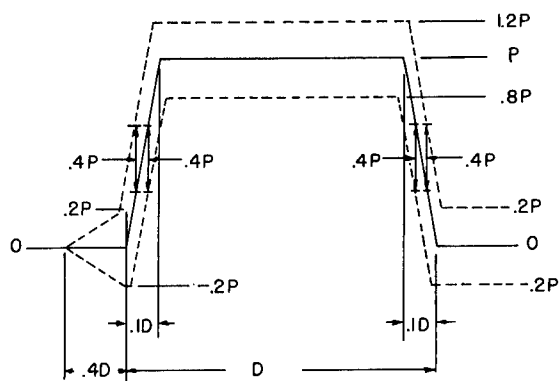
175

Fig. 8. Trapezoidal acceleration pulse with tolerance envelopes. Maximum value is P and duration is D. Velocity change associated with pulse is ΔV_i = 0.9DP (D expressed in seconds and P as acceleration).

If an acceleration record of the pulse has been obtained, the velocity change can be determined from the area under the pulse. The following is an example of graphically integrating the area under the pulse.

The area under the pulse, as shown in Fig. 9, is divided into 5 rectangular and triangular areas. Areas 1 through 5 are, respectively, equal to $0.002 \times 5g/2$, $0.004 \times 45g/2$, $0.004 \times 5g$, $0.002 \times 51g$, and $0.0054 \times 51g/2$. Their sum is equal to 0.355 g, or 11.4 fps. The velocity associated with an "ideal" sine pulse of 11 ms duration and 50 g amplitude is 11.3 fps. It will be observed that the velocity change determined from the measured pulse will be within a few percent of the nominal value if the pulse can be contained within the tolerance envelopes.

The measured pulse of Fig. 9 has been retraced in Fig. 10 to illustrate how it fits within
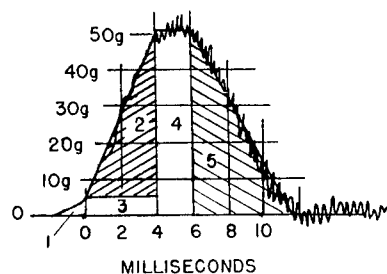

Fig. 9. Graphical determination of pulse area. Pulse area is approximated by sum of five triangular and rectangular sections.

the tolerance limits of Fig. 2. As the fit is acceptable, the pulse can be considered a nominal half-sine pulse having a nominal amplitude of 50 g and a nominal duration of 11 ms.
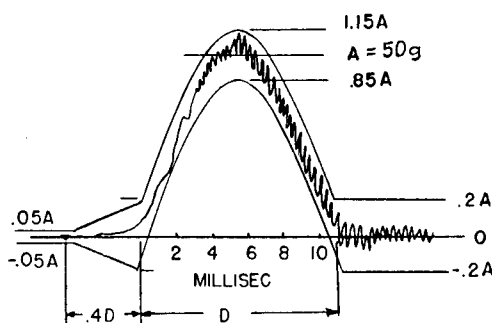

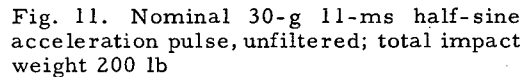Fig. 10. Pulse of Fig. 9 contained within the tolerance limits of 50-g 11-ms half-sine acceleration pulse

COLLECTION OF MEASURED SHOCK PULSES FOR DETERMINATION OF PRACTICAL TOLERANCE LIMITS
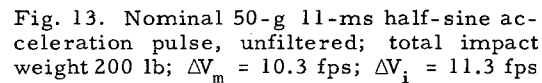
Measured Shock Pulses

In requesting the illustrations of shock pulses from various laboratories, it was asked that they represent normal laboratory procedures, and that no effort be taken to obtain pulses other than those usually obtained during routine test procedures. In addition, as it was merely desired to illustrate the average state of the art at good laboratories and not to provide comparisons of different types of machines or techniques, no identification is made as to the machine type or laboratory source of the illustrations. They merely illustrate typical shapes for shock pulse excitation as obtained by good laboratories at this time.

The overall instrumentation response for all unfiltered records was essentially flat for frequencies between several cycles per second and about 10 times the reciprocal of the pulse duration. For long-duration pulses (10 ms) this factor might extend to 50 times and for very short-duration pulses (0.1 ms) the factor might be 5. For many records, the frequencies of the high frequency components were so high that they could be largely eliminated by instrumentation. This elimination would be regarded as acceptable; i.e., their overall response would meet the above requirements.
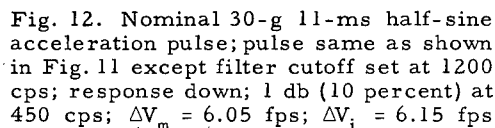
The curves in Figs. 10 through 27 illustrate that experienced personnel in laboratories with

176

Fig. 11. Nominal 30-g 11-ms half-sine
acceleration pulse, unfiltered; total impact
weight 200 lb

good facilities can comply with the tolerance
limits given, although in many cases some
extra effort would be required.

It also appears that a 10 percent tolerance
for velocity change, as compared with the nomi-
nal (ideal) value, is easily complied with. Pres-
ent skills are such as to cause the measured
acceleration curve to approach both upper and
lower tolerances, thus forcing the average to be
near that of the ideal acceleration curve. Unless
present skills improve, or unless some filtration
is used, it may be unnecessary to require the
velocity tolerance when the shape tolerances
are as given. Of course, if the shape tolerances
were increased, the velocity tolerance would
again be important.

Fig. 12. Nominal 30-g 11-ms half-sine
acceleration pulse; pulse same as shown
in Fig. 11 except filter cutoff set at 1200
cps; response down; 1 db (10 percent) at
450 cps; ΔV_m = 6.05 fps; ΔV_i = 6.15 fps

As pulse durations become very short, the
velocity change, or impulse, becomes increas-
ingly important as compared to factors related
to the shape of the pulse. While it can be seen
(Fig. 24) that it is possible to generate accept-
able pulse shapes down to about 0.1 ms duration,
it is doubtful that much effort is warranted to
require that the pulse shape be closely defined.
It is therefore suggested that for pulses of less
than a few milliseconds duration, the pulse can

Fig. 13. Nominal 50-g 11-ms half-sine ac-
celeration pulse, unfiltered; total impact
weight 200 lb; ΔV_m = 10.3 fps; ΔV_i = 11.3 fps

be adequately specified in terms of its maximum
magnitude, its maximum faired magnitude, its
duration, and its associated velocity change.

It may happen that the faired, or filtered,
pulse will comply with the tolerances, whereas
the unfiltered pulse (Figs. 13, 16, 19, 20, and
26) will not. Under such circumstances, the
damage potential of the pulse will be greater
than that of the specified pulse. If it should be
difficult to clean up the pulse, and if the test
item survives the test in an acceptable manner,
then it should be considered that the item has
qualified under the terms of the test as speci-
fied. Of course, if the item does not pass the
test the vendor has a legitimate complaint.

Some experimentation may be required with
the test setup to make adjustments so that the
test machine will deliver an acceptably shaped
shock pulse. It may not be desirable to have
the test load on the machine during this adjust-
ment period. It is suggested, therefore, that
either a dynamically equivalent load, or a rigid
load having the same center-of-mass location,
be permitted to be used instead of the test load.
The mounting methods should be equivalent in
the two cases. After test machine operating
procedures have been adjusted to give satisfac-
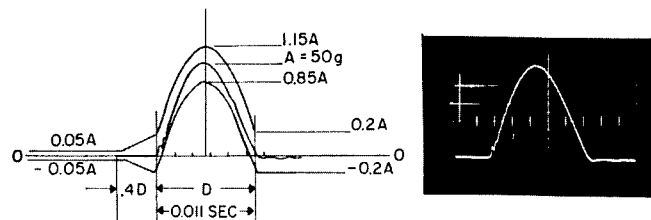tory excitation with the equivalent or rigid load,

177

Fig. 14. Nominal 50-g 11-ms half-sine acceleration pulse; pulse same as shown in Fig. 13 except filtered with filter cutoff set at 1200 cps; response down 1 db (10 percent) at 450 cps; ΔV_m = 10.3 fps; ΔV_i = 11.3 fps
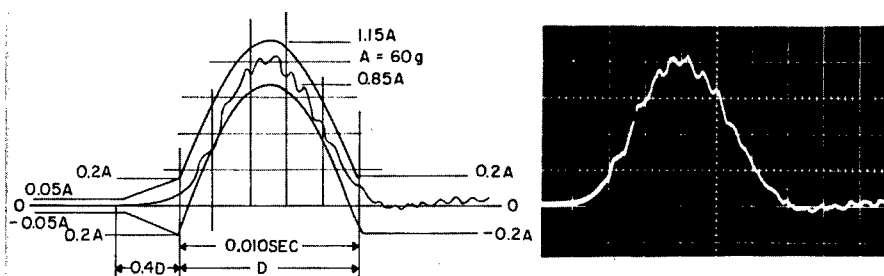

Fig. 15. Nominal 60-g 10-ms half-sine acceleration pulse, unfiltered; total impact weight 230 lb; ΔV_m = 11.9 fps; ΔV_i = 12.3 fps
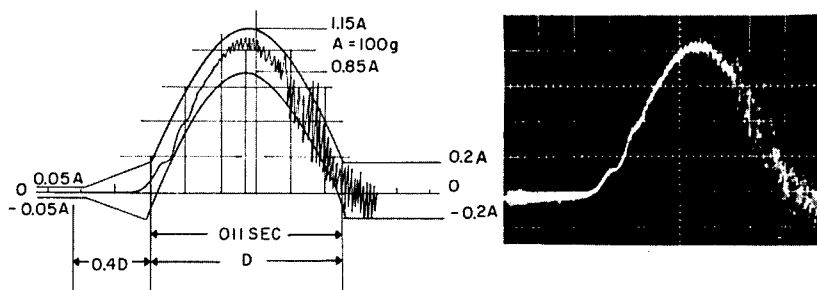

Fig. 16. Nominal 100-g 11-ms half-sine acceleration pulse, unfiltered; total impact weight 240 lb; ΔV_m = 24 fps; ΔV_i = 22.5 fps
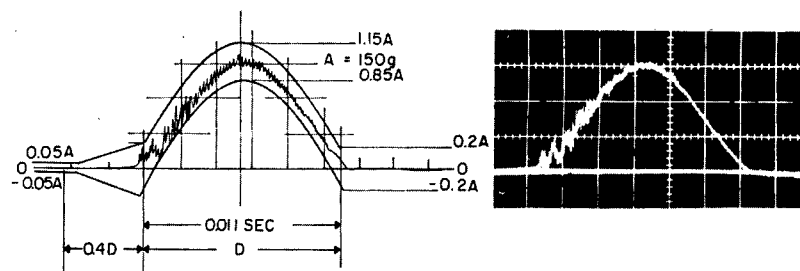

Fig. 17. Nominal 150-g 11-ms unfiltered pulse; total impact weight 330 lb; ΔV_m = 34.1 fps; ΔV_i = 33.8 fps
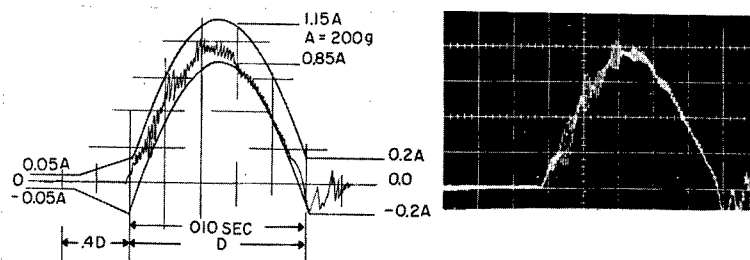
Fig. 18. Nominal 200-g 10-ms unfiltered pulse; total impact weight 400 lb; ΔV_m = 39.6 fps; ΔV_i = 41.0 fps
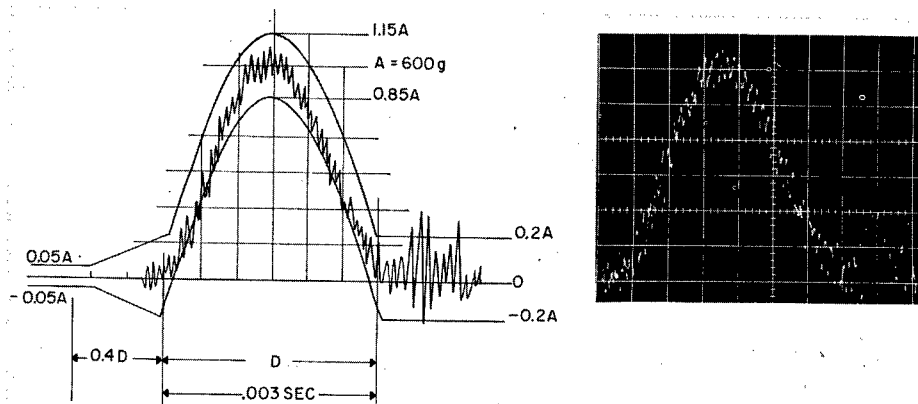

Fig. 19. Nominal 600-g 3-ms unfiltered pulse; total impact weight 240 lb; ΔV_m = 33.6 fps; ΔV_i = 36.9 fps
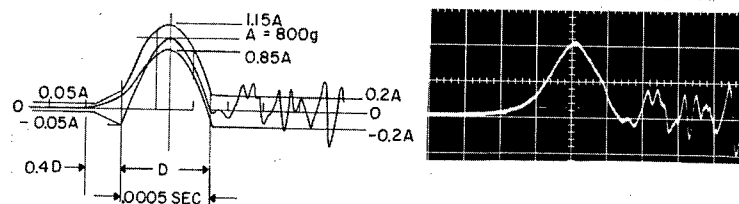

Fig. 20. Nominal 800-g 0.5-ms unfiltered pulse; total impact weight 240 lb; ΔV_m = 7.8 fps; ΔV_i = 8.2 fps
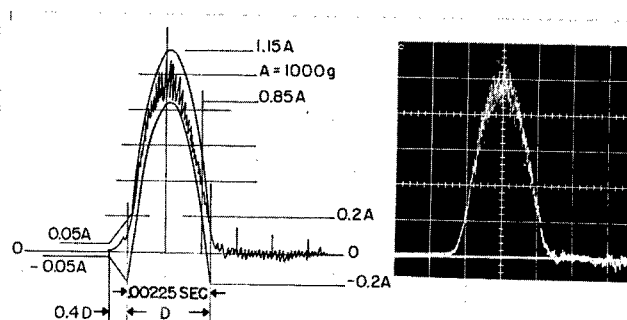

Fig. 21. Nominal 1000-g 2.25-ms unfiltered pulse; total impact weight 91 lb; ΔV_m = 48.3 fps; ΔV_i = 46.1 fps
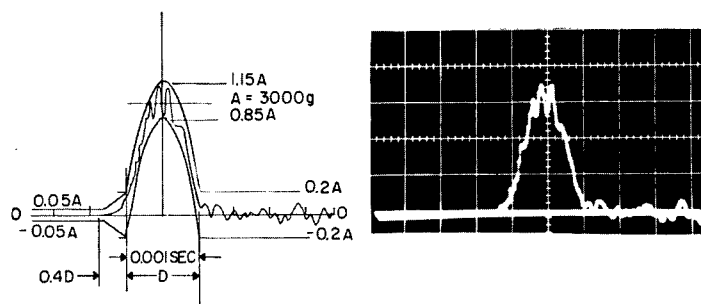
179

Fig. 22. Nominal 3000-g 1-ms unfiltered pulse; total impact weight 89 lb; ΔV_m = 64.7 fps; ΔV_i = 61.4 fps
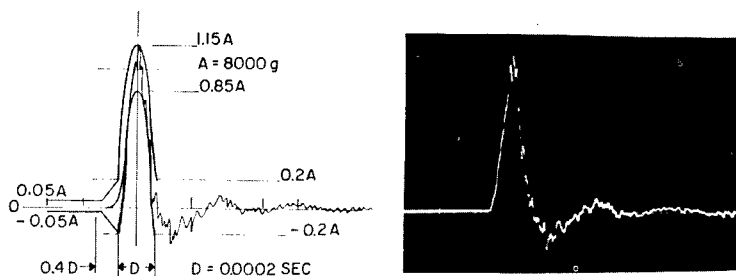
Fig. 23. Nominal 8000-g 0.2-ms unfiltered pulse; total impact weight 13 lb; ΔV_m = 29.5 fps; ΔV_i = 32.8 fps. Triangular pulse was requested and measured pulse fits symmetrical triangle better than half-sine.
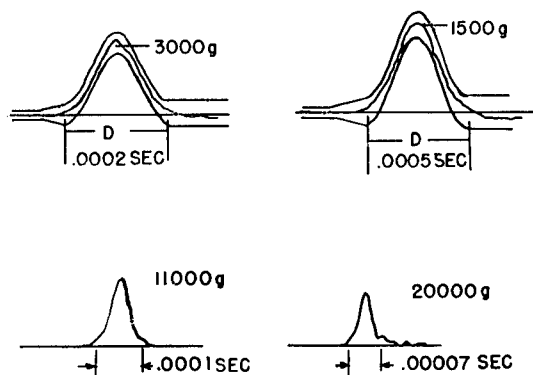
Fig. 24. Pulses from small machine which might be used for testing semiconductor devices. Accelerometer provided a load similar to semiconductor. Pulses fit a versed-sine curve better than half-sine, but either would be acceptable.

this same operating procedure will be considered to provide an acceptable test for the test item. It is not implied that the waveform generated by the test machine will not have changed; it is suggested that the test has been satisfactorily performed and that further consideration of the waveform is unnecessary.

ACKNOWLEDGMENTS

180
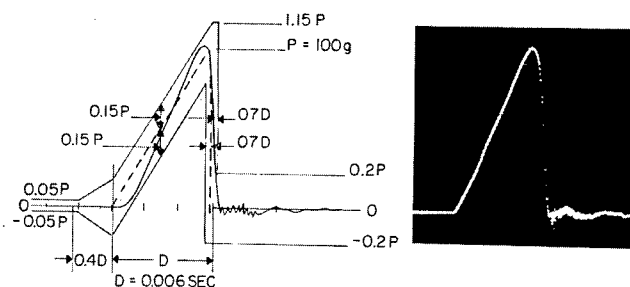
Fig. 25. Nominal 100-g 6-ms terminal-peak sawtooth pulse, unfiltered; total impact weight 98 lb; ΔV_m = 10 fps; ΔV_i = 9.66 fps
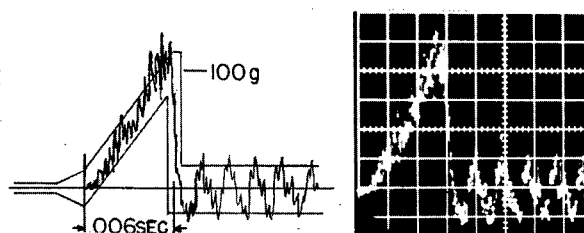
Fig. 26. Nominal 100-g 3-ms terminal-peak sawtooth pulse, unfiltered; total impact weight 375 lb
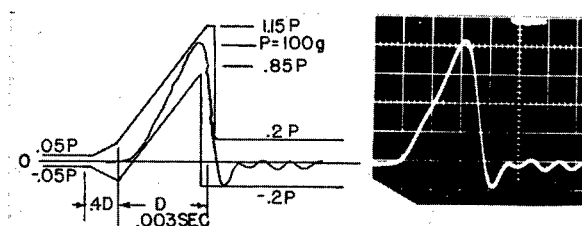
Fig. 27. Conditions same as for Fig. 25, except 0.2- to 800-cps filter used

Appendix

DEFINITIONS

The following definitions are taken from a draft proposal being assembled by the International Standards Organization.

Shock Pulse. A shock pulse is a form of shock excitation characterized by a rise and decay of acceleration in a relatively short period of time.

Ideal Shock Pulse. An ideal shock pulse is a pulse that is described exactly, usually by a simple mathematical description, i.e., half-sine pulse, a sawtooth pulse.

Measured Shock Pulse. A measured shock pulse is a representation of a measured shock motion.

Duration of Shock Pulse. The duration of a shock pulse is the interval between the time the acceleration rises above some stated fraction of the maximum value to when it decays to this value.

181

Note 1: This definition is limited to pulses of simple shape.

Note 2: For an ideal shock pulse the "stated fraction" would be taken as zero.

Duration of Ideal Shock Pulse. The duration of an ideal shock pulse is equal to the length of time over which the pulse is active.

Rise Time (Pulse Rise Time). The rise time is the interval of time required for the leading edge of a curve representing a function of time to rise from some specified small fraction to some specified large fraction of the maximum value.

Pulse Drop-Off Time (Pulse Drop Time). The pulse drop time is the interval of time for the trailing edge of a pulse to drop from some specified large fraction of the maximum value to some specified small fraction of the maximum value.

Nominal Shock Pulse (Nominal Pulse). A nominal shock pulse is descriptive of a measured shock pulse which does not differ from an ideal pulse by more than a specified amount.

Note 1: Nominal shock pulse is a generic term. It requires an additional modifier to make its meaning specific, i.e., nominal half-sine shock pulse or nominal sawtooth shock pulse.

Note 2: The tolerances of the nominal pulse from the ideal may be expressed in terms of pulse shapes (including area), or corresponding spectra.

Nominal Values of Shock Pulses. The nominal values of a measured shock pulse are the values descriptive of an ideal pulse (half-sine, sawtooth, etc.) from which the measured pulse does not differ by more than a specified amount.

Note: Spectra are included among the values descriptive of shock pulses.

Nominal Duration of Shock Pulse. The nominal duration of a measured shock pulse is equal to the duration of an ideal shock pulse which does not differ from the given pulse by more than specified amounts. See Duration of Shock Pulse.

Faired Curve (Smoothed Curve). A faired curve contains only the low-frequency components of a curve that has high-frequency components superimposed upon it.

Amplitude. Amplitude is the maximum value of a simple harmonic quantity.

Note: In vibration theory the use of "amplitude," for purposes other than to describe the maximum value of a sinusoid, is deprecated.

Instantaneous Value (Instantaneous Magnitude, Value, Magnitude). The instantaneous value of a variable quantity is the value of the quantity at a given instant.

Note: The modifier "instantaneous" is omitted if the meaning is apparent.

Peak Value (Peak Magnitude, Maximum Magnitude), Positive Peak Value, Negative Peak Value. A peak value is the maximum of the values of a quantity during a given interval.

Note: A peak value of an oscillating quantity is usually taken as the maximum deviation of that quantity from the mean value. A positive peak value is the maximum positive deviation and a negative peak value is the maximum negative deviation.

DISCUSSION

Mr. Bort (David Taylor Model Basin): I presume there are frequency response requirements on the instrumentation and on any filters used, because some of the hashy pulses could be smoothed off beautifully by running them through the proper filter.

Dr. Vigness: For all of these pulses, filtration was practically nonexistent. For the last pulses shown, the pass was up to about 100

kc, so if there had been any hash it would have been recorded. In the specifications which may use some of these pulse shapes, there are additional requirements for accuracy of the instrumentation and the frequency range required. That would be covered in a general specification.

Mr. Bresk (Monterey Research Lab.): Would you comment on which specifications will be changed to incorporate these

modifications and when the changes will be made?

Dr. Vigness: You are asking me something with which I have nothing to do directly. I merely talk with the people responsible for making these specifications. I believe, however, both MIL-STD-810 and MIL-STD-202 will be modified somewhat in the not too distant future. Within the last week, the International Electrotechnical Commission, which is standardizing shock specifications internationally, has agreed to include the same approach. It will not include everything we have here, but will include some things we do not have. It will use the half-sine pulse, the rectangular pulse and the terminal-peak pulse.

Mr. Painter (Lockheed-California Co.): I have a comment that relates to both Mr. Rouchon's paper and this one. It might be assumed that the complex transient synthesis method of which Mr. Rouchon spoke is confined to the simulation of the rather jagged spectra that are characteristic of aerospace vehicles. But, if one desired to do so, he could very readily simulate the response spectrum of any of these classical pulses. I believe that this could be done with a considerably closer approximation to the theoretical spectrum of an idealized pulse and, possibly, to the variations shown in the slides. I might add that the ringing phenomena that were shown can be virtually removed in the synthesis procedure simply by putting a deep notch at that particular frequency in the synthesizing filters.

Dr. Morrow (Aerospace Corp.): Whether the infinite Q shock spectrum exaggerates the damage potential, I think, depends on whether we are trying to use the shock spectrum as a way of standardizing a pulse or as a basis for design. For example, if we have the same pulse it does not make too much difference whether we use a spectrum with a Q of 3 or an infinite Q spectrum. I prefer the infinite Q spectrum, but it is the same pulse, so obviously the test is not made too severe. On the other hand, if the designer is going to take the infinite Q spectrum as a direct estimate of what happens inside, it is clear that with a large amount of damping this might be reduced. There are ways of estimating this, so I am not too concerned. I did want to point out one feature of the shock spectrum which I rather like in comparison with this method of doing it. I think these tolerances that you worked out are very valuable to have and I do not know for sure what else you can do when working with pulses. However, if the specification writer writes his tolerances in this way, he is putting a good deal of emphasis on insuring that the pulse is not too severe rather than that it is severe enough. I think insuring that the pulse is severe enough is the primary job of the specification writer. After all, if somebody tests something to twice the shock pulse and it passes, he is not going to ask for a rejection. If you have a shock spectrum to a first approximation, you can say that if you increase the level the shock is worse. If you set a lower limit on the shock spectrum, then the specification writer has done his primary duty. I think quite a bit of effort would be saved if we let the designer and the people subject to the specification worry about just how severe they are willing to let it go above that required by the specification.

Dr. Vigness: I really was not opposing the use of shock spectra as a specification means, but there is a practical consideration to take into account here. There are many laboratories throughout the United States and the world that are going to use these techniques. It is not easy to obtain shock spectra from the measured values so, from a practical point of view, I do not think we are quite ready to require a lot of small laboratories in various places to determine the shock spectrum of the shock pulse.

Dr. Mains (Washington Univ.): One very important field in which the Q used in determining the shock spectrum is earthquake spectrum analysis. The difference between the Q you usually get in a building, down around 1, 2, or 3, and an infinite Q is significant there.

*   *   *

SHOCK TESTING TO SHOCK SPECTRA SPECIFICATIONS

S. M. Ostergren
General Electric Company
Re-entry Systems Department
Philadelphia, Pennsylvania

Shock test requirements are appearing more consistently in specifications in the form of a shock spectrum rather than a shock pulse. A shock pulse is described by a g level, pulse duration and shape, with tolerances on these parameters. A spectrum typically has no tolerance placed on it and is presented graphically. The problems the test engineer is faced with in utilization of a shock spectrum are: (a) to determine which shock pulse will produce the required shock spectrum, and (b) to demonstrate that the test requirement has been met. The paper considers theoretical and empirical methods that the engineer can use to deal with these problems. Examples are given showing how the pulse height, duration, and waveform can be determined from a given shock spectrum.

The test method of demonstrating compliance to a shock spectrum is to measure reed gage responses to a shock pulse input. Consideration of weight and number of channels of instrumentation required using this approach make it uneconomical and impractical. It is more feasible to measure the pulse computed from the spectrum and then, using analytical calculations or comparison with known spectra and pulses, to deduce whether the test requirement has been met. In some cases a machine computation of the shock spectrum may be required. This is normally accomplished by establishing an analog or digital computer program.

INTRODUCTION

Shock test requirements are appearing more consistently in the form of a shock spectrum rather than a shock pulse. A shock pulse is described by a g level, pulse duration, and pulse shape, with tolerances on these parameters. A shock spectrum is typically presented graphically as a plot of g vs frequency and represents the response of single degree of freedom systems with different natural frequencies to shock pulse inputs. The problems that the test engineer is faced with in utilization of shock spectra to conduct shock tests are: (a) determining which shock pulse will produce the required shock spectrum, and (b) demonstrating that the test requirement has been met.

This paper discusses theoretical and empirical methods that the engineer can use to deal with these two problems.

CURRENT APPROACH

Current shock testing machines are usually designed to produce the desired shock pulses in one of two ways:

1. Impact on a specific shock pad or hydraulic spring, or

2. Pneumatic-type excitation of a piston created by the release of gas through an orifice.

The most common shock pulses, and the easiest to obtain, are the half-sine and the terminal-peak sawtooth pulses. Other pulses are, of course, possible to obtain, but they are much less frequently called for.

A typical tolerance on the shock pulse is ±10 percent on amplitude (general acceleration), ±10 percent on pulse duration, and stringent control of waveform. In some cases, the tolerances are even closer.

The production of a shock time history is directly related to the problem of accurately measuring shock motion. The overall bandwidth of the pickup and recording instrument has a significant effect on a shock pulse's time history. If, for instance, the frequency response of the measuring system is not low enough, general distortion of the pulse will

result. Conversely, if the frequency response of the measuring system is high, "hash" will result both during and after the pulse. Furthermore, there will be a corresponding increase in "hash" as the frequency response of the measuring systems becomes higher (Fig. 1).

ACTUAL
PULSE

TOO MUCH LOW
FREQUENCY FILTERED OUT
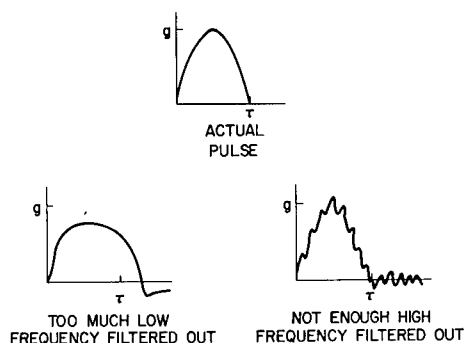
NOT ENOUGH HIGH
FREQUENCY FILTERED OUT

Fig. 1. Effect of filtering
on shock pulses

This high-frequency "hash" is usually not caused by the device producing the pulse; rather it is generated by the resonance of the shock table, fixtures and specimen. Therefore, we can reason that while "hash" is measured on a shock pulse, it is not the input to the specimen but an effect caused by the response of the system that produces it. Generally, a great deal of "hash" makes the curve unintelligible for visual examination. For this reason, a measuring system with unfiltered frequency response is seldom employed. A narrow bandwidth filter is preferable since it makes possible a clean pulse which we can observe, describe, compare, and measure and on which we can place tolerances.

SHOCK SPECTRUM

A shock pulse or transient disturbance results in motion that acts over a certain period of time. We will call this motion $x_i(t)$, the input acceleration, as shown in Fig. 2; it is a function of time.

When a shock pulse acts on a single degree of freedom system, it produces a response $x_r(t)$ in the system. This response is also a function of time (Fig. 2).

The information in the response x_r can be classified into four parts: primary, residual, maximum, and minimum. The primary information is the response information obtained
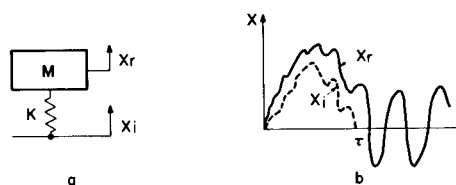

Fig. 2. Response of single
degree of freedom system

during the interval $0 < t < \tau$, that is, during the pulse. The residual information is the information obtained after the pulse has been completed. The residual response is always a sine wave with the frequency of the spring mass system and a specific constant maximum amplitude. The maximum response is equal to the maximum of either primary or residual response. The minimum response is equal to the negative of the residual response.

A shock spectrum is the response of several single degree of freedom systems having different natural frequencies. There are several types of shock spectra in general use.

Maximum Response Shock Spectrum

This is a plot of the maximum response of the single degree of freedom system as a function of frequency. It is the most commonly used spectrum, and when a shock spectrum is called for, it will be the presumed requirement unless the specifications state otherwise.

Residual Response Shock Spectrum

This is a plot of the maximum response of the single degree of freedom system after the pulse has been completed. It is of general interest since for some pulses it goes to zero at certain frequencies; that is, there is no "ringing" after the pulse at these frequencies.

Primary Response Shock Spectrum

A plot of the maximum response of the single degree of freedom system occurring during the pulse, this spectrum is usually, in itself, of minor interest.

Minimum Response Shock Spectrum

This plot of the minimum response of a single degree of freedom system is negative in

value and equal to the negative of the residual response shock spectrum.

CHARACTERISTICS OF SHOCK SPECTRA

The shock pulses most typically produced on shock machines are the half-sine, the terminal-peak sawtooth, triangular spike, and the square wave. The shock spectra of these pulses are shown in Fig. 3.
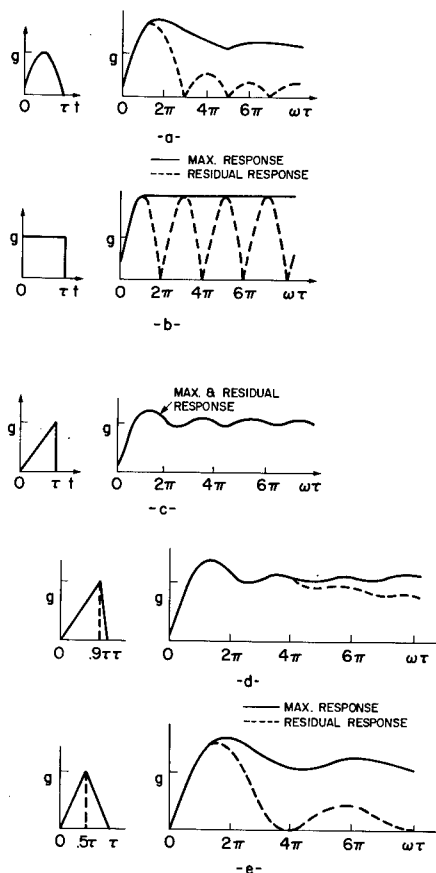
Fig. 3. Shock spectra for half-sine, square triangular and spike pulses

A number of important and pertinent observations can be made regarding the maximum response shock spectrum by studying these curves:

1. A shock spectrum is always zero at 0 cps;

2. It rises to a maximum level and never exceeds this level;

3. Within certain bounds, it then stays flat as the frequency increases; and

4. The pulse shape has comparatively little effect on the shape of the shock spectrum, as seen from Fig. 4.

Some characteristics of the residual response shock spectrum are also pertinent to the problem of shock testing. The residual response spectrum for both the half-sine pulse and the square pulse goes to zero at certain frequencies, indicating that there is no "ringing" after the pulse at these frequencies. By contrast, the residual response shock spectrum for the sawtooth shock pulse is the same as the maximum response shock spectrum and, therefore, produces a maximum amount of "ringing" at all frequencies. We also know the equation for the residual response shock spectrum and, therefore, the equation for the maximum response shock spectrum for the sawtooth pulse:

$$M(\omega) = g \left(1 + \frac{4}{(\omega\tau)^2} \sin^2 \frac{\omega\tau}{2} - \frac{2}{\omega\tau} \sin \omega\tau\right)^{1/2}.$$

This is the only pulse for which we know the equation for the maximum response shock spectrum.

SHOCK SPECTRA TEST SPECIFICATIONS

The problem we are faced with is to conduct a shock test once given a shock spectrum as a test requirement. Figure 5 shows four typical shock spectra that appear in our shock test specifications. Since we cannot control our shock spectra, we must determine which pulse will produce the desired spectra. This requires solving the Inverse Problem for the maximum response shock spectrum. This cannot be done rigorously, but good approximations can be obtained empirically. The shock pulse parameters we are looking for are g level, pulse duration and pulse shape. Figure 5 indicates that the first two of these spectra bear obvious resemblance to most maximum response shock spectra and that the second also calls for a minimum response spectra which we know to be equal to the residual response shock spectrum.

EMPIRICAL TECHNIQUE FOR SELECTING SHOCK PULSES

Since we cannot analytically solve the Inverse Problem for the maximum response shock spectrum, it is necessary to take an
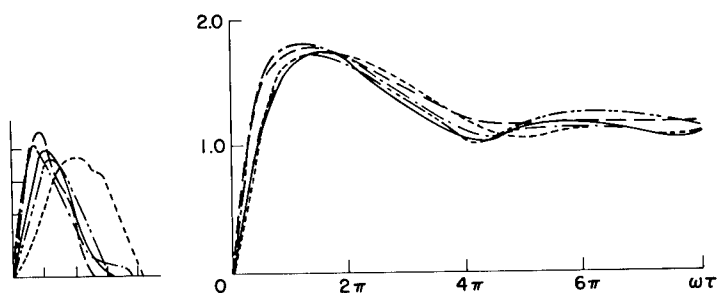
Fig. 4. Example of effect of variation in
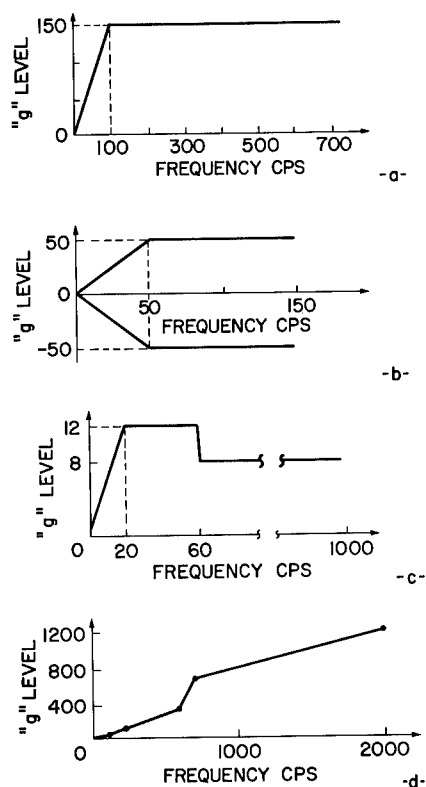pulse shape on shock spectra

Fig. 5. Typical shock
spectra specifications

of the maximum response shock spectrum. It
does, however, have a great effect on the shape
of the residual response shock spectrum.

The terminal-peak sawtooth pulse gives
the highest residual spectrum and we have
therefore selected it as a good shape on which
to standardize. However, since the rear portion
of the pulse is not vertical, we are confronted
with a very practical problem; i.e., an exact
sawtooth shock pulse cannot be obtained. There-
fore, the residual response shock spectrum will
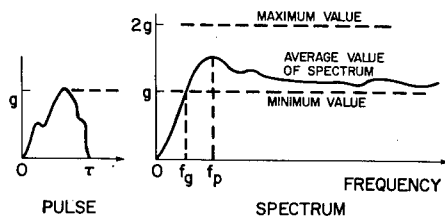be less than the maximum response shock
spectrum.

It is, however, well within the state of the
art to get a less than 10 percent decay in the
rear slope of the pulse, and it can be seen from
Fig. 5d that only at high frequency is the resid-
ual response spectrum lower than the maximum
response shock spectrum, and at less than 8
the drop is less than 25 percent. However, if
we have a 50 percent decay, the residual re-
sponse shock spectrum does go to zero at cer-
tain frequencies, as shown in Fig. 3e.

The half-sine pulse can be obtained on most
shock machines but the residual spectra goes to
zero and is generally low at all high frequencies.

g Level

From observing pulses and their spectra,
we can see that the amplitude of the pulse is at
least half the value of the highest point on the
spectrum and not more than the lowest point.
Those are the upper and lower bounds for all
pulses. We can see that the pulse amplitude is
about the same as the average value of the
spectrum (Fig. 6).

In general, if a pulse having an amplitude
greater than the average value of the maximum
response shock spectrum is selected, it will

empirical approach to the problem. By observ-
ing the shock pulses shown in Fig. 3 and by
studying the spectra in the appendices, the Shock
and Vibration Handbook and in other literature,
some general observations about the relation-
ship of shock spectra and certain properties of
shock pulses can be made.

Pulse Shape

We can see that the shape of a shock pulse
does not have a significant effect on the shape

188

$$\frac{1}{f_p} \geq \tau \geq \frac{1}{2f_p}$$

$$\frac{1}{2f_g} \leq \tau \leq \frac{1}{4f_g}$$

Fig. 6. Typical bounds for
shock spectra

produce a pulse with an average value greater than the specification calls for, except for some points on a sawtooth spectrum.

Pulse Duration

The object here is to determine the pulse duration once we are given a spectrum. When we inspect maximum response shock spectra, we can observe that they all start at zero, then rise to a level at which they remain relatively constant within certain bounds. The response frequency at which the spectrum reaches this level is related to the pulse duration by the approximate formula $1/f_p \geq \tau \geq 1/(2f_p)$, where f_p is the frequency at which the spectrum slope first reaches zero (Fig. 6). This approximation is good for shock machine pulses.

However, if a particular pulse shape is first chosen, the required pulse duration can be calculated more accurately from the point at which it first reaches the g level of the pulse,

$$\frac{1}{2f_g} \leq \tau \leq \frac{1}{4f_g}.$$

For example, for a perfect sawtooth pulse

$$\tau = \frac{1}{2.0f_g},$$

for a half-sine pulse

$$\tau = \frac{1}{4f_g},$$

and for a perfect rectangular pulse

$$\tau = \frac{1}{4f_g} = \frac{1}{2f_p}.$$

These relationships were all obtained by examining normalized pulses and spectra. Anyone can do the same thing and get similar results for different pulses.

EXAMPLES

Four shock spectra are shown in Fig. 5. These are typical of those presently appearing in our shock test specifications. Now we can calculate a shock pulse for each of these spectra and show how closely they can be approximated.

We can start with the specification in Fig. 5a. For pulse shape we select the terminal-peak sawtooth pulse. The amplitude of the pulse is the same as that of the spectrum, 100 g in this case. The specification and test shock spectra are shown in Fig. 7.
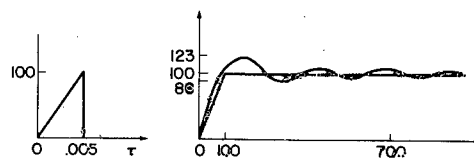

Fig. 7. Shock spectra and specification for 5-ms 100-g sawtooth pulse

Since the equation for the maximum response shock spectra of a terminal-peak sawtooth shock pulse is known to be

$$M(\omega) = g \left(1 + \frac{4}{(\omega\tau)^2} \sin^2 \omega\tau - \frac{2}{\omega\tau} \sin \omega\tau\right)^{1/2},$$

the frequency at which the spectrum first crosses the 100-g level can be calculated:

$$100 = 100 \left(1 + \frac{4}{(\omega\tau)^2} \sin^2 \frac{\omega\tau}{2} - \frac{2}{\omega\tau} \sin \omega\tau\right)^{1/2},$$

if $\omega\tau = 0, \pi, 2\pi$. Therefore, $\omega\tau = \pi$ at $f_g = 100$, and

$$\tau = \frac{\pi}{\omega} = \frac{\pi}{2\pi f_g} = \frac{1}{2f_g} = \frac{1}{2(100)} = 0.005 \text{ sec}.$$

The maximum and minimum values of the shock spectrum occur at $(3\pi)/2$ and $(5\pi)/2$, respectively, and are 120 and 88 g.

In this particular case, there was no tolerance on the shock spectrum and the type of shock spectrum was not defined. The normal

189

test procedure would be to place the specimen on a drop test shock machine with an impact device producing 5-ms sawtooth pulse and drop the table about 26 in. The 700-cps upper limit on the shock spectrum is taken to mean that information above this frequency is not of interest and should be filtered out. We would, therefore, want our measuring system to only pass data below 700 cps.

The specification shown in Fig. 5b is different in that it also shows a requirement on the negative shock spectrum. Since the negative shock spectrum is equal to the residual shock spectrum, we presume this to be a convenient way of placing a requirement on the residual spectrum. This requirement dictates that a terminal-peak sawtooth pulse must be used because its residual response shock spectrum is equal in magnitude to the maximum response shock spectrum. The pulse duration would be $\tau = 1/(2f_g) = 1/(2 \times 50) = 0.010$ sec or 10 ms. The equivalent drop height would be about 12.5 in. with the high-frequency filter set at 150 cps. The 150-cps high-frequency limit is typically low for shock measurement.

In practice, a perfect terminal-peak sawtooth shock pulse cannot be obtained, and there is no finite slope on the rear of the pulse (Fig. 8b). Typical tolerance on the rear slope of the pulse is 10 percent of τ, which is close, but feasible. Fortunately, this phenomenon does not cause the residual spectrum to go to zero at certain frequencies like the square pulse and half-sine pulse. In fact, this specification goes to 150 cps and the residual and maximum response shock spectra are very close in this region with the 10 percent of τ decay. It is not until 450 cps that the residual level is 25 percent below the maximum response level as shown in Fig. 8b.
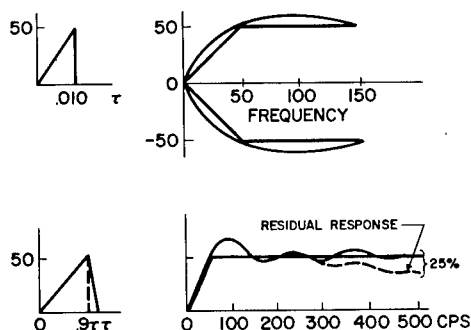

Fig. 8. Shock spectra and specification for 10-ms 50-g sawtooth pulse

The shock spectrum shown in Fig. 5c is a little unusual in that it has a stepdown at 60 cps. Shock spectra of pulses that can be produced on shock machines are flat within certain bounds. As we have observed before, however, a half-sine pulse produces a greater hump at its maximum level at f_p than the terminal-peak sawtooth pulse. To meet this specification we could use either of two shock pulses:

1. An 8-g 20-ms half-sine pulse (Fig. 9a), or

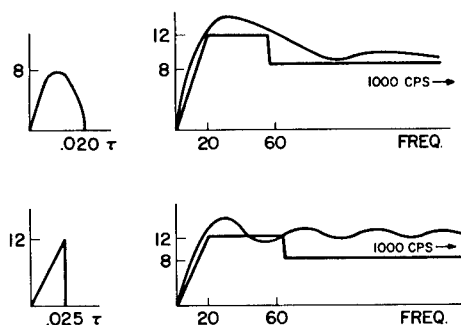2. A 12-g 25-ms terminal-peak sawtooth pulse (Fig. 9b).

Fig. 9. Shock spectra and specification that can be satisfied by two pulses

Since there is no specification on the residual spectrum in this case, we assume that we are at liberty to produce either shock pulse. The filters in the measuring system would be set to 1000 cps as indicated in the specification.

The last shock spectrum is shown in Fig. 5d. It, too, is unusual. It appears to have been taken from field data or perhaps a computation of a component environment. It is, in any case, different from the others, both in amplitude and frequency.

Using our standard technique, we select a 1200-g terminal-peak sawtooth pulse with a pulse duration of $\tau = [1/(2.0f_g)][1/(2.0 \times 2000)] = 0.00025$ sec or 0.25 ms. This we obtained by an approximately 2.8-in. drop height and a 2000-cps upper frequency on the measuring system. In practice, this pulse can only be obtained on a small shock machine because of the very short pulse duration.

It is difficult to produce this type of sawtooth pulse for two seemingly conflicting

190

reasons: (a) there is a high g level; and (b) the energy of the pulse, which is proportional to terminal velocity and drop height, is low as evidenced by the 2.8-in. drop height.

The pulse actually obtained is more closely described as a spike or triangular pulse. However, this is not really a problem since the shock spectrum will still meet the specifications as shown in Fig. 10b, only it will be somewhat higher. The maximum value will go to 1470 g at higher frequencies for the sawtooth pulse and 1750 g for the spike pulse.
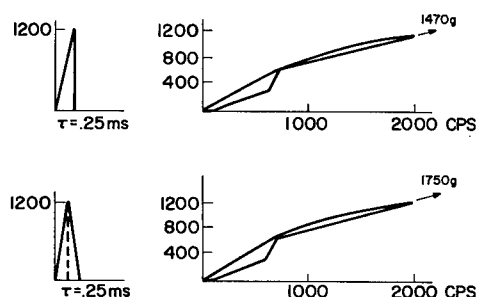

Fig. 10. Shock spectra and specification for 0.25-ms 1200-g pulse

DEMONSTRATING TEST COMPLIANCE

Having selected a shock pulse to perform a shock test, we must next demonstrate to a customer that the test requirements have indeed been met. There are basically three approaches we can use.

We can measure the shock spectrum directly with a reed gage which would consist of a series of cantilever beams with weights on them having different natural frequencies. This method is feasible, but undesirable for three reasons: (a) only a limited amount of data can be obtained, (b) an adequate reed gage would be heavy compared to the weight capabilities of most shock machines, and (c) it requires measuring many channels of information making the measuring system expensive.

We can record the pulse on magnetic tape and compute the spectrum on an analog or digital computer. This method is practical only if one has available a computer and programs. It

is used mostly in experimental work and for field data reduction.

Excellent use is, of course, made of computer analysis of field data to compute shock spectra, since field data are usually in the form of transient random vibration rather than a simple shock pulse.

We can record the pulse and then demonstrate that requirement has been met by the same logic that was used to determine the pulse, that the shock spectrum for the same pulse meets the requirement.

For most cases, especially quality control testing, the third method, which is simply to measure the pulse, appears to be the most realistic. In cases where a residual spectrum is called for, and it is difficult to get good pulse cutoff, it might be necessary to compute the spectrum.

SUMMARY AND CONCLUSION

Our studies indicate that testing to a shock spectrum is really not much different than testing to a shock pulse. However, it does have the decided advantage of allowing the test engineer more freedom in the conduct of his tests.

Most of what we have discussed is the application of known information to develop empirical techniques for finding pulses from shock spectra.

We are convinced that the basic technique, selecting a terminal-peak sawtooth pulse having an amplitude equal to the average maximum level of the shock spectrum, and then computing the pulse duration, filtering out the portion of the signal over the upper frequency limit of the shock spectrum, will enable us to fully satisfy the requirements of our customers.

One point of caution, however. The methods discussed here are applicable to shock testing because shock test machines limit us to shock pulses. There is no basis for applying these techniques to the reduction of field test data, since these are typically made up of transient vibrations.

191

BIBLIOGRAPHY

Barton, M. V., "Shock and Structural Response," ASME Colloquium, Nov. 1960

Barton, M. V., Y. C. Fung, and V. Chobotov, "A Collection of Information on Shock Spectrum of a Linear System," Space Technology Labs., Inc., EM 11-9, July 1961

Fung, Y. C. and M. V. Barton, "Some Characteristics and Uses of Shock Spectra,"Ramo-Wooldridge Corp., GM-TR-82, 15 Oct. 1956

Goldman, S., "Frequency Analysis, Modulation and Noise" (McGraw-Hill, New York), 1948

Harris, C. M. and C. E. Crede, "Shock and Vibration Handbook," Chap. 8, 23 (McGraw-Hill, New York), 1961

Jacobsen and Ayre, "Engineering Vibrations" (McGraw-Hill, New York), 1958

Lowe, R. and R. D. Cavanaugh, "Correlation of Shock Spectra and Pulse Shape With Shock Environment," Environ. Eng. (Feb. 1959)

Mains, R. M., "Structural Response to Dynamic Load," General Engineering Lab. Rept. No. 60GL228, 9 Dec. 1960

Mindlin, R. D., "Dynamics of Package Cushioning," Bell System Tech. J. (July-Oct. 1949)

Morrow, C. T., "The Shock Spectrum," Electrical Manufacturing (Aug. 1959)

Southworth, H., Jr., "Derivation of the Relationship Between the 'Residual' Shock Spectra and the Fourier Integral Spectra," Shock, Vibration and Associated Environments Bull. No. 29, Part IV, pp. 408-411, June 1961

Appendix A

SHOCK SPECTRA WITH PEAKS AND NOTCHES

Shock pulses produce shock spectrum that are flat within certain bounds in the high-frequency region. Testing to these shock pulses is the state of the art at the present time. It has been observed from field data that shock spectra have peaks and notches as roughly indicated in Fig. A-1. These phenomena would be associated with the mechanical impedance of the table of the shock machine and the filters employed in the measuring system.

The type of peak in a shock spectrum shown in Fig. A-2 could be caused by constant frequency lash or distortion of the shock pulse as shown in Fig. A-2. It is probable that this results from "ringing" of the fixture or shock table due to their resonant frequencies and high Q. This phenomenon would not normally be generated by the impacting device of most shock machines, but would get measured on the pulse.

The presence of a notch in a shock spectrum is called shock spectrum dip. It can be caused by the presence of a large resonant mass on the shock table as shown in Fig. A-3.

These phenomena are real and, since they exist, could theoretically be utilized to "shape" a shock spectrum for a test. However, at the present time, the techniques are best categorized as impractical and cumbersome.
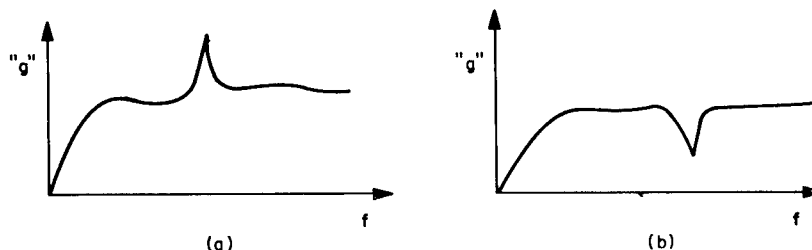

(a)   (b)

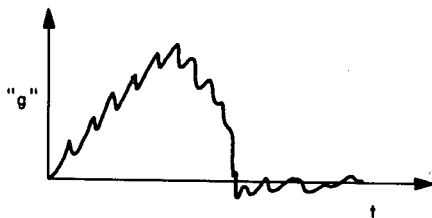Fig. A-1. Peaks and notches in shock spectra

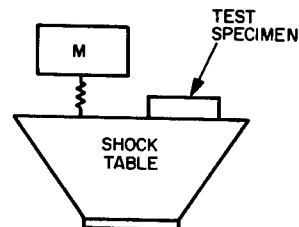Fig. A-2. Peak in shock spectrum perhaps caused by constant frequency lash or distortion of shock pulse

Fig. A3. Large resonant mass on shock table

Appendix B

SHOCK SPECTRA FROM STEP-TYPE PULSES

The shock spectra for step-type pulses presented in Fig. B-1 are from a previous work by the author (B-1) and are presented for the insight they give into the relationship of the pulse to the main response shock spectrum and residual response shock spectrum. One interesting observation that can be made is that if the pulses have equal area, height duration and front slope, they have the same maximum response shock spectrum even if the near slope is not the same. This, of course, means that more than one shock pulse can produce the same shock spectrum. In other words, a shock spectrum does not have a unique pulse.

REFERENCE

B-1. S. M. Ostergren, "The Inverse Problem for the Maximum Response Shock Spectrum," General Electric Co. Tech. Info. Series No. 65SD259, May 14, 1965.
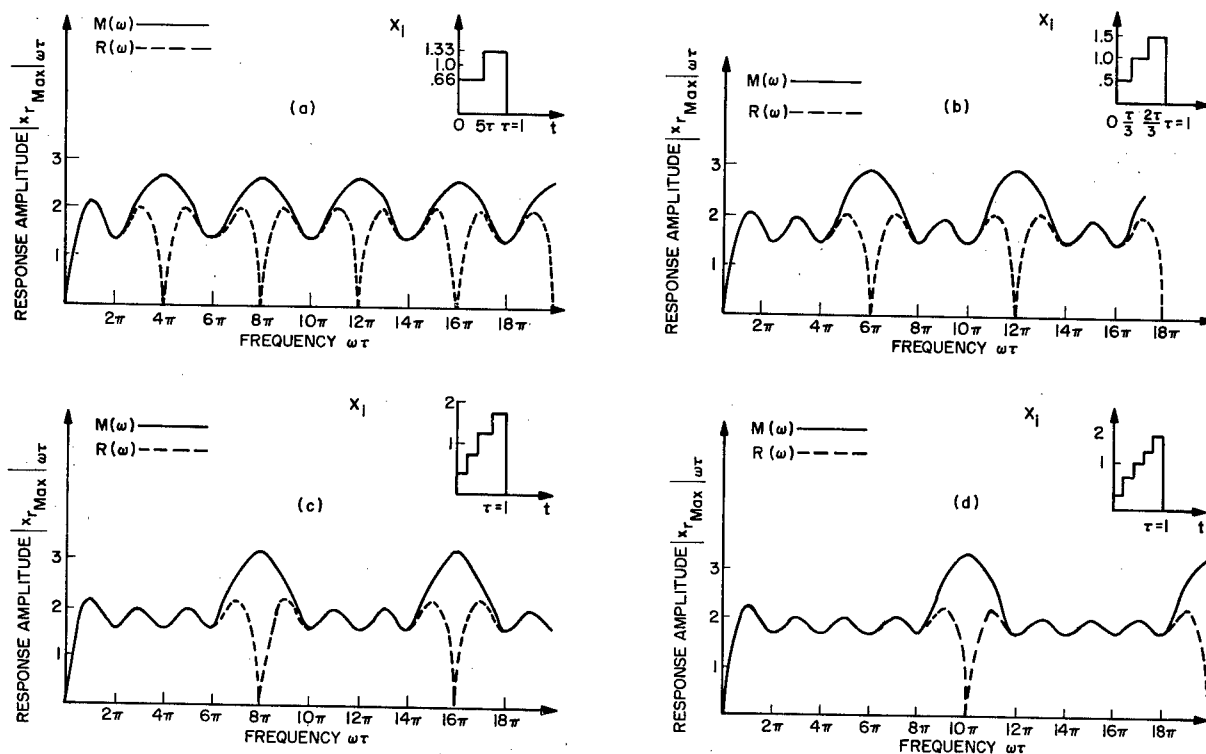
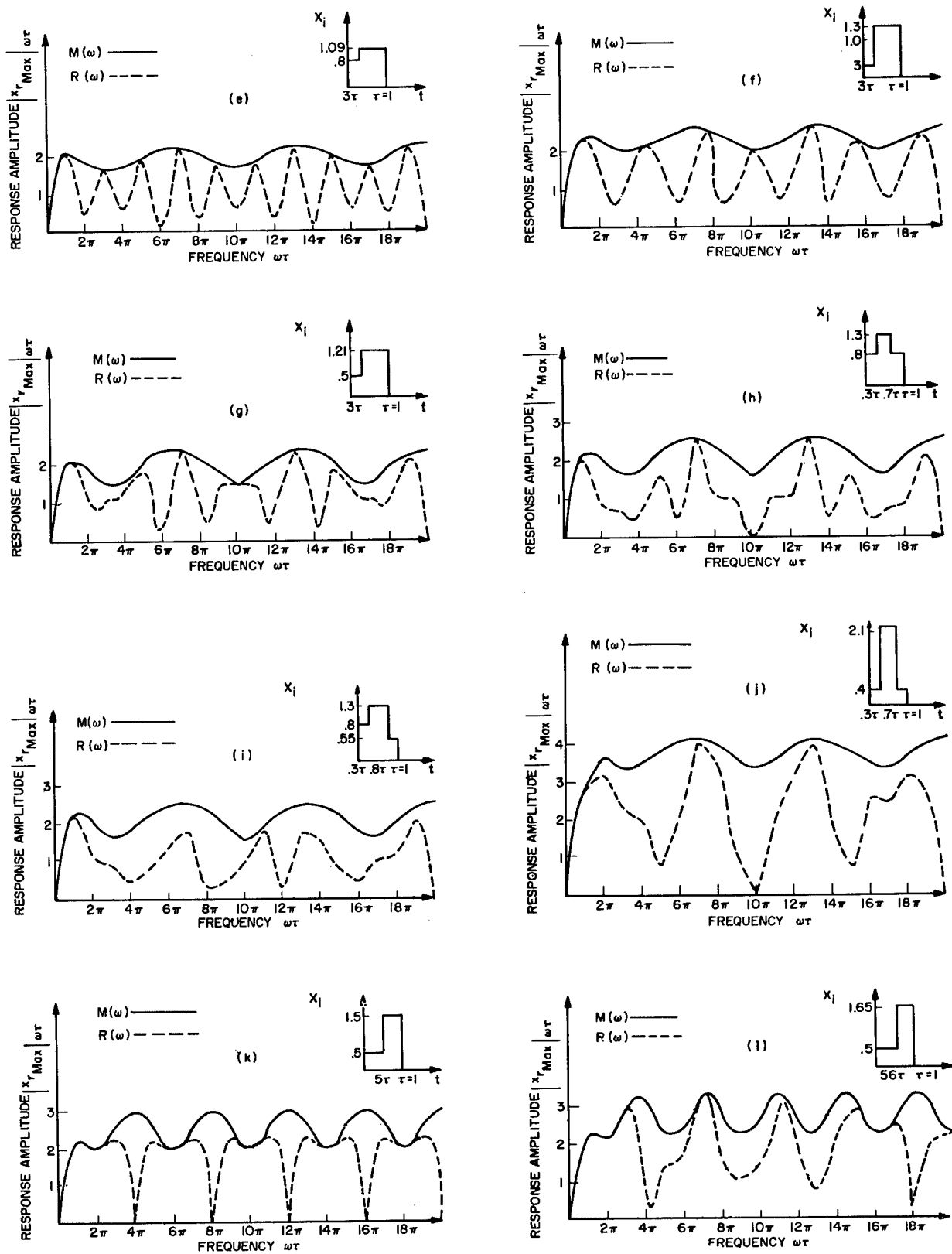Fig. B-1. Shock spectra for step-type pulses

Fig. B-1. (Continued) Shock spectra for step-type pulses

194
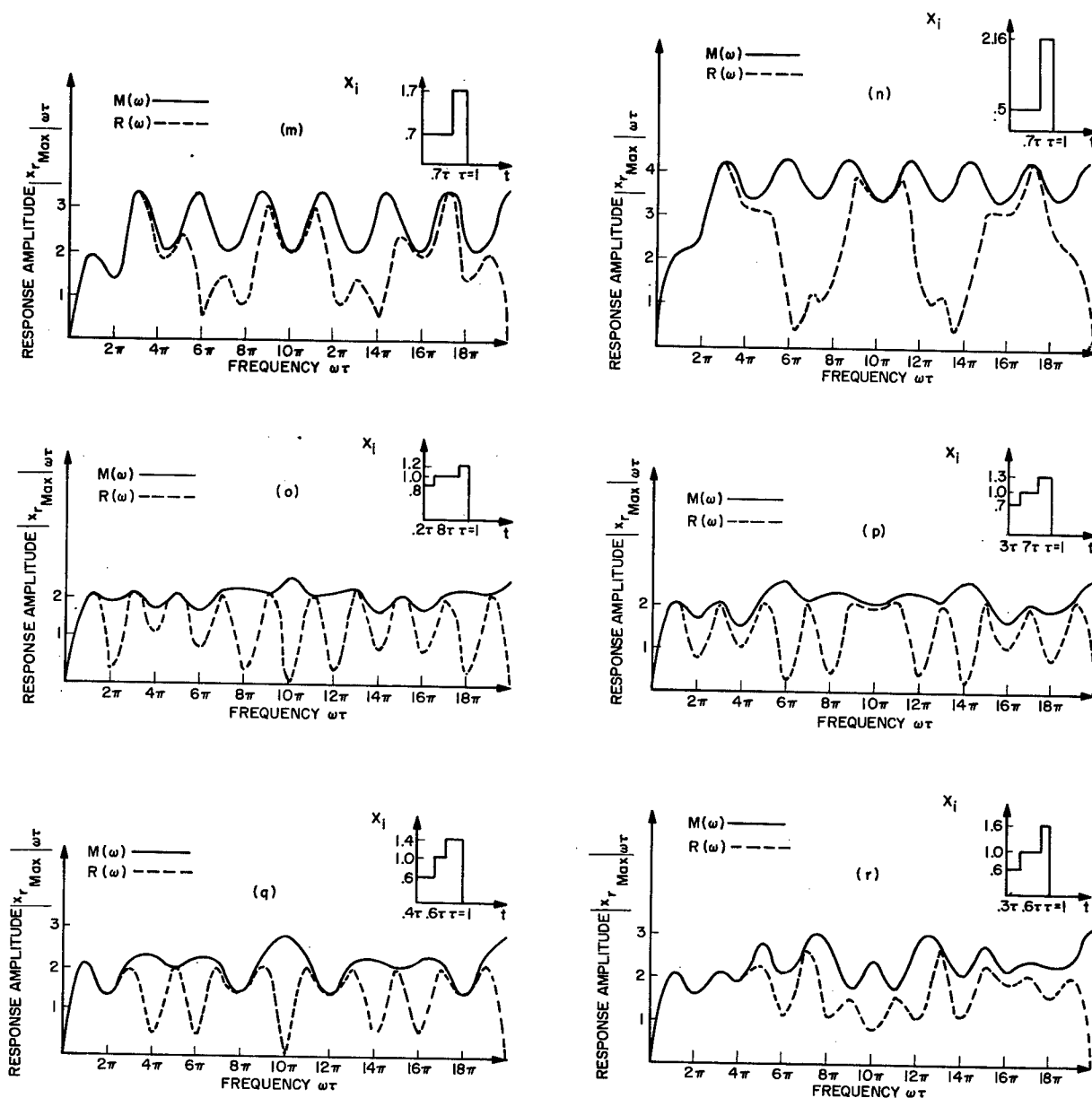
Fig. B-1. (Continued) Shock spectra for step-type pulses

DISCUSSION

Mr. Schell (AF Flight Dynamics Lab.): I want to make a comment and get Mr. Ostergren's reaction. This shock spectrum is based on the response of a simple single degree of freedom system which is linear up to the point of failure. For that type of system the shock spectrum is a criterion for damage potential of the motion. As Mr. Ostergren showed us, there are many ways to meet a shock spectrum requirement with different waveforms. Now, it is my

experience with respect to failure that most equipment goes nonlinear before it fails. There are very few cases of linear-type failures in which equipment actually breaks up. In this case, especially in a hardening system, you are stiffening the system so that it will transmit some very high-frequency components to the equipment being tested. For this reason, I feel that the high-frequency content and the negative content of a shock pulse is rather important in

the performance of a test. I prefer to specify a waveform knowing that, if different laboratories run this test, it will always be run with the same waveform. The frequency components of the waveform, insofar as is possible for the man to create this shock pulse within the tolerance limits, will be the same.

Mr. Ostergren: I tend to agree with you. I think a very important point to be made is that, when we are given a shock spectrum as a test requirement, we can satisfy this requirement with more than one pulse, such as a half-sine or a triangular peak sawtooth. We can also use the methods developed by Lockheed to generate the spectrum directly, using a vibration exciter. There is no reason to assume that the three methods would produce consistent failure data. You would get better failure criteria by standardizing on a single pulse. The question is, how accurately are you simulating the environment to which you expect your equipment to be subjected? Can this be simulated by a half-sine pulse or triangular pulse, or should we be doing something else?

Dr. Morrow (Aerospace Corp.): I want to comment on Mr. Echell's comment. The problem I have observed in pulse testing is that it is difficult to insure that people are using the same pulse or that they really arrive at the same damage potential because of the variation in "hash" on the pulse from one laboratory to another. The shock spectrum provides one way of controlling this. I also want to comment on the limitations that the shock spectrum appears to have as a result of being defined as the response of a linear single degree of freedom system. Again, I think this is primarily a matter of whether you are trying to compare shock severities, or whether you are trying to use the numbers as they come out for design purposes. I agree that there are a lot of things one would like to look at in particular cases, such as the initial spectrum and the high-frequency content. But, if you look at the residual spectrum, it differs from the Fourier transform only by a factor of 2 pi times the frequency. We can infer that the Fourier transform is also a measure of severity. I think it is interesting to compare the Fourier transform with the sort of thing that we work with when we have a complex periodic excitation. It is quite generally accepted that to a first approximation the magnitudes of the individual sinusoids constitute a measure of severity. This information by itself does not completely determine the response of any one system because there are phase effects too. It is hard to tell which phase is worse because the phases get altered in transmission.

Nevertheless, having nothing better that we can do, we generally think of the magnitudes as a reasonably adequate description. Now the Fourier transform is a very closely related idea with magnitude and phase as a function of frequency. Considering the magnitude spectrum to be a first approximation measure of severity, it is no wilder than doing the same thing for the complex periodic case. Using the residual shock spectrum for this purpose amounts to the same thing.

Mr. Ostergren: Dr. Morrow, do you feel that the residual spectrum or the Fourier spectrum should be specified as a test requirement? If so, how would you produce it?

Dr. Morrow: Actually, it does not matter very much whether one specifies the Fourier transform or the residual shock spectrum because if one uses one curve on a piece of graph paper with two sets of rulings, it is essentially the same thing. For most of the shocks induced by such things as igniters and explosives, it is very difficult to distinguish between an initial shock and a residual shock because the common pulse has two discontinuities. You can examine what happens after the first one and this is of some interest. Then you can examine what happens after the second one and this is the one related to the Fourier transform. It is more indicative of what, if anything, is going to persist in the way of continuing vibration. I think it is a little more fundamental. At any rate, if our problem is to simulate what happens in flight, then the residual spectrum or the Fourier transform is a pretty good tool. If we were trying to compare two standard pulses and insure that their effects will be the same for the various types of resonators, nonlinear and otherwise, that might be subjected to it, then I think we would have to look at the initial spectrum as well.

Mr. Foley (Sandia Corp.): It would seem to me that the specification of shock in spectral form in a shock specification might be inappropriate. Although the environmentalist may measure the environment and present it in terms of shock spectra, there should be an intermediate step by a dynamicist to evaluate the spectra and apply proper techniques in order to establish a good shape for a test specification.

Dr. Mains: As far as I know, in each case where a specification has been written, there certainly have been dynamicists in the loop, so that their thoughts and points of view have not been missed, I am sure.

* * *

ANALOG METHOD FOR STUDY OF SHOCK
SPECTRA IN NONLINEAR SYSTEMS

Theodore F. Bogart, Jr.
Ling Electronics Division
LTV Ling-Altec, Inc.
Anaheim, California

An analog technique is described which was used in conjunction with shock spectrum synthesis equipment to study shock spectra in a system containing a common nonlinearity. Operational amplifiers were used to solve the simultaneous differential equations describing the response of a simulated shaker armature and mass load joined by a nonlinear spring element in the presence of damping. A cubic function generator was developed to simulate the nonlinear terms in the equations.

Studies were made using both hardening and softening springs for values of μ^2 ranging up to 59.3×10^6 (corresponding to a 10X spring constant change for a 0.225-in. displacement change) and for various system resonant frequencies and Q's. In each case, shock spectrum synthesis equipment was used to generate a low-level shock pulse at the armature of the simulated nonlinear system. The gain of the synthesis equipment was then increased by a known amount, and shock spectrum analysis equipment was used to determine the modified spectrum.

These studies showed that very severe nonlinearities cause a "peak-notch" to appear in the high-level shock spectrum; in the vicinity of the resonant frequency of the system. In systems with hardening springs the peak was found to precede the notch, and the reverse order was observed in systems with softening springs. Relationships between the magnitudes of the peaks and notches and the other controlled parameters in the simulation were observed. For the most severe nonlinearity studied ($\mu^2 = -45.3 \times 10^6$), at $Q = 20$ and $\omega_r = 1240 \ sec^{-1}$, a -11.5 percent deviation from a linearly predicted high-level shock spectrum was observed. It was concluded that shock spectra are not significantly affected by spring nonlinearities of practical magnitudes.

INTRODUCTION

In recent months new techniques have been developed for performing shock tests with electrodynamic shakers and shock spectrum synthesis equipment (1,2). Experience with these methods has raised certain questions about the effect of system nonlinearities on the synthesized shock spectra. The purpose of this paper is to describe an analog technique which may be used to study the effect of such nonlinearities on shock spectra, and to present the results of studies that were made using the analog to investigate a shock system with a nonlinear spring.

A system for synthesizing a time transient with a specified shock spectrum is shown in Fig. 1. The pulse generator provides a source of transient energy in the form of a short-duration high-level pulse. This pulse is delivered to a set of equalizers, which consists of twenty-six 1/3-octave filters covering the frequency range from 12.5 cps to 8 kc and associated level controls, so that the energy in each of the spectral bands may be controlled independently. The outputs of the 26 channels are summed in one of the equalizers and the synthesized transient is delivered to a line amplifier with a calibrated gain control. The line amplifier drives the power amplifier, which drives the electrodynamic shaker. The accelerometer signal is delivered to a shock spectrum analyzer, via impedance matching and normalizing amplifiers, where the shock spectrum is determined by analysis at the 26 resonant frequencies corresponding to the twenty-six
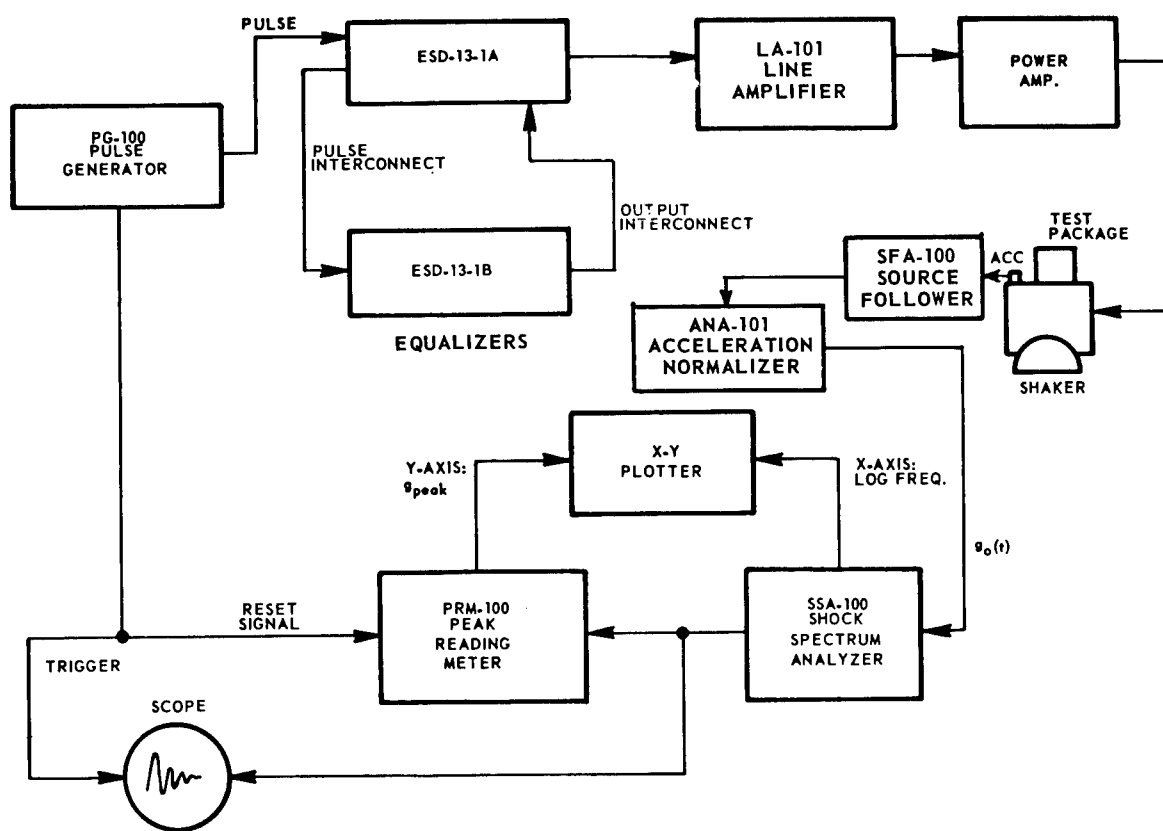
Fig. 1. Electrodynamic shaker shock synthesis and analysis system

1/3-octave frequencies of the equalizer. The shock spectrum analyzer is a special purpose analog computer designed to solve the differential equations governing the motion of the hypothetical spring-mass system by which the shock spectrum concept is defined. The output of the analyzer represents the response of the hypothetical spring-mass system with a selected resonant frequency and Q, when driven by a signal representing the acceleration-time waveform applied to the system. This response waveform is applied to a peak-reading meter, which reads and holds the value of the peak acceleration response occurring during the transient acceleration. The peak acceleration response may then be displayed on the x-y plotter as a function of the resonant frequency selected on the analyzer.

In a typical shock spectrum synthesis procedure, the shaker and test package would be subjected to a series of low-level transients (perhaps 40 db below the actual test level), while the operator simultaneously adjusted the equalizer level controls and observed the peak reading meter. While adjusting the level in a particular frequency band, the analysis frequency

of the shock spectrum analyzer would be selected to correspond to the center frequency of that band. The trigger and reset signals shown in Fig. 1 are used to synchronize this synthesis operation, by insuring that the peak reading meter is reset in advance of every transient pulse. A variable pulse delay control is provided to adjust the reset timing and to trigger a display on the oscilloscope. By successively adjusting the levels in all frequency bands while the analyzer frequencies are set to corresponding bands, an acceleration-time waveform with a specified shock spectrum may be synthesized.

Once a low-level transient with a specified shock spectrum has been synthesized, the gain of the system may be increased to the actual test level with the calibrated gain control on the line amplifier. A manual control on the pulse generator is then used to generate a single high-level test pulse. If the shaker, fixture, and test package all comprise a linear mechanical system, then the shock spectrum associated with the test-level transient will be a linear magnification of the shock spectrum associated with the low-level transient. On the other hand, the presence of the nonlinear mechanical

198

elements can be expected to alter the shape of the spectrum as a function of the level. The nature and degree of the alteration will depend not only on the kind of nonlinearity but also on its severity. In a practical situation it becomes very difficult to account for the many nonlinearities which may be present, and it is therefore necessary to restrict a quantitative investigation to a particular kind of nonlinearity, such as a nonlinear spring. The knowledge gained from investigation of particular cases should then lead to an insight and understanding of the behavior of the more general, practical system involving many nonlinearities.

ANALOG SIMULATION

The study of nonlinear mechanical elements is accomplished much more readily by analog simulation than by fabrication of the elements themselves. Operational amplifiers and nonlinear electrical elements may be used to solve analogous equations describing nonlinear mechanical elements, and if the analog thus constructed is properly designed, it can be inserted directly into a large-scale system to study its effect on that system. This use of simulated mechanical elements for study purposes has the further advantage that parameters in the analog (such as the severity of the nonlinearity) can be changed much more conveniently than corresponding mechanical parameters. For purposes of the investigation described here, the mechanical components shown in Fig. 1 were replaced by an analog consisting of amplifiers wired to solve the differential equations of a two-mass system. A cubic function generator was added to the analog and the resulting system was used directly with the remaining shock synthesis equipment (less power amplifier) shown in Fig. 1 to study the effects of a nonlinear fixture.

Consider the two-mass system shown in Fig. 2. Let M_1 represent a mass load attached to an armature of mass M_2. Suppose the attachment is made by a fixture with spring constant K and damping B. The simultaneous differential equations describing the behavior of this system are:

$$M_2 \ddot{X}_2 + B(\dot{X}_2 - \dot{X}_1) + K(X_2 - X_1) = F(t), \quad (1)$$

$$M_1 \ddot{X}_1 + B(\dot{X}_1 - \dot{X}_2) + K(X_1 - X_2) = 0, \quad (2)$$

where

X = displacement,
$\dot{X}$ = velocity, and
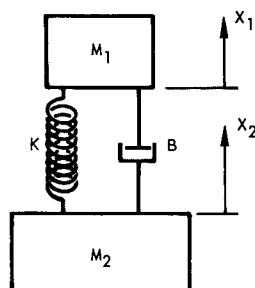$\ddot{X}$ = acceleration.

Fig. 2. Simple two-mass system

The standard procedure used to solve differential equations with operational amplifiers may be summarized as follows:

1. Solve the differential equation for the highest order derivative;

2. Assume that a voltage proportional to this derivative is available at some arbitrary point in the analogous circuit;

3. Integrate the voltage with an operational amplifier to obtain the next lower order derivative;

4. Scale the voltage thus derived by a factor corresponding to its coefficient in the differential equation of step 1, and feed this voltage back to a summing amplifier;

5. Continue to integrate, scale, and feed back voltages as prescribed by the differential equation of step 1 until a summation of all the terms equal to the highest order derivative is obtained; and

6. The summation of these terms as prescribed by the differential equation then yields the voltage (initially assumed) that is proportional to the highest order derivative.

It is necessary in setting up the analog to insure that scale factors are chosen so that the range of operation does not cause amplifier saturation due to overvoltages. The procedure outlined above may be extended to apply to simultaneous differential equations by simply adding voltages proportional to the other variables at the summing amplifiers. This summation is again performed in accordance with equations which have been solved for the highest order derivatives. Much has been written on these techniques of analog simulation, and the reader is referred to standard References (3-5) for further details. Figure 3 illustrates an analog setup that could be used to solve simultaneously the differential Eqs. (1) and (2).
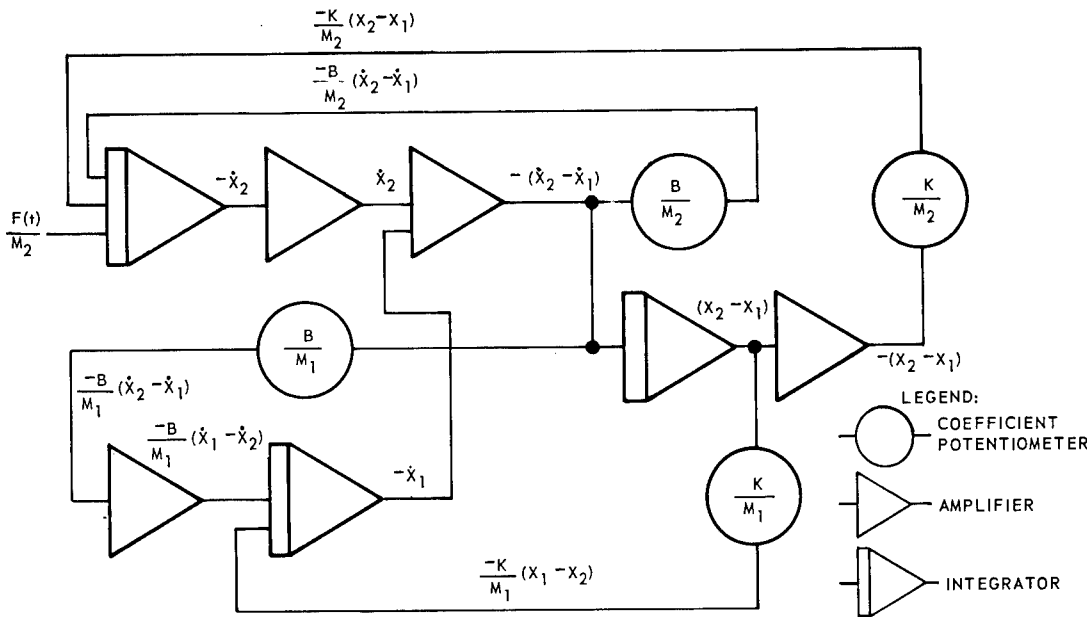
Fig. 3. Analog setup for two-mass system

Consider now a nonlinear spring with a force-displacement relation given by (6):

$$F = K(X \pm \mu^2 X^3) , \qquad (3)$$

where μ^2 determines the severity of the nonlinearity and carries a positive sign for a hardening spring and a negative sign for a softening spring. This relation could represent the nonlinear characteristic of a fixture attached between a shaker armature and a test package. Equations (1) and (2) modified for inclusion of the nonlinear fixture then become:

$$M_2 \ddot{X}_2 + B(\dot{X}_2 - \dot{X}_1) + K\left[(X_2 - X_1) \pm \mu^2 (X_2 - X_1)^3\right] = F(t),$$
$$(4)$$

$$M_1 \ddot{X}_1 + B(\dot{X}_1 - \dot{X}_2) + K\left[(X_1 - X_2) \pm \mu^2 (X_1 - X_2)^3\right] = 0.$$
$$(5)$$

Figure 4 shows an analog setup used to solve these equations in conjunction with the shock synthesis and analysis equipment shown in Fig. 1.

Analog simulation of nonlinear elements is a technology in its own right, and many different methods have been used to achieve various kinds of nonlinear functions. One very popular and versatile device that is used for this purpose is the diode function generator, which employs biased diodes and variable attenuators to provide a piecewide linear approximation to a given nonlinear transfer characteristic. Details

and means of simulating nonlinearities other than that described by Eq. (3) may be found elsewhere (4,5). The cubic function generator shown in Fig. 4, which is used to generate a voltage proportional to the cube of the relative displacement of M_1 and M_2, was designed using three field-effect transistor squaring circuits (7). The squaring circuit is the basis of a very versatile means for simulating nonlinearities of integer degree. For this purpose, two squaring circuits are used to form a multiplier, by implementing the "quarter-square" equation:

$$4xy = (X + Y)^2 - (X - Y)^2 . \qquad (6)$$

The cubic function generator used for this study consisted of a quarter-square multiplier driven by a squaring circuit:

$$4(X_1 - X_2)^3 = \left[(X_1 - X_2)^2 + (X_1 - X_2)\right]^2$$

$$- \left[(X_1 - X_2)^2 - (X_1 - X_2)\right]^2 . \qquad (7)$$

SHOCK STUDIES

To investigate the effect of a nonlinear fixture on a typical shock test, it is necessary to assign values to and scale the simulated elements M_1, M_2, B, K, and μ^2. By reference to Fig. 4, it can be seen that except for μ^2 and $F(t)/M_2$, only ratios (K/M_2, K/M_1, B/M_2 and B/M_1) need be specified. For this investigation, an armature mass 10 times the load mass was
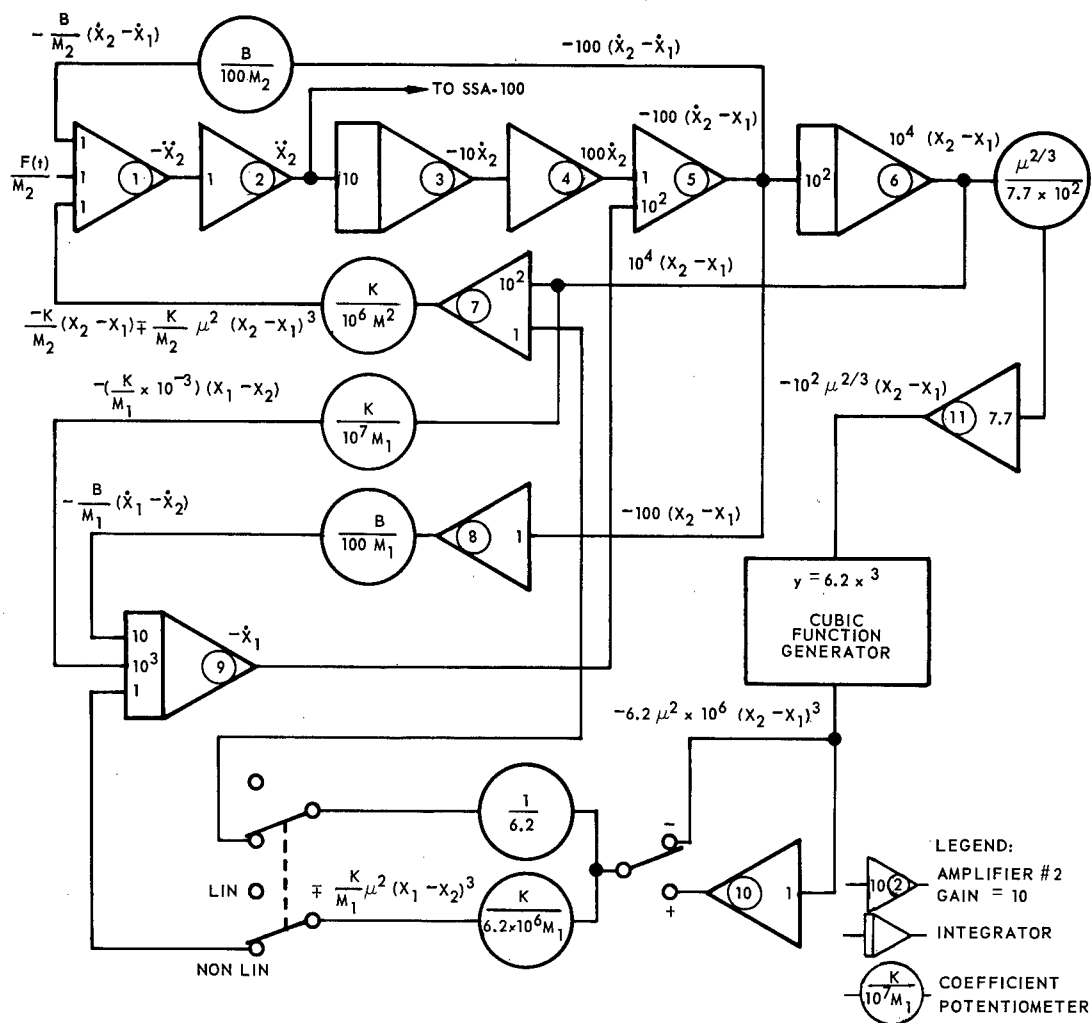
200

Fig. 4. Simulated load and armature dynamics

assumed. For a spring constant of $K = 40,000$ lb/in. and an armature weight of 100 lb, $K/M_2 = 0.1544 \times 10^6$, $K/M_1 = 1.54 \times 10^6$, $B/M_2 = 12.4$, and $B/M_1 = 124$.

It is sometimes convenient to assign values in terms of the more familiar constants of the system, such as the resonant frequency ω_r and the Q. The linear Eqs. (1) and (2) may be written:

$$\ddot{X}_2 + \omega_{r2} Q_2 (\dot{X}_2 - \dot{X}_1) + \omega_{r2}^2(X_2 - X_1) = \frac{F(t)}{M_2} , \quad (8)$$

$$\ddot{X}_1 + \omega_{r1} Q_1 (\dot{X}_1 - \dot{X}_2) + \omega_{r1}^2(X_1 - X_2) = 0 ,$$

where

$$\omega_{r2} \triangleq \frac{K}{M_2} ,$$

$$\omega_{r1} \triangleq \frac{K}{M_1} ,$$

$$Q_2 \triangleq \frac{M_2 \omega_{r2}}{B} ,$$

and

$$Q_1 \triangleq \frac{M_1 \omega_{r1}}{B} .$$

Then, in terms of the ratio of the armature mass to load mass:

$$\frac{\omega_{r2}}{\omega_{r1}} = \sqrt{\frac{M_1}{M_2}} ,$$

and

$$\frac{Q_2}{Q_1} = \sqrt{\frac{M_2}{M_1}} .$$

201

The values chosen above lead to $\omega_{r1} = (2\pi)(200$ cps$)$, and $Q_1 = 10$.

The value of μ^2, which determines the severity of the nonlinearity, can be expected to have a significant influence on the shape of the synthesized shock spectrum when the system gain is increased to the actual test level. Therefore, the choice of this parameter must be considered in some detail. A convenient means for gaining an insight into the severity of the nonlinearity as a function of the magnitude of μ^2 is to determine the effective change in spring constant, from its static value K, for a given change in relative displacement. The effective spring constant as a function of the relative displacement may be found by differentiating Eq. (3):

$$\frac{dF}{dx} = K \left[1 \pm 3\mu^2 X^2\right]. \tag{10}$$

The spring constant at zero relative displacement is clearly equal to K, and the value of μ^2 required to change this spring constant by a factor of C over a relative displacement

range d (measured from zero), for the hardening spring, may be found by substitution into Eq. (10):

$$\mu^2 = \frac{C-1}{3d^2}. \tag{11}$$

For the softening spring the value of C is less than 1, and Eq. (11) may be written:

$$\mu^2 = \frac{(1-C)}{3d^2}. \tag{12}$$

The minimum and maximum values of μ^2 used in this study were $\mu^2_{min} = 1.6 \times 10^6$ and $\mu^2_{max} = 59.3 \times 10^6$. From Eq. (11), the spring constant is changed by a factor of 10 for a 1.37×10^{-3}-in. relative displacement with the minimum value of μ^2, and for a 0.225×10^{-3}-in. relative displacement with the maximum value of μ^2. Figure 5 is a plot of Eq. (3) for the minimum and maximum values of μ^2, and $K = 40,000$ lb/in.

The procedure used to determine the effect of the spring nonlinearity was to synthesize a
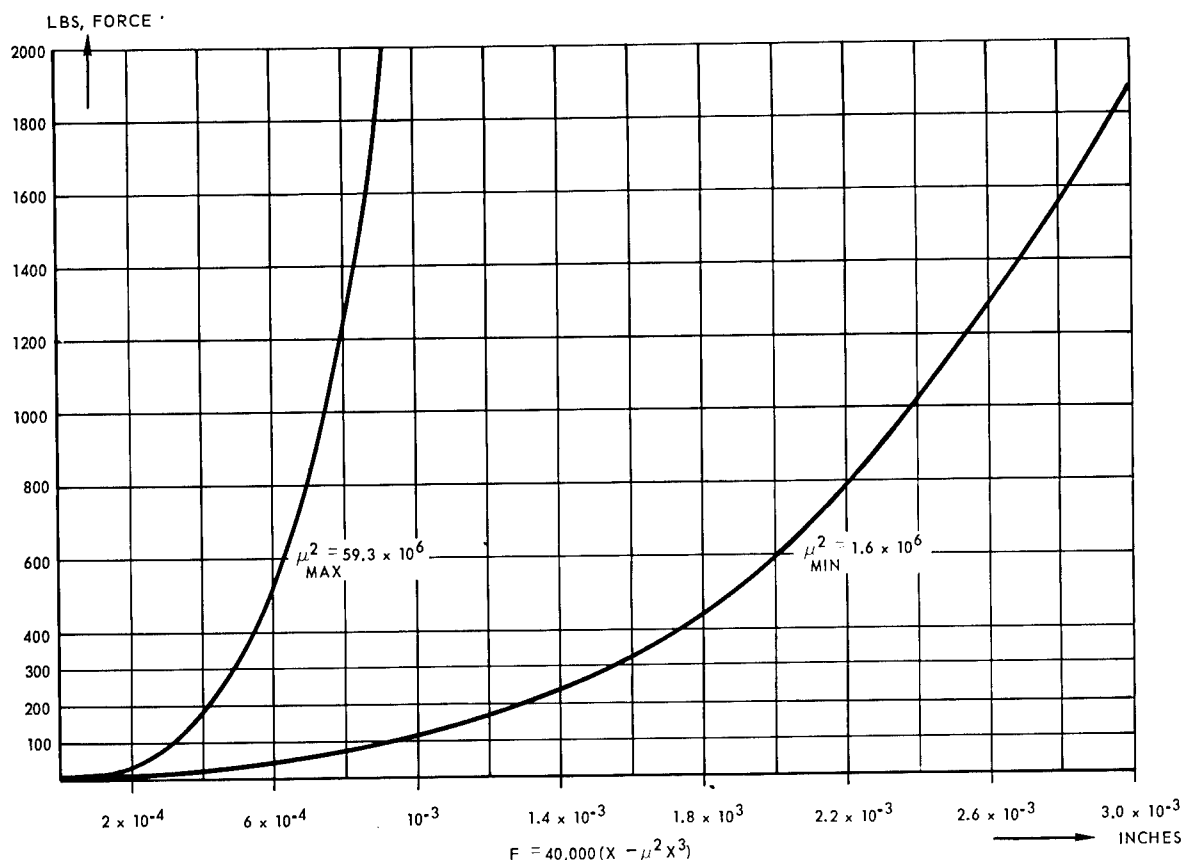

Fig. 5. Nonlinear spring force vs displacement

202

transient waveform with a flat shock spectrum, increase the level of this waveform by 20 db, and determine the shock spectrum of the resulting waveform. In both the low-level synthesis and high-level analysis operations, the waveform of concern was the acceleration $\ddot{X}_2$ at the armature. This would be the normal location of an accelerometer in an actual shock test using the shock spectrum synthesis method. The equalizers shown in Fig. 1 were used to synthesize a waveform with a flat shock spectrum. When parameters in the analog were changed, it was found that only two or three of the 1/3-octave filters adjoining the 200-cps band needed to be adjusted to reestablish a flat spectrum. On the other hand, for shock spectrum analysis a continuously variable frequency control on the spectrum analyzer was used, so that the analysis resolution would be much finer than the 1/3-octave synthesis resolution. It was necessary to record the "flat" spectrum of the low-level transient because small deviations in the immediate vicinity of 200 cps cannot be compensated for with the synthesizer. Thus, deviations in the spectrum due to the nonlinearity, as determined by analysis of the high-level transient at identical frequencies, could be distinguished from deviations due to the broadness of the synthesis bands. The synthesized low-level transient, which has the form of a damped sinusoid of decreasing frequency typical to this application, had a maximum peak-to-peak value of 35 g.

Figures 6 through 9 are plots of the percentage deviation of the high-level spectrum from a linear prediction of the high-level spectrum, based on measured values of the low-level spectrum, versus analysis frequency. By definition,

$$D = \% \text{ deviation} = \left[\frac{H - 10L}{10L}\right] 100 , \qquad (13)$$

where H and L are, respectively, the high- and low-level measured values of the shock spectrum at a particular frequency. Figure 6 is a plot of D versus analysis frequency for a fixed resonant frequency $(\omega_{r1} = 1240 \text{ sec}^{-1})$ and a fixed $Q_1 = 10$, as μ^2 is varied. It is interesting to note that the deviation peaks positively in the frequency range immediately preceding ω_{r1} and is negative in a small frequency range following ω_{r1}. The high-level shock spectrum is thus higher than a linear prediction would indicate at frequencies just below ω_{r1} and lower than a linear prediction for frequencies above ω_{r1}. By reference to Fig. 7, which shows D for the same values of Q_1 and ω_{r1} but with softening springs, it can be seen that the opposite situation is true. Here, the high-level shock spectrum was found to be lower than a linear prediction in the frequency range immediately preceding ω_{r1} and lower at frequencies above ω_{r1}. In both cases it is obvious that increasing the magnitude of μ^2, which corresponds to increasing the severity of the nonlinearity,
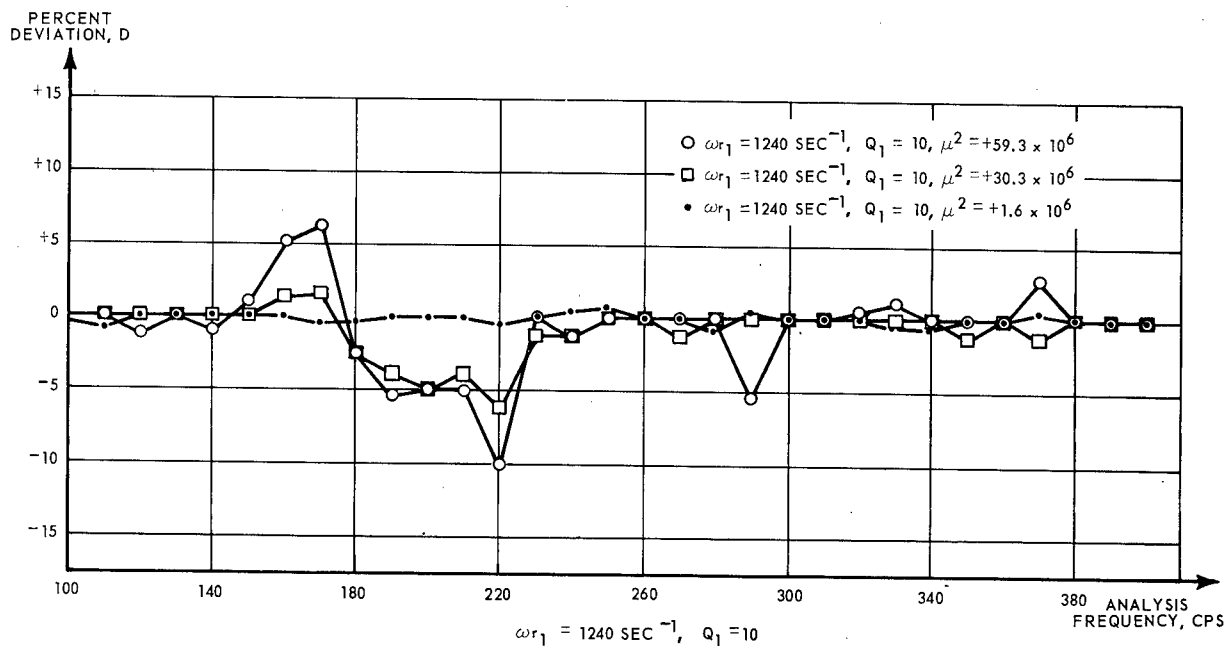

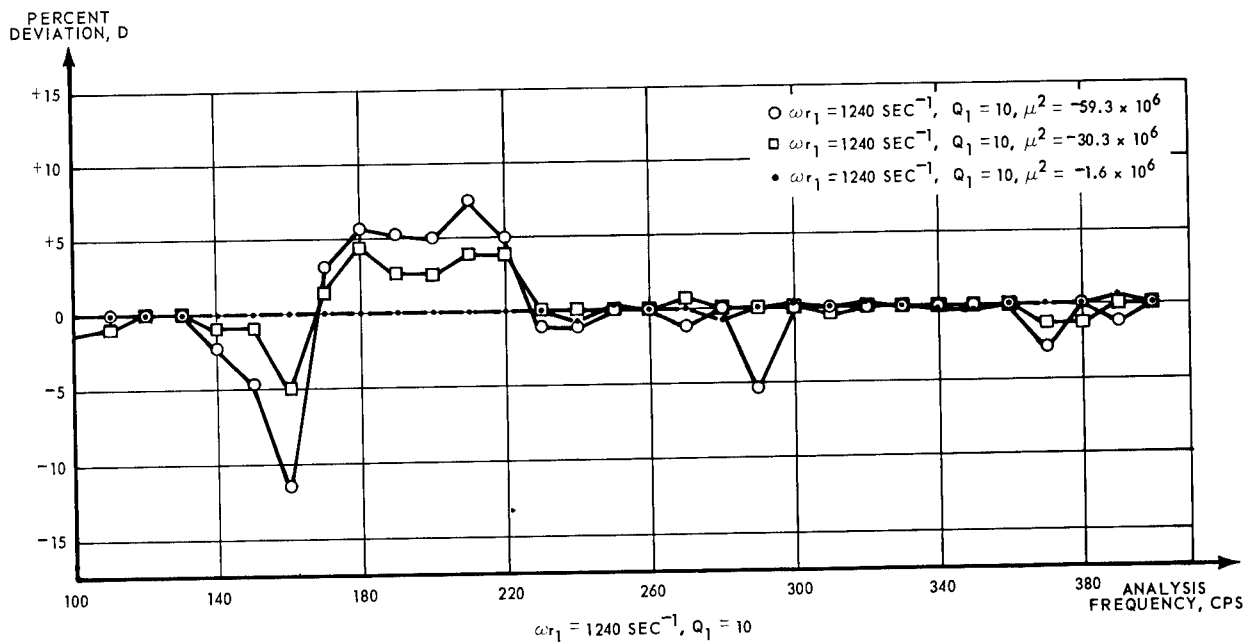Fig. 6. Deviations in shock spectra due to magnitude of $+\mu^2$

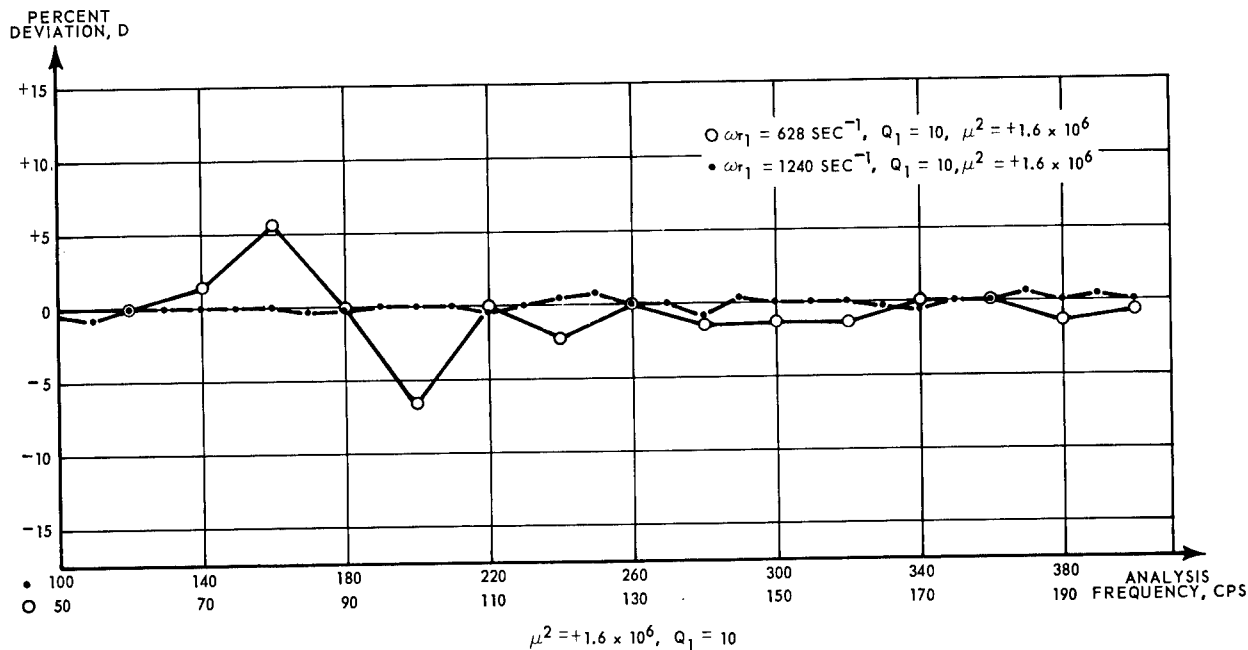Fig. 7. Deviations in shock spectra due to magnitude of $-\mu^2$

Fig. 8. Deviations in shock spectra due to ω_{r1}

increases the percent deviation of the high-level spectrum from a linear prediction of its value.

The existence of this "peak-notch" in the shock spectrum can be explained qualitatively by recognizing that an instantaneous change in spring constant results in an instantaneous change in resonant frequency. The low-level synthesis procedure, in effect, compensates for the usual notch-peak which is observed in the frequency response of the two-mass system shown in Fig. 2. This compensation results in the addition of energy to the synthesized transient

204

PERCENT
DEVIATION, D

$$\times \quad \omega_{r_1} = 1240 \text{ SEC}^{-1}, \quad Q_1 = 10, \quad \mu^2 = +45.3 \times 10^6$$
$$\bullet \quad \omega_{r_1} = 1240 \text{ SEC}^{-1}, \quad Q_1 = 20, \quad \mu^2 = +45.3 \times 10^6$$
$$\bigcirc \quad \omega_{r_1} = 1240 \text{ SEC}^{-1}, \quad Q_1 = 10, \quad \mu^2 = -45.3 \times 10^6$$
$$\square \quad \omega_{r_1} = 1240 \text{ SEC}^{-1}, \quad Q_1 = 20, \quad \mu^2 = -45.3 \times 10^6$$

$$\omega_{r_1} = 1240 \text{ SEC}^{-1}, \mu^2 = \pm 45.3 \times 10^6$$
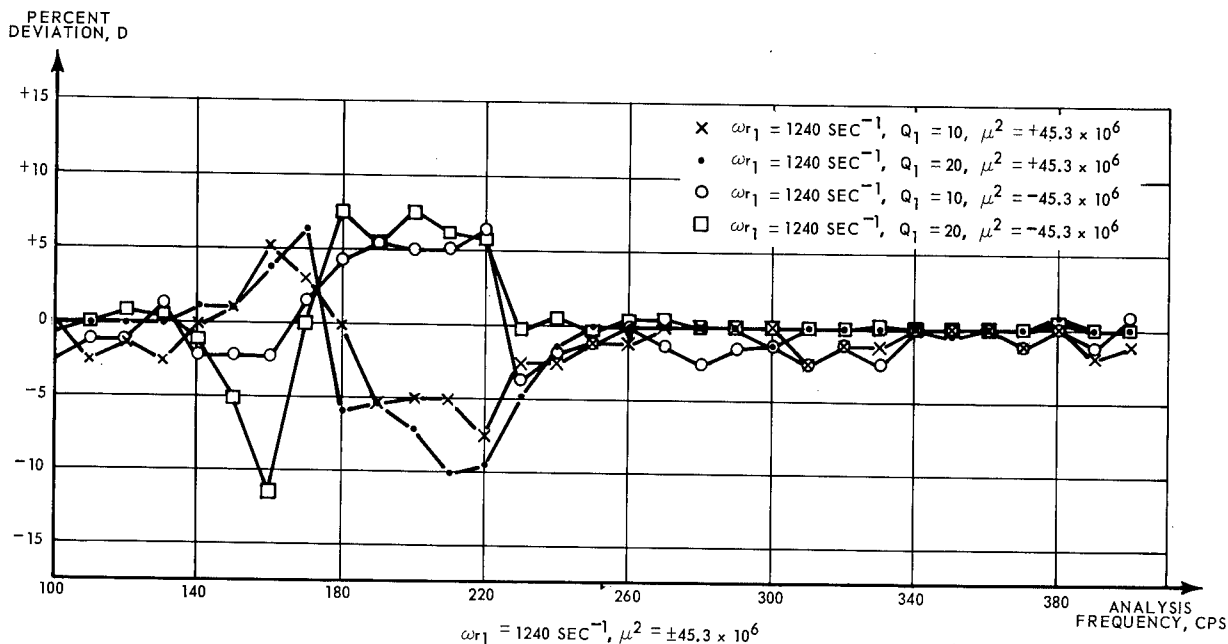
ANALYSIS FREQUENCY, CPS

Fig. 9. Deviations in shock spectra due to Q_1

in the frequency range (the "notch") preceding ω_{r1} and attenuation of energy in a band just following ω_{r1}. When the level of a transient synthesized under these conditions is increased, in a system with a hardening spring, the effective increase in resonant frequency thus results in excess energy at frequencies in the vicinity of the "notch."

Similarly, this instantaneous shift in resonance results in a relative attenuation of energy in the vicinity of the "peak." Increasing the level of a synthesized transient in a system with a softening spring shifts the resonant frequency in the opposite direction, and the opposite effect occurs. It must be appreciated that the preceding is only a qualitative analysis, using the more familiar sine wave response characteristics of such a system as an analogy, and that the actual process is complicated by the facts that: (a) the system is subjected to a short-duration nonsinusoidal transient rather than a sustained sine wave, and (b) the "shift" in resonant frequency is not a fixed amount but depends on the instantaneous level of an oscillatory waveform.

Figures 8 and 9 show the effects of changing the resonant frequency ω_{r1} and the value of Q in systems with hardening springs. The resonant frequency ω_{r1} was changed by reducing the values of K/M_1 and K/M_2 in the analog shown in Fig. 4, which in effect reduced the value of K, since all other parameters were left unchanged.

From Fig. 8, it is evident that reducing ω_{r1} produces greater deviations in the high level shock spectrum. This effect is the result of increased relative displacement, since the applied force remained the same. The value of Q was increased by reducing the values of B/M_1 and B/M_2 in the analog, which effectively reduced the damping in the system. From Fig. 9 it is evident that increasing the Q, which increases the severity of the notch-peak in the system frequency response, also produces greater deviations in the high-level shock spectrum. This is clearly the result of the increased compensation which is required when synthesizing the low-level transient for a flat shock spectrum.

SUMMARY

From a practical standpoint, the quantitative results of this study indicate that the nonlinear spring coupling has very little effect on the magnification of a shock spectrum. Of all the cases shown by Figs. 6 through 9, the maximum deviation was only -11.5 percent. More significantly, the severities of the nonlinearities studied, as indicated by the magnitudes of μ^2 used in the analog, are much greater than the severity of a nonlinearity which might be encountered in a practical test. Even the smallest value of μ^2 used in the study would, from Eq. (11), produce a 120 times change in the effective spring constant for a 0.005-in. relative displacement.

205

Although it is not possible to generalize these conclusions to include all types of nonlinearities subjected to all test conditions, the result nonetheless indicate that nonlinearities of sufficient severity to affect the shock spectrum synthesis method are several orders of magnitude greater than those encountered in practice.

REFERENCES

1. G. W. Painter and H. J. Parry, "Simulating Flight Environment Shock on an Electrodynamic Shaker," Shock, Vibration and Associated Environments Bull. No. 33, Part III, pp. 85-96, March 1964

2. J. D. Forte, "Shock Analysis and Synthesis," Proc. IES (1965)

3. G. A. Korn and T. M. Korn, Electronic Analog and Hybrid Computers (McGraw-Hill, New York), 1964

4. N. R. Scott, Analog and Digital Computer Technology (McGraw-Hill, New York), 1960

5. W. J. Karplus and W. W. Soroka, Analog Methods (McGraw-Hill, New York), 1959

6. H. N. Abramson, "Non-linear Vibration," in Shock and Vibration Handbook (C. M. Harris and C. E. Crede, Ed.) (McGraw-Hill, New York), Vol. 1, 1961

7. L. J. Sevin, Field Effect Transistors Application Report (Texas Instruments, Inc.), 1964

DISCUSSION

Mr. Gertel (Allied Research Assoc.): I am curious about the nonlinearity. Was that something to do with the calculation of the shock spectrum, or did it have something to do with the compensation of the shaker system?

Mr. Bogart: That particular nonlinearity does not represent any specific nonlinearity. It happens to be a general representation in the Harris and Crede Handbook and has no particular significance.

Mr. Gertel: By definition, shock spectrum involves linear single degree of freedom systems as the means of calculation. I was trying to relate this nonlinearity to that.

Mr. Bogart: There is no relation. The linear single degree of freedom system which is used to analyze a transient to determine its shock spectrum was also used in this system. Simulation of that linear single degree of freedom system is by the shock spectrum analyzer and that was unchanged. The linear single degree of freedom system which defines the shock spectrum concept is a purely hypothetical thing. It does not really exist. But, we inserted a nonlinear spring into the hardware in the place where it would exist. Does that answer the question?

Mr. Zell (Picatinny Arsenal): Was the effect of Q on the spectrum investigated?

Mr. Bogart: Yes, it was. We must be careful to distinguish between the Q of the shock spectrum and the Q of the two-mass system. Changing the Q of the shock spectrum does not really mean much as long as the results are consistent. We did change the Q of the two-mass system and found, in general, that the deviation increases as the Q increases.

Mr. Zell: And the case that you presented was for the maximum deviation?

Mr. Bogart: That is correct.

Mr. Forkois (U.S. Naval Research Lab.): Would you say, then, that there is an optimum amount of damping that could be put into the system? Is it or is it not good to put damping into a shock-mitigating system?

Mr. Bogart: We found that the deviation in the high-level shock spectrum increases as we increase the Q or, in effect, reduce the damping. What we have done is to synthesize a low-level transient and compensate for the notch-peak effect. In effect, we have equalized it out in the synthesis procedure and the notch-peak actually reverses. The peak becomes a notch and the notch becomes a peak at high level. There is an excess of energy due to our effective compensation at low level and this excess of energy at high level results in the peak and causes a deviation. Increasing the Q of the system or reducing the damping means that you have to compensate more for the notch at low levels. Consequently, at high levels, you end up with even more energy than is required and there is a greater deviation.

Dr. Mains (Washington Univ.): Damping in a shock-mitigating system can be very useful in that it allows you to shape the character of the response. If what you want to protect against is peak acceleration, you shape one way. If you want to protect against velocity, you shape another way. If you want to protect against total excursion, a different shaping is required. The damping is the means by which you can do this most readily. In particular, as in the case of your problem below decks with electronic equipment, a properly programmed viscous damper can help either limit acceleration or excursion in an optimum fashion.

*   *   *

A MECHANICAL SHOCK PULSE SURVEY

Francesco Palmisano
U.S. Army Electronics Command
Fort Monmouth, New Jersey

A survey of the shock pulse shapes produced by eight mechanical shock machines used in the evaluation of electronic piece parts is discussed. The shock machines include the general types of free-fall, pendulum, and cam-activated. The shock pulses range in nominal time duration of from 40 to 1150 g.

Details of the recording and instrumentation techniques employed to obtain survey data are presented. Instrumentation calibration and problems of undershoot are also discussed, as is the reduction of the raw data from their original collected form to a form suitable for analysis and storage.

The methods of analysis, quantitative and qualitative, of the shock pulse curves obtained from the mechanical shock machines surveyed were to first determine shock pulse curves amplitude-frequency spectrum by use of a special-purpose analog computer designed specifically to compute Fourier integrals. The frequency spectrum is then converted to a Bode diagram from which a graphical comparison of the shock pulse is made.

Analysis of the results of the survey shows that major characteristics of the amplitude-frequency spectrum of each mechanical shock ma-. chine surveyed are mainly dependent on peak amplitude, shock pulse duration, and the area under the shock pulse curve.

INTRODUCTION

The purpose of this survey, performed by personnel of the Techniques Branch Environmental Research Group, Electron Tubes Division, Electronic Components Laboratory, of the U.S. Army Electronics Command (USAECOM), was to classify and compare the shock pulses produced by eight typical mechanical shock machines currently used to evaluate electronic piece parts. Both amplitude-versus-time spectra and amplitude-versus-frequency spectra were used in the analysis of each shock pulse. Table 1 lists the mechanical shock machines analyzed, together with the amplitude-time characteristics of primary concern.

Inspection of Table 1 reveals that large variations exist in the pulse time duration of the individual mechanical shock machines, the longest pulse lasting more than 50 times the shortest pulse. The highest peak amplitude is more than 25 times the lowest peak amplitude, the higher amplitudes being associated with the shorter pulse durations. Comparison of the acceleration-versus-time record of these shock pulses shows that each of the shock pulse machines produces a unique pulse shape. In spite of these differences, there are similarities; chiefly the areas under the shock pulse curves are each within one order of magnitude and each shock pulse curve displays a predominant positive area readily identified as the main accelerating force. This report deals with the significance of these variations and similarities.

DISCUSSION

Background History

The mechanical shock machine, as is true of many environmental test equipments, was born of necessity. Early in World War II, military requirements demanded that heretofore carefully handled electronic equipments be made to withstand the severe treatment imposed by normal combat and logistic conditions.

TABLE 1
Amplitude-Versus-Time Characteristics of Mechanical Shock Machines

Mechanical Shock Machine	Nominal Time Duration of Major Positive Pulse (ms)	Peak Amplitude (g)	Area under Major Positive Pulse (g/sec)
180-JAN (Navy Flyweight)	0.60	1150	0.442 (see Fig. 4)
254-JAN (drop tester)	0.75	480	0.204 (see Fig. 6)
123-JAN (pendulum type)	4.75	90	0.222 (see Fig. 8)
SRDE-RSC-11 (British Bump)[a]	5.00	40	0.098 (see Fig. 10)
JAN-S-44 (drop tester)	5.50	85	0.270 (see Fig. 12)
Barry 20VI (sand drop)	10.00	70	0.246 (see Fig. 14)
Barry Varipulse (modified Type 15575)	11.00	62	0.285 (see Fig. 16)
Controlled motion[b]	32.00	45	0.300 (see Fig. 18)

[a]Developed by the Signals Research and Development Establishment, Christ Church, Hants, England.
[b]Manufactured by the N. J. Dynamic Company, Livingston, New Jersey.

The first mechanical shock machine design to evolve as a result of field experience was a pendulum-type bump tester (now 123-JAN). Other early devices included a package drop tester which simulated the dropping of a package from a moving vehicle and the Navy Flyweight shock machine (now 180-JAN). The 180-JAN shock machine was one of a series of mechanical shock machines of ascending load capacity which were the direct result of experiences in naval engagements. It was found that during a near-miss, the mechanical shocks generated caused severe damage to electronics mounted on bulkheads. The 180-JAN shock machine proved to be extremely successful in evaluating electronic equipment. The success with this machine led to the development of other mechanical shock machines which were designed, in the main, to meet a special shock environment. Among these shock machines are the drop tester (254-JAN) and the sand-drop tester (Barry 20VI) which was designed to simulate the long pulse of aircraft landings.

Because the design of the above mentioned mechanical shock machines was motivated to a great extent by a specific crisis or special shock environment to be overcome, it is not surprising that the shock pulses produced by these machines are quite complex with respect to shock pulse shape. Although certain shock parameters, e.g., shock pulse duration and peak amplitude, can be controlled to a great extent, shock pulse shape or the amplitude-versus-frequency spectrum is a function of many factors in addition to shock machine design. Fabrication, installation conditions, type and size of the item to be tested, and fixture mounting also play roles. It is not uncommon, therefore, for two mechanical shock machines of apparently identical design to present quite different shock pulse spectra, even though each has similar peak amplitude and time duration. This difference in shock pulse spectra has sometimes been used as an explanation when electronic piece parts which have successfully passed a shock test on one shock machine fail on another machine of similar design.

The need for a mechanical shock pulse survey becomes immediately apparent when one considers the many problems which confront the military and commercial specification writer. In attempting to specify shock pulse criteria, he is confronted with various schools of thought on the subject each with different

basic concepts. To some extent he is also bound by past traditions in the methods of specifying a shock pulse and by shock machine histories which have been marked by both success and failure. All suitable specifications require that some agreeable compromise be reached. The specification must satisfy the user by insuring that he has obtained a reliable electronic piece part. It must also satisfy the manufacturer that he has produced an electronic piece part which is reliable for the application and has not become prohibitive in price because of the high initial cost of the shock test equipment. Thus, the method of specifying a mechanical shock test has an effect on final design application and cost of an electronic piece part.

At present, there are at least three methods of specifying mechanical shock tests. The first (1,2) stipulates the use of a specific mechanical shock machine. Advocates of this method feel that with strict adherence to detailed techniques of calibration, mounting, and maintenance, comparable tests can be performed between two shock machines of the same design. The strongest argument in favor of this method is that many piece parts evaluated in this manner have been used successfully in the field.

The second method (3) stipulates the specification of a specific shock pulse shape without reference to a specific shock machine. One advantage of this method is that it does not limit the tester to individual types of mechanical shock machines. However, it is not certain that one can assure the reliability of an electronic piece part which has been tested with a simple shock pulse shape, as most field environments are characterized by rather complex shock pulse shapes. Also, it is not certain whether comparison tests between two testers would be valid, since both tolerance limits and instrumentation used to measure the applied shock pulse could have a significant effect on the test results.

The third method (4,5) suggests the specification of three parameters: peak amplitude, shock pulse duration, and area under the shock pulse curve. This method leaves the means of producing the shock pulse to the discretion of the tester. However, rigid specification of instrumentation is required. Justification for this method is based on the fact that the energy available in the shock pulse is directly proportional to the terminal velocity of any acceleration-versus-time record. The area under the acceleration-versus-time record is, of course, also the terminal velocity and does not vary directly with shock pulse shape.

In summary, the three methods for specifying shock tests each have advantages and disadvantages.

1. Specifying an individual type of shock machine to test a piece part is supported by many years of laboratory experience and successful field applications; however, the method restricts the tester's ingenuity and does not allow him good control of the shock pulse experienced by the piece part.

2. Specification by shock pulse shape gives the tester more freedom in his choice and design of a shock machine but restricts the tester to the use of simple shock pulse shapes which are not characteristic of those experienced in the field.

3. The use of only peak amplitude, time duration and area under the shock pulse curve to specify a mechanical shock test is the method which is least restrictive to the tester. Some objections to this method are that the amplitude spectrum is given no consideration and it allows the manufacturer to select those shock pulse shapes which are least destructive to his products.

The differences in the methods for specifying shock tests involve the importance of the shock pulse shape. It is expected that by examining typical shock pulse shapes, information will be obtained which can aid in the specification of mechanical shock testing.

Experimental Procedure

Data Acquisition — The standard procedure used in the survey in making reproductions of the shock pulse shapes produced by each of the eight mechanical shock machines consisted first of calibrating all the instrumentation used. The most insensitive component in the instrumentation scheme was the piezoelectric mechanical-to-electrical transducer, the accelerometers. The devices used weighed 15 gm and were specified as having sensitivities of 1.18 and 1.29 mv/g with a ±0.05 mv/g deviation. However, calibration of the accelerometers by absolute measurements using interferometers and traveling microscope techniques showed a standard deviation of 10 percent from mean sensitivities of 1.11 and 0.93 mv/g, respectively. This indicated that, through natural aging or some unnoticed unknown environmental stress, the accelerometers had become less sensitive and less stable. It is interesting to note that this deviation was apparent throughout the frequency range investigated, 20 to 10,000

cps, indicating that the deviation was not localized in any internal band of the total frequency spectrum. This, at least, gave an assurance that no portion of the measured frequency spectrum was distorted.

The instrumentation was triggered by a small magnet attached to a moving part of each mechanical shock machine under investigation. The magnet was allowed to pass a stationary coil. This triggering method could be used since each of the shock machines has a member, e.g., pendulum, carriage, table, or cam, which is in motion just prior to the occurrence of the actual shock. Locating the stationary coil judiciously with respect to the magnet permitted close control of the leadtime and triggering voltage level. This triggering method also eliminated any retrace of the triggering pulse over the recorded shock pulse and any initial triggering transients. The triggering device, which was developed within the Techniques Branch Environmental Research Group, was quite simple to fabricate and use and provided a reliable, rapid, and versatile method of triggering the instrumentation.

Figure 1 shows the basic instrumentation scheme used to measure and record the shock pulse data taken in the survey. Prior to each shock event, the instrumentation sensitivity was tested by applying a calibrated 1-v, 1-kc sinusoidal wave to both the tape recorder and oscilloscope. During the shock event, two records were made: a photograph of the oscilloscope trace and a magnetic tape recording of the accelerometer output. The magnetic tape recording was checked by playing it back through the oscilloscope and comparing its trace with the trace photographed during the event.

Documentation — The photographic record produced during the described measuring procedure was for immediate use in performing a qualitative analysis and for use in a numerical analog computational technique using a specialized Fourier spectrum analyzer. The taped data were maintained for convenient storage and for conversion to digital data for later analysis with computers available within the USA-ECOM.

Various loading conditions were used, including changes in amplitude of drop height or angle of arc, and changes in table load. This was done to insure that the analysis was performed with data obtained on the linear portion of the individual shock machine's capability. In general, three conditions of filtering were used: no filter, 5,000 to 0.2 cps, and 1,000 to 0.2 cps. All analyses except one were performed using the 5,000- to 0.2-cps filtering condition. The lone exception was the controlled-motion shock machine. Because of its long pulse duration and vibration of the mounting table, this shock machine required the use of a 1,000- to 0.2-cps filter to produce a shock pulse shape suitable for analysis. The problem of undershoot was effectively resolved by using a filter with a lowest cutoff frequency of 0.2 cps (Fig. 2).

Method of Analysis

Quantitative Analysis — The method used to analyze the mechanical shock pulses produced by the mechanical shock machines surveyed consisted of a computation of a Fourier spectrum for each shock pulse. All numerical values of the time history of each shock pulse were normalized with respect to the peak
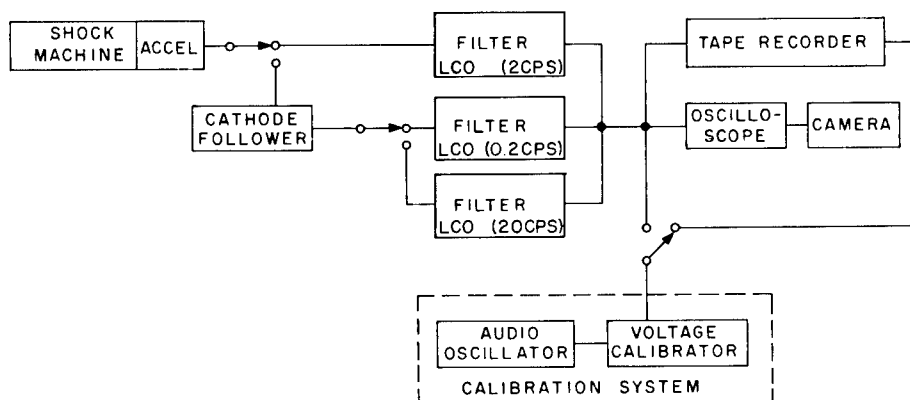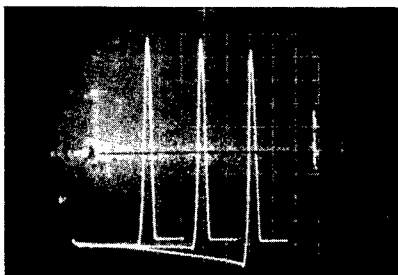

Fig. 1. Typical pulse recording system

Fig. 2. Undershoot effects at
low cutoff frequencies of 0.2,
2, and 20 cps, respectively

amplitude prior to computation of the Fourier spectrum. The amplitude components, $|\bar{F}(\omega)|$, of the Fourier spectrum were then normalized with respect to the zero frequency component, $|\bar{F}(0)|$, of the shock pulse or the net area under the shock pulse and converted to decibels by use of the following formula:

$$20 \log_{10} \frac{|\bar{F}(\omega)|}{|\bar{F}(0)|} .$$

The results were plotted against a normalized frequency scale on semilog paper in the form of a Bode diagram. (The Bode diagram enables the investigator to predict what effect the shock pulse produces on an electronic piece part if the transform of the piece part is known.) The electronic piece part response, $X(\omega)$, to any shock pulse is proportional to the product of the Fourier transform of the shock pulse, $\bar{F}(\omega)$, and the reciprocal of the electronic piece part transform, $G(\omega)$, or $\bar{F}(\omega) \, G(\omega) \approx X(\omega)$. There-fore, in general, when the amplitude component of the Fourier spectrum at a particular fre-quency is very small, only a small response is produced in the electronic piece part under test at that frequency. This is especially true in the practical sense where, because of damping, sustained oscillations of the electronic piece part from a single mechanical shock are not possible.

Computation of the Fourier spectrum was accomplished with the aid of a special-purpose analog computer, Procedyne Associates Ana-lyzer M-101A (6). This computer is designed to evaluate numerically the Fourier integral of any shock pulse shape. The integral evaluated was

$$\bar{F}(\omega) = \int_0^T f(t) \, [\cos \omega t - j \sin \omega t] \, dt$$

$$\approx \sum_{n=0}^{32} f(n\Delta t) \, (\cos \omega n\Delta t - j \sin \omega n\Delta t) ,$$

where $\Delta t = T/32$. The function $f(t)$ is the re-sponse of the instrumentation to the input shock pulse. This response gives the best possible reproduction of the input shock pulse which is being transmitted to the test specimen during an actual test. Introduction of function $f(t)$ into the computer was accomplished by a photograph of the shock pulse shape as it appeared on the screen of the oscilloscope. The trace on the photograph was then transferred to a function generator which approximated the shock pulse shape by a best-fit technique using 32 straight-line segments.
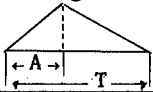
The numerical calculation was repeated each time a new frequency point was chosen. Depending on the smoothness of the Bode dia-gram, from 15 to 25 discrete frequencies were plotted for each shock pulse over a normalized frequency range of 0 to 10.

Readouts on Analyzer M-101A were ac-complished with a polar coordinate recorder. The readout plots amplitude versus phase angle on polar coordinate paper. This type of plot is commonly known as a Nyquist diagram. Ana-lyzer M-101A uses a normalized frequency scale where $\omega_k = T\omega/\pi = \omega/\omega_0$ and little restric-tion is placed on the frequency scale by the computer. The 10 ω_0 upper limit was chosen because the amplitudes of all Fourier compo-nents above 10 ω_0 are at least 20 db below the zero reference level.

The final steps consisted of converting the Fourier component amplitudes to decibels and plotting a Bode diagram for the shock pulse from each mechanical shock machine surveyed. Bode diagrams for the half-sinusoidal, triangu-lar, and square pulses were also derived (see appendix) for purposes of comparison.

Qualitative Analysis — A qualitative analy-sis of Bode diagrams of the shock pulse shapes of the individual mechanical shock machines was performed by comparison of these pulse shapes with the half-sinusoidal, triangular, and square pulse shapes. The pertinent

213

TABLE 2
Bode Diagram Characteristics of Mechanical Shock Pulses

Mechanical Shock Pulse	Relative Minimum		Maximum ω/ω_0			Av. Slope (db/octave)			
	ω/ω_0	Level (db)	-5 db Level	-10 db Level	-20 db Level	0.5 to 1	1 to 2	2 to 4	4 to 8
180-JAN	3	-15	2.8	4.2	6	-0.5	0.5	NA[a]	18
	9	-32							
254-JAN	6	-40	1.2	2	3	-1	8.6	15	NA[a]
	8	-∞							
123-JAN	None	None	2.2	2.4	2.5	-2	-2	-15	-9
SRDE-RSC-11 (British Bump)	3.2	-32.2	1.5	2	2.5	-1.6	-4	-18	NA[a]
	4.8	-42.2							
	8	-39.5							
	10	-38.3							
JAN-S-44	1.6	-35	0.7	1.1	1.3	-6.5	-15	NA[a]	NA[a]
	2.4	-∞							
	3.4	-50.3							
	6.4	-39.1							
Barry 20VI	2.6	-30	1	1.5	2.2	-2.4	-14	NA[a]	NA[a]
	6	-50							
	7.8	-37							
Barry Varipulse (modified Type 15575)	3.5	-38	1	1.5	1.7	-2.5	-15	NA[a]	NA[a]
	5	-37							
	7.2	-40							
Controlled motion	3.6	-8.7	1.6	3	4.7	+2.5	NA[a]	NA[a]	NA[a]
	7.5	-∞							
Half sinusoidal	3	-∞	1.5	2	2.3	-2	-8	NA[a]	NA[a]
	5	-∞							
	7	-∞							
	9	-∞							
Triangular m = T/A, n = 1,2,3,...	2nm	-∞	1.5	2.3	3 to 7	-1 to -4	-4 to -6	-4 to -6	NA[a]
Square n = 1,2,3,...	2n	-∞	1.2	1.5	3.3	-3	NA[a]	NA[a]	NA[a]

[a]NA = Excessive fluctuation within octave makes average readings meaningless.

characteristics of each Bode diagram are given in Table 2. The Bode diagram of each mechanical shock machine pulse is discussed qualitatively in the following section of this report.

RESULTS*

180-JAN (Navy Flyweight) Shock Machine

Shock Pulse:

Shape	as shown in Fig. 3
Nominal time duration of major positive pulse	0.60 ms
Peak amplitude	1150 g
Area under major positive pulse	0.442 g/sec (Fig. 4)

Discussion — From Fig. 4, the Bode diagram of the 180-JAN shock machine pulse, it

─────────
*On oscilloscope pictures, t is from right to left.
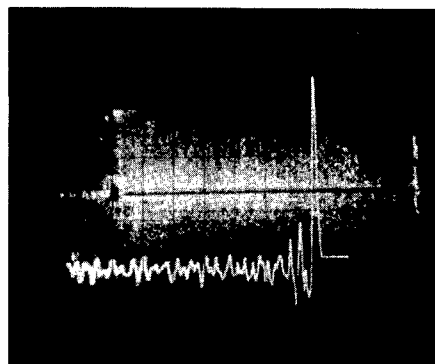
Fig. 3. 180-JAN shock pulse shape

can be seen that the slope of the Bode diagram changes sharply at $\omega/\omega_0 = 2.5$ ($\omega_0 = \pi/T$, T = duration of pulse), such that the amplitude spectrum above $\omega/\omega_0 = 3$ is located mainly below the 10-db level. Above $\omega/\omega_0 = 6$, the amplitude spectrum is below the 20-db level. The spectrum above $\omega/\omega_0 = 6$ can be ignored because of its small amplitude. Comparison with the Bode diagrams of the half-sinusoidal, triangular, and square shock pulses does not yield any
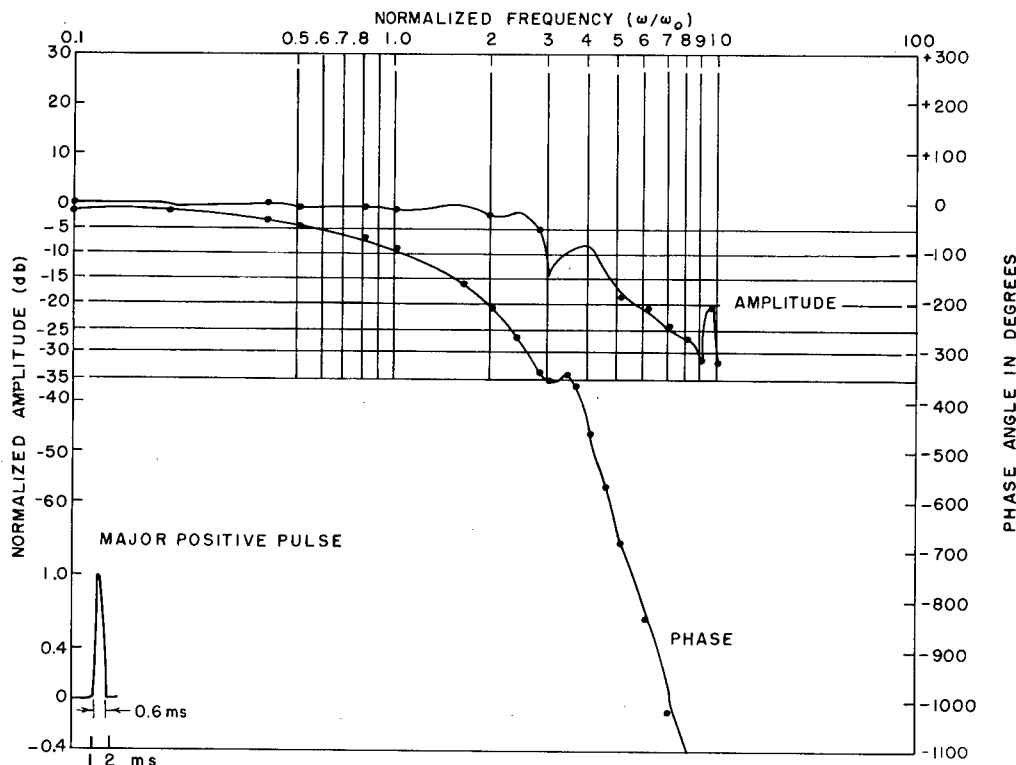
Fig. 4. Typical Bode diagram of 180-JAN shock machine pulse (major positive pulse)

215

apparent similarities other than the general decrease of the amplitude at the higher frequencies.

For the 180-JAN shock pulse to be most effective, it should be applied to an electronic piece part whose natural frequency is less than 5.1×10^3 cps, or $\omega/\omega_0 = 6$.

254-JAN (Drop Tester)
    Shock Machine

    Shock Pulse:

Shape	as shown in Fig. 5
Nominal time duration of major positive pulse	0.75 ms
Peak amplitude	480 g
Area under major positive pulse	0.204 g/sec (Fig. 6)

Discussion — Figure 6 shows that the amplitude spectrum falls off rapidly above $\omega/\omega_0 = 1$.
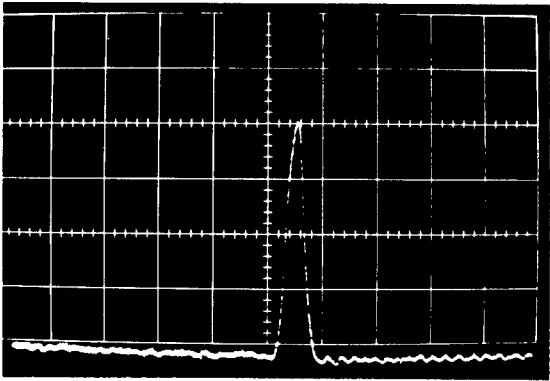
Fig. 5. 254-JAN shock pulse shape

Fluctuations present at ω/ω_0 higher than 2 can be ignored as they occur well below the 30-db level. The diagram is similar to Bode diagrams of the triangular shock pulses.

The 254-JAN shock pulse is most effective when applied to an electronic piece part whose natural frequency is below 2,000 cps, or $\omega/\omega_0 = 3$.
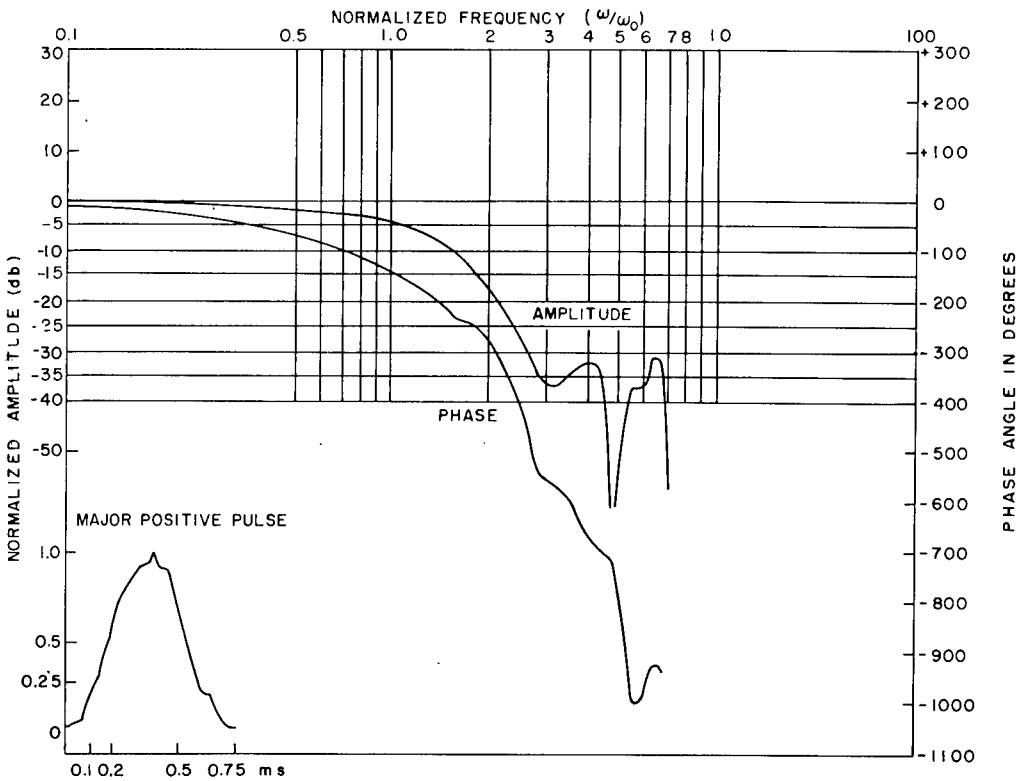
Fig. 6. Typical Bode diagram of 254-JAN shock machine pulse

123-JAN (Pendulum-Type)
Shock Machine

Shock Pulse:

Shape | as shown in Fig. 7

Nominal time duration of major positive pulse | 4.75 ms
Peak amplitude | 90 g
Area under major positive pulse | 0.222 g/sec (Fig. 8)

Discussion — Figure 8 shows that the frequency spectrum above $\omega/\omega_0 = 3$ is below the 20-db level. The diagram is similar to those associated with triangular shock pulses of the sawtooth variety.

The most effective use of the shock produced by the 123-JAN shock machine would be on electronic piece parts whose major response lay below 330 cps, or $\omega/\omega_0 = 3$.
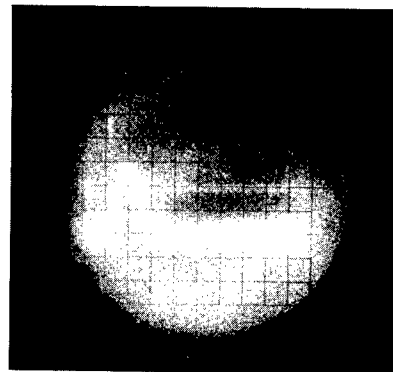
Fig. 7. 123-JAN shock pulse shape
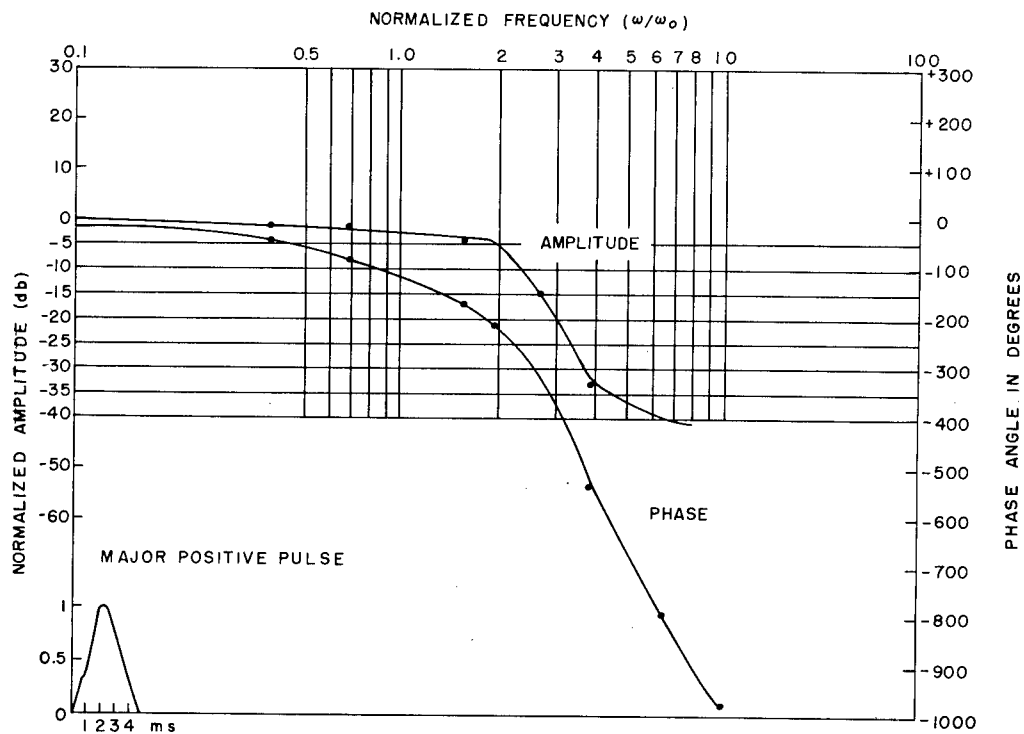
Fig. 8. Typical Bode diagram of 123-JAN shock machine pulse

SRDE-RSC-11 (British Bump)
Shock Machine

Shock Pulse:

Shape   as shown in
Fig. 9

Nominal time duration of
major positive pulse   5.00 ms
Peak amplitude   40 g
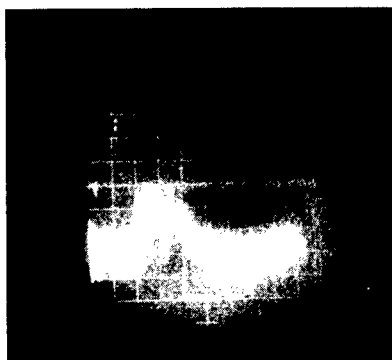Area under major posi-
tive pulse   0.098 g/sec
(Fig. 10)

Discussion — Examination of the Bode dia-
gram of the shock pulse of the SRDE-RSC-11
shock machine (Fig. 10) shows that the ampli-
tude above ω/ω_0 = 3 lies below the 25-db level.
The diagram fluctuations at the higher frequen-
cies show some similarities to the half-
sinusoidal pulse.

The effective portion of the frequency
spectrum lies below 300 cps, or ω/ω_0 = 3. In
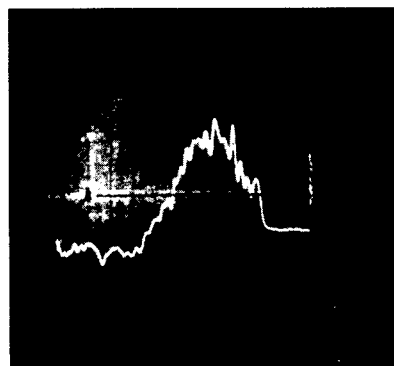
Fig. 9. SRDE-RSC-11
shock pulse shape

view of this, one should not test electronic piece
parts which have characteristic frequencies
above 300 cps with this machine.
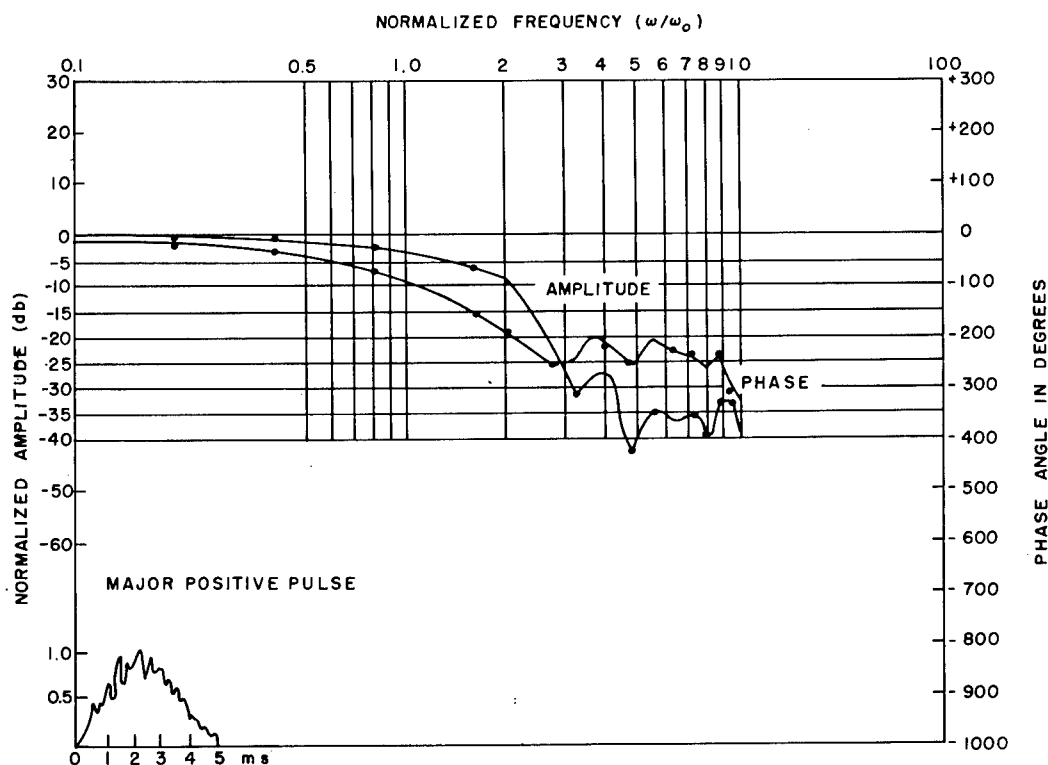
Fig. 10. Typical Bode diagram of SRDE-RSC-11
shock machine pulse (British Bump)

JAN-S-44 (Drop Tester)
  Shock Machine

  Shock Pulse

      Shape   as shown in
                                        Fig. 11
      Nominal time duration of
          major positive pulse   5.50 ms
      Peak amplitude   85 g
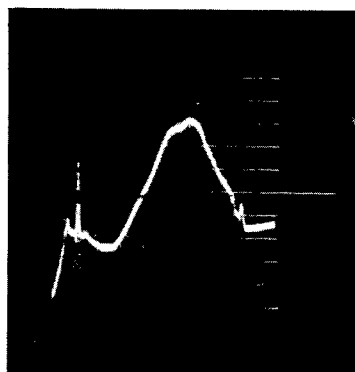   Area under major posi-
          tive pulse   0.270 g/sec
                                        (Fig. 12)
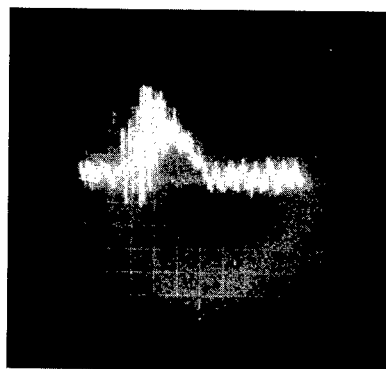
Fig. 11. JAN-S-44
shock pulse shape

      Discussion — Figure 12 shows that above
$\omega/\omega_0 = 1.3$, the amplitude is completely below
the 20-db level. Comparison of the JAN-S-44
shock pulse with the derived Bode diagrams of
half-sinusoidal, triangular, and square pulses
does not yield any significant similarities with
these pulse shapes.

      The JAN-S-44, to be effective, should be
limited to investigations where the frequency
range of interest is not above 117 cps, or
$\omega/\omega_0 = 1.3$.
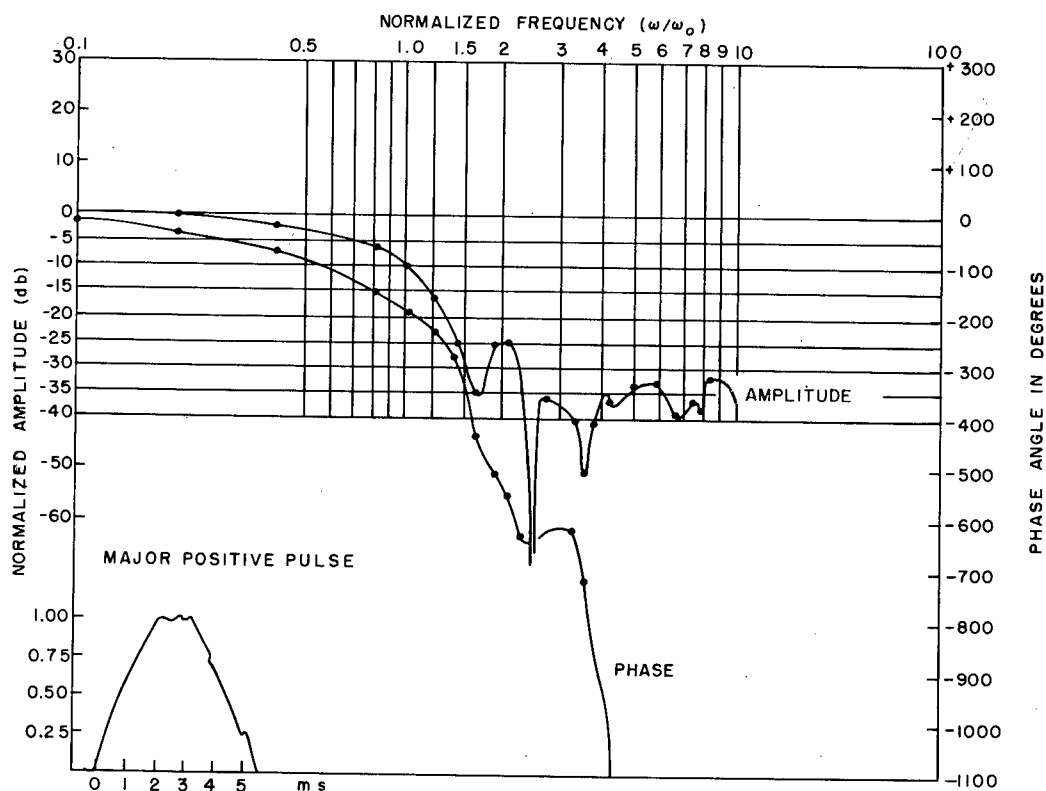
Fig. 12. Typical Bode diagram of JAN-S-44 shock machine pulse

Barry 20VI (Sand Drop)
  Shock Machine*

  Shock Pulse:

Shape	as shown in Fig. 13
Nominal time duration of major positive pulse	10.00 ms
Peak amplitude	70 g
Area under major positive pulse	0.246 g/sec (Fig. 14)

Discussion — The Bode diagram of the shock produced by the Barry 20VI shock machine (Fig. 14) shows that the amplitude of the spectrum above $\omega/\omega_0 = 2$ lies well below the

---

*This machine was converted by personnel of the Techniques Branch, Electronic Components Laboratory, USAECOM. The modification consisted of isolating the table hook from the electric release mechanism. This reduced any shock pulses which might be introduced to the table by the release solenoid.

Fig. 13. Barry 20VI
shock pulse shape

20-db level. Comparison with the Bode diagrams of the standard pulse shapes does not reveal any apparent similarities, aside from decreasing amplitude with increasing frequency.

The effective portion of the amplitude spectrum of the Barry 20VI shock machine lies between 0 and 100 cps.
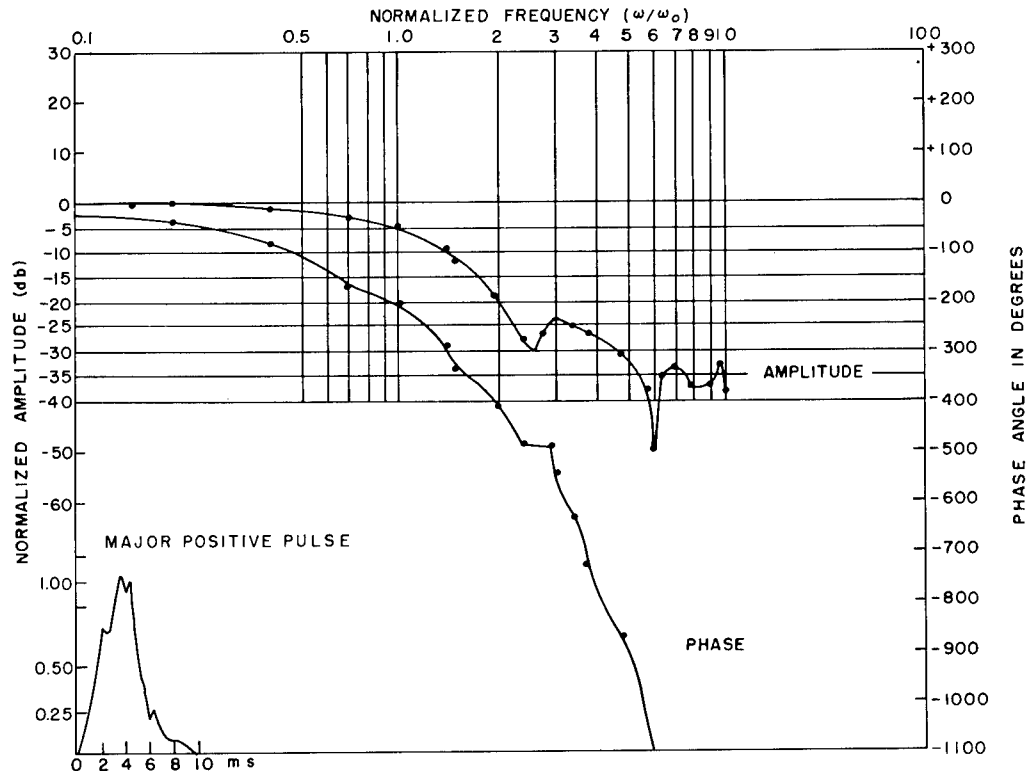
Fig. 14. Typical Bode diagram of Barry 20VI shock machine pulse

Barry Varipulse (Modified Type
15575) Shock Machine

Shock Pulse:

Shape	as shown in Fig. 15
Nominal time duration of major positive pulse	11.00 ms
Peak amplitude	62 g
Area under major positive pulse	0.285 g/sec (Fig. 16)

Discussion — The shock produced by the
Barry Varipulse (modified Type 15575) shock
machine yields a Bode diagram (Fig. 16), in
which the amplitude spectrum above $\omega/\omega_0 = 2$
lies below the 20-db level. Comparison with
the Bode diagrams of the half-sinusoidal, tri-
angular, and square shock pulses does not show
any easily discernible similarities.

Fig. 15. Barry Varipulse
(modified Type 15575)
shock pulse shape

As the predominant portion of the spectrum
energy lies between 0 and 90 cps, the Barry
Varipulse (modified Type 15575) shock machine
is primarily useful when the frequency range
of interest is below 90 cps.
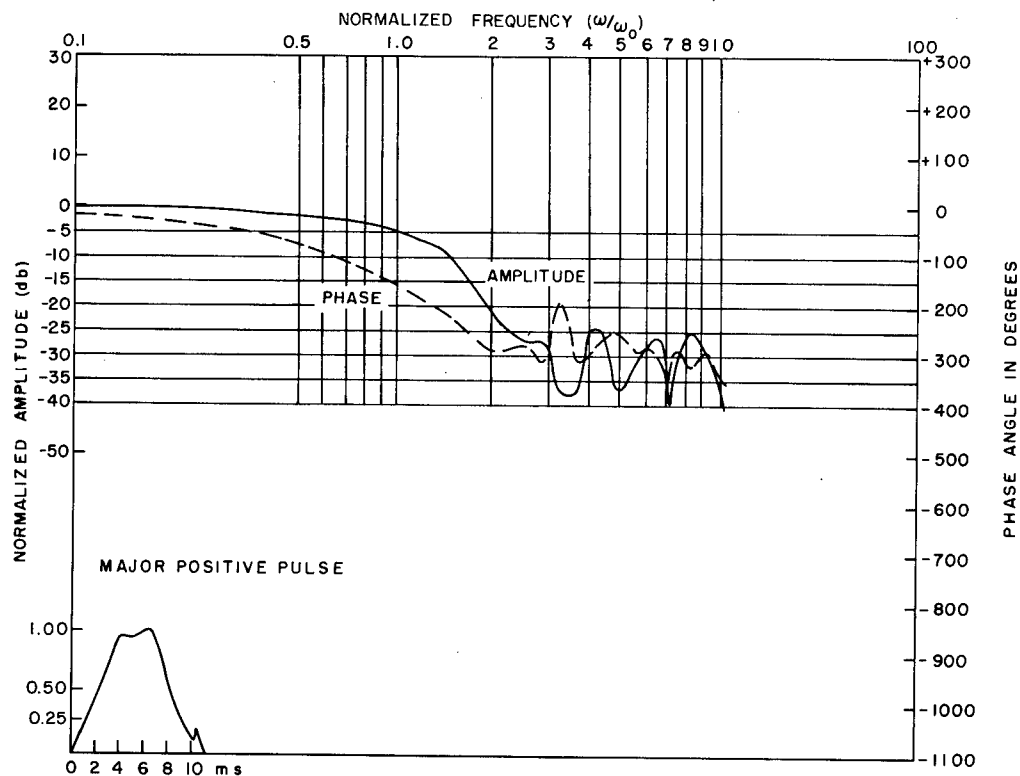
Fig. 16. Typical Bode diagram of Barry Varipulse
(modified Type 15575) shock machine pulse

221

Controlled-Motion Shock Machine

Shock Pulse:

Shape	as shown in Fig. 17
Nominal time duration of major positive pulse	32.00 ms
Peak amplitude	45 g
Area under major positive pulse	0.300 g/sec (Fig. 18)

Discussion — In the Bode diagram of the shock produced by the controlled-motion shock machine (Fig. 18), all the amplitudes were further normalized to $\omega/\omega_0 = 1.6$ so that the complete spectrum would lie below the 0-db level.

The spectrum has components greater than the zero-frequency component, -12.5 db, in the range $\omega/\omega_0 = 0.1$ to 3.2. Above $\omega/\omega_0 = 3.2$, the spectrum falls off very rapidly and, except for the interval between $\omega/\omega_0 = 3.8$ to 4.7, the spectrum remains below the -20-db level. This indicates that the pulse energy is concentrated
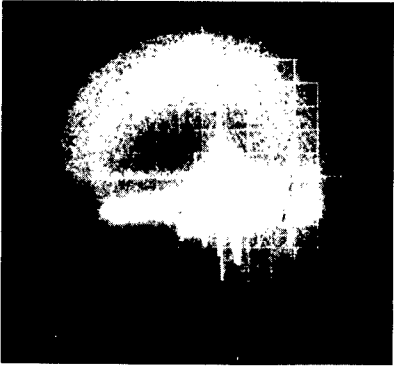
Fig. 17. Controlled-motion shock pulse shape

in frequencies below 50 cps. The effectiveness of the controlled-motion shock machine is restricted to the frequency band from 0 to 50 cps. Unlike other shock machines investigated, this machine does not exhibit decreasing amplitude with increasing frequency below 50 cps. Above 50 cps, however, the amplitude does decrease rapidly with increasing frequency.
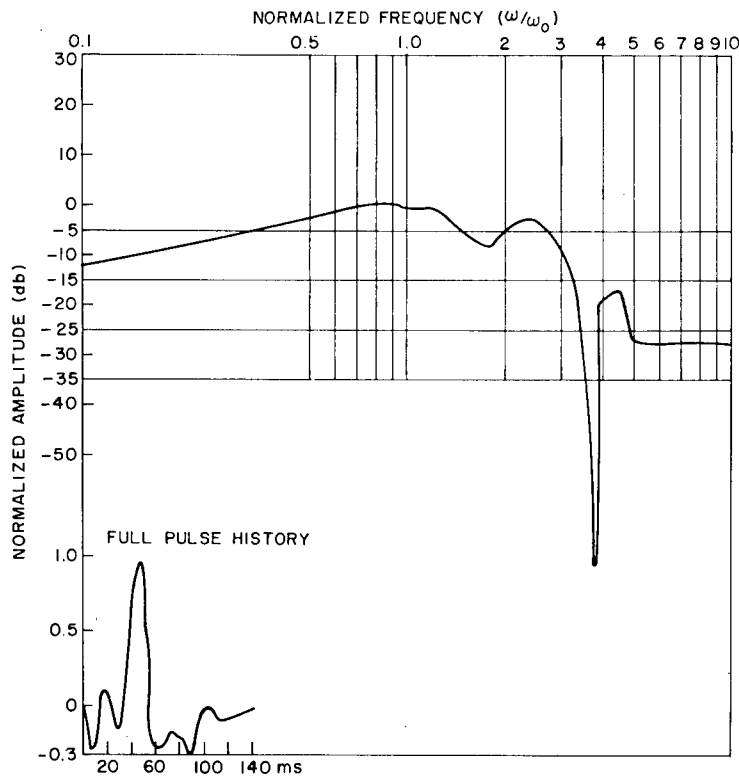
Fig. 18. Typical Bode diagram of controlled-motion shock machine pulse (full pulse history)

CONCLUSIONS

The fact most evident from inspection of the Bode diagrams of the eight mechanical shock machines is that, with two exceptions, the 180-JAN and the controlled-motion shock machines, the amplitude level above $\omega/\omega_0 = 3$ of any shock pulse is negligible. In all other shock pulses, the amplitude level above $\omega/\omega_0 = 3$ is at least 20 db below zero frequency level. The reason for the sustained amplitude level, in the case of the controlled-motion shock machine, is that the shock pulse time used to normalize the frequency scale was approximately 100 ms. The major positive peak of the controlled-motion shock pulse has a duration of 32 ms. If this time duration were used to normalize the frequency scale, the $\omega/\omega_0 = 3$ point would appear at approximately 45 cps. This point is well below the 20-db level. It seems safe to say that, for all practical purposes, mechanical shock pulses will not show any significant components above the third harmonic unless the shock pulse has an extremely high peak amplitude with respect to its duration, e.g., the 180-JAN shock machine pulse. It can be said that the most effective means of mechanically shock testing electronic piece parts with high-frequency characteristics is to subject them to short-duration high-peak-amplitude shock pulses. The shock pulse selected should have a duration less than $1/2 \ f_0$, where f_0 is the characteristic frequency of the electronic piece part being evaluated.

With respect to standard shock pulse shapes, the appendix shows that the different shock pulse shapes (half-sinusoidal, triangular, and square) have similar Bode diagrams. There are no significant Fourier components above the fourth harmonic, or $4 \ \omega/\omega_0$ frequency. The greatest difference between shock pulses before $4 \ \omega/\omega_0$ frequency, is the manner in which they fall off. The half-sinusoidal, triangular,

and square shock pulses remain fairly constant up to 1 ω/ω_0 frequency, after which the half-sinusoidal and square shock pulses fall off more rapidly than the triangular shock pulse. The triangular shock pulse starts its falloff immediately, but it has a more gradual negative slope. The radical fluctuations in the amplitude spectrum of the half-sinusoidal and square shock pulses which occur above the $\omega/\omega_0 = 2$ point can be ignored as they usually occur below the 15-db level.

From the above, it is apparent that mechanical shock pulse shapes obtainable in practice do not have significant amplitude levels at the higher frequencies. For the greater majority of pulses, the amplitude spectrum above $\omega/\omega_0 = 3$ can be neglected. For all practical purposes, rigid specification of the shock pulse shape is not necessary. The important parameters for shock specification are the peak amplitude, the shock pulse duration, and the area under the shock pulse curve. These three parameters restrict the shock pulse shape sufficiently to insure that any differences in the Fourier spectrum become negligible.

ACKNOWLEDGMENTS

REFERENCES

1. Military Specification MIL-E-1E, "Electron Tubes, General Specification For," Dec. 20, 1963, Appendix E, "Test Conditions and Methods," Method 1041, "Shock"

2. Military Standard MIL-STD-202C, "Test Methods for Electronic and Electrical Component Parts," Sept. 12, 1963, Method 205C, "Shock, Medium Impact" and Method 207A, "High-Impact Shock"

3. Military Standard MIL-STD-810A(USAF), "Environmental Test Methods for Aerospace and Ground Equipment," June 23, 1964, Method 516.1, "Shock"

4. J. T. Muller, "Shock in Dynamic Systems," Sperry Eng. Review (July-Aug. 1954), pp. 9-12

5. J. T. Muller, "Notes on Shock Specifications for Electron Tubes," J T-15 Committee on Environments for Electron Tubes, Doc. 15-121, Sec. 2, p. 7, Feb. 12, 1962

6. K. Staffin and R. Staffin, "The Procedyne Analyzer M-101A," Procedyne Assoc., New Brunswick, N. J., 1962
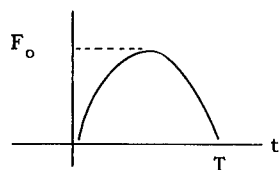
7. S. J. Mason and H. J. Zimmerman, Electronic Circuits, Signals, and Systems (John Wiley and Sons, New York), 1960, Ch. 6

8. S. Rubin, "Concepts in Shock Data Analysis," Ch. 23, Vol. 2, Shock and Vibration Handbook (C. M. Harris and C. E. Crede, Ed.) (McGraw-Hill, New York), 1961

Appendix

FOURIER SPECTRA OF STANDARD SHOCK PULSE SHAPES

Half-Sinusoidal Shock Pulse (see Table A-1 and Fig. A-1)

1. $f(t) = t < 0; \quad t > T$

$f(t) = F_0 \sin \omega_0 t; \quad 0 < t < T$

2. $\overline{F}(\omega) = F_0 \int_0^T \sin \omega_0 t \; e^{-j\omega t} dt$

3. $\overline{F}(\omega) = F_0 \int_0^T \left[\left(e^{j(\omega_0 - \omega)t} - e^{-j(\omega_0 + \omega)t} \right) / 2j \right] dt$

4. $\overline{F}(\omega) = F_0 \omega_0 (e^{-j\omega t} + 1)/(\omega_0^2 - \omega^2)$

5. $\overline{F}(\omega) = F_0 \left(\cos \pi\omega/\omega_0 - j \sin \pi\omega/\omega_0 + 1 \right)/\omega_0 \left[1 - (\omega/\omega_0)^2 \right]$
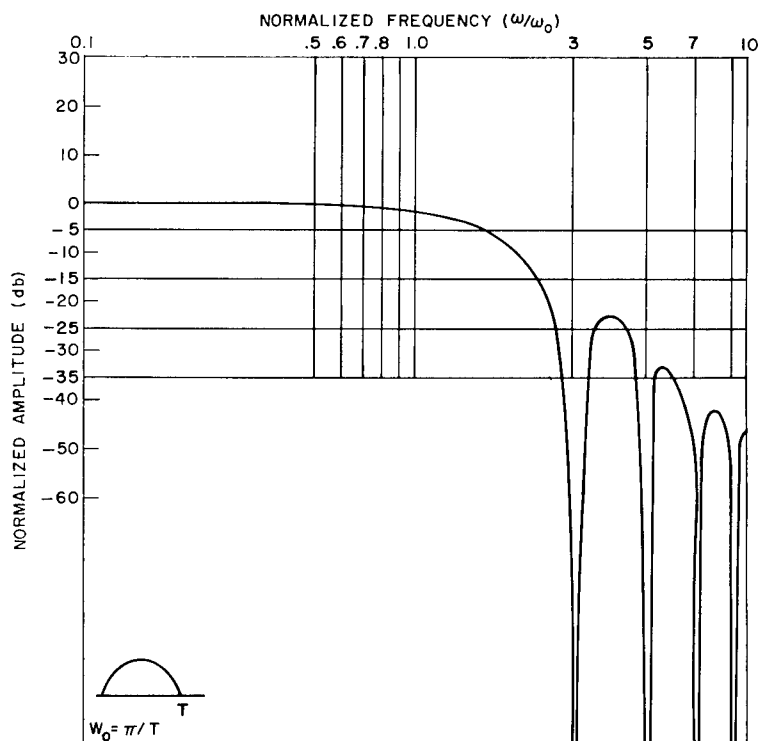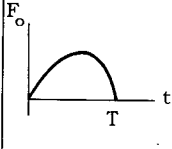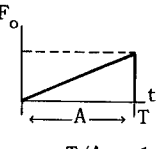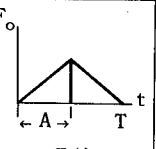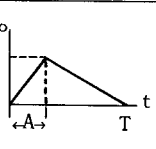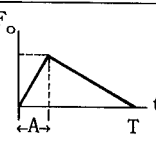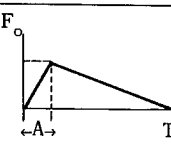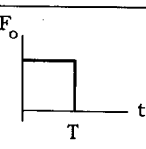

Fig. A-1. Bode diagram of half-sinusoidal shock pulse

TABLE A-1
Bode Diagram Data for Derived Shock Pulses

Half Sinusoidal		Triangular										Square	
		m = T/A = 1		m = T/A = 2		m = T/A = 3		m = T/A = 4		m = T/A = 6			
ω/ω_0	-db	ω/ω_0	-db	ω/ω_0	-db	ω/ω_0	-db	ω/ω_0	-db	ω/ω_0	-db	ω/ω_0	-db
0.0	0.00	0.0	0.00	0.0	0.00	0.0	0.00	0.00	0.00	0.0	0.00	0.00	0.0
0.1	0.09	0.1	0.08	0.1	0.09	0.1	0.03	0.10	0.01	0.1	0.166	0.33	0.4
0.3	0.17	0.4	0.40	0.4	0.26	0.5	0.54	0.50	0.50	0.2	0.17	0.50	0.9
0.5	0.54	0.8	1.56	0.8	1.20	0.75	0.92	0.75	1.10	0.6	0.86	0.66	1.4
0.7	1.12	1.0	2.45	1.0	1.83	1.0	1.89	1.00	4.66	1.0	2.00	1.00	3.9
0.9	1.83	1.4	4.90	1.4	3.60	1.5	4.36	1.33	3.71	1.5	4.90	1.33	7.4
1.0	2.05	2.0	10.03	2.0	7.75	2.0	8.09	2.0	8.40	2.0	8.74	1.50	10.4
1.2	3.05	2.5	13.00	2.5	13.55	2.5	13.00	2.7	14.00	2.5	13.70	1.66	14.3
1.6	5.68	3.0	13.20	3.0	20.80	3.0	17.30	3.0	15.40	3.0	12.80	2.0	∞
1.8	7.51	3.5	14.06	3.5	33.55	3.5	18.80	3.7	21.40	3.5	14.50	2.5	14.7
2.0	9.63	4.0	16.00	4.0	∞	4.0	20.20	4.0	17.40	4.0	14.80	3.0	13.5
2.5	17.06	5.0	17.80	5.0	30.50	5.0	29.80	5.0	23.00	5.0	20.54	3.5	18.0
3.0	∞	6.0	19.60	6.0	29.60	6.0	∞	6.0	27.00	6.0	23.70	4.0	∞
3.5	24.40	7.0	20.80	7.0	35.80	7.0	35.60	7.0	38.40	7.0	25.60	5.0	18.0
4.0	23.05	8.0	22.00	8.0	∞	8.0	32.20	8.0	∞	8.0	28.00	6.0	∞
4.5	27.08	9.0	23.10	9.0	40.00	9.0	36.40	9.0	43.00	9.0	33.00	7.0	20.5
5.0	∞	10.0	24.00	10.0	36.00	10.0	36.00	10.0	36.40	10.0	36.40	8.0	∞
6.0	37.00											9.0	22.7
7.0	∞											10.0	∞
8.0	42.00												
9.0	∞												
10.0	46.00												

6. $R\overline{F}(\omega/\omega_0) = F_0(\cos \pi\omega/\omega_0 + 1)/\omega_0 [1 - (\omega/\omega_0)^2]$
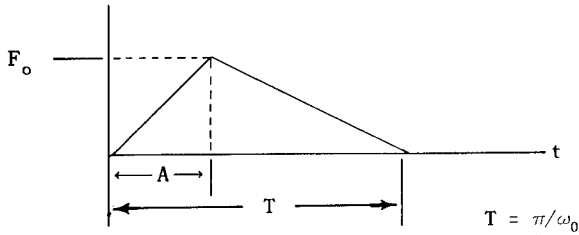
$R\overline{F}(1) = 0$

7. $I\overline{F}(\omega/\omega_0) = -F_0 \sin \pi\omega/\omega_0/\omega_0 [1 - (\omega/\omega_0)^2]$

$I\overline{F}(1) = -F_0\pi/2\omega_0$

8. $|\overline{F}(\omega/\omega_0)| = |F_0 2 \cos \pi\omega/2\omega_0/\omega_0 [1 - (\omega/\omega_0)^2]|$

Triangular Shock Pulse (see Table A-1 and Fig. A-2)

$T = \pi/\omega_0$

1. $f(t) = F_0 t/A; \quad 0 < t < A$

$f(t) = F_0(T - t)/(T - A); \quad A < t < T$

$f(t) = 0; \quad t < 0, \quad t < T$

2. $\overline{F}(\omega) = F_0/A \int_0^A t e^{-j\omega t} dt$

$\quad + F_0/(T - A) \int_0^A (T - t) e^{-j\omega t} dt$

3. $\overline{F}(\omega) = F_0(Te^{-j\omega A} - Ae^{-j\omega T} - T + A)/\omega^2 A(T - A)$

4. $R\overline{F}(\omega) = F_0(T \cos \omega A - A \cos \omega T + A - T/\omega^2 A(T - A)$

5. $I\overline{F}(\omega) = F_0(A \sin \omega T - T \sin \omega A) \omega^2 A(T - A)$

6. $|\overline{F}(\omega)| = F_0 \sqrt{2} [T^2 - TA + A^2 - TA \cos \omega(T - A)$

$\quad + (T - A)(A \cos \omega T$

$\quad - T \cos \omega A)]^{1/2}/\omega^2 A(T - A)$

If we let $T/A = m$ or $m/(m - 1)$ and substitute in Step 6, we get the following for $|\overline{F}(\omega)|$:

7. $|\overline{F}(\omega)| = F_0 \sqrt{2} m\omega_0 [m^2 - m + 1$

$\quad - (m^2 - m) \cos \pi\omega/m\omega_0$

$\quad + (m - 1) \cos \pi\omega/\omega_0$

$\quad - m \cos \pi\omega m - 1/m\omega_0]^{1/2}/\pi\omega^2(m - 1)$

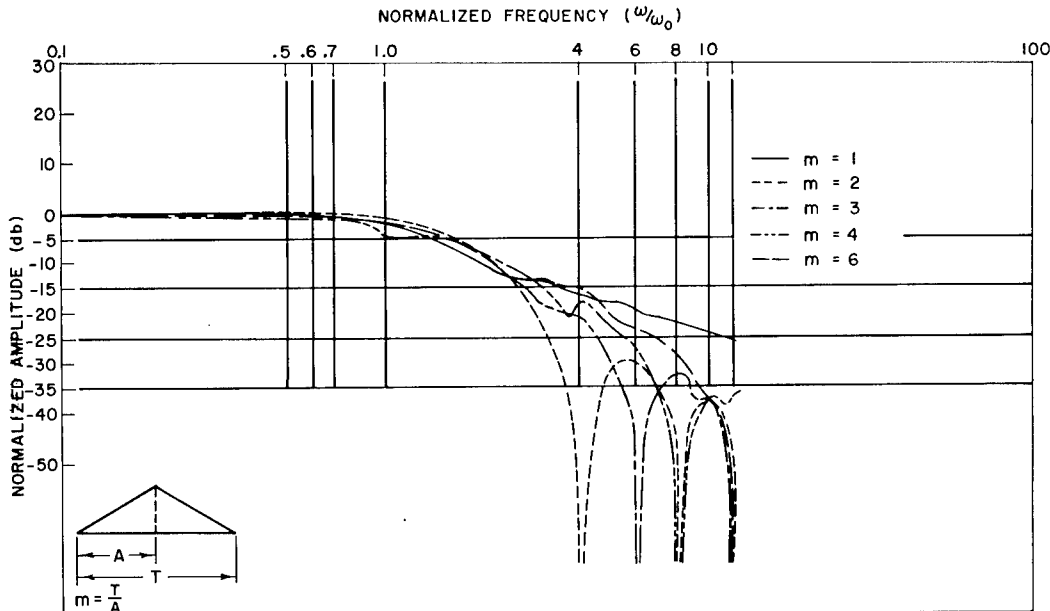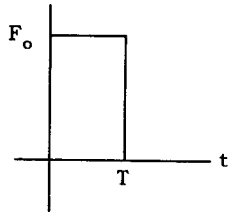

Fig. A-2. Bode diagram (typical) of triangular shock pulses

226

8. $|\overline{F}(0)| = F_0 T/2$

It can be seen that a triangular pulse will have zero amplitude when $(m-1)\,\omega/m\omega_0$, $\omega/\omega_0 m$, and ω/ω_0 all equal $2n$ where $n = 1, 2, 3, 4, \ldots$.

Square Shock Pulse (see Table A-1 and Fig. A-3)

1. $f(t) = F_0 ;\quad 0 < t < T$

$f(t) = 0 ;\quad t < 0 ,\quad t > T$

2. $\overline{F}(\omega) = F_0 \displaystyle\int_0^T e^{-j\omega t}\,dt = F_0 j\,(e^{-j\omega T} - 1)/\omega$

3. $F(\omega) = F_0\,[\sin \omega T + j(\cos \omega T - 1)]/\omega$

4. $R\overline{F}(\omega/\omega_0) = F_0\,\sin \pi\omega/\omega_0 /\omega$

5. $I\overline{F}(\omega/\omega_0) = F_0(\cos \pi\omega/\omega_0 - 1)/\omega$

$T = \pi/\omega_0$

6. $|F(\omega/\omega_0)| = 2F_0\,\sin \pi\omega/2\omega_0 ;\ |\overline{F}(0)| = F_0\pi/\omega_0$
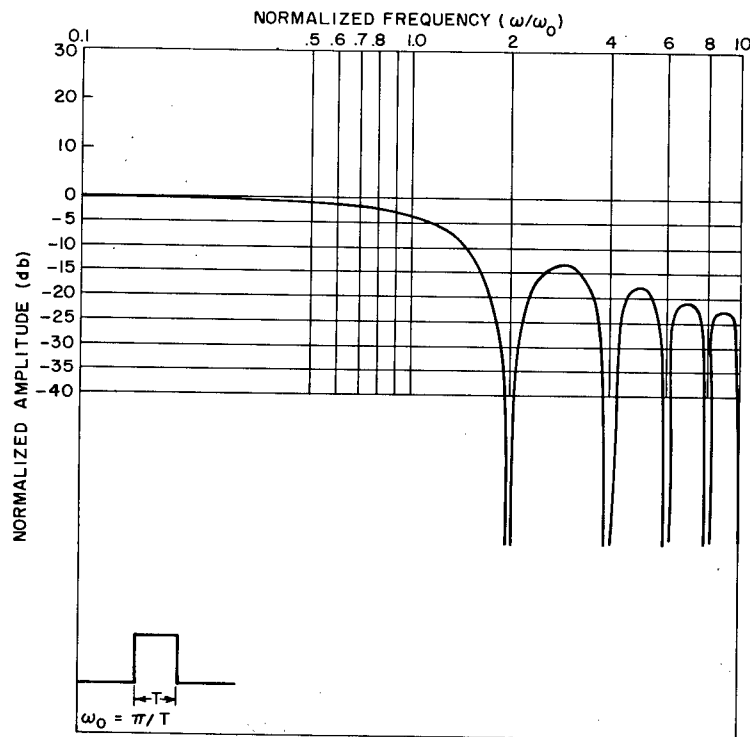

Fig. A-3. Bode diagram of square shock pulse

*   *   *

PROXIMITY SPECTRUM—A NEW MEANS OF

EVALUATING SHOCK MOTIONS

Edward H. Schell
Air Force Flight Dynamics Laboratory
Wright-Patterson AFB, Ohio

The concept of a "proximity criterion" was developed in a paper pre-
sented at the 34th Shock and Vibration Symposium. It was suggested
that this concept could be expanded to a "proximity spectrum" which
would provide useful insights into the effects of shock motions not ob-
tainable from either the Fourier spectrum or the shock spectrum. The
proximity criterion indicates the effects of shock on a simple idealized
equipment consisting of two uncoupled linear single degree of freedom
systems mounted to a common rigid base. When the base undergoes a
shock motion, the distance between the two masses varies. The change
in the distance between these two systems is called the proximity cri-
terion. In some types of failure (e.g., electrical malfunctions and colli-
sion of parts), this criterion is important.

This paper develops the proximity criterion into the proximity spec-
trum by varying the natural frequencies of the two systems so that data
can be obtained for spectral plots. Digital computation is employed for
obtaining data from a mathematical model.

The technique provides means of comparing different shock motions in
terms of their effects on a standard equipment. Proximity spectra of
the half-sine, terminal-peak sawtooth, and rectangular shock motions
are presented.

INTRODUCTION

One of the most important characteristics
of a shock is its ability to excite all modes of
vibration of a piece of equipment. Because of
this feature, several types of equipment failure
can occur as a result of the dynamic interaction
of two or more response modes of the equipment.

These failures fall into two general cate-
gories, based on the nature of the equipment.
The first of these is mechanical, and the fail-
ures are directly attributable to increased or
decreased friction or interference between
parts. The second of these categories is elec-
tromagnetic, in which the direct cause of failure
may be changes in dielectric strength, loss of
insulation resistance, and variations in magnetic
and electrostatic field strengths. These, in turn,
cause insulation breakdowns, changes in capaci-
tance, inductance, mutual inductance, current,
etc. A large number of malfunctions or perma-
nent failures can result in either of these
categories.

The shock spectrum, of course, indicates
that many modes of vibration are excited. It is
deficient in that it does not indicate the possi-
bilities of modal interactions.

This paper, coupled with a previous paper
(1), develops the concept of a "proximity spec-
trum" which gives some insight into the ability
of an excitation to cause these types of failures
in a simple model equipment. To rephrase this,
the proximity spectrum is a means of analyzing
a shock motion to determine its potential for
producing simultaneous frequency responses or
modal interactions.

Examples of proximity spectra are pre-
sented for several commonly applied design and
test waveforms.

The application of this concept to several
shock problems is discussed. The first appli-
cation shows that better simulation waveforms
for the environment can be derived. The second
discusses the possibility of simulating random

vibration environments on an inexpensive shock machine. The third discusses the possibility of eliminating certain shock tests when the random vibration test is considered to be more severe. Finally, a direct design method is given to show the application of the spectrum to the design of simple systems.

These discussions will also relate the applications to improvements in design, reliability, and significant monetary savings.

NOMENCLATURE

a,b,C   Constants

c   Viscous damping coefficient

D   Proximity or distance between masses of Fig. 1 at any time ($D_{st} + \Delta$)

D_{st} Static value of D; i.e., value when masses are at rest

e   Base of Napierian logarithms (2.7183)

f   Cyclic frequency

H   Subscript meaning homogeneous solution

i $\sqrt{-1}$

K   Stiffness

M   Mass

m   Indicial variable

n   0, 1, 2, 3, ..., etc.

P   Subscript meaning particular solution

R   Generalized response of linear single degree of freedom system

t   Instantaneous time

u   Absolute displacement excitation

x   Absolute displacement response

δ Relative displacement response

Δ Proximity criterion or change in D under influence of u ($X_2 - X_1$ of Fig. 1)

ζ Fraction of critical damping

θ Phase angle

τ Duration of applied excitation

ϕ Phase

ω_n Angular natural frequency

PROXIMITY CRITERION

The criterion was first presented at the 34th Symposium on Shock and Vibration (1). However, it is appropriate to present a brief review of the proximity criterion at this time.

The proximity criterion is a direct measure of the ability of an excitation to produce failures in a simple model equipment due to changes in the distance between two elements of the equipment. These failures are referred to as proximity failures, and collision between the elements is considered an extreme case of proximity failure.

This criterion is a means of analyzing different excitations to compare their potential for exciting proximity failures. If the proximity criterion for one excitation is greater than that for another excitation, the one with the greater value will be more likely to produce a proximity failure.

Figure 1 shows the model equipment used to derive the method of computing the proximity criterion. A dynamic input is applied to the left side of the rigid base. Two uncoupled spring-mass-damper systems are attached to the base. These masses respond with displacements X_1 and X_2. The distance between the two masses at any time is D. This distance is composed of the static distance between the masses, D_{st}, plus the dynamic change Δ of distance under excitation. D is called the proximity, and Δ is called the proximity criterion. The ability of an excitation to create relatively large values of Δ is a measure of the ability of the excitation to cause proximity failures.

Figure 2 shows an analog computer record of the undamped proximity criterion for two waveforms. The waveforms are displayed on the third line of the data and are the common half-sine and terminal-peak sawtooth test pulses. The top two rows show the responses of the two masses. The fourth row shows the results of computing the difference of the responses of mass 2 and mass 1 to obtain the proximity criterion. The last row shows the absolute value of the proximity criterion, which becomes important when an equipment is tested in both the positive and negative directions along a given axis (1).
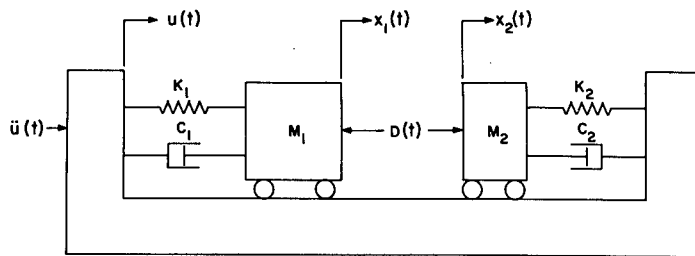
Fig. 1. Model equipment for determining proximity
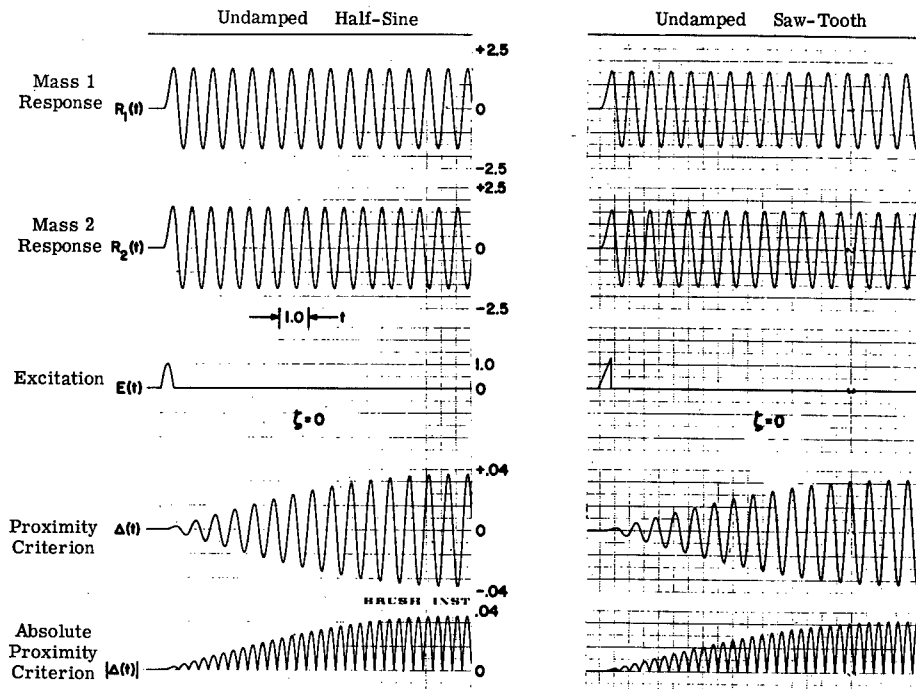failure criteria for given excitation

Fig. 2. Proximity criteria for half-sine and sawtooth pulses

Figure 3 shows several time histories for the undamped proximity criterion when the excitation is a half-sine. These are actual analog computer records. The top trace is typical of frequency ratios f_1/f_2 or f_2/f_1 intermediate between zero and unity and intermediate between one and large values (e.g., ten). When the frequency ratios approach unity, the records exhibit the typical beat pattern shown in the center trace. When the ratio becomes unity, both masses have the same motion and the proximity criterion is zero. When the frequency ratio is small or large, the proximity criterion approaches the response of the lowest frequency system and is nearly a pure sinusoid in the residual era (after the excitation has ceased). The bottom record shows the special case

encountered when the 350-cps system is timed for cancellation in the residual response era. During application of the excitation, the proximity criterion shows the effect of both system responses, but after the input ceases, the proximity criterion consists of the free vibrations of the 300-cps system only.

While the complete time history of the proximity criterion may be somewhat more enlightening, most engineers would be more concerned with the extreme values (positive and negative) of the proximity criterion. By restricting ourselves to the maxima and minima of the proximity criterion, we can expand this concept into that of the proximity spectrum.

231

30 and 10 cps
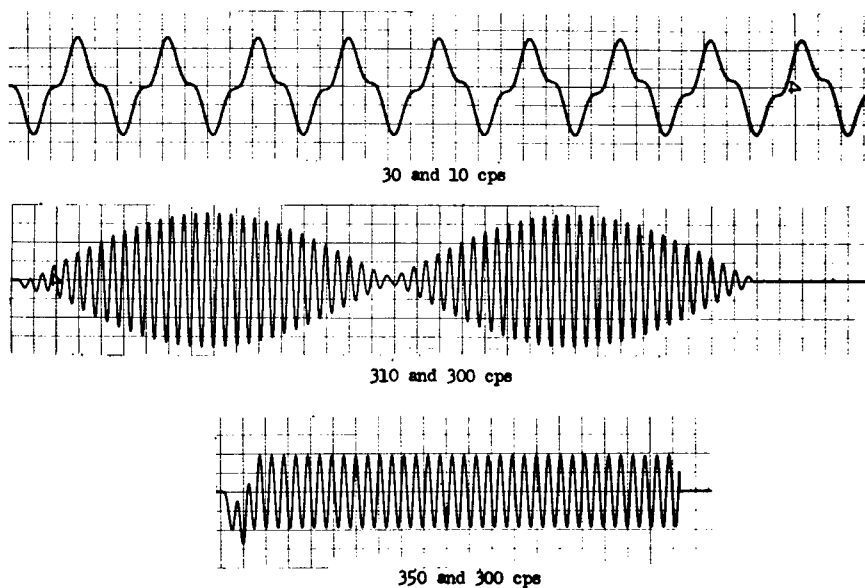
310 and 300 cps

350 and 300 cps

Fig. 3. Typical analog computer records
of proximity criterion time history

PROXIMITY SPECTRUM

If the frequencies of the two systems are varied over a range of values likely to be of significance in the response spectrum, data can be generated for a three-dimensional proximity spectrum. The maximum positive and negative values of the proximity criterion would be plotted on the vertical axis, and the frequencies of the two systems would be plotted on the two horizontal axes. This would generate positive and negative proximity surfaces, indicative of the maximum changes in proximity. These surfaces would then serve as a comparison of the ability of different excitations to produce this type of failure.

Figure 4 shows a cubical coordinate system for such plots. While proximity surfaces are conceptually interesting and lend themselves very well to solid models of the data, they do not lend themselves to plots on a plane surface, such as the pages of this paper, except in the simplest cases where the proximity surfaces are not too irregular. The surfaces in the case of the proximity spectrum are usually irregular. Therefore, we have plotted the intersections of the surfaces with planes parallel to the f_2 plane at selected f_1 frequency increments. The plane ABCD is an example of this process. Line AB is then the plot of the proximity spectrum for the value of frequency f_1 represented by point D. Other planes passed through the solid parallel to ABCD will intersect the proximity surface, so that the intersections are proximity

spectra for other values of f_1. Thus, we get a family of proximity spectra for a range of values of f_1, the natural frequency of the system composed of M_1, K_1, and C_1 in Fig. 1.

COMPUTATION OF UNDAMPED SPECTRA

The method of computing the proximity criterion (1), although technically correct, was not used in computing the undamped spectra of this paper. The algebra of the undamped case shows that the proximity criterion will be zero when the frequencies of the two systems are equal. When this happens, the responses of the two systems will be equal, and their difference will therefore be zero. It can also be shown that the phase difference and frequency ratios would not often be so related that the two systems would ever reach either a peak response or a minimum response simultaneously. It is shown, however (see Appendix), that an infinitesimal change in either system's frequency would cause the peak and minimum residual responses (those that occur after the shock is over) to be reached simultaneously. In this case, the maximum and minimum values of the proximity criterion will be merely the algebraic summation of the peak and minimum values of the response.

Since real systems can never be related by exact frequency ratios, it is more reasonable to determine the maxima and minima in this
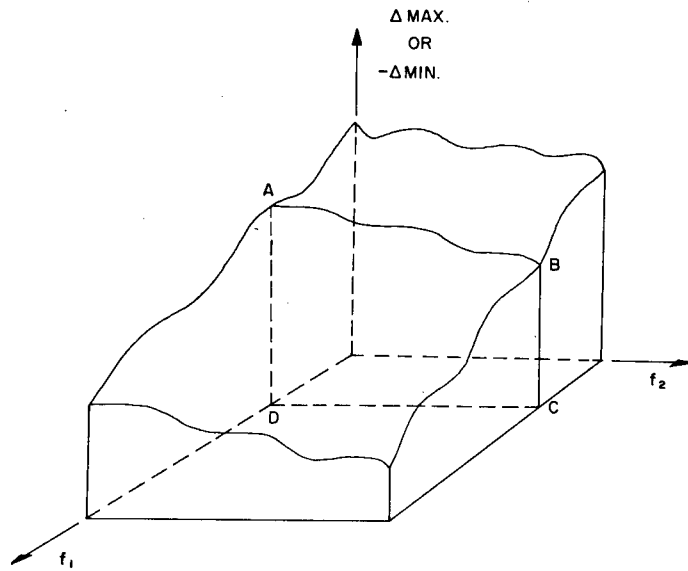
232

Fig. 4. Hypothetical proximity surface generated
by three-dimensional plots of proximity spectra

manner. This statement is not true, however, for the damped case. In the damped case, the responses will be damped out prior to the occurrence of the correct conditions for coincidence. In computing the values for the undamped proximity spectra, the initial values (those that occur while the shock excitation is being applied) of the proximity criterion are computed as time-dependent maxima and minima, and the residual values are computed independent of time, as indicated in the foregoing discussion. The maxima and minima of the proximity criterion obtained for the initial and residual eras are then compared, and the highest of the maxima and the lowest of the minima are the values plotted in the proximity spectrum.

PRESENTATION AND DISCUSSION OF SPECTRAL PLOTS

Proximity spectra were computed for three common test and design waveforms: the half-sine, terminal-peak sawtooth, and square wave. The undamped cases and cases with viscous damping ratios of 0.005 and 0.1 were computed. Both systems were assigned the same representative values of damping.

Figure 5 shows the undamped proximity spectra of the terminal-peak sawtooth waveform. This is a very special case; other cases of the spectra are not nearly as simple. The undamped proximity spectra of the terminal-peak sawtooth are merely the sums of the shock spectrum values. The positive and negative values are equal,

just as they are in the undamped shock spectrum. The ordinate scale is logarithmic and represents the difference of the displacement of the two systems multiplied by the input wave duration squared and divided by the peak value of the input wave acceleration. Each curve represents a different value of f_1, and is normalized by multiplying by τ, the duration of the excitation. The abscissa values are normalized in the same manner and represent the frequencies of mass 2.

Examination of the figure shows that the proximity spectrum becomes nearly constant above some value of f_2 and that, when f_1 is small, the value of f_2 at which the spectrum become nearly constant is small. For example, when τf_1 is 0.1, the spectrum is nearly constant for values of τf_2 greater than 1.0. For τf_1 equal to 0.6, the spectrum is nearly constant for values of τf_2 above 2.4. The reason for this is readily discerned when one realizes that, as the frequency f_2 increases, the response of M_2 becomes smaller and smaller. Eventually the response of M_2 will become insignificant when compared with that of M_1, and the entire proximity spectrum will be due merely to the response of M_1 at the constant frequency f_1. This fact helps to simplify the computation of the spectra, since one can arbitrarily select some response amplitude of M_2 which he considers to be insignificant in comparison with the response of M_1. For example, when the response of M_2 contributes less than 5 percent of the total proximity spectrum value, further computations can be terminated, and the maximum and minimum
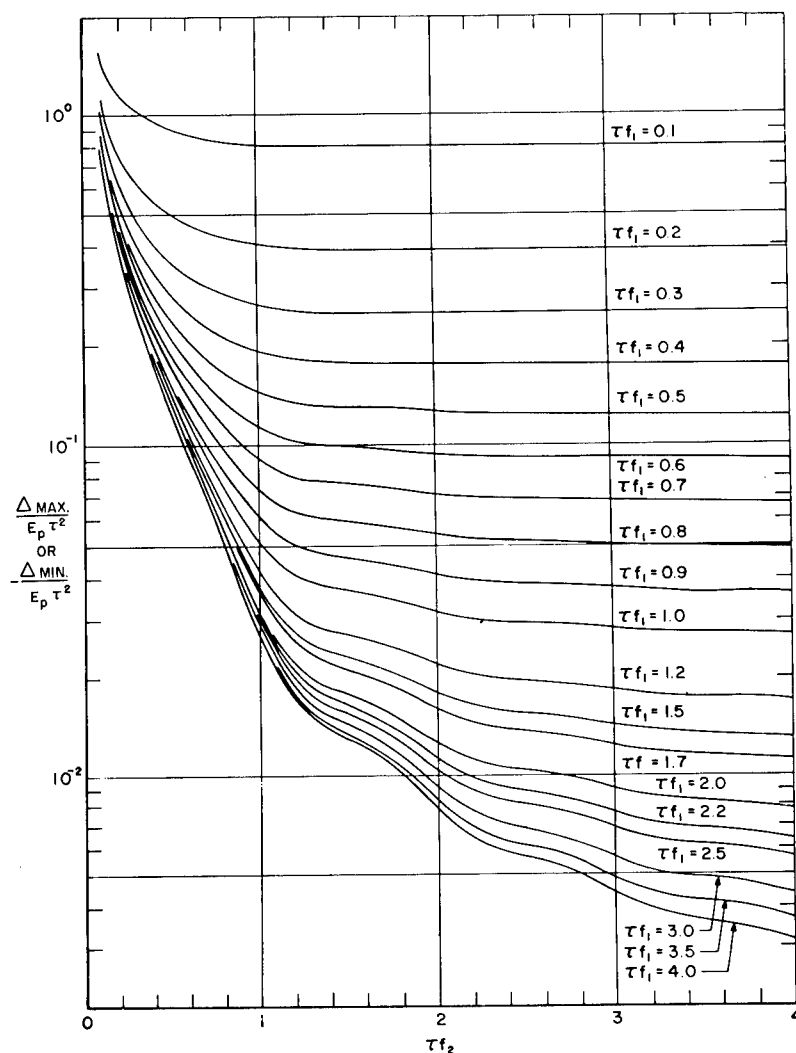
233

Fig. 5. Undamped proximity spectra of terminal-peak sawtooth excitation function

values of the response of M_1 can be printed out on the computer as the proximity spectrum values. The same logic can also be applied when the response of M_1 is insignificant in comparison with that of M_2. In this case, proximity spectrum values for lower values of the abscissa are almost entirely due to the response of M_2.

Figure 6 shows the undamped positive proximity spectra for a square wave excitation. This graph is presented mainly to show the difficulty encountered when one tries to present the proximity spectra as families of curves on a single plot. This is one of the least confusing

examples. Those cases plotted with damping are even more confusing. Note that the curves above a τf_1 value of 0.9 are quite orderly. For curves with τf_1 values greater than 0.9, there is very little order with the curves crowding, intersecting, and exhibiting sudden trend changes. For this reason, such a plot is much less useful than the method shown in Fig. 7. This figure shows the undamped positive and negative proximity spectra of a square wave excitation for a τf_1 value of 3.0. This presentation is much clearer, but requires entirely too much space for a short paper. The number of curves for which data were generated is 720. If they were printed 2 per plot and 4 plots per page, it would require
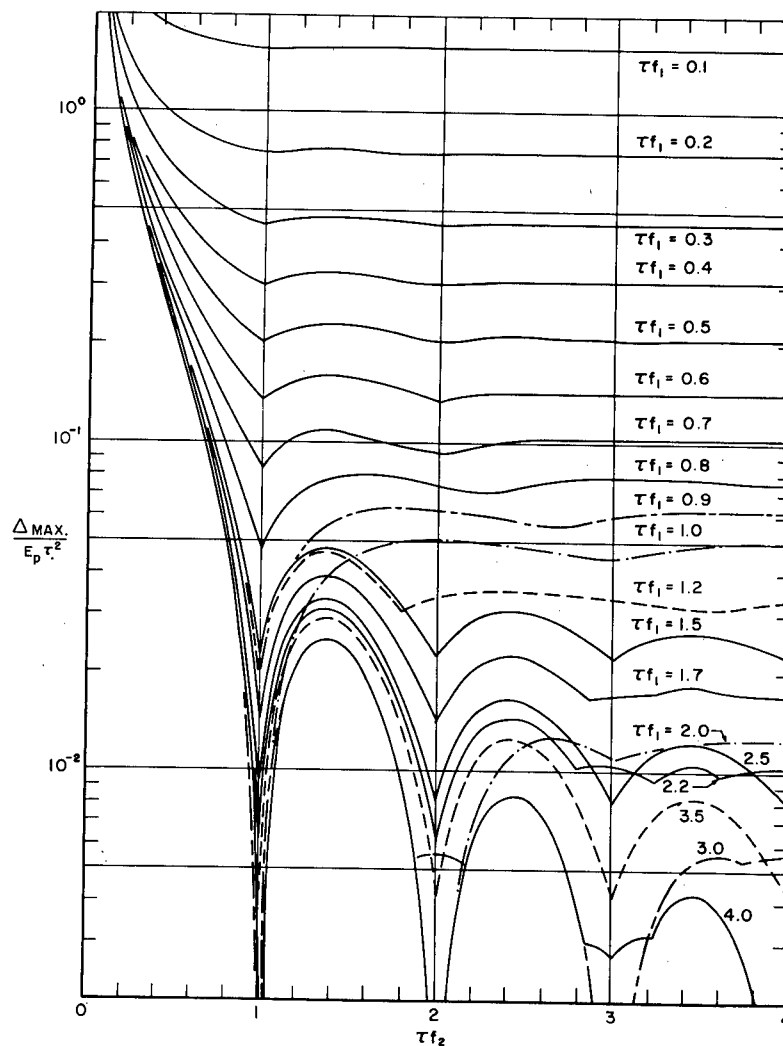
Fig. 6. Undamped positive proximity spectra of square wave excitation function

90 pages to present the data.* For this reason, only illustrative examples are given here. Returning to the Fig. 7, we see that a region of very low values exists near the value τf_2 equals 3.0. This is due to the fact that, as f_2 approaches f_1, the two systems tend to respond in phase with each other during the pulse. When f_2 equals f_1, the systems are exactly in phase and have exactly the same motion. The proximity spectrum is zero at this point. Ordinarily, however, if the two systems were not exactly in phase, they would get further and further out of

phase in the residual time era, and the differences of the responses would fill in the hole in the spectrum occurring at $\tau f_2 = 3.0$. Because of the symmetry of the square wave, however, the residual responses are almost entirely cancelled as τf_n approaches a whole number (i.e., 1, 2, 3, ..., etc.) and are completely cancelled for whole number values of τf_n. The hole in the positive spectrum at τf_2 equals 1.0 is partially explained by cancellation of the residual responses, since τf_1 and τf_2 are both whole numbers. However, the two systems do not have the same frequency and do not respond in the same way, so the difference is not always zero. The relationship between the two frequencies is such that the maximum occurs at t equal to zero and t equal to τ when the responses are exactly zero and the positive
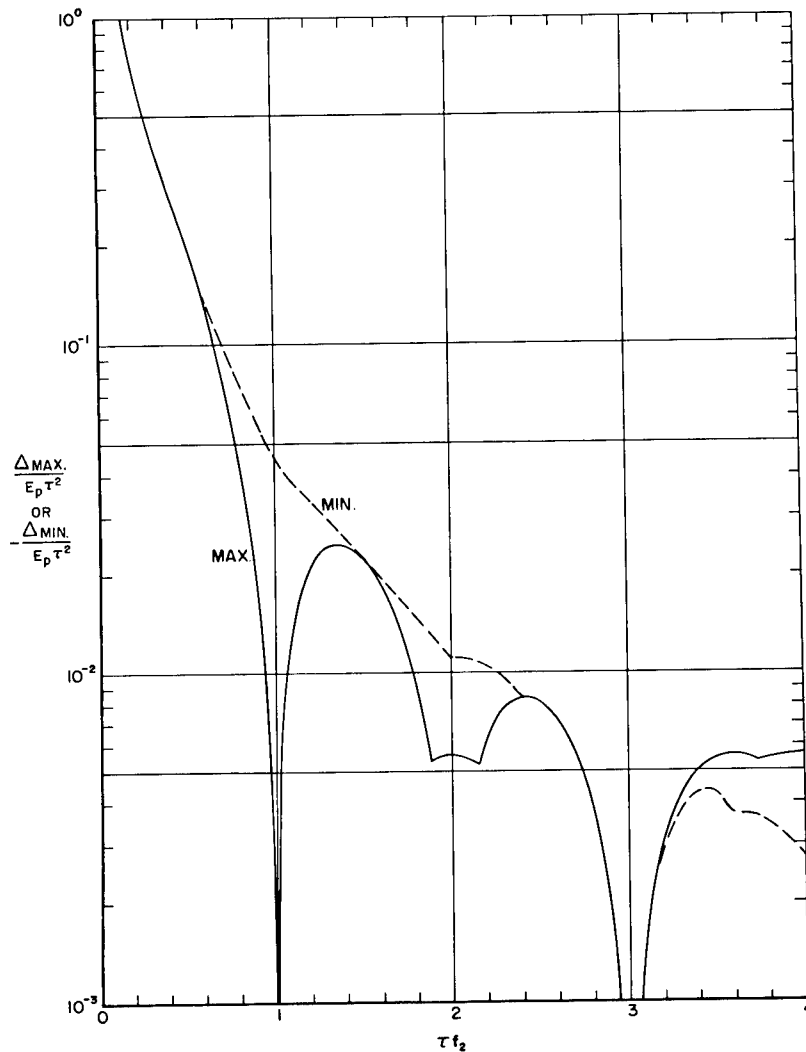
235

Fig. 7. Proximity spectra of square wave excitation
function when $\zeta = 0$ and $\tau f_1 = 3.0$

proximity spectrum is, therefore, zero. The maximum negative value is as shown on the minimum curve. The same reasoning holds for the positive spectrum at τf_2 equals 2.0, with the exception that the maximum proximity spectrum values during the pulse are greater than zero and the trend toward zero, which occurs in the residual time era, is stopped.

We can now point out that, at least for the undamped spectra, some of the sudden changes in trends are accounted for by the fact that the maximum or minimum spectral values in the residual and initial spectra are exhibiting opposite trends. Thus, a point occurs on the curves where the one becomes greater or lesser than the other. Since we are plotting only the largest and smallest values irrespective of the time

interval (initial or residual) in which they occur, a sudden trend reversal results. Where the minimum curve departs from the maximum curve, minima occur during the initial time era, but we still see sudden changes in the trends. These changes can be explained by the following: (a) the minima occur at a time when the response of system 1 is zero, and the response of system 2 is maximum, in which case the phase relationship is correct for producing the smallest of the possible minima for the two frequencies involved; (b) the phase relationship is such that the largest of the minima is produced; or (c) intermediate minima are produced. Examples of (a) can be seen when τf_2 has values of 0.75, 1.5, 2.25, 3.5 and 3.75. Examples of (b) are seen at 1.0, 2.0, 3.0 and 3.6. All other values on the dashed curve are examples of (c).

236

Figure 8 shows the proximity spectra for the same input when the damping is 0.005. For this particular case, where τf_1 is 3.0, there is little difference from the undamped case of the previous figure. The shapes of the curves are nearly the same and the values are only slightly less than those in the undamped case. It will be shown later that this similarity for the undamped and lightly damped spectra does not always occur.

Figure 9 shows the case of the square wave when the damping is 10 percent. This case is, of course, drastically different from those with little or no damping. The curves are higher in some regions and lower in others. The general effect of damping is to provide less erratic behavior in the proximity spectra. The same

effect is also evident in the shock spectra (i.e., the deep nulls become less apparent) (1).

Figures 10, 11, 12, 13, and 14 show examples of the proximity spectra of the half-sine and sawtooth waveforms. Figures 10 and 11 show the undamped and lightly damped half-sine cases. As in the square wave, there is little difference between the two, but the null of Fig. 11, when τf_2 is 1.5, is not as deep. In Fig. 12, we see again that the proximity spectra are drastically affected by the addition of 10 percent damping. The behavior of the sawtooth spectra when the damping ratio is one-half percent (Fig. 13) is somewhat more erratic than that exhibited in the undamped spectra of the sawtooth (Fig. 5) but much less erratic than the square wave and half-sine wave for the
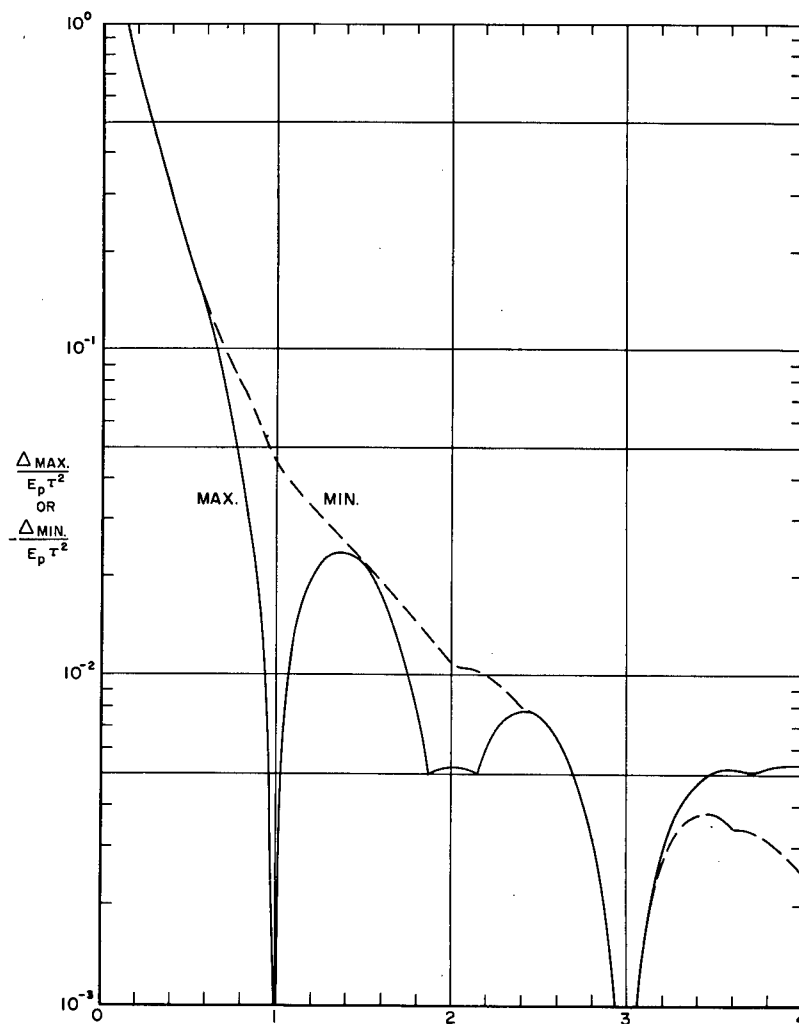

Fig. 8. Proximity spectra of square wave excitation function when $\zeta = 0.005$ and $\tau f_1 = 3.0$
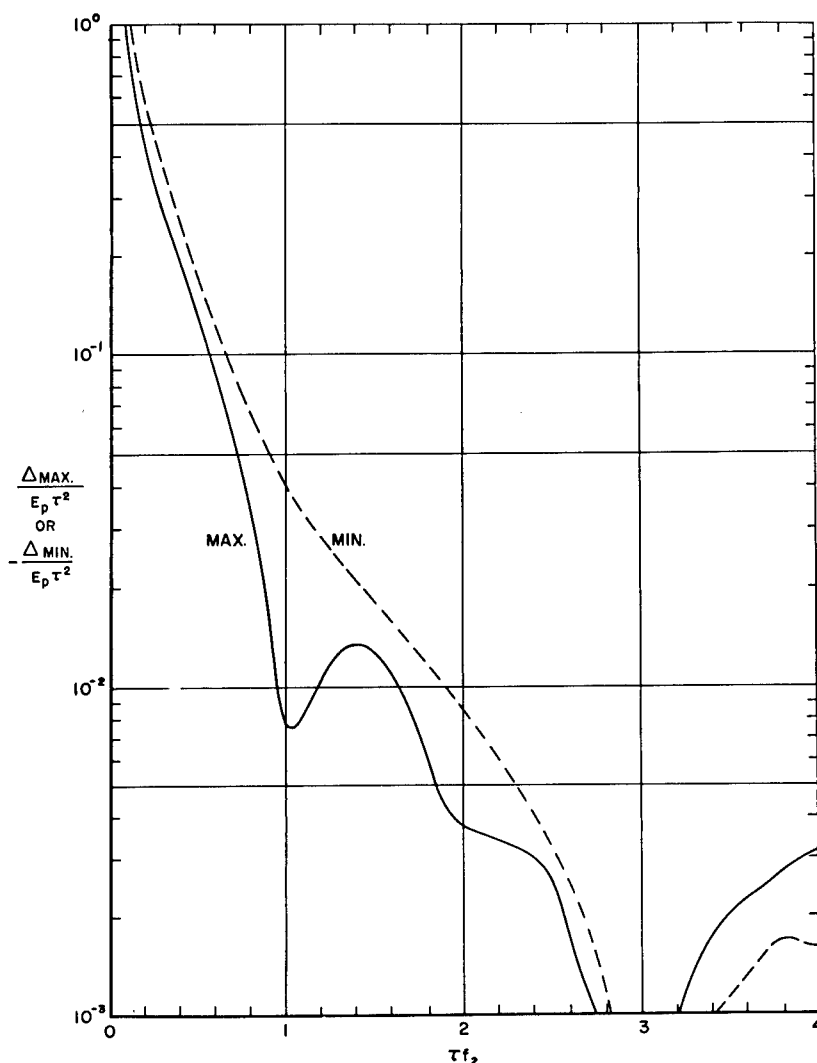
Fig. 9. Proximity spectra of square wave excitation
function when $\zeta = 0.1$ and $\tau f_1 = 3.0$

same damping (Figs. 8 and 11). The behavior
at f_2 equal to 2.5 (Fig. 13) is as expected, since
the damped spectra always approach zero as
the frequency of M_2 approaches that of M_1. No
attempt has been made to explain the somewhat
irregular behavior of the rest of the curve, but
it is assumed that these are the effects of the
actual phase relationships rather than those
assumed in the undamped sawtooth spectra.*

---

*The sawtooth proximity spectrum is entirely
residual. Since the method of computation of
undamped residual spectra, as previously ex-
plained, results in an algebraic summation of
peak and minimum responses independent of
time, this is the same as saying that the max-
ima and minima are assumed to occur at a time
when the responses are 180 degrees out of phase.

Concerning Fig. 14, it should be noted again
that the damping has smoothed the spectra con-
siderably, and that they are less erratic than
the square wave and half-sine of Figs. 9 and 12.

Figure 15 shows a plot of the square wave
data when τf_1 is 2.5 (the same value used for
the half-sine and sawtooth cases). Only the
positive (maximum) spectra are plotted, and
they compare the effects of the various amounts
of damping. In the regions near τf_2 equals 2.5,
the two systems are nearly equal in frequency.
The undamped curve indicates a proximity
spectrum value at least several orders of mag-
nitude greater than those values on the steep
sides of the lightly damped curve (0.005) as it
extends below the graph. This difference in

magnitudes, coupled with the knowledge that actual systems always have some degree of damping, would indicate that it is unrealistic to compute such spectra with zero damping. The curve for 10 percent damping shows much smoother characteristics than either of the other two. The two damped curves bracket the values of the proximity spectra which might be realistically interpreted in terms of application to most military equipments.

APPLICATION OF PROXIMITY SPECTRUM

Simulating Environment for Design and Test

Perhaps the most important use of the proximity spectrum of an excitation is in evaluating its ability to produce proximity failures in the system of Fig. 1. More fundamental than this, however, the model enables us to analyze the simultaneous occurrence of responses at two discrete frequencies. The importance of this method can be seen if we imagine a slowly swept vibration applied to the model. If the input is swept over a range large enough to include the resonant frequencies of both systems, and if the resonant frequencies are sufficiently far apart, both systems will be excited to large relative responses at resonance. However, the two resonant responses will occur at different times.

When only one of the systems is in resonance, the relative response of the nonresonant system will either be zero (if it is at a frequency below the excitation frequency) or a
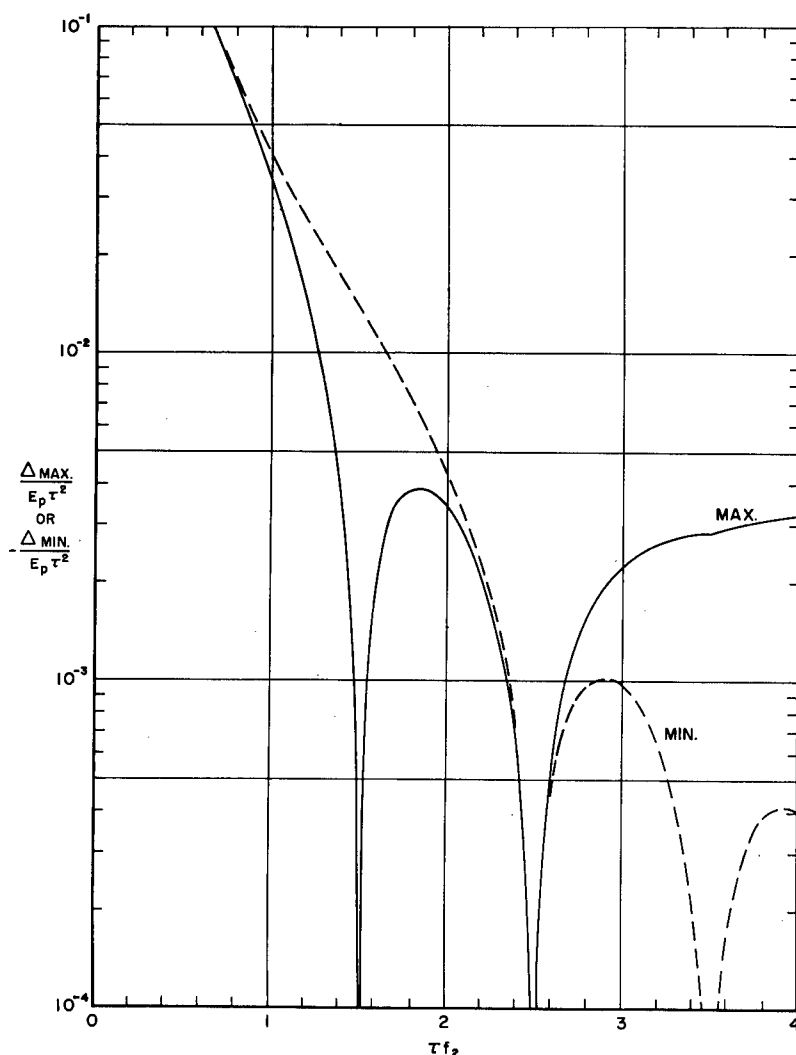

Fig. 10. Proximity spectra of half-sine excitation
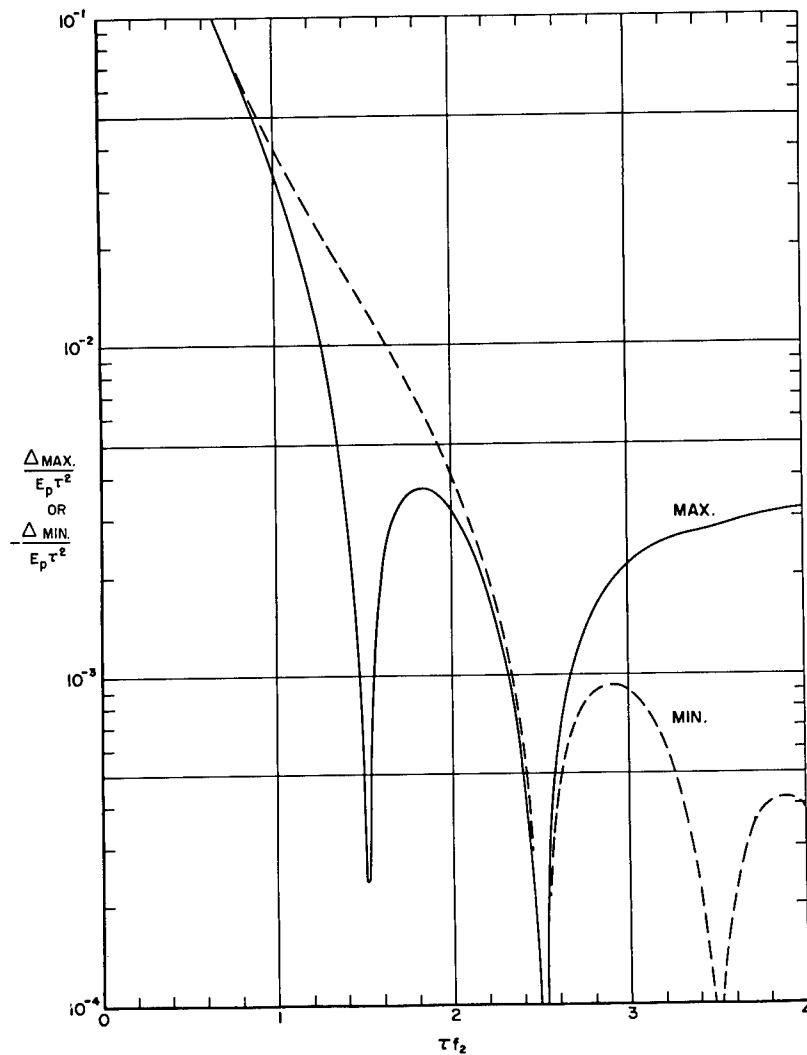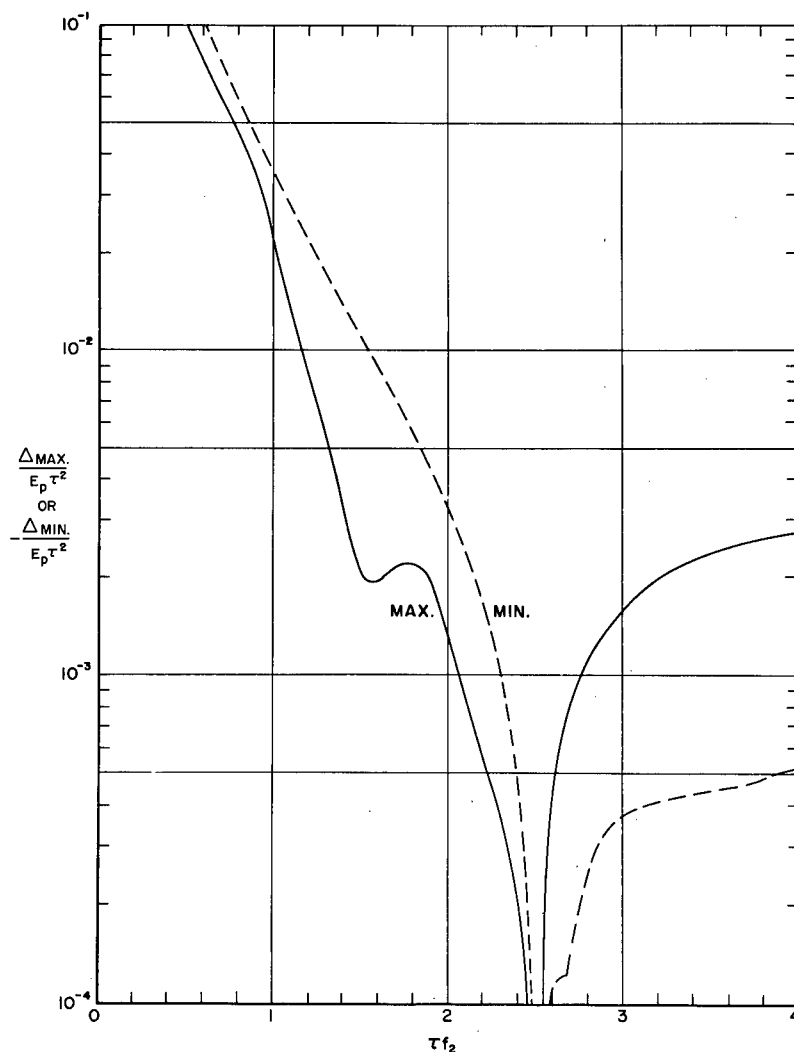function when $\zeta = 0$ and $\tau f_1 = 2.5$

Fig. 11. Proximity spectra of half-sine excitation
function when $\zeta = 0.005$ and $\tau f_1 = 2.5$

response value slightly less than the excitation value (if it is at a frequency above the excitation frequency). Now, assume that a simple shock pulse can be applied which will produce the same peak responses. The shock spectra of both the sweep and pulse excitations will be the same at the resonant frequencies, but in the second case, the responses will occur simultaneously, or nearly so, while in the first case they were separated in time. One would hardly consider a slow sinusoidal sweep to be a shock. (Here, slow sinusoidal sweep is relative to the response buildup time of the systems.)

The difficulty arises when the sweep becomes relatively rapid, and the vibration then becomes a transient. Under these circumstances, the question of whether or not the

responses occur simultaneously is not so easily answered. Since most environmental transients fall into the gray area between vibration and a simple pulse-type shock, environmental transients are somewhat analogous to the case of the rapidly swept vibration. All of these excitations may have the same shock spectra values at the natural frequencies of the two systems, but no two of them will have the same proximity spectra.

The shock spectrum is indicative of one kind of damage potential to a hypothetical system, and the proximity spectrum is indicative of another kind of damage which depends on the simultaneous response of two hypothetical systems. The proximity spectrum concept can, therefore, be used to compare test and design

240

waveforms with the environment to obtain a more realistic test or design waveform than can be obtained by comparison of the shock spectra alone. It is not yet clear whether or not we can ignore the shock spectra.

Since the proximity spectrum is a result of the simultaneous analysis of two shock spectra (single degree of freedom) systems, it is reasonable to suspect that waveforms whose proximity spectra equal or exceed the envelopes of the proximity spectra of the environment might also have a shock spectrum that equals or exceeds the shock spectrum envelope of the environment. At the present time, however, one should also choose a waveform whose shock spectrum equals or exceeds the positive and negative envelopes of the shock spectra of the environments.

The procedure would be to prepare environmental proximity spectrum envelopes by reducing many measurements of environmental conditions. Design and simulation waveforms whose proximity spectra equal or exceed those of the environmental envelopes could then be chosen.

Determining Equivalence of
    Shock and Random Vibration

One of the essential features of random vibration is its ability to excite simultaneously

Fig. 12. Proximity spectra of half-sine excitation
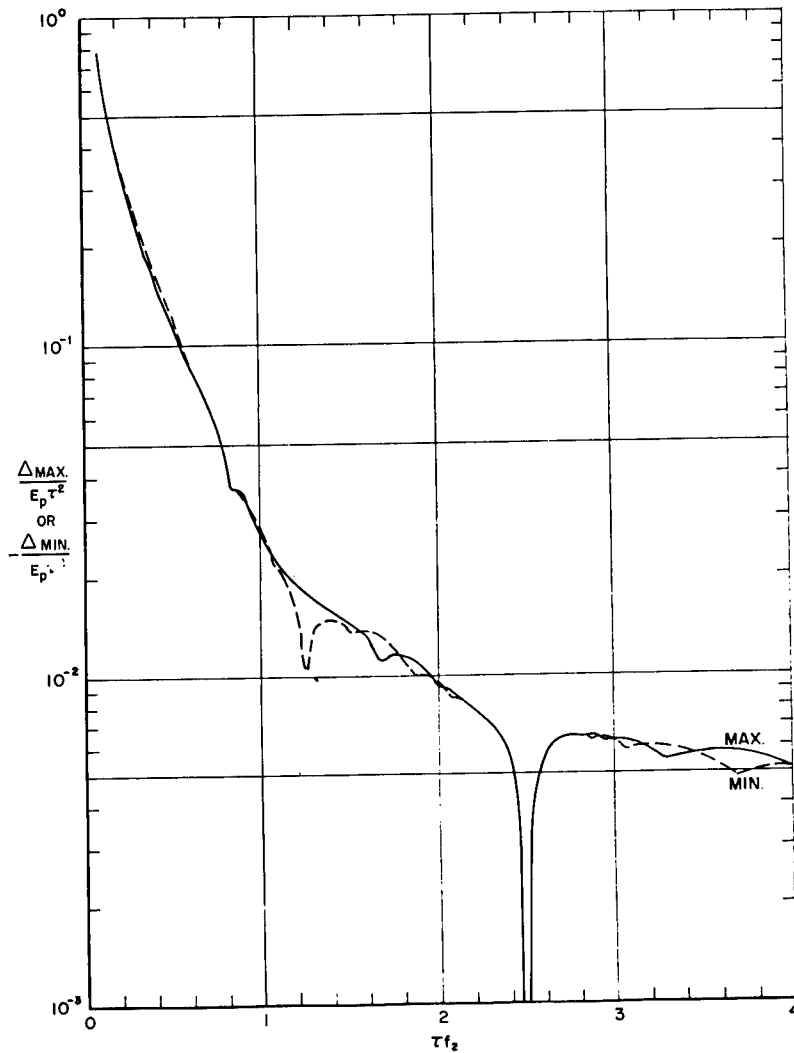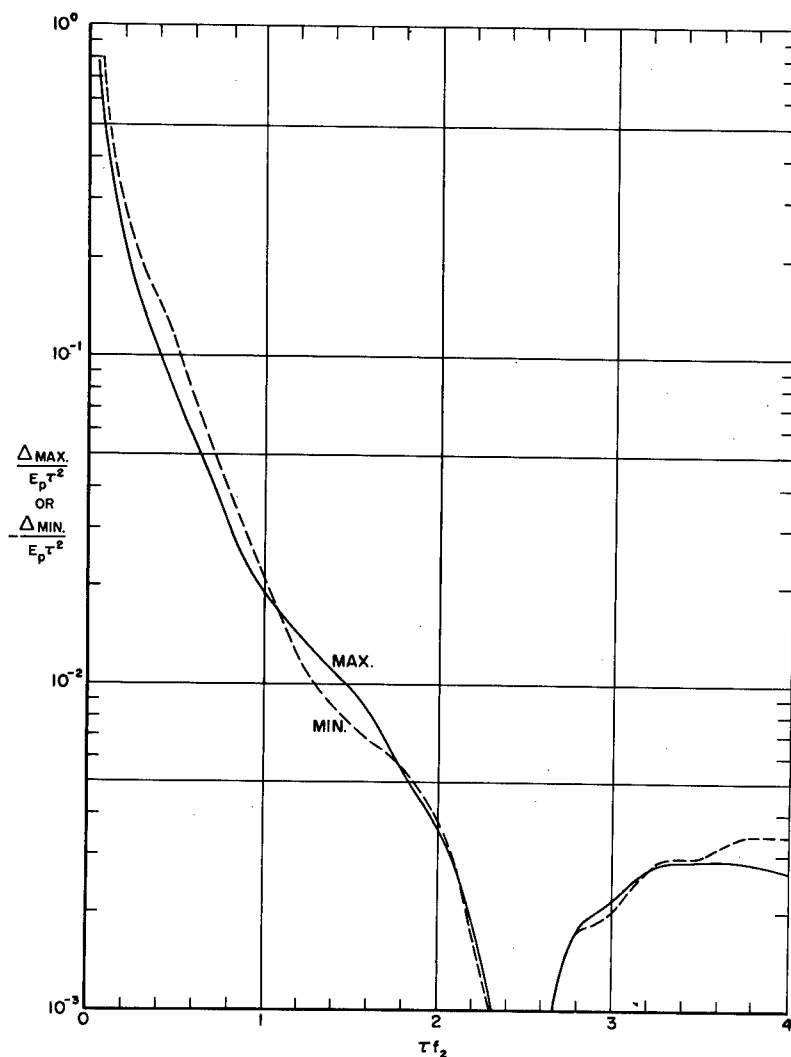function when $\zeta = 0.1$ and $\tau f_1 = 2.5$

241

Fig. 13. Proximity spectra of terminal-peak sawtooth
excitation function when $\zeta = 0.005$ and $\tau f_1 = 2.5$

two or more response modes of an equipment. Theory also tells us that a terminal-peak sawtooth can excite all response modes simultaneously. However, if one runs a random test long enough, one can assume that all possible combinations of two response modes will occur simultaneously. The proximity spectra of the random vibration would indicate the validity of this assumption. Since the random vibration takes a long time in comparison with the duration of the sawtooth, it appears that the sawtooth may be superior for producing this characteristic of the excitation. In a terminal peak sawtooth shock, a broadband excitation occurs in a very short period of time. In random vibration, the broadband characteristics accumulate over a relatively long period of time. One other

aspect of a random vibration is that it produces fatigue damage. Neither the shock spectrum nor the proximity spectrum can give a direct indication of cumulative fatigue potentials of a given excitation. However, in 1954, Crede, Gertel and Cavanaugh proposed a three-dimensional response surface which can be used to evaluate the cumulative damage potential of the shock. When the proper number of shocks has been applied, the cumulative damage should equal the cumulative damage under random vibration as determined by the methods of Fuller (3) or Fruedenthal (4).

These ideas are, of course, not applicable at present and require more study. If such a project were successful, it is believed that a

242

shock machine could be developed to sell for $10,000 or less to replace a $100,000 random vibration system. Thus, the savings in equipment would mount into the millions of dollars. Further savings would be realized from maintenance ease and reliability of the shock machine which is a basically simple device.

Decision Tool for Elimination of Shock Tests

It appears that an application similar to that of the preceding paragraphs is now possible. The author has had the opportunity to examine trip reports of Dr. W. W. Mutch's group at the Department of Defense Shock and Vibration

Information Center. One repeated comment was noted: "It is a waste of time and money to perform shock tests on an item which receives a random vibration test much more severe in its effects than the shock test." For this reason, some method is needed for deciding whether or not a random vibration test is more severe than the shock test so that the shock test might be eliminated, resulting in large savings of manpower, equipment, and money.

The following method may possibly be utilized by the Air Force in the near future to eliminate some shock tests. Since shock produces relatively few reversals of stress as compared with random vibration, it is safe to assume that fatigue effects of the random

Fig. 14. Proximity spectra of terminal-peak sawtooth excitation function when $\zeta = 0.1$ and $\tau f_1 = 2.5$
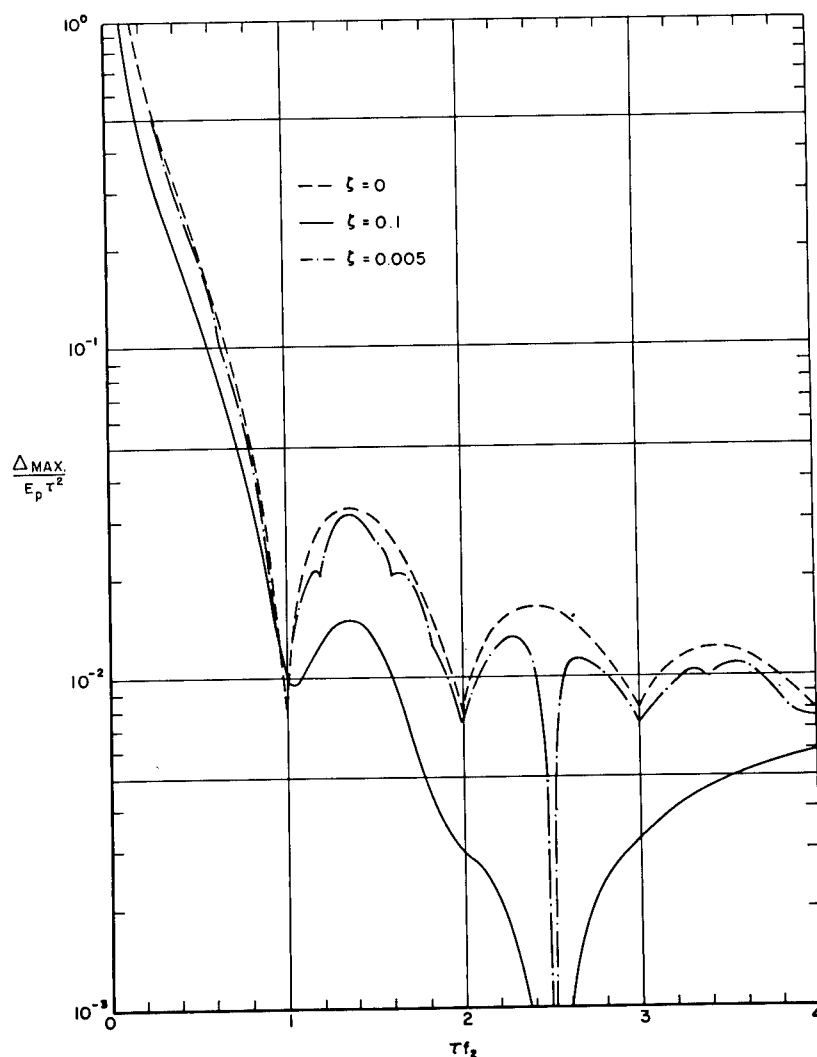
Fig. 15. Effects of damping on positive proximity spectra of square wave excitation function when $\tau f_1 = 2.5$

vibration will be much greater than those produced by the shock test. The next step in eliminating certain shock tests will involve computation of the response spectra of the random vibration and the shock. The proximity spectra of both the random vibration and the shock will then be computed. If both the response spectrum and the proximity spectra of the random vibration exceed the values of the same spectra for the shock, the shock test could be eliminated. For a general specification, this problem will have to be solved only once. The results will provide a simple numerical comparison for deciding whether or not to run the shock test. The results would then be incorporated into the specification or some other implementing document.

A pessimistic upper limit for the cost of refining and documenting these relationships if performed "in-house" would be $10,000. If one assumes a cost of $1,000 per test, the potential savings to the Air Force (and other federal agencies as well) could run well into the millions. This application will be the subject of a forthcoming technical report.

Design of Simple Systems

From a design standpoint, the first three applications, which affect design indirectly by selecting waveforms or excitations to which a designer must work, are the most important. However, in some rather simple cases, when

244

Fig. 1 is a reasonable model of the equipment masses, numbers can be obtained from the spectra which have more direct application. This method is also of use in relating the spectra to the model of Fig. 1 and to physical reality. When such simple cases exist, the extremes of proximity under a given excitation can be conservatively estimated for design and failure analysis as follows, assuming a damping ratio of 0.005 (see conclusion 4):

1. Determine the absolute static distance (always positive) between the masses of interest (M_1 and M_2 of Fig. 1). This determination should include any gravitational effects present. The model of Fig. 1 does not include them.

2. Determine the natural frequencies of the two spring-mass-damper systems and multiply them by τ, the duration of the excitation.

3. Find the positive and negative spectral values for τf_2 on the curves marked τf_1, for the given excitation. For example, assume that the waveform is a half-sine of 100 g peak acceleration, the duration is 10 ms, and the frequencies of the two systems are $f_1 = 250$ and $f_2 = 140$. Then $\tau f_1 = 2.5$ and $\tau f_2 = 1.4$. Using the curves of Fig. 11, the positive spectrum value of 3.25×10^{-3} is obtained from the curve marked "MAX" and the negative spectrum value of -1.65×10^{-2} is found on the curve marked "MIN." The ordinate values are in inches per unit peak acceleration of the input waveform times the square of its duration. The acceleration is in inches per second squared, and the duration is in seconds.

4. Convert the values from step 3 to inches, multiplying by the peak acceleration and the duration square of the half-sine excitation. For example, if the peak input is 100 g and the duration is 0.01 sec, the peak acceleration is 3.86×10^4 in./sec^2, and the duration squared is 10^{-4} sec^2. The positive change in proximity is then $3.86 \times 10^4 \times 3.25 \times 10^{-3} \times 10^{-4}$, which gives us 0.0125 in. The negative change is $-1.65 \times 10^{-2} \times 3.86 \times 10^4 \times 10^{-4}$, which gives us -0.0637 in.

5. Calculate the actual extremes of proximity by adding the static distance $|D_{st}|$ and the dynamic changes ($\triangle$ MAX and $\triangle$ MIN). For example, if $|D_{st}|$ is 0.05 in., the maximum distance separating the masses D_{MAX} will be 0.05 + 0.0125, or 0.0625 in.; D_{MIN} will be 0.05 - 0.0637 = 0.0137 in. The negative value indicates a collision which may or may not be considered a failure, depending on the particular design. (If the static distance $|D_{st}|$ is greater than the negative value $\triangle_{MIN}$, collision will not occur, but this does not eliminate the possibility of other types of failure.)

CONCLUSIONS

1. The proximity spectrum concept is a means of evaluating shock motions (environmental, test, or design) which shows the potential of the motion for producing simultaneous responses at many frequencies.

2. The model equipment of Fig. 1 makes it possible to visualize situations where damage might occur. This gives the proximity spectrum a physical significance not possible with an analogous approach that does not consider the behavior of physical systems.

3. The proximity spectrum can be used to indicate the essential differences between transients which excite sequential responses and those which excite simultaneous responses, although the shock spectra are similar or even identical.

4. The proximity spectrum computed with a viscous damping ratio of 0.005 is considered to be more realistic than the undamped spectrum and provides a conservative value for most equipments.

5. The proximity spectrum can be used directly to determine the approximate maximum and minimum values of proximity in simple cases for design or failure analysis.

6. The proximity spectrum can be used to determine a single test and design waveform which will produce proximity failures equal to, or conservatively in excess of, those produced by the environment.

7. More realistic designs and tests will result from application of the proximity spectrum. This should result in a considerable improvement in reliability of equipment, with a correspondingly large savings in dollars.

8. If methods of eliminating certain shock tests can be derived from applications of the proximity spectrum, this concept may produce savings well into the millions of dollars for the Air Force and other Government agencies when adopted.

9. The proximity spectrum, in conjunction with the response spectrum, with the response surface (2), and with methods of predicting random fatigue (3,4), can be used to evaluate a means of simulating random vibration on inexpensive shock machines. If successful, this means of simulating random vibration will result in large monetary savings.

REFERENCES

1. E. H. Schell, "Spectral Characteristics of Some Practical Variations in the Half-Sine and Sawtooth Pulses," Shock and Vibration Bull. 34, Part 3:223 (1964). Also published as AFFDL TR 64-175, Air Force Flight Dynamics Laboratory, Wright-Patterson AFB, Ohio (1965).

2. C. E. Crede, M. Gertel, and R. D. Cavanaugh, "Establishing Vibration and Shock Tests for Airborne Electronic Equipment," Wright-Patterson AFB, Ohio, WADC TR-54-272, 1954

3. J. R. Fuller, "Research on Techniques of Establishing Random Type Fatigue Curves for Broad-band Sonic Landing," Flight Dynamics Lab., Wright-Patterson AFB, Ohio, ASD-TDR 62-501, 1962

4. A. M. Freudenthal, "The Safety of Aircraft Structures," Wright-Patterson AFB, Ohio, WADC TR 57-131, ASTIA Doc. AD 130 910

Appendix

METHODS OF COMPUTATION*

The first step in obtaining the data for the proximity spectrum was to find the solution to the following linear differential equation:

$$\frac{\ddot{R}}{\omega_n^2} + \frac{2\zeta\dot{R}}{\omega_n} + R = E, \qquad 0 \le \zeta < 1, \quad \text{(A-1)}$$

where R is the generalized response of a single degree of freedom system, and E is a generalized excitation function.

Associated with the homogeneous case of Eq. (A-1) is an auxiliary or indicial equation

$$\left(\frac{1}{\omega_n^2}\right) m^2 + \frac{2\zeta}{\omega_n} m + 1 = 0. \qquad \text{(A-2)}$$

This equation will have two roots of the form $m_1 = a + ib$ and $m_2 = a - ib$.

The solution to the homogeneous case of Eq. (A-1) is then known to be of the form

$$R_H = C_1 e^{at} \cos(bt) + C_2 e^{at} \sin(bt), \quad \text{(A-3)}$$

where C_1 and C_2 are constants determined from the given initial conditions $R(0+)$ and $\dot{R}(0+)$.

By letting $C = \sqrt{C_1^2 + C_2^2}$, and

$$\phi = \tan^{-1}\left(\frac{C_2}{C_1}\right),$$

we can express R_H in the form:

$$R_H = C e^{at} \sin(bt + \phi). \qquad \text{(A-4)}$$

The particular solution to Eq. (A-1), call it R_P, was determined by the "variation of parameters" technique (A-1), and the total solution to Eq. (A-1) is then

$$R = R_H + R_P. \qquad \text{(A-5)}$$

The form of Eq. (A-5) is used as a solution to Eq. (A-1) for values of $0 \le t \le \tau$, where τ is the time at which the excitation is terminated. At that time, we again solve Eq. (A-1) for the homogeneous case, using $R(\tau)$ and $\dot{R}(\tau)$ as initial conditions to determine new constants C_1 and C_2, and since $E(t) = 0$ for $t > \tau$, the solution thus obtained will be the total solution to Eq. (A-1) for $t > \tau$.

It now remains to solve for the maximum and minimum values of

---

$$\Delta(t) = \delta_2(t) - \delta_1(t) = \frac{R_1(t)}{\omega_1^2} - \frac{R_2(t)}{\omega_2^2} . \quad (A-6)$$

The search for the extremal values of $\Delta(t)$ proceeded in the following manner. Using a suitably small time increment, we look for local maxima and minima of $\Delta(t)$, i.e., points where $\Delta(t)$ has positive or negative peaks. Using three points which straddle a peak, we then fit a second degree polynomial to these points and solve for the root of the corresponding derivative. This yields the time at which the local extremum occurs; i.e., $t = t_0$. We then compare $\Delta(t_0)$ with the previous local maximum or minimum, and let the larger one be the temporary maximal or minimal value.

In the cases where we had damping, the search was terminated as follows. At every occurrence of an extremal value for $\Delta(t)$, we compare the upper or lower bound for $\Delta(t)$ at this point in time with the previously computed maximum or minimum. If this upper or lower bound is less in absolute value than the extremal point with which we compare it, the computation is terminated.

Where there was no damping, the search for extremal points proceeded as above up to the time when the excitation was terminated. At this point we compare the computed maximum and minimum to this time with

$$\max |\delta_2(t)| + \max |\delta_1(t)| ,$$

and choose the larger values as our desired maxima and minima.

In doing this, we make the assumption that in the residual era $\max \Delta(t)$ equals $\max \delta_2(t) + \max \delta_1(t)$, and $\min \Delta(t)$ equals $\min \delta_2(t) + \min \delta_1(t)$. This is not strictly true for all the given frequency combinations, but it is true if we make an arbitrarily small change in ω_2 for any given ω_1 (or vice-versa, of course).

Now, let $\Delta\omega$ be the change in ω_2. We want to show that there exists a time t_0 for which

$$\delta_1(t_0) = \frac{C_1}{\omega_1^2} \sin (\omega_1 t_0 + \phi_1) = \left| \frac{C_1}{\omega_1^2} \right| , \quad (A-7)$$

and

$$\delta_2(t_0) = \frac{C_2}{\omega_2^2} \sin \left[(\omega_2 + \Delta\omega) t_0 + \phi_2 \right]$$

$$= \left| \frac{C_2}{\omega_2^2} \right| . \quad (A-8)$$

Clearly there exists a phase angle θ such that

$$\frac{C_2}{\omega_2^2} \sin (\omega_2 t_0 + \phi_2 + \theta) = \left| \frac{C_2}{\omega_2^2} \right| , \quad (A-9)$$

but then our desired $\Delta\omega$ is equal to θ/t_0.

Since

$$\sin (\omega_2 t_0 + \phi_2) = \sin \left[\omega_2 \left(t_0 + \frac{2n\pi}{\omega_2} \right) \right.$$

$$\left. + \phi_2 \right] , \quad n = 0, 1, 2 \ldots , \quad (A-10)$$

$$\Delta\omega = \frac{\theta}{t_0 + \frac{2n\pi}{\omega_2}} , \quad (A-11)$$

and clearly $\Delta\omega \to 0$ as $n \to \infty$.

All computations were performed on an IBM 7094-7044 Directly Coupled System.

REFERENCE

A-1. W. Leighton, An Introduction to the Theory of Differential Equations (McGraw-Hill, New York), 1952

DISCUSSION

Dr. Morrow (Aerospace Corp.): If you want to simulate random vibration by shock, you should be able to do it if the pulses are quite close together, preferably with a random variation in timing; otherwise you get a periodic excitation. You might consider plotting contours of equal proximity instead of the present presentation of your proximity spectrum. You might be able to get the essential information on one sheet of paper.

Mr. Schell: We will have to discuss this further. It sounds interesting to me. I am quite anxious to get all these data on one sheet of paper because it is very cumbersome the way it is. We could normalize the amplitudes. That would help in making the plots a little easier to present.

Dr. Mains (Washington Univ.): It might interest some of you to know that before the words

"random vibration" were used as a combination to represent a particular concept, we were analyzing the flight vibration data from Talos and Terrier weapons. We decided that what we were seeing looked for all the world like a series of repeated shocks. We started analyzing the data to see what more we could find out, and working on this series of repeated shocks, we came up with the fact that we did indeed have a random vibration with a Gaussian distribution of amplitude in any given band. That is how some of this grew up. There has also been a good bit of analytical work done on calculating just what kind of a repeated ping model has to be generated analytically to get the same response that one gets with random vibration. That was about 7 or 8 years ago.

*　　*　　*

DEFINITION OF SHOCK DESIGN AND TEST
CRITERIA USING SHOCK AND FOURIER
SPECTRA OF TRANSIENT ENVIRONMENTS

M. Gertel and R. Holland
Allied Research Associates, Inc.
Concord, Massachusetts

In connection with recent environmental studies, shock and Fourier spectra for a variety of measured and idealized acceleration pulses and complex waveforms have been computed on an IBM 7094 digital computer using O'Hara's recursion equations for the Duhamel integral. These spectra have been machine-plotted in a normalized four-coordinate format similar to that proposed by Vigness using a General Dynamics SC4020 computer plotter. Several samples of computed spectra are presented and discussed. The application of shock and Fourier spectra for deriving shock design and test criteria is discussed in connection with recent measured shocks representative of missile pyrotechnic stage separation and Army tank turret gunfiring conditions.

INTRODUCTION

At the present state of the art, it has become more or less standard practice to define environmental design goals for equipment indirectly by laboratory environmental qualification tests. In the early days of the development of the environmental testing science (or art), it was sufficient to establish a shock or vibration testing requirement by completely intuitive and arbitrary means. In some instances, this involved specifying the machine or method of testing, rather than quantitatively or numerically defining the environment. If the test appeared to reproduce or resemble particular aspects of the environment, this was coincidental. The principal justification was that the test accomplished its purpose if it successfully reproduced or "simulated" the damaging effects of the environment, and thereby screened out equipment which would have failed in service.

In the post World War II years, and particularly with the advent of missiles and spacecraft, there have been increasing efforts to measure and define quantitatively service environments for the purpose of incorporating more realism in laboratory qualification testing of equipment. To a very great extent, the results of these efforts are reflected in the random vibration tests which are currently standard practice in most missile and spacecraft environmental qualification test programs.

By contrast with the advancements which have been made in improving laboratory vibration simulation, no similar progress appears evident in the area of making laboratory shock tests more representative of field conditions. In retrospect, this seems quite strange because shock and Fourier spectral techniques for quantitatively defining shock transients were well advanced and understood long before the concept of defining missile random vibration by spectral density functions became accepted practice.
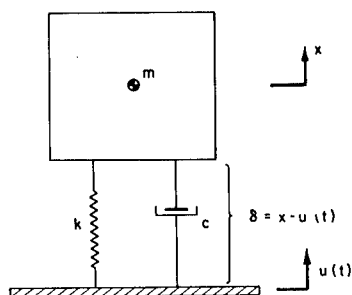
SHOCK SPECTRUM DEFINITION
OF TRANSIENTS

Definition of transient shock environments by a shock spectrum represents a special form of single degree of freedom response analysis. This response concept is regarded as representative of the "damaging effects" of the environment and is thoroughly documented in the technical literature. References (1-5), for example, contain varied presentations of the basic concepts involved in the development of shock spectra and their application to environmental shock analysis.

In brief, the shock spectrum is a plot of the maximum relative deflection responses of many simple single degree of freedom systems such as shown in Fig. 1, presented as a function of system natural frequency. Using the nomenclature in Fig. 1, the equation of motion for the simple system is

$$m\ddot{x} = -k(x - u) - c(\dot{x} - \dot{u}) , \qquad (1a)$$

or simply,

$$\ddot{x} = -\frac{k}{m} \delta - \frac{c}{m} \dot{\delta} . \qquad (1b)$$

$$\ddot{x} = -\frac{k}{m}\delta - \frac{c}{m}\dot{\delta} = -\omega_n^2 \delta - 2\zeta\omega_n\dot{\delta}$$

$$\delta(t) = \delta_0 e^{-\zeta\omega_n t}\left(\cos \omega_n\sqrt{1-\zeta^2}\,t + \frac{\zeta}{\sqrt{1-\zeta^2}}\sin \omega_n\sqrt{1-\zeta^2}\,t\right)$$

$$+ \frac{\dot{\delta}_0}{\omega_n\sqrt{1-\zeta^2}} e^{-\zeta\omega_n t}\sin \omega_n\sqrt{1-\zeta^2}\,t$$

$$- \frac{1}{\omega_n\sqrt{1-\zeta^2}}\int_0^t \ddot{u}(\tau)e^{-\zeta\omega_n(t-\tau)}\sin \omega_n\sqrt{1-\zeta^2}(t-\tau)d\tau$$

Fig. 1. Single degree of freedom system used for shock spectrum analysis

The maximum relative deflection d of a simple system response to a foundation shock acceleration input $\ddot{u}(\tau)$ may be determined experimentally with a multifrequency reed gage, by simulation techniques with an electronic or mechanical analog computer, or analytically by Duhamel's integral or an equivalent numerical method.

Duhamel's integral (sometimes called the convolution integral) for the system relative deflection response $\delta(t)$ to a foundation acceleration input may be stated as:

$$\delta(t) = \delta_0 e^{\zeta\omega_n t}\left(\cos \omega_d t + \frac{\zeta}{\sqrt{1-\zeta^2}}\sin \omega_d t\right) \qquad (2)$$
$$\text{(Cont.)}$$

$$+ \frac{\dot{\delta}_0}{\omega_d} e^{\zeta\omega_n t}\sin \omega_d t$$

$$- \frac{1}{\omega_d}\int_0^t \ddot{u}(\tau)e^{-\zeta\omega_n(t-\tau)}\sin \omega_d(t-\tau)d\tau, \qquad (2)$$

where

$\omega_n = \sqrt{k/m}$ = undamped radian natural frequency,

$\omega_d = \omega_n\sqrt{1-\zeta^2}$ = damped radian natural frequency,

$\zeta = c/2\sqrt{km}$ = ratio of critical damping,

δ_0 = initial relative deflection, and

$\dot{\delta}_0$ = initial relative velocity.

Equation (2) and its derivative have been transformed by O'Hara (6) into pairs of recursion equations which are more readily suited to numerical computation. These may be written for an acceleration input which is replaced by a sequence of n incremental steps of equal time duration to approximate closely the original function, as follows:

$$\omega_n\delta_{n+1} = A_1\omega_n\delta_n + A_2\dot{\delta}_n + A_3\ddot{u}_n + A_4\Delta\ddot{u}_n , \qquad (3)$$

$$\dot{\delta}_{n+1} = A_5\omega_n\delta_n + A_6\dot{\delta}_n + A_7\ddot{u}_n + A_8\Delta\ddot{u}_n , \qquad (4)$$

where

$\delta_n = \delta(t_n) ,$

$\dot{\delta}_n = \dot{\delta}(t_n) ,$

$\delta_{n+1} = \delta(t_n + h) ,$

$\dot{\delta}_{n+1} = \dot{\delta}(t_n + h) ,$

$h = t_{n+1} - t_n ,$

$A_1 = a + \zeta b ,$

$A_2 = b ,$

$A_3 = \frac{1}{\omega_n}(A_1 - 1) ,$

$A_4 = \frac{1}{\omega_n}\left\{\frac{1}{\omega_n h}\left[(1 - 2\zeta^2)b + 2\zeta^2(1 - a)\right] - 1\right\} ,$

$A_5 = -b ,$

$A_6 = a - \zeta b ,$

$A_7 = -\frac{b}{\omega_n} ,$

250

$$A_8 = \frac{A_3}{\omega_n h} ,$$

$$a = e^{-\zeta \omega_n h} \cos \omega_d h ,$$

$$b = \left(e^{-\zeta \omega_n h} \sin \omega_d h \right) \sqrt{1 - \zeta^2} ,$$

$$\omega_d = \omega_n \sqrt{1 - \zeta^2} ,$$

$$\zeta = c/2 \sqrt{km} ,$$

and

$$\omega_n = \sqrt{k/m} .$$

The general nature of the relative deflection response of a simple system to an arbitrary input is predominantly sinusoidal at its own natural frequency ω_n, especially if the damping is very slight. Accordingly, peak sinusoidal velocity v and acceleration a parameters can be computed from the relative deflection response d, as follows:

$$v = \omega_n d , \tag{5}$$

$$a = \omega_n v = \omega_n^2 d . \tag{6}$$

When the system damping is zero, the peak velocity of Eq. (5) corresponds exactly with the peak velocity of the mass relative to its foundation, and the peak acceleration of Eq. (6) corresponds exactly with the absolute acceleration of the mass. These are only approximately true when damping is present. In recognition of this approximation, v in Eq. (5) is referred to as "pseudo-velocity." Similarly, a in Eq. (6) is called the "equivalent static acceleration" because this is the steady acceleration which will produce the same peak relative response deflection d. It is significant to note here that the maximum relative deflection, with and without damping, is perhaps the most important of all the shock spectrum parameters. This parameter makes it possible to perform simple stress analysis in systems subjected to complex shock motions when the stress-deflection relationship has been determined for the system.

FOURIER SPECTRUM DEFINITION OF TRANSIENTS

Although historically the Fourier spectrum, which transforms a function from the time domain into the frequency domain, is the oldest known technique for defining shock transients, this approach has never been widely exploited. The principal difference between the Fourier and shock spectrum is that while the latter is exclusively a function of system response, the Fourier spectrum can be used to define either the system input or its response. Moreover, the system transfer or transmissibility function $T(\omega)$ relates the input Fourier spectrum $F_i(\omega)$ and the response Fourier spectrum $F_r(\omega)$ in the frequency domain as follows:

$$F_r(\omega) = F_i(\omega) \times T(\omega) . \tag{7}$$

Another advantage cited for the application of Fourier techniques is that the transformation of a time function $f(t)$ to a Fourier frequency function $F(\omega)$ is a reversible process. This is indicated by the following equations defining the Fourier transformation and its inverse:

$$F(\omega) = \int_{-\infty}^{\infty} f(t) \, e^{-j\omega t} dt , \tag{8}$$

$$F(t) = \frac{1}{2\pi} \int_{-\infty}^{\infty} F(\omega) \, e^{j\omega t} d\omega . \tag{9}$$

It is argued by many environmental engineers that the potential implementation of Eqs. (7), (8) and (9) makes the Fourier spectrum approach a much more powerful method than the statement of "damaging effects" which can be inferred from shock spectra. Nevertheless, the mathematical operational advantages of Fourier spectra are seldom utilized.

Recently it has been shown by O'Hara (6) and Rubin (7) that there is a fixed relationship between the Fourier spectrum and the undamped shock spectrum of the residual vibration d_r which exists after an acceleration shock pulse ends:
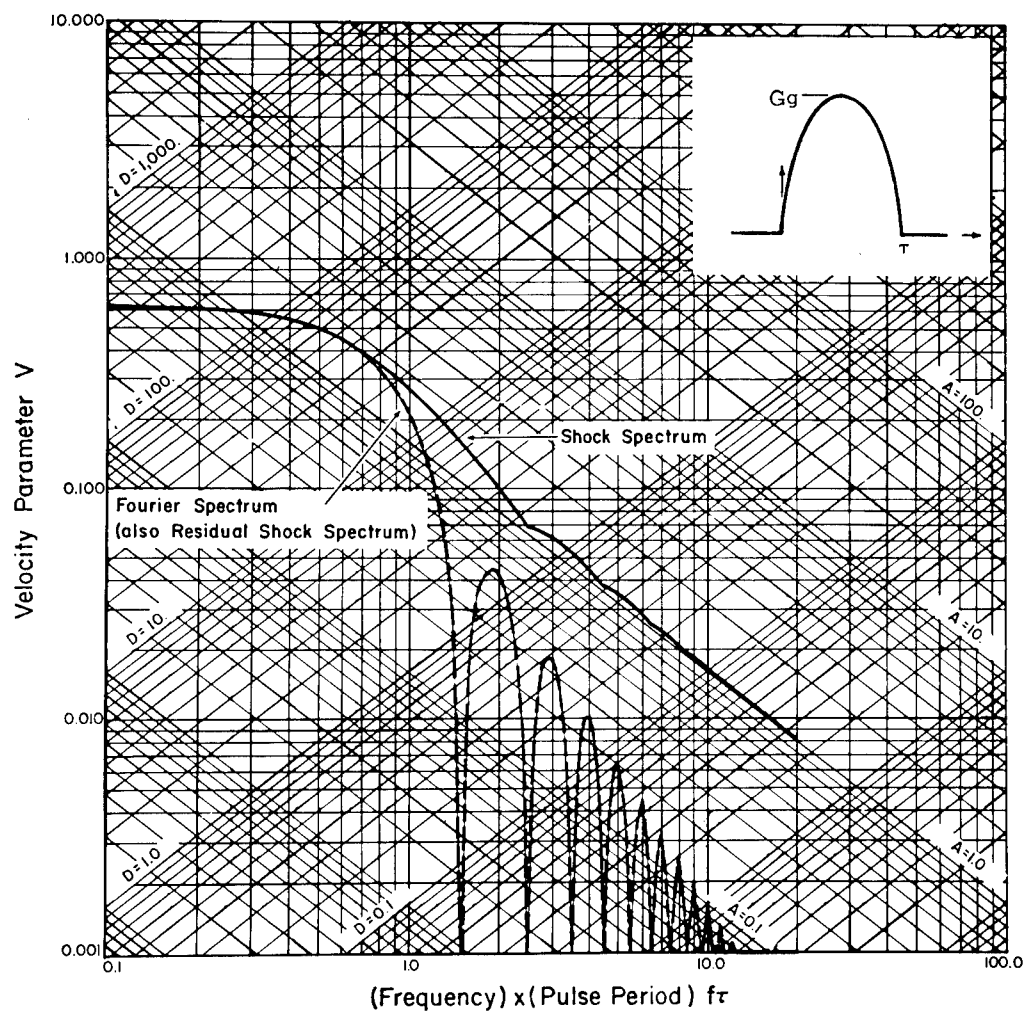
$$\omega_n d_r = F(\omega) . \tag{10}$$

This, in effect, states that the pseudo-velocity of the residual shock spectrum for an acceleration pulse is identical to the Fourier amplitude spectrum of the acceleration pulse. (Fourier phase angle information is, of course, not included here.) Thus, if the undamped "maximax" shock spectrum (plot of relative deflection maxima whether or not occurring during or after the shock pulse) is plotted superimposed on the residual shock spectrum, there effectively results a combined plot of the shock and Fourier (amplitude) spectrum for any given shock motion. It is particularly convenient for this combined spectrum plot to use a logarithmic four-coordinate nomograph, similar to the well-known vibration nomograph. This can then be read directly for displacement, velocity and acceleration parameters.

Figure 2 presents an example of a combined shock and Fourier spectrum plot for a half-sine pulse. The coordinates of the plot are presented in dimensionless form as indicated in the table at the bottom of the figure. This plot is essentially the same as presented by Vigness (8), except that the sloping reference lines of constant displacement have been shifted by the constant $g = 386$ in./sec^2 to simplify deflection computations.

SAMPLE SHOCK AND FOURIER SPECTRA FOR IDEALIZED AND COMPLEX TRANSIENTS

Although the application of shock and Fourier spectra as a means for defining shock transient environments have been discussed at great length in many Shock and Vibration Symposia, there is still only a limited utilization of these concepts to define actual field conditions.

PARAMETER	FOURIER SPECTRUM	SHOCK SPECTRUM
$d = (G_T^2) \cdot (D)$ in.	deflection component	relative deflection response
$v = (G_g\tau) \cdot (V)$ in./sec	velocity component	pseudo velocity response
$a = (Gg) \cdot (A)$ in./sec^2	acceleration component	equivalent static acceleration

Fig. 2. Fourier and shock spectra for half-cycle sine acceleration pulse

Perhaps the principal deterrent here has been that until recently analog computation techniques have been considered exclusively for determination of shock and Fourier spectra. Although analog techniques can provide an instantaneous display of system response, the spectral plotting of the response peaks must be done manually; this can become quite laborious and time consuming if many shock records are to be analyzed. Further, there may be additional problems and delays if the field shock records are recorded on oscillographic films. The film records of the shocks must be transformed into equivalent electrical signals before they can be used as shock inputs to an analog computer.

The application of high-speed digital computers coupled with automatic computer plotters to process shock and Fourier spectra will greatly advance the application of these concepts to the definition of shock environments. Figures 2 to 12 present samples of computed shock and Fourier spectra for many idealized and complex shock pulses which are considered representative of various types of field conditions; these have been reproduced from Refs.
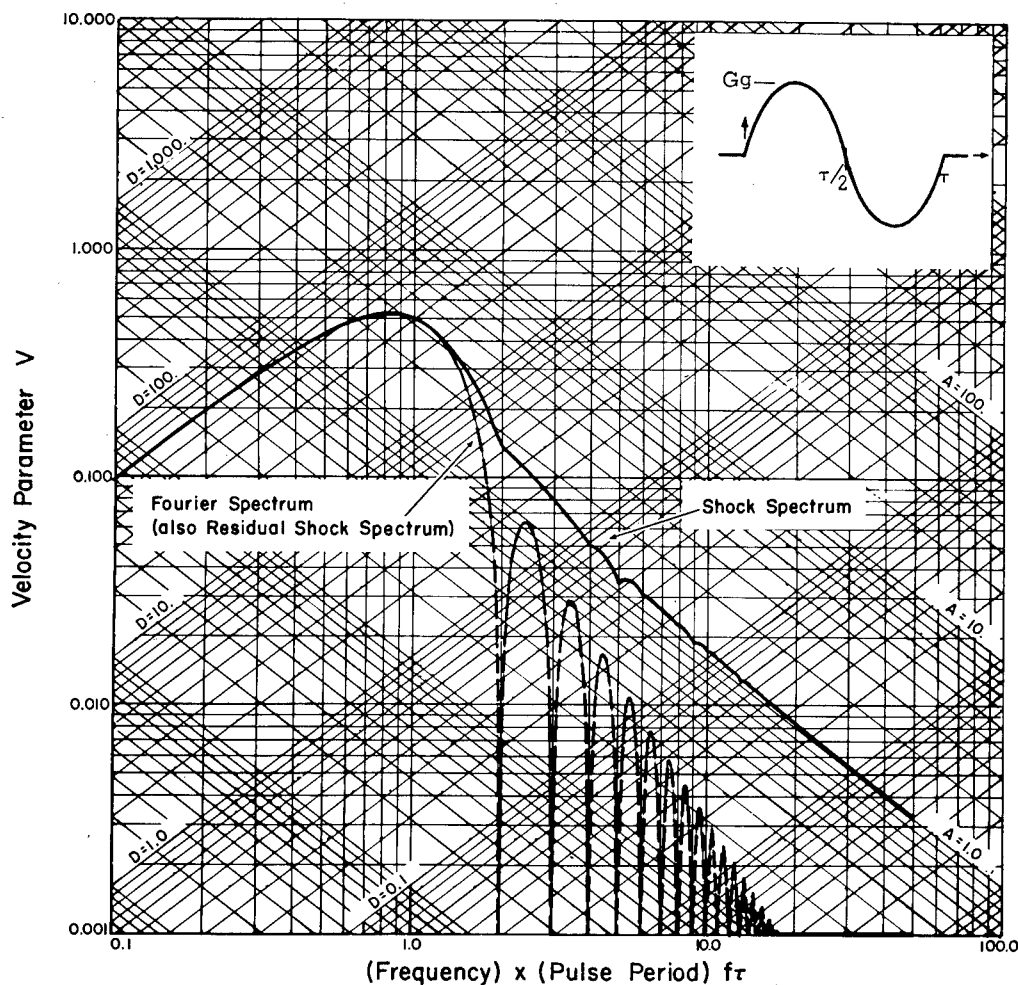
PARAMETER	FOURIER SPECTRUM	SHOCK SPECTRUM
$d = (G\tau^2) \cdot (D)$ in.	deflection component	relative deflection response
$v = (Gg\tau) \cdot (V)$ in./sec	velocity component	pseudo velocity response
$a = (Gg) \cdot (A)$ in./sec^2	acceleration component	equivalent static acceleration

Fig. 3. Fourier and shock spectra for full-cycle sine acceleration pulse

Fig. 4. Fourier and shock spectra for decaying sinusoidal acceleration
pulse with 8 cycles and amplitude ratio = 1/2

PARAMETER	FOURIER SPECTRUM	SHOCK SPECTRUM
$d = (G_T^2) \cdot (D)$ in.	deflection component	relative deflection response
$v = (G_T) \cdot (V)$ in./sec	velocity component	pseudo velocity response
$a = (Gg) \cdot (A)$ in./sec^2	acceleration component	equivalent static acceleration

(9) to (15). With the exception of the spectra in
Fig. 5 and curve (1) of Fig. 6, which are drawn
from Refs. (9) to (11), all the spectra presented
herein have been computed with Eqs. (3) and (4),
using an IBM 7094 computer. The computed
spectral points were then plotted automatically
with a General Dynamics SC 4020 computer
plotter. This plotter not only plots the spectra,
but also draws and labels the axes of the four-
coordinate nomograph. This is all accomplished
in a matter of a few minutes per graph, and

compares with one or more days which might
be required to do an equivalent amount of anal-
ysis by analog techniques.

IDEALIZED SHOCK TRANSIENTS

There are two significant properties of
shock spectrum plots of acceleration pulses
which are important to note. First, the low-
frequency portion of the shock spectrum

254

approaches a value of constant velocity which corresponds to the net velocity change embodied in the shock pulse. This can be seen in Fig. 2, for example, where the low-frequency portion of the half-sine pulse shock spectrum approaches a constant value of $v = 0.63\,G_g\,\tau$. This checks with the theoretical value for the area under a half-sine pulse. Systems in this low-frequency range are said to be "velocity sensitive." The second property to be noted in shock spectra for acceleration pulses is that the high-frequency portion of the curve approaches a value of constant acceleration which corresponds to the

peak acceleration of the pulse. This can only be seen in Fig. 2, where the high-frequency portion of the half-sine pulse of the shock spectrum is asymptotic to $a = G_g$, the peak value of the input. Systems in this high-frequency range are said to be "acceleration sensitive."

The Fourier spectrum of the half-sine pulse in Fig. 2 is of great interest because it indicates that all frequency components are present in the shock except certain well-defined multiples of the dimensionless parameter $f\tau$.

(A) and (B) R. Blake (Proc. IES, April 1964) ——————

(C) V. R. Paul (Proc. 33rd Shock and Vibration Symposium) ——·——·——

(D) D. E. Hines (Proc. IES, April 1964) — — — — — — — —
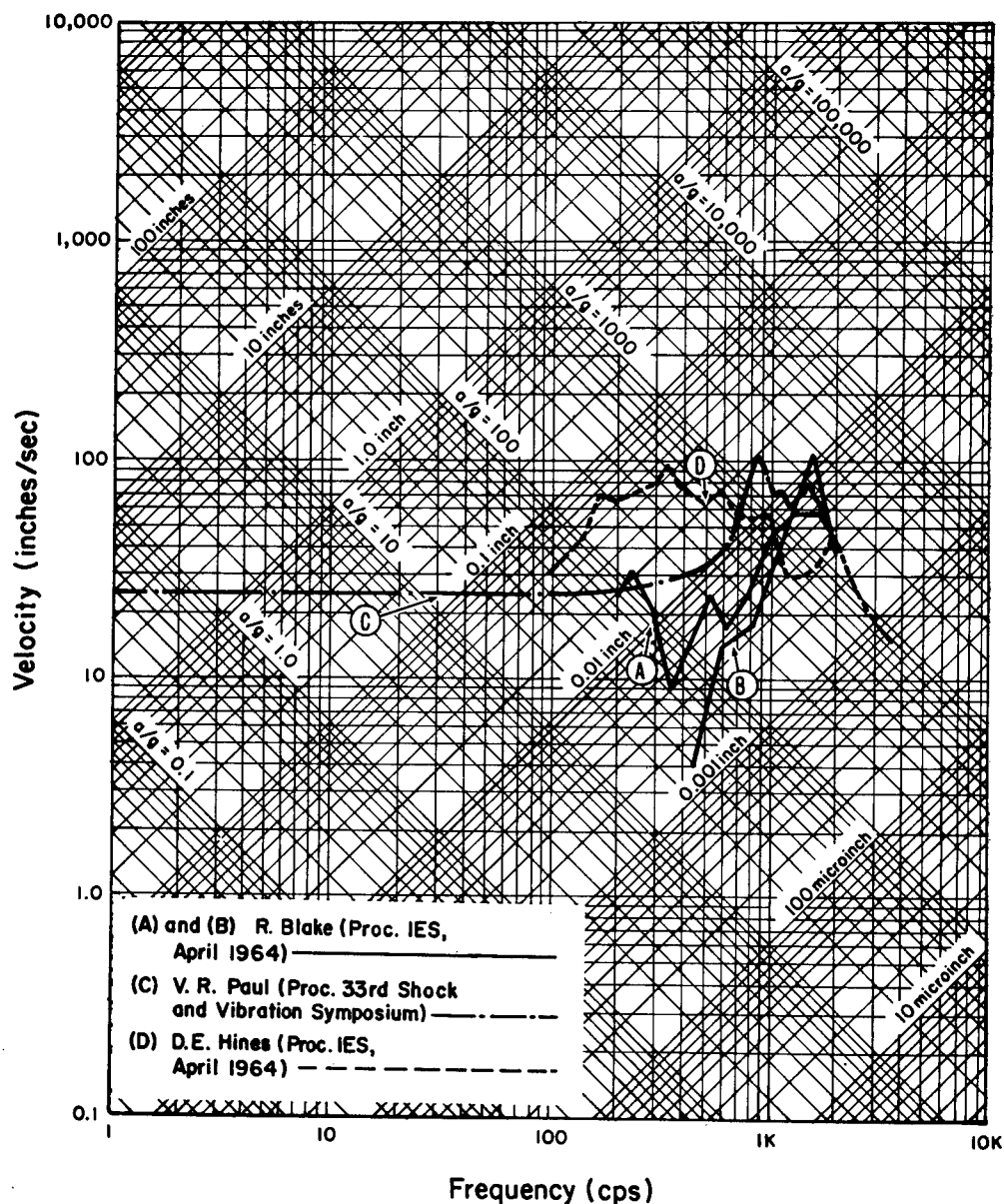
Fig. 5. Typical separation shock spectra

255
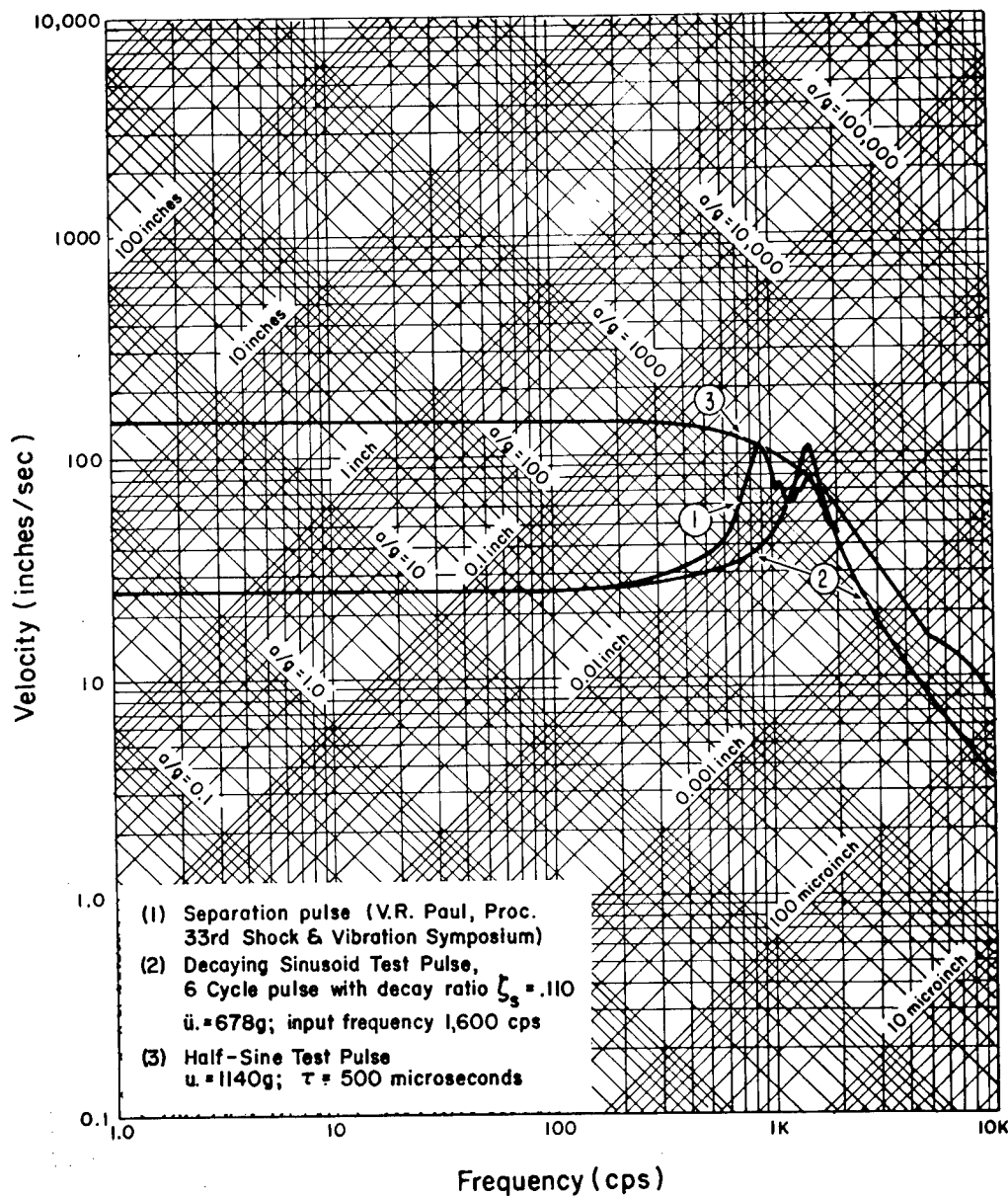
Fig. 6. Separation shock test pulse comparison

Within the figure:

Velocity (inches/sec)

(1) Separation pulse (V.R. Paul, Proc.
33rd Shock & Vibration Symposium)

(2) Decaying Sinusoid Test Pulse,
6 Cycle pulse with decay ratio ζ_s = .110
ü.=678g; input frequency 1,600 cps

(3) Half-Sine Test Pulse
u.=1140g; τ = 500 microseconds

Frequency (cps)

The missing frequency components appear as "notches" in the Fourier spectrum. Consequently, in a particular design problem involving a system to be subjected to a half-sine shock pulse, it would be definitely advantageous to design or select the system's natural frequency to correspond with a frequency void or notch in the Fourier spectrum. This idea of frequency selectivity in designing a system for shock is confirmed by recalling the relationship between the Fourier and residual shock spectrum. The notches in the Fourier spectrum correspond to those in the residual shock

spectrum and, therefore, indicate the natural frequencies of systems which will remain absolutely stationary at the end of the shock pulse. Accordingly, these systems will be subjected to negligible vibration fatigue damage. In this sense, therefore, the combined Fourier and shock spectrum plot may be regarded as providing a type of fatigue cycling information which is analogous to the three-dimensional shock spectrum described in Ref. (12).

For purposes of comparison with the "single polarity" shock pulse of Fig. 2, the spectra

for an "alternating polarity" full-cycle sine acceleration pulse are presented in Fig. 3. It is significant to note here that there is no low-frequency constant-velocity asymptote for the shock and Fourier spectra. This results because the net velocity change is zero at the end of the pulse. This is an important point to note and will be discussed later in connection with selecting shock test parameters to correspond with the damaging aspects of service conditions. Although the low-frequency portion of the full-sine pulse shock spectrum curve differs from the single polarity shock pulse, the high-frequency portion of the spectrum behaves as expected and becomes asymptotic to the peak acceleration of the shock.

For further comparison with the idealized cases of Figs. 2 and 3, Fig. 4 shows the shock and Fourier spectra of a decaying sinusoidal acceleration pulse. Two points of interest may be noted here. First, unlike the full-sine pulse, the low-frequency shock spectrum approaches a low value of constant velocity. This is due to the fact that each alternating polarity half cycle of the transient differs from the previous half

cycle by a constant factor related to the log decrement of the decay rate. Second, due to the fact that a short-term condition of resonance can occur at the input frequency, the maximum shock amplification factor can become quite large for this type of transient.

Missile Separation Shock Transients

Figure 5 shows typical shock spectra which have been reported (9-11) for missile stage separation and pyrotechnic type shocks. It seems characteristic that each of the three spectra indicates high-frequency accelerations in excess of 1000 g, yet the low-frequency region shows that negligible velocity change is involved in producing the shock.

For purposes of illustrating how the testing parameters might be established for this type of shock, Fig. 6 shows two idealized forms of shock pulse spectra superimposed on one of the separation shock spectra of Fig. 5. The idealized forms used here are a half-sine pulse and a decaying sinusoidal transient. Both of these
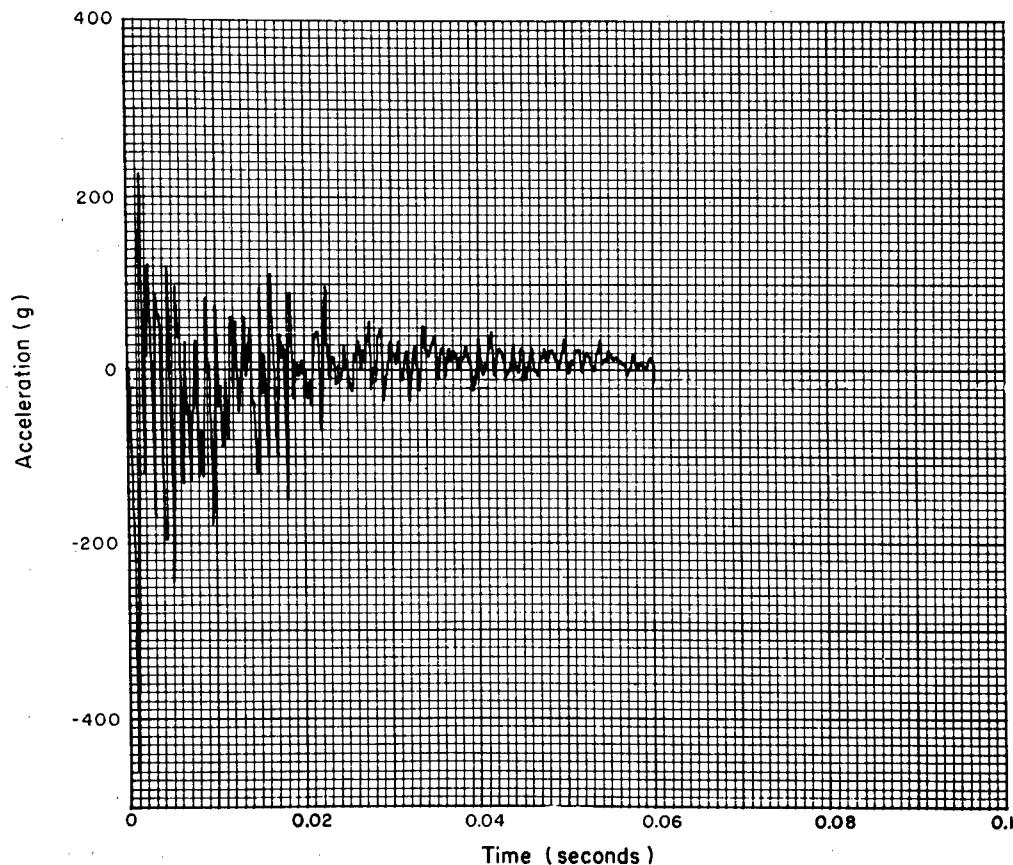
Fig. 7. Shock input time history for record 4
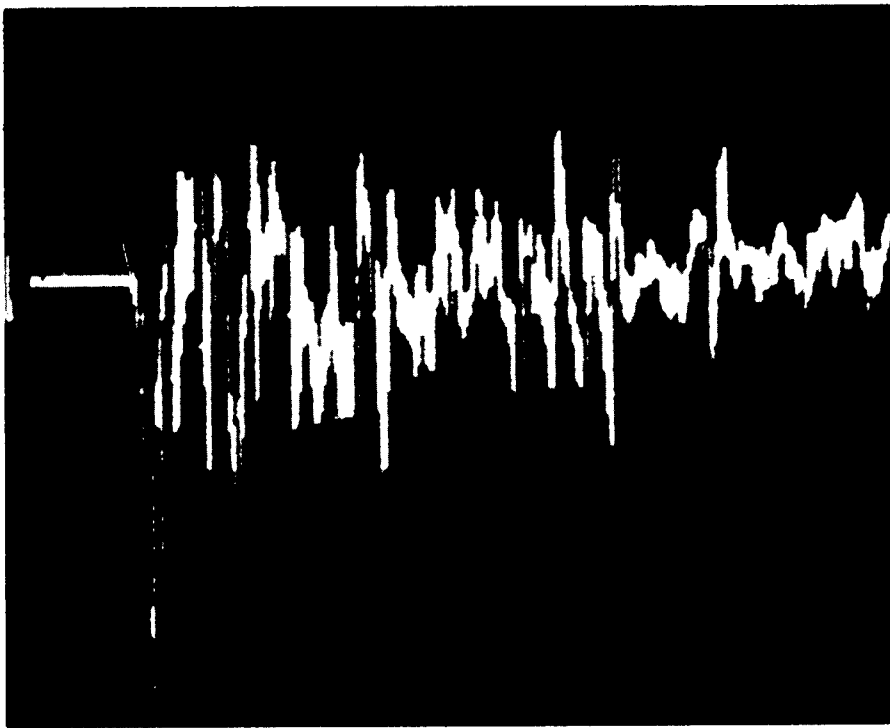
Fig. 8. Analog playback of high-speed digitized
time history input of record 4

have been shifted and adjusted to provide a maximum response of 2000 g at 1600 cps to match the highest acceleration point on the sample separation shock spectrum. For purposes of simplicity, no attempt was made to match the 900-cps component in the separation shock. The decaying sinusoidal transient can be adjusted to provide a reasonable match with both the high- and low-frequency ranges of the separation shock. In contrast, the half-sine pulse (or other single polarity pulses) can only be adjusted for either a high- or a low-frequency match, but not both. It seems evident here that simple pulses are far from ideal for testing the ability of components to withstand the type of missile pyrotechnic separation shocks reported in Refs. (9) to (11).

Gunfire Shock Transients in
    Tank Vehicles

Figures 7 to 10 describe a typical shock condition produced by the Frankford Arsenal's 32,000-ft-lb shock machine (15). This shock is considered representative of the complex shocks experienced by fire control equipment in tank turrets during gunfire conditions. The

Environmental Division of the Frankford Arsenal is planning an extensive field testing program which will involve making gunfire shock measurements and then correlating shock and Fourier spectra for the field data with laboratory test machine spectra.

Figure 7 presents a sample of one of the Frankford Arsenal's shock records as replotted by a General Dynamics SC-4020 computer plotter from manually digitized data. Figure 8 shows a plot of the same shock record from digitized data obtained by a high-speed optical-electronic scanning process. This is included here for information purposes only to indicate that high-speed automatic digitizing of visual records can be readily accomplished at the present state of the art.

The shock and Fourier spectra of Figs. 9 and 10 were computed using the manually digitized data of Fig. 7. Figure 9 presents the undamped shock and Fourier spectra, while Fig. 10 shows the "smoothing" effect that small amounts of damping will have on the resulting shock spectra.

As a by-product, the spectra of Figs. 9 and 10 can be utilized to aid in the selection of an

258

"optimum" shock mount with minimum deflection to attenuate the transmitted shock to delicate equipment. To illustrate this, in Figs. 9 and 10, the shock spectrum exhibits approximately a 90-g "plateau" or constant "equivalent static acceleration" below 80 cps. Inasmuch as the shock spectrum indicates the "response" of simple single degree of freedom systems, this can also be taken as the output of a single degree of freedom "c.g. type" isolation system. The four-coordinate nomograph shows that the 80-cps isolation system will exhibit the minimum deflection response for the indicated 90-g output; hence, this can be selected as an "optimum" isolator. This will eliminate the possibility of higher frequency equipment components experiencing responses in excess of 1000 g, as indicated by the maximax shock spectrum.

ACCURACY CHECK OF DIGITAL COMPUTER SHOCK PROGRAM

As noted earlier, an IBM 7094 digital computer has been programmed to obtain relative deflection shock responses for any arbitrary shock pulse using Eqs. (3) and (4). The program computes the complete time history of the response and then keeps only the maximax and residual peak values. In the shock work conducted for the Environmental Division of the Frankford Arsenal (15), an accuracy check of the computer program was conducted. In this work, theoretical responses for a complex shock motion were computed by classical Laplace transformation means and with the digital computer. The complex shock selected for this is the two-component decaying sinusoidal
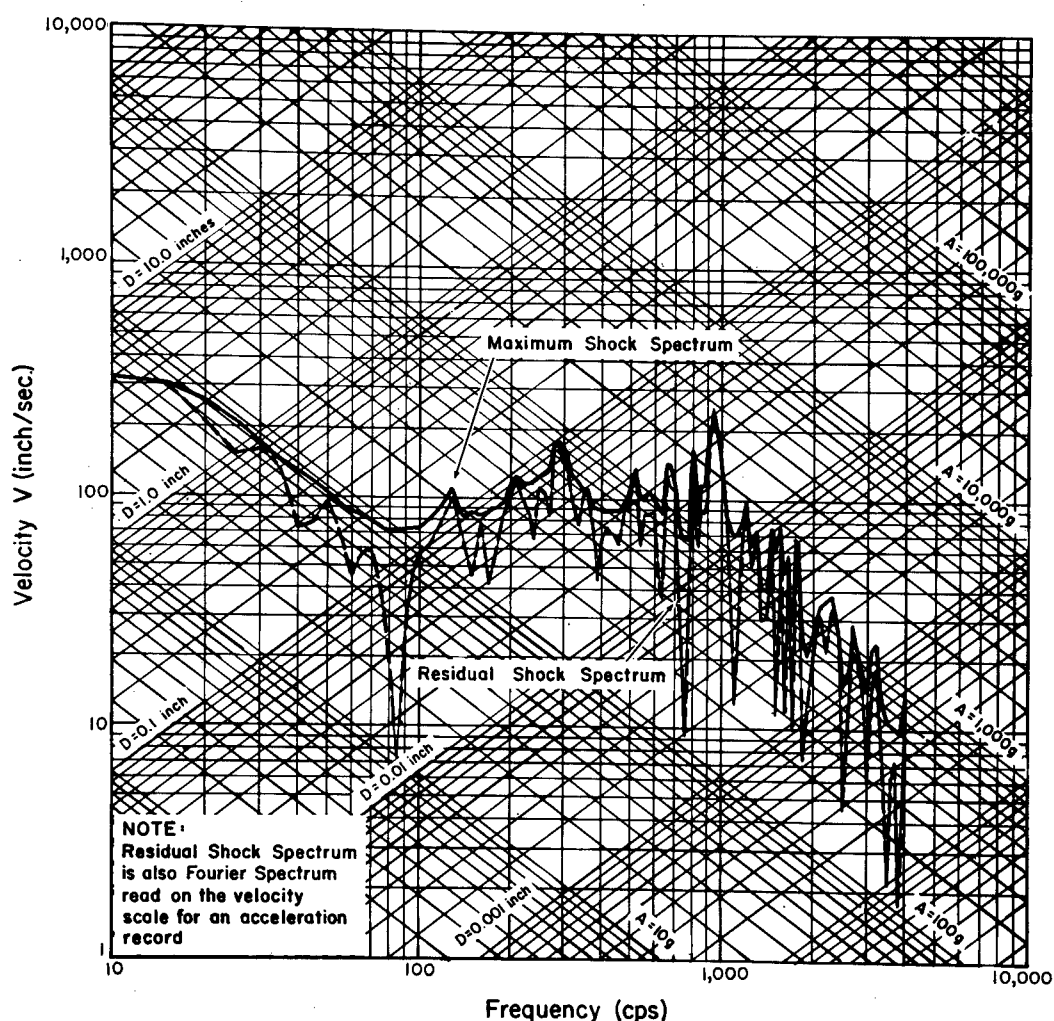
Fig. 9. Maximax and residual spectra for record 4
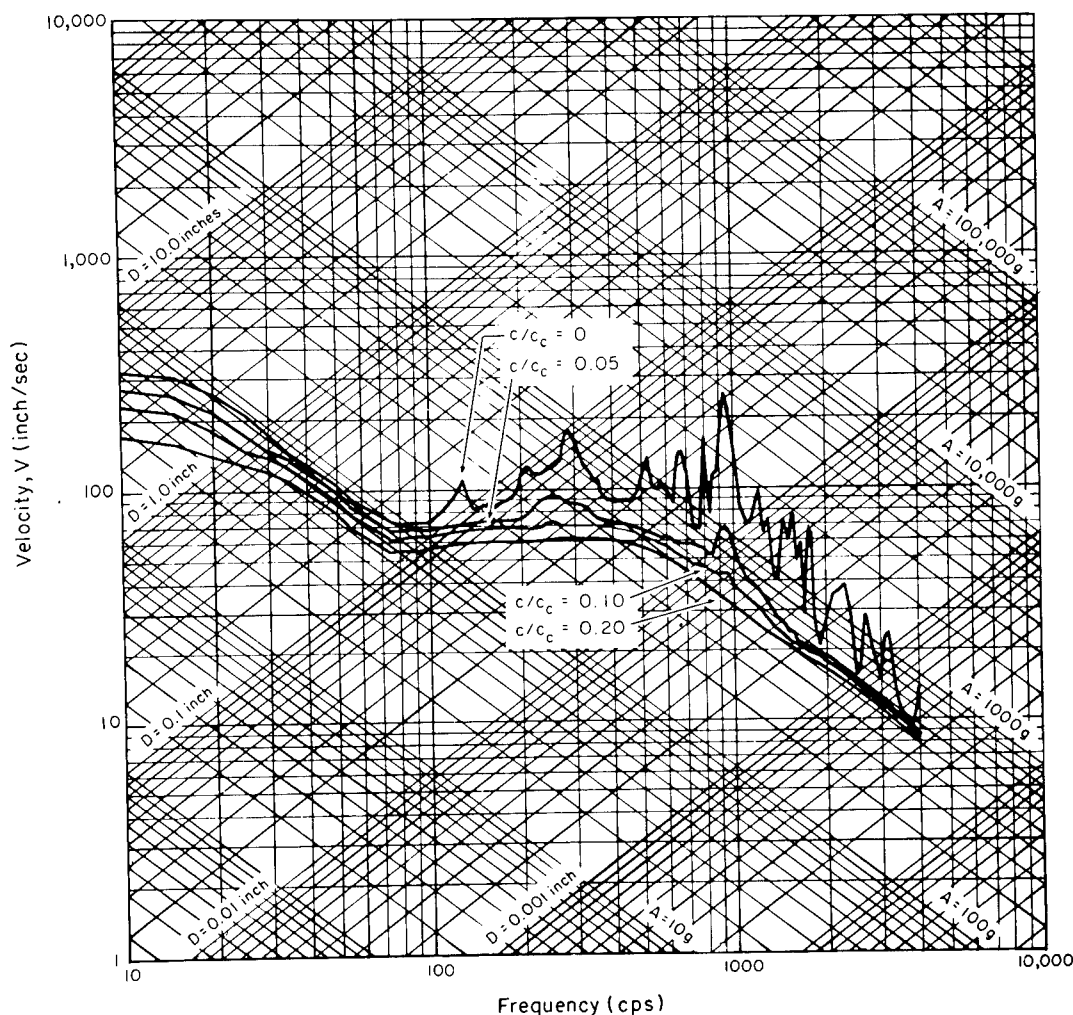
Fig. 10. Damped shock spectra for record 4

transient shown in Fig. 11. Table 1 summarizes the peak relative deflection responses computed for ten different system natural frequencies by the classical method and with the digital computer. It can be seen that the worst error is a relatively insignificant 0.34 of 1 percent. For purposes of reference, the digitally computed shock and Fourier spectra for the reference shock transient in Fig. 11 are presented in Fig. 12.

In addition to the foregoing check on the accuracy of the peak response computation by the digital computer, an analysis was made of the frequency resolution of the computer program in Ref. 15. The frequency resolution in the response is a function of the number of points used to digitize the shock input. If M is the total number of digitized points for a shock record of duration τ seconds, then the number

of points N in one period or complete cycle at frequency f, is defined by:

$$N = \frac{M}{f\tau} \text{ points/cycle.} \qquad (11)$$

The maximum possible error in obtaining the peak amplitude of a response sinusoid occurs when the digitizing points "straddle" the peak. The maximum error E in percent is then

$$E = 100 \left(1 - \cos\frac{\pi}{N}\right). \qquad (12)$$

The error indicated by Eq. (12) is plotted in Fig. 13 as a function of a frequency parameter which is the inverse of Eq. (11). It may be noted that Fig. 13 indicates that the error in frequency resolution of peaks can be maintained constant at approximately 5 percent by linear
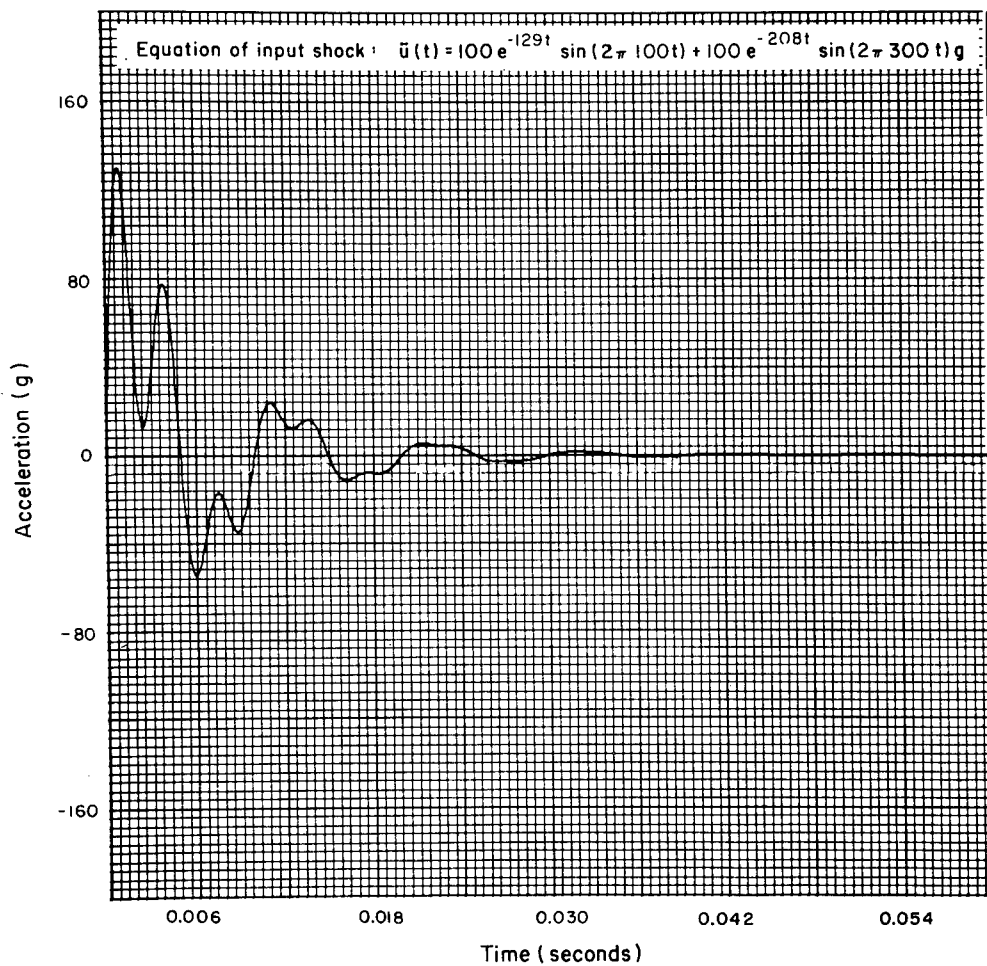
Fig. 11. Shock input time history for two-component
superimposed decaying sinusoidal acceleration

TABLE 1
Sample Comparison of Theoretical and Computer Program
Peak Responses for Two-Component Decaying
Sinusoidal Acceleration Shock Inputs

Frequency (cps)	Peak Response (in.)			Error (%)
	Theoretical Solution	Shock Program	Difference	
10	-1.27048	-1.2701	+0.0004	0.0315
30	-0.480569	-0.48040	+0.00017	0.0354
80	-0.278056	-0.27797	+0.00009	0.0323
100	-0.246923	-0.24680	+0.00012	0.0485
120	-0.131544	-0.13153	+0.00001	0.00761
200	-0.0457847	-0.045753	-0.000011	0.024
280	-0.0476972	-0.047644	+0.000053	0.111
300	-0.0497754	-0.049824	-0.000049	0.0988
350	-0.0272114	-0.027138	+0.000073	0.269
1000	-0.00174328	-0.0017374	+0.0000059	0.339

261

$$\ddot{u}(t) = 100\,e^{-129\,t}\sin(2\pi 100\,t) + 100\,e^{-208\,t}\sin(2\pi 300\,t)\,g$$

Equation of input shock:

1000.0

100.0

Velocity, V (inch/sec)

10.0

1.0

0.1

D = 1.0 INCHES

D = 0.1 INCH

D = 0.01 INCH

D = 0.001 INCH

D = 0.0001 INCH

A = 10,000 g

A = 1,000 g

A = 100 g

A = 10 g

Maximax Shock Spectrum

Residual Shock Spectrum

Note:
Residual shock spectrum
is also Fourier spectrum
read on the velocity scale
for an acceleration record

10   100   1000   10,000

Frequency (cps)

Fig. 12. Maximax and residual spectra for two-component
superimposed decaying sinusoidal acceleration

interpolation of the input. To accomplish this, it is necessary to maintain N = 10 for high-frequency response computations. This was done automatically by the computer program for the shock and Fourier spectra of Figs. 7 to 10. For example, the digitizing point density utilized in Fig. 7 is

$$\frac{M}{\tau} = \frac{200}{0.010} = 20{,}000 \ \text{points/sec} .$$

By requiring that N = 10 points/cycle, the frequency resolution provided by Fig. 7 is

$$f = \frac{M}{N\tau} = \frac{20{,}000}{10} = 2000 \ \text{cps} .$$

The spectral plots of Figs. 9 and 10 are carried out to 4000 cps. Consequently, the computer program in this particular case was called upon to provide linear interpolation of the input to maintain N = 10 from 2 to 4 kc.
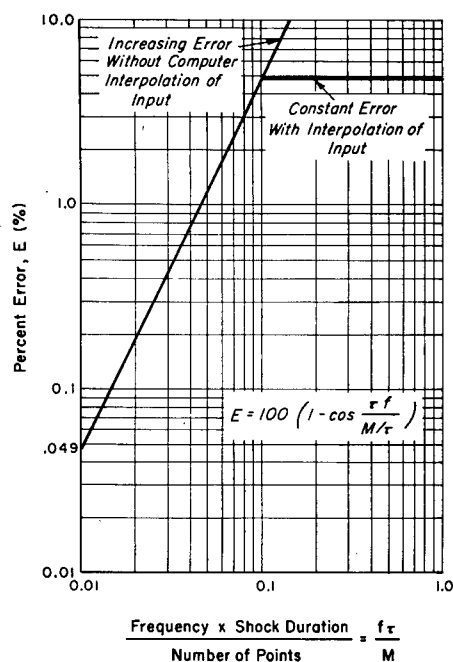
Fig. 13. Maximum possible frequency component error due to digital conversion of shock input

$$E = 100 \left(1 - \cos \frac{r f}{M/r} \right)$$

$$\frac{\text{Frequency} \times \text{Shock Duration}}{\text{Number of Points}} = \frac{f\,\tau}{M}$$

REFERENCES

1. J. P. Walsh and R. E. Blake, "The Equivalent Static Accelerations of Shock Motions," Proc. SESA 6 (2) (1949)

2. C. E. Crede, M. Gertel, and R. D. Cavanaugh, "Establishing Vibration and Shock Tests for Airborne Electronic Equipment," WADC Tech. Rept. 54-272 (ASTIA Doc. AD 45-696), 1954

3. T. K. Caughey and D. E. Hudson, "A Response Spectrum Analyzer for Transient Loading Studies," Proc. SESA 13 (1) (1955)

4. A. F. Dick and R. E. Blake, "Reed-Gage Shock-Spectrum Characteristics of Navy Mediumweight High-Impact Shock Machine," NRL Rept. 4750, July 1956

5. C. T. Morrow, "The Shock Spectrum," Electrical Manufacturing 64 (1959)

6. G. J. O'Hara, "A Numerical Procedure for Shock and Fourier Analysis," NRL Rept. 5772, June 1962

7. S. Rubin, "Concepts of Data Reduction," Ch. 23 in Shock and Vibration Handbook (C. M. Harris and C. E. Crede, Ed.) (McGraw-Hill, New York), 1961

8. I. Vigness, "Elementary Considerations of Shock Spectra," Shock and Vibration Bull. No. 34, Part 3, pp. 211-222, Dec. 1964

9. R. E. Blake, "Problems of Simulating High Frequency Mechanical Shocks," Proc. IES, April 1964

10. V. R. Paul, "Mechanical Shock from Frangible Joints," Shock and Vibration Bull. No. 33, Part IV, pp. 63-71, Dec. 1964

11. D. E. Hines, "Generation and Propagation of Stage Separation Shocks in Missiles and Space Vehicles," Proc. IES, April 1964

12. M. Gertel, "Specification of Laboratory Tests," Ch. 24 in Shock and Vibration Handbook (C. M. Harris and C. E. Crede, Ed.) (McGraw-Hill, New York), 1961

13. M. Gertel and R. Holland, "Methods for Specifying and Extrapolating Shock Conditions," Final Rept.; Vol. I, NASA-MSFC Contract NAS-8-11090; MITRON R&D Corp., Rept. 607-4-I, Dec. 1964

14. M. Gertel and R. Holland, "Compilation of Four Coordinate Shock and Fourier Spectra for Simple and Complex Shock Motions,"

263

Final Rept.; Vol. II; NASA-MSFC Contract
NAS-8-11090; MITRON R&D Corp. Rept.
607-4-II, Dec. 1964

15. M. Gertel and R. Holland, "Analysis of
Shock Records Using a Digital Computer,"
Frankford Arsenal Rept. R-1763 (ASTIA
AD 465410), May 1965

*   *   *

STRUCTURAL RESPONSE TO IMPULSIVE LOADING
(PYROTECHNIC DEVICES)

Vincent S. Noonan and William E. Noonan
McDonnell Aircraft Corporation
St. Louis, Missouri

The flexible linear shaped charge and other pyrotechnic devices are used during various separation phases in the Gemini Mission Profile. Concern has been expressed regarding structural response and/or equipment malfunctions resulting from the high-acceleration high-frequency transient motions (shocks) induced in vehicle structures by separation events. In particular, separation techniques employing cutting by flexible linear shaped charges have been known to cause relay chatter and fractures of brittle parts or structure. Therefore, the structural response to impulsive loading of spacecraft structure and the effects on the performance of electronic equipment mounted to such structure have been investigated.

Two test programs were conducted, one primarily to determine the type of instrumentation needed to obtain reliable transient data and the other to obtain the transient response data of the Gemini Adapter due to firing. Fourier transforms were calculated for the data obtained. A Fourier transform computer program was set up and checked out by using the data from a known square pulse. The desired frequency range for the analysis was not compatible with the computer sampling rate; therefore the time duration of the pulse was increased (frequency decreased) by utilizing tape recorder speed changes.

The maximum accelerations recorded by the adapter shell mounted accelerometers, for both the longitudinal and radial directions during the two tests, were 6500 g and 4100 g, respectively. Some scatter is associated with the data from the two tests, and the attenuation of the initial impulse is not always consistent with distance. However, when all the known facts are associated with each data point, a curve can be obtained showing the attenuation of the impulse due to Gemini structure.

INTRODUCTION

The Gemini spacecraft employs over 100 pyrotechnic devices that are used at various times during a typical Gemini mission profile. Each device imparts a transient acceleration wave into the spacecraft structure of varying amplitude, and must be considered as part of the total dynamic environment to which the spacecraft structure and equipment are subjected.

The types of pyrotechnics used on the Gemini spacecraft and target docking adapter include flexible linear shaped charges (FLSC), mild detonating fuses (MDF), explosive bolts, and numerous cartridge-type devices. The location of these devices is shown in Figs. 1 and 2. In most cases, all are mounted directly to rigid structure and provide a direct path for the generated transient to be transmitted through the spacecraft and its equipment.

The flexible linear shaped charge and mild detonating fuse are used during critical separation phases in the Gemini Mission Profile. Concern has been expressed in the spacecraft and missile industry regarding the separation transient problem as related to structural response and/or equipment malfunctions resulting from the high-acceleration high-frequency transient motions (shocks) induced in vehicle structures by separation events. In particular, separation techniques employing cutting by flexible linear shaped charges have been known to cause relay chatter and fractures of brittle parts or structure. Since there are several critical separation phases involving configuration
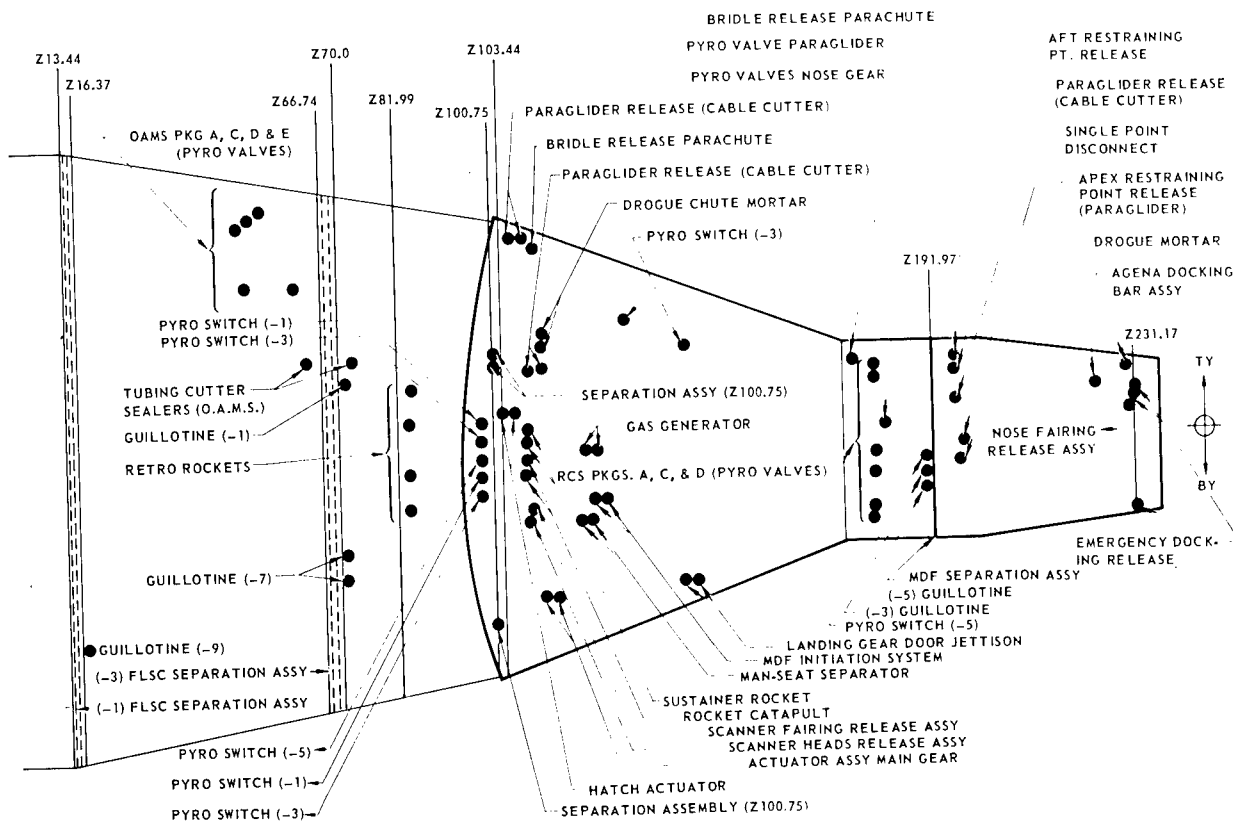
Fig. 1. Gemini spacecraft pyrotechnic locations

changes in the Gemini Mission Profile, the structural response of spacecraft structure to impulsive loading and the effects on the performance of electronic equipment mounted to such structure, have been investigated.

Two test programs were conducted on the spacecraft adapter module by McDonnell Aircraft Corporation to determine the structural response to impulsive loading. The first test was conducted primarily to determine the type of instrumentation needed to obtain reliable transient data. On completion of the first test, a second test was then conducted to obtain response data of the Gemini Adapter due to firing of the FLSC. A third test program was conducted for the target docking adapter to obtain response data during the FLSC firing for the transponder door separation. The overall effect of pyrotechnic detonations as they occur in the spacecraft adapter and target docking adapter are discussed in this paper. Time histories and Fourier spectra of the transient accelerations are presented.

PYROTECHNIC DESCRIPTION

Flexible linear shaped charge (FLSC) is a V-shaped, flexible lead sheathing containing a high-explosive core. FLSC is used in separation assemblies to sever various types, thicknesses, and shapes of materials. The specific type, shape, and thickness of the material to be separated dictates the amount of explosive contained in the FLSC. In the Gemini spacecraft and target docking adapter, the FLSC is provided in four different core loadings: 8, 10, 20, and 25 grains/ft. When installed, as shown in Fig. 3, the open portion of the V-shaped FLSC is placed towards the item to be severed. The FLSC is detonated by a booster charge that has been initiated by a detonator. The explosive core of the FLSC detonates, resulting in collapse of the sheathing in the V groove, which produces a cutting jet composed of explosive products and minute metal particles. The FLSC burns at an approximate rate of 20,000 ft/sec. This jet produces extremely high localized pressures, resulting in stress far above the yield strength of the target material.

266
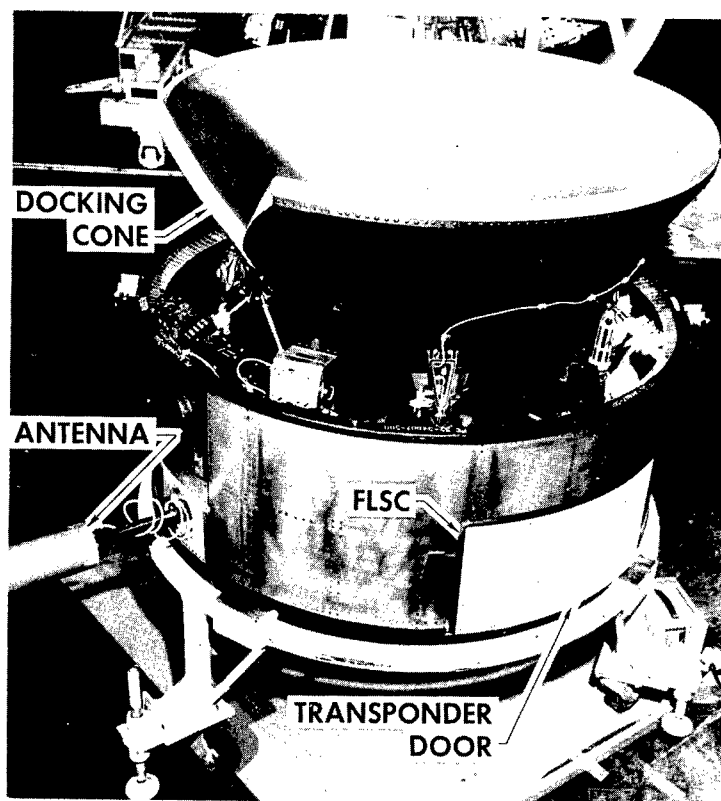
Fig. 2. Target docking adapter

FLSC ASSY

MDF ASSY
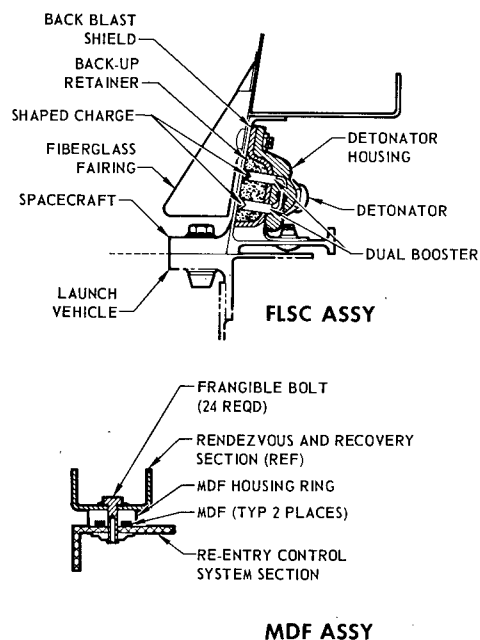
Fig. 3. Pyrotechnic assemblies

Mild detonating fuse (MDF) is a strand of high explosive encased in a lead sheathing with a circular cross section. MDF is used as a separation device and as an explosive interconnect. As a separation device, the strand contains 5 grains of explosive per foot. As an explosive interconnect, the strand contains 2 or 3.3 grains of explosive per foot. The MDF used as a separation device is placed in a groove milled in a magnesium ring, as shown in Fig. 3. The ring is formed to the shape of the items to be separated, and is placed between the mating surfaces. The assembly to be jettisoned is attached to the main structure by frangible bolts. The bolts have been axially drilled to reduce tensile strength to a specified breaking point. When detonated, the MDF exerts a force against the mating surface greater than the tensile strength of the frangible bolts. The MDF, used as an explosive interconnect, is initiated when a detonator or booster charge propagates a detonation wave to the MDF booster. The booster strengthens the wave and transmits it linearly through the length of the MDF strand. The booster, at the opposite end, propagates the detonation wave to the device to which it is attached.

267

TEST BACKGROUND

The tests by McDonnell Aircraft Corporation were conducted to determine the magnitude of the pyrotechnic transient and the transmission characteristics throughout the spacecraft due to firing the FLSC at adapter stations Z-13 (spacecraft-booster separation plane) and Z-69 (spacecraft retro adapter and equipment adapter separation plane). In addition, it was also required that adapter-mounted electronic equipment be operational during these tests to determine if any anomalies occurred due to the transient environment.

The approach taken to test and obtain the necessary data for this particular problem was influenced by the time schedule to which Project Gemini was committed. This required that all tests conducted to determine the transient acceleration produced by firing the FLSC be completed prior to launch of Spacecraft 2 to assure that the transient environment would not impair spacecraft system performance. One test was initiated to determine the type of instrumentation required to record accurately the transient response at various stations along the Gemini adapter shell. A second test was conducted which employed the necessary instrumentation determined from the first test and measured the amplitude and frequency content of the transient and how the shock was propagated throughout the Gemini adapter.

INSTRUMENTATION

The selection of proper instrumentation and its proper mounting are by far the most difficult part of obtaining valid pyrotechnic transient data. It is important that all the accelerometers used in the test are rigidly bolted to the structure to assure that the response data obtained is not biased by the inclusion of frequencies associated with accelerometer mounting. In view of the high-acceleration high-frequency content associated with the pyrotechnic transient, only a small number of the available accelerometers and amplifiers are capable of accurately recording this phenomenon.

On the first test, a number of different accelerometers and amplifiers were used to determine which type would produce the most accurate data. A summary of these data is presented in Table 1, with the mounting locations shown in Fig. 4. From the Endevco instrumentation that was used for this test, only the 2225 accelerometer (Fig. 6, accelerometer No. 7) recorded the high acceleration pyrotechnic

transient accurately. All other accelerometers mounted to rigid structure in the direct path of the transient were either saturated or had large dc shifts. As a result, valid data were not obtained from these transducers. In accelerometers, dc shifts are a function of the type of crystal and the initial strain placed in the accelerometer crystal during manufacturing (1). Saturation of an accelerometer circuit occurs by overloading the accelerometer amplifier and is normally attributed to excessive acceleration, dc shifts in the accelerometer, and excitation of the natural frequency of the transducer due to the high-frequency content of the transient pulse. Voltage amplifiers as used in the first test have a very slow recovery from overload, and are considered unacceptable for use in tests where the time duration of the transient is very short. In general, this test did produce the desired results, in that it provided a background on the type of instrumentation required for measuring the acceleration transient.

During the second test conducted by McDonnell, 30 accelerometers were used to obtain data for the Z-13 firing and 16 accelerometers were used for the Z-69 firing. This instrumentation is summarized in Tables 2 and 3, with the mounting locations shown in Fig. 5. All data obtained from this test were considered valid with little or no evidence of dc shift present. A change was made in the amplifier used for this test. The Endevco amplifiers used in the first test were replaced by Unholtz Dickie 8PCX charge amplifiers. This change was made because of availability and versatility, not for technical reasons. A charge amplifier is considered more versatile and has instantaneous recovery from overload. At the time of the second test, only a sufficient number of the Unholtz Dickie charge amplifiers were available to assure that the same type of amplifier was used on all data channels. This was not a strict requirement for the test, but it was a recommendation of the test engineers.

TIME HISTORIES

The time history responses of the transient accelerations for the Gemini adapter and target docking adapter are shown in Figs. 6 through 11. The time histories for the Gemini adapter longitudinal response exhibit the same basic characteristics; that is, an initial high-acceleration peak with a very rapid decay back to the null position. However, the adapter radial response time histories differ primarily in the time it takes for the response to decay to the null position. The initial high-acceleration peak is still present, but the response does not decay for at

<div align="center">

TABLE 1
Test 1, Z-13 Firing

</div>

Accel. No.	Accelerometer Type	Amplifier Type	Accel. Axis[a] and Sensitivity Range (g pk)	Location		Comments
				Z Sta.	Degrees[b]	
1	Endevco 2242	Endevco 2702C	6000 – L	16.37	119	Saturated — no data
2	Endevco 2242M4	Endevco 2702C	6000 – R	41.17	0	Saturated — no data
3	Endevco 2242M4	Endevco 2702C	3000 – L	41.17	119	dc shift — data questionable
4	Endevco 2213C	Endevco 2702C	3000 – R	66.74	119	dc shift – data questionable
5	Endevco 2215	Endevco 2702C	3000 – L	66.74	119	dc shift — data questionable
6	Endevco 2215	Endevco 2702C	3000 – L	Relay Panel		Valid data — low accelerations
7	Endevco 2225	Endevco 2614	6000 – R	16.37	119	Valid data — high accelerations
8	Endevco 2215	Endevco 2614	2000 – R	Relay Panel		Valid data — low accelerations
9	Endevco 2242M4	Endevco 2614	5000 – R	41.17	119	dc shift — data questionable
10	Endevco 2242	Endevco 2614	5000 – R	41.17	238	dc shift — data questionable

[a] L = longitudinal direction; R = radial direction.
[b] Measured clockwise from top of spacecraft (TY = 0 degree).

STRINGER 30 STRINGER 1 STRINGER 60

Z STA 69.00

Z STA 41.17

Z STA 13.00

● ACCEL. AXIS NORMAL TO OUTSIDE SKIN OF ADAPTER
▲ ACCEL. AXIS PARALLEL TO OUTSIDE SKIN OF ADAPTER
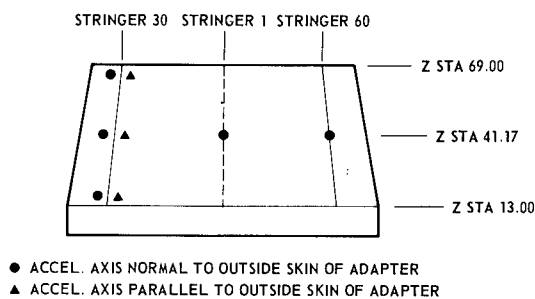
Fig. 4. Accelerometer locations on equipment section of adapter -- test 1

least a period of 30 to 50 ms, as compared to the longitudinal response which decays in 10 to 15 ms. This longer response time for the radial axis does provide the source for a high overall acceleration input to equipment located directly in the high shock path.

Figures 9, 10 and 11 are the response plots for the target docking adapter during shroud separation and transponder door separation. These time histories are similar to those shown before; however, the acceleration levels are of a higher magnitude and frequency than those for the Gemini adapter. This is due in part to the difference in material and also to the fact that in the Gemini adapter FLSC firing, the transient pulse propagates away from the recording transducer, while for the target docking adapter FLSC firing, the transient pulse propagates in a 360-degree circle around the recording transducer. It is interesting to note that in Fig. 11, the accelerometers at the transponder door are mounted back to back, 180 degrees out of phase. However, at the time zero, both accelerometers start in phase for approximately 1/4 ms and then clearly remain out of phase until the signal attenuates to the null position. This is explained by the fact that initially the accelerometers are recording the natural frequency of the mounting column to which they are attached and not the response of the door. After a short time duration, the response of the door becomes predominant and the accelerometers record out of phase.

TABLE 2
Test 2, Z-13 Firing

Accel. No.	Accelerometer Type[a]	Sensitivity Range (g pk)	Location Z Sta.	Location Degrees[b]	Accel. Axis[c]
1R	Endevco 2225	6000	16.37	12	R
1L	Endevco 2225	6000	16.37	12	L
2R	Endevco 2225	5000	28.61	41	R
2L	Endevco 2225	5000	28.61	41	L
3R	Endevco 2225	3000	41.17	84	R
3L	Endevco 2225	3000	41.17	84	L
4R	Endevco 2225	3000	53.74	127	R
4L	Endevco 2225	3000	53.74	127	L
5R	Endevco 2235C	3000	66.74	168	R
5L	Endevco 2225	3000	66.74	168	L
6R	Endevco 2235C	3000	70.00	200	R
6L	Endevco 2235C	3000	70.00	200	L
7R	Endevco 2235C	3000	81.97	245	R
7L	Endevco 2235C	3000	81.97	245	L
8R	Endevco 2235C	3000	94.40	305	R
8L	Endevco 2235C	3000	94.40	305	L
9R	Endevco 2235C	3000	103.44	335	R
9L	Endevco 2235C	3000	103.44	335	L
10	Endevco 2235C	600	Relay panel		N
11	Endevco 2235C	600	Relay panel		R
12	Endevco 2235C	600	Relay panel		N
13	Endevco 2235C	600	Relay panel		R
14	Endevco 2235C	600	Relay panel		N
15	Endevco 2235C	600	Relay panel		R
16	Endevco 2235C	600	Relay panel		Z axis
17	Endevco 2235C	600	Relay panel		N
18	Endevco 2235C	3000	66.74	15	R
19	Endevco 2235C	3000	66.74	15	L
20	Endevco 2235C	3000	81.97	15	R
21	Endevco 2235C	3000	81.97	15	L

[a]Unholtz Dickie 8PCX amplifier used in all cases.
[b]Measured clockwise from top of spacecraft (TY = 0 degree).
[c]L = longitudinal direction; R = radial direction; N = normal.

TABLE 3
Test 2, Z-69 Firing

Accel. No.	Accelerometer Type[a]	Sensitivity Range (g pk)	Location Z Sta.	Location Degrees[b]	Accel. Axis[c]
6R	Endevco 2225	6000	70.00	200	R
6L	Endevco 2225	6000	70.00	200	L
7R	Endevco 2225	5000	81.97	245	R
7L	Endevco 2225	5000	81.97	245	L
8R	Endevco 2225	3000	94.40	305	R
8L	Endevco 2225	3000.	94.40	305	L
9R	Endevco 2235C	3000	103.44	335	R
9L	Endevco 2225	3000	103.44	335	L
10	Endevco 2235C	2000	Relay panel		N
11	Endevco 2235C	2000	Relay panel		R
12	Endevco 2235C	2000	Relay panel		N
13	Endevco 2235C	2000	Relay panel		R
14	Endevco 2235C	2000	Relay panel		N
15	Endevco 2235C	2000	Relay panel		R
20	Endevco 2235C	5000	81.97	15	R
21	Endevco 2235C	5000	81.97	15	L

[a]Using Unholtz Dickie 8PCX amplifier in all cases.
[b]Measured clockwise from top of spacecraft (TY = 0 degree).
[c]L = longitudinal direction; R = radial direction; N = normal.
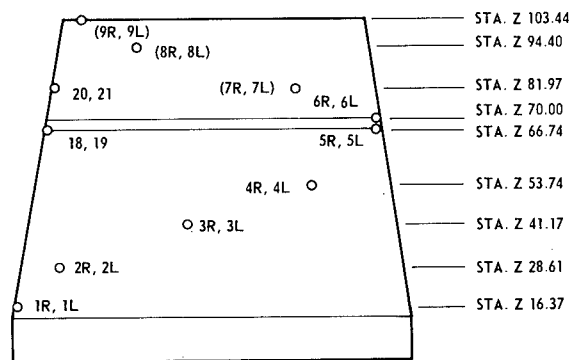
Fig. 5.   Accelerometer locations on
adapter skin -- test 2
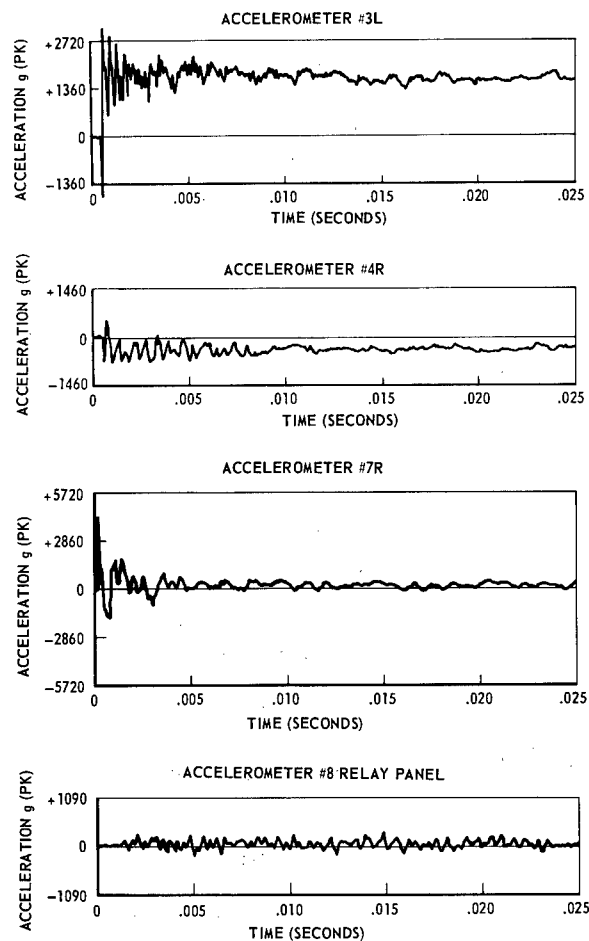
Fig. 6.   Shaped charge firing at
Z-13 -- test 1

271

Fig. 7. Shaped charge firing at
Z-13 -- test 2

ACCELEROMETER #6L

ACCELEROMETER #6R

ACCELEROMETER #9L

ACCELEROMETER #9R
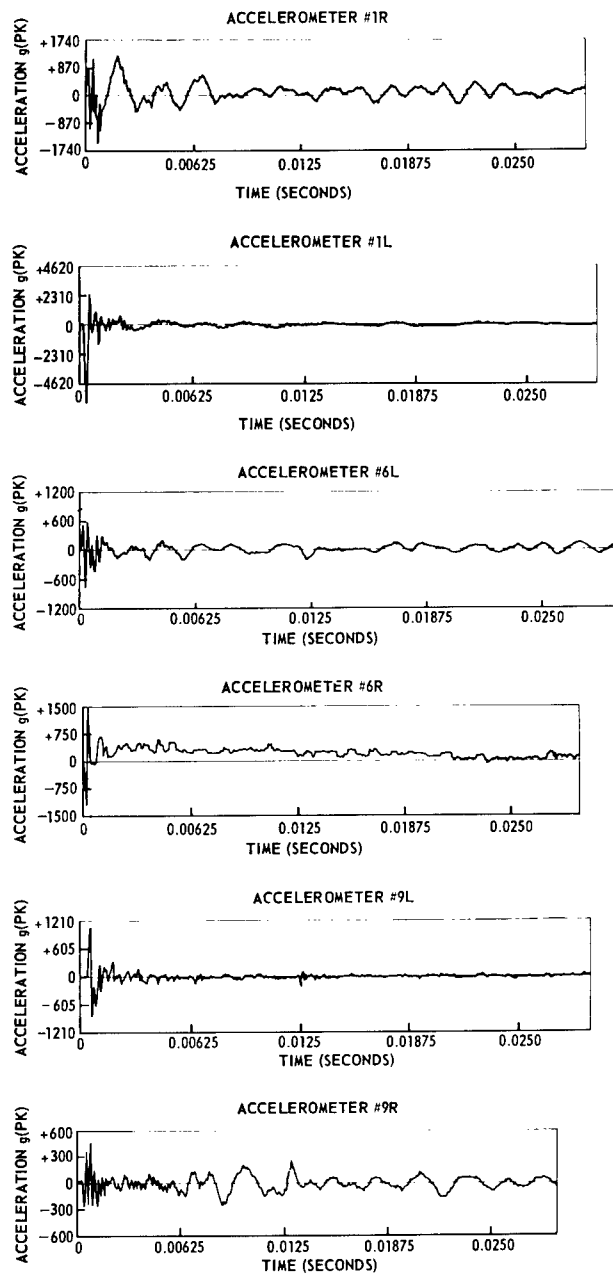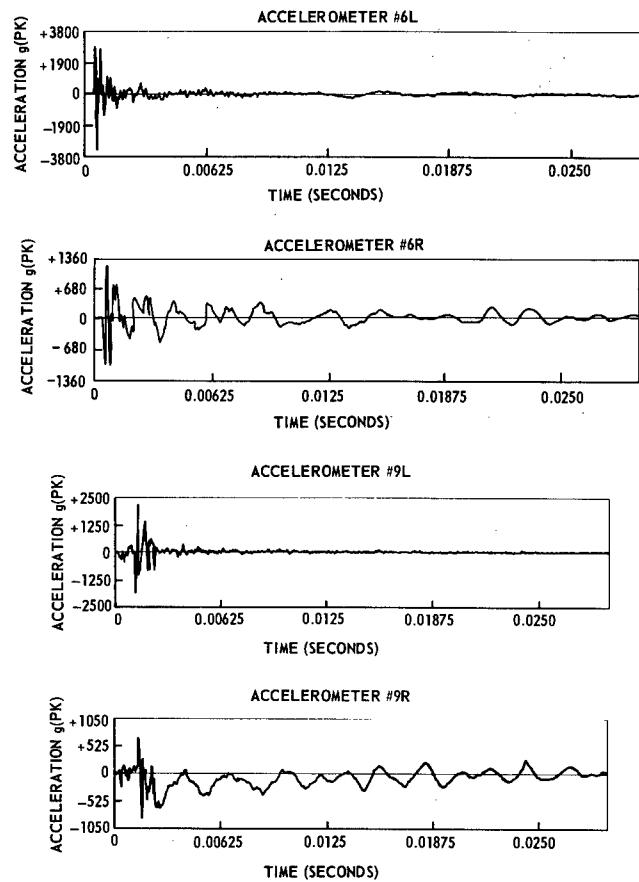
Fig. 8. Shaped charge firing at Z-69 -- test 2

TRANSPONDER

ANTENNA
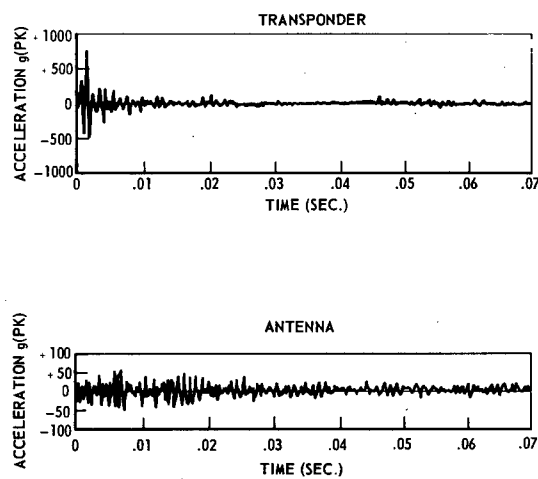
Fig. 9. Target docking adapter
(shroud separation)

273

TRANSPONDER DOOR (CENTER)

TRANSPONDER DOOR (RH CORNER)
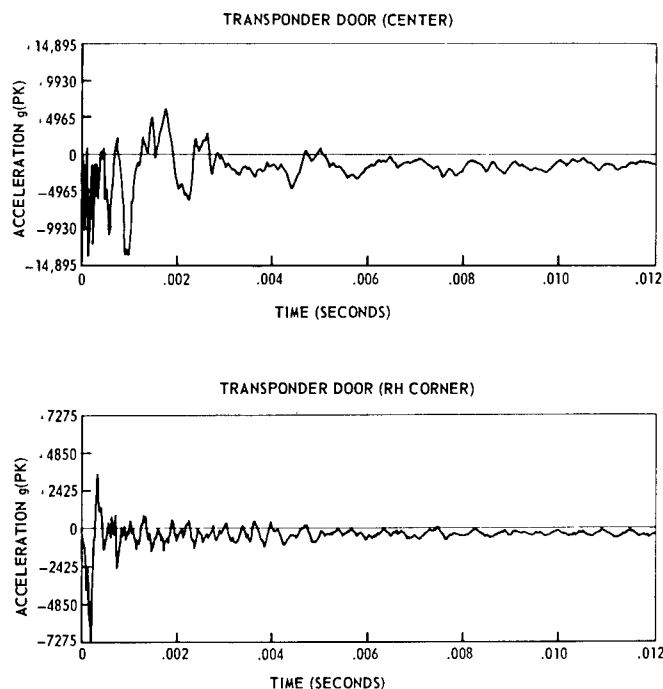
Fig. 10. Target docking adapter

Figure 12 envelops the maximum peak accelerations recorded at various distances from the adapter Z-13 firing of the FLSC. A peak acceleration of 6500 g was recorded in the longitudinal direction and 4100 g in the radial direction at Z-16 station, approximately 3 in. from the FLSC. The peak accelerations were attenuated to 1200 and 200 g, respectively, at Z-104 station. Measurements made on equipment located at the center of the adapter away from the direct shock path recorded peak accelerations of 200 g. The time duration of this response compares closely to the time duration of the radial response recorded on the adapter shell.

FOURIER ANALYSIS

Complex Fourier transforms were conducted on the response data obtained from the pyrotechnic firing. A Fourier transform was initiated so that the frequency content could be extracted from the time histories. It was felt that a Fourier analysis would be more useful if a linear analysis of the structure is to be performed.

The Fourier transform reduces the acceleration time function into a frequency function which consists of sinusoidal components, each with its characteristic amplitude $Z(\omega)$ and $\Phi(w)$.

The parameters obtained from the Fourier analysis were the absolute value of the amplitude of the Fourier spectrum or the amplitude density and the phase angle of the sinusoidal components. The parameters were obtained by first determining the sine and cosine coefficients of the Fourier analysis. These coefficients were defined as follows:

$$A(\omega) = \int_0^\infty f(t) \cos \omega t \, dt ,$$

$$B(\omega) = \int_0^\infty f(t) \sin \omega t \, dt .$$

The amplitude density of the spectrum was then obtained by taking the square root of the sum of the squares of the sine and cosine coefficients. The phase angle of the sinusoidals was obtained by taking the arctan of the sine divided by the cosine coefficients.

The following experimental method was used to obtain these results. The time functions, which were recorded in an FM mode on magnetic tape, were sampled at a high rate and converted into a digital format. The desired integrations were performed on a 7094 digital computer. Since a sample rate of 1 ms was the only rate available, the time axis of the data had

274
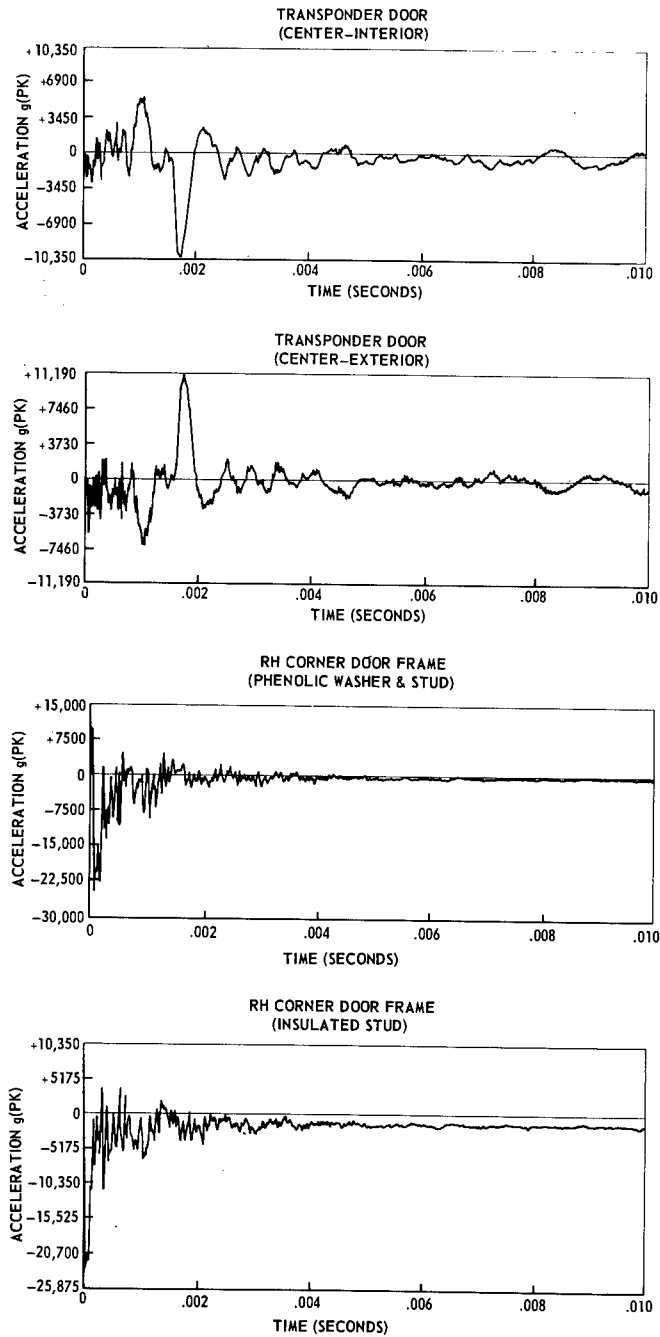
Fig. 11. Target docking adapter (boiler plate)

275
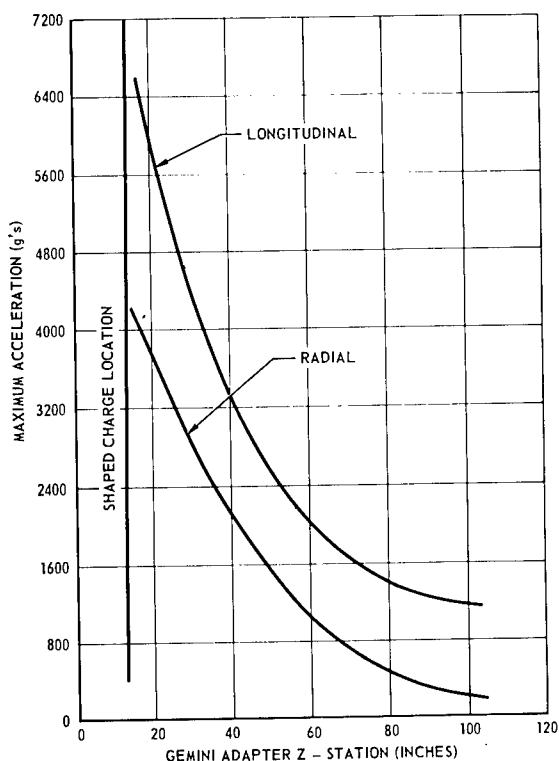
Fig. 12. Impulse attenuation -- Z-13
firing, 10 grains/ft

to be expanded by a factor of 64 so that the specified frequency range would be compatible with the sampling rate. The expansion of the time axis was accomplished by the process of re-recording, making speed changes in the tape recorder.

The Fourier analysis was then conducted from 0 to 156 cps in 1-cps increments. These data, when related back to actual test time, covered a frequency range from 0 to 10 kcps in 64-cps increments. The expansion of the time axis also resulted in an increase in the amplitude of the desired Fourier spectrum by a factor of 64. This increase was reduced by inserting a constant in the computer program. The expansion of the time axis had no effect on the phase angle of the sinusoids.

The expanded time histories had non-zero amplitudes, ranging in time from 2 to 4 sec. The data from the first test were integrated for a 10-sec period. To insure that the integration was conducted over all non-zero amplitudes, sampling of the analog tape was started at some arbitrary point, approximately 2 to 3 sec before the start of the transient. This arbitrary starting point did not affect the amplitude density, but did shift the phase angle by a factor of $\omega\tau$

(τ being the time from the start of sampling to the start of the transient). A simple mathematical analysis of the Fourier integral will show this result (2). It is interesting to note that the arbitrary starting point did affect the value of the sine and cosine coefficients, but was eliminated in the computation of the amplitude density (square root of the sum of the squares).

The data obtained from the second adapter test and the transponder door test of the target docking adapter were reduced in a similar manner, except that a modification was introduced in the computer program. This modification allowed the integration to start within 0.01 sec of the shock initiation and to continue for a 4-sec period. This eliminated the ($\omega\tau$) phase shift encountered in the first program.

DISCUSSION OF FOURIER SPECTRA

The Fourier spectra (Figs. 13-30) present the amplitude density of the recorded acceleration transients. These data, which have the units of g-sec or g per unit of angular frequency, indicate only the relative magnitude of the acceleration at the various frequencies contained in the aperiodic functions. These sinusoids have infinitesimal amplitudes, and the maximum amplitude is given by the expression $Z(\omega)\,d\omega$ (3). This results because the period of the time function extended to infinity. It was felt that a better comparison of the data could be obtained from this manner of presentation than by averaging the spectra over some selected finite period.

The frequency content of the data obtained from the Z-13 firing in both adapter test programs is similar. The differences in the amplitude density at the predominant frequencies might be explained by the difference in the adapter boundary conditions for the two test programs. The first program was conducted using only the equipment section, while the second program was conducted using a full adapter, including both the equipment and retrograde section. A difference in response from one FLSC firing to another can be expected because of the difference in detonation initiation time. An FLSC normally has more than one detonator distributed along the length of the charge. The initiation time of these detonators, as compared to the burning rate of the FLSC, cannot be closely controlled. This time difference causes phase shifts in the distributed forcing function, which when summed with the transfer functions will result in a difference in response.

276
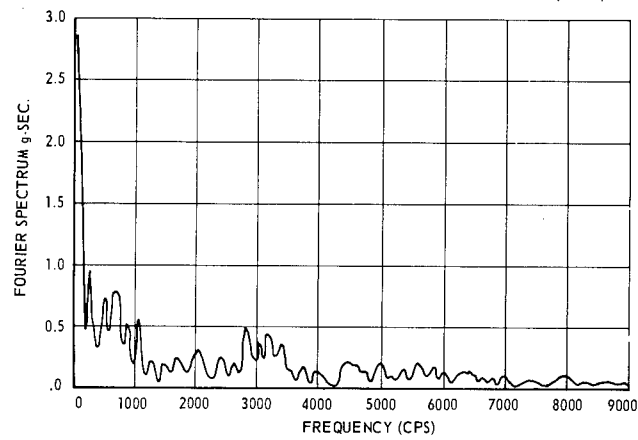
Fig. 13. Fourier amplitude spectrum --
test 1, accelerometer 4R
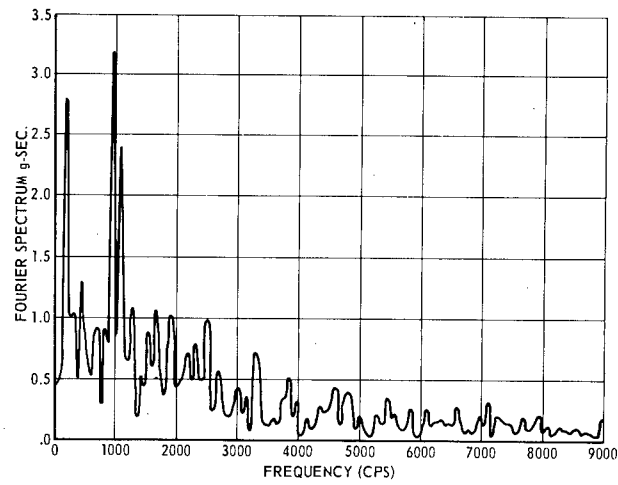
Fig. 14. Fourier amplitude spectrum --
test 1, accelerometer 7R
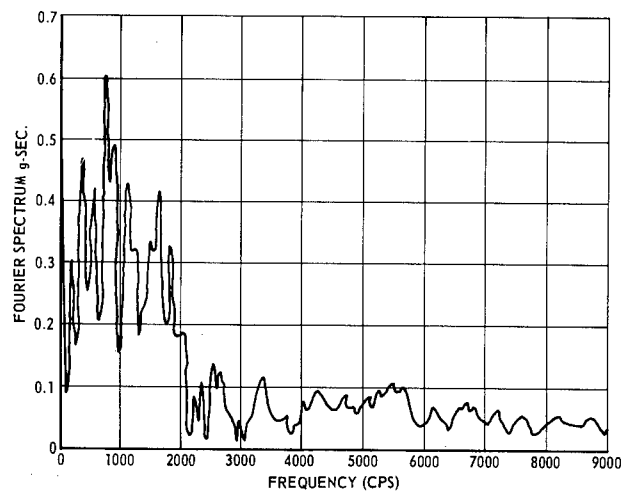
Fig. 15. Fourier amplitude spectrum --
test 1, accelerometer 8, relay panel

277
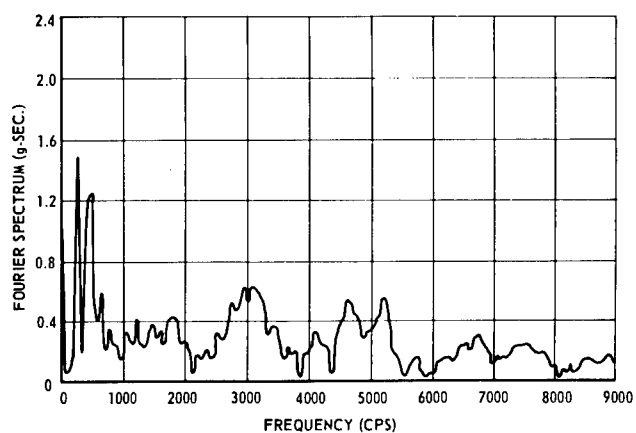
Fig. 16. Fourier amplitude spectrum --
test 2, accelerometer 1 L
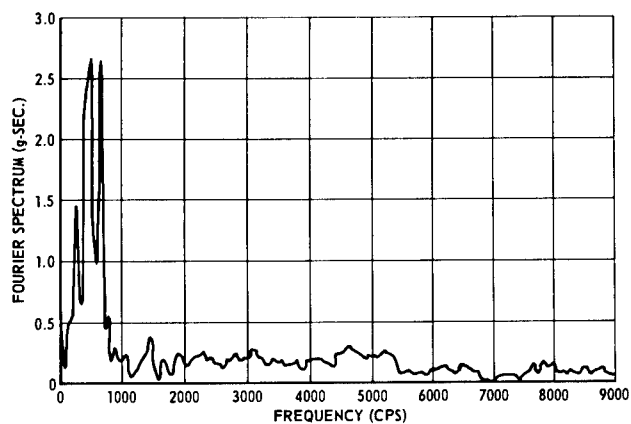
Fig. 17. Fourier amplitude spectrum --
test 2, accelerometer 1R
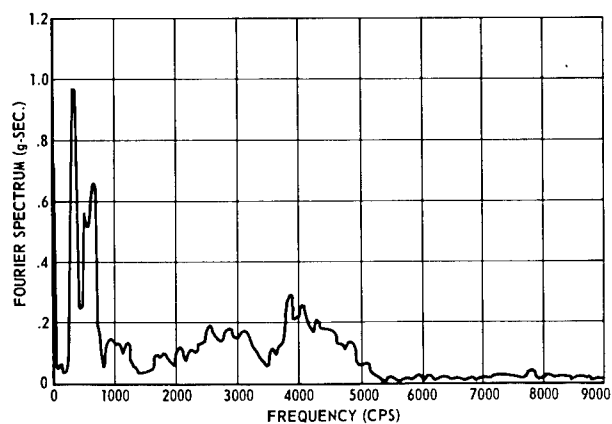
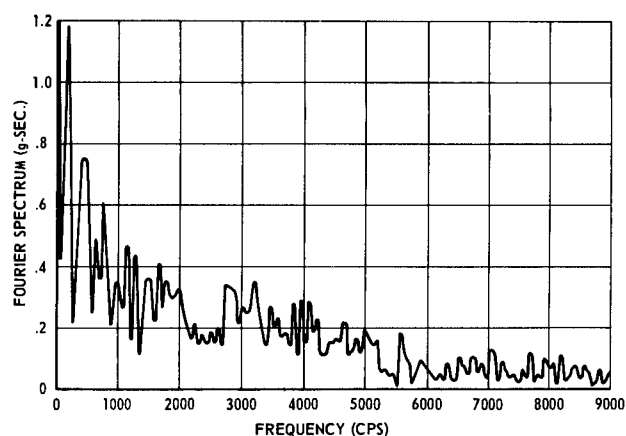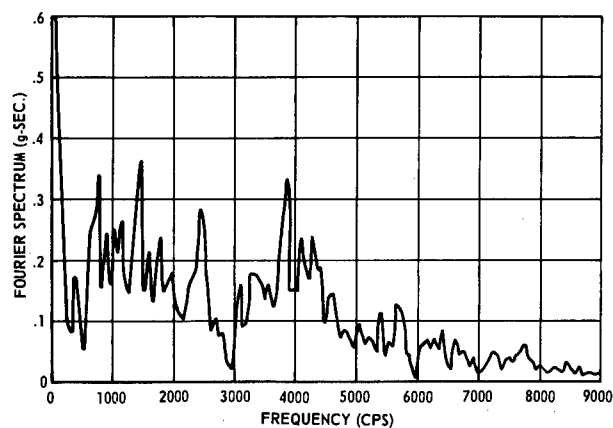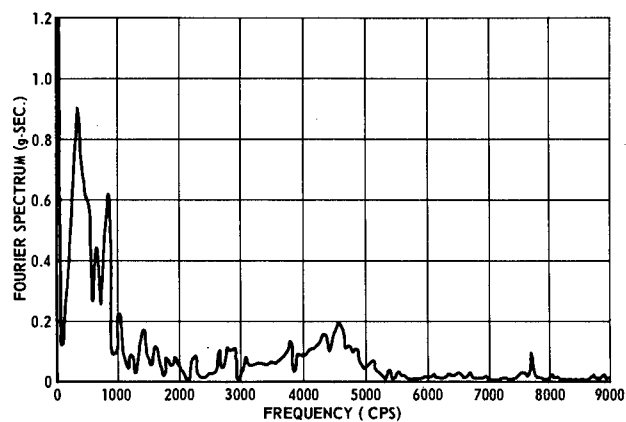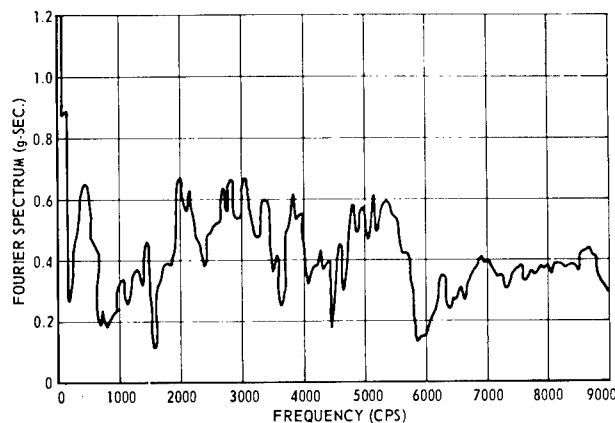Fig. 18. Fourier amplitude spectrum --
test 2, accelerometer 6 L

278

Fig. 19. Fourier amplitude spectrum --
test 2, accelerometer 6R

Fig. 20. Fourier amplitude spectrum --
test 2, accelerometer 9L

Fig. 21. Fourier amplitude spectrum --
test 2, accelerometer 9R

279

Fig. 22. Shaped charge firing at Z-69 --
test 2, accelerometer 6L
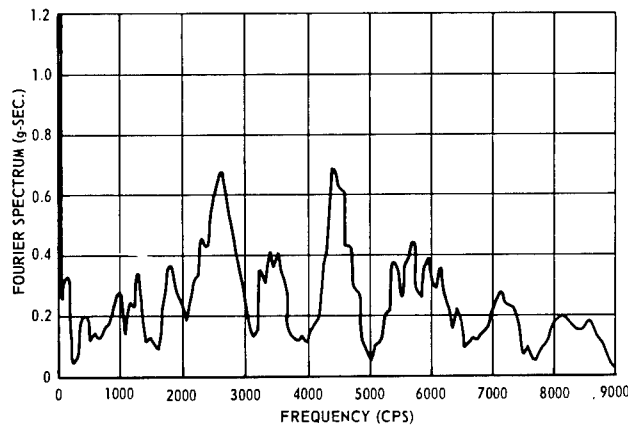
Fig. 23. Shaped charge firing at Z-69 --
test 2, accelerometer 9L

The data obtained from the Z-69 firing of the second adapter (Figs. 22, 23, and 24) have a higher frequency content than any of the data obtained from the Z-13 firing (Figs. 16-21). This can be expected, since the retrograde adapter, because of its construction and size, has the higher frequency shell modes.

During the target docking adapter boiler plate program, redundant transducers were installed on both the door and the boiler plate to investigate various transducer installations. Figures 27 and 28, spectra of back-to-back transducers mounted on an Endevco Model 2980B insulated stud, show good frequency and amplitude correlation. The small amount of time that the transducers exhibited in-phase relationship and a different frequency content near time zero (see time history, Fig. 11) is

not distinguishable in the amplitude density spectrum. This difference, which is attributed to the transducer installation, is only a minute part of the overall response and is not considered to have an appreciable effect on the accuracy of the data. The response of the target docking adapter boiler plate was different from the rest of the presented data in that it did not exhibit numerous lightly damped resonant modes. This boiler plate was constructed from rolled 0.25-in. aluminum plate and, being in a yielded condition, would have highly damped low-frequency resonant modes. This can be seen by comparing Figs. 25 and 28.

DATA USAGE

The data obtained from the transform can be expressed in terms of the complex Fourier spectrum:

280

$$F(\omega) = Z(\omega) \ e^{j\,\Phi(\omega)} ,$$

or in terms of the real and imaginary components:

$$F(\omega) = Z(\omega) \times \cos \Phi(\omega) + jZ(\omega) \times \sin \Phi(\omega) .$$

The Fourier spectrum at other points on the structure could be predicted if the transfer functions were available from the point of measured response to the point of interest. The transfer function in this case is the steady state sinusoidal acceleration transmissibility, both in amplitude and phase. The correspond-

ing acceleration time function could also be predicted by performing the inverse transform.

In a similar manner, the forcing function per unit of shaped charge length could be estimated, based on the availability of transfer functions from various points along the linear shaped charge to the points of measured response. In this case, the transfer functions would be the steady state sinusoidal inertance (acceleration per pound of input force). A matrix corresponding to the following expression could then be set up, and the unit forcing function could be determined by solving the set of simultaneous equations on a digital computer:

$$Z(\omega)_x = H(\omega)_{xy} \ F(\omega)_y ,$$
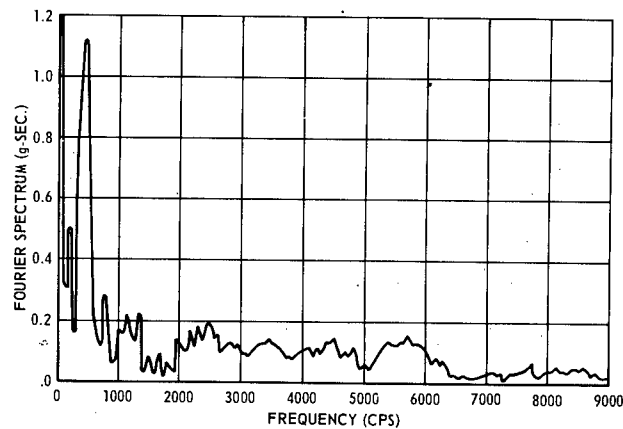
Fig. 24. Shaped charge firing at Z-69 -- test 2, accelerometer 9R

FREQUENCY (CPS)
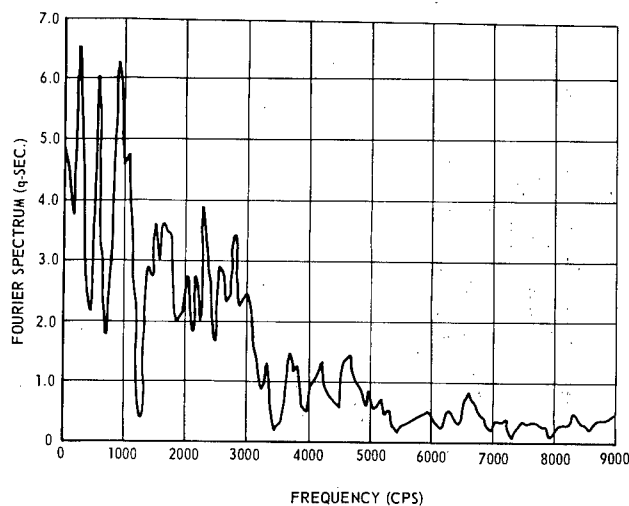
Fig. 25. Target docking adapter, center of door at right corner of door

281
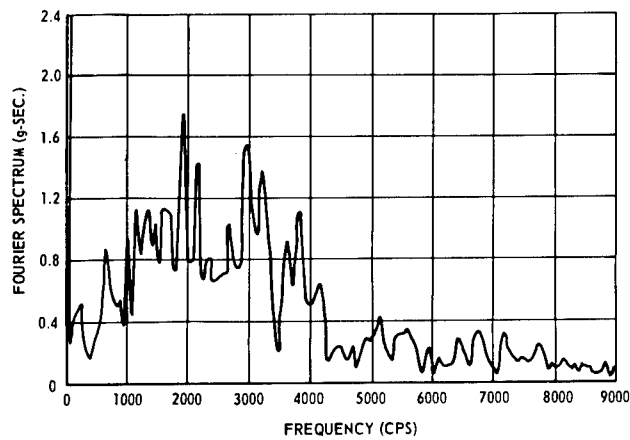
Fig. 26. Target docking adapter, on structure right-hand corner of door
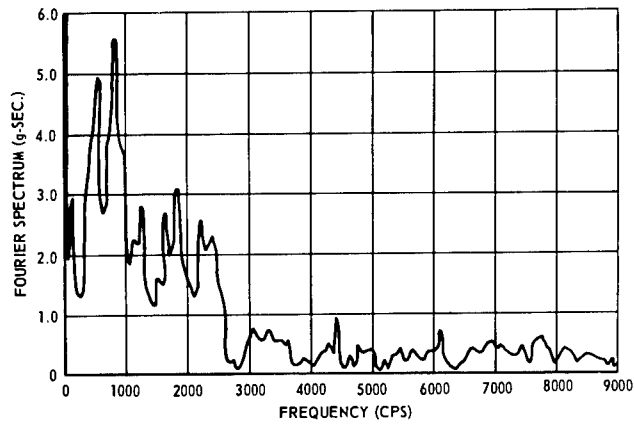
Fig. 27. Target docking adapter -- boiler plate, center of transponder door (interior)
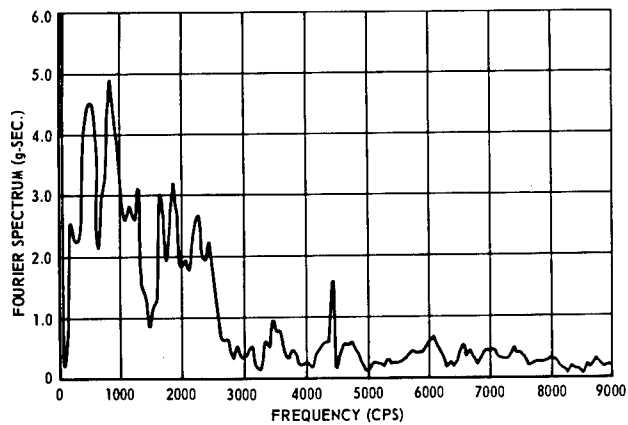
Fig. 28. Target docking adapter -- boiler plate, center of transponder door (extended)
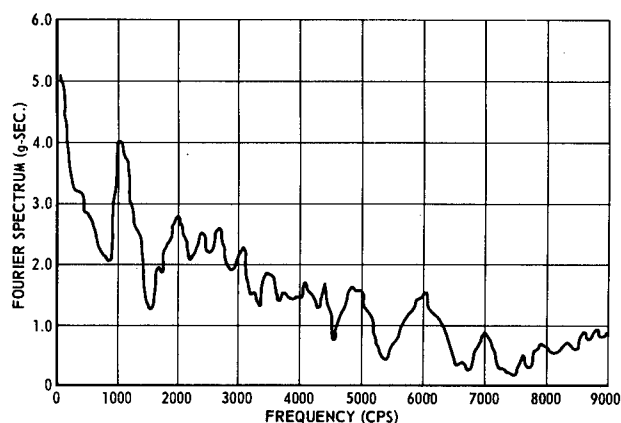
Fig. 29. Target docking adapter -- boiler plate, right corner of door frame (insulated stud)
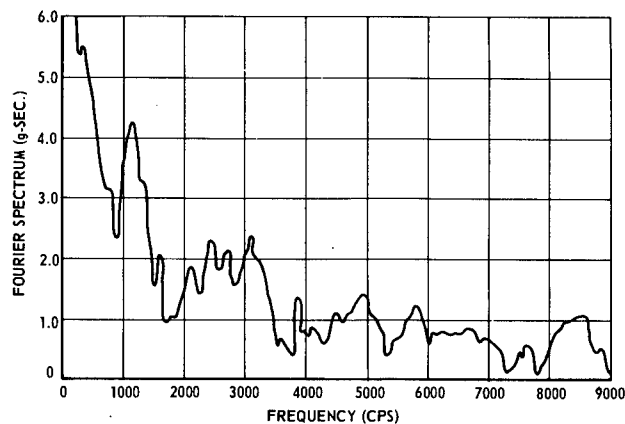
Fig. 30. Target docking adapter -- boiler plate, right corner of door frame (phenolic washer and stud)

where

x = location of point of response,

y = location of unit forcing function,

$Z(\omega)$ = response,

$H(\omega)$ = transfer function, and

$F(\omega)$ = unit forcing function.

Once this is accomplished, detonator initiation time could be varied to determine "worst condition" criteria. The response of other equipment could be predicted and compared with qualification tests results to insure compatibility.

EQUIPMENT PERFORMANCES

During the FLSC firings on the Gemini adapter and target docking adapter, various electronic components were monitored to detect possible failures that might occur because of the transient acceleration.

Thyratron circuits were set up to monitor spacecraft relay contacts of the installed retrofire relay panel and discrete command system relay panel for relay chatter. The normally closed relay contact thyratron channels were set up to indicate any opening exceeding 500 ms, and the normally open relay contact thyratron channels were set up to indicate any closure

283

exceeding 10 ms. These times were predetermined by circuit analysis. No chatter was detected.

For the shaped charge firing at Z-13, the power input to the S-band beacon, digital command system, and acquisition aid beacon was monitored to observe any variation of input power resulting from the shaped charge firing. No variation was observed.

During the shaped charge firing at Z-69, eight simulated retro-rocket pyrotechnic circuits were made up for use with the retro-rocket relay panel. The circuits consisted of actual spacecraft production wiring, with a 1-ohm resistor substituted for the retro-rocket igniter squib. A tape recorder was used to record any stray voltages that might appear across the resistor because of relay chatter. No stray voltages were recorded.

A production transponder was installed during the transponder door separation test conducted on the TDA. The transponder was checked before and after the FLSC firing, and no malfunctions were detected.

CONCLUSIONS

The accelerations recorded on the adapter shell for both the longitudinal and radial directions and on the target docking adapter, reveal that large transient accelerations propagate throughout the structure as a result of firing the FLSC. The frequency content of the transient ranged from 0 to 10 kcps. Fourier spectra of the transient acceleration reveal that structural resonances associated with the shell and panel modes are clearly excited.

Some scatter was associated with the data from the various tests, and the attenuation of the initial impulse was not always consistent with distance. However, many of the inconsistencies can be associated with the mounting techniques used for the accelerometers during these tests. Due to the high temperatures employed during the second test, rigid installation of all accelerometers was not possible. (Note: For the first test conducted, all accelerometers

were rigidly mounted to the adapter shell at the intersections of the rings and stringers.)

As a result, when all known facts are associated with each data point, curves can be drawn showing the maximum acceleration at each Z-station and the attenuation of the impulse through the Gemini structure. This is illustrated in Fig. 12 for both the longitudinal and radial directions.

All electronic equipment and relays mounted in the adapters during the shaped charge firings performed within specification, without any evidence of variations in equipment performance or of relay chatter. Pre-delivery acceptance tests on the electronic equipment used in the tests verified that all components would operate satisfactorily in the orbital mode after being subjected to this environment. In the case of the transponder located in the target docking adapter, the high transient accelerations recorded directly on the unit caused serious concern since reliability is necessary so that all future transponder units will function properly after being exposed to a high transient acceleration environment. As a result, a redesign effort has been made in this one instance to eliminate the high transient acceleration input to the transponder.

Qualification of adapter equipment to a transient acceleration spectrum produced by the FLSC has not been required for the Gemini spacecraft. In general, this decision is based on the fact that the Gemini adapter equipment is located well away from the high shock path. However, if in the future, Gemini equipment is either added or relocated to the adapter wall area or to an area considered to be a direct path for the high transient acceleration, then this equipment will be evaluated on an individual basis as to necessity for testing to the spectrum produced by the shaped charge firing. Because of the high-frequency nature of the transient acceleration and the high acceleration levels, the only realistic method of testing would be to subject the equipment to an actual firing of the FLSC, using simulated production structure. Transient analysis should be performed prior to testing to verify that such a test actually is required.

REFERENCES

1. R. R. Bouche, "Survey Report on Quasi-Constant Voltage Outputs," Endevco Technical Data No. 521

2. R. Legros, and A. V. J. Martin, Transfer Calculus for Electrical Engineering

(Prentice Hall, New Jersey), 1961, pp. 92-97

3. Y. W. Lee, Statistical Theory of Communication (John Wiley and Sons, New York), 1964, pp. 32-49

ANALYTIC DYNAMIC MODELING FOR
IMPULSIVE ENVIRONMENTS*

William C. Broding and John R. Henry
AVCO Corporation
Research and Advanced Development Division
Wilmington, Massachusetts

Analytic dynamic modeling techniques of suitable simplicity for the de-
sign engineer have been used successfully for the study of impulsive
conditions created by pyrotechnic devices, blast, or impact. The scope
of modeling considered covers only linear theory for the definition of
structural overall damage within the early response time of the entire
structure.

Although it may appear that the development of an analytic dynamic
model is a series of compromises and assumptions, reasonable suc-
cess has been achieved in modeling for a variety of geometric shapes.
The quality of instrumentation is acceptable so that the analytical defi-
nition of the forcing function can be made with reasonable accuracy.
Comparisons are shown of various approaches to the definition of the
physical characteristics of the dynamic system, using three methods:
direct-stiffness, lumped-parameter, and the Houbolt finite-difference
approaches. Geometries considered are shallow spherical shells,
sphere-cones, axially and laterally loaded cylinders, and elastic bars.
These examples indicate that adequate analytical techniques are avail-
able for the analysis of impulsively loaded structures.

INTRODUCTION

Impulsive loading is commonly encountered
in design environments for aerospace systems.
Pyrotechnic devices are usually used for sepa-
ration or ejection mechanisms. Weapon systems
designed for encounter with nuclear defense sys-
tems experience large pressures. High-intensity
short-duration forces are produced when high-
velocity vehicles impact with objects, for exam-
ple, as when arresting the vehicle or encounter-
ing micrometeroid hazards. It is therefore
imperative during design to use test or analytical
methods to ascertain the structural integrity of
the design to withstand these impulsive loads.

Impulsive loading considered in a design
may be imposed directly to the structural item
or may be the result of load transmission
through supporting structure external to the
design configuration. For directly applied pres-
sure loads, the characteristic type of load input
to the design consists of a short time to peak
load, generally in the microsecond range, and
then a logarithmic decay into the millisecond
range. Total impulse duration for x-ray loading
is in the microsecond range. For structurally
transmitted loads, the design experiences com-
plicated accelerations whose spectrum covers
a broad range of frequencies (2 to 2000 cps) and
levels up to 4000 g.

The characteristic response to impulsive
loads consists of high-frequency high-g oscilla-
tions which are complicated by the higher
modes of the many elements of the structural
system. During the response, mechanical dam-
age of two types can be produced: material
damage and structural damage. Material dam-
age is caused by stress wave interactions;
typical examples are spalling and corner frac-
tures. This damage occurs within microsec-
onds of the arrival of the loading. Structural
damage, on the other hand, consists of bending,
buckling, or twisting of the structural configura-
tion; such damage occurs in the same order of
magnitude of time for response times of the
structural elements (generally hundreds of
microseconds). Structural damage can be di-
vided into two parts: overall damage, and local

damage. Analytical dynamic modeling is used for the evaluation of overall damage, which involves entire vehicle motion, such as bending of the vehicle as a beam. Local failure, on the other hand, is that in which the kinetic energy imparted by the applied load is dissipated locally, resulting in damage such as wrinkling, denting, and cracking.

In the definition of overall damage, the structural response to impulsive loading can be divided into two distinct parts for the convenience of analysis. The first phase is the early response of the entire structure, which can be studied on the basis of linear theory. Such studies establish the overall response characteristics and determine the initial regions of high stress and deformations. The second phase, which is beyond the scope of linear analysis, considers the instability, collapse, or rupture in certain critical regions. Analytic dynamic modeling is, therefore, the basis for investigating the first phase, while rigorous detail analysis is the only meaningful approach to the second.

In the support of weapon system design and evaluation at AVCO/RAD, many studies and tests have been performed for definition of structural deformation and damage due to impulsive loads. It is the purpose of this paper to present the results of these studies, which may serve as guidelines to an analyst formulating a dynamic model of an impulsively loaded system. It must be recognized that for analytical expediency, any continuous physical system must be simplified, idealized, and approximated to formulate the mathematical expressions of motion. The modeling techniques and simplifying assumptions used by the analyst should be drawn from experiences obtained by closely controlled physical tests. Correlation of test data with analytically determined values best establishes confidence in the analytical approach. When testing costs are prohibitive, comparisons often can be drawn from theoretical "exact" solutions.

THEORETICAL CONSIDERATIONS FOR ANALYTICAL MODELING

The analytical approaches used in evaluating time-varying behavior are significantly different when considering linear or nonlinear systems. Most analytical techniques have been developed for linear systems represented by sets of integro-differential equations, which are simultaneous ordinary or partial differential equations where each term contains no more than the first power of a dependent

variable and its derivatives. At the present, little is known about the solutions of nonlinear systems (which contain higher powers or cross products of the dependent variable and its derivatives) other than brute-force approximations using analog or digital computers. The engineer today, therefore, is restricted to the use of linear models or elementary nonlinear forms.

Four basic approaches have been used by analysts to reduce a physical system to a model consisting of finite sets of linear simultaneous equations in the independent variable time:

1. The first approach assumes that the use of a finite number of degrees of freedom, rather than an infinite number, are sufficient to describe the motion and that the deformation can be represented by the superposition of explicitly defined continuous functions. This modal approach employs the use of a finite number of numerically determined natural mode shapes and normal coordinates to define the deformation of the structure.

2. The Rayleigh-Ritz method approximates the deflection in a manner similar to the modal approach but utilizes the superposition of assumed deflection shapes. Since this method requires knowledge of the dynamic system to provide insight for properly assuming the mathematical form of the deflection shape, it is unsuitable for impulsively loaded structural designs.

3. The lumped parameter method approximates the deformation of a continuous structure by a finite number of discrete generalized displacements of various parts of the structure. This method involves the replacement of a continuous system by a pattern of discrete points and instead of obtaining a continuous solution for deformation throughout the system, the displacements are approximated at only the points. Intermediate values, derivatives, or integrals may be obtained from the solutions at the discrete points by interpolation. Implicit to the formulation of the model is the necessity to approximate the continuous system with lumped physical characteristics.

4. The use of digital computers allows for the direct solution of the integro-differential equations by finite difference methods. Application of this approach is restricted to those structural geometries which can be represented by continuous mathematical functions. The accuracy of the solution is dependent on the numerical technique used for solution of the

286

equations. In practice, it is generally difficult to define continuous functions, and the finite difference techniques for solution of the equations are combined with lumped parameter approximations of the system to provide a suitable analysis.

Physical characteristics of a structure are defined by similitude to common structural forms:

1. Beam;

2. Beam with shear flexibility;

3. Beam with shear flexibility and rotary inertia;

4. Shell without longitudinal, circumferential, or radial inertia; and

5. Shell with longitudinal, circumferential, or radial inertia.

A problem common to all of these models is the means of establishing load-deflection relations for the system. Deflection influence coefficients are widely used for beam models based on deflection obtained by application of Castigliano's theorem, and redundant internal loads are solved by the principle of least work. Difficulties in the application of influence coefficients arise when one underestimates the degree of redundancy. The use of static deflection influence coefficients determined by static shell analysis has allowed use of the modal approach for the dynamic analysis of shells. During recent years, significant progress made at AVCO/RAD in the static analysis of shells (1-3) has provided numerical means of accurately defining shell influence coefficients. Application to the digital computer often presents difficulties. Because of matrix size and machine storage capability, feasible description of shells requires the uncoupling of longitudinal and lateral response. Also, it has been found that many higher modes are significant for definition of shell response under impulse loading, so that direct time integration of the shell equations is often required (4).

The direct stiffness method is a different approach, in which displacements of the joints of the structure are unknown quantities. Analytical expressions are formed for mutually compatible deformations in the structure, and the pattern of displacements is one for which the equations of equilibrium are satisfied.

Standard numerical techniques are available for solving the equations of the beam models by simply replacing derivatives with finite-difference approximations. The shell models employ essentially the same schemes but are limited by the efficiency of the finite-difference numerical analysis and by the number of degrees of freedom. Although there is considerable literature available on the numerical solution of parabolic and hyperbolic partial differential equations, few applications have been made to the shell dynamics problem area. An implicit integration technique has been applied to the beam vibration problem by Leonard (5) but an explicit integration technique such as used by Witmer et al. (6) on the axisymmetric shell problem has been successful for linear problems, as well as for more complicated nonlinear physical models. The explicit technique has computational limitations because of the time interval used and spatial mesh size which is required to insure numerical stability. A successful numerical integration has been employed on simpler problems utilizing the techniques of Houbolt (7).

The application of plasticity theories to the dynamics solution are still being formulated for basic shell shapes. The underlying techniques required for more complex shell structures exhibiting elastic-plastic and creep behavior are matrix methods of structural analysis. Recent work by Turner, Percy et al. (8-10) has produced successful matrix methods for geometric description of a structure with proper boundary conditions. There are two methods available for inelastic analyses of general shell shapes, that of Denke and Warren (11-13) and that of Gallagher, Padlog et al. (14-16). Adapting these techniques to computers produces the expected difficulty of excessive computing time required for the incremental or iterative solution of the nonlinear governing equations. An elastic-plastic analysis is no better than the basic elastic analysis with which it begins; similarly, a time-dependent elastic-plastic-creep analysis is no better than the time independent elastic-plastic analysis with which it begins. If the element size is large, the matrix analysis does not account for high stress gradients. The inelastic behavior of an element is strongly dependent on all components of stress. Thus, the scheme for matrix analysis must retain all components of stress for each discrete element. The behavior cannot be properly represented, for example, by an idealization of a plate into a network of axially loaded linear elements.

EXPERIENCES IN FORMULATING
ANALYTICAL MODELS

The formulation of a dynamic model is based on the understanding of three areas of compromise: (a) the definition of the forcing

function in a form which is adaptable to analytical solutions, (b) the definition of the physical characteristics of the dynamic system, and (c) the numerical techniques used for solution of the equations of motion. Each of these areas of interest requires simplification for ease of solution, while not losing accuracy. The success of a model rests on the ingenuity and judgment of the engineer making these approximations.

Forcing Function

The most critical simulation in modeling is the forcing function. Only when the form and distribution of the forcing function is known does the engineer have a basis for selecting a model of the physical system. Generally, engineering design can use crude estimates of loading environments with factors for conservatism. This does not hold entirely true when designing for impulsive loads. The shape of the impulse is usually critical, and one must have a reasonable limit defined for total impulse, duration, and peak load. If too much uncertainty is involved, the only recourse is to make a parametric study using given total impulses with a variety of pulse shapes to determine the envelope of peak response levels.

The most difficult situation exists when the mathematical form of the environmental loading has been chosen and then it is desired to simulate this forcing function in a laboratory test. Similarly, it is extremely difficult to evaluate test data because of the assumptions required for mathematically describing the forcing function observed in the test.

A direct impulsive load applied to the surface of a dynamic system is generally considered to be a step function of a given total impulse. This type of forcing function is a good representation for radiation-induced vaporization of the surface material but generally is not acceptable for pressure loadings created by blast. A step function is entirely unacceptable for describing structurally transmitted loads.

In the laboratory, the step function is simulated by applying sheet explosive directly to the surface of the structure. The total impulse is obtained from a pre-test calibration on an identical cylinder mounted on a ballistic pendulum. Various weights of sheet explosive are applied to the calibration cylinder to establish the relationship of weight of the sheet explosive and the total impulse imparted to the calibration cylinder. The actual total impulse imparted to each test cylinder is obtained by analyzing the Fastax film data. Cylinder velocities are calculated from the film data, and impulse is calculated from the velocities.

When the impulsive load is produced by a pressure wave, the forcing function is suitably measured by pressure transducers. For example, the idealized forcing function defined for a cylinder sustaining a blast wave is shown in Fig. 1. The pressures were obtained by mounting several pressure transducers around the circumference of the cylinder. The distribution of pressure around the cylinder is then determined to be that shown in Fig. 2. The most significant time effect is the engulfment, shown in Fig. 3. Another example is a sphere-cone configuration whose pressure transducers obtained the type of pressure histories shown in Fig. 4.

Another type of impulsive loading is that transmitted through structural media to the item under question. An example is an
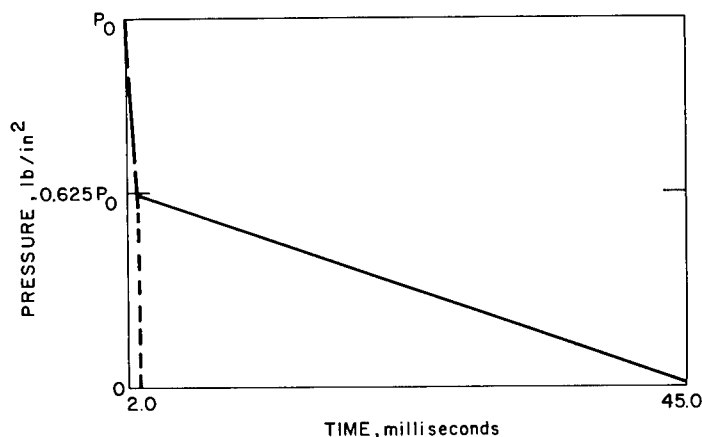
Fig. 1. Idealized pressure pulse

288
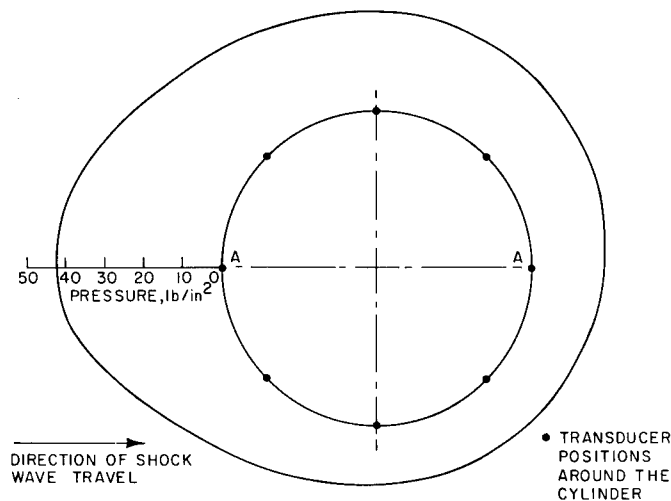
Fig. 2. Distribution of initial peak pressures
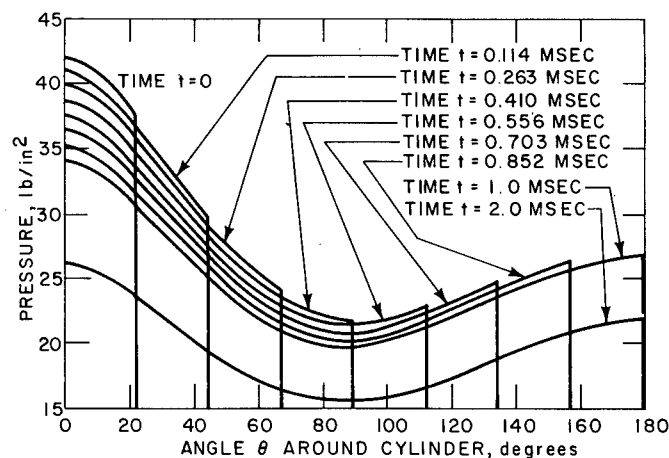
Fig. 3. Pressure distributions around
cylinder during engulfment by blast

equipment item mounted some distance from a pyrotechnic separation device. Accelerometers are used to measure the input to the equipment box. The measurements are usually highly random vibrations covering a wide range of frequencies and g levels. The only means of identifying this response as an input to the box is by generating a power spectral density plot of the random vibration. This may not be acceptable if the response was of short duration, which is generally the case for impulsive loadings. In that event it is common practice to use the tape recordings of the measured test accelerations directly as the forcing functions in the equations of motion of the box and then to solve the equations by finite-difference techniques.

It can be seen from these examples that the mathematical form of the forcing function for impulsive loading is not a simple mathematical expression. For meaningful results, the computing equipment used for the solution of the dynamic equations must be able to accept the random vibratory forms of the forces.

Physical Characteristics

In forming the dynamic model, the physical characteristics are categorized into three areas: mass, stiffness, and damping characteristics of the system. The description of the mass distribution in general can be quite crude. Usually

289
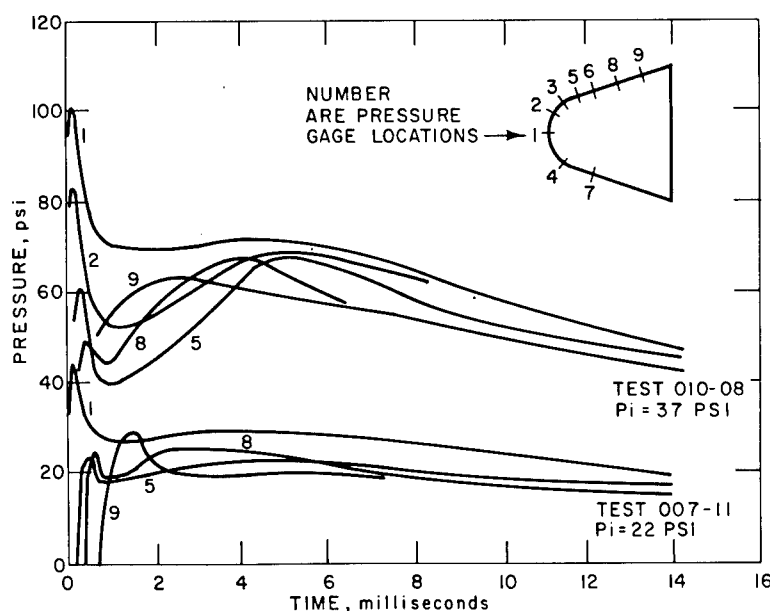
Fig. 4. Smoothed pressure-time functions
for specific calibration tests

the mass is well regulated, such as sheet material having uniform thickness, or components of high density easily defined as lumped masses. The most accurate form of describing the mass distribution is by writing explicit dynamic equations of motion in which the inertia terms are mathematical functions. Success is dependent on the ability to describe the distribution by continuous functions.

The use of lumped masses for defining continuous systems has been a long-standing engineering practice. It is somewhat surprising that such an approximation can provide good results, even in sensitive problems such as stress wave studies. The case of an elastic disturbance propagating in a one-dimensional homogeneous bar of finite length having free-fixed and free-free boundary conditions was solved using classical stress wave theory, and then compared to solutions obtained by using an equivalent dynamic lumped mass approach. It was found that solutions to beam impact problems pertaining to particle velocity, stress magnitude, wave periods, and impact duration, as obtained by classical theory, agree very well with that obtained by using the lumped mass modeling technique. It is evident from the results of these studies (17) that the lumped mass technique is capable of accounting for internal reflection and transmission activities, as well as those by external boundary constraints.

A study was made of an elastic bar of unit cross-sectional area, fixed at one end, and struck at the free end by an absolutely rigid mass having a velocity, v_o, at time of impact. Figures 5 and 6 indicate the stresses versus time for the first and last spring, respectively, of a 60-mass lumped mass system. The values shown are identical to those obtained for a 30-mass system.

Another study was made of a bar of unit cross-sectional area whose length consisted of two materials, fixed at one end and struck at the free end by an absolutely rigid mass having a velocity, v_o, at time of initial impact. Figure 7 is a graphical representation of the theoretical reflection and transmission activities of the initial wave front during the first 1-1/2 cycles. Figure 8 is a stress history plot of the first spring of the lumped mass model. The lumped mass model stress levels at the time for a wave to start from its origin, propagate through materials 1 and 2, reflect off the fixed end, propagate through materials 2 and 1, and return to its origin agrees very well with the values obtained theoretically.

In the evaluation of shallow spherical caps, it was found that distribution of mass by the lumped mass technique, in which the mass was represented by a series of concentric rings, was acceptable. A reasonable comparison of frequencies and mode shapes were obtained with a small number of masses for the spherical cap shown in Fig. 9. A study was made to determine the number of lumped masses required for

290
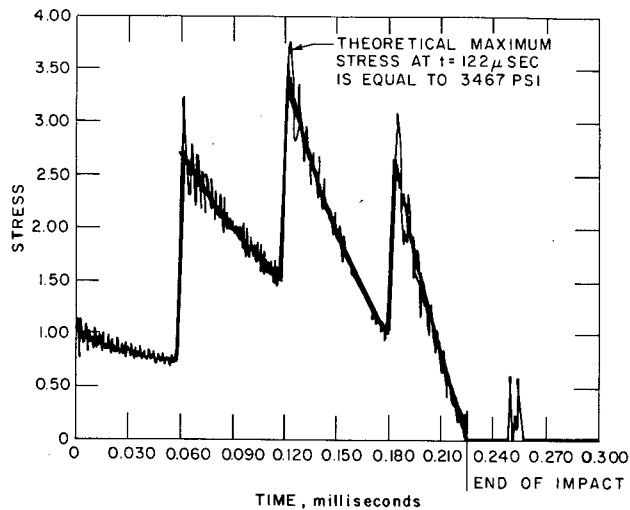
Fig. 5. Stress vs time for first spring of
elastic bar sustaining impact
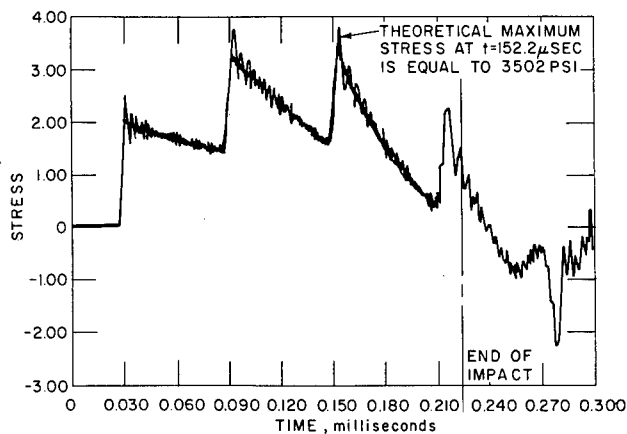
Fig. 6. Stress vs time for last spring of
elastic bar sustaining impact

acquiring suitable accuracy (Figs. 10-12). This
type of modeling was acceptable for the cap be-
cause an element in the cap deflected as a beam,
not a membrane. However, the deflection of an
arbitrary shell does not act as a beam, and the
lumped mass technique is unacceptable. For
this reason, the numerical schemes chosen for
arbitrary shells use the smallest grid size
possible within the limits of the computer to al-
low the finest detail definition possible of the
mass elements.

A study was made of a thin-walled axially
loaded cylinder subjected to pressure blast
loading. Repetitive data from several tests are
in good agreement, indicating that the test setup

and support system were successful in simulat-
ing a restrained fixed-free axially loaded sys-
tem. The cylinder was modeled as an axial
array of 30 masses. Pressure gages recorded
the impulsive load, and the resulting idealized
pressure pulse applied to the cylinder end is
shown in Fig. 13. The cylinder was modeled as
an axial array of 30 lumped masses. The com-
parison of test results and analytically deter-
mined compressive strains in the thin-walled
cylinder are shown in Fig. 14.

In the use of numerical schemes for defi-
nition of physical systems, it is difficult to
assess the influence of the mass distribution
approximations from the effects created by the

291
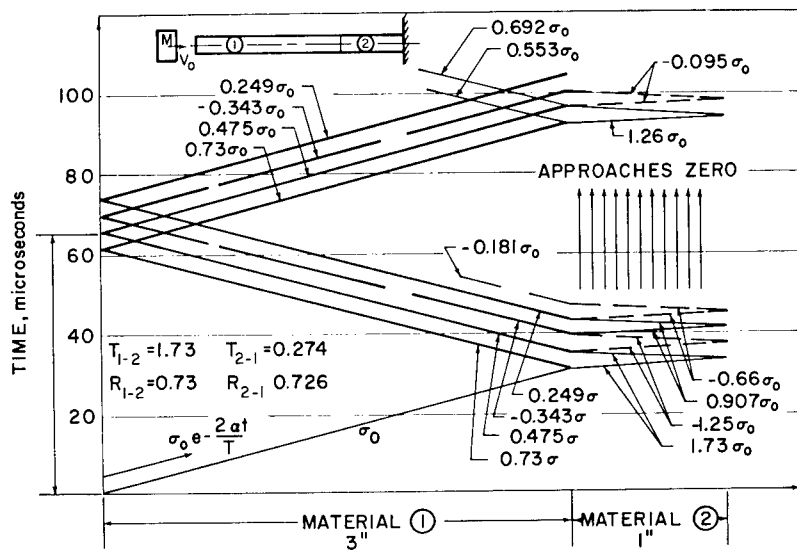
Fig. 7. Reflection and transmission of initial wave
front (σ_0) in elastic bar of two materials
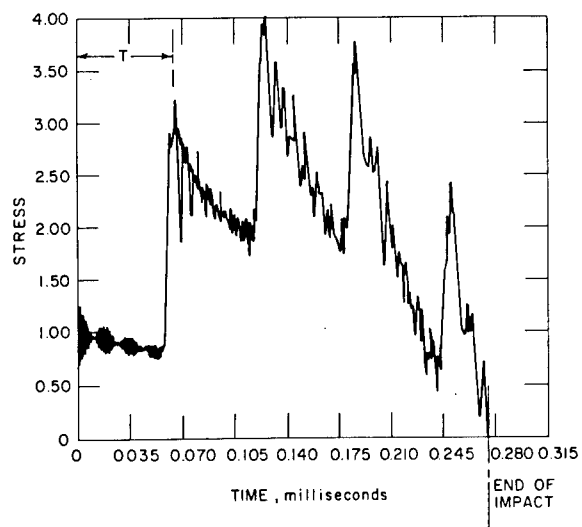
Fig. 8. Stress vs time for elastic bar
of two materials sustaining impact

C G OF MASS

h

r_0

r

Z

θ

θ_{ci}

θ_0

$\Delta\theta$

R

BOUNDARY
CONDITIONS
AT EDGE
U = 0
β = 0

DISPLACEMENTS

W

U

β

MATERIAL PROPERTIES

$E = 30.0 \times 10^6$ psi

$\nu = 0.3$

$\rho = 0.283$ lb m/in^3

DIMENSIONS

$\theta_0 = 8.0$ deg

$r_0 = 10.0$ in   EXACT

R = 71.853 in

h = 0.195 in
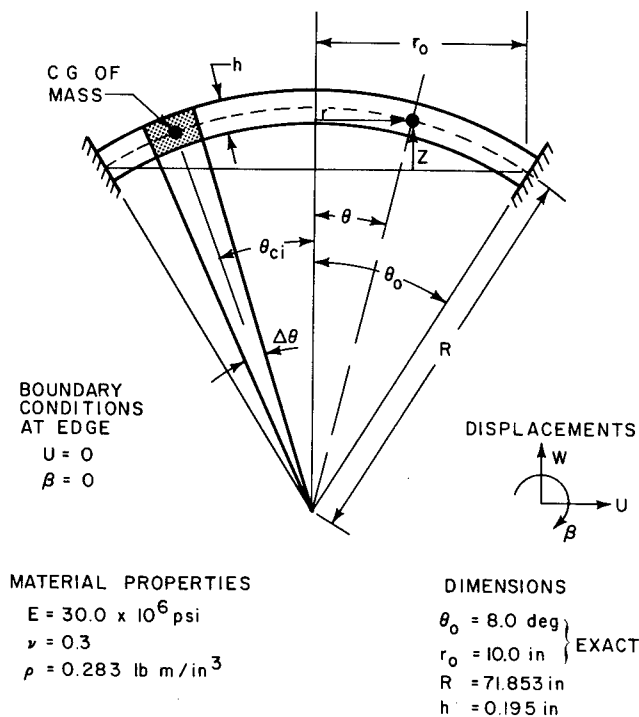
Fig. 9. Spherical cap model
used for analytical study

stiffness or damping assumptions. Therefore, it is difficult to comment on the benefits of one numerical method over another. The definition of the stiffness characteristics of a dynamic system is a more difficult part of the formulation of a dynamic model. Complex structures require a great amount of detail when there exist cutouts, access doors, and varieties of constraints.

The most common practice for defining the stiffness characteristics is to use beam strain energy principles for definition of the deflection influence coefficients, and the inverse produces the stiffness. With the advent of large digital computers, the use of the direct-stiffness approach has become more in favor because of its engineering utility for defining geometric detail.

A comparison was made of the techniques using beam deflection influence coefficients, direct-stiffness methods, and the direct solution by finite differences of a cylindrical shell (21). In all cases, the dynamic models used were limited by the computer storage available on the IBM 7094.

Figure 15 shows a cylindrical shell, clamped-free with uniform geometry. Boundary

conditions for this cylinder at the clamped end are comprised of three zero displacement components and zero rotation. The free end conditions consisted of three zero force components and zero moments. The problem is to find the dynamic response of this shell when it is subjected to a uniform external pressure consisting of the first unsymmetrical harmonic with the time variation, as shown in Fig. 15.

The direct-stiffness modal approach uses finite elements to obtain the stiffness and mass matrices, as well as a modal analysis for the response calculations. The modal analysis used in obtaining the dynamic response is limited to a maximum of 100 degrees of freedom. Since each mode of the shell structure has 4 degrees of freedom, the maximum number of shell elements is thus controlled. It was found convenient to use 24 elements (described in Fig. 15). Using this model, a static analysis was obtained by the direct stiffness methods developed by Percy et al. (18). From this analysis resulted the mass and stiffness matrices. The results of the static analysis appear to be good, except for the meridional moment M(s) in the membrane region of the shell. A residual value of M(s) existed in this region, where it should have been zero.

293
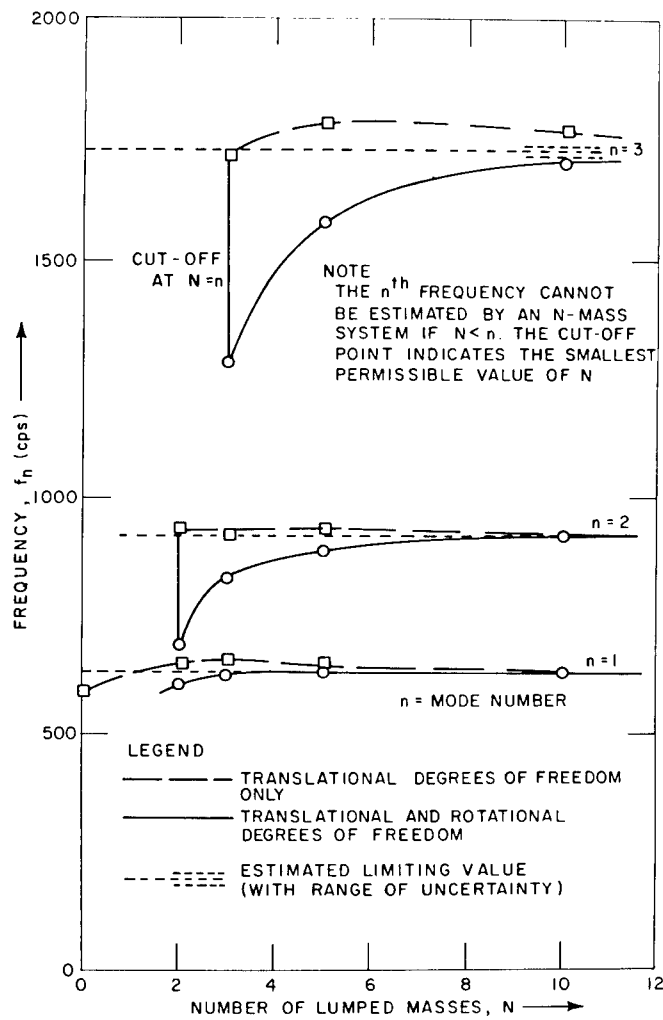
Fig. 10. Frequency vs number of masses
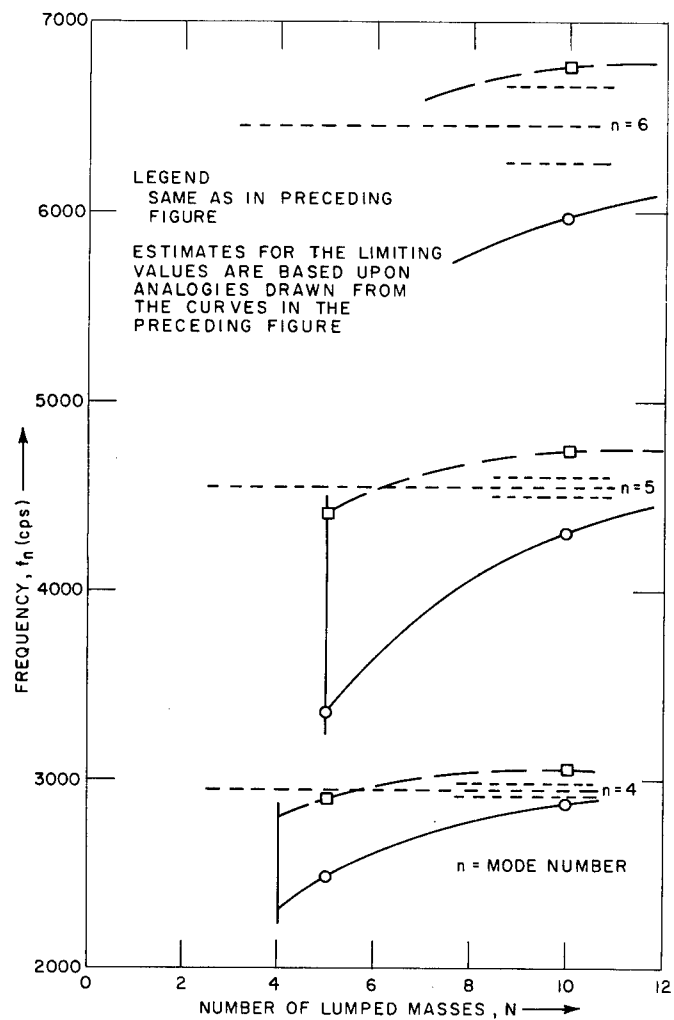
Fig. 11. Frequency vs number of masses
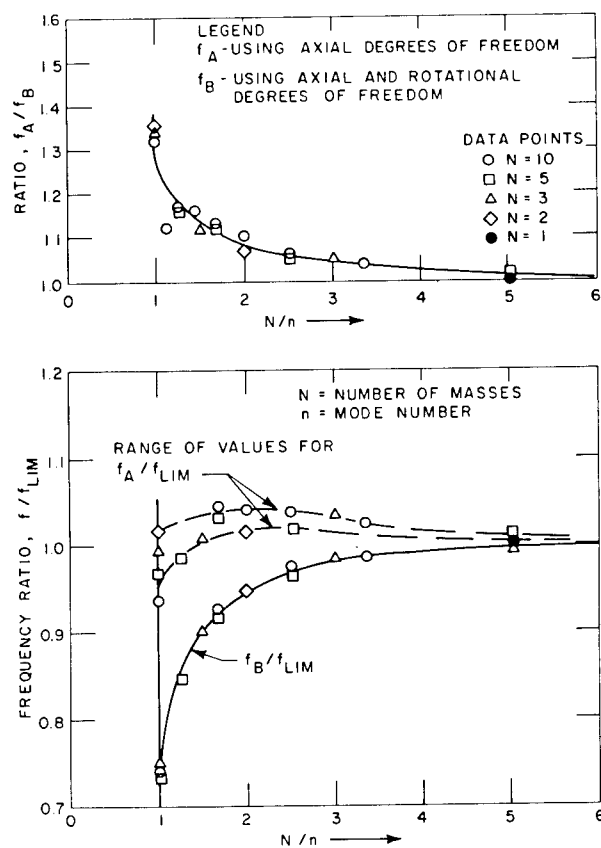
Fig. 12. Correlation of frequency
ratios with N/n
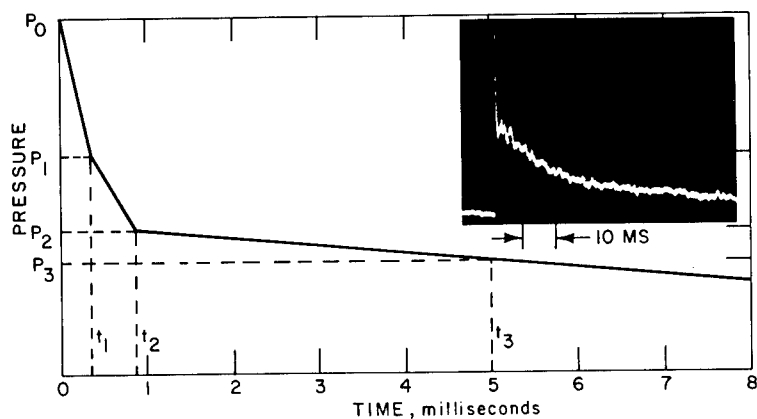
Fig. 13. Idealized pressure pulse
applied to cylinder end
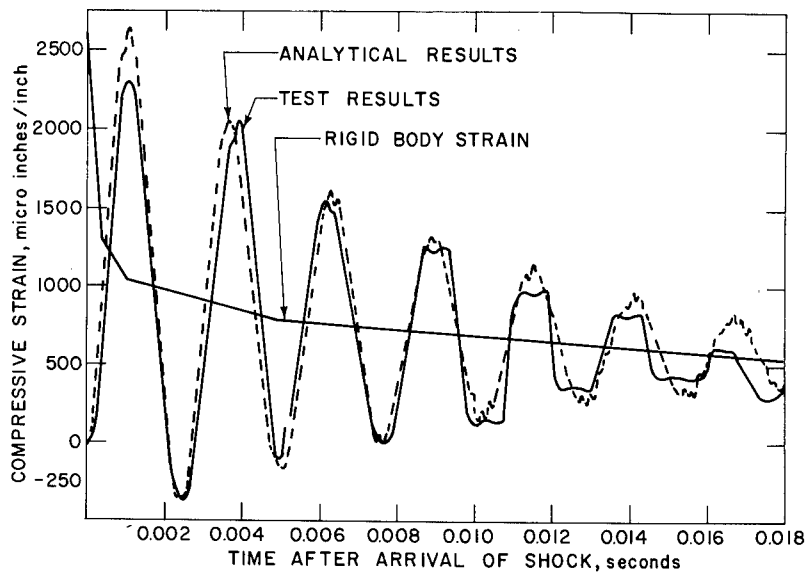
Fig. 14. Comparison of test results and analytical study of
thin-walled cylinder subjected to axial shock load
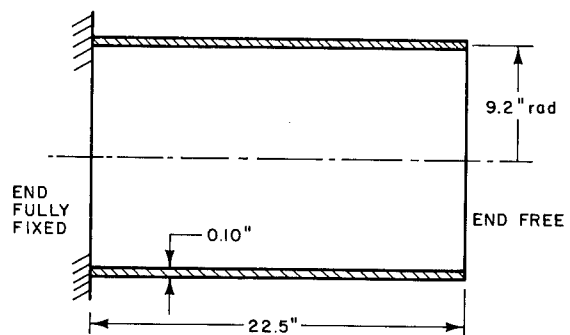
READING FROM THE FULLY-FIXED END THE MODEL IS
COMPOSED OF THE FOLLOWING ELEMENTS
(i)   6 ELEMENTS EACH 0.25" LONG
(ii) 2 ELEMENTS EACH 0.50" LONG
(iii) 12 ELEMENTS EACH 1.50" LONG
(iv) 4 ELEMENTS EACH 0.50" LONG

EXTERNAL PRESSURE
LOADING = 10 COS θ PSI
THE PRESSURE
PULSE SHAPE IS
SHOWN OPPOSITE
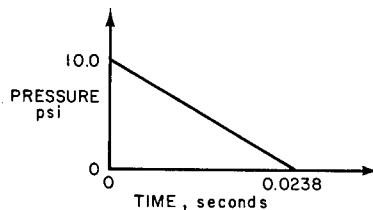
Fig. 15. Cylindrical shell
and loading function

The Houbolt technique for dynamic analysis for shells (4) solves for the time-varying response of the shell and provides the deflections, meridional moment, and stresses at selected intervals during the analysis. The equations of motion are obtained by adding the appropriate inertia terms to the equations of equilibrium for a cylindrical shell, using Sander's theory (19). The resulting equations of motion were integrated timewise using an explicit method of numerical integration. As the applied load varies with time, the analysis linearly interpolates between the values given at particular instants. The input to the analysis is comprised of the geometry description, material properties, length of time for which the response is required, the boundary conditions, and the Fourier coefficients for the load for each axial position, and each time at which the load is stipulated. The output consists of the time variation of the displacements, the components of both membrane and bending stress, and the three strain components for selected points on the surface of the shell. The values of strain calculated are those on the inside surface, thus allowing direct comparison with the strain readings from laboratory tests. Six Fourier coefficients may be used to describe the load, and the output is the summation of the results for each harmonic.

The beam deflection influence coefficients/modal analysis utilizes strain energy principles to arrive at the stiffness matrix, and a modal analysis is used to obtain the response. The beam analysis was conducted on the cylinder, assuming it to be a uniformly loaded cantilever beam divided into 20 equal lengths and 19-1/2 masses. Deflection influence coefficients for the individual sections were determined by considering the strain energies due to bending and shear. The mass matrix consisted of the mass values of the individual sections and their polar moments of inertia about the centroidal axis of the individual sections.

Figure 16 compares the natural frequencies and mode shapes of the direct stiffness methods and beam analysis. No frequency values of mode shapes were obtained from the Houbolt shell analysis. The differences noted can be attributed largely to the absence of strain energy in the beam analysis due to tensile forces.

Figure 17 shows the normal deflection at the free end of the cantilever for theta equal to zero as obtained from the three analytical techniques. The results from the direct-stiffness method and the Houbolt approach show close agreement. Results from the beam analysis

are approximately 20 percent low. As can be observed from the figures, the second peak is slightly higher than the first for the shell analysis. This can be attributed probably to the presence of axial inertia generating stress waves in the cylinder. The behavior of the meridional and circumferential displacements at the free end of the cylinder from the two shell programs show almost identical results, except for the small variation in the meridional displacements. Similar comparisons were made at the clamped end of the cylinder for evaluating beam bending moment.

To amplify this comparison, a study was made comparing the dynamic response by the direct stiffness method and the Houbolt finite-difference techniques to measured responses in a cylinder subjected to lateral blast loading (22,23). Because of the uniform loading along the shell and the symmetry of the boundary conditions, it is possible to consider only half of the cylinder for the analysis. The geometry analyzed is shown in Fig. 18. It was concluded from the study that the direct stiffness method shows fair comparison with the Houbolt finite-difference methods. A static analysis of the shell produced favorable comparisons as shown in Figs. 19, 20, and 21. At the centerline of the shell, comparable results were obtained under dynamic loading, as shown in Figs. 22 and 23, while variations exist in the description of the displacements close to the clamped end, as shown in Figs. 24 and 25. These differences can be explained by observing the displacements along the meridian of a cylinder as calculated for a clamped-free cylinder, as shown in Fig. 26. The complex deformation patterns existing near the restrained ends can be determined by highly theoretical means, but not as accurately by mere engineering approaches.

Damping is included in dynamic models as a modal quality factor and expressed as percent critical damping per mode. Damping is usually not significant during initial responses. However, the peak levels attained at later times are significantly reduced. For example, responses to blast in a sphere-cone-cylinder are shown in Figs. 27 and 28 where structural damping was varied from 0 to 5 percent of critical damping level, and the changes in response accelerations are noted. These plots represent envelopes of maximum accelerations.

It is recognized that actual vehicle damping consists of a combination of material and system damping. However, no methods exist to determine these effects separately. For small amounts of damping, any form of damping (viscous, Coulomb, joint) introduced into
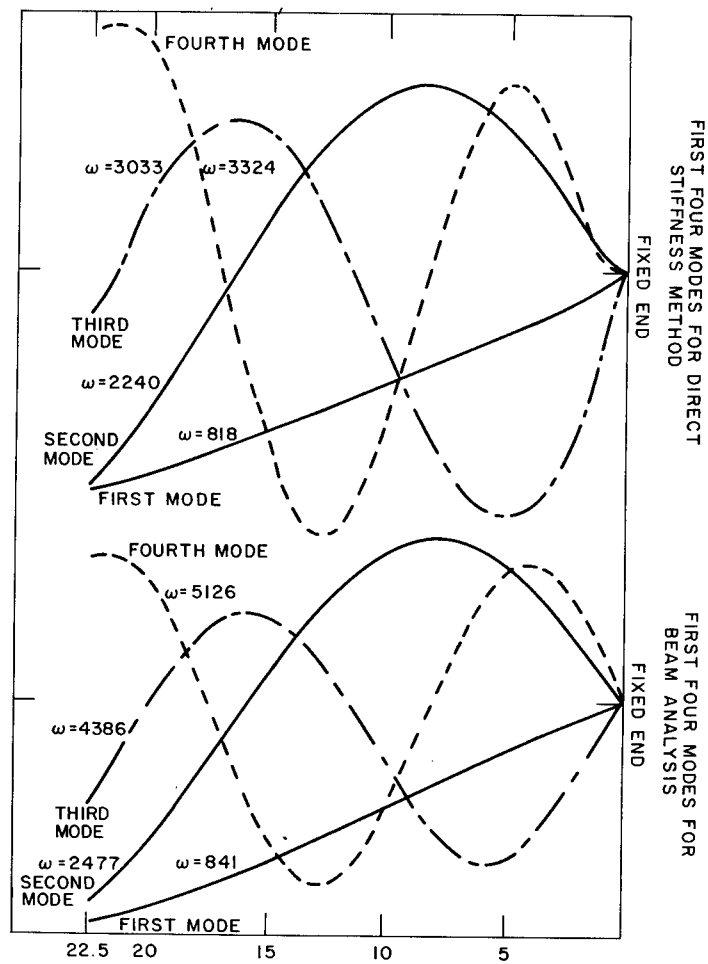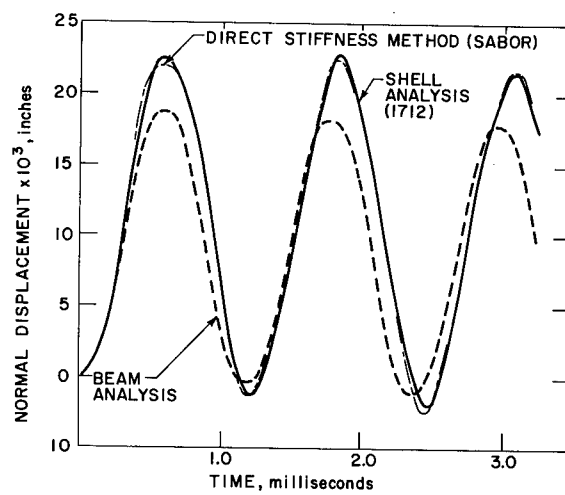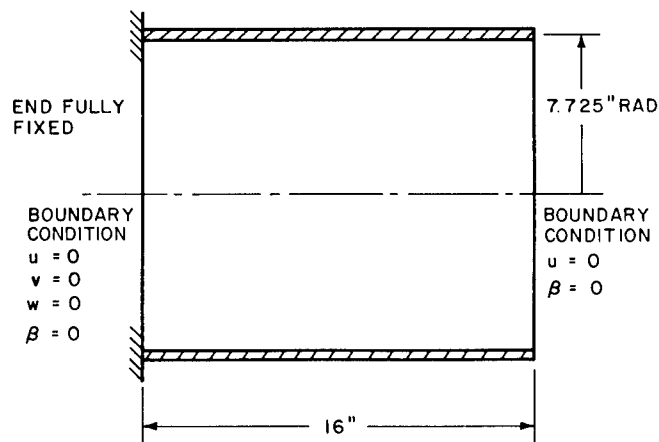
Fig. 16. Mode comparison

Fig. 17. Displacement at free end of
cantilever for theta equal to zero
degrees

END FULLY
FIXED

7.725" RAD

BOUNDARY
CONDITION
u = 0
v = 0
w = 0
β = 0

BOUNDARY
CONDITION
u = 0
β = 0

16"

READING FROM THE FULLY FIXED END THE MODEL
WAS COMPOSED OF THE FOLLOWING ELEMENTS
(i)   4 ELEMENTS EACH 0.25" LONG
(ii)   2 ELEMENTS EACH 0.50" LONG
(iii) 12 ELEMENTS EACH 1.00" LONG
(iv)   2 ELEMENTS EACH 0.50" LONG
(v)   4 ELEMENTS EACH 0.25" LONG

Fig. 18. Geometry of cylinder subjected to
lateral blast loading
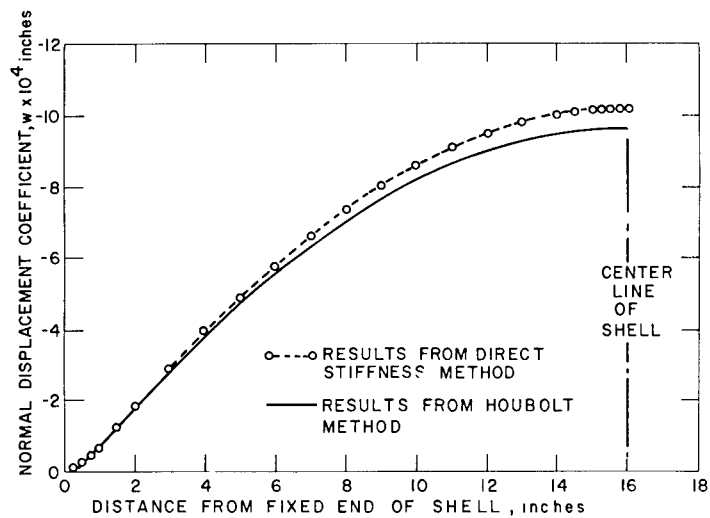
Fig. 19. Comparison of static analyses
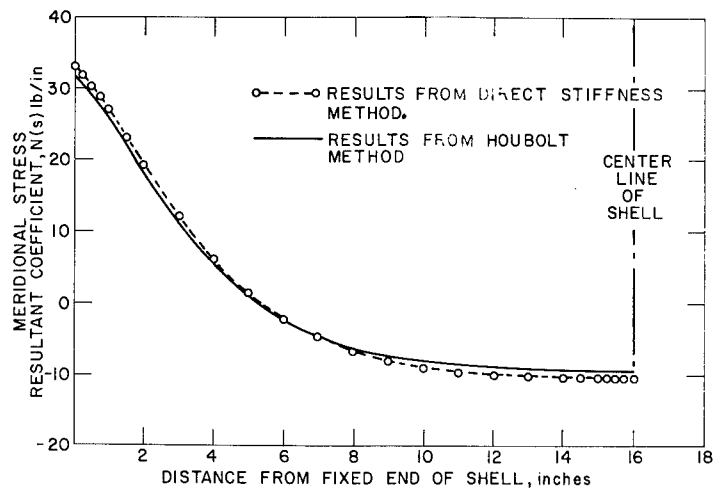
Fig. 20. Comparison of static analyses
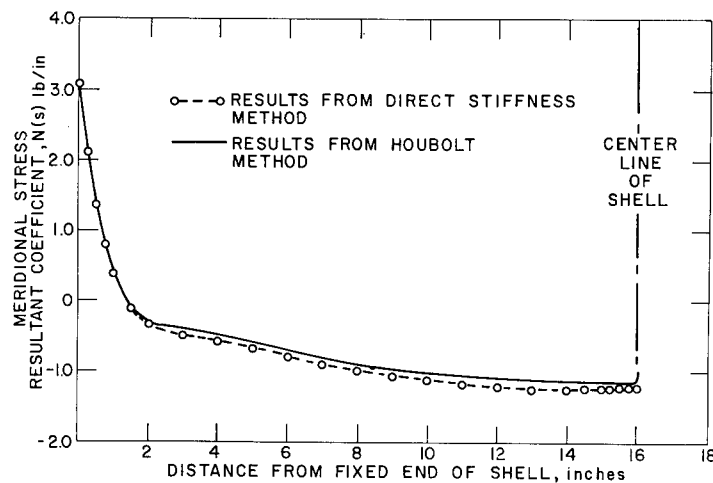
Fig. 21. Comparison of static analyses

the response will yield similar results. Thus, if the combined effect of the various damping forms is known, such as from a resonant survey, then the response effects of damping can be adequately defined. Most vibration surveys indicate that damping levels as calculated by the bandwidth method described in Ref. (20), are 3 to 7 percent of critical damping. For metal structures, analytical results indicate that damping must be included in the structural response analyses. However, the influence of the damping decreases with increase in damping. Generally the amount of damping selected is 3 percent, since it is considered a conservative estimate of damping and because higher damping will not drastically reduce the initial response value.

Solutions of the Equations

The solution to any impulsively loaded dynamic model requires the use of electronic computers. It is difficult to generalize about the methods which best lend themselves to numerical analysis of impulse problems. Since the engineer is restricted to the machine at his disposal, the numerical techniques available to him are constrained by the size and capacity of his machine. In general, the finite-difference techniques are only suitable to the largest digital computers. For smaller computers, accuracy in the solution of the simultaneous equations or iteration schemes for natural modes is the limiting factor.

301
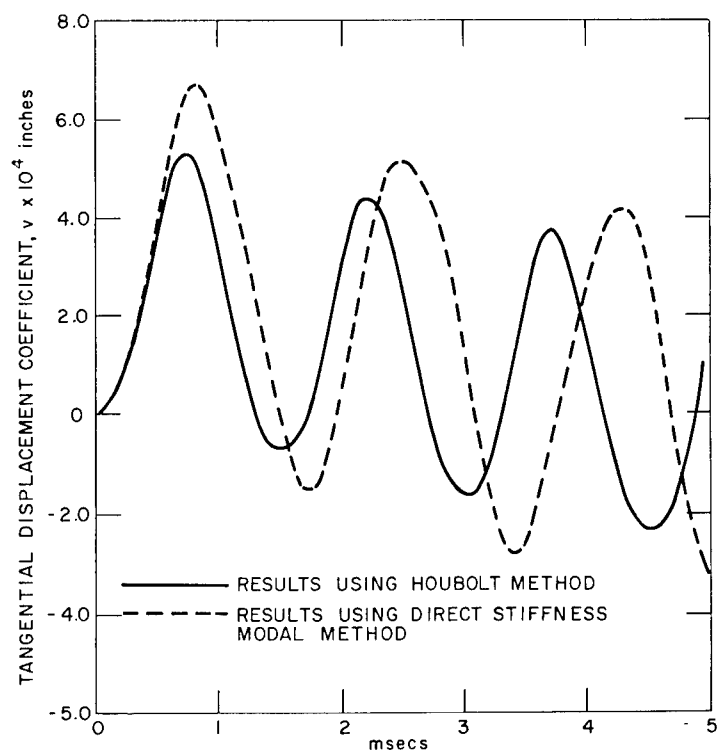
Fig. 22. Comparison of dynamic response at centerline of shell -- tangential displacement , coefficient V
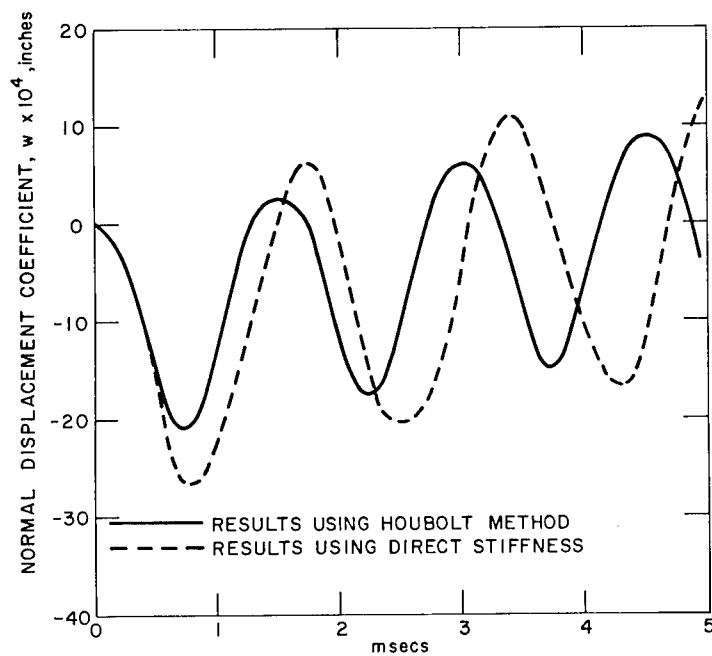
Fig. 23. Comparison of dynamic response at centerline of shell -- normal displacement coefficient W

302
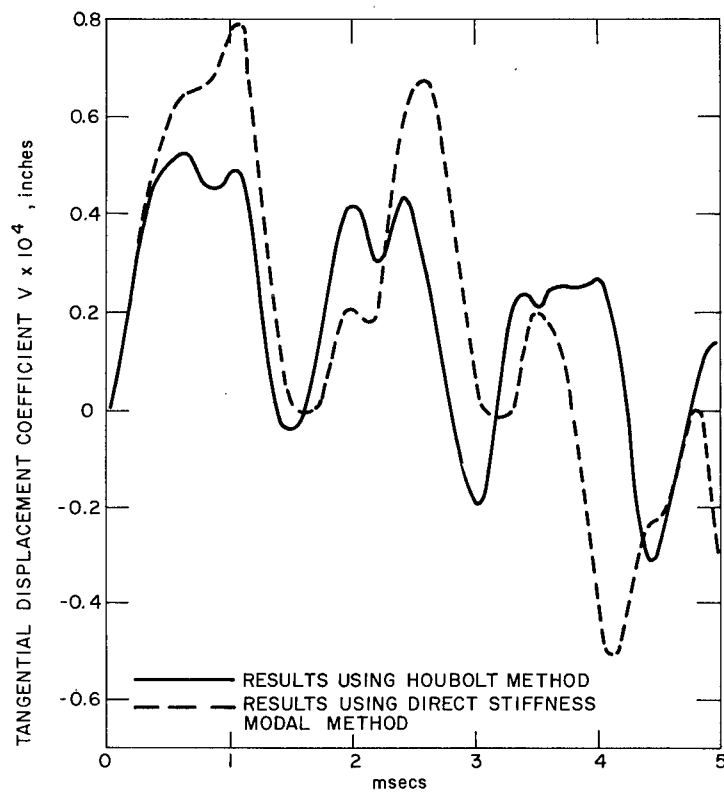
Fig. 24. Comparison of dynamic response at 2 in.
from end of shell -- tangential displacement coef-
ficient V
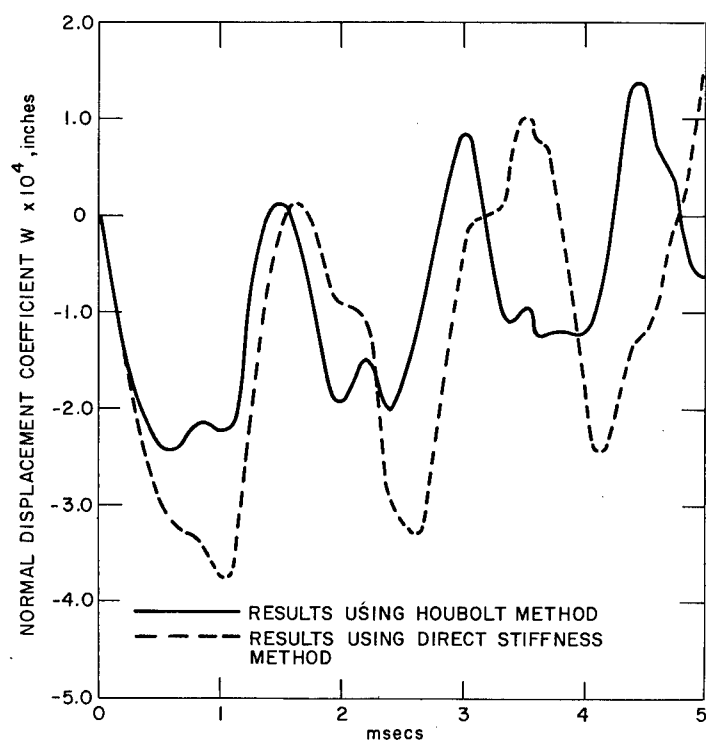
Fig. 25. Comparison of dynamic response
at 2 in. from end of shell -- normal dis-
placement coefficient W
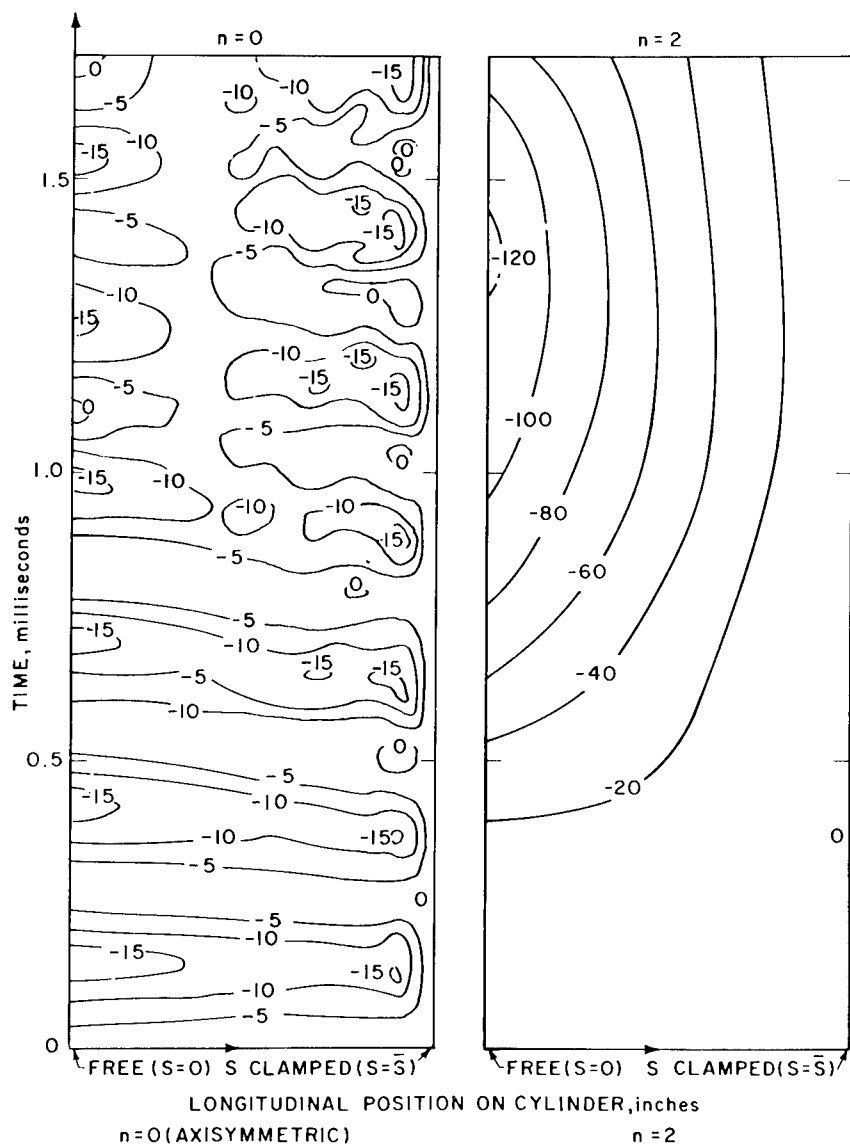
Fig. 26. Contour plot of $w^{(n)}$ for $n = 0$ and $n = 2$ (nondimensional Fourier coefficient of normal displacement)

304
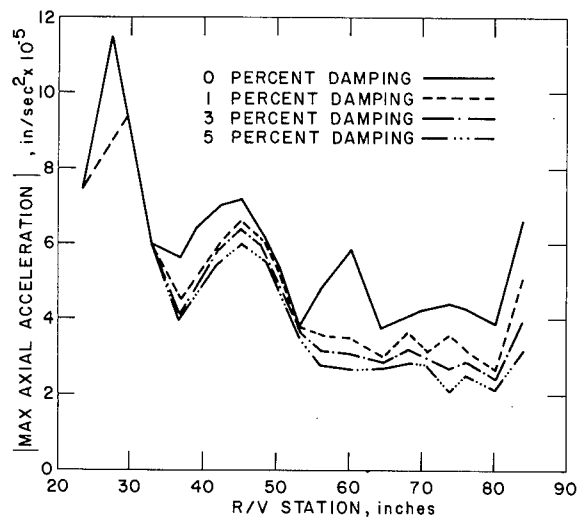
Fig. 27. Absolute max acceleration
vs station axial model
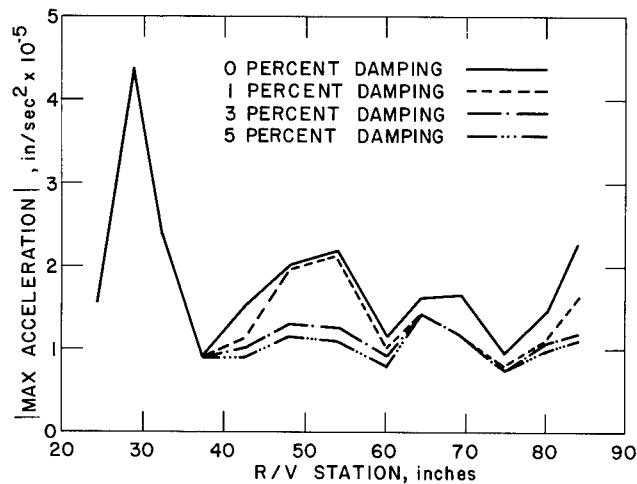
Fig. 28. Absolute max acceleration
vs station lateral model

CONCLUSIONS AND RECOMMENDATIONS

The following conclusions can be made about the current status of analytical modeling for evaluation of response to impulsive loads:

1. The quality of instrumentation is acceptable, allowing definition of the forcing functions with a good degree of accuracy.

2. Several techniques are available to the engineer for formulating the dynamic model. These techniques are a function of the complexity of the system. The more complex the system is, the more difficult the model and the more complex the model required.

3. With the existence of larger computers (such as the IBM 360), the analyst has at his disposal the means of attaining the higher accuracy required by the more complex models.

4. The particular technique used for a model in many cases can be based on existing engineering techniques which surprisingly enough are applicable.

305

5. Since it is recognized that acceptable means exist for the analysis of impulsively loaded structures, a larger amount of work should be expended in the establishment of reasonable design criteria for the design of structures to impulsive loads.

REFERENCES

1. P. P. Radkowski, R. M. Davis, and M. R. Bolduc, "Numerical Analysis of Equations of Thin Shells of Revolution," Am. Rocketry Soc. J. 32:36-41 (1962)

2. P. P. Radkowski, "Stress Analysis of Orthotropic Thin Multilayer Shells of Revolution," AIAA Launch and Space Vehicle Shell Structures Conference, Palm Springs, Calif., 1-3 April 1963 (Preprint 2889-63)

3. B. Budiansky and P. P. Radkowski, "Numerical Analysis of Unsymmetrical Bending of Shells of Revolution," AIAA J. 1(8) (Aug. 1963)

4. D. E. Johnson and R. Greif, "Dynamic Response of a Cylindrical Shell: Two Numerical Methods," Avco/RAD Tech. Memo. RAD-TM-65-33, 19 July 1965

5. R. Leonard, "On Solutions for the Transient Response of Beams," NASA TR-4-21, 1959

6. E. A. Witmer et al., "Large Dynamic Deformations of Beams, Rings, Plates, and Shells," AIAA J. 1:1848 (Aug. 1963)

7. J. C. Houbolt, "A Recurrence Matrix Solution for the Dynamic Response of Aircraft in Gusts," NACA Rept. 1010, 1953

8. J. G. Percy, W. A. Loden, and D. R. Navaratna, "A Study of Matrix Analysis Methods for Inelastic Structures," AF Flight Dynamics Lab., Rept. RTD-TDR-63-4032, Oct. 1963

9. J. J. Turner et al., "Stiffness and Deflection Analysis of Complex Structures," J. Aeronautical Sci. 23 (1956)

10. W. J. Turner, H. C. Martin, and R. C. Weikel, "Further Development and Applications of the Stiffness Method," paper presented at AGARD Structures and Materials Panel, Paris, France, July 1962; published as report by Aerospace Div., Boeing Co., Seattle, Washington

11. P. H. Denke, "The Matrix Solution of Certain Nonlinear Problems in Structural Analysis," J. Aeronautical Sci., 23 (1956)

12. D. S. Warren, "A Matrix Method for the Analysis of the Buckling of Structural Panels Subjected to Creep Environments," ASD-TDR-62-740, Nov. 1962

13. P. H. Denke, "Digital Analysis of Plasticity in Plates," Appendix C, pp. 145-157, "Effect of Compressive Loads on Structural Fatigue at Elevated Temperatures," ASD-TDR-62-448, Oct. 1962

14. R. H. Gallagher, J. Padlog, and P. P. Bijlaard, "Stress Analysis of Heated Complex Shapes," Am. Rocket Soc. J. 32 (1962)

15. J. Padlog, R. D. Huff, and G. F. Holloway, "Unelastic Behavior of Structures Subjected to Cyclic, Thermal and Mechanical Stressing Conditions," WADD-TR-60-271, Dec. 1960

16. R. H. Gallagher, J. F. Quinn, and J. Padlog, "Deformational Response Determinations for Practical Heated Wing Structures," Proc. Symposium on Structural Dynamics of High Speed Flight, ONR ACR-62, Vol. 1, April 1961

17. D. T. Mooney and R. H. Coco, "The Evaluation of Lumped Mass Techniques for Solving Stress Wave Propagation Problems," Avco/RAD Tech. Release S310-T-150, 5 Dec. 1965

18. J. H. Percy et al., "Application of the Matrix Displacement Method to the Linear Elastic Analysis of Shells of Revolution," M.I.T. Aeroelastic and Structures Research Lab., ASRL TR 121-7, Jan. 1965

19. B. Budiansky and J. Lyell Sanders, Jr., "On the 'BEST' First-Order Linear Shell Theory," ONR Contract No. 1886102, Harvard Univ. Div. of Eng. and Appl. Physics, Tech. Rept. No. 14, Sept. 1962

20. Structural Damping (J. E. Ruzicka, Ed.), ASME, 1959

21. W. Hadley, J. McLean, and C. Sve, "Comparison of Dynamic Response Methods," Avco/RAD Tech. Release S310-T-183, 4 Aug. 1965

22. J. L. McLean, "Comparison of the Dynamic Response of a Cylinder Subjected to Lateral Blast Loading," Avco/RAD Tech. Release S310-T-182, 30 July 1965

23. J. L. McLean and D. E. Johnson, "Theoretical-Experimental Comparison of the Dynamic Response of a Circular Cylinder Subjected to Lateral Loading," Avco/RAD Tech. Memo. RAD-TM-65-37, 5 Aug. 1965

DISCUSSION

Dr. Sevin (IIT Research Inst.): It seems to me that for impulsive loading, where the time details get very small relative to the natural periods of the structure, the actual time details are less important. I believe that there is an alternate way for analysis, and I wonder whether you have considered this. In some work which we published 7 or 8 years ago we learned a few things. One may be uncertain about the details of the inputs for these very short duration loads. One may know more about the total impulse and duration and may only be able to define the forcing function within a class of forcing functions such as those having a prescribed impulse, duration, limited peak force, and so on. In this case, one can still handle a response problem and answer such questions as: What are the bounds on the possible response? What is the largest possible maximum displacement of some element of the model? What is the smallest possible maximum displacement? If these bounds are between a mil and a mile, one has not learned a great deal. If they are much narrower, one may have learned a lot, both about the likely response and the definition of the forcing function. It seems to me that, in principle, there is no reason why these techniques, which have been published for very simple models, cannot be extended to more complex models.

Mr. Broding: That is very true. For example, on a shaped charge, if you know the total impulse from the separation joint you can experiment parametrically with various time durations that you feel exist and then you can bound the problem.

Mr. Kapur (Aerospace Corp.): The speaker has given the impression that the finite-difference method is better than the stiffness method. I would say that if there is a grid at the fixed end, one will get much better results using the stiffness method. Also, for structures which have cutouts, such as windows, the stiffness method will prove much more useful than the finite difference method.

Mr. Broding: That is an old argument. For comparative purposes we have fixed the size of the problem to the size of the 7094 computer. We had a very simple problem so that the mesh size on the finite-difference method gave very good results. We went to the largest size matrices we could use with the SABRE program and one could see the differences. From a practical engineering point of view, I think the direct stiffness method is more advantageous, but I do not see how it can be useful until we get the IBM 360 computers in operation.

Mr. Howard (Aerospace Corp.): I think that a more efficient allocation of the grid size is what Mr. Kapur was talking about, that is, putting more breakdowns close to the load and more breakdowns close to the clamped edge.

Mr. Broding: We tried that, but there just are not enough sides. As soon as you start putting all of the mesh sides down at the constraint, the other end of the cylinder is lost.

*   *   *

PYROTECHNIC SHOCK ANALYSIS AND

TESTING METHODS*

Alan R. Hoffman and James E. Randolph
Jet Propulsion Laboratory
Pasadena, California

Explosive separation devices employed during the launch phase and
space flight generate a shock environment that could have a deleterious
effect on the spacecraft hardware. The interpretation and simulation
of these shocks in ground tests are necessary to insure equipment in-
tegrity during this phase.

A detailed analysis of certain pyrotechnic shocks is presented. The
data used are from the Ranger Block III and Mariner Mars test pro-
grams. Shock spectra form the basis of correlation between similar
shocks of various spacecraft and assembly testing. Comparisons of
shock data using statistical methods are also included. Since a wealth
of shock data was available, the statistical analysis is significant. The
results indicate the necessity for a system level pyrotechnic test pro-
gram if the environment is to be properly simulated.

INTRODUCTION

Explosive separation devices are charac-
terized by relatively short-duration shocks of
high magnitude. The separation events near
the payload area of a vehicle may include
shroud separation, electrical separation, and
mechanical separation. Also, pyrotechnic
devices are used to deploy such items as solar
panels or scientific instruments. The pyro-
technics generate shock pulses that could have
a deleterious effect on the spacecraft operability.

This paper does not consider transients
associated with booster staging or engine start-
shutdown or those associated with lunar or
planetary impact. Only shock transients re-
lated to pyrotechnics near the payload area are
discussed.

Most of the data used come from the Ranger
test program. The rest is drawn from the
Mariner Mars test program. Both programs
were conducted at the Jet Propulsion Labora-
tory, Pasadena, California from 1963 to 1965.

Ranger was an unmanned lunar probe 9.25
ft high (launch configuration) and weighing

approximately 804 lb. Mariner IV flew by
Mars July 14, 1965, on a scientific and photo-
graphic mission. Its weight was approxi-
mately 575 lb.

The launch vehicle for Ranger was the
Atlas/Agena B, and for Mariner was the Atlas/
Agena D.

Figures 1, 2, and 3 show three typical pin-
pullers used for the Ranger program. The
electrical separation pinpuller (Fig. 1) drives
pins against the brackets. The spin collar
releases the connector, and a spring pulls the
lower connector away from the spacecraft.
The mechanical separation pinpuller (Fig. 2)
retracts a pin, and spring loading separates the
spacecraft from the launch vehicle. The shroud
separation pinpullers operate in an identical
manner. The solar panel pinpullers (Fig. 3)
release the panels after launch by retracting a
pin. The panels are slowly extended by an
actuator. Figure 4 shows the location of these
pinpullers. Similar pinpullers were utilized on
the Mariner for solar panel and scan platform
deployment, but V bands affected both shroud
and mechanical separation.
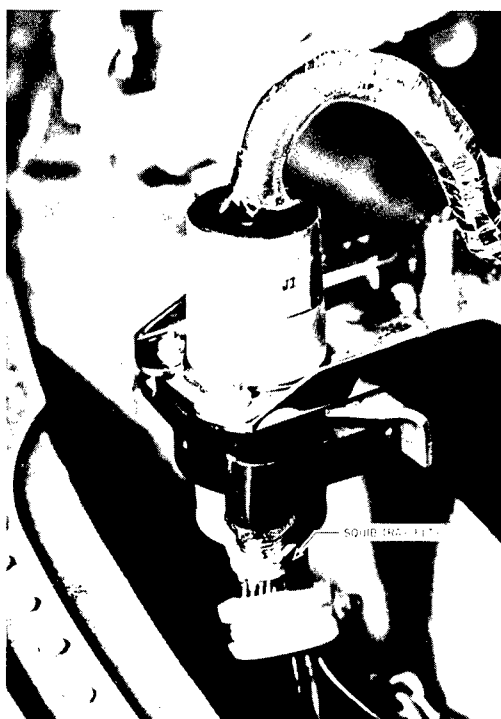
Fig. 1. Ranger electrical
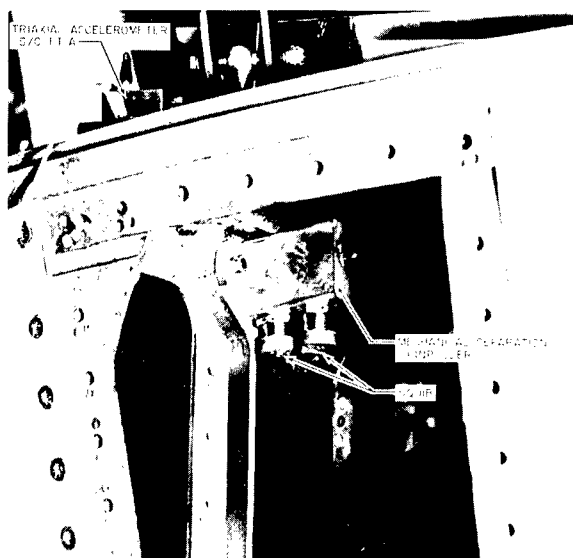separation pyrotechnic

Fig. 2. Ranger mechanical
separation pinpuller

The number of pinpullers used on Ranger
and Mariner is given in Table 1. For reliability,
two squibs are mounted in the pinpullers, either
one of which could cause actuation. Also, for
reliability, separate circuitry for firing of each
squib was used.

TESTING METHODS

Hardware integrity and operability in the
environment were demonstrated on the assem-
bly level and system level prior to the commit-
ment to flight.

The assembly shock test requirement for
the type approval (TA) assembly consisted of a
terminal-peak sawtooth 0.5 to 1.5 ms in dura-
tion and 100 or 200 g in magnitude, depending
on installation. The test was repeated five
times in each orthogonal axis for a total of 15
shocks.

The shock test requirements were based
on experience obtained from earlier programs.
Since the present-day shock machines cannot
excite the high frequencies associated with
pyrotechnic devices without excessive test
response at the low frequencies, a tradeoff in
test duration had to be made. In other words,
the shock from a shock machine does not simu-
late the shock from the pyrotechnic. This
point is considered in detail later.

The shock machine shown in Fig. 5 was the
one used for the majority of the Ranger-Mariner
testing.

Ranger had no failures reported during TA
testing. Mariner had three failures in 116 tests,
all latching-relay malfunctions.

To demonstrate the proper operation of the
spacecraft in the environments, especially the
high-frequency transients not covered by the
TA tests, a series of tests using flight-type
pyrotechnics was performed at the spacecraft
level.

For system level tests, the Ranger proof
test model (PTM) was mounted on the adapter
and the forward equipment rack of the launch
vehicle. The test configuration for Ranger is
shown in Fig. 4. The pinpullers actuated were
electrical separation, mechanical separation,
and solar panel. These were chosen because:
(a) each of these transmit loading through dif-
ferent paths, and (b) the magnitude of the tran-
sients associated with these pinpullers is sig-
nificant. The shroud-separation pinpullers
were not used because the loading path and
transient magnitude are similar to the me-
chanical separation pinpullers, i.e., are located
in close proximity. The most severe shocks
occurred during mechanical separation.

A typical Mariner Mars test configuration
is shown in Fig. 6. The shock test consisted
of the actual firing of the pyrotechnic devices
on board the spacecraft. The following tests
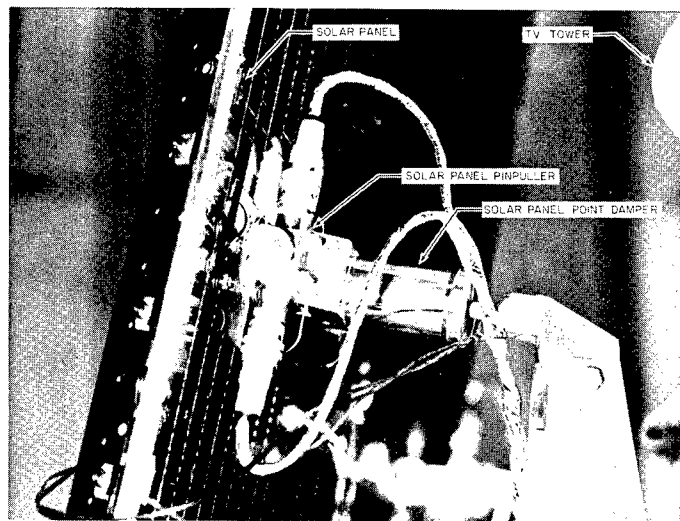
Fig. 3. Ranger solar panel pinpuller
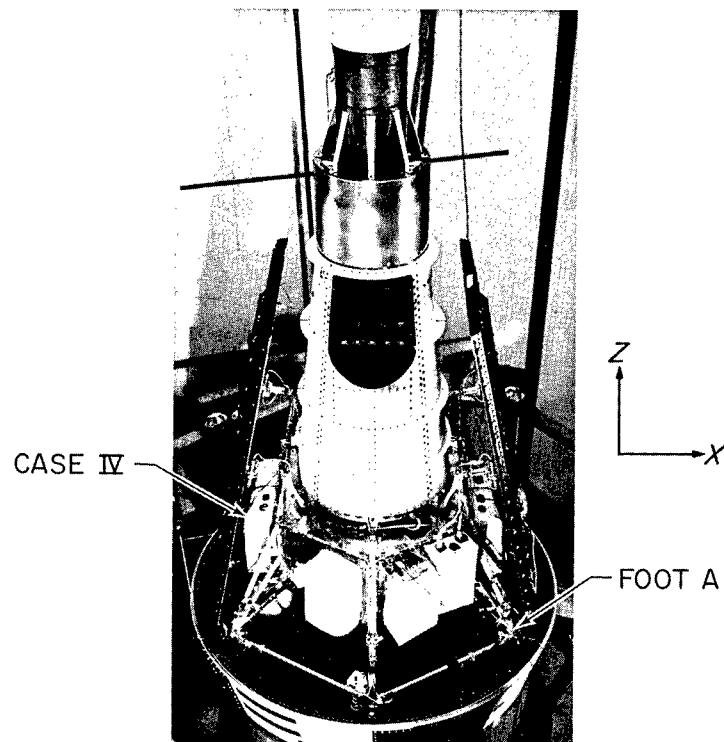
Fig. 4. Ranger pyrotechnic test configuration

TABLE 1
Number of Pinpullers for Ranger-Mariner Mars

Pyrotechnic Events	Ranger	Mariner
Shroud separation	3	V-band
Electrical separation	2	(Not pyrotechnically separated)
Mechanical separation	3	V-band
Solar panel deploy	4	8
Scan platform	---	1
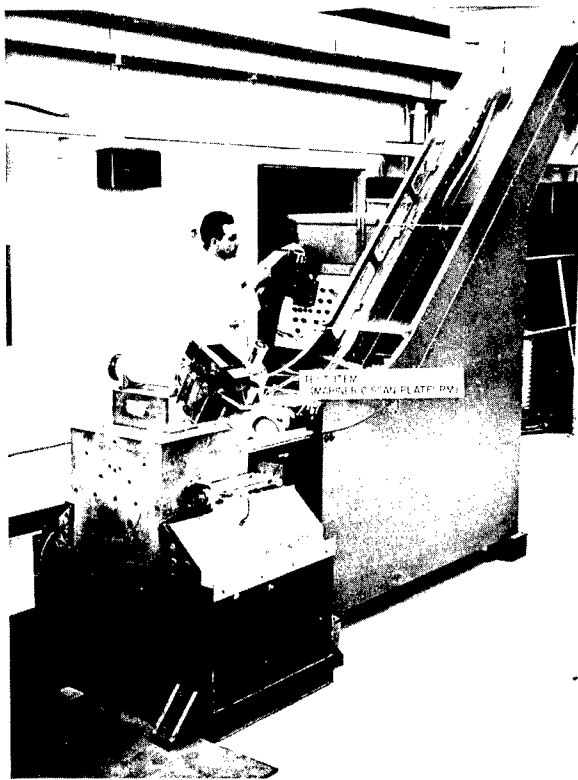
Fig. 5. Shock machine for assembly level testing
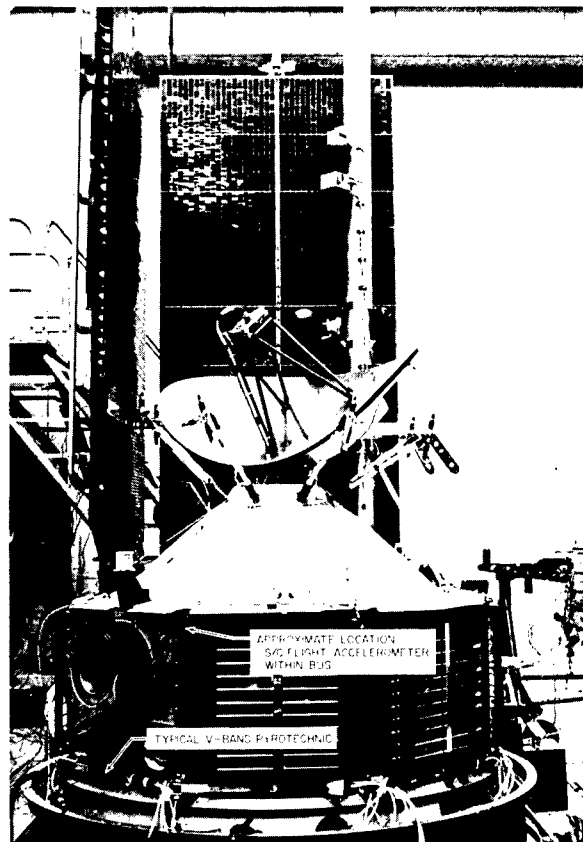
Fig. 6. Mariner Mars test configuration (two solar panels removed)

were performed: (a) shroud V-band release, (b) spacecraft V-band release, (c) solar panel release, and (d) science platform release. The most severe shocks occurred during the spacecraft V-band release. Low-frequency ring-out due to the release of the stored energy in the deformed structure was detected.

For the Ranger PTM, the electrical separation was performed twice, the mechanical separation five times, and solar panel deployment six times. Transient simulation was the primary objective during the electrical separation and mechanical separation.

312

A special test, in which the pyrotechnically actuated midcourse motor valves were fired, demonstrated that there were not significant responses to the other parts of the spacecraft.

Each Ranger spacecraft had the solar panel pinpullers fired at least once. The primary purpose was to verify circuitry with live squibs installed. The transient simulation was a secondary consideration.

Environmental data were measured on all these tests. The frequency response of typical accelerometers has been checked. The results are given in Table 2. A description of the special test performed to verify the response of accelerometers used in the test programs to transient excitation is given in the appendix.

For this reason, the decision was made to test the accelerometer limitations of the data analyzed in this paper. In general, the results of the accelerometer test, included in Table 2, have demonstrated the adequacy of the instrumentation.

The test is described in detail in the appendix. It consisted principally of analyzing the data from a reference standard accelerometer mounted back to back with the accelerometer to be calibrated. The same analysis parameters were utilized with this test as with the spacecraft environmental test analyses, to insure the same type of comparison.

Other equipment in the data channels can be considered flat to 10 kc. These include

TABLE 2
Typical Accelerometer Characteristics

| Accelerometer | Manufacturer's Specifications | | | Frequency Response from Special Transient Test[c] | Ranger Spacecraft Location |
	Frequency Response[a]	Accel. Mounted Resonance Frequency[b] (kc)	Amplitude Linearity		
Endevco 2225	±10%, 2 cps-15 kc	80	±2%, 0-20,000 g	+0% -8% 200 cps-10 kc	Case IV[d]
Columbia 514[e]	±5%, 2 cps-5 kc	30	±1%	+6% -0% 200 cps-8kc / +46% -0% 8 kc-10 kc	Foot A
Endevco 2213	±5%, 2 cps-7 kc	35	±2%, 0-500 g	+5% -1% 100 cps-10 kc	Case I, Leg A
Endevco 2217	±5%, 2 cps-6 kc	30	±2%, 0-300 g	+0% -3% 200 cps-10 kc	Flight position (Ranger and Mariner)
Endevco 2226	±5%, 2 cps-5 kc	25	±2%, 0-1000 g	+3% -2% 200 cps-10 kc	Solar panel tip

[a] With 1000-MΩ load.
[b] Term taken from vendor literature.
[c] Data evaluated to 10 kc; see appendix for details.
[d] Also type approval assembly.
[e] Three-hole, data from three-point mounting Columbia 514tx (Z axis).

INSTRUMENTATION

It is a foregone conclusion that results from any dynamic test are only as reliable as the instrumentation utilized to obtain the data.

the tape recorders and amplifiers in the channels.

Endevco Model 2217 accelerometers were used in the actual flight measurements of both

Ranger and Mariner Mars. The remainder of the flight telemetry consisted of a standard Inter-Range Instrumentation Group (IRIG) package mounted in the Agena second-stage vehicle. Present analysis techniques can limit the frequency response of such a system to the standard bandwidth frequency for the particular channel involved. However, as a result of the end-to-end calibration performed on the Ranger 8 and 9 systems, it seems reasonable to extend the cutoff frequency of the channels to twice the nominal IRIG values without introducing a significant decrease in the signal-to-noise ratio.

The extended frequency range does limit the frequency response to 2000 cps. This is a small fraction of the possible response of test instrumentation.

To compare flight and test data at the present time, the test data must be modified by low-pass filtering at approximately twice the IRIG cutoff frequency. (Extending the IRIG limits using an inverse frequency response analysis may be possible in the future.) In Fig. 9a, the Mariner Mars PTM data have been low-passed at 2000 cps (utilizing a digital filter) and are thus comparable with the Channel 17 flight data at twice IRIG. Both of these measurements were taken at the same location on the internal section of Leg B (Fig. 7).
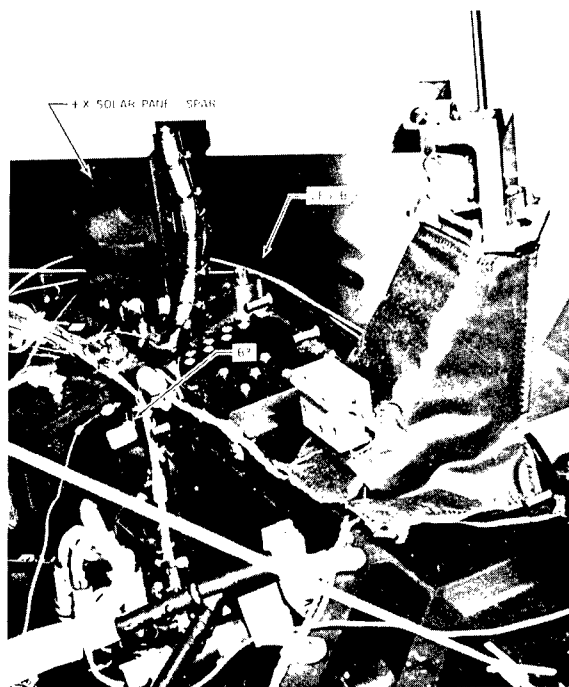
Fig. 7. Mariner Mars flight location B-3

The most significant flight pyrotechnic event seems to be the mechanical separation of the spacecraft. This event was lost on both Ranger and Mariner due to a channel switch-over to another monitoring instrument just before the separation took place. This would have been useful in defining the maximum pyrotechnic shock environment.

ANALYSIS TECHNIQUES

Shock Spectrum Program

Pyrotechnic transients are, in general, so highly unstationary that no statistical methods of analysis are applicable. Also, an attempt to analyze these types of shock in the time domain would be of little value. Interpretation of these data in the frequency domain requires the use of a type of analysis such as shock spectra.

A digital program (JPL 5352) has been used to compute the spectra included in this paper.

The maximum response of a tuned simple resonator, excited by the transient, defines a single ordinate at one tuned frequency (abscissa) of a shock spectrum. By varying the tuned frequency of the resonator and plotting the peak response for each frequency, the shock spectrum is generated. The resulting plot is a specific type of frequency content of the transient pulse input. The units of the ordinate are peak g's response, while the abscissa is plotted as tuned frequency in cycles per second. Another parameter associated with each spectrum is the zeta or percent of critical damping of the resonator which has the effect of smoothing the spectrum.

The IBM 7094 program computes the shock spectrum by solving the differential equation of motion of a simple resonator due to the applied transient and detecting the peak response. Eulerian numerical integration techniques are utilized in the solution of the equation. A Stromberg Carlson 4020 plotter produces the output, including the observed transient and the shock spectra associated with that transient. Various zeta values are usually used with each analysis, resulting in more than one shock spectrum for each transient. Included here are the spectra for 2.5 percent damping only. Typical data analysis output is shown in Fig. 8.
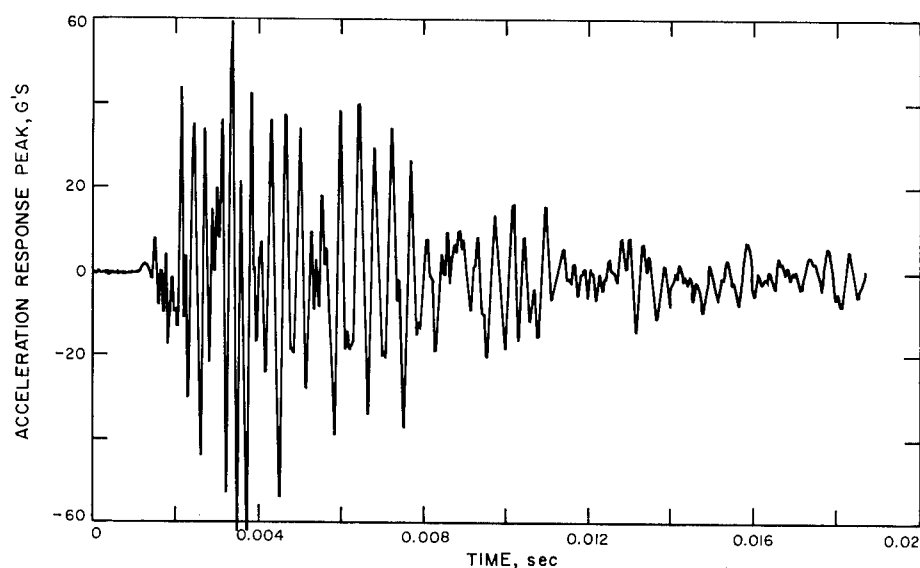
(a) Transient response

ZETA=0.025
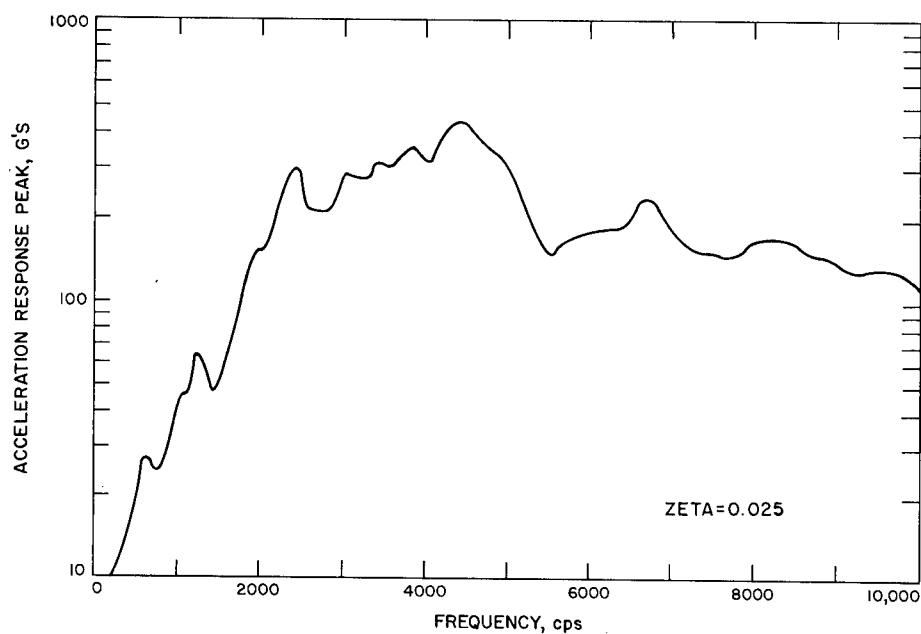
(b) Shock spectrum

Fig. 8. Typical data analysis output -- Ranger
mechanical separation test at flight location

SPECTRA MANIPULATION PROGRAM

An advantage of digital processing is the convenient format of the output which lends itself to further comparison and compression of the data. The shock spectrum program has an output of punched IBM cards of the frequency spectra. Supplementary calculations can be performed using these cards as input data to an IBM 7094 computer.

The JPL program 5574 can be utilized for comparison and manipulation of these data. There are seven manipulation operations available in the program as follows: mean, percentile

levels (normal), percentile levels (log-normal), maximum envelope, minimum envelope, product, and ratio. Output data of this program are either IBM cards or SC 4020 plots, or both. Typical examples of the output of this program are shown in Fig. 9.

TEST DATA

Several comparisons using flight data, spacecraft test data, and assembly test data have been made.

The shock spectra for the Ranger VIII and IX shroud separation event is compared to the ground tests of the mechanical separation on the PTM in Fig. 10. The data were recorded from the accelerometer near Case IV, shown in Fig. 11.

The filtering effect of the telemetry system is apparent in the flight curve. The mechanical separation data could be filtered using a digital filter and a comparison made to the flight data as they are. But this would limit the data to 2000-cps frequency range.

The Ranger bus response to the mechanical separation transient is given in Fig. 12. Several accelerometer locations in and on

electronic Case IV were used. The sensitive axis was the spacecraft X axis. The PTM and Ranger VI were the test vehicles for these data. Thirteen data samples from five separate runs were used to compute the maximum–minimum envelope and the 95 and 50 percentile levels (assuming a normal distribution). It is interesting to note that the maximum envelope and the 95 percentile level are comparable. Figure 12 shows the amount of dispersion in the response that equipment would see when exposed to a severe pyrotechnic environment. A necessity for repeated firings is indicated. That is, the statistical variations associated with pyrotechnic devices cause a variation in the response experienced by the test hardware. To increase the probability that a flight shock would be within the test limits, a series of repeated runs should be performed. Assuming a t distribution and small sample size, four or five runs would give significant results. Another possible method would be to increase the charge of the pyrotechnic, i.e., use a larger squib, for the environmental tests using live pyrotechnics.

In Fig. 13, the maximum envelope described above is compared to the maximum envelope from the TA shock test of the Case IV assembly which utilized the shock machine in Fig. 5. Three accelerometers (Endevco 2225) at various locations in the assembly were used
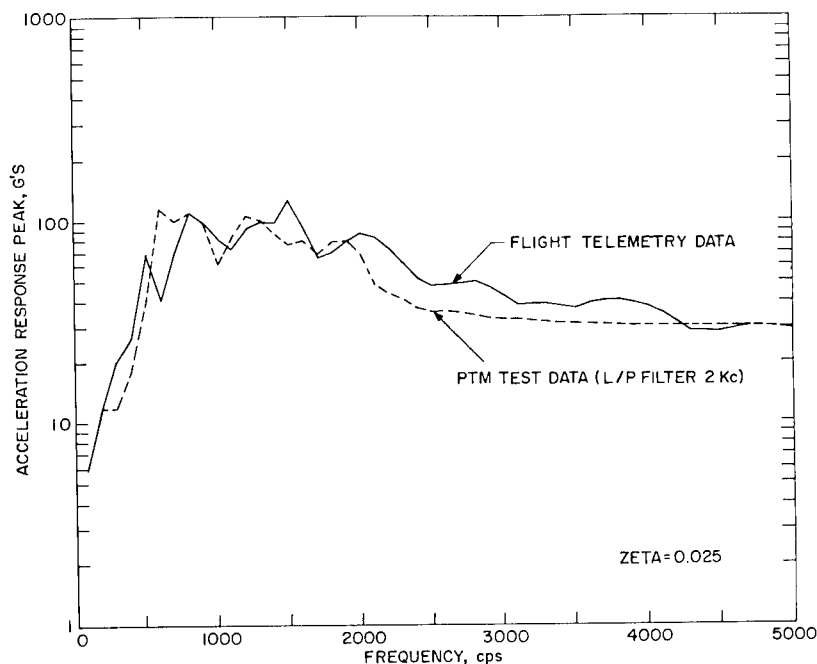
(a) Maximum envelopes

Fig. 9. Typical data manipulation examples--shock spectra of Mariner Mars shroud separation event

316
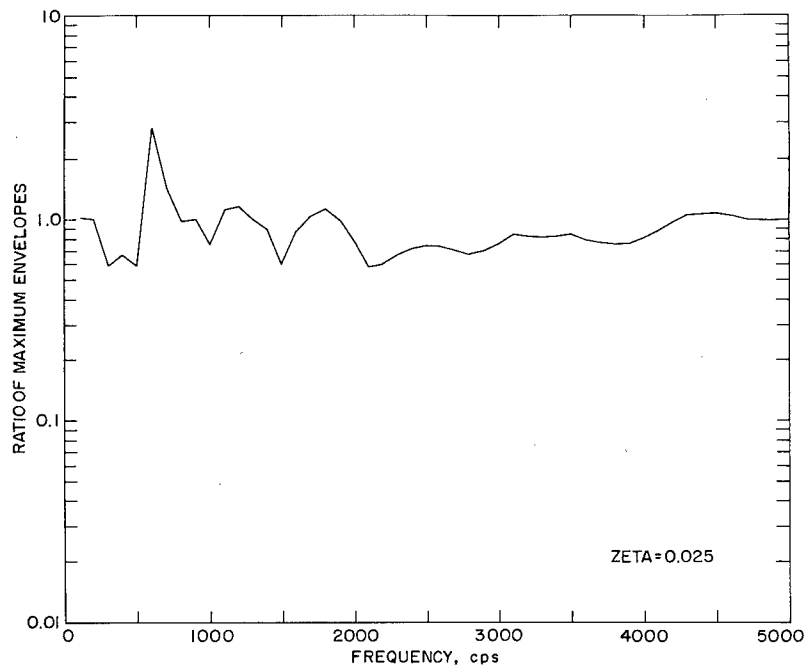
(b) Ratio of maximum envelopes, test data/flight data

Fig. 9 (Continued). Typical data manipulation examples -- shock
spectra of Mariner Mars shroud separation event
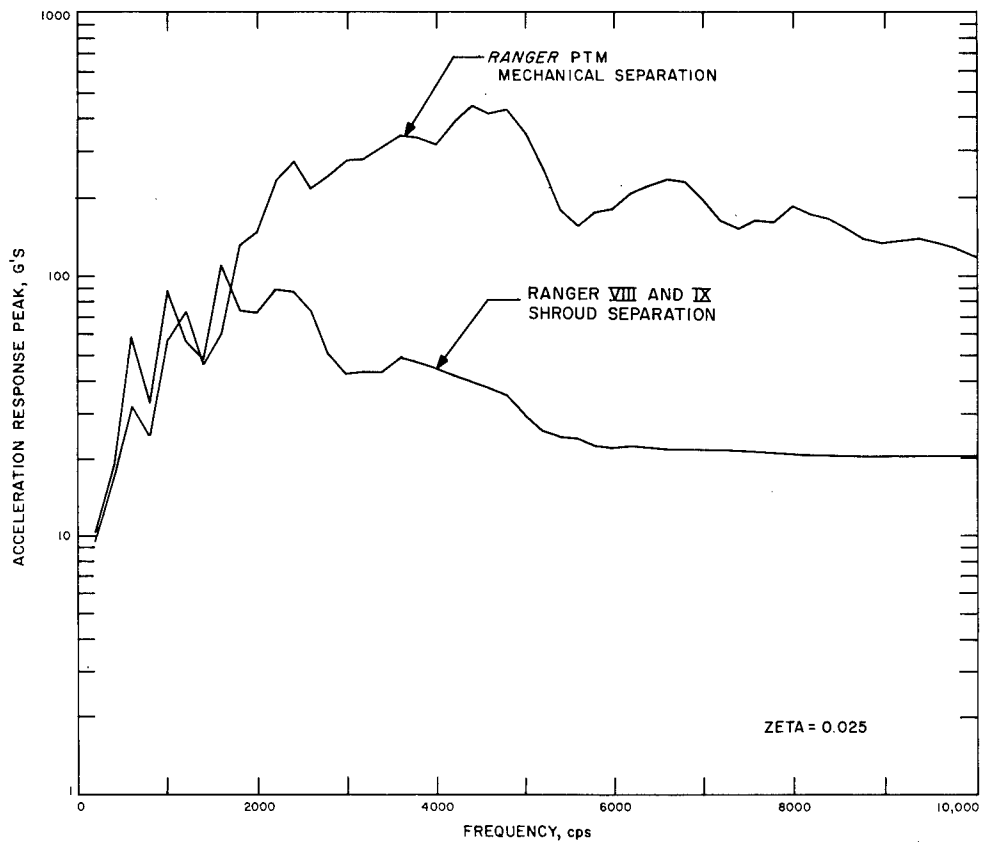
Fig. 10. Maximum envelopes of shock spectra, Ranger flight
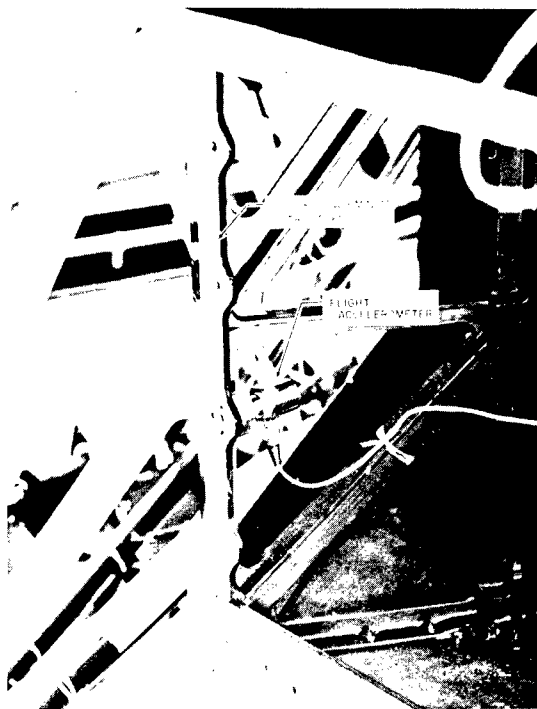shroud separation and PTM mechanical separation test

317

Fig. 11. Flight location of accelerometer on Ranger VIII, IX spacecraft bus (Case IV) removed

as inputs. The test configuration and accelerometer locations are shown in Fig. 14. The transducers are sensitive in the spacecraft X axis. All data from the five TA runs in the X axis were used in the analyses. Figure 13 shows that TA shock does not adequately cover the mechanical separation shock at the higher frequencies. The TA shock does, however, cover the solar panel deployment shocks at the high frequencies, as shown in Fig. 15.

The idealized TA shock spectrum would be one bracketing the shock spectra of the mechanical separation event. However, this is not within the state of the art of present-day shock machines.

The responses to different events (electrical separation, mechanical separation, and solar panel deployment) as measured at the interior center web of Case IV on the Ranger PTM are shown in Fig. 16. Both 5 and 95 percentile levels are given. The data show that the mechanical separation produces the highest response. The same general trend can be noted in all the spectra; i.e., the highest response is at the higher frequencies, even though the different pyrotechnics are located at several locations on the spacecraft. The results would indicate

that for ground testing of spacecraft systems, the minimal requirement would be the mechanical separation test. The solar panel deployment has considerable dispersion at the high frequencies, resulting in a low confidence level in this portion of the spectra.

Figure 17 compares the shock spectra of a mechanical separation as seen at different locations on the spacecraft. The spacecraft Foot A response is very high because it is located directly above a pinpuller, as shown in Fig. 2. The case I, Leg A location is directly above the Foot location. The solar panel location shock spectrum is different from other shock spectra, as could be anticipated because of the structural differences. These curves show that responses at different locations during the same test are widely scattered. This well-known result is emphasized to demonstrate the necessity for pyrotechnic tests at the system level. It would be very difficult to design an assembly level test that matches all of the spectra or even covers them adequately. If a test were specified to bracket all the responses adequately, then based on present shock machine capability, severe damage would occur due to the low-frequency content characteristic of shock test machines.

318
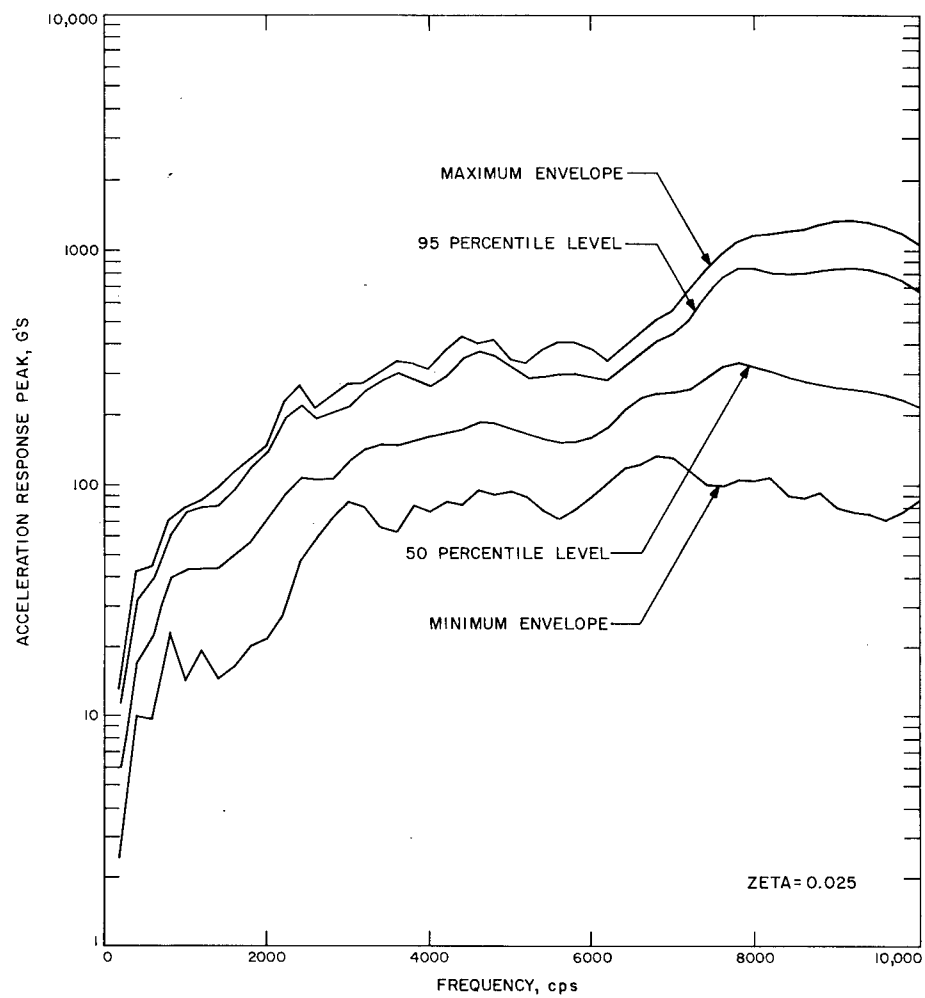
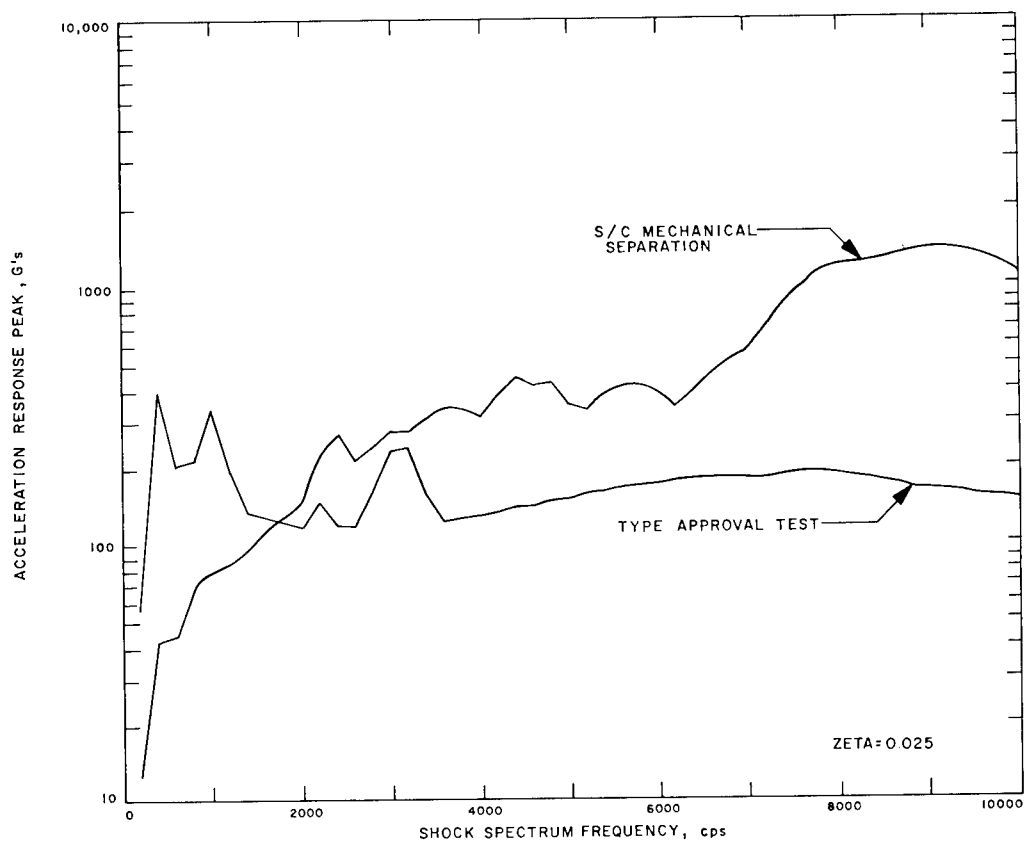Fig. 12. Ranger Case IV response to mechanical separation

319

Fig. 13. Maximum envelopes of shock spectra, Ranger Case IV TA
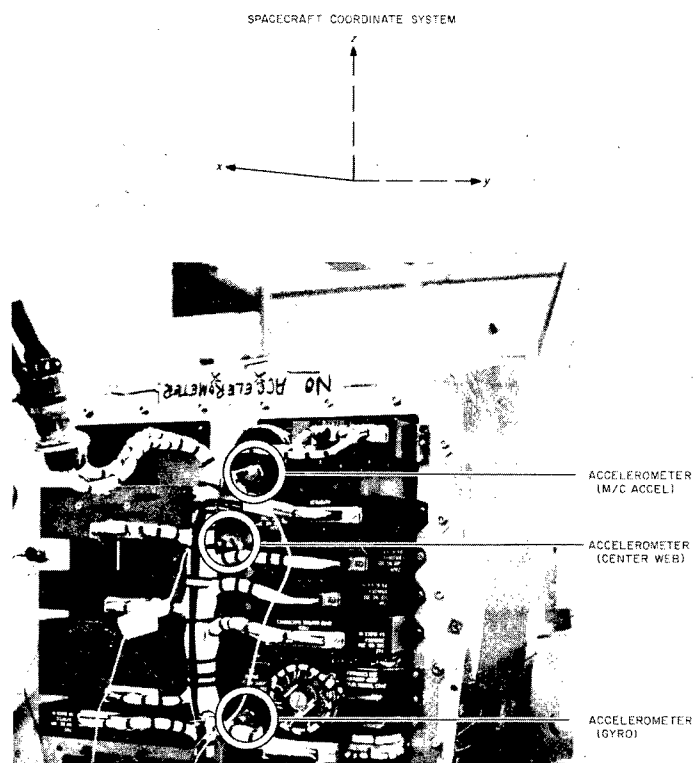assembly shock and spacecraft mechanical separation test

Fig. 14. Ranger TA Case IV shock test
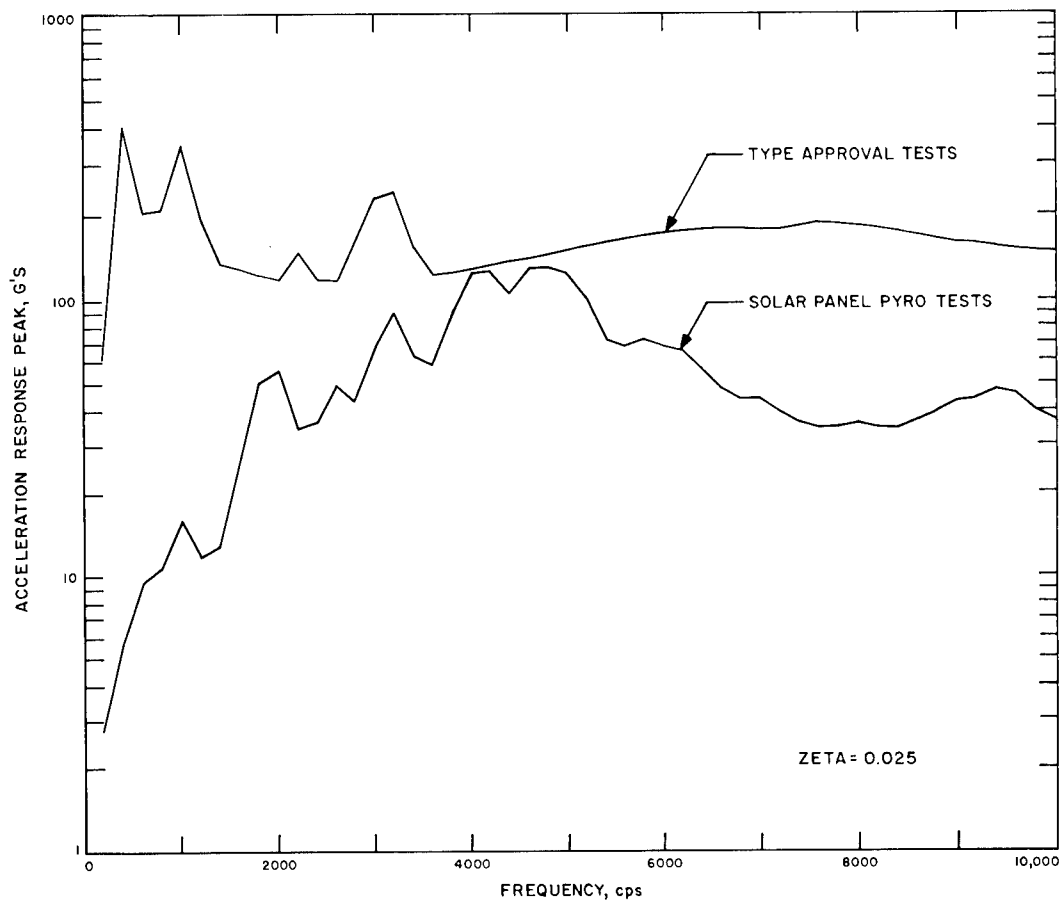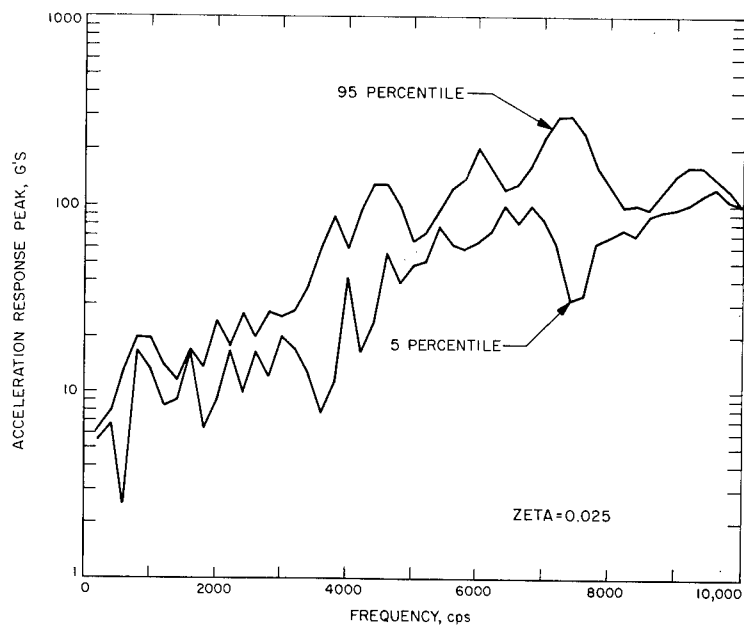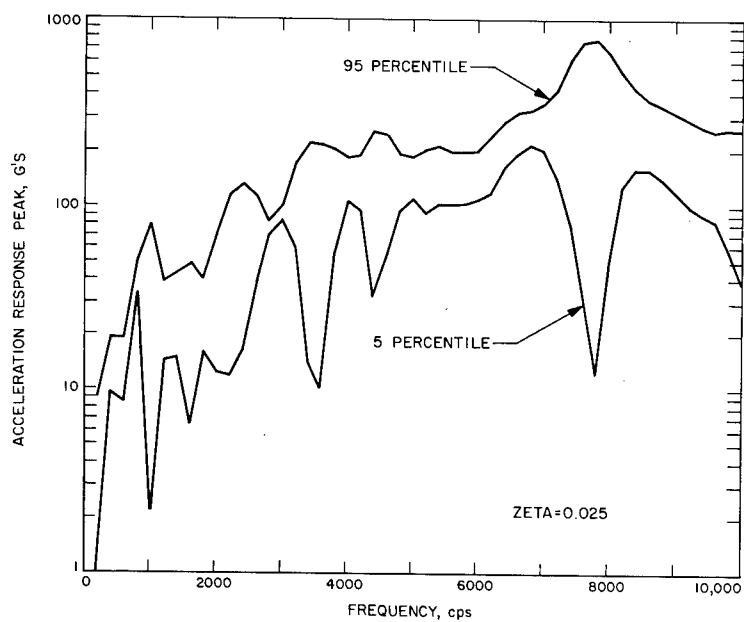configuration, spacecraft X axis

Fig. 15. Maximum envelopes of shock spectra, Ranger Case IV TA
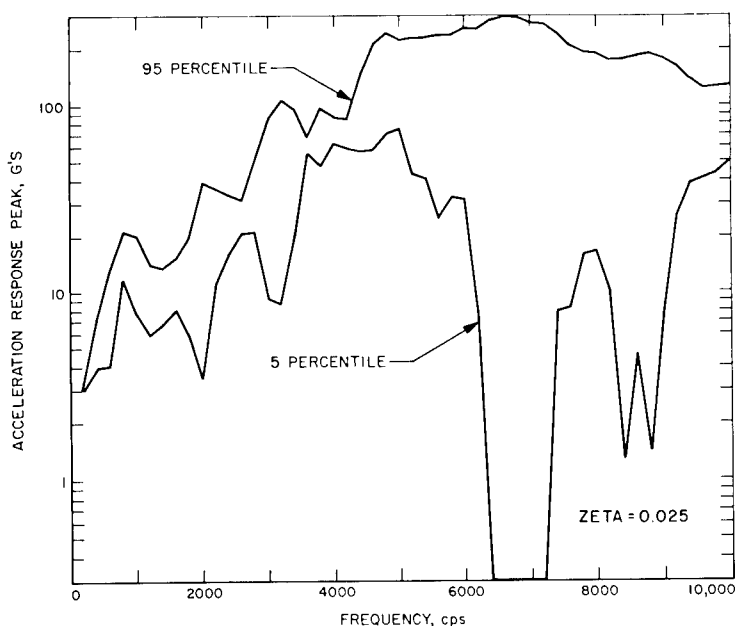assembly shock and spacecraft solar panel development

(a) Electrical separation

(b) Mechanical separation

Fig. 16. Shock spectra, Ranger
Case IV center web

323

(c) Solar panel deployment

Fig. 16 (Continued). Shock spectra, Ranger Case IV
center web

The reproducibility of the TA shock is demonstrated in Fig. 18. Five consecutive shocks measured at the gyroscope location and at the midcourse guidance accelerometer location, shown in Fig. 14, were used in the plot. The envelope shown is the percentile envelope using a normal distribution and computing 95 and 5 percentile levels. These data show that the TA shock produced by the shock machine is very reproducible.

The maximum-minimum envelopes of the solar panel shock at several locations on the Ranger spacecraft show that the responses are dispersed (Fig. 19). This is typical of pyrotechnic data. Seven separate tests were used to compute the envelope indicated at each location. Consequently, the results are statistically significant and give an indication of the amount of variation that could be expected from several repetitions of the same test on different vehicles. The vehicles used were Rangers PTM, VI, VII, VIII, and IX.

CONCLUSIONS

Extensive pyrotechnic shock measurements have been obtained from the ground testing of the Ranger and Mariner spacecraft using the actual explosive devices in their flight configuration.

The analysis of the data using shock spectra and statistical techniques has shown that:

1. The mechanical separation shock is generally the most severe pyrotechnic shock experienced by the spacecraft. There is reason to believe, based on flight data from vehicle staging and shroud separation, that the shroud separation pyrotechnic is more severe in amplitude at the spacecraft flight location than the staging transients. The shock spectra from flight data, which are meaningful up to 2 kc, tend to support this. The shroud separation (on Ranger) was comparable to the mechanical separation shock, although a direct comparison of flight data could not be made because of telemetry problems.

2. The flight telemetered data are inadequate for shock measurement because of the lack of high-frequency response and absence of measurements of spacecraft separation.

3. Although results from the shock machine were highly reproducible, the responses did not cover those from pyrotechnic tests. Repeated firings, four or five, of the pyrotechnics on at least PTM-type spacecraft will demonstrate the reliability of the spacecraft in the environment. Although no system level failures have occurred during either the Ranger or Mariner
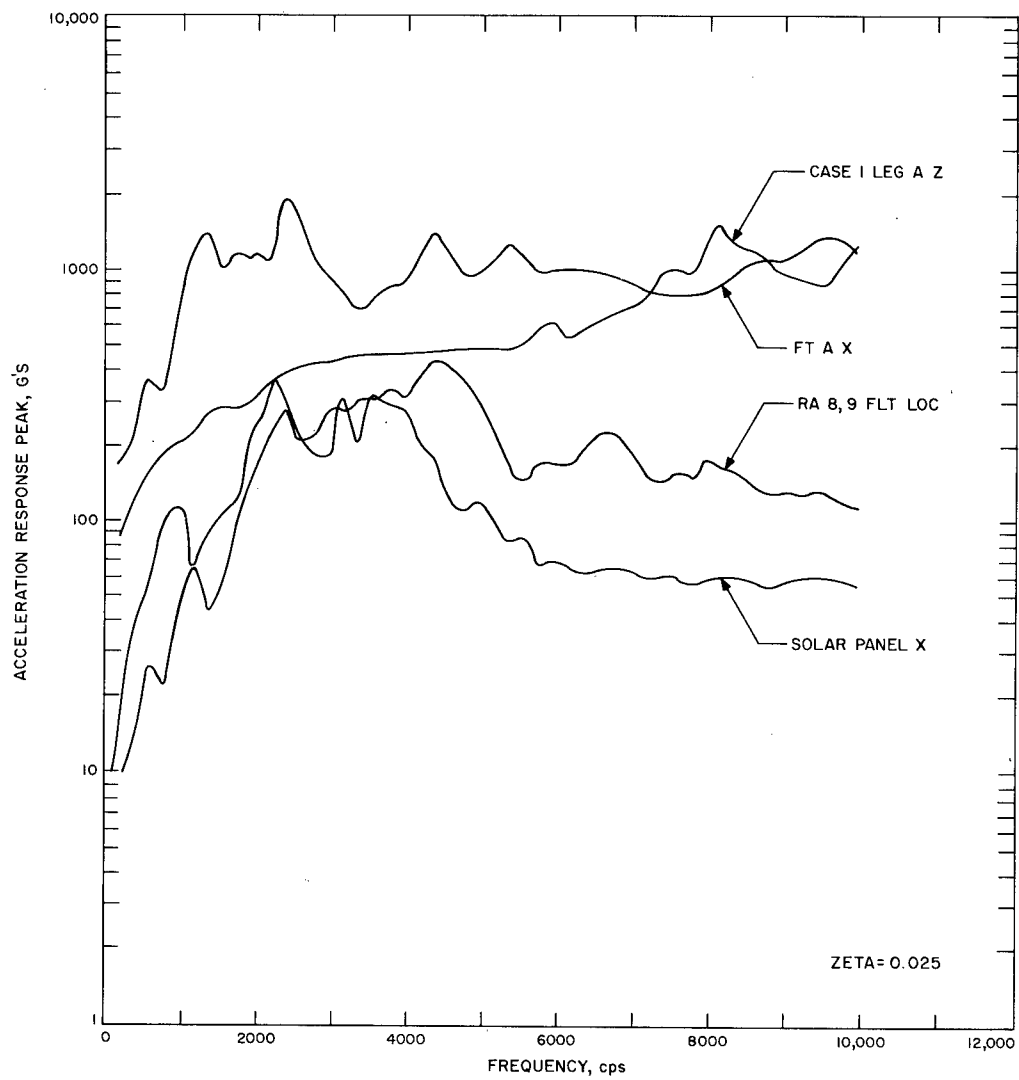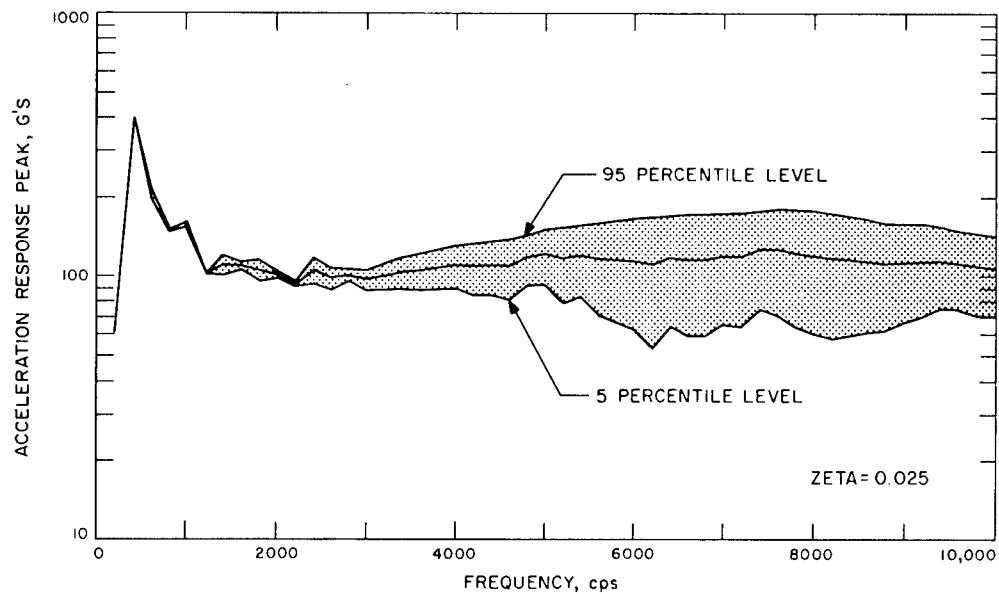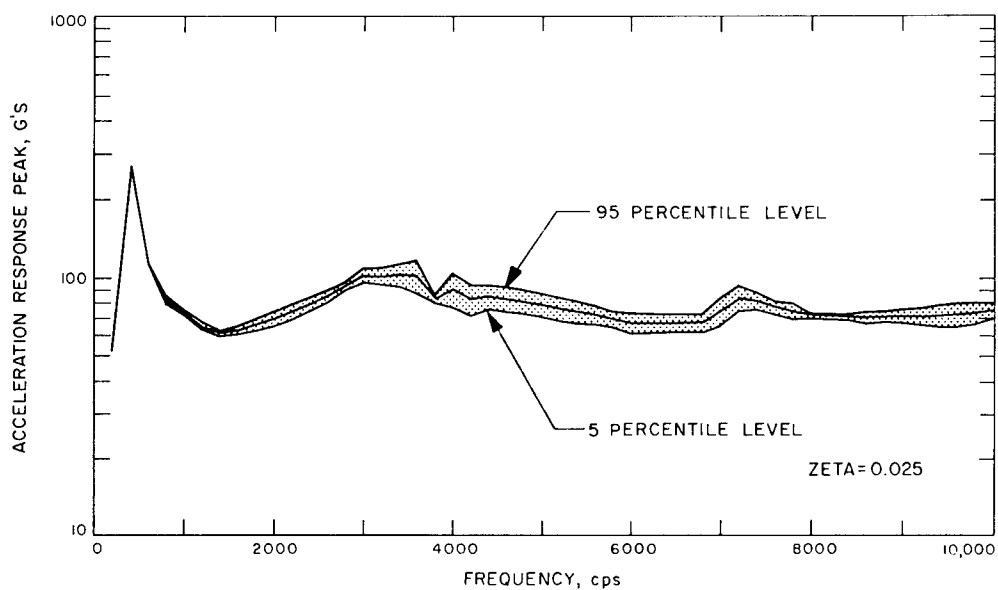
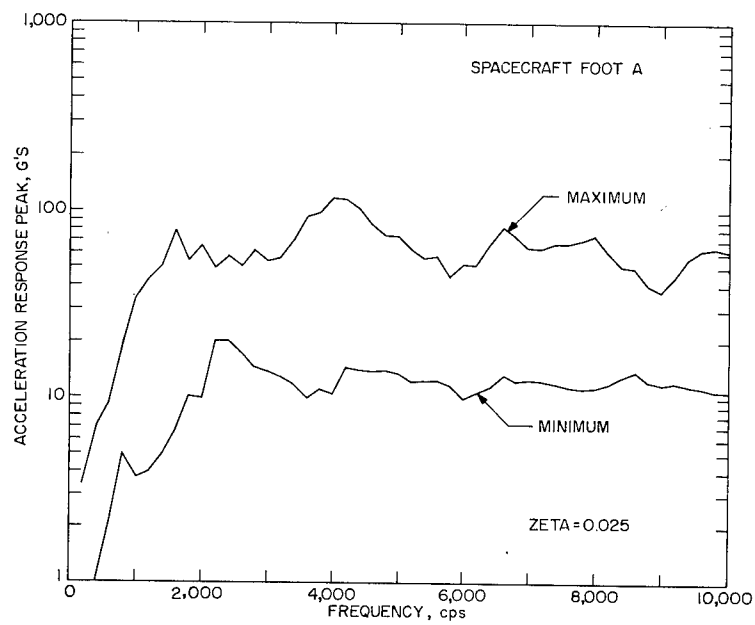Fig. 17. Shock spectra, Ranger mechanical separation test
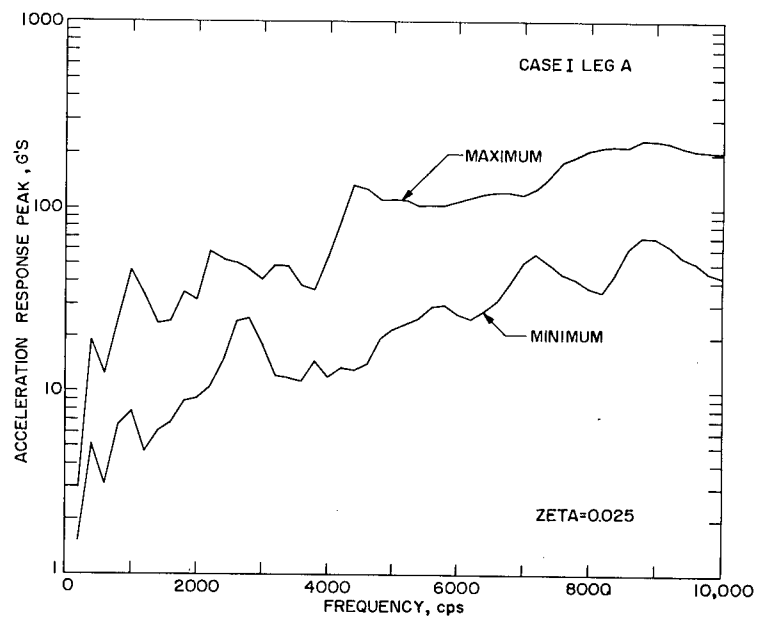
(a) Gyro

(b) Center web

Fig. 18. Percentile levels of shock spectra—Ranger Case IV TA
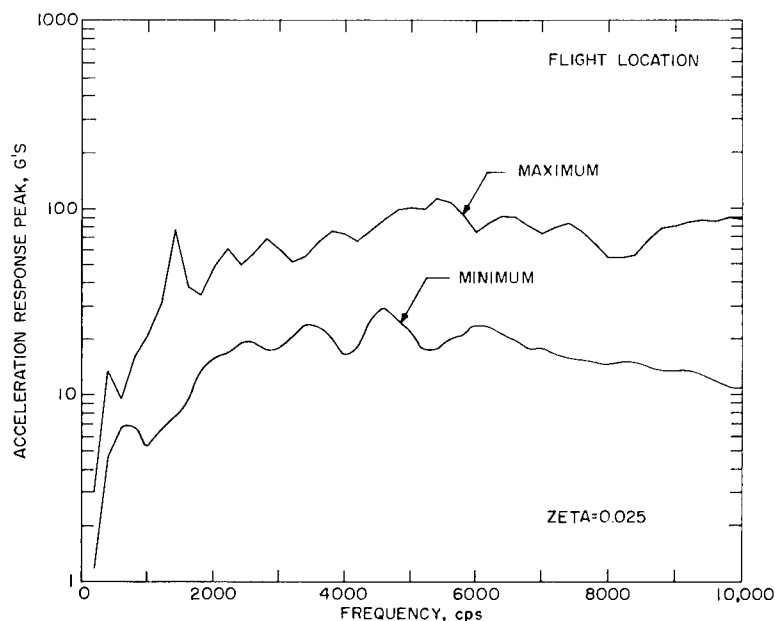assembly shock

(a) Spacecraft Foot A

(b) Case I, Leg A

Fig. 19. Maximum and minimum envelopes of shock
spectra -- Ranger solar panel deployment

(c) Flight location

Fig. 19 (Continued). Maximum and minimum envelopes
of shock spectra -- Ranger solar panel deployment

test programs, there is no indication that the environment should be ignored.

4. The responses at the same location for different pyrotechnic devices (as used on the Ranger) tend to give the same spectra shape. Specifically, the highest response always occurs at a high frequency.

Appendix

ACCELEROMETER CHARACTERISTICS UNDER TRANSIENT CONDITIONS

A special test was performed to determine the frequency response of typical accelerometers used for measurement of pyrotechnic shock data under a shock environment. The accelerometers are normally calibrated using a sinusoidal input. The response to transient excitation above 4 or 5 kc was not known.

A cylindrical projectile with a hemispherical end was dropped 12 in. onto a lead target 1/4 by 1 by 1 in. The test accelerometer was mounted on top of the projectiles. The standard accelerometer, a Kistler standard directly traceable to NBS, was mounted in the interior cavity of the mounting block. The accelerometers were mounted back to back in the mounting block with a single stud, except for the Columbia 514 and Endevco 2226. The Columbia 514 has a three-hole mount. The Endevco 2226 was attached with dental cement.

The projectile was suspended by an electromagnet. Data were recorded at 60 ips on an Ampex 1300 double-band tape recorder. The five accelerometers used are given in Table 2. Each accelerometer was tested five times.

The height of the drop was determined by the objective of achieving approximately a 500-g shock.

The data were digitized at 160,000 samples per second and played through the shock program. The frequency response up to 10 kc, as determined by comparing all accelerometers to the Kistler standard Model 808K2, is given in Table 2.

DISCUSSION

Mr. Clevenson (Langley Research Center): You emphasized that the zeta you use is 2-1/2 percent of critical damping. In a number of other papers where the shock spectrum has been described as using 5 percent critical damping, the Q's which they have presented are reduced. Have you noticed in your spacecraft that there is more response at 2-1/2 percent damping than at greater damping values?

Mr. Hoffman: The computer gives shock spectra computed for zero, 2-1/2 and 5 percent critical damping. We have chosen to use the 2-1/2 percent damping throughout this presentation for comparative reasons.

Mr. Clevenson: There was no other reason for choosing 2-1/2 percent?

Mr. Hoffman: No, sir.

Mr. Harvey (Goodyear Aerospace Corp.): What was the information on the Mariner shroud separation? Did this use "FLSC," and was it a longitudinal or a circumferential separation?

Mr. Hoffman: This uses a V-band which is attached all the way around.

Mr. Harvey: I am familiar with the bottom portion of it. Was this also separated longitudinally?

Mr. Hoffman: Yes, it is over the nose.

Mr. Condos (Martin Co.): Did you mention the pulse shape that you were trying to get on the shock machine?

Mr. Hoffman: I did not mention that. It is a terminal-peak sawtooth.

Mr. Condos: Why did you not try for a half-sine pulse? It looked as if it would match your spectrum much better.

Mr. Hoffman: In reality, there is no such thing as a terminal-peak sawtooth pulse, as I am sure you are aware. The data actually looks more like a half-sine than a terminal-peak sawtooth pulse.

Mr. Condos: We have been able to match spectra of that shape with an approximate half-sine pulse on the order of 0.2 ms.

Mr. Hoffman: Up to 10 kc?

Mr. Condos: At least to 4 or 5 kc.

Mr. Hoffman: As in most of these pyrotechnic data, we are peaking out as indicated between 5 and 8 kc.

Mr. Condos: We found that there was an advantage in running laboratory tests, as opposed to complete systems tests, on vehicles a little bigger than this.

*　　*　　*

SHAPED CHARGE SHOCK ENVIRONMENT

FOR CENTAUR VEHICLE COMPONENTS

E. C. Noble, Jr. and R. L. Batten
General Dynamics Convair
San Diego, California

This paper describes the acquisition and analysis of high-frequency shock data recently obtained during three ground tests of a full-scale Centaur vehicle. These shocks were usually measured at the equipment mounts. The mounting structure shocks were produced by a linear shaped charge separation system (approximately 127 ft in length) that cuts the structural joints of the external insulation panels. A comparison is made between a ground test shock measurement and a similar flight measurement. Also, the shaped charge acoustic environment in the Centaur forward equipment area is evaluated. Shock spectra of the shock measurements several inches to 219 in. away from the shaped charge severed joints are presented and analyzed. An experience with hardware is discussed that consisted of measurement and analysis of the shock environment, as well as laboratory shock tests that aided in verifying the adequacy of the equipment to the expected shock.

INTRODUCTION

The upper stage Centaur vehicle has a high specific impulse (400 sec). The vehicle uses a cryogenic propellant of liquid hydrogen (LH_2) and liquid oxygen (LO_2). An external insulation panel system covers the Centaur propellant tanks. This insulation panel system is used to minimize propellant boil-off losses during the booster phase of flight, and the panels are jettisoned after the Centaur vehicle has left the Earth's atmosphere (Fig. 1). A shaped charge separation system is used to sever four structural joints that run longitudinally along the insulation panels. In addition, two circumferential seals at the forward and aft ends of the insulation panels are cut (Fig. 2). A high-frequency shock environment is produced throughout the entire vehicle when these structural joints and seals are cut. During the early development of the shaped charge separation system, shock measurements and analyses of the environment were done, and shock tests were made to verify that the electronic and mechanical equipment of the vehicle would operate satisfactorily.* The early development program included ground tests similar to the tests described in this paper.

Recently two ground separation tests of a full-scale insulation panel separation system (referred to as Run I and Run II) were completed to qualify the present design of the separation system and to obtain more high-frequency shock data. A third insulation panel separation test (Run III) was also conducted with small changes incorporated into the shaped charge separation system. The reduced shock data from these three runs are included herein. The data analysis is presently being used to improve the shock qualification test requirements.

The objectives of this paper are to:

1. Describe the three test configurations and instrumentation;

2. Present an analysis of the shock environment;

3. Discuss a shock response problem on a staging disconnect located 2 to 4 in. from the shaped charge cutting surface; and

4. Present a general discussion of shock test requirements.

TEST CONFIGURATION AND INSTRUMENTATION

The Centaur vehicle was mounted vertically on a short adapter section. The LH_2 tank

---
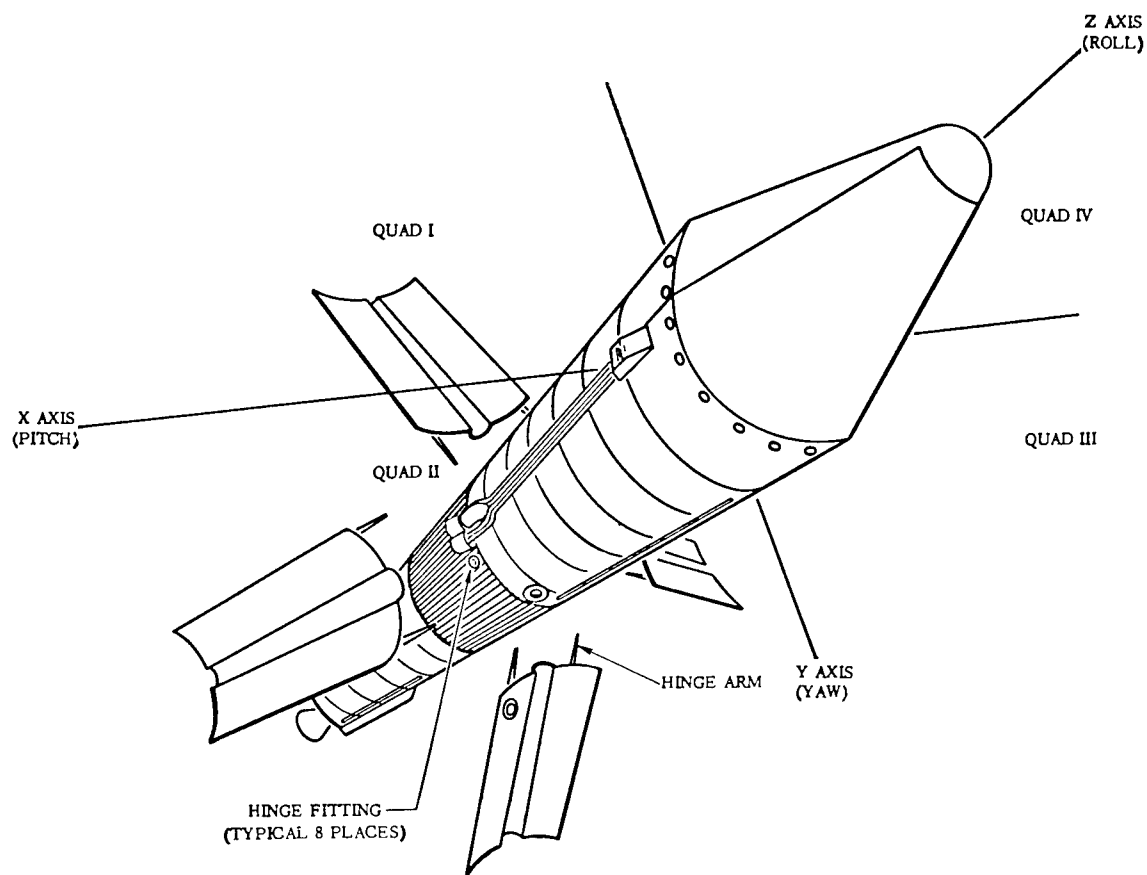
Fig. 1. Centaur jettisonable insulation system

ELECTRICALLY INITIATED
DUAL DETONATOR ASSEMBLY
(TYPICAL 4 PLACES)

TO ATLAS PROGRAMMER

FLEXIBLE LINEAR SHAPED CHARGE
(7 GR/FT-RDX)

END - PRIMERS (TYPICAL 16 PLACES)

Y AXIS (STATION 219.0)

MILD DETONATING FUSE
(2 GR/FT. PETN)-(TYPICAL)

FLEXIBLE LINEAR SHAPED
CHARGE (10 GR/FT-RDX)

Y AXIS (STATION 412.0)

TO ATLAS PROGRAMMER
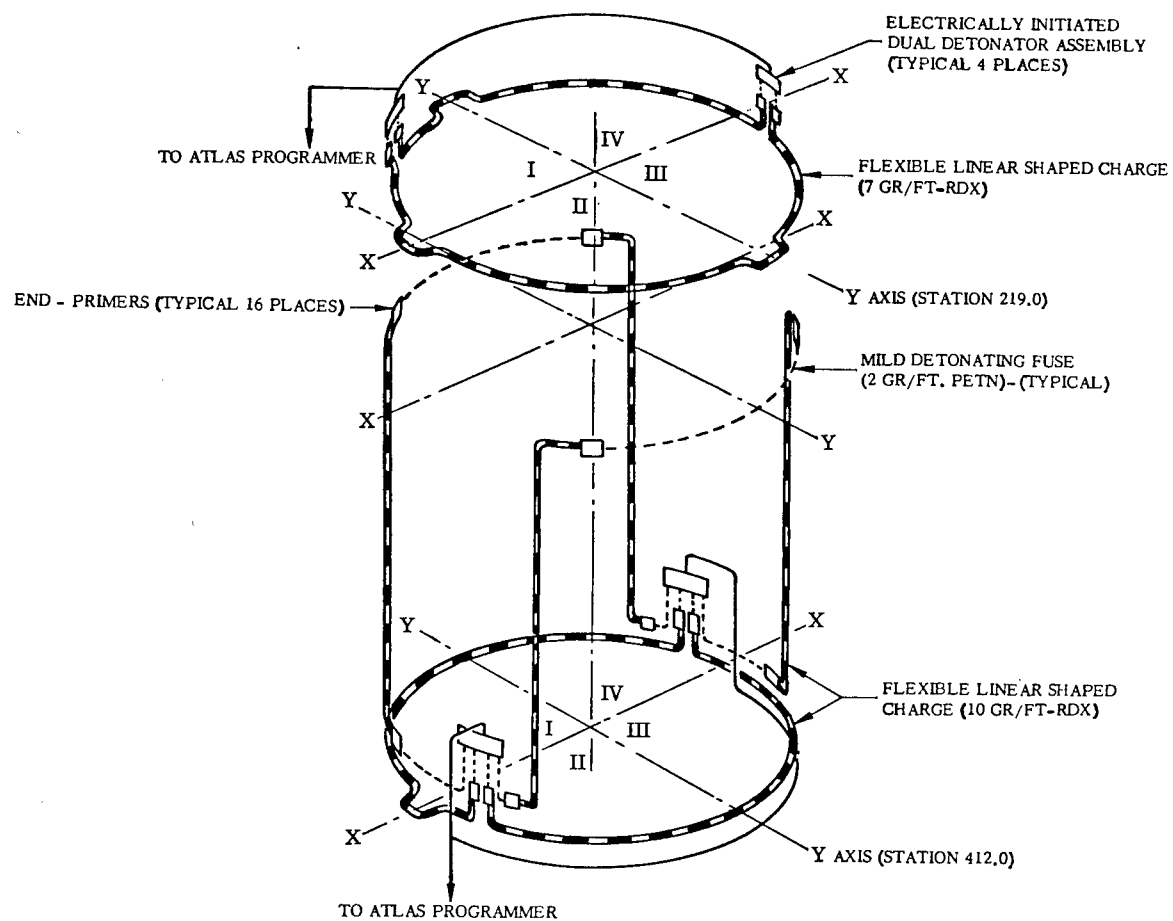
Fig. 2. Insulation panel shaped charge separation system
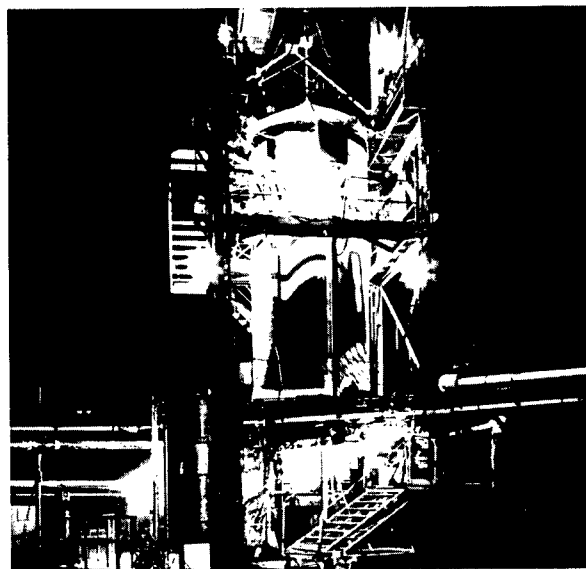
Fig. 3. Insulation panel test setup

was two-thirds full of LH_2 and the LO_2 tank was full of LN_2. Figure 3 shows an overall view of the test setup. The equipment in the forward bulkhead area was installed either by using actual test specimens or by using dummy packages. Approximately 14 accelerometers were located on the mounts of the equipment. A dynamic model of a payload and a payload adapter were also installed with two accelerometers on a payload latch. A payload shroud (nose fairing) simulation was installed and instrumented with two accelerometers. Several equipment packages in the propulsion area were installed and also instrumented with accelerometers. The insulation panels were installed and were severed by shaped charge during these tests. Table 1 lists the shock measurement number, location, sensitive axis, missile station, quadrant, and the type of accelerometer. Figure 4 shows the measurement locations on the upper and lower tier of the equipment shelf. An overall view of the missile is also shown. Several accelerometer installations are shown in Figs. 5 and 6. The instrumentation system block diagram is shown in Fig. 7.

Acoustic measurements were also made in the atmosphere to determine the shaped charge-produced acoustic environment near the forward equipment area. Several measurements were made to determine the acoustic response of several types of accelerometers in the same environment. The measured acoustic environment was less than 145 db (ref. 0.0002 microbar). The acoustic response of the Endevco accelerometers, Models 2225 and 2221, could

not be detected in the 10- to 20-g noise floor. It was concluded that the acoustic environment had little or no effect on most of the shock measurements.

SHOCK TEST DATA

Data Reduction

All shock data were recorded on FM tape with a system frequency response that was essentially flat to 10,000 cps. Four types of accelerometers were used (Table 1). Endevco Model 2252 accelerometer was used in cold temperature areas. After the initial test (Run I), it was found that an apparent dc shift occurred on these accelerometer outputs during high shock loads. The shock spectrum in the frequencies below 700 cps was found to reflect this effect; and this portion of the data is not presented.

A shock spectrum analyzer was designed and built to determine an approximate description of the shock response spectrum. Shock response spectrum analysis is generally recognized as an analytical tool that aids in determining the severity of an impulse or a transient load. The shock spectrum analyzer used is described by the block diagram of Figs. 8 and 9. For the data analyzed here, 10 equivalent resonators were used and the natural frequencies were selected between 50 and 5000 cps. Each electrical circuit (resonator) of the analyzer was considered to represent a second-order single degree of freedom system, in mechanical terms, a spring,

334

TABLE 1

Shock Measurements[a]

Measurement No.	Location	Sensitive Axis	Station	Quad.	Type of Endevco Accel.
1	Guidance computer base	X	172	III	2221D
2	Guidance computer base	Y	172	III	2221D
3	Guidance computer base	Z	172	III	2221D
7	Destruct package	Radial	400	I-IV	2252
8	Destruct package	Z	400		2252
9	Propellant utilization electronics package	Normal to blkhd	437	IV	2252 Run I & II 2225 Run III
10	Propellant utilization electronics package	Tangent to blkhd	437	IV	2252
11	Missile inverter base	Z	184	IV	2221D
12	Power changeover switch	Radial	184	IV	2242C Run II - 2215 Run III
13	Azusa transponder dummy package	Normal to blkhd	184	III	2221D
14	Payload separation and electrical disconnect relay	Z	172	I	2242C
15	Payload separation and electrical disconnect relay	Radial	172	I	2221D
16	Range safety power control box	Z		I	2221D
19	Inside range safety power control box next to relay		180	I	2221D
20	Near payload latch	Z	128	III	2221D
21	Near payload latch	Radial	128	III	2221D
22	Nose fairing barrel near relays	Z	169	I-IV	2221D
23	Nose fairing barrel near relays	Radial	169	I-IV	2221D
24	A/P sequence timer base	Z	172	IV	2221D
25	A/P sequence timer base	Radial	172	IV	2225 Run I - 2242C Run II
26	AFT seal plate near staging disconnect	Z	408	II-III	2252
27A	Staging disconnect mount	Z	408	II-III	2252 Run II - 2225 Run III
28	AFT seal plate near staging disconnect	X	408	II-III	2252
29	AFT seal plate near staging disconnect	Y	408	II-III	2252
30	Accel. Model 2225 acoustic sensitivity	-	120		2225
31	Accel. Model 2221 acoustic sensitivity	-	120		2221D
32	Mounted on 219 ring structure	Radial	219	III	2252
33	Base of relay inside Telepak	Z	170		2221D

[a]See Fig. 4 for equipment location.

VIEW LOOKING AFT
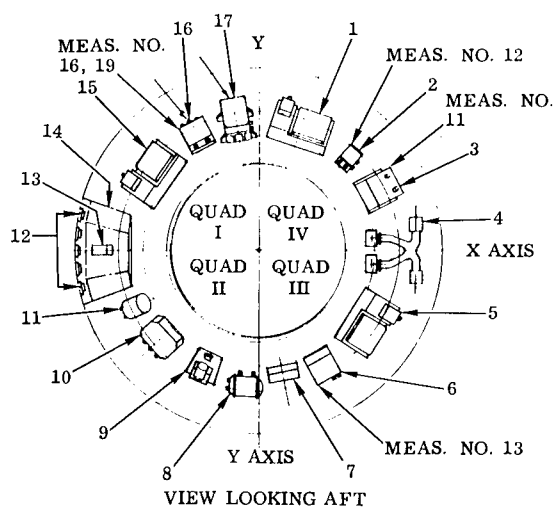
1. TLM NO. 2
2. POWER CHANGEOVER SW.
3. MISSILE INVERTER
4. BOIL-OFF VALVE
5. TLM SPARE PROVISION
6. AZUSA TRANSPONDER
7. FORWARD INSTRUMENTATION
8. GUIDANCE SIGNAL CONDITIONER
9. C-BAND TRANSPONDER
10. NASA STRAIN GAGE
11. ADDED GUIDANCE (SIG. COND.)
12. UMBILICAL RECEPTACLES
13. TLM RF ANTENNA
14. GROUND PLANE
15. TLM NO. 1
16. R/S POWER CONTROL
17. A/P SERVO AMP.

CENTAUR AC-6
ELECTRICAL/ELECTRONIC EQUIPMENT INSTALLATIONS —
LOWER TIER SHOCK MEASUREMENT NUMBERS

VIEW LOOKING AFT
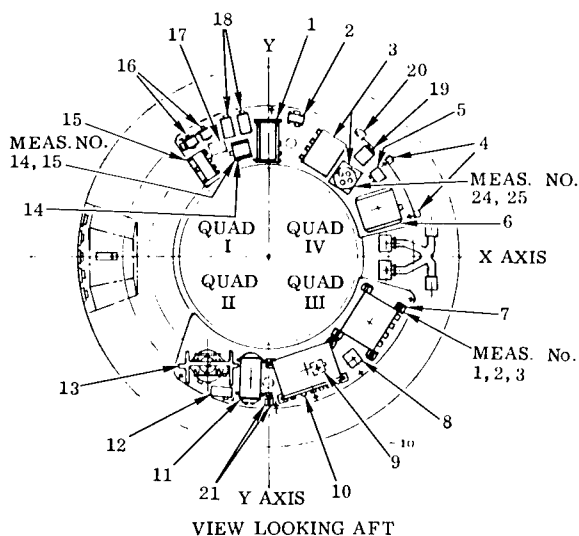
1. A/P RATE GYRO
2. SURVEYOR ARM SAFE
3. AUX. MODULE AND SEQ. TIMER
4. FUSING AND INSTALLATION
5. INSTR. T/C REF. JUNCTION
6. MAIN VEHICLE BATTERY
7. GUIDANCE COMPUTER
8. INSTR. ACCELEROMETER
9. AZUSA FILTER
10. GUIDANCE POWER SUPPLY
11. GUIDANCE ELECTRONIC PLATFORM
12. GUIDANCE 'PAST' PROVISIONS
13. GUIDANCE PLATFORM INSTL.
14. RELAY ASSY. - INSTL. SURVEYOR
15. MULTIPLEXER
16. R/S RECEIVER (2)
17. R/S RING COUPLER
18. R/S BATTERY (2)
19. PUVEP FILTER
20. ISOLATION UNIT - AC POWER
21. INSTL. - ISOLATION AND FUSE

CENTAUR AC-6
ELECTRICAL/ELECTRONIC EQUIPMENT INSTALLATIONS —
UPPER TIER SHOCK MEASUREMENT NUMBERS
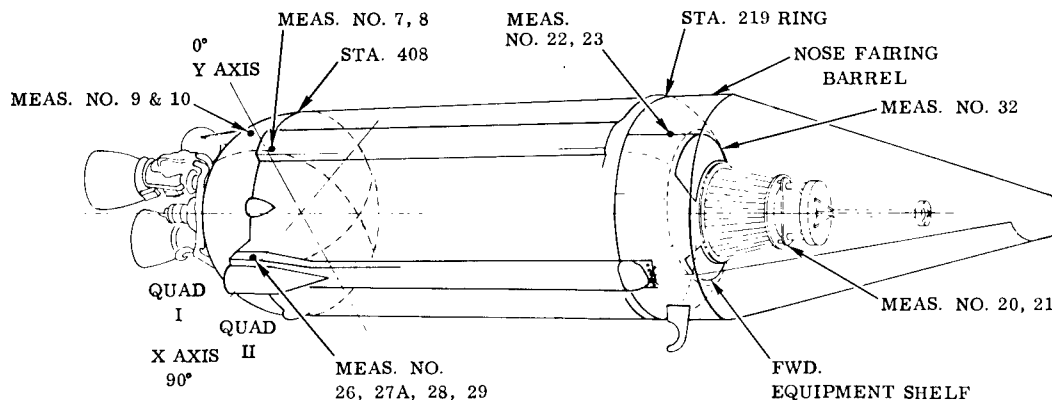
Fig. 4. Accelerometer locations for insulation panel jettison test
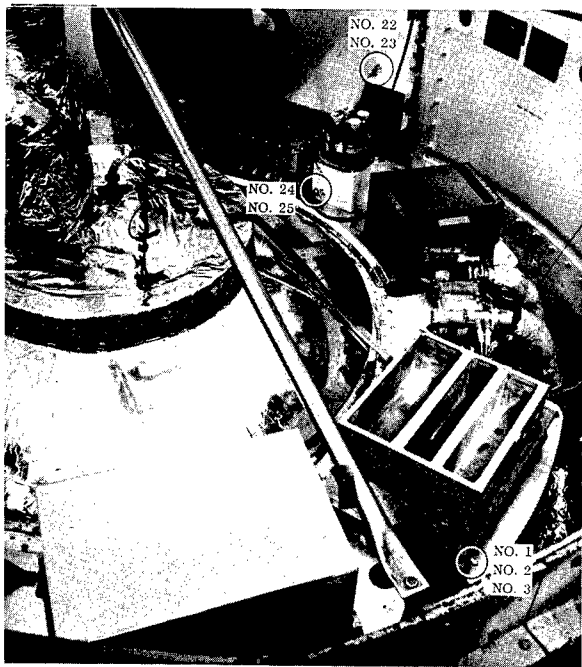
Fig. 5. Shock measurements made on test specimen equipment simulated in forward bulkhead area
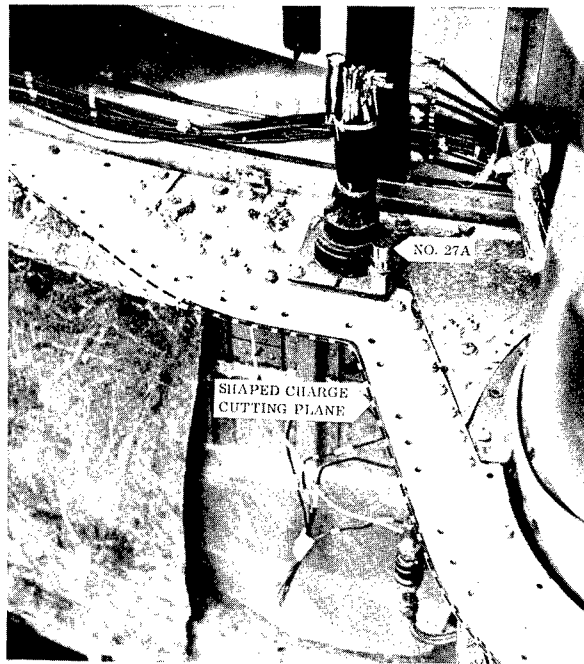
Fig. 6. Accelerometer on electrical wiring staging disconnect
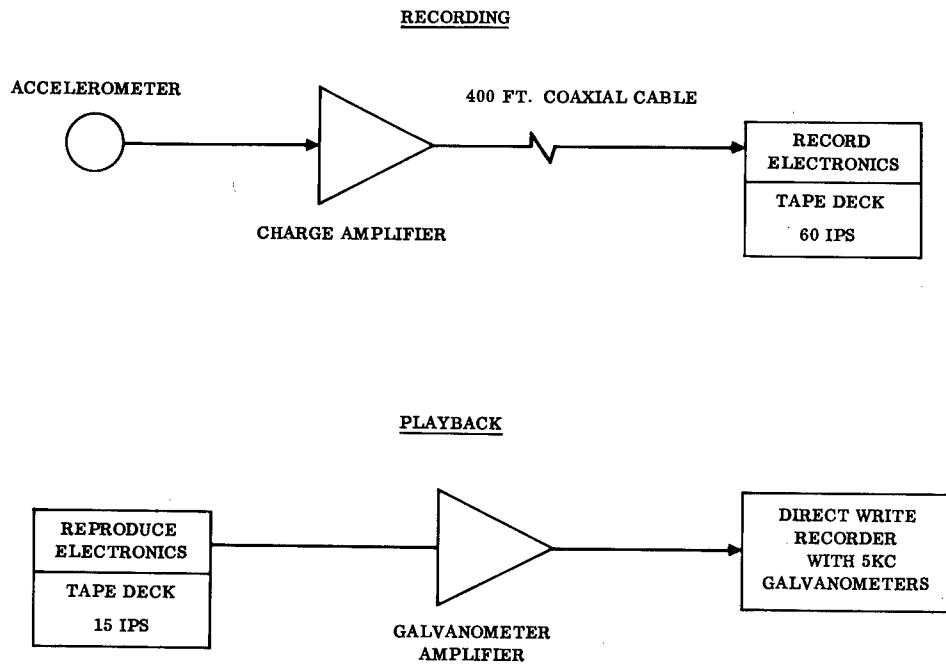
RECORDING

Fig. 7. Instrumentation recording system block diagram

SIMULATED SYSTEMS (10)
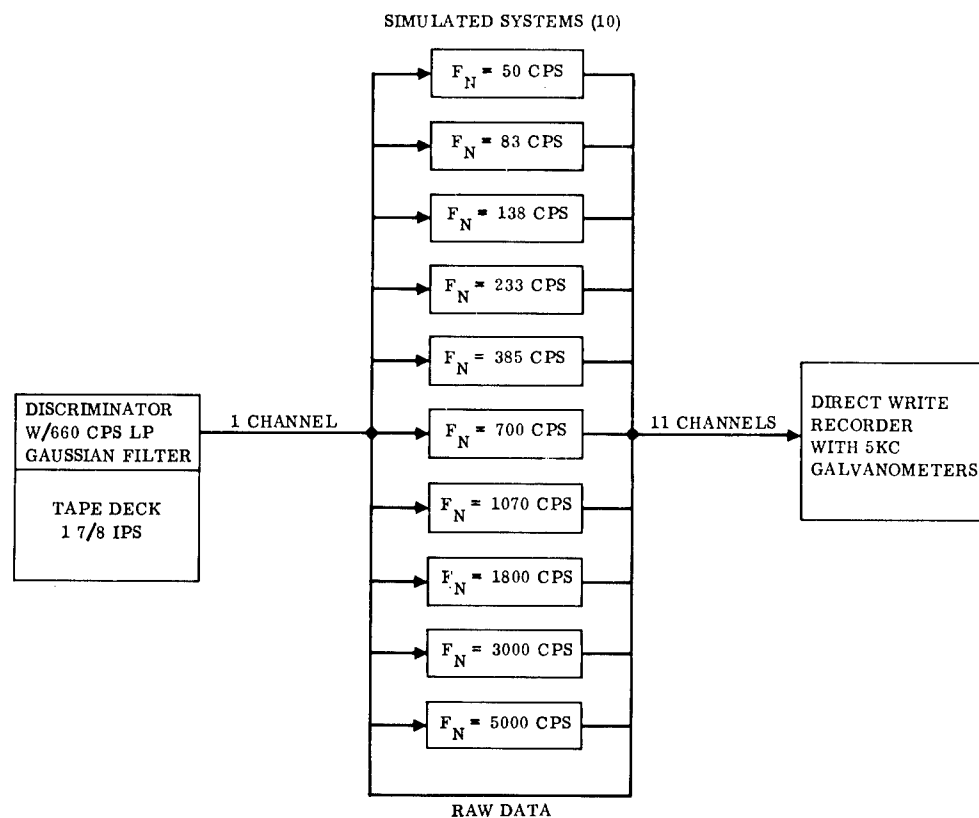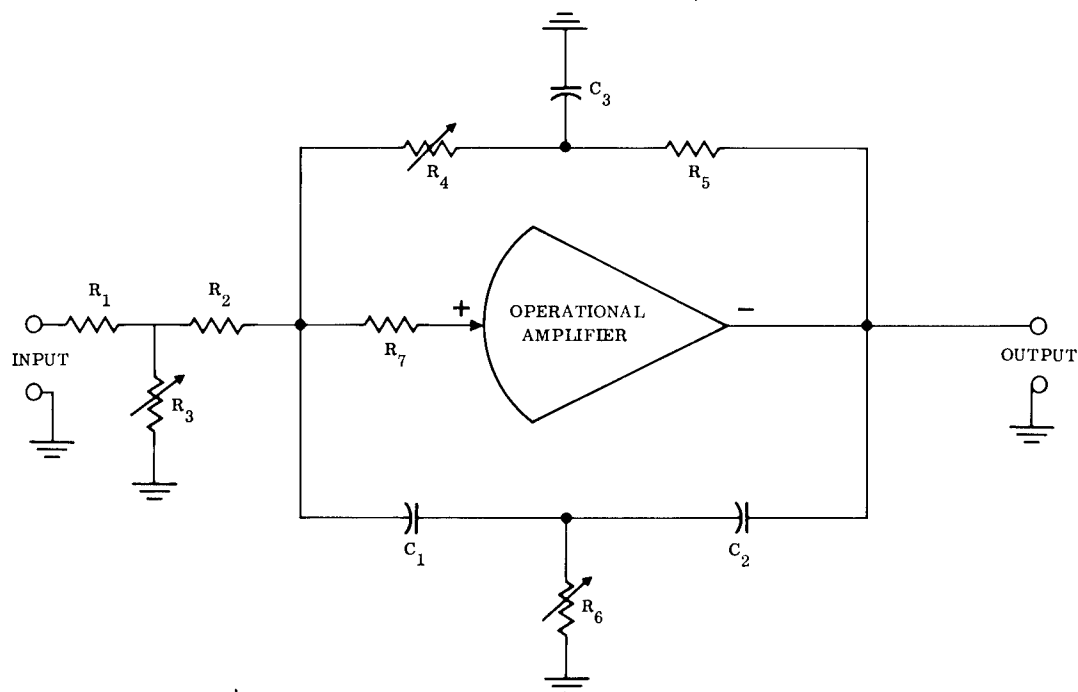

Fig. 8. Shock spectrum analyzer block diagram

Fig. 9. Schematic of typical simulated system

dashpot, and mass. The damping used corresponds to an amplification (Q) of 5 at resonance, chosen because equipment structures generally have an amplification less than 8. These reduced data form a basis for further analysis of the more important shock measurements in each area. A more complete shock response description is being obtained and cannot be included in this paper. The work being done includes determination of a more continuous shock spectrum and evaluation of the effects of different amplification factors on the shock response spectrum.

Each equivalent electrical resonator within the shock analyzer was calibrated by driving the system at resonance and measuring the output. When the shock spectrum was determined from the measured shock data, the transient amplitudes from the shock analyzer were measured on the same amplitude scale as the analyzer output at resonance.

Shock Data Analysis

An analysis of the waveforms and shock spectra (Figs. 10 through 17) reveal the following points. The measured flight data and the

ground test data at the payload latches (Z axis) during insulation panel shaped charge firing are similar. A frequency comparison shows a maximum transient response near 600 cps in the flight measurement CY54Ø (Fig. 18). The shock spectrum of measurement 20 (Fig. 14a) indicates a maximum shock response near 700 cps. The maximum amplitude of measurement 20 (Fig. 10) was 39 g o-p. The range of the flight measurement CY54Ø (Fig. 18) was ±10g and some clipping of the waveform peaks was occurring. The clipping did not saturate the accelerometer system; therefore, a comparison of maximum amplitudes between flight and ground test measurements was approximated and indicates a maximum ratio of 2 or 3. The conclusion that the acoustic environment had little or no effect on a majority of the shock measurements (discussed earlier) leads one to believe that the agreement between the ground test shock data and flight data may be better than indicated.

The shock response is very high (4000 to 13,500 g o-p at 3000 to 5000 cps) at distances of 2 to 4 in. from the shaped charge. Measurements 26, 27A, 28, 29, and 32 were within 6 in. of the charge (Figs. 15 and 17). Measurement 27A, Run III is considered to be the most
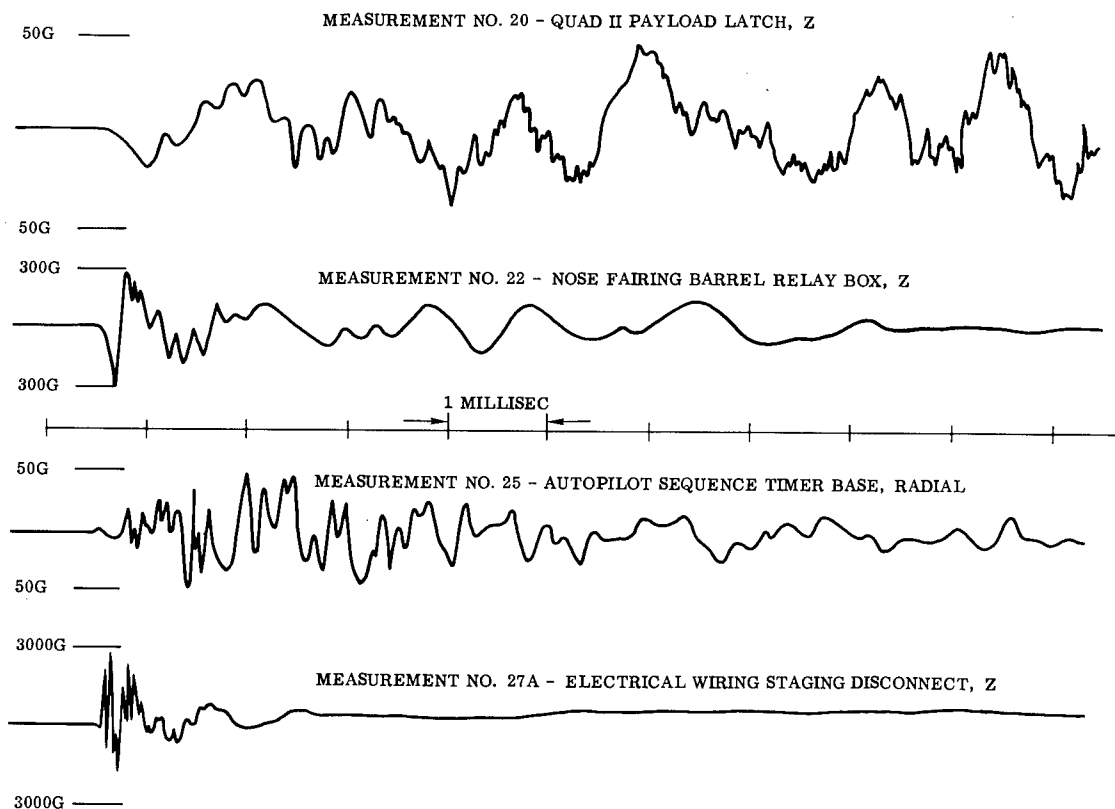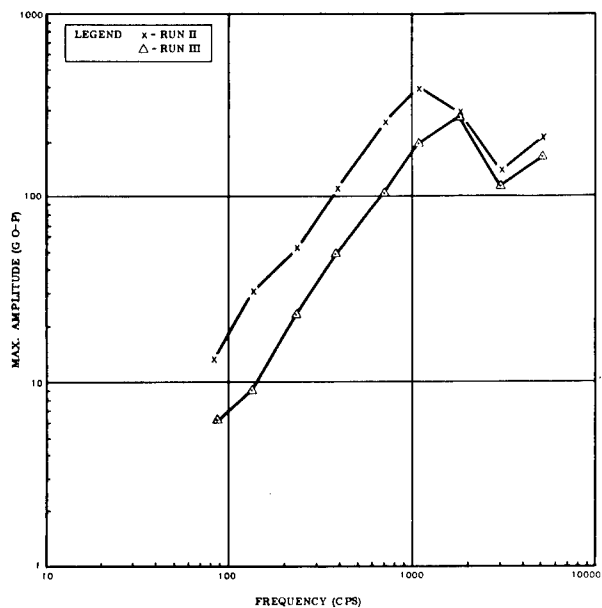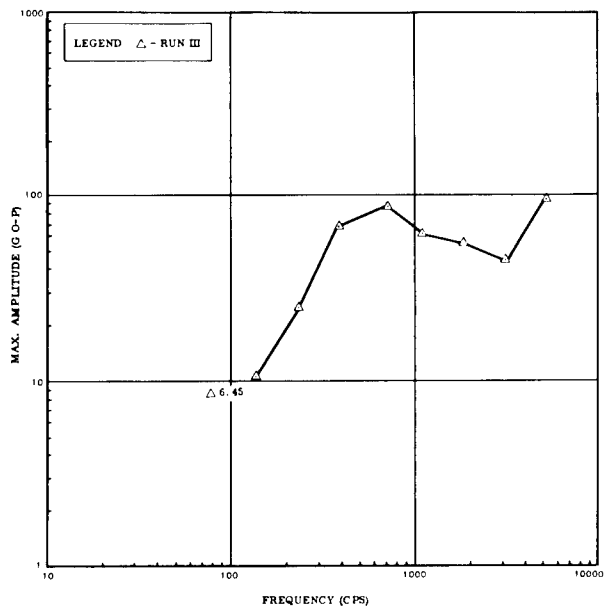

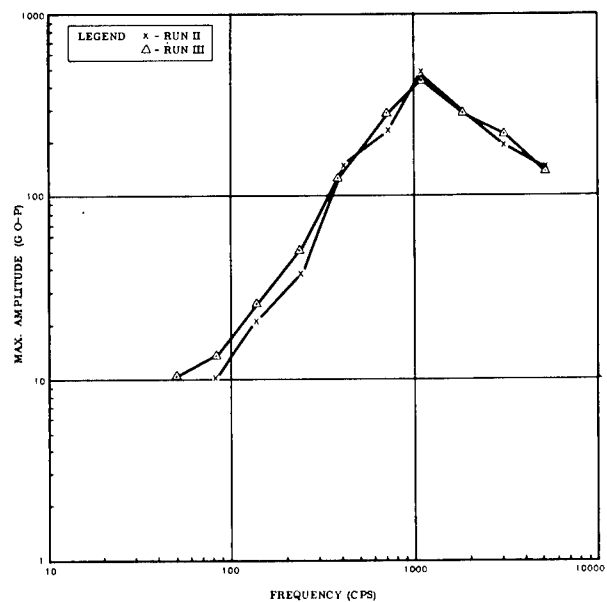Fig. 10. Selected waveforms from insulation panel separation tests

339

LEGEND   x – RUN II
          △ – RUN III

SHOCK RESPONSE SPECTRUM OF MEAS. NO. 1
(GUIDANCE COMPUTER BASE X AXIS STA. 172)

(a)

LEGEND   △ – RUN III

△ 6. 45

SHOCK RESPONSE SPECTRUM OF MEAS. NO. 3
(GUIDANCE COMPUTER BASE Z AXIS STA. 172)

(b)

LEGEND   x – RUN II
          △ – RUN III

SHOCK RESPONSE SPECTRUM OF MEAS NO 2
(GUIDANCE COMPUTER BASE Y AXIS STA 172)

(c)

LEGEND   ◯ – RUN I
          △ – RUN III
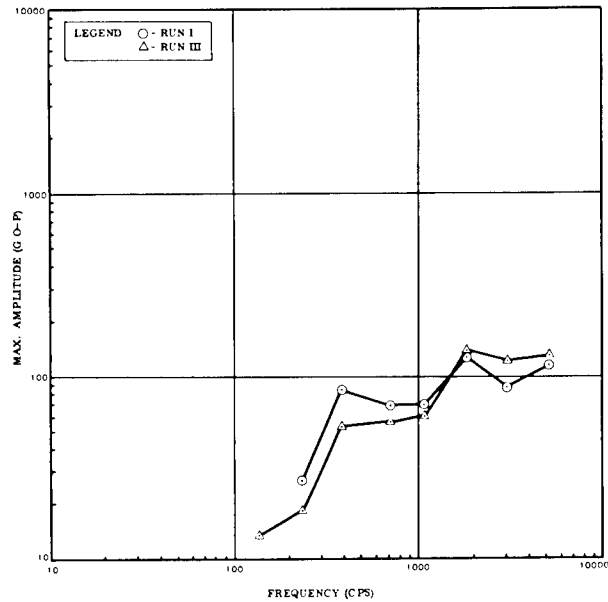
SHOCK RESPONSE SPECTRUM OF MEAS NO 11
(MISSILE INVERTER BASE Z AXIS STA 184)

(d)

Fig. 11. Shock response spectra of forward bulkhead area measurements (Q = 5)

340
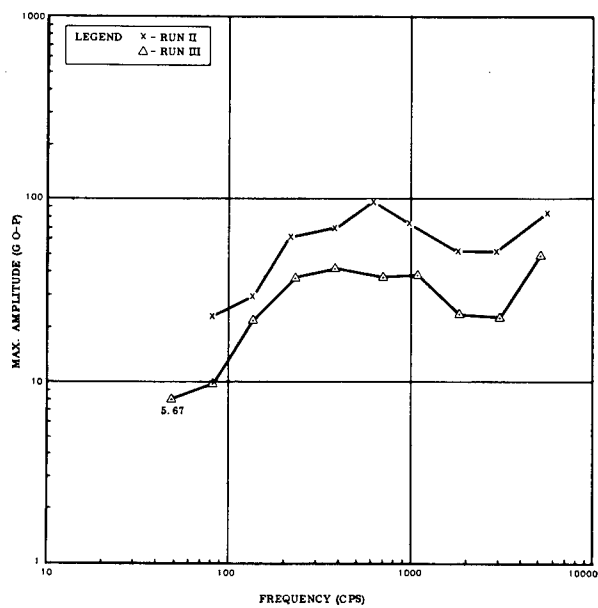
SHOCK RESPONSE SPECTRUM OF MEAS. NO. 12
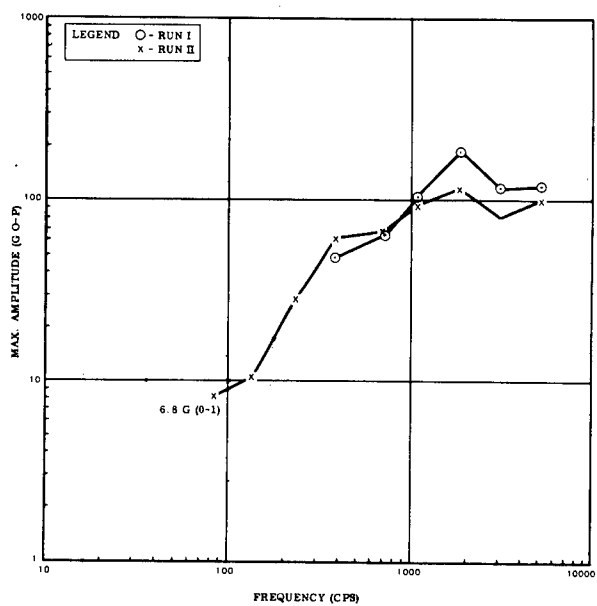(POWER CHANGEOVER SWITCH RADIAL, STA. 184)

(a)
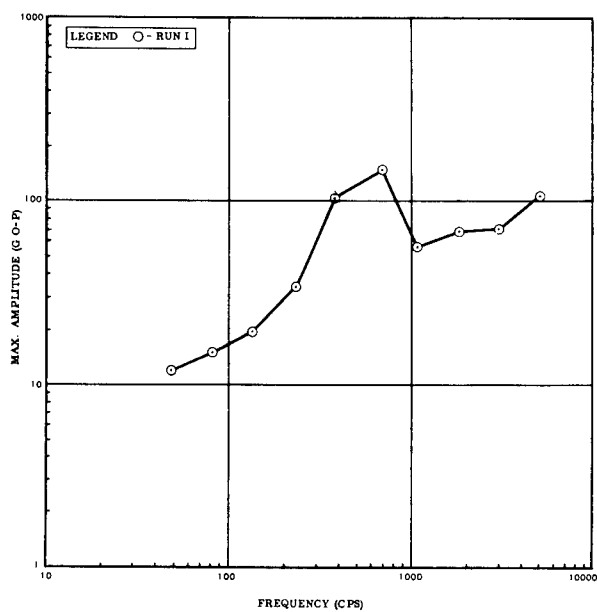
SHOCK RESPONSE SPECTRUM OF MEAS. NO. 14
(PAYLOAD SEPARATION AND ELECTRICAL
DISCONNECT RELAY BASE Z AXIS STA. 172)

(b)
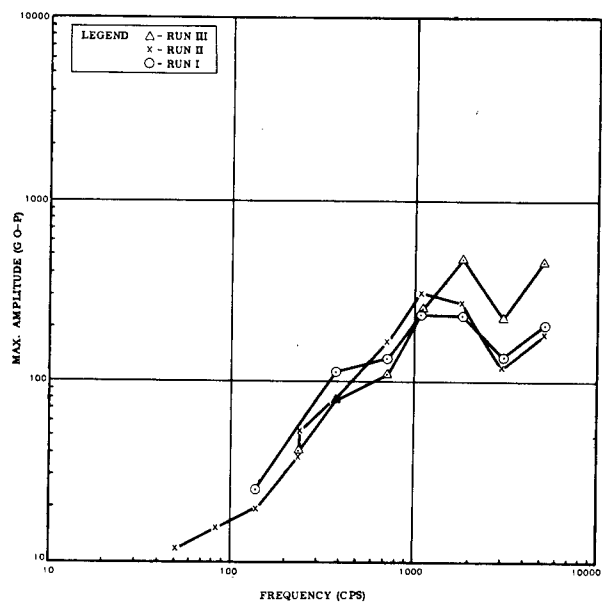
SHOCK RESPONSE SPECTRUM OF MEAS. NO. 13
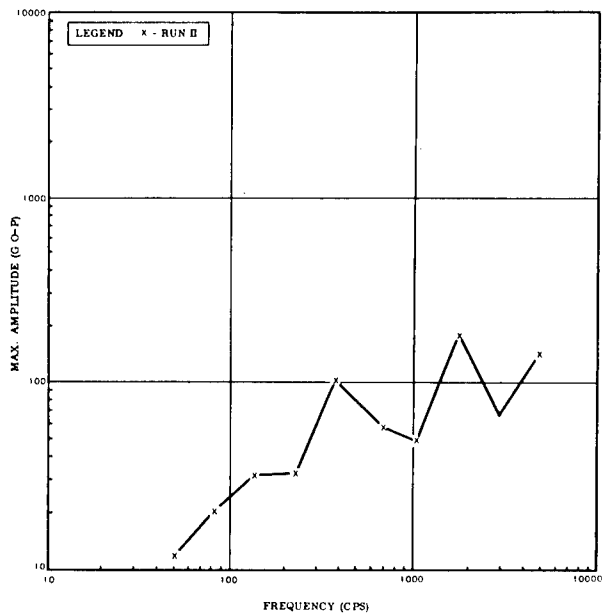(AZUSA TRANSPONDER DUMMY PACKAGE NORMAL
TO BHD. STA. 184)

(c)

SHOCK RESPONSE SPECTRUM OF MEAS. NO. 15
(PAYLOAD SEPARATION AND ELECTRICAL
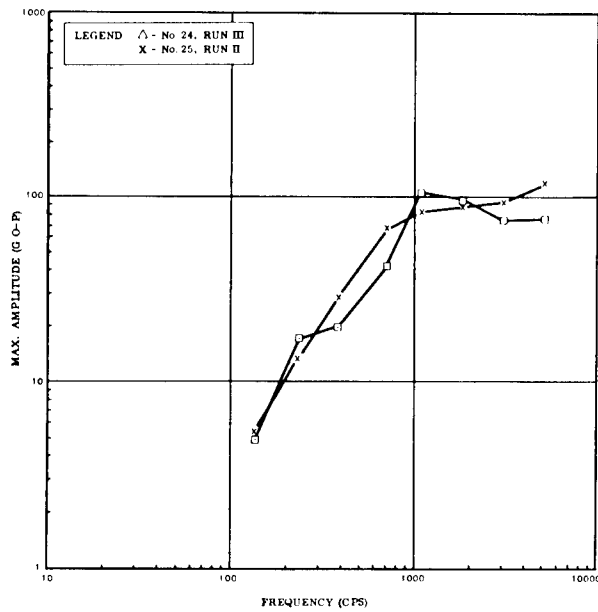DISCONNECT RELAY BASE, RADIAL STA. 172)

(d)

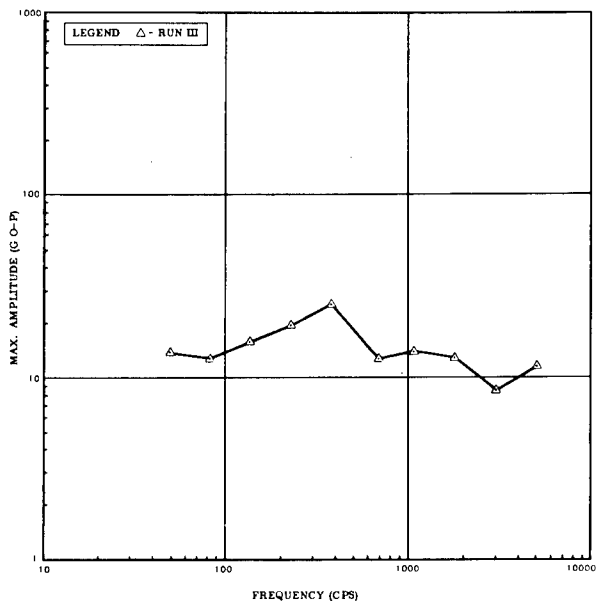Fig. 12. Shock response spectra of forward bulkhead area measurements (Q = 5)

(a)

SHOCK RESPONSE SPECTRUM OF MEAS NO 16
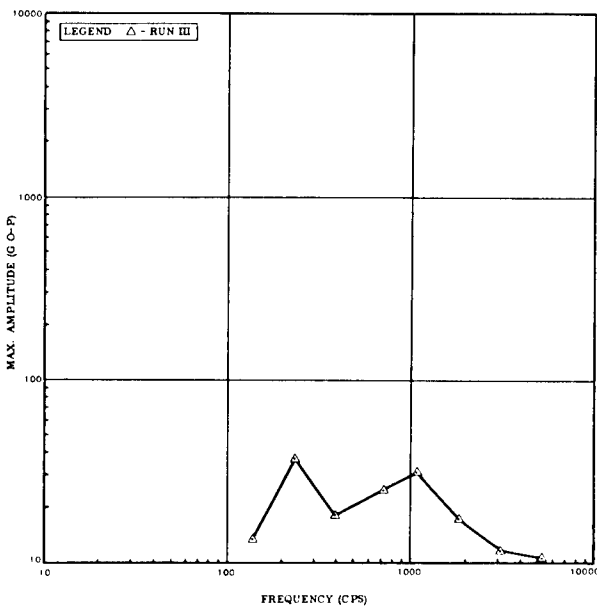(RANGE SAFETY POWER CONTROL BOX Z AXIS
STA 184)

(b)

SHOCK RESPONSE SPECTRUM OF MEAS NO 24 & 25
(A/P SEQUENCE TIMER BASE Z AXIS MEAS No 24,
RADIAL MEAS No 25)

(c)

SHOCK RESPONSE SPECTRUM OF MEAS NO 19
(LOCATED INSIDE OF RANGE SAFETY POWER
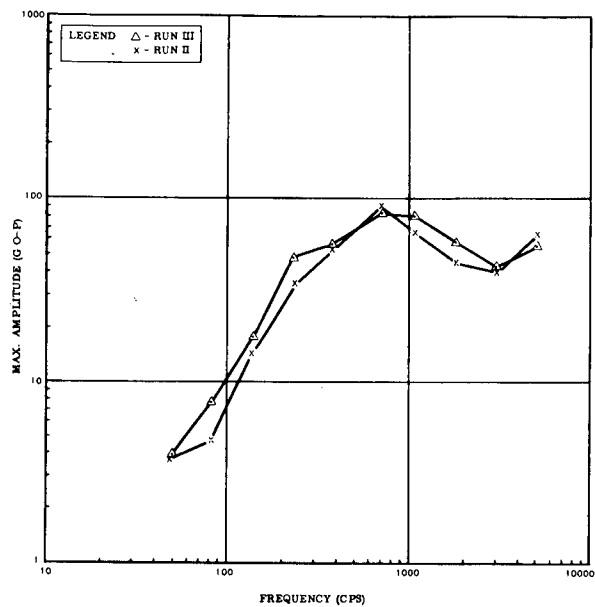CONTROL BOX NEXT TO RELAY)

(d)

SHOCK RESPONSE SPECTRUM OF MEAS NO 33
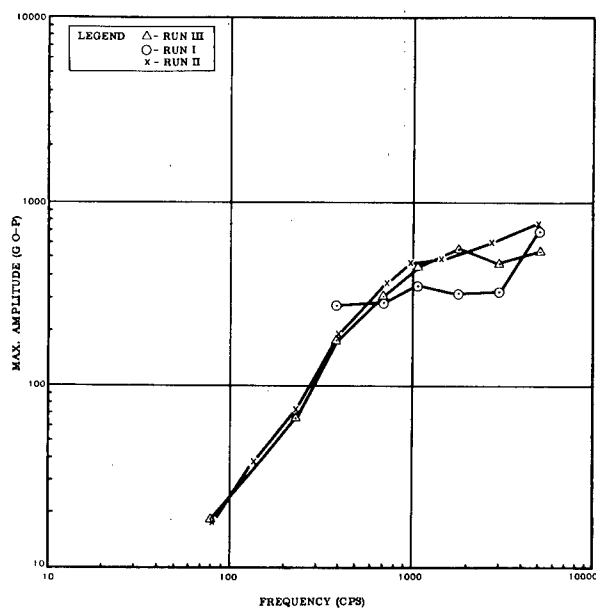(AT BASE OF RELAY INSIDE OF TELEPAK, STA 170)

Fig. 13. Shock response spectra of forward bulkhead area measurements (Q = 5)

SHOCK RESPONSE SPECTRUM OF MEAS. NO. 20
(AT PAYLOAD LATCH Z AXIS STA. 128 - 120°)

(a)

SHOCK RESPONSE SPECTRUM OF MEAS. NO. 22
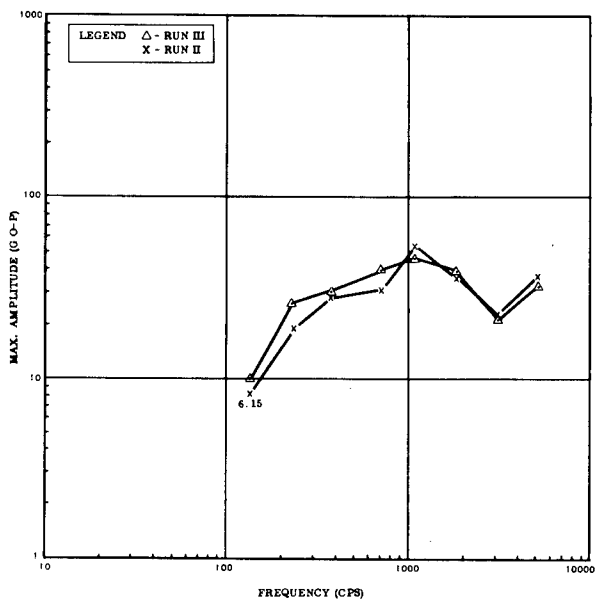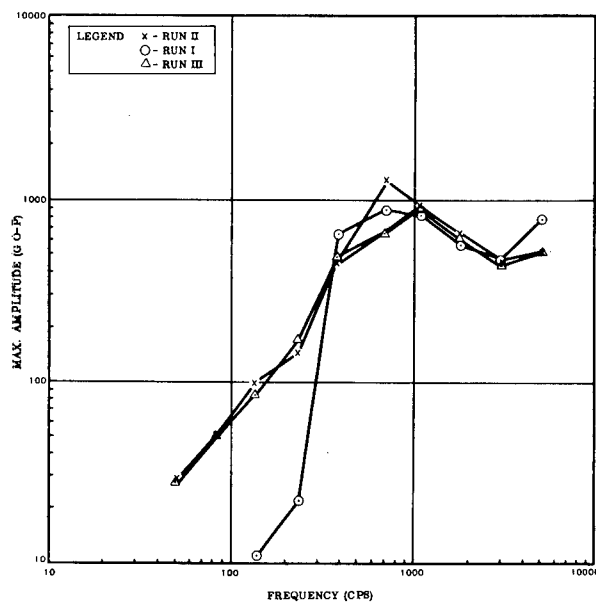(NOSE FAIRING BARREL AT RELAYS Z AXIS STA. 169)

(b)

SHOCK RESPONSE SPECTRUM OF MEAS. NO. 21
(AT PAYLOAD LATCH RADIAL STA. 128 - 120°)

(c)

SHOCK RESPONSE SPECTRUM OF MEAS. NO. 23
(NOSE FAIRING BARREL NEAR RELAY BOX,
RADIAL STA. 169)

(d)

Fig. 14. Shock response spectra of payload and
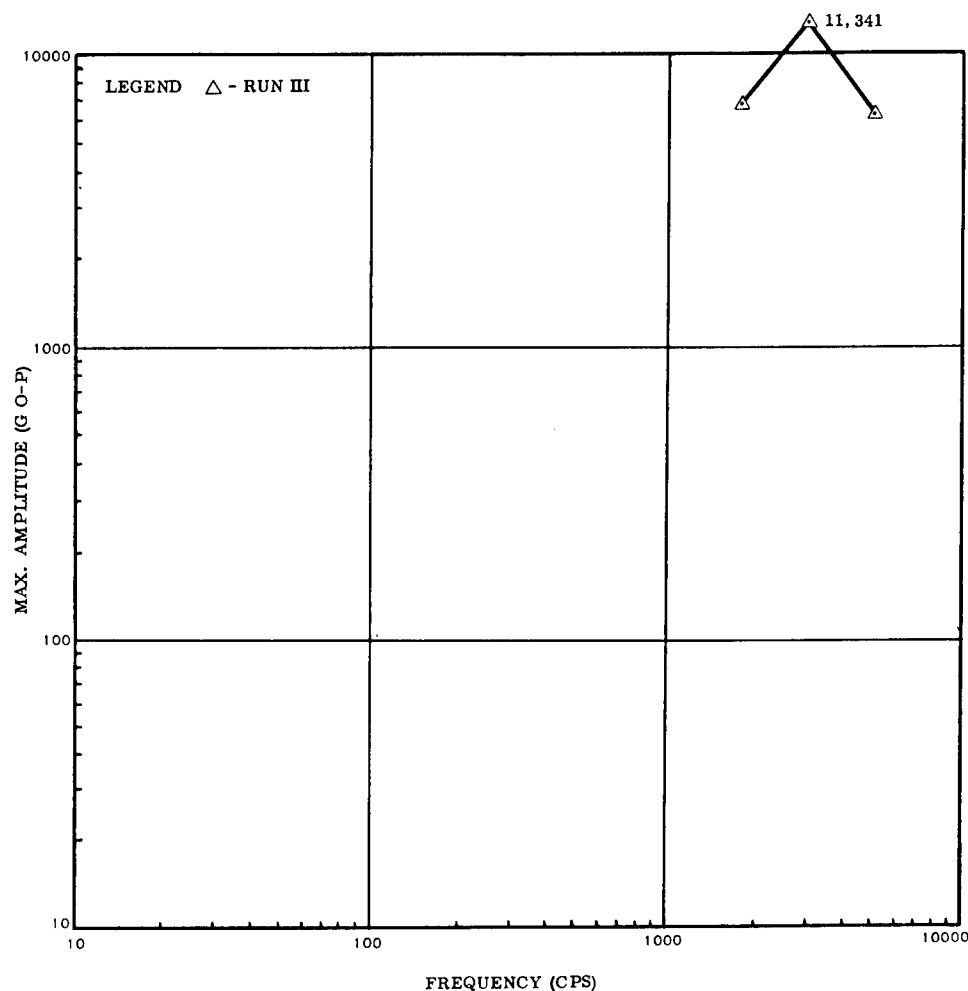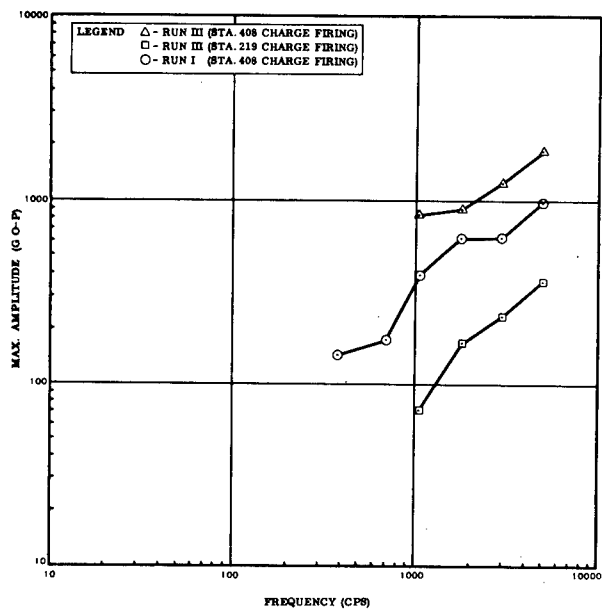nose fairing area measurements (Q = 5)

Fig. 15. Shock response spectrum of measurement 32
(at sta. 219 radial, Q = 5)

reliable. This measurement was taken on the mounting bolt of the electrical staging disconnect (1 to 2 lb wt). A part of the disconnect and the accelerometer were potted with Stafoam for temperature and sealing considerations. The Stafoam almost eliminated acoustic blast pressures on the accelerometer and minimized the motion of the accelerometer electrical cable. The measurements 26, 27A of Run II, 28, 29, and 32 were made with the Model 2252 accelerometer. The apparent dc shift (mentioned earlier) may be adding an error to the shock frequency spectrum above 700 cps. With the exception of measurement 27A, these accelerometers were mounted on structure that has little concentrated weight compared to an equipment package.

The most severe shock response in several zones of the Centaur vehicle appears to be between shock frequencies of 700 and 1800 cps. Shock measurements located in the forward equipment area (sta. 170 to sta. 184) indicate a range of shock spectra with a majority of the shock response below 200 g o-p (Table 2). Several of the highest shock responses are shown by measurement 2 (460 g near 1070 cps) and by measurement 13 (480 g near 1070 cps and 460 g near 5000 cps) (Figs. 11c and 12c).

By using the shock response spectrum as a comparison, a large number of the shock response spectra showed small variations from run to run (Figs. 11 through 17). Some of the measured shock responses, usually in the forward equipment area, were of a very dominant transient nature where relatively large amplitude responses would exist from 2.5 to 7 ms (Fig. 10). The shock measurements several inches from the charge were more of an impulsive nature.

344

LEGEND △ - RUN III (STA. 408 CHARGE FIRING)
□ - RUN III (STA. 219 CHARGE FIRING)
○ - RUN I (STA. 408 CHARGE FIRING)

SHOCK RESPONSE SPECTRUM OF MEAS. NO. 7
(DESTRUCT PACKAGE RADIAL AXIS STA. 400)

(a)

LEGEND × - RUN II (CHARGE AT STA. 408 FIRING)
△ - RUN III (CHARGE AT STA. 408 FIRING)
□ - RUN III (CHARGE AT STA. 219 FIRING)
⊙ - RUN I (CHARGE AT STA. 408 FIRING)
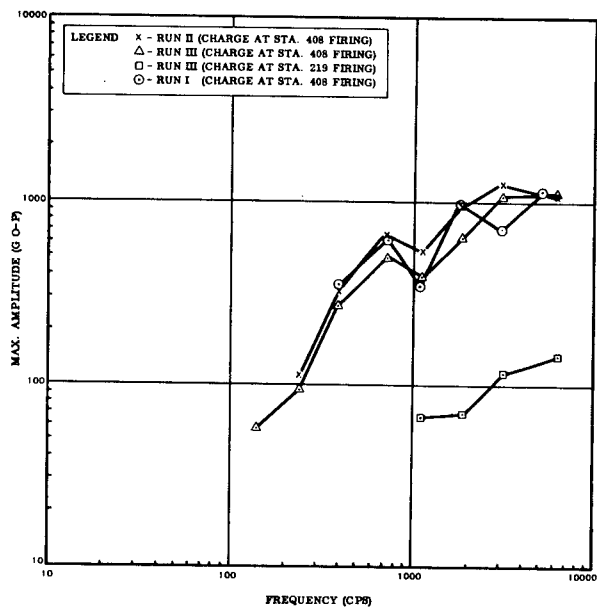
SHOCK RESPONSE SPECTRUM OF MEAS. NO. 9
(PROPELLANT UTILIZATION ELECTRONICS
PACKAGE ACCEL. NORMAL TO BHD. AT
STA. 437)

(b)

LEGEND ○ - RUN I
△ - RUN III (STA. 408 FIRING)
□ - RUN III (STA. 219 FIRING)
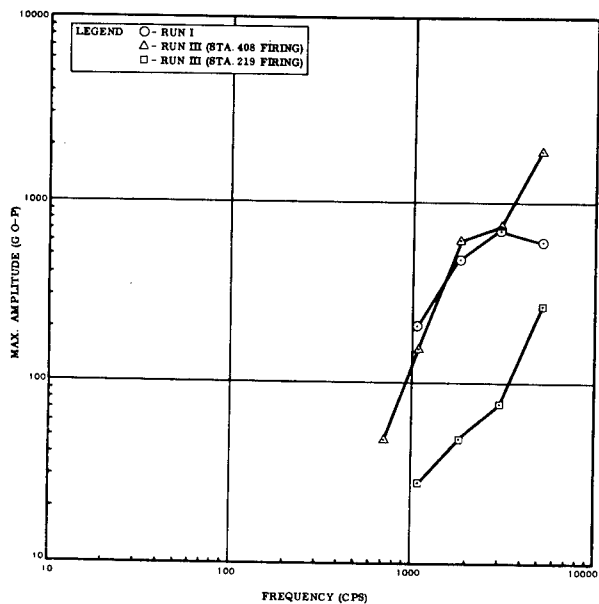
SHOCK RESPONSE SPECTRUM OF MEAS. NO. 8
(DESTRUCT PACKAGE Z AXIS STA. 400)

(c)

LEGEND △ - RUN III (AFT SEAL PLATE STA. 408 FIRING)
□ - RUN III (STA. 219 CHARGE FIRING)
× - RUN II (AFT SEAL PLATE STA. 408 FIRING)
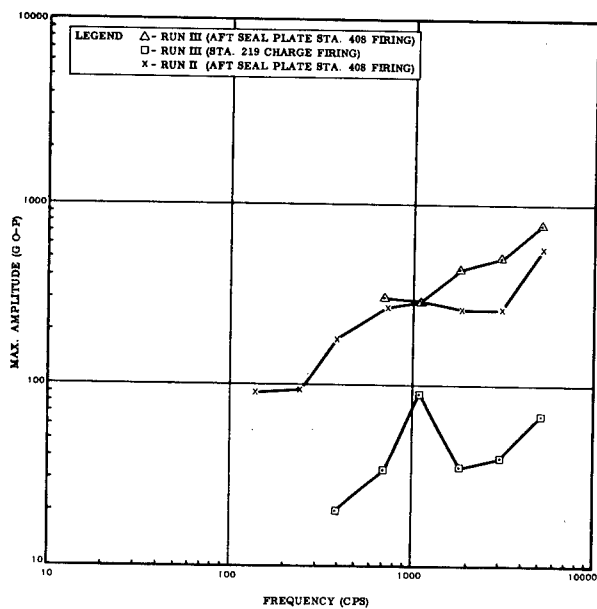
SHOCK RESPONSE SPECTRUM OF MEAS. NO. 10
(PROP. UTILIZATION ELECT. PACK. TANG. TO
BHD. STA. 437)

(d)

Fig. 16. Shock response spectra of tank and aft bulkhead area measurements (Q = 5)

345

(a)
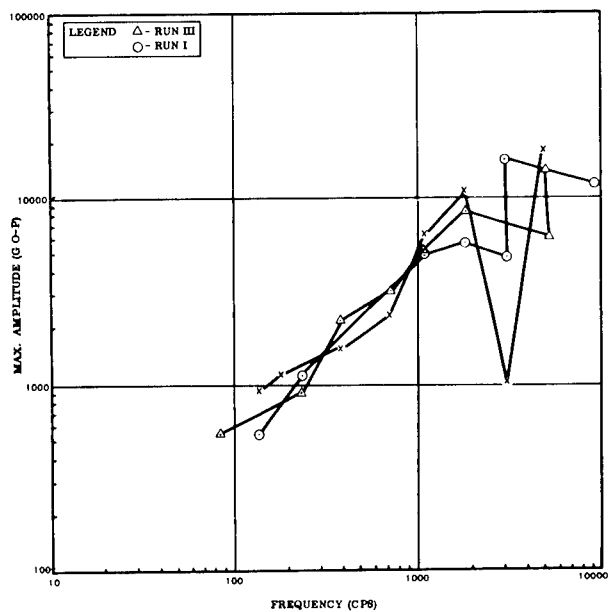
SHOCK RESPONSE SPECTRUM OF MEAS. NO. 26
(AFT SEAL PLATE, Z AXIS STA. 408)

(b)
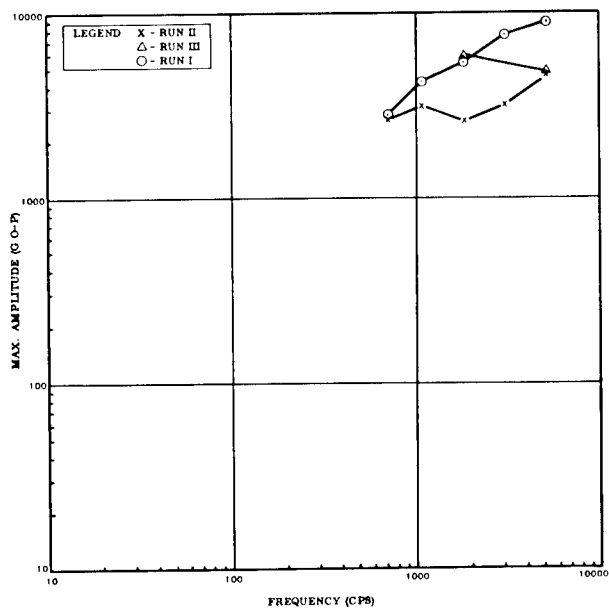
SHOCK RESPONSE SPECTRUM OF MEAS. NO. 28
(AFT SEAL PLATE, X AXIS STA. 408)

(c)

SHOCK RESPONSE SPECTRUM OF MEAS. NO. 27A
(ELECTRICAL STAGING DISCONNECT MOUNT
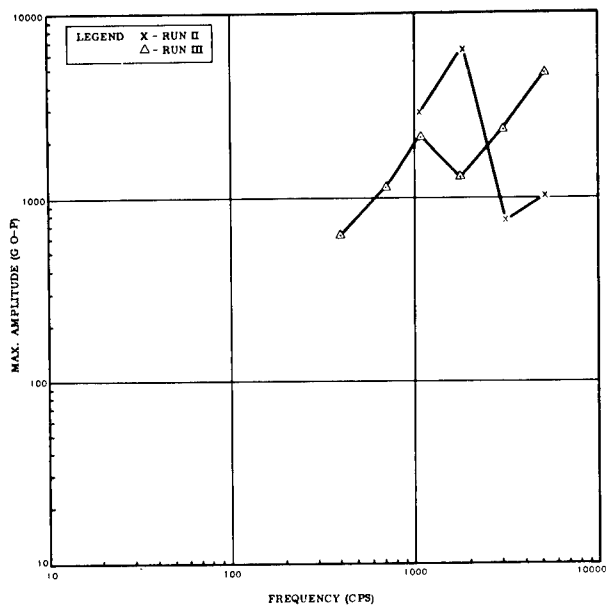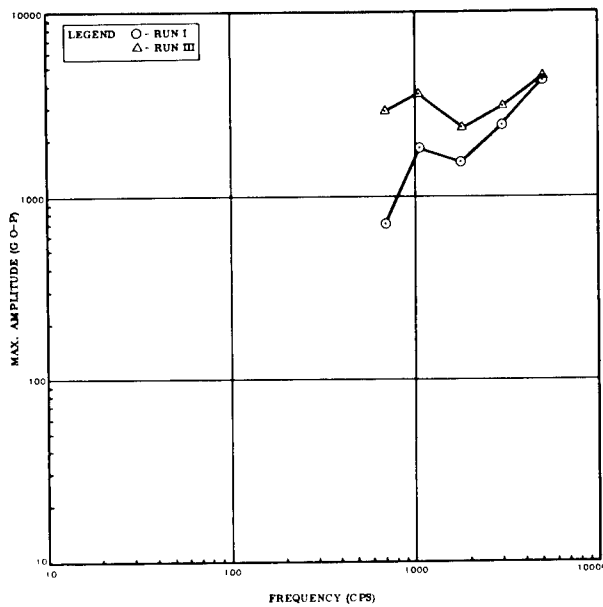Z AXIS STA. 408)

(d)

SHOCK RESPONSE SPECTRUM OF MEAS. NO. 29
(AFT SEAL PLATE NEAR STAGING DISC Y AXIS STA. 408)

Fig. 17. Shock response spectra of aft bulkhead area measurements (Q = 5)
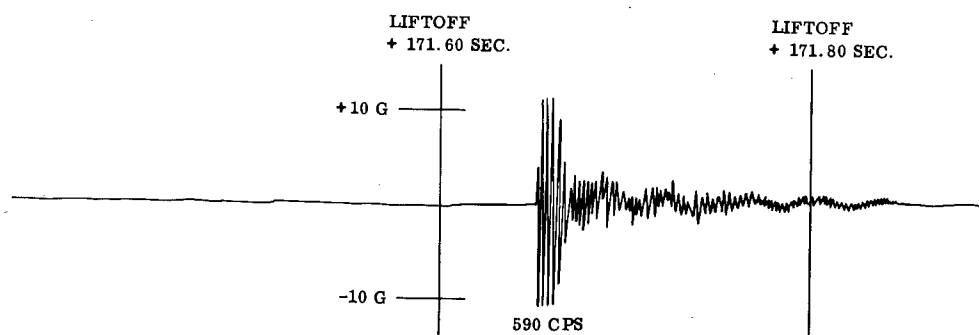
346

Fig. 18. Atlas-Centaur flight measurement CY540 (payload attachment No. 3, sta. 128, Z axis, IRIG telemetry channel 18)

TABLE 2
Summary of Maximum Shock Levels Measured During Insulation Panel Tests

Measure No.	Sensitive Axis	Tests Monitored	Maximum Measured Input (g peak)	Maximum Shock Spectral Level (Q = 5)	
				g peak	Frequency
(a) Forward Bulkhead Area					
1	X	2	128	398	1070–1800
2	Y	1	146	463	1070
3	Z	1	27	99	5000
11	Z	2	55	142	1800
12	Radial	2	36	98	700–5000
13	Normal to blkhd	3	135	478	1800
14	Z	1	58	148	700
15	Radial	2	71	183	1800
16	Z	1	27	178	1800
19	Z	1	10	25	385
24	Z	2	--	100	1070
25	Radial	1	51	120	5000
33		1	9	38	233
(b) Payload and Nose Fairing Area					
20	Z	2	39	90	700
21	Radial	2	24	54	1070
22	Z	3	337	770	5000
23	Radial	3	363	1,313	700–1070
(c) Tank and Aft Bulkhead Area					
32	Radial	1	4774	11,341	3000
7	Radial	3	485	1,832	5000
8	Z	3	394	647	3000–5000
28	Z	3	6580	9,214	1800–5000
29	Y	2	3390	4,450	5000
26	Z	3	7100	13,400	5000
27A	Z	2	5769	6,500	5000
9	Normal to blkhd	3	525	1,258	3000–5000
10	Tang. to blkhd	2	470	785	5000

Significant shocks were measured more than 100 in. away from the charge. When the sta. 219 shaped charge was fired, shocks were recorded by measurements 9 and 10 located 218 in. from the charge (Figs. 16b and d). The largest shock responses were 90 g near 1070 cps and 70 g near 5000 cps. Figure 19 shows a comparison of these shock spectra with distance.

EXAMPLE OF SHOCK PROBLEM

Electrical Staging Disconnect

During the development of the insulation panel separation system, the cutting surface of the shaped charge had been located several inches from the subject staging disconnect. An early measurement and analysis program had determined a 2500 g half-sine (0.4-ms) pulse (input) shock test requirement for this area.

During laboratory shock tests, the staging disconnect separated when a 700 g (0.4-ms) half-sine pulse shock input was applied. The shock impulse caused a spring preloaded collar to displace enough to allow the locking collets to disengage. This mode of separation would ordinarily occur when a lanyard pull would cause the staging disconnect to separate.

During ground tests of the full-scale insulation panel separation system, the disconnect was installed on the vehicle and a relative displacement on the staging disconnect indicated that the collar had moved 90 percent of the distance required to separate it. These data verified the results of the above laboratory test, and the conclusion was that the existing design of the disconnect was marginal.

More shock measurements several inches from the staging disconnect (Fig. 17) were obtained, the shock data were analyzed, and the
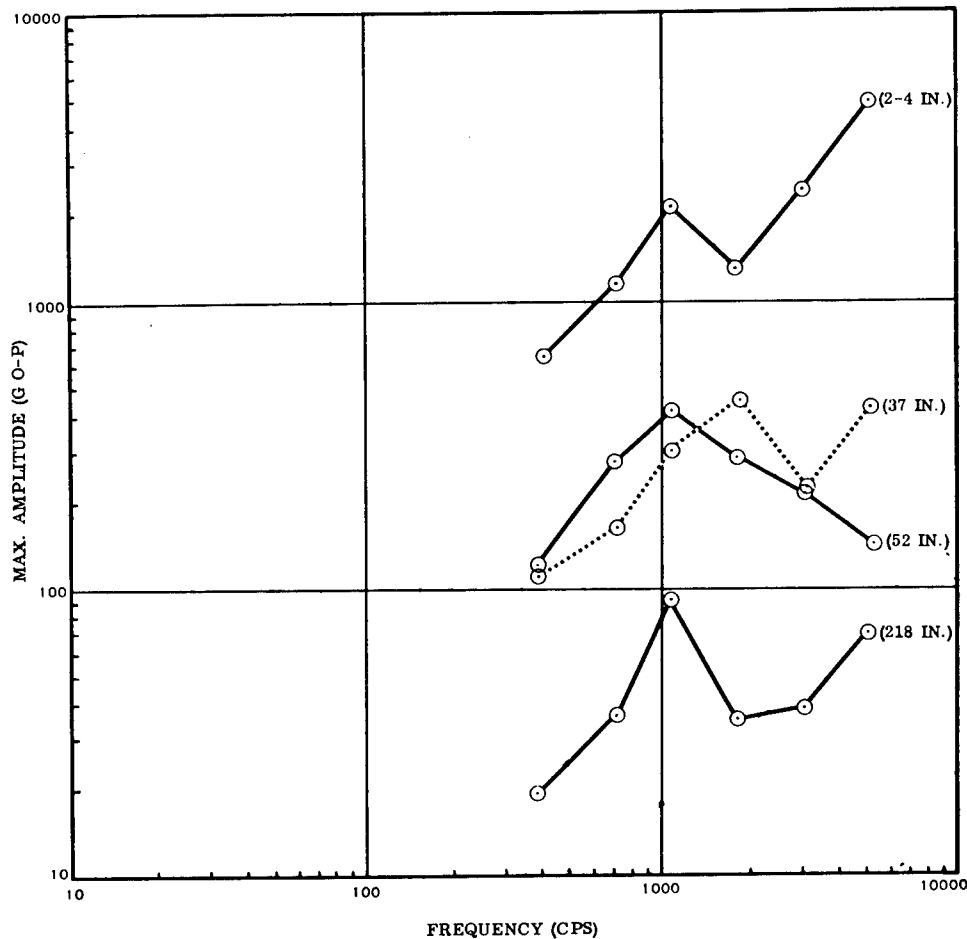

Fig. 19. Comparison of shock spectra and distance from shaped charge (Q = 5)

348

shock test requirement was changed to a 2100 g (0.4-ms) half-sine shock test that included a factor of safety (Fig. 20). After analysis, redesign, and retest, the staging disconnect was able to pass a 2400 g (0.4-ms) shock including side loads due to shock. The last shaped charge separation test of the series (Run III) was conducted using the redesigned staging disconnect, and the measured relative displacement was only 16 percent of that producing separation. For this problem, it was shown that half-sine pulse shock tests tend to be more severe than the actual environment.

SHOCK QUALIFICATION TEST REQUIREMENTS

Existing Techniques

The present approach to the high-frequency shock problem relies heavily on half-sine pulse

shock tests based on the most severe portion of the shock frequency spectrum. Most equipment on Centaur is located in a relatively low-shock environment; however, this environment is considered to be severe enough to warrant shock qualification tests. There are indications that a high-vibration qualification test requirement (11 g rms combined sine plus random) has significantly reduced the number of shock problems in the Centaur forward equipment area. In the high shock level areas, the equipment is usually tested to a shaped charge-produced shock response and tested to one or more different half-sine pulse shocks.

Techniques Under Consideration

Low shock environment, less than 60 g input (Table 2), may be reproduced by an electrodynamic shaker. A simulation of the complex transient response shock environment may be
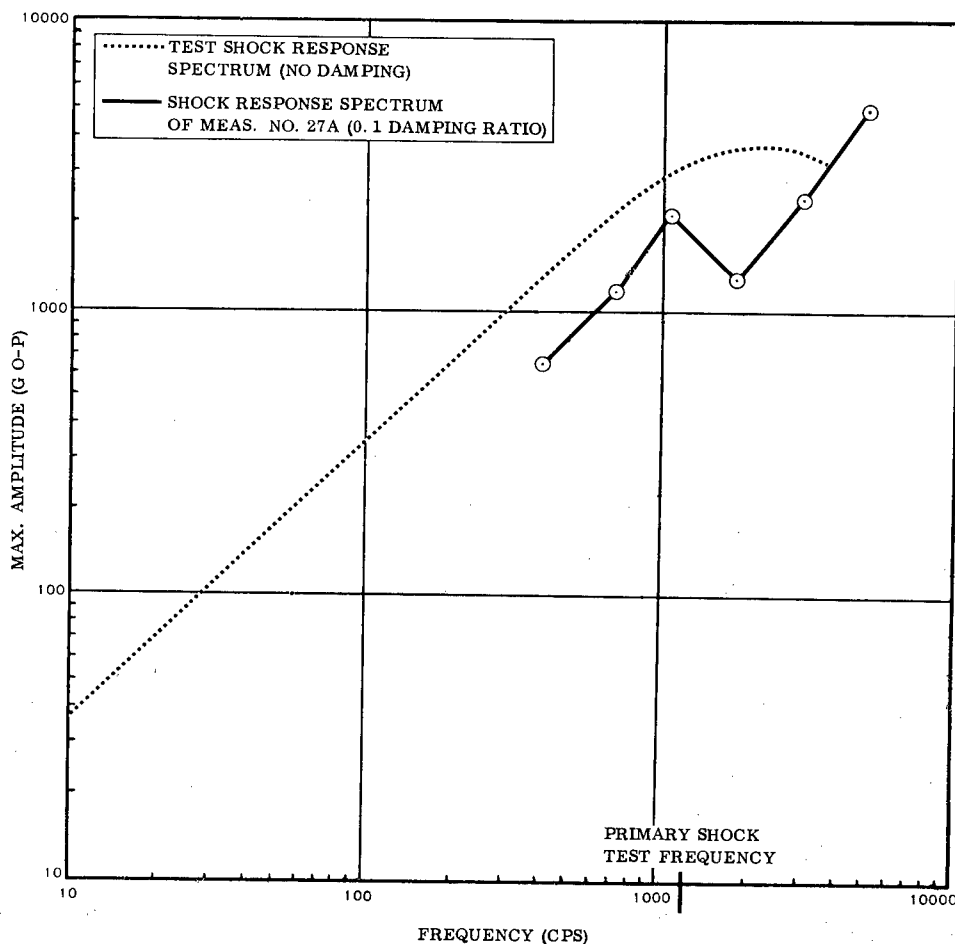

Fig. 20. Comparison of measured and laboratory test shock spectra on electrical staging disconnect

possible. This approach could be used as soon as practical techniques are available. It is conceivable that this approach may make some of the assumptions in a shock response spectrum analysis less important. For example, an amplification fact of 1 could be used if the number of cycles at a frequency would be reproduced. The complex high-amplitude shock environment simulation (more than 250 to 500 g input) may require using a pyrotechnic method to reproduce the shock. This technique needs more refinement. This method is not now very predictable. Some testing along these lines has been conducted on a substructure configuration. The complexity and high costs of adequately simulating the Centaur structure precluded the approach of establishing a pyrotechnic shock facility where test specimens could be tested and operated simultaneously.

CONCLUSIONS

1. The data from the ground tests indicate that the whole vehicle is subjected to high-frequency shock when the linear shaped charge is fired. A limited comparison of ground and flight test data indicated that the ground test vehicle provided similar response. A need for additional flight data is apparent before it can be verified that the ground test criteria truly simulate the flight environment.

2. The shaped charge-induced acoustic environment has little or no effect on most of the shock data.

3. The shock magnitude within 6 in. of the shaped charge installation is extremely high (approaching 10^4 g o-p in some cases), and it is recommended that designers refrain from locating equipment or relays within 6 in. of the charge. Beyond 6 in., a significant attenuation in shock response was observed.

4. The ground test data indicate that added mass can provide a large attenuation in shock response within the 6 in. distance; however, the resulting response is still considered prohibitive for critical components.

5. Repeatability of structural response was demonstrated since many shock spectra were similar from run to run.

6. Recent experiences, not discussed in this paper, indicate that a high-vibration qualification test (11 g rms combined sine plus random) has significantly reduced the number of shock problems.

7. Significant shock responses exist above 5000 cps, and since some of the more recent microminiature electronic circuits are utilizing mechanical reeds (natural frequencies near 8000 cps with damping ratios corresponding to Q's of 150), the reeds can serve as very selective electrical oscillators and may be affected by the shock environment.

DISCUSSION

Mr. Blake (Lockheed Missiles & Space Div.): In the matter of qualification testing we have adopted the attitude that the shock spectrum is not a reliable measure of the shock, and that any shock machine is also likely to be unreliable. To provide some degree of confidence in a full system test, we have used an overtest by increasing the size of the charge and simultaneously increasing the size of the joint which it breaks.

Mr. Noble: We considered this in the beginning when we were developing this concept. One of the difficulties with our particular problem is that it is very expensive to run a full-scale system test, and management is very reluctant to spend this kind of money.

Mr. Lesem (Litton Industries): I have a question regarding the measurement of the shock, particularly in your forward equipment area. Were measurements made primarily on the structure, or was an attempt made to determine the shock level experienced by the equipment mounted in the bay?

Mr. Noble: Primarily, the measurements were made at the feet of components. We did make some measurements inside electronic packages, for example, next to relays, to evaluate several different commercial isolators used on these equipment packages. One of these isolators was very soft. Isolator resonance was around 50 cps, and in this environment the relay was chattering. Its natural frequency was around 300 cps, and we were able to reduce the environment at the relay very significantly with this isolator. Another isolator that was not primarily designed for this application but was used to minimize the vibration response, was a little harder, resonating around 110 to 160 cps. This isolator did not work very well for this application.

Mr. Lesem: Was there a significant difference between points on the structure away from heavier packages compared with the response of the heavier packages themselves?

Mr. Noble: Yes, there was. Mass attenuation seems to work.

Mr. Gertel (Allied Research Assoc.): I have some comments on the presentation of the shock spectra. In the very high-frequency range, where you presented spectral results going up from 1000 cps, I noticed that you only plot points every 1000 cps. With the complex frequency composition of shock waves indicated in your slides, it is more than likely that there will be frequency components which fall in between these points. At these particular component frequencies of the shock wave, you will get extremely high shock spectrum results. In addition, with respect to the use of such a low Q for the shock spectrum presentation, it has been found that the shock spectrum results are very sensitive to the value of Q used. When you use such a low value of Q and high value of damping, there is a tremendous smoothing effect, especially in the high-frequency range where you have shown your primary concern. Another reason that it is disadvantageous to use such low Q's is the age-old problem of comparing the data of two or more people. Your Q is 5, my Q is 100, and someone else may use 300. If we are going back to the application of shock spectra and similar techniques for presenting complicated shock waveform results, we ought to be thinking again about the use of standardized Q's, zero Q possibly, for presenting shock spectra. This has been suggested for many years at previous symposia. My last comment is on the use of the half-sine pulse for shock testing. Equipment failures tend to fall in two broad categories: velocity sensitive and peak acceleration sensitive groups. When you use a half-sine pulse with the complicated kind of shock spectrum that you have, it seems that you can only match one aspect of the shock spectrum, usually the peak g. Consequently, you will overtest in the low frequency or velocity sensitive range of the spectrum.

Mr. Noble: I agree with everything you say. On the second point that you made, if there is a standard Q, I would like to know what it is. The reason we chose a Q of 5 was that most of our equipment located in the forward bulkhead area usually has a Q of less than 8. We are analyzing these data with different Q's, all the way up to 25 and higher. You also mentioned that we only plotted close to octave band frequencies. We also ran a continuous spectrum analysis, but it was not available for this presentation. We do not worry very much about the continuous spectrum, because we played back the data before analysis, and we have a rough idea of what frequency spectrum to expect. I have a table in the paper listing the input shock level and the response spectrum shock level on all of these measurements, which gives an idea of how significant the transient vibration is in terms of the number of cycles that would occur at a particular input. No measurements were analyzed where the shock response spectrum was 5 times the input, indicating that we had enough for a steady state vibration to occur. I thought this was significant.

Mr. Kirkley (Martin Co.): I was interested in why you picked the 5000-cps upper limit. Is it that you do not expect any resonances to exist in fragile parts of the equipment above this frequency? We've been confronted with this same problem.

Mr. Noble: Yes, that was one of the reasons, although we are starting to be more concerned about the shock levels above 5000 cps. For example, some of the recent electronics use cantilever beams in microminiature circuits to take the place of an inductance. The natural frequency of these little cantilever beams starts at 8000 cps and goes up. I would certainly recommend that anyone working on this type of component be very careful in this kind of environment.

*   *   *

VIBRATION AND SHOCK DATA
FROM THE ATHENA BOOSTER

C. J. Moening and F. J. Benedetti
Aerospace Corporation
San Bernardino, California

Vibration and shock data measured on the ATHENA intermediate size solid propellant booster are presented. These data were measured in three orthogonal axes at two missile stations on broadband FM/FM telemetry. The two locations selected for the flight measurements were at the missile attitude controller base plate (Stage 3) and at the payload interface plate (Stage 4). During eleven flights, measurements were made in each of three orthogonal axes at the Stage 3 location. On six of these flights, measurements were also made in each of the three axes at the Stage 4 location. In addition, ground tests were instrumented to measure the magnitude of shock induced as a result of pyrotechnic separation devices.

The vibration data are presented as acceleration spectral densities and the shock data are presented as response spectra.

INTRODUCTION

This paper presents shock and vibration data measured on the ATHENA intermediate size solid propellant booster. Since only limited data on this size booster have been published previously, it is hoped that the data presented will be of assistance in predicting the environment of future vehicles of this category.

A description of the vehicle configuration and structural aspects pertinent to the evaluation of the dynamic environments is presented. In addition, the data acquisition and analysis techniques are included to provide as lucid a description of the data as possible.

DESCRIPTION OF VEHICLE

The ATHENA vehicle is a four-stage solid propellant booster used for subscale reentry vehicle testing as part of the Advanced Ballistic Reentry System (ABRES) program. The first two stages boost to altitude a velocity package consisting of the third and fourth stages and the reentry vehicle. After second stage burnout, the velocity package is released and oriented to the proper attitude during a coast period. On attaining this attitude, the third and fourth stages accelerate the reentry vehicle to high velocity to obtain reentry physics data.

The vehicle, illustrated in Fig. 1, has the following physical characteristics:

Length,	51 ft;
Diameter:	
1st stage,	31 in.;
2nd stage,	28 in.;
Exit heat shield,	28 in.; and
Weight,	16,000 lb.

Additional details showing the velocity package contained within the exit heat shield and its attachment to the forward end of the second stage are shown in Fig. 2. It should be noted that the heat shield, in addition to providing protection from aerodynamic heating during boost, also attenuates acoustically and aerodynamically induced vibrations on the velocity package.

The first stage propulsion system consists of three motors, one Castor and two Recruit. Vehicle stability is maintained by fins on the first and second stages and by body rotation. The body rotation is imparted by spin rockets mounted on the trailing edge of each second stage fin and by canting the fins. The spin rockets are initiated at launch and impart an initial spin rate of 1 rps to the vehicle. The canted fins increase the spin rate to a maximum of approximately 3 rps at Stage 2 burnout. A listing of the motors employed on each flight and their performance characteristics are given in Tables 1 and 2, respectively.

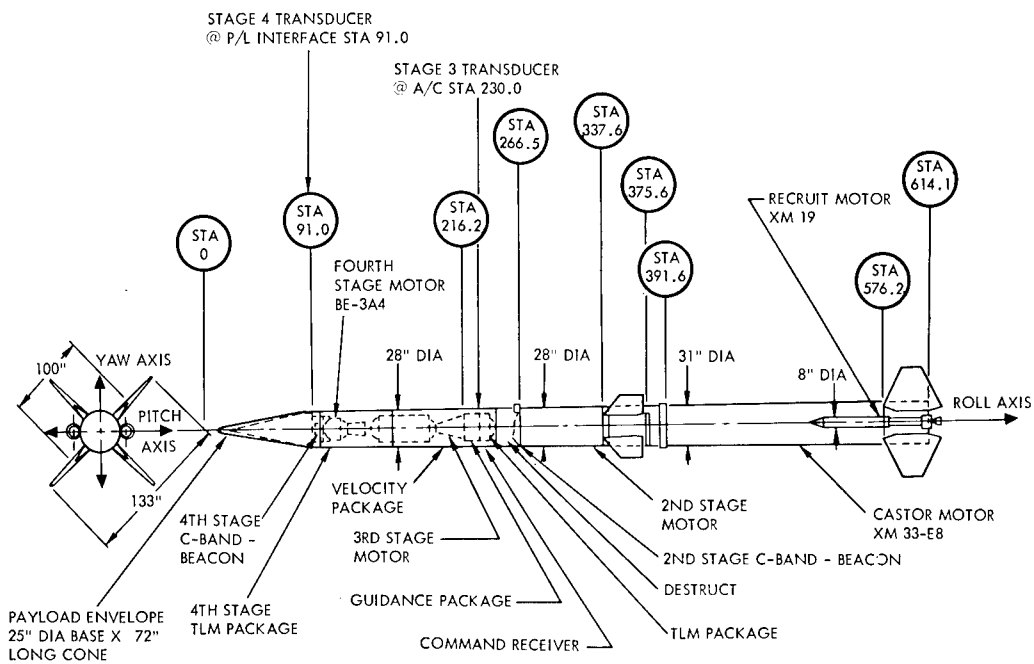Separation of the first stage is accomplished by detonation of two explosive nuts which release
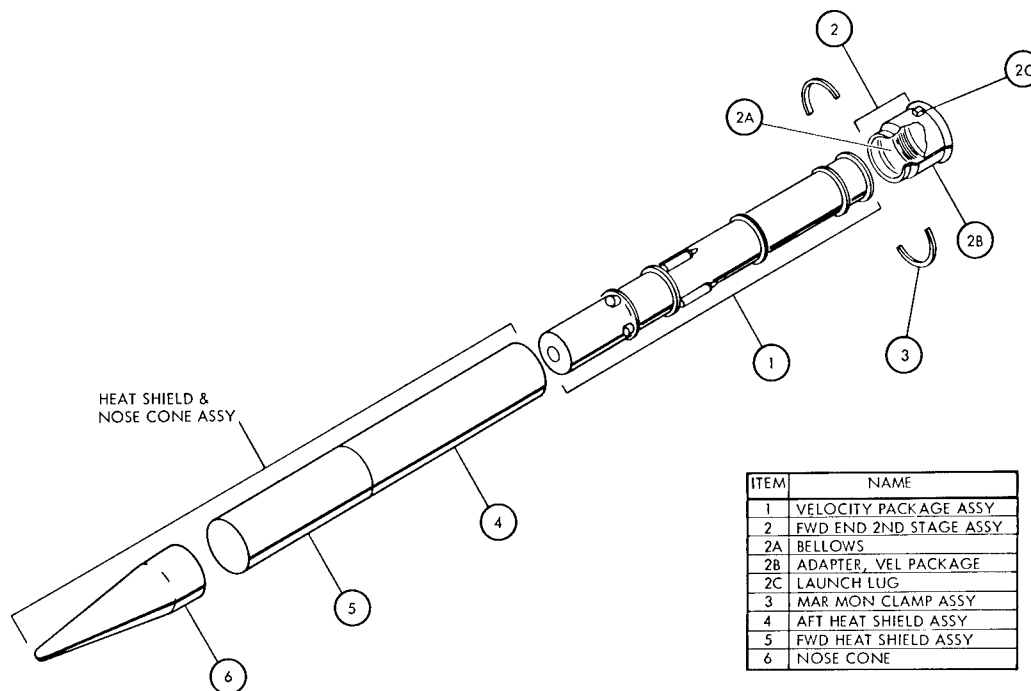
Fig. 1. Configuration of ATHENA vehicle

STAGE 4 TRANSDUCER
@ P/L INTERFACE STA 91.0

STAGE 3 TRANSDUCER
@ A/C STA 230.0

STA 266.5

STA 337.6

STA 375.6

STA 91.0

STA 216.2

STA 391.6

STA 614.1

STA 0

STA 576.2

RECRUIT MOTOR XM 19

YAW AXIS

100"

PITCH AXIS

133"

28" DIA

28" DIA

31" DIA

8" DIA

ROLL AXIS

FOURTH STAGE MOTOR BE-3A4

VELOCITY PACKAGE

4TH STAGE C-BAND - BEACON

3RD STAGE MOTOR

2ND STAGE MOTOR

CASTOR MOTOR XM 33-E8

2ND STAGE C-BAND - BEACON

DESTRUCT

PAYLOAD ENVELOPE 25" DIA BASE X 72" LONG CONE

4TH STAGE TLM PACKAGE

GUIDANCE PACKAGE

COMMAND RECEIVER

TLM PACKAGE

HEAT SHIELD & NOSE CONE ASSY

ITEM	NAME
1	VELOCITY PACKAGE ASSY
2	FWD END 2ND STAGE ASSY
2A	BELLOWS
2B	ADAPTER, VEL PACKAGE
2C	LAUNCH LUG
3	MAR MON CLAMP ASSY
4	AFT HEAT SHIELD ASSY
5	FWD HEAT SHIELD ASSY
6	NOSE CONE

Fig. 2. Velocity package assembly

354

TABLE 1
Propulsion Systems Employed on ATHENA Flights

Vehicle No.	Recruit Motor	1st Stage Motor	2nd Stage Motor	3rd Stage Motor	4th Stage Motor
A-002	XM-19	XM33-E8	X259-A4	None	None
A-003	XM-19	XM33-E8	X259-A4	None	None
C-001	XM-19	XM33-E8	TX261-4	30KS8000	BE3-A4
C-002	XM-19	XM33-E8	TX261-4	30KS8000	BE3-A4
C-003	XM-19	XM33-E8	TX261-4	30KS8000	BE3-A4
C-004	XM-19	XM33-E8	TX261-4	30KS8000	BE3-A4
D-001	XM-19	XM33-E8	X259-A4	30KS8000	BE3-A4
D-002	XM-19	XM33-E8	X259-A4	23KS11000	BE3-A4
D-003	XM-19	XM33-E8	X259-A4	23KS11000	BE3-A4
B-001	XM-19	XM33-E8	X259-A4	23KS11000	None
B-003	XM-19	XM33-E8s	X259-A4	23KS11000	None

TABLE 2
Vacuum Thrust and Propellant Flow Rate of ATHENA Motors

Motor	Maximum Ignition Thrust (lb)	Maximum Propellant Flow Rate at Ignition (lb/sec)	Nominal Thrust (lb)	Nominal Propellant Flow Rate (lb/sec)	Nozzle Exit Diameter (in.)
Recruit (XM-19) Thiokol	41938 at 0.5 sec	185.73	38,000	168	11.4
Castor (XM33-E8) Thiokol	75055 at 0.16 sec	297.07	60,000	238	23.75
2nd Stage (X259-A4) Naval Propellant Plant	24153 at 0.16 sec	86.61	23,000	83	28.244
2nd Stage (TX261-4) Thiokol	66403 at 2.50 sec	248.42	62,000	232	23.266
3rd Stage (30KS8000) Aerojet	No ignition maximum	No ignition maximum	10,000	36	16.68
3rd Stage (23KS11000) Aerojet	No ignition maximum	No ignition maximum	11,000	40	16.68
4th Stage (BE3-A4) Hercules	6002 at 2.50 sec	21.59	5,600	20	12.2

a double segmented Marman clamp. On exit from the atmosphere, separation of the velocity package from the second stage is accomplished by the following sequential events:

1. The exit heat shield nose cone fairing is separated by severing the structure around its periphery with a shaped charge explosive and ejecting the fairing by preloaded springs; and

2. An air spring bellows assembly is activated, ejecting the velocity package from the cylindrical heat shield and the second stage (Fig. 2).

Separation of the third from the fourth stage is accomplished with a Marman clamp similar to Stage 1 separation. The method used to separate the reentry vehicle from the fourth stage varies with the type of payload being carried, but is generally a pyrotechnic activated device. The timed sequence of separation and other events for a nominal flight are given in Table 3.

TABLE 3
Timed Events for Typical ATHENA Flight

Event	Function	Time (sec, ref. to lift-off)
1	1st stage ignition	-0.05
2	Recruit motors squib initiate	0.01
3	Spin motors squib initiate	0.48
4	Vehicle clears launcher rail	0.48
5	Spin motors — Ignition	0.62
6	Spin motor burnout	1.50
7	Recruit motors burnout	2.30
8	1st stage burnout	40.22
9	1st stage separation	46.00
10	2nd stage ignition	53.22
11	2nd stage burnout	66.27
12	Nose fairing release — shaped charge initiate	96.23
13	Velocity package release	106.49

TABLE 3—Continued

Event	Function	Time (sec, ref. to lift-off)
14	3rd stage motor ignition	234.50
15	3rd stage burnout	268.51
16	3rd/4th stage separation	269.51
17	4th stage ignition	273.61
18	4th stage burnout	283.11
19	Payload release	285.71

DISCUSSION OF DATA

Vibration

The vibration data presented were measured during 11 ATHENA flights. Two sets of triaxial piezoelectric accelerometers were oriented along the major missile axes at two locations, one set on stage 4 and one set on stage 3. Table 4 gives specific locations along with pertinent instrumentation information. All data were continuously transmitted on FM/FM telemetry. All vehicles carried the third stage measurements, whereas only six of the vehicles carried the fourth stage measurements.

TABLE 4
Telemetry Calibration Ranges
for Vibration Measurements

Meas. Location	Meas. No.	Axis	Peak g	T/M Channel
Payload interface Plate, stage 4 at	B463V	Roll	±48	18
missile sta. 91	B464V	Pitch	±20	16
	B465V	Yaw	±20	15
Missile attitude	A323V	Yaw	±10	15
Controller base	A324V	Roll	±10	16
Plate, stage 3 at				
missile sta. 230	A325V	Pitch	±10	17

The most significant structural characteristic of the ATHENA vehicle to consider when evaluating the measured data is the lack of a shear path between the exit heat shield and the velocity package. The guide rails take only bearing loads and have contact surfaces which

are faced with 1/4 in. of Teflon on the velocity package and 1/4 in. of brass on the heat shield. As a result, it was anticipated that the acoustically and aerodynamically induced vibrations on the velocity package would be minimized. This was proven to be the case because the only vibration of significance, with the exception of ignition and staging transients, occurs at launch. This is unlike measurements on other boosters which also exhibit significant vibrations during the transonic and maximum dynamic pressure periods. As is readily discernible by review of Figs. 3 and 4, the vibration magnitude does not significantly increase with a large increase in dynamic pressure. The data for the two measurement locations are presented in Figs. 5 and 6. The data represent an envelope of the measured levels for all flights. The acceleration spectral density analyses were performed on launch data samples of 0.4 to 1.0 sec duration with an effective analysis filter bandwidth of 25 cycles.

The heat shield weights and dimensions are provided in Table 5 for utilization of the data for the prediction of vibration levels on other rocket vehicles.

TABLE 5
Heat Shield Properties

Heat Shield	Materiel	Weight (lb)	Diameter (in.)	Length (in.)
Forward section	Fiberglass	79.9	28	60.5
Aft section	Aluminum	160.7	28	102
Total		240.6		162.5
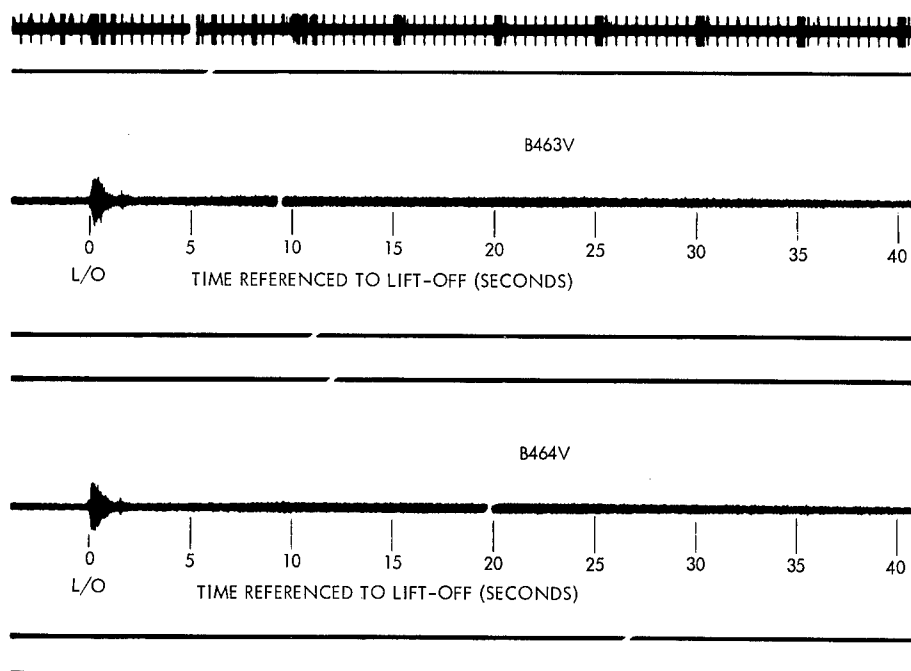
Fig. 3. Vibration amplitude vs time
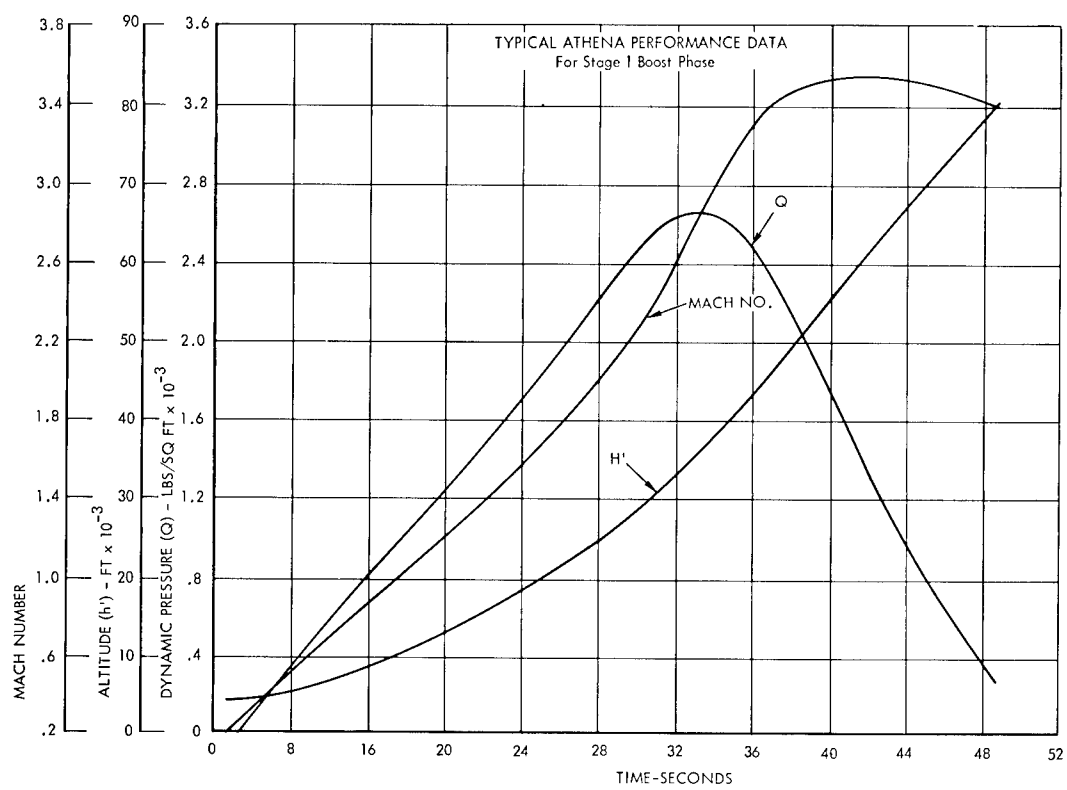
Fig. 4. ATHENA performance data
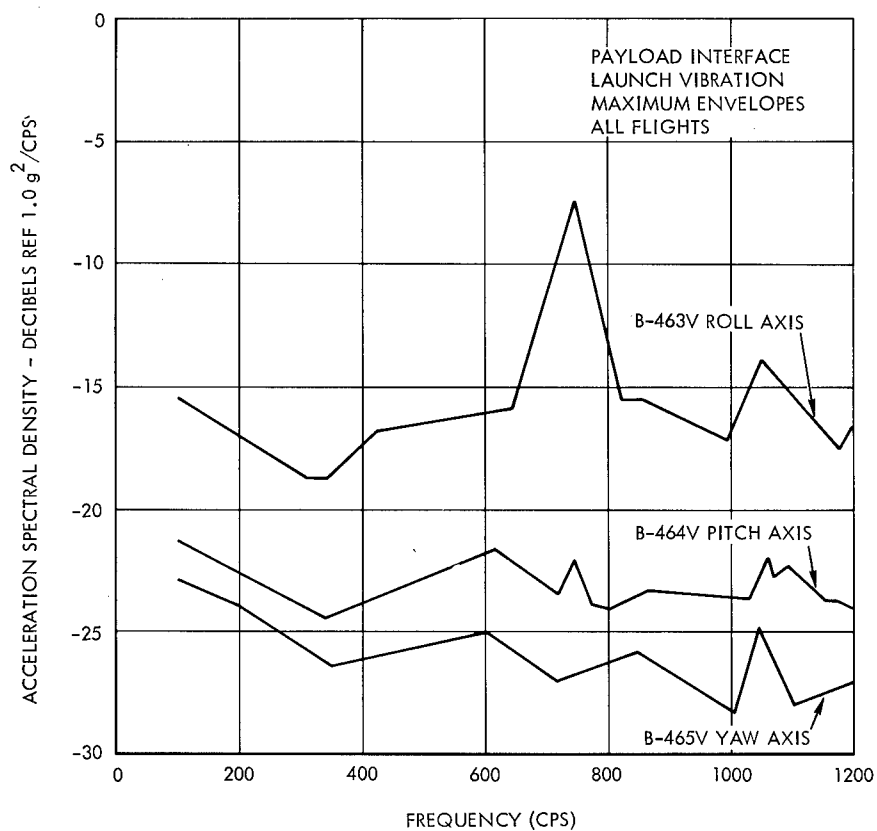
Fig. 5. Acceleration spectral density, Stage 4
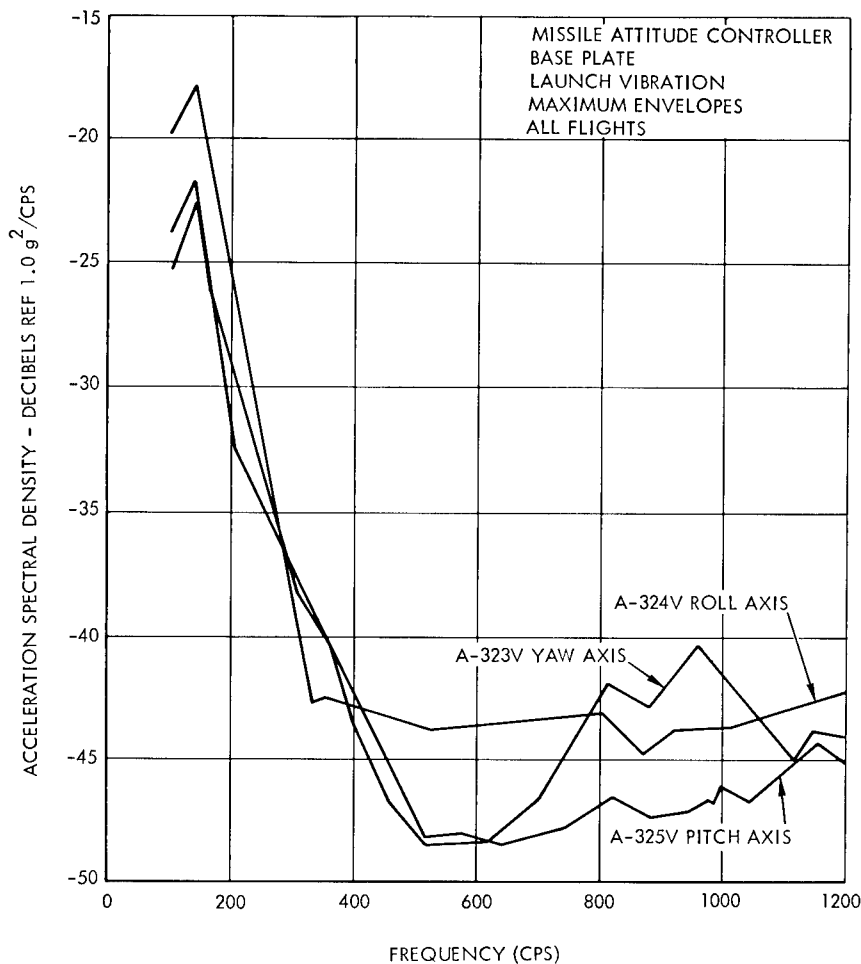
Fig. 6. Acceleration spectral density, Stage 3

Shock

The transients associated with ignition and separation events were analyzed in terms of response spectra. A typical transient acceleration time history is shown in Fig. 7. Transients were noted at Stage 2 ignition, exit heat shield nose cone separation, velocity package ejection, third stage separation, Stage 3 ignition, and Stage 4 ignition. Reentry vehicle separation data were not measured during flight; however, some data were obtained during a ground test.

A channel 18 IRIG filter was used in playback of all flight data to obtain a maximum frequency response of 1050 cps. The response spectra were computed at 10-cps intervals using a damping ratio of 5 percent. The envelopes of the response spectra for each measurement are presented in Figs. 8 through 13.

The shock environment associated with ignition of the 23KS11000 motor as compared to the 30KS8000 motor was so diverse that separate spectral envelopes of the roll axis data were included for both motors. These data are presented in Fig. 14.

The shock magnitude associated with a Primacord reentry vehicle separation device was evaluated during a full-scale ground test since these shocks could not be measured in flight because of the limited telemetry bandwidth and dynamic range. The ground instrumentation had a frequency response of 5000 cps and the accelerometers were calibrated for 2000 g. Measurements were located adjacent to component mountings on both the reentry vehicle and on the fourth stage. Table 6 gives the measurements with their approximate axial distance from the pyrotechnic charge.

360

Fig. 7. Typical third stage ignition acceleration transient

MEAS B-464V

PAYLOAD INTERFACE PITCH AXIS

+20 g's

0 g's

-20 g's

+48 g's

65 MILLISECONDS

MEAS B-463V

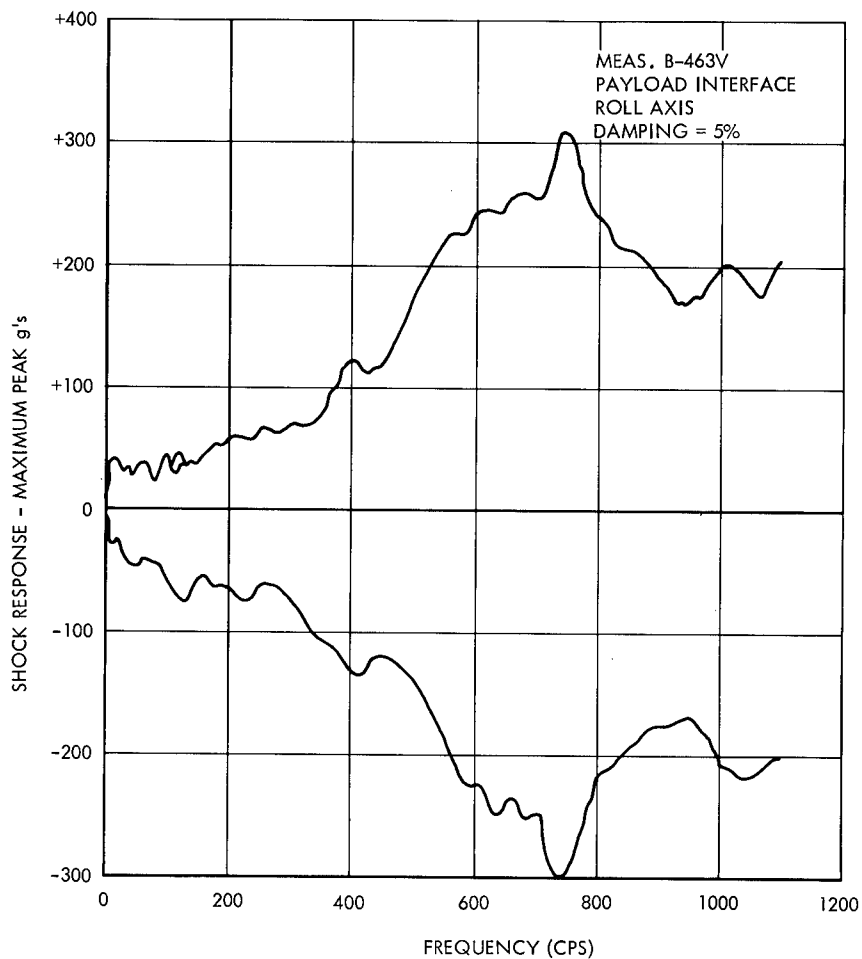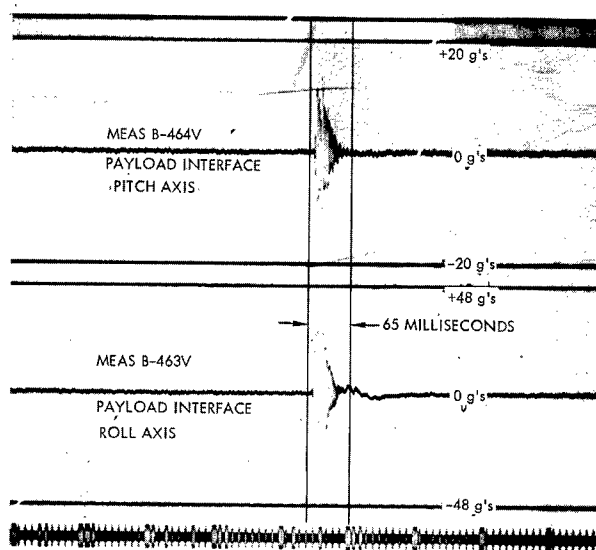PAYLOAD INTERFACE ROLL AXIS

0 g's

-48 g's

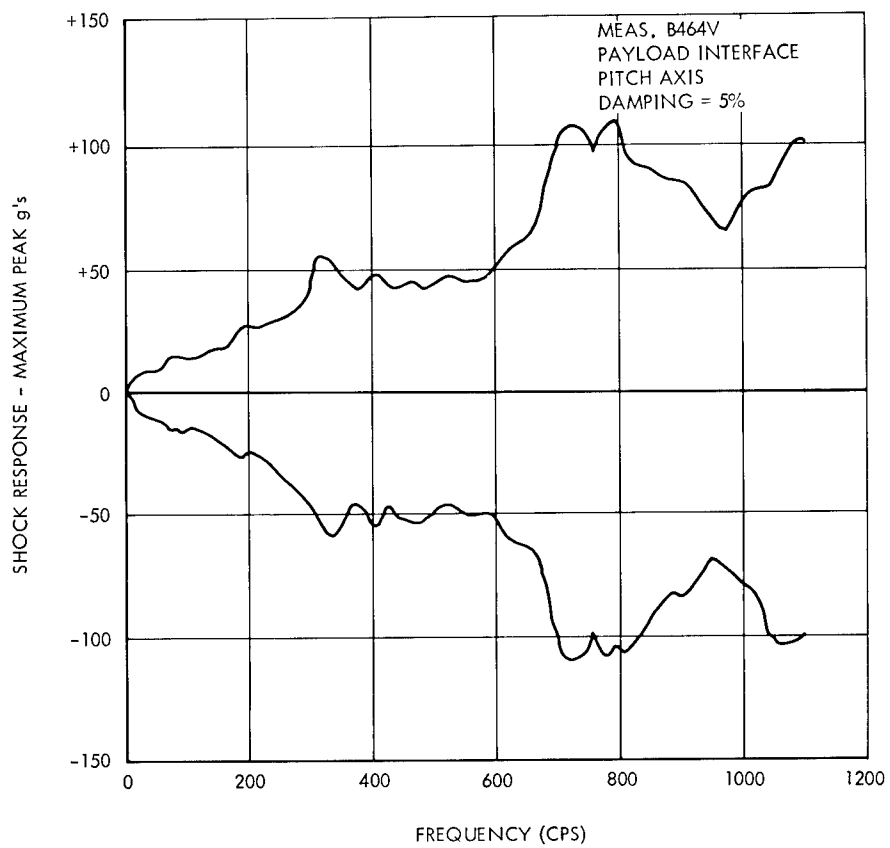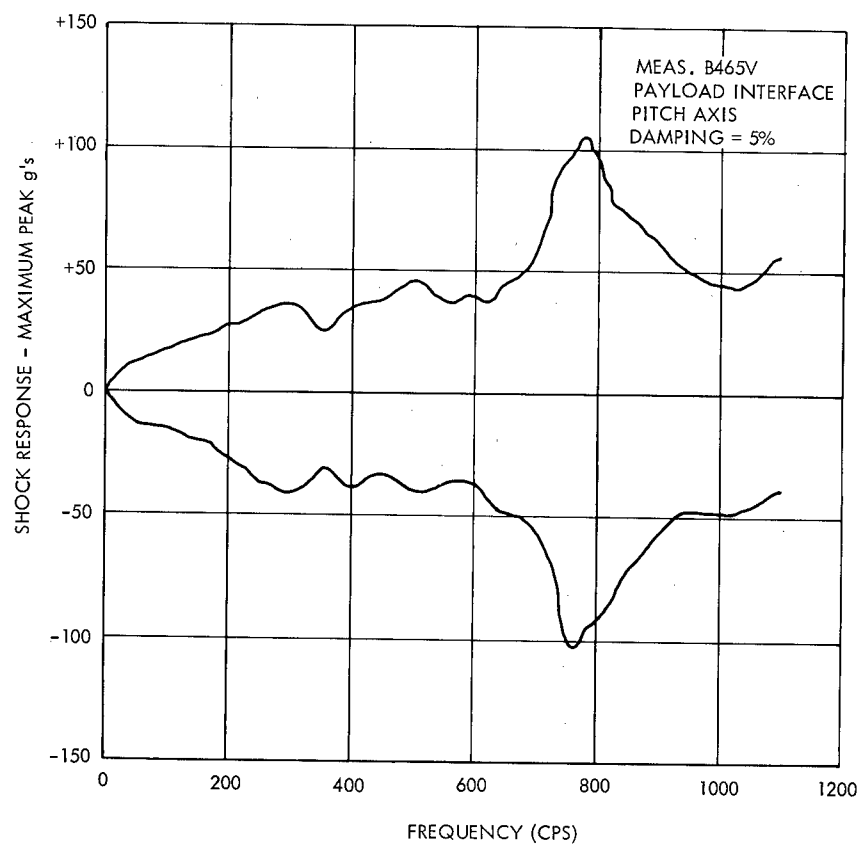Fig. 8. Shock response spectrum, maximum envelope B-463V

Fig. 9. Shock response spectrum, maximum envelope B-464V

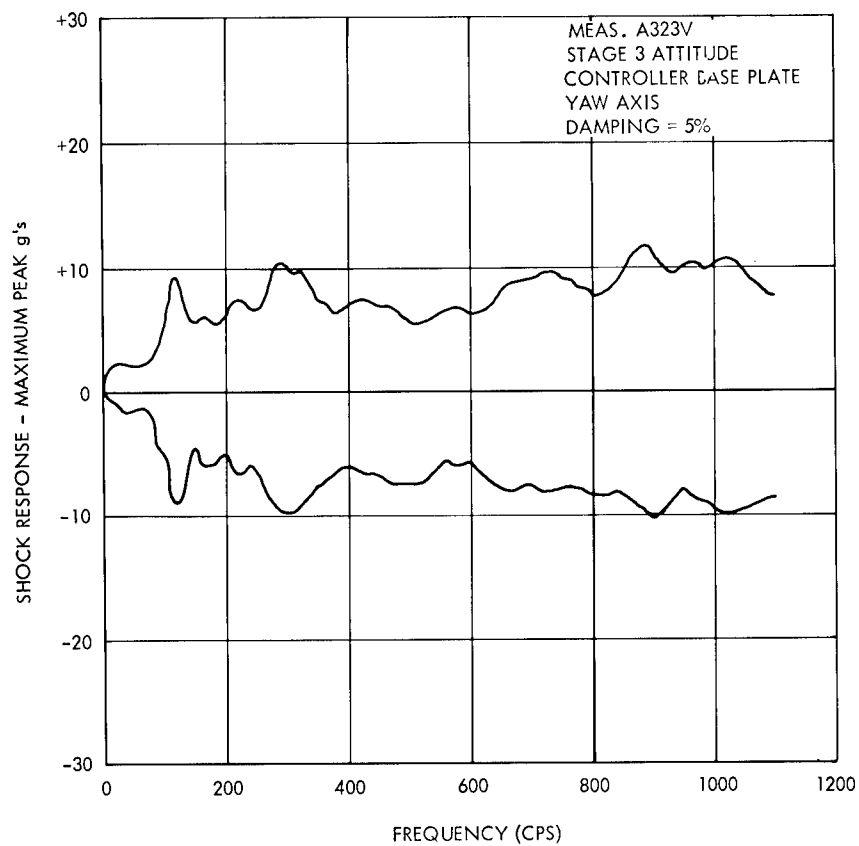362

Fig. 10. Shock response spectrum, maximum envelope B-465V
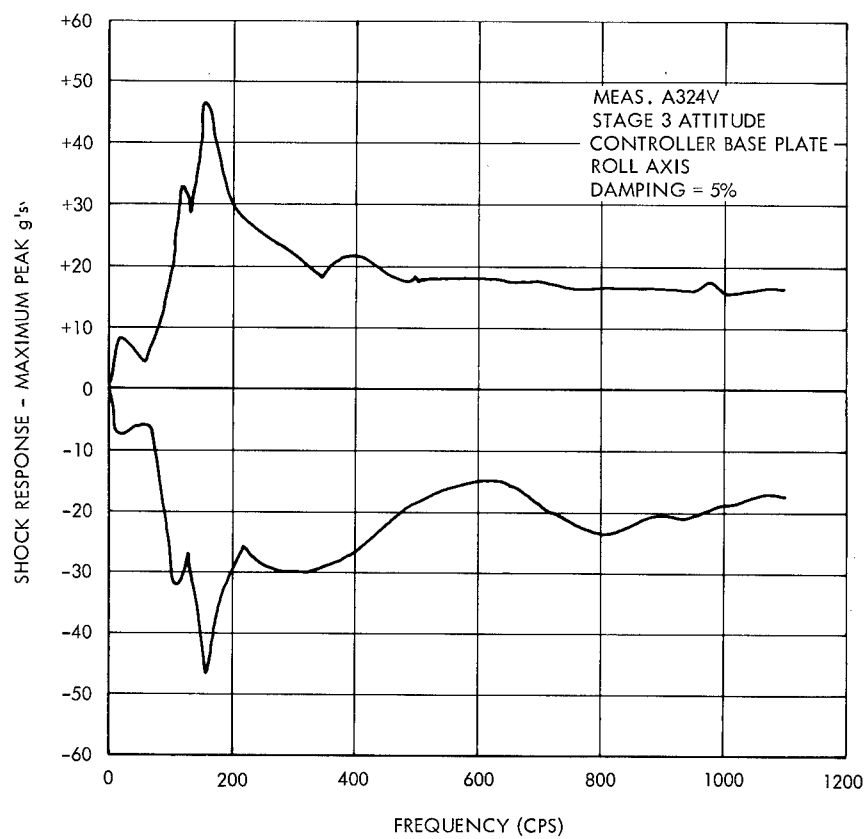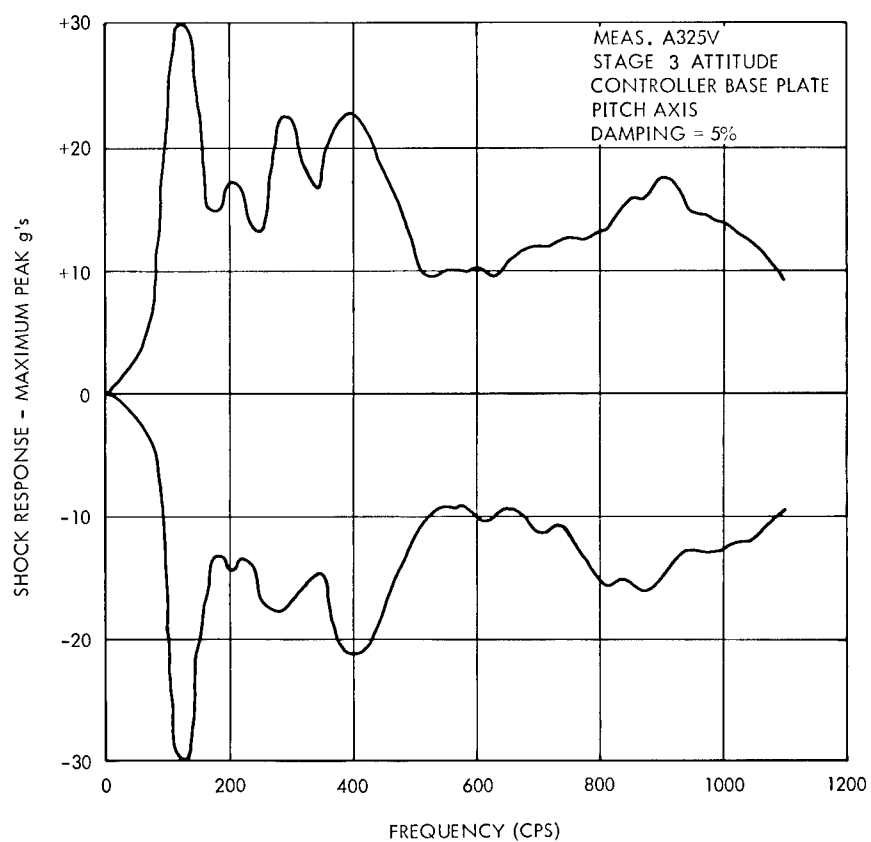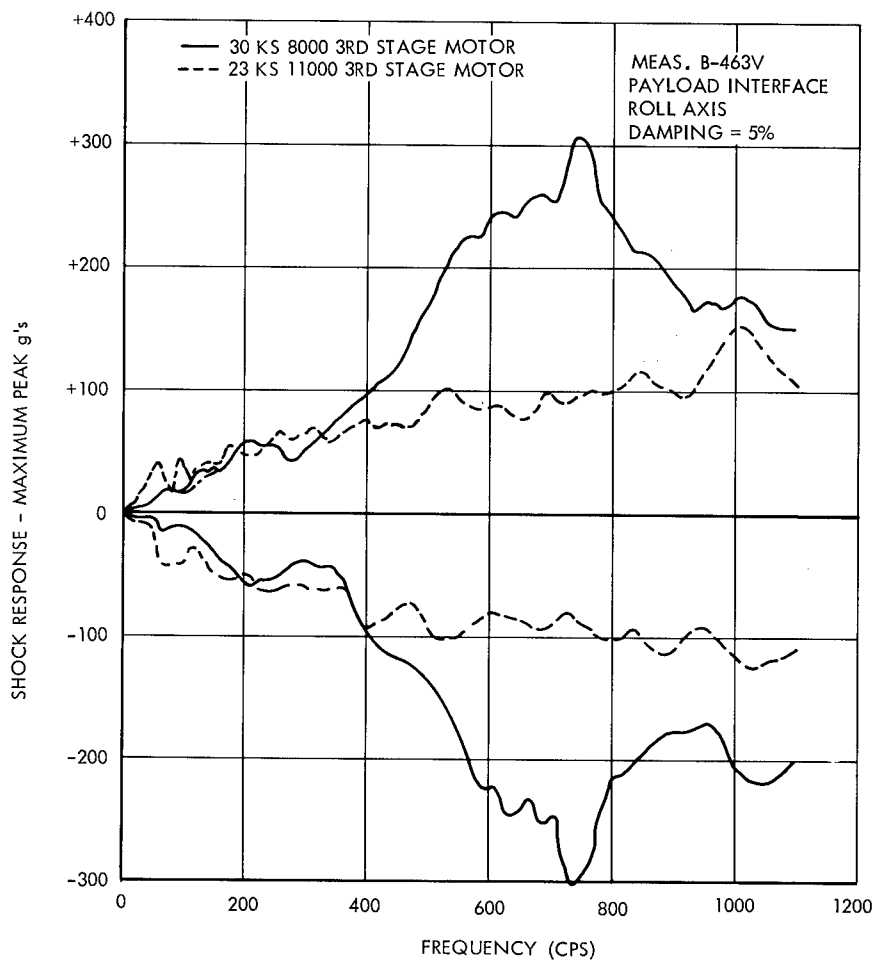
Fig. 11. Shock response spectrum, maximum envelope A-323V

Fig. 12. Shock response spectrum, maximum envelope A-324V

Fig. 13. Shock response spectrum, maximum envelope A-325V

Fig. 14. Shock response spectra, third stage ignition

TABLE 6
Ground Separation Test Shock Measurements

Meas. Location	Meas. No.	Axis	Approx. Axial Distance from Shock Source (in.)
Reentry body	V-1 V-2	Transverse Roll	10
4th stage airframe	V-3 V-8 V-9	Roll Transverse, 135° Transverse, 225°	25
4th stage internal structure on T/M tray	V-4 V-5 V-6	Transverse, 225° Transverse, 135° Roll	20

Response spectra for each of the three locations given in Table 6 are presented in Figs. 15 through 17. The spectra are typical for shocks induced by pyrotechnic separation mechanisms in that the acceleration is a maximum in the high frequencies. In general, these shocks are not damaging to structure but can cause certain component malfunctions such as relay contact chatter.
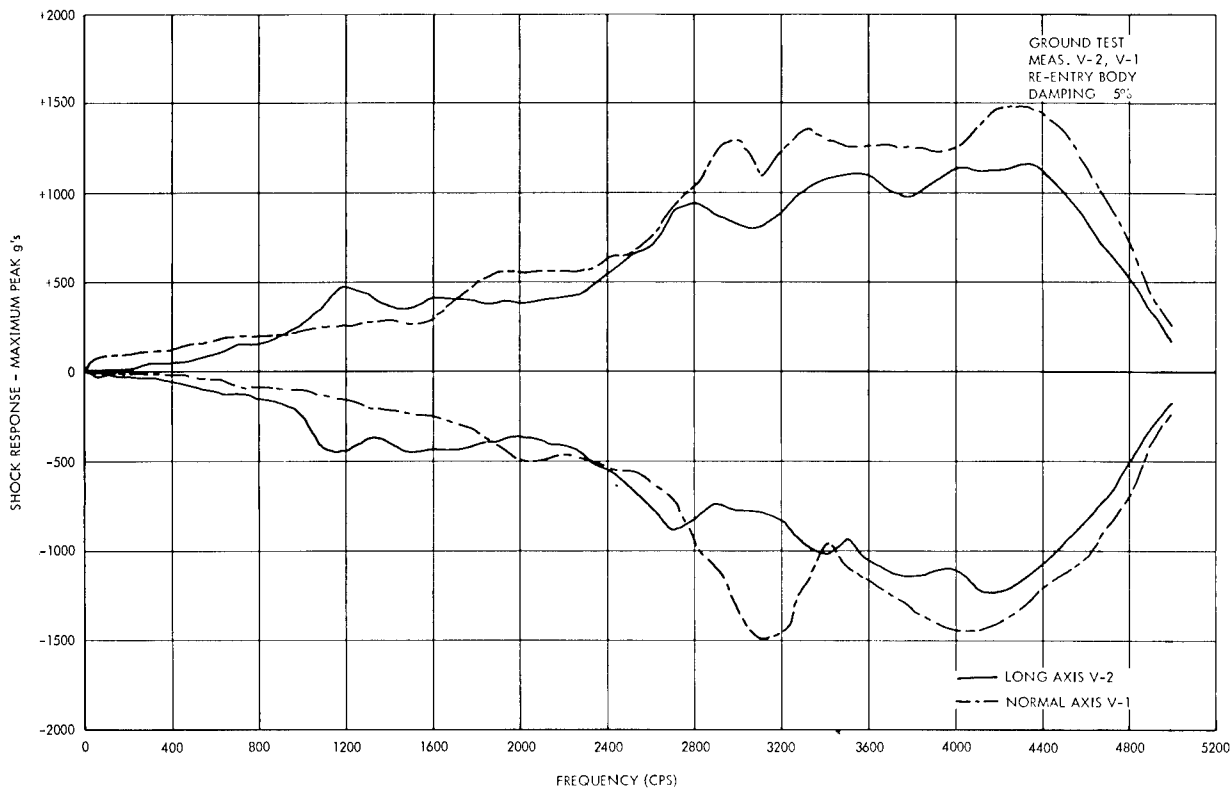

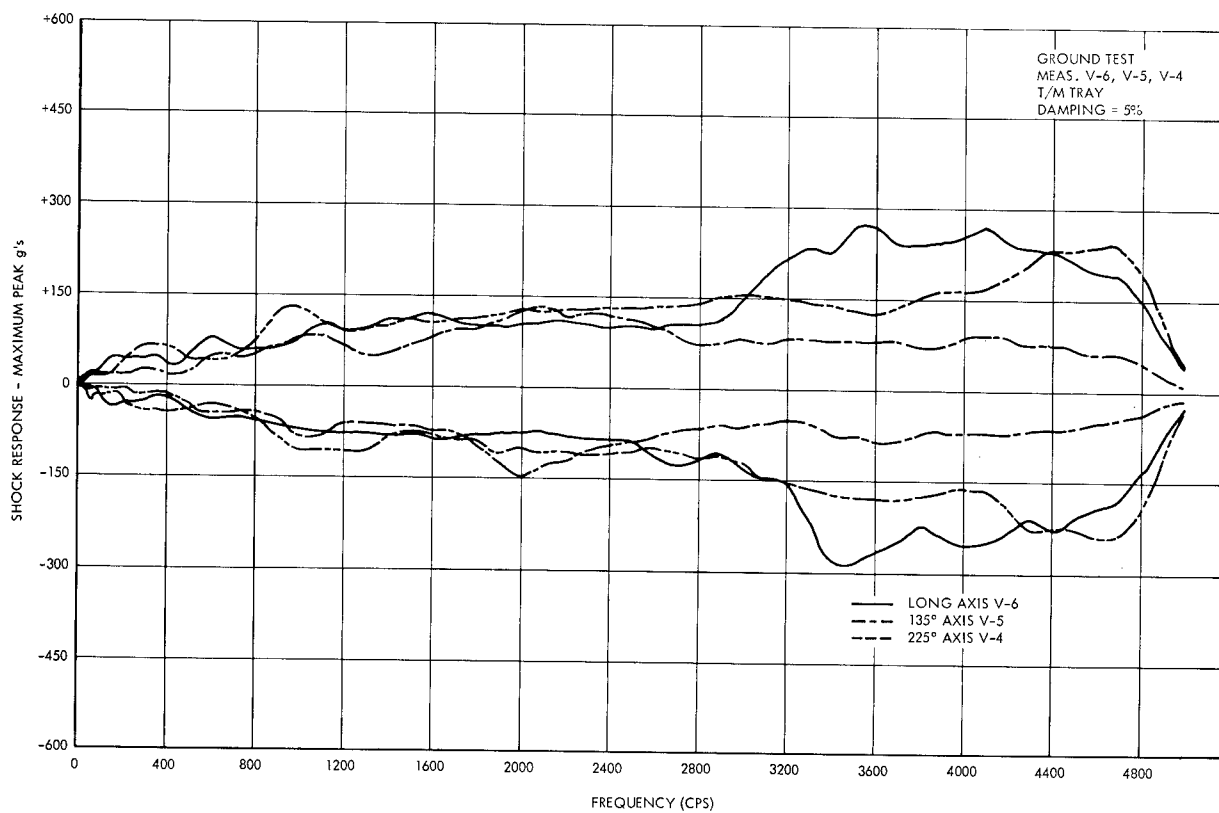Fig. 15. Shock response spectra, ground separation test, reentry vehicle

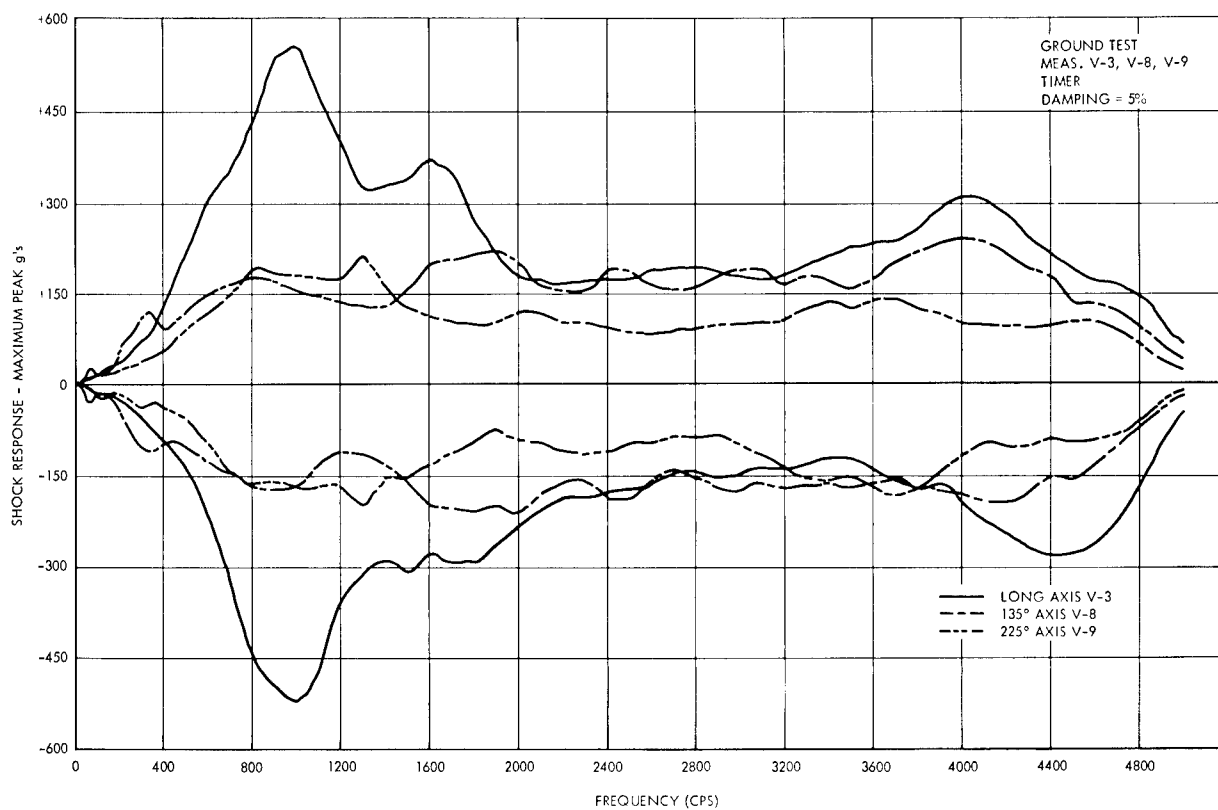Fig. 16. Shock response spectra, ground separation test, telemetry tray

Fig. 17. Shock response spectra, ground separation test, timer

CONCLUSIONS

1. The ATHENA vibration environment is only significant at launch. An envelope of the acceleration spectral densities has a peak value of 0.178 g^2/cps.

2. The maximum powered flight shock transients (measured on the velocity package) occur at third stage ignition. This environment is more severe with the 30KS8000 motor as compared to the 23KS11000. The maximum response acceleration levels associated with these motors are, for 30KS8000, 310 g at 750 cps, and for 23KS11000, 153 g at 1000 cps.

DISCUSSION

Mr. Davis (Fairchild-Hiller): You chose to present some of the data that you analyzed in terms of shock spectra, yet when you analyzed the initial launch vibration you chose to present it as spectral density. It appeared that the launch vibration was really a shock transient; therefore, would it not be more consistent to present it also as a shock spectrum?

Mr. Moening: We did not feel that the launch vibration was best represented as a shock transient. The time scale on the slide that was presented was condensed so that it may have looked as if we had essentially a transient similar to stage ignition. However, when we examined an expanded time scale of the launch vibration, we obtained a 1-sec sample of stationary data. For the upper stage separations, the transient might have existed for not much longer than 35 ms.

Mr. Mahaffey (LTV Astronautics): Did you measure any significant structurally trans-mitted vibration which could be attributed to rocket motor burning?

Mr. Moening: No, not at the measurement locations available to us at the forward end. These measurements were fairly close to the third and fourth stage motors during the upper stage flight, and vibration levels were insignifi-cant. They are down on the noise floor. Inci-dentally, I do not know whether it was shown on the slide, but the calibration range for the roll axis was 48 g and for the pitch and yaw axes was 20 g. I feel this is low enough to measure any vibrations of significance.

*　　*　　*

DISTRIBUTION

Aberdeen Proving Ground, Md.
    Att: Ballistic Research Lab.   1
    Att: Development & Proof Services   1
    Att: Physical Test Lab.   1

Air Defense Command, Ent AFB
    Att: Deputy for Civil Engineering   1
    Att: ADIRP   1

Air Force Academy, Colo.
    Att: Dept. Mech. DFME   1
        (UNCLASSIFIED)

Air Force Packaging Evaluation Agency,
Brookley AFB
    Att: MOSPR   1
    Att: MONE   1

Air Proving Ground Center, Eglin AFB
    Att: PGTRI, Technical Library   1

Air Force Headquarters, DC
    Att: Operations Analysis Off.,
        Off. Vice Chief of Staff, Library   2
    Att: AFDRD-GW   1

Air Force Logistics Command, W-PAFB
    Att: Mr. G. P. Civille, MCTEP   1

Air Force Missile Development Center,
Holloman AFB
    Att: RRRT/Miss R. Porter   1
    Att: MDS/Dr. M. G. Jaenke   1
    Att: MDLR/Mr. H. J. Dunbar   1
    Att: MDSGS/Mr. G. R. Moser   1
    Att: MDSTE/Mr. J. M. Mapes   1

Air Force Missile Test Center, Patrick AFB
    Att: MT LLL-3 (Classified Material)   2
    Att: MU-135, Technical Library
        (UNCLASSIFIED)   1

Air Force Office of Scientific Research, DC
    Att: Library (UNCLASSIFIED)   1

Air Force Regional Civil Engineer
    Att: North Atlantic Region,
        AFRCE-NA-A   1
    Att: South Atlantic Region,
        AFRCE-SA-E   1

Air Force Rocket Propulsion Lab., Calif.
    Att: Mr. A. J. Davies (RPFDE)   1
    Att: Mr. R. A. Silver   1

Air Force Systems Command, Andrews AFB
    Att: Technical Library   2

Air Force Weapons Laboratory,
Kirtland AFB
    Att: Development Test Division   1
    Att: Dr. W. E. Fisher, WLRS   1
    Att: SWOI 631-276   1

Army Air Defense Center, Ft. Bliss
    Att: Technical Library   1

Army Chemical Center, Maryland
    Att: Library   1

Army Electronics Materiel Agency, Phila.   1

Army Electronics Command, Ft. Monmouth
    Att: AMSEL-RD-ADT   1
    Att: AMSEL-RD-PEE   1
    Att: AMSEL-RD-PRT   1
    Att: AMSEL-RD-G   1
    Att: AMSEL-RD-GTF   1
    Att: Mr. J. J. Oliveri   1

Army Engineer District, New York
    Att: NANGD   1

Army Engineer R&D Laboratories, Ft. Belvoir
    Att: Package Development Branch   1
    Att: Mr. A. Carolla   1
    Att: Director of Research   1
    Att: Chief, Spec. Proj. Branch   4

Army Engineer Waterways Experiment
Station, Vicksburg
    Att: Mr. J. M. Strange   1

Army Materials Research Agency, Watertown
    Att: Dr. Reinier Beeuwkes, Jr.   2

Army Materiel Command, DC
    Att: AMCRD-RS-CM   1

Army Materiel Command, Redstone Arsenal
    Att: Technical Library   4

Army Missile Command, Redstone Arsenal
    Att: AMSMI-RB   1
    Att: AMSMI-RG   1
    Att: AMSMI-RL   1
    Att: AMSMI-RS   1
    Att: AMSMI-RT   1
    Att: AMSMI-RTR, Mr. J. M. Taylor   1
    Att: AMSMI-RSM, Mr. E. J. Wheelahan   1

Army Mobility Command, Centerline
    Att: Mr. Otto Renius   1

Army Natick Laboratories, Mass.
    Att: Technical Library   2
    Att: Mr. W. B. Brierly   1
    Att: Chief, Container Div.   1

Army, Office Chief of Engineers, DC
    Att: ENGMC-EM   2

Army, Office Chief of Research &
Development, DC
    Att: Scientific & Technical
            Information Div.   1

Army, Office Chief of Transportation, DC
    Att: Director of Transportation
            Engineering   1

Army Ordnance Ammunition Command, Joliet
    Att: ORDLY-T   1
    Att: NNSC/A   1

Army Staff Group, DC
    Att: Mr. J. Valler (UNCLASSIFIED)   1

Army Tank-Automotive Center, Warren
    Att: SMOTA-RRS, Tech. Library   1
    Att: SMOTA-RCE.3,
          Mr. D. J. Hackenbruch   1
    Att: SMOTA-RRC   1

Army Transportation Engineering Agency,
Ft. Eustis
    Att: Library   1
    Att: Mr. L. J. Pursifull   1

Army Transportation Research Command,
Ft. Eustis
    Att: Dr. R. L. Echols,
          Physical Sci. Res. Group   1

Arnold Engineering Development Center,
Arnold AFS
    Att: AEOIM   1

Atomic Energy Commission, Oak Ridge
    Att: Office of Technical Information   6

Atomic Energy Commission, DC
    Att: Library   1

Aviation Supply Office, Philadelphia
    Att: Code TEP-1   1

Ballistic Systems Division, USAF, Norton AFB
    Att: Technical Data Division   3

Boston Naval Shipyard, Mass.
    Att: Library   1

Bureau of Medicine & Surgery, USN, DC
    Att: Research Division   1

Bureau of Naval Weapons, USN, DC
    Att: DLI-3   2
    Att: FWAA, Mr. C. H. Barr   1
    Att: RREN-5   5
    Att: RRMA   1
    Att: RAAE-2   1
    Att: RM-3   2
    Att: RM-2   1
    Att: RSSH   2
    Att: FWAE   1
    Att: RREN-8   1

Bureau of Naval Weapons Rep., E. Hartford   2

Bureau of Naval Weapons Rep., Pomona
    Att: Chief Engineer   1
    Att: Metrology Dept. Code 60   1

Bureau of Naval Weapons Rep., Sunnyvale   1

Bureau of Ships, USN, DC
    Att: Code 423   20

Bureau of Supplies & Accounts, USN, DC
    Att: Library   1

Bureau of Yards & Docks, USN, DC
    Att: Code D-440   1
    Att: Code D-220   1
    Att: Code D-220 (UNCLASSIFIED)   6

Coast Guard Headquarters, DC   1

David Taylor Model Basin, UERD, Portsmouth
    Att: Code 281A   1

David Taylor Model Basin, DC
    Att: Library   3
    Att: Mr. Harry Rich   1
    Att: Code 591L, Mr. J. A. Luistro   1
    Att: Contract Res. Administrator   1

Defense Atomic Support Agency, DC
    Att: Technical Director   1
    Att: Weapons Development Division   1
    Att: Mr. John G. Lewis   1

Defense Atomic Support Agency, Livermore
    Att: Administrative Officer   1

Defense Documentation Center, Va.   100

Defense Intelligence Agency, Va.
    Att: DIAAP-1K2   1

District Public Works Office,
14th Naval District   1

Electronic Systems Division,
L. G. Hanscom Field
    Att: ESTI   1

Electronics Supply Office, USN, Great Lakes   1

Erie Army Depot, Ohio
    Att: Chief, Materiel Testing Div.   1

Federal Aviation Agency, DC
    Att: Emergency Readiness Div.,
          Off. Plans & Requirements   2
    Att: Chief, Tech. Processing Br.,
          Library Serv. Div.
            (UNCLASSIFIED)   1

Forest Products Laboratory,
Dept. of Agriculture, Madison
    Att: Mr. Robert Stern (UNCLASSIFIED)   1

Frankford Arsenal, Philadelphia
    Att: Library Branch, CC 0270/40   1
    Att: Mr. David Askin, CC 1730/230   1

Harry Diamond Laboratories, DC	
Att: Chief, Lab. 700	1
Att: Chief, Branch 850	1
Att: Technical Information Officer	2
Inspector of Naval Material, San Francisco	1
Library of Congress, DC (UNCLASSIFIED)	2
Long Beach Naval Shipyard, Calif.	
Att: Code 240	1
Mare Island Naval Shipyard, Vallejo	
Att: Library	1
Marine Corps Equipment Board, Quantico	1
Marine Corps Headquarters, DC	
Att: Research & Development Section	1
Att: Code AO4E	1
Maxwell AFB, Alabama	
Att: Air University Library	1
NASA, Ames Research Center, Moffett Field	
Att: Tech. Management Office N203-5	1
NASA, Flight Research Center, Edwards	
Att: Library	1
NASA, Goddard Space Flight Center, Greenbelt	
Att: Code 320, Mr. J. C. New	1
Att: Code 623.3, Mr. G. Hinshelwood	1
Att: Code 321.2, Mr. K. M. Carr	1
Att: Code 321.2, Mr. F. Lindner	1
Att: Dr. Elias Klein	1
Att: Mr. W. R. Forlifer	1
Att: Library	1
NASA, Langley Research Center, Hampton	
Att: Library	2
Att: Mr. S. A. Clevenson	1
Att: Mr. D. J. Martin	1
NASA, Lewis Research Center, Cleveland	
Att: Library	2
NASA, Manned Spacecraft Center, Houston	
Att: Technical Library	1
NASA, Marshall Space Flight Center, Huntsville	
Att: Mr. J. H. Farrow, M-P&VE-ST	1
Att: Mr. R. M. Hunt, M-P&VE-S	1
Att: Mr. R. E. Jewell, R-P&VE-SVR	1
Att: AMSMI-RBLD	1
NASA, Michoud Operations, New Orleans	
Att: Mr. H. L. Williams, QR (UNCLASSIFIED)	1
NASA, Scientific & Technical Info. Facility, Bethesda	
Att: NASA Representative	1
NASA, Headquarters, DC	
Att: Mr. D. Michel, RV-2	1

National Bureau of Standards, DC	
Att: Mr. B. L. Wilson	1
Att: Mr. S. Edelman, Mech. Div.	1
National Security Agency, DC	
Att: Engineering	1
Naval Air Development Center, Johnsville	
Att: Mr. E. R. Mullen	1
Att: Aeronautical Instruments Lab.	1
Att: NADC Library	2
Naval Air Engineering Center, Philadelphia	
Att: Library	1
Naval Air Test Center, Patuxent River	
Att: Electronics Test Div.	1
Att: VTOL/STOL Branch	1
Att: Instrumentation Br., Flight Test Div.	1
Naval Ammunition Depot, Crane	
Att: Code 3540	1
Att: Code 3400	1
Naval Ammunition Depot, Portsmouth	
Att: Mr. Jerome Smith, Code QALE	1
Naval Ammunition Depot, Red Bank	
Att: Chief Engineer	1
Naval Ammunition Depot (Oahu)	
Att: Weapons Technical Library	1
Naval Applied Science Laboratory, Brooklyn	
Att: Library	3
Naval Attache, Navy No. 100, NY	
Att: Logistics Division	1
Naval Avionics Facility, Indianapolis	
Att: MAL Library	1
Naval Civil Engineering Lab., Pt. Hueneme	
Att: Library	2
Naval Construction Battalion Center, Pt. Hueneme	
Att: Civil Engineer Corps Officers	1
Naval Medical Field Research Lab., Camp Lejeune	1
Naval Mine Engineering Facility, Yorktown	
Att: Library	1
Naval Missile Center, Pt. Mugu	
Att: Library, N-03022	1
Att: Env. Div., N314	2
Naval Operations, Office of Chief, DC	
Att: Op 31	1
Att: Op 34	1
Att: Op 75	1
Att: Op 07T6, Mr. T. Soo-Hoo	1
Att: Op 725	1

Naval Ordnance Laboratory, Corona
    Att: Code 234, Technical Library   1
    Att: Code 56, Sys. Eval. Division   1

Naval Ordnance Laboratory, Silver Spring
    Att: Technical Director   1
    Att: Library   3
    Att: Environmental Simulation Div.   6
    Att: Mr. George Stathopoulos   1

Naval Ordnance Plant, Forest Park
    Att: Mr. R. E. Seely, Div. 5600   1

Naval Ordnance Test Station, China Lake
    Att: Technical Library   1
    Att: Code 3023   1
    Att: Code 3073   1
    Att: Code 4062   2
    Att: Code 4533   1
    Att: Code 5516   1

Naval Ordnance Test Station, Pasadena
    Att: P8087   3
    Att: P8092   1
    Att: P8073   1
    Att: P80962   1

Naval Postgraduate School, Monterey
    Att: Library   1

Naval Propellant Plant, Indian Head
    Att: Library   1

Naval Radiological Defense Lab.,
San Francisco
    Att: Library   3

Naval Research Laboratory, DC
    Att: Code 6250   1
    Att: Code 6260   1
    Att: Code 6201   1
    Att: Code 6020   2
    Att: Code 2027   2

Naval Security Engineering Facility, DC
    Att: R&D Branch   1

Naval Supply R&D Facility, Bayonne
    Att: Library   1

Naval Torpedo Station, Keyport
    Att: QEL, Technical Library   1

Naval Training Device Center, Pt. Washington
    Att: Technical Library   1

Naval Underwater Ordnance Station, Newport
    Att: Technical Documents Library   1

Naval Underwater Weapons Systems Engrg.
Center, Newport
    Att: Library   1

Naval Weapons Evaluation Facility,
Albuquerque
    Att: Library, Code 42   1

Naval Weapons Laboratory, Dahlgren
    Att: Technical Library   1

Navy Electronics Laboratory, San Diego
    Att: Library   1
    Att: Code 3360   1

Navy Marine Engineering Laboratory,
Annapolis
    Att: Library   1

Navy Mine Defense Laboratory, Panama City
    Att: Library   1

Navy ROTC and Administrative Unit,
Cambridge   1

Navy Underwater Sound Laboratory,
New London
    Att: Technical Director   1
    Att: Mr. J. G. Powell,
        Engrg. & Eval. Div.   1

Navy Underwater Sound Reference Lab.,
Orlando
    Att: Mr. J. M. Taylor, Code 120   1

Norfolk Naval Shipyard, Portsmouth
    Att: Design Superintendent   1

Norton AFB, Off. of Inspector General
    Att: AFIMS-2-A   1

Office Director of Defense R&E, DC
    Att: Technical Library   3
    Att: Mr. Melvin Bell   1
    Att: Mr. W. M. Carlson   1

Office of Naval Material, DC   1

Office of Naval Research, DC
    Att: Code 439   6
    Att: Code 104   1

Office of Naval Research Branch Office,
Boston   1

Office of Naval Research Branch Office,
Pasadena   1

Office of Naval Research Branch Office,
San Francisco   1

Ogden Air Materiel Area, Hill AFB
    Att: Service Engineering Dept.,
        OONEOO   1

Oklahoma City Air Materiel Area, Tinker AFB
    Att: Engineering Division   1

Pearl Harbor Naval Shipyard
    Att: Shipyard Tech. Library, Code 246P   1

Philadelphia Naval Shipyard, Pa.
    Att: Ship Design Section   1
    Att: Naval Boiler & Turbine Lab.   1

Picatinny Arsenal, Dover
    Att: Library SMUPA-VA6   1
    Att: SMUPA-VP7, Mr. R. G. Leonardi   1
    Att: SMUPA-T, Mr. R. J. Klem   1
    Att: SMUPA-D, Mr. E. Newstead   1
    Att: SMUPA-VP3, Mr. A. H. Landrok   1

Portsmouth Naval Shipyard, NH
Att: Code 246 — 1
Att: Mr. E. C. Taylor — 1

Puget Sound Naval Shipyard, Bremerton
Att: Code 275 — 1
Att: Material Laboratories — 1
Att: Code 242, Mr. K. G. Johnson — 1
Att: Code 281 — 1

Randolph AFB, School of Aviation Medicine, Texas — 1

Rome Air Development Center, Griffiss AFB
Att: Mr. Dana Benson, RASSM — 1

6511th Test Group (Parachute), USAF, El Centro
Att: Mr. E. C. Myers, Tech. Director — 1

6570th Aerospace Medical Research Labs., W-PAFB
Att: MRMAE — 1
Att: Mr. R. G. Powell, MRBAE — 1

San Francisco Naval Shipyard, Calif.
Att: Design Division — 1

Savanna Ordnance Depot, Illinois
Att: OASMS — 1

Sheppard AFB, Texas
Att: Dept. of Missile Training — 1

Special Projects Office, USN, DC
Att: SP Technical Library — 1

Strategic Air Command, Offutt AFB
Att: Operations Analysis Office — 1

Supervisor of Shipbuilding, USN, Camden
Att: Code 299 — 2

Tobyhanna Army Depot, Pa.
Att: SMC Packaging and Storage Center — 1

Watervliet Arsenal, New York
Att: ORDBF-RR — 2

White Sands Missile Range, New Mexico
Att: STEWS-AMTED-E — 2

Wright-Patterson AFB, Dayton
Att: AFFDL (FDFE, E. H. Schell) — 1
Att: AFFDL (FDFE, C. W. Gerhardt) — 1
Att: AFFDL (FDD, H. A. Magrath) — 1
Att: AFFDL (FDDS, C. A. Golueke) — 1
Att: AFML (MAMD, J. P. Henderson) — 1
Att: SEG (SEFSD, R. F. Wilkus) — 1

Yuma Proving Ground, Arizona
Att: Library — 1